

# **Numerical modelling and simulation of atmospheric entrained flow gasification of surrogate fuels**

Zur Erlangung des akademischen Grades eines

DOKTORS DER INGENIEURWISSENSCHAFTEN (DR.-ING.)

der KIT-Fakultät für Chemieingenieurwesen und Verfahrenstechnik des  
Karlsruher Instituts für Technologie (KIT)  
genehmigte

DISSERTATION

von

Maximilian Dammann

Tag der mündlichen Prüfung: 02.05.2024

Erstgutachter: Prof. Dr.-Ing. Thomas Kolb

Zweitgutachter: Prof. Dr.-Ing. Roman Weber

Dissertation, KIT, Department of Chemical and Process Engineering

Date of the oral exam: 02 May 2024

Examination chair: Prof. Dr. rer. nat. habil. Sabine Enders

First supervisor: Prof. Dr.-Ing. Thomas Kolb

Second supervisor: Prof. Dr.-Ing. Roman Weber

Examiner: Prof. Dr.-Ing. Dieter Stapf

© Maximilian Dammann, ORCID: 0000-0002-2851-7787, Germany, 2024

This is an open access document distributed under the terms of the CC-BY-NC-ND license (<http://creativecommons.org/licenses/by-nc-nd/4.0/>).

Registered names, trademarks, etc. used in this document, even when not specifically marked as such, are not to be considered as unprotected by law.

DOI: 10.5445/IR/1000172116

Printed in Germany, 2024





# Abstract

Entrained flow gasification is the prevailing gasification technology for the production of tar-free synthesis gas. However, in view of the rapid climate changes, the technology needs to be adapted to biogenic and anthropogenic feedstocks. Therefore, new validated mathematical models are required for design, optimisation and scale-up.

This thesis focusses on the numerical modelling and simulation of atmospheric entrained flow gasification of surrogate fuels to accelerate the model development for high-pressure entrained flow gasification of biomass. Firstly, RANS based models were developed to describe the gasification of ethylene glycol and of mixtures of ethylene glycol and wood char. Specifically, improved inlet conditions and injection properties and new wood char devolatilisation kinetics were derived using data from laboratory-scale experiments. Subsequently, numerical simulations of gasification experiments with ethylene glycol and with mixtures of ethylene glycol and wood char were performed using improved implementations and meshes to close the elemental and energy balances. The predictions were compared with experimental flame shape observations, experimental axial droplet velocities and experimental radial profiles of gas temperature and dry gas species concentrations. Furthermore, sensitivity analyses were carried out to investigate the impact of the homogeneous reaction kinetics, the vapourisation model, the turbulence model, the thermal gas radiation property model, the inlet conditions, the injection properties and the wood char kinetics.

The comparisons show that (i) appropriate inlet conditions and injection properties are essential for accurate predictions of flame shape and recirculation strength when using the RANS approach and (ii) predictions of gas temperature and dry gas species concentrations outside the flame region can even be accurate when applying strongly simplified injection properties or kinetics. Specifically, for both the gasification of ethylene glycol and the gasification of mixtures of ethylene glycol and wood char, the predictions of gas temperature and dry gas species concentrations outside the flame region were mainly in good to excellent agreement with the experimental data. Larger deviations were found for the conversion of ethylene glycol and of wood char in the near-axis region as the adopted common models for turbulent mixing and turbulent dispersion led to erroneous predictions. Thus, the mathematical description of the physical and thermo-chemical process steps in the flame region of entrained flow gasification processes should be further improved in future studies. Furthermore, the sensitivity analyses have shown three major findings. Firstly, the HVI1

mechanism is highly recommended for preliminary simulations due to its low stiffness while the DLR2017/RM mechanism provides the most reasonable flame temperature predictions at adequate computing times. Secondly, the specific models for turbulence and the thermal gas radiation properties are not decisive for accurate predictions of gas temperature and dry gas species concentrations. Thirdly, for the gasification of mixtures with wood char contents of up to 30 %, accurate predictions of gas temperature and dry gas species concentrations outside the flame region are possible within the uncertainty limits of the wood char kinetics.

# Kurzfassung

Flugstromstromvergasung ist die dominierende Vergasungstechnologie für die Produktion von teerfreiem Synthesegas. Die Technologie muss jedoch in Anbetracht der rapiden Klimaveränderungen an biogene und anthropogene Ausgangsmaterialien angepasst werden. Daher sind neue validierte mathematische Modelle für die Auslegung, Optimierung und Hochskalierung erforderlich.

Diese Dissertation fokussiert sich auf die numerische Modellierung und Simulation der atmosphärischen Flugstromvergasung von Ersatzbrennstoffen, um die Modellentwicklung für die Hochdruckflugstromvergasung von Biomasse zu beschleunigen. Zunächst wurden auf dem RANS-Ansatz basierende Modelle entwickelt, um die Vergasung von Ethylenglykol sowie von Mischungen aus Ethylenglykol und Holzkoks zu beschreiben. Insbesondere wurden verbesserte Eintrittsbedingungen und Injektionseigenschaften und neue Holzkoksentsgasungskinetiken aus Daten von Experimenten im Labormaßstab entwickelt. Anschließend wurden numerische Simulationen von Vergasungsexperimenten mit Ethylenglykol bzw. mit Mischungen aus Ethylenglykol und Holzkoks unter Anwendung von verbesserten Implementierungen und Netzen zur Schließung von Element- und Energiebilanzen durchgeführt. Die Vorhersagen wurden mit experimentellen Flammenformbeobachtungen, experimentellen axialen Tropfengeschwindigkeiten und experimentellen Radialprofilen von Gastemperaturen und trockenen Gaskomponentenkonzentrationen verglichen. Darüber hinaus wurden Sensitivitätsanalysen durchgeführt, um den Einfluss der homogenen Reaktionskinetiken, des Verdampfungsmodells, des Turbulenzmodells, des thermischen Gasstrahlungseigenschaftsmodells, der Eintrittsbedingungen, der Injektionseigenschaften und der Holzkoks kinetiken zu untersuchen.

Die Vergleiche zeigen, dass (i) geeignete Eintrittsbedingungen und Injektionseigenschaften für genaue Vorhersagen von Flammenform und Rezirkulationsstärke bei Anwendung des RANS-Ansatzes erforderlich sind und (ii) Vorhersagen von Gastemperaturen und trockenen Gaskomponentenkonzentrationen außerhalb der Flammenregion auch genau sein können, wenn die Injektionseigenschaften oder die Kinetiken stark vereinfacht beschrieben werden. Für die Vergasung von Ethylenglykol sowie von Mischungen aus Ethylenglykol und Holzkoks waren insbesondere die Vorhersagen von Gastemperaturen und trockenen Gaskomponentenkonzentrationen außerhalb der Flammenregion überwiegend in guter bis exzellenter Übereinstimmung mit den experimentellen Daten. Größere Abweichungen wurden für den

Umsatz von Ethylenglykol und von Holzkoks an axialen Reaktorpositionen gefunden, da die eingesetzten üblichen Modelle für turbulente Vermischung und turbulente Dispersion zu fehlerbehafteten Vorhersagen führten. Folglich sollte die mathematische Beschreibung der physikalischen und thermisch-chemischen Prozessschritte in der Flammenregion von Flugstromvergasungsprozessen in künftigen Arbeiten weiter verbessert werden. Darüber hinaus haben die Sensitivitätsanalysen drei Erkenntnisse aufgezeigt. Erstens ist der kürzlich entwickelte HVI1-Mechanismus auf Grund seiner geringen Steifigkeit sehr empfehlenswert für Vorberechnungen, während der DLR2017/RM-Mechanismus die vernünftigsten Vorhersagen für die innere Flammenregion in angemessenen Rechenzeiten liefert. Zweitens sind die konkreten Modelle für Turbulenz und thermische Gasstrahlungseigenschaften für genaue Vorhersagen von Gastemperaturen und trockenen Gaskomponentenkonzentrationen nicht entscheidend. Drittens sind für die Vergasung von Mischungen mit Holzkoksanteilen von bis zu 30 % genaue Vorhersagen von Gastemperaturen und trockenen Gaskomponentenkonzentrationen außerhalb der Flammenregion innerhalb der Unsicherheiten der Holzkokskinetiken möglich.

# Acknowledgements

This thesis was written during my research activities for (i) the Engler-Bunte-Institute, Fuel Technology (EBI ceb) of Karlsruhe Institute of Technology (KIT), (ii) the Institute for Technical Chemistry, Gasification Technology (ITC vgt) of Karlsruhe Institute of Technology (KIT) and (iii) the Institute for Energy Process Engineering and Fuel Technology (IEVB) of Clausthal University of Technology (TU Clausthal).

The research activities were financially supported (i) by the Helmholtz Association of German Research Centres (HGF) in the frame of the programmes Energy Efficiency, Materials and Resources (EMR) and Materials and Technologies for the Energy Transition (MTET) and of the project Helmholtz Virtual Institute for Gasification Technology (HVI GasTech, VH-VI-429) and (ii) by the German Federal Ministry for Economic Affairs and Energy (BMWi) / Project Management Jülich (PtJ) in the frame of the project Huntorf2020 (03ET6139A).

I am very grateful that I got the opportunity to work on so many research and teaching projects together with numerous people from Karlsruhe Institute of Technology, Clausthal University of Technology, RWTH Aachen University, Forschungszentrum Jülich, German Aerospace Center and Technical University of Denmark. My sincere thanks go to all colleagues and students.

I would like to express my particular gratitude to Prof. Thomas Kolb, Prof. Roman Weber and PD Marco Mancini for the supervision, the funding acquisition and the thriving personal and research discussions.

I would like also to thank Michael Alberti, Pia Bengert, David Böning, Sabine Fleck, Manuel Haas, Christian Hotz, Fabian Hüsing, Tobias Jakobs, Thobias Kreitzberg, Ulrike Santo, Alexander Sängler, Christoph Schneider and Stella Clara Walker for the collaboration and the helpful discussions within the dissertation project.



*Meiner Familie*



# Contents

<b>Abstract</b>	<b>v</b>
<b>Kurzfassung</b>	<b>vii</b>
<b>Acknowledgements</b>	<b>ix</b>
<b>List of figures</b>	<b>xxvi</b>
<b>List of tables</b>	<b>xxx</b>
<b>List of symbols</b>	<b>xxxix</b>
Latin symbols . . . . .	xxxix
Greek symbols . . . . .	xxxiv
Diacritic symbols . . . . .	xxxvi
Indices . . . . .	xxxvii
<b>List of acronyms</b>	<b>xlvi</b>
<b>1 Introduction</b>	<b>1</b>
1.1 Gasification . . . . .	2
1.2 Gasification technologies . . . . .	3
1.3 bioliq process . . . . .	4
1.4 Laboratory-scale plants . . . . .	6
1.5 Preceding works . . . . .	7
1.6 Objectives . . . . .	11
<b>2 Model fundamentals</b>	<b>13</b>
2.1 Physical and thermo-chemical process steps . . . . .	13
2.2 Multiphase flows . . . . .	16
2.2.1 Continuous gas phases . . . . .	18
2.2.1.1 Continuity equation . . . . .	18
2.2.1.2 Species balance equation . . . . .	18
2.2.1.3 Momentum equation . . . . .	19
2.2.1.4 Energy equation . . . . .	20
2.2.2 Turbulent flows . . . . .	21

2.2.2.1	Reynolds averaging . . . . .	22
2.2.2.2	Favre averaging . . . . .	23
2.2.2.3	Favre averaged Navier-Stokes equations . . . . .	23
2.2.2.4	Standard $k$ - $\epsilon$ model . . . . .	24
2.2.2.5	Shear-stress transport (SST) $k$ - $\omega$ model . . . . .	25
2.2.3	Boundary conditions . . . . .	26
2.2.3.1	Inlet . . . . .	26
2.2.3.2	Outlet . . . . .	27
2.2.3.3	Wall . . . . .	27
2.2.4	Atomisation . . . . .	30
2.2.4.1	Experiments of Sanger and Jakobs . . . . .	31
2.2.4.2	Experiments of Haas . . . . .	32
2.2.4.3	Previous initial particle state properties for liquid gasification . . . . .	33
2.2.4.4	Improved initial particle state properties for liquid gasification . . . . .	34
2.2.4.5	Initial particle state properties for slurry gasification . . . . .	36
2.2.5	Dispersed phases . . . . .	37
2.2.5.1	Drag coefficient . . . . .	38
2.2.5.2	Turbulent dispersion . . . . .	39
2.2.5.3	Heat and mass transfer . . . . .	40
2.2.5.4	Source terms . . . . .	42
2.2.5.5	Physical properties . . . . .	44
2.2.5.6	Initial particle state properties . . . . .	44
2.3	Homogeneous reaction kinetics . . . . .	44
2.3.1	Detailed, reduced and global reaction mechanisms . . . . .	45
2.3.2	Reaction rates . . . . .	47
2.4	Turbulence-chemistry interactions . . . . .	49
2.5	Thermal radiation . . . . .	52
2.5.1	Discrete ordinates model . . . . .	53
2.5.2	Thermal gas radiation property models . . . . .	55
2.5.2.1	Grey-gas model . . . . .	55
2.5.2.2	Weighted-sum-of-grey-gas model . . . . .	56
2.5.3	Thermal particle radiation property models . . . . .	57
2.5.4	Thermal wall radiation property models . . . . .	60
2.6	Ethylene glycol vaporisation . . . . .	60
2.6.1	Classical model . . . . .	61
2.6.2	Model of Abramzon and Sirignano . . . . .	63
2.6.3	Model of Sazhin . . . . .	63

---

2.6.3.1	Temperature distribution in presence of intra-droplet radiation . . . . .	64
2.6.3.2	Temperature distribution in absence of intra-droplet radiation . . . . .	66
2.6.3.3	Thermal radiation power distribution . . . . .	66
2.6.4	Comparisons and conclusions . . . . .	67
2.6.4.1	Thermal radiation power distribution . . . . .	67
2.6.4.2	Single-droplet vaporisation . . . . .	68
2.7	Wood char conversion . . . . .	71
2.7.1	Chemical properties . . . . .	72
2.7.1.1	Simplified elemental and proximate compositions . . . . .	73
2.7.1.2	Equilibrium contents and equilibrium volatiles compositions . . . . .	74
2.7.1.3	Compositions during devolatilisation and heterogeneous gasification . . . . .	75
2.7.2	Physical properties . . . . .	76
2.7.2.1	Experiments of Gupta et al. . . . .	77
2.7.2.2	Experiments of Dupont et al. . . . .	78
2.7.2.3	Experiments of Brewer et al. . . . .	78
2.7.2.4	Experiments of Dubil . . . . .	78
2.7.2.5	Experiments of Arnold et al. . . . .	79
2.7.2.6	Conclusions . . . . .	79
2.7.3	Morphology . . . . .	79
2.7.3.1	DTR experiments of Schneider et al. . . . .	81
2.7.3.2	REGA experiments of Fleck et al. . . . .	81
2.7.3.3	Experiments of Kreitzberg et al. . . . .	84
2.7.3.4	Experiments of Müller et al., Dubil, Stösser and Schneider et al. . . . .	84
2.7.3.5	Conclusions concerning fragmentation . . . . .	85
2.7.3.6	Conclusions concerning particle shape . . . . .	86
2.7.3.7	Conclusions concerning particle shrinking . . . . .	86
2.7.3.8	Conclusions concerning particle pore structures . . . . .	86
2.7.3.9	Particle pore diameter . . . . .	87
2.7.3.10	Initial effective solid density . . . . .	88
2.7.3.11	Initial particle diameter . . . . .	89
2.7.3.12	Particle diameter . . . . .	89
2.7.4	Devolatilisation . . . . .	92
2.7.4.1	Detailed network models and global models . . . . .	92
2.7.4.2	Previous studies and HVIGasTech kinetics . . . . .	93
2.7.4.3	New HVIGasTech kinetics, comparisons and conclusions . . . . .	94

---

2.7.4.4	Heat and mass transfer . . . . .	96
2.7.4.5	Volatiles compositions . . . . .	97
2.7.5	Heterogeneous gasification . . . . .	98
2.7.5.1	Reaction regimes . . . . .	99
2.7.5.2	Previous studies and HVI GasTech kinetics . . . . .	102
2.7.5.3	Heat and mass transfer . . . . .	103
2.7.5.4	Comparisons and conclusions . . . . .	104
<b>3</b>	<b>Simulation and evaluation methods</b>	<b>107</b>
3.1	Settings . . . . .	107
3.2	Experimental data for comparison . . . . .	110
3.3	Numerical data for comparison . . . . .	111
3.4	Recirculation strengths and lengths . . . . .	111
3.5	Relative deviations . . . . .	111
3.6	Cumulative mass flow rates . . . . .	112
3.7	Solid conversions . . . . .	112
<b>4</b>	<b>Results</b>	<b>115</b>
4.1	Flame shapes . . . . .	115
4.2	Recirculation zones . . . . .	117
4.3	Droplet dispersions . . . . .	119
4.4	Droplet velocities . . . . .	121
4.5	Homogeneous reaction kinetics . . . . .	122
4.6	Vaporisation . . . . .	131
4.7	Turbulence . . . . .	134
4.8	Thermal gas radiation properties . . . . .	134
4.9	Inlet conditions and injection properties . . . . .	138
4.10	Wood char kinetics . . . . .	140
<b>5</b>	<b>Conclusions</b>	<b>147</b>
<b>A</b>	<b>Plant descriptions</b>	<b>151</b>
A.1	bioliq entrained flow gasifier (bioliq EFG) . . . . .	151
A.2	Atmospheric research entrained flow gasifier (REGA) . . . . .	153
A.3	Atmospheric spray test rig (ATMO) . . . . .	156
A.4	Drop-tube reactor (DTR) . . . . .	158
<b>B</b>	<b>Gasification experiments</b>	<b>161</b>
<b>C</b>	<b>Technical drawings</b>	<b>165</b>
C.1	Nozzles . . . . .	165
C.2	Reactors . . . . .	166

---

<b>D</b>	<b>Experimental results</b>	<b>169</b>
D.1	ATMO experiments . . . . .	169
D.1.1	Droplet diameter distributions . . . . .	169
D.1.2	Characteristic values . . . . .	172
D.2	REGA experiments . . . . .	174
<b>E</b>	<b>Injection properties</b>	<b>181</b>
E.1	Mathematical methods . . . . .	181
E.2	Gamma and Weibull distributions . . . . .	181
E.3	Normalised distributions . . . . .	183
E.4	Injection distributions . . . . .	185
<b>F</b>	<b>Physical properties</b>	<b>195</b>
F.1	Molar masses . . . . .	195
F.2	Molar standard enthalpies and molar standard entropies . . . . .	195
F.3	Specific standard enthalpies and specific standard entropies . . . . .	196
F.4	Lennard-Jones diameters and Lennard-Jones energy parameters . . . . .	196
F.5	Gas phase . . . . .	196
F.5.1	Molar mass . . . . .	197
F.5.2	Density . . . . .	197
F.5.3	Dynamic viscosity . . . . .	197
F.5.4	Thermal conductivity . . . . .	198
F.5.5	Diffusion coefficients . . . . .	199
F.5.6	Specific heat capacity . . . . .	202
F.5.7	Specific physical enthalpy . . . . .	202
F.5.8	Specific entropy . . . . .	203
F.6	Liquid phase . . . . .	204
F.6.1	Vapour pressure . . . . .	204
F.6.2	Specific enthalpy of vaporisation . . . . .	204
F.6.3	Density . . . . .	204
F.6.4	Dynamic viscosity . . . . .	205
F.6.5	Thermal conductivity . . . . .	205
F.6.6	Vapour diffusion coefficient . . . . .	205
F.6.7	Specific heat capacity . . . . .	206
F.6.8	Specific physical enthalpy . . . . .	206
F.7	Solid phase . . . . .	207
F.7.1	Density . . . . .	207
F.7.2	Specific heat capacity . . . . .	209
F.7.3	Specific physical enthalpy . . . . .	211
<b>G</b>	<b>Reaction mechanisms</b>	<b>213</b>

---

G.1	The WD mechanism . . . . .	213
G.2	The JL mechanism . . . . .	213
G.3	The JL/A mechanism . . . . .	214
G.4	The HVI1 mechanism . . . . .	214
G.5	The eJL mechanism . . . . .	215
G.6	The eJL/A mechanism . . . . .	215
G.7	The DLR2017/RK mechanism . . . . .	216
G.8	The DLR2017/RM mechanism . . . . .	216
<b>H</b>	<b>Vaporisation simulation results</b>	<b>217</b>
<b>I</b>	<b>Wood char properties</b>	<b>221</b>
I.1	Chemical properties . . . . .	221
I.2	Morphology measurements . . . . .	224
I.3	Heterogeneous gasification kinetics . . . . .	229
<b>J</b>	<b>CFD simulation results</b>	<b>233</b>
	<b>Bibliography</b>	<b>235</b>

# List of figures

2.1	Physical and thermo-chemical process steps and sub-processes of entrained flow gasification. . . . .	15
2.2	Sub-processes of entrained flow gasification. . . . .	16
2.3	Predicted gas temperature distributions for the REGA experiments TUC3 V479 and TUC5 V1105. . . . .	34
2.4	Fluid zones assumed by the eddy-dissipation-concept model. . . . .	50
2.5	Spectral refractive index and spectral absorption index of ethylene glycol. . . . .	59
2.6	Particle absorption efficiency and particle scattering efficiency of ethylene glycol. . . . .	59
2.7	Spectral particle absorption efficiencies based on Mie theory or Dombrovsky approximation. . . . .	67
2.8	Thermal radiation powers based on Mie theory or Dombrovsky approximation. . . . .	68
2.9	Predicted gas temperature distributions for the REGA experiment TUC3 V786. . . . .	69
2.10	Predicted gas temperatures and predicted gas velocities along the reactor axis and the reactor diagonal for the REGA experiment TUC3 V786. . . . .	69
2.11	Simulated particle temperatures and simulated particle diameters along the reactor axis and the reactor diagonal based on the classical model, the model of Abramzon and Sirignano and the model of Sazhin et al. in absence of thermal radiation. . . . .	70
2.12	Simulated particle temperatures and simulated particle diameters along the reactor axis and the reactor diagonal based on the classical model, the model of Abramzon and Sirignano and the model of Sazhin et al. in presence of thermal radiation. . . . .	71
2.13	Mass fractions of the volatiles and equilibrium volatiles compositions in mass fractions. . . . .	74
2.14	Cumulative particle size distributions of the wood chars HK01, HK06, HK06-1400-200 and HK07 based on laser diffraction measurements, interpolated cumulative particle size distributions of the wood chars HK06 and HK06-1400-200 and calculated cumulative particle size distributions based on simplified break-up approaches. . . . .	82

2.15	SEM images of particles of the wood chars HK01 and HK07 and of particles collected in the REGA experiments TUC5 GHKS10 V1071 and TUC5 GHKS30 V1284. . . . .	83
2.16	Normalised particle diameters during heterogeneous gasification based on measurements, fitting and extrapolation. . . . .	90
2.17	Simulated particle diameters during heterogeneous gasification at constant gas condition and based on different approaches. . . . .	91
2.18	Simulated mean particle devolatilisation conversions in comparison with balanced devolatilisation conversions of various DTR experiments. . . .	95
2.19	Simulated particle devolatilisation conversions at constant heating rate and constant temperature based on various devolatilisation kinetics. . . . .	96
2.20	Kinetic regimes for the heterogeneous gasification of porous carbonaceous particles. . . . .	99
2.21	Simulated particle gasification conversions and effectiveness factors at constant gas condition and various constant particle pore diameters based on various heterogeneous gasification kinetics. . . . .	105
2.22	Simulated particle gasification conversions and effectiveness factors at constant gas condition and various constant particle diameters based on various heterogeneous gasification kinetics. . . . .	106
4.1	Predicted gas temperature distributions for the REGA experiment TUC3 V479/TUC3 V786: comparison of results from the preceding work and this work. . . . .	116
4.2	Predicted gas temperature distributions for the REGA experiment TUC5 V1105: comparison of results from the preceding work and this work. . .	116
4.3	Predicted stream function distributions for the REGA experiment TUC3 V479/TUC3 V786: comparison of results from the preceding work and this work. . . . .	118
4.4	Predicted stream function distributions for the REGA experiment TUC5 V1105: comparison of results from the preceding work and this work. . .	118
4.5	Predicted droplet concentration distributions for the REGA experiment TUC3 V479/TUC3 V786: comparison of results from the preceding work and this work (I). . . . .	119
4.6	Predicted droplet concentration distributions for the REGA experiment TUC5 V1105: comparison of results from the preceding work and this work (I). . . . .	119
4.7	Predicted droplet concentration distributions for the REGA experiment TUC3 V479/TUC3 V786: comparison of results from the preceding work and this work (II). . . . .	120

---

4.8	Predicted droplet concentration distributions for the REGA experiment TUC5 V1105: comparison of results from the preceding work and this work (II). . . . .	120
4.9	Measured axial droplet velocities, predicted axial droplet velocities and predicted axial gas velocities for the REGA experiment TUC3 V786. . . . .	121
4.10	Measured axial droplet velocities, predicted axial droplet velocities and predicted axial gas velocities for the REGA experiment TUC5 V1105. . . . .	121
4.11	Predicted gas temperature distributions for the REGA experiment TUC3 V786: comparison of results based on the HVI1 mechanism and the DLR2017/RM mechanism. . . . .	122
4.12	Predicted gas temperature distributions for the REGA experiment TUC5 V1105: comparison of results based on the HVI1 mechanism and the DLR2017/RM mechanism. . . . .	122
4.13	Predicted gas temperature distributions for the REGA experiment TUC3 V786: comparison of results based on the DLR2017/RM mechanism and the eJL mechanism. . . . .	123
4.14	Predicted gas temperature distributions for the REGA experiment TUC5 V1105: comparison of results based on the DLR2017/RM mechanism and the eJL mechanism. . . . .	123
4.15	Predicted gas temperature distributions for the REGA experiment TUC3 V786: comparison of results based on the DLR2017/RM mechanism and the eJL/A mechanism. . . . .	123
4.16	Predicted gas temperature distributions for the REGA experiment TUC5 V1105: comparison of results based on the DLR2017/RM mechanism and the eJL/A mechanism. . . . .	124
4.17	Predicted gas temperature distributions for the REGA experiment TUC3 V786: comparison of results based on the DLR2017/RM mechanism and the DLR2017/RK mechanism. . . . .	124
4.18	Predicted gas temperature distributions for the REGA experiment TUC5 V1105: comparison of results based on the DLR2017/RM mechanism and the DLR2017/RK mechanism. . . . .	124
4.19	Predicted profiles of gas temperature and dry gas species volume fractions for the REGA experiment TUC3 V786 in comparison with measured profiles: comparison of results based on the HVI1 mechanism and the DLR2017/RM mechanism. . . . .	127
4.20	Predicted profiles of gas temperature and dry gas species volume fractions for the REGA experiment TUC5 V1105 in comparison with measured profiles: comparison of results based on the HVI1 mechanism and the DLR2017/RM mechanism. . . . .	127

---

4.21	Predicted profiles of gas temperature and dry gas species volume fractions for the REGA experiment TUC3 V786 in comparison with measured profiles: comparison of results based on the DLR2017/RK mechanism and the eJL mechanism. . . . .	128
4.22	Predicted profiles of gas temperature and dry gas species volume fractions for the REGA experiment TUC5 V1105 in comparison with measured profiles: comparison of results based on the DLR2017/RK mechanism and the eJL mechanism. . . . .	128
4.23	Predicted profiles of gas temperature and dry gas species volume fractions for the REGA experiment TUC3 V786 in comparison with measured profiles: comparison of results based on the DLR2017/RK mechanism and the eJL/A mechanism. . . . .	129
4.24	Predicted profiles of gas temperature and dry gas species volume fractions for the REGA experiment TUC5 V1105 in comparison with measured profiles: comparison of results based on the DLR2017/RK mechanism and the eJL/A mechanism. . . . .	129
4.25	Predicted profiles of gas temperature and dry gas species volume fractions for the REGA experiment TUC3 V786 in comparison with measured profiles: comparison of results based on the DLR2017/RK mechanism and the DLR2017/RK mechanism. . . . .	130
4.26	Predicted profiles of gas temperature and dry gas species volume fractions for the REGA experiment TUC5 V1105 in comparison with measured profiles: comparison of results based on the DLR2017/RK mechanism and the DLR2017/RK mechanism. . . . .	130
4.27	Predicted cumulative mass flow rates of vaporised ethylene glycol for the REGA experiment TUC3 V786: comparison of results based on various reaction mechanisms and film factors. . . . .	132
4.28	Predicted cumulative mass flow rates of vaporised ethylene glycol for the REGA experiment TUC5 V1105: comparison of results based on various reaction mechanisms and film factors. . . . .	132
4.29	Predicted profiles of gas temperature and dry gas species volume fractions for the REGA experiment TUC3 V786 in comparison with measured profiles: comparison of results based on various film factors. . . . .	133
4.30	Predicted profiles of gas temperature and dry gas species volume fractions for the REGA experiment TUC5 V1105 in comparison with measured profiles: comparison of results based on various film factors. . . . .	133
4.31	Predicted profiles of gas temperature and dry gas species volume fractions for the REGA experiment TUC3 V786 in comparison with measured profiles: comparison of results based on various turbulence models. . . . .	135

---

4.32	Predicted profiles of gas temperature and dry gas species volume fractions for the REGA experiment TUC5 V1105 in comparison with measured profiles: comparison of results based on various turbulence models. . . .	135
4.33	Predicted profiles of gas temperature and dry gas species volume fractions for the REGA experiment TUC3 V786 in comparison with measured profiles: comparison of results based on various thermal gas radiation property models. . . . .	136
4.34	Predicted profiles of gas temperature and dry gas species volume fractions for the REGA experiment TUC5 V1105 in comparison with measured profiles: comparison of results based on various thermal gas radiation property models. . . . .	136
4.35	Predicted gas temperatures and heat fluxes at wall for the REGA experiment TUC3 V786: comparison of results based on various thermal gas radiation property models and various reaction mechanisms. . . . .	137
4.36	Predicted gas temperatures and heat fluxes at wall for the REGA experiment TUC5 V1105: comparison of results based on various thermal gas radiation property models and various reaction mechanisms. . . . .	137
4.37	Predicted profiles of gas temperature and dry gas species volume fractions for the REGA experiment TUC5 V1105 in comparison with measured profiles: comparison of results based on various injection properties. . .	138
4.38	Predicted gas temperature distributions for the REGA experiment TUC5 V1105: comparison of results based on various injection properties. . .	139
4.39	Predicted gas temperature distributions for the REGA experiment TUC5 V1105 and the REGA experiment TUC5 V1374. . . . .	139
4.40	Predicted profiles of gas temperature and dry gas species volume fractions for the REGA experiment TUC5 GHKS10 V1071 in comparison with measured profiles (I). . . . .	143
4.41	Predicted profiles of gas temperature and dry gas species volume fractions for the REGA experiment TUC5 GHKS30 V1284 in comparison with measured profiles (I). . . . .	143
4.42	Predicted profiles of gas temperature and dry gas species volume fractions for the REGA experiment TUC5 GHKS10 V1071 in comparison with measured profiles (II). . . . .	144
4.43	Predicted profiles of gas temperature and dry gas species volume fractions for the REGA experiment TUC5 GHKS30 V1284 in comparison with measured profiles (II). . . . .	144
4.44	Predicted profiles of gas temperature and dry gas species volume fractions for the REGA experiment TUC5 GHKS30 V1284 in comparison with measured profiles (II). . . . .	145

---

4.45	Predicted gas temperature distributions for the REGA experiment TUC5 GHKS10 V1071. . . . .	146
4.46	Predicted gas temperature distributions for the REGA experiment TUC5 GHKS30 V1284. . . . .	146
A.1	Sketch of the bioliq EFG plant. . . . .	152
A.2	Sketch of the REGA plant. . . . .	153
A.3	Sketch of the REGA reactor. . . . .	156
A.4	Sketch of the ATMO plant. . . . .	157
A.5	Sketch of the DTR plant. . . . .	158
C.1	Cross-sections of nozzle D1 and nozzle D2. . . . .	166
C.2	Cross-sections of nozzle D1.1 and nozzle D2.1. . . . .	166
C.3	Cross-section of the REGA reactor. . . . .	166
C.4	Cross-section of the DTR reactor. . . . .	167
D.1	Number-based cumulative distributions and mass-based cumulative distributions of the particle diameters at various radial positions based on the ATMO experiment TUC3 D1. . . . .	169
D.2	Number-based cumulative distributions and mass-based cumulative distributions of the particle diameters at various radial positions based on the ATMO experiment TUC5 D2. . . . .	170
D.3	Global number-based cumulative distributions and global mass-based cumulative distributions of the particle diameters based on the ATMO experiments TUC3 D1 and TUC5 D2. . . . .	170
D.4	Number-based cumulative distributions and mass-based cumulative distributions of the particle diameters at various axial positions based on the ATMO experiment TUC5 D2.1. . . . .	171
D.5	Number-based cumulative distributions and mass-based cumulative distributions of the particle diameters based on the ATMO experiments TUC3 D1, TUC5 D2, TUC5 D1.1, TUC5 D2.1 and TUC5 PO D2.1. . . . .	171
D.6	Characteristic particle diameters, characteristic axial particle velocities, characteristic radial particle velocities, characteristic axial gas velocities and characteristic radial gas velocities based on the ATMO experiment TUC3 D1. . . . .	172
D.7	Characteristic particle diameters, characteristic axial particle velocities, characteristic radial particle velocities, characteristic axial gas velocities and characteristic radial gas velocities based on the ATMO experiment TUC5 D2. . . . .	173
E.1	Normalised mass flux and velocity distributions based on the ATMO experiment TUC3 D1 and applied to derive the injection properties for the CFD simulations of the REGA experiments TUC3 V479 and TUC3 V786. . . . .	183

---

E.2	Normalised mass flux and velocity distributions based on the ATMO experiment TUC5 D2 and applied to derive the injection properties for the CFD simulations of the REGA experiment TUC5 V1105. . . . .	183
E.3	Normalised mass flux and velocity distributions based on the ATMO experiment TUC5 D2.1 and applied to derive the injection properties for the CFD simulations of the REGA experiment TUC5 V1105. . . . .	184
E.4	Normalised mass flux and velocity distributions based on the ATMO experiment TUC5 D1.1 and applied to derive the injection properties for the CFD simulations of the REGA experiment TUC5 V1374. . . . .	184
E.5	Injection distributions of the ethylene glycol droplets based on the ATMO experiment TUC3 D1 and used for the CFD simulations of the REGA experiment TUC3 V479. . . . .	185
E.6	Injection distributions of the ethylene glycol droplets based on the ATMO experiment TUC3 D1 and used for the CFD simulations of the REGA experiment TUC3 V786. . . . .	186
E.7	Injection distributions of the ethylene glycol droplets based on the ATMO experiment TUC5 D2 and used for the CFD simulations of the REGA experiment TUC5 V1105. . . . .	187
E.8	Injection distributions of the ethylene glycol droplets based on the ATMO experiment TUC5 D2.1 and used for the CFD simulations of the REGA experiment TUC5 V1105. . . . .	188
E.9	Injection distributions of the ethylene glycol droplets based on the ATMO experiment TUC5 D1.1 and used for the CFD simulations of the REGA experiment TUC5 V1374. . . . .	189
E.10	Injection distributions of the ethylene glycol droplets used for the CFD simulations of the REGA experiment TUC5 GHKS10 V1071. . . . .	190
E.11	Injection distributions of the wood char particles used for the CFD simulations of the REGA experiment TUC5 GHKS10 V1071. . . . .	191
E.12	Injection distributions of the ethylene glycol droplets used for the CFD simulations of the REGA experiment TUC5 GHKS30 V1284. . . . .	192
E.13	Injection distributions of the wood char particles used for the CFD simulations of the REGA experiment TUC5 GHKS30 V1284. . . . .	193
F.1	Comparison of simulated solid densities at constant heating rate and constant temperature based on various models. . . . .	209
F.2	Comparison of simulated specific solid heat capacities at constant heating rate and constant temperature based on various models. . . . .	210
H.1	Simulated particle temperatures and simulated particle diameters along the reactor axis and the reactor diagonal based on the model of Sazhin et al. in presence of thermal radiation. . . . .	217

---

H.2	Simulated particle temperatures and simulated particle diameters along the reactor axis and the reactor diagonal based on the classical model and the model of Abramzon and Sirignano in presence of thermal radiation and on two different approaches for the particle emissivity. . . . .	218
H.3	Simulated particle temperatures and simulated particle diameters along the reactor axis and the reactor diagonal based on the model of Abramzon and Sirignano and the model of Sazhin et al. in presence of thermal radiation and on two different approaches for the vapour film diffusion coefficient. . . . .	219
J.1	Predicted profiles of gas temperature and dry gas species volume fractions for the REGA experiments TUC3 V479 and TUC3 V786 in comparison with measured profiles. . . . .	233
J.2	Predicted profiles of gas temperature and dry gas species volume fractions for the REGA experiments TUC3 V479 and TUC3 V786 in comparison with measured profiles. . . . .	234

# List of tables

1.1	Conditions of the REGA experiments. . . . .	8
2.1	Conditions of the ATMO experiments. . . . .	31
2.2	Characteristic results from the ATMO experiments. . . . .	31
2.3	Equivalent nozzle diameters based on the ATMO experiments and applied for the CFD simulations of the REGA experiments TUC3 V479/TUC3 V786, TUC5 V1105 and TUC5 V1374. . . . .	35
2.4	Equivalent nozzle diameters applied for the CFD simulations of the REGA experiments TUC5 GHKS10 V1071 and TUC5 GHKS30 V1284. . . . .	37
2.5	Coefficients for the calculation of the drag coefficient using the Morsi-Alexander equation. . . . .	39
2.6	Particle conversion processes for the different particle types. . . . .	40
2.7	Conditions for the particle conversion processes. . . . .	41
2.8	Typical gas species mole fractions of carbon monoxide, carbon dioxide and water vapour in the CFD simulations of the REGA experiments TUC3 V786 and TUC5 V1105. . . . .	56
2.9	Solid densities of wood char HK02-1600 based on measurements and predictions. . . . .	78
2.10	Carbon conversions of the particles collected in the REGA experiment TUC5 GHKS30 V1284. . . . .	82
2.11	Initial effective solid densities, initial effective solid porosities and initial solid densities based on the REGA experiments TUC5 GHKS10 V1071 and TUC5 GHKS30 V1284. . . . .	89
2.12	Parameters for the devolatilisation kinetics of Stösser based on a single first-order reaction Arrhenius law model (SFORALM) and of Dammann et al. based on a single first-order reaction Arrhenius law model or a modified Yamamoto model, coefficients of determination and ranges of relative deviations between balanced and simulated particle devolatilisation conversions for various DTR experiments. . . . .	94
2.13	Specific standard combustion enthalpies of the wood chars HK01 (EF simple) and HK07 (EF simple) based on heating value analyses and corresponding specific standard combustion enthalpies of the volatiles and specific standard enthalpies of devolatilisation based on calculations. . . . .	97

---

2.14	Volatiles compositions in mass fractions based on equilibrium calculations for the wood chars HK01 (EF simple) and HK07 (EF simple) and based on measurements and estimations. . . . .	98
3.1	Baseline sub-models used for the CFD simulations. . . . .	108
3.2	User-defined functions used for the CFD simulations. . . . .	109
3.3	Spatial discretisation schemes used for the CFD simulations. . . . .	110
3.4	Under-relaxation factors used for the CFD simulations. . . . .	110
4.1	Predicted maximum gas temperatures for the REGA experiments TUC3 V479, TUC3 V786 and TUC5 V1105: comparison of results from the preceding works and this work. . . . .	117
4.2	Predicted strengths and lengths of the recirculation zones for the REGA experiments TUC3 V479, TUC3 V786 and TUC5 V1105: comparison of results from the preceding works and this work. . . . .	118
4.3	Predicted maximum gas temperatures for the REGA experiments TUC3 V786 and TUC5 V1105: comparison of results based on various reaction mechanisms. . . . .	125
4.4	Relative deviations concerning the profiles of gas temperature and dry gas species volume fractions and absolute relative deviations at the nozzle distance of 300 mm for the REGA experiment TUC3 V786. . . . .	125
4.5	Relative deviations and absolute relative deviations concerning the profiles of gas temperature and dry gas species volume fractions at the nozzle distance of 680 mm for the REGA experiment TUC3 V786. . . . .	126
4.6	Relative deviations concerning the profiles of gas temperature and dry gas species volume fractions and absolute relative deviations at the nozzle distance of 300 mm for the REGA experiment TUC5 V1105. . . . .	126
4.7	Relative deviations concerning the profiles of gas temperature and dry gas species volume fractions and absolute relative deviations at the nozzle distance of 680 mm for the REGA experiment TUC5 V1105. . . . .	126
4.8	Normalised computing times for the CFD simulations of the REGA experiments TUC3 V786 and TUC5 V1105: comparison of results for various reaction mechanisms. . . . .	131
4.9	Predicted strengths and lengths of the recirculation zones for the REGA experiments TUC3 V479, TUC3 V786 and TUC5 V1105: comparison of results based on various turbulence models. . . . .	134
4.10	Predicted total and radiation heat flow rates at wall for the REGA experiments TUC3 V786 and TUC5 V1105: comparison of results based on various thermal gas radiation property models. . . . .	137
4.11	CFD simulations of the REGA experiments TUC5 GHKS10 V1071 and TUC5 GHKS30 V1284. . . . .	140

---

4.12	Predicted solid devolatilisation conversions, predicted solid gasification conversions and predicted solid carbon conversions for the REGA experiments TUC5 GHKS10 V1071 and TUC5 GHKS30 V1284 at a nozzle distance of 680 mm and near axis. . . . .	142
4.13	Balanced solid gasification conversions of particles collected in the REGA experiment TUC5 GHKS30 V1284. . . . .	145
A.1	Characteristic plant properties of the bioliq EFG reactor. . . . .	151
A.2	Characteristic properties of slurries applied in the bioliq EFG reactor. . . . .	151
A.3	Characteristic properties of synthesis gas produced in the bioliq EFG reactor. . . . .	152
A.4	Characteristic properties of slag discharged from the bioliq EFG reactor. . . . .	152
A.5	Characteristic plant properties of the REGA reactor. . . . .	154
A.6	Measurement ranges and measurement accuracies for the flow rates at the REGA plant. . . . .	154
A.7	Measurement principles and measurement ranges for gas species concentrations at the REGA plant. . . . .	155
A.8	Characteristic plant properties of the ATMO plant. . . . .	156
A.9	Characteristic plant properties of the DTR plant. . . . .	159
B.1	Inlet conditions of the REGA experiments. . . . .	162
B.2	Characteristic parameters of the REGA experiments. . . . .	163
B.3	Inlet conditions applied for the REGA simulations. . . . .	163
D.1	Measured axial droplet velocities from the REGA experiments. . . . .	174
D.2	Measured gas temperatures and dry gas species volume fractions from the REGA experiments. . . . .	175
E.1	Shape parameters for the gamma distributions used to approximate the number-based droplet diameter distributions. . . . .	182
E.2	Shape parameters for the Weibull distributions used to approximate the mass-based droplet diameter distributions. . . . .	182
F.1	Coefficients for the calculation of the collision integral for the dynamic gas viscosity. . . . .	198
F.2	Coefficients for the calculation of the collision integral for the gas diffusion coefficients. . . . .	202
F.3	Coefficients for the calculation of the solid density using the model of Merrick. . . . .	207
F.4	Coefficients for the calculation of the solid density using the models of IGT. . . . .	208
G.1	Chemical equations of the reaction mechanism of Westbrook and Dryer. . . . .	213

---

---

G.2	Parameters of the reaction mechanism of Westbrook and Dryer. . . . .	213
G.3	Chemical equations of the reaction mechanism of Jones and Lindstedt. . . . .	213
G.4	Parameters of the reaction mechanism of Jones and Lindstedt. . . . .	213
G.5	Chemical equations of the alternative reaction mechanism of Jones and Lindstedt. . . . .	214
G.6	Parameters of the alternative reaction mechanism of Jones and Lindstedt. . . . .	214
G.7	Chemical equations of the first reaction mechanism of HVIGasTech for the gasification of ethylene glycol. . . . .	214
G.8	Parameters of the first reaction mechanism of HVIGasTech for the gasification of ethylene glycol. . . . .	214
G.9	Chemical equations of the extended reaction mechanism of Jones and Lindstedt for the gasification of ethylene glycol. . . . .	215
G.10	Parameters of the extended reaction mechanism of Jones and Lindstedt for the gasification of ethylene glycol. . . . .	215
G.11	Chemical equations of the alternative extended reaction mechanism of Jones and Lindstedt for the gasification of ethylene glycol. . . . .	215
G.12	Parameters of the alternative extended reaction mechanism of Jones and Lindstedt for the gasification of ethylene glycol. . . . .	216
G.13	Adapted chemical equations of the reduced DLR2017 mechanism of Kathrotia et al. for the gasification of ethylene glycol. . . . .	216
G.14	Adapted chemical equations of the reduced DLR2017 mechanism of Methling et al. for the gasification of ethylene glycol. . . . .	216
I.1	Origins and applications of wood chars focussed in the characterisation and gasification experiments and in the numerical simulations. . . . .	222
I.2	Proximate and ultimate compositions of wood chars focussed in the characterisation and gasification experiments and in the numerical simulations. . . . .	223
I.3	Mean particle pore diameters obtained by measurements, numerical regressions or estimations. . . . .	225
I.4	Measured specific surface areas obtained in the frame of HVIGasTech. . . . .	226
I.5	Heterogeneous gasification kinetics developed in the frame of HVIGasTech. . . . .	230
I.6	Parameters of heterogeneous gasification kinetics developed in the frame of HVIGasTech for regime I. . . . .	231
I.7	Parameters of heterogeneous gasification kinetics developed in the frame of HVIGasTech for regime II. . . . .	232

# List of symbols

## Latin symbols

---

Symbol	Description
$a$	model parameter (used in bell functions)
$a$	weight; fraction of black body emission
$\mathbf{a}$	weight vector
$A$	coefficient (used in empirical correlations)
$A$	general parameter
$b$	model parameter (used in bell functions)
$b$	temperature exponent (used in homogeneous reaction kinetics)
$B$	coefficient (used in empirical correlations)
$B$	Spalding number
$Bi$	Biot number
$c$	model parameter (used in bell functions)
$c$	molar concentration
$C$	coefficient (used in empirical correlations)
$C$	heat capacity
$C$	model constant (for example, used in turbulence models or in the eddy-dissipation-concept model)
$C$	model parameter (used for fall-off reaction rates)
$d$	diameter
$d$	model parameter (used in bell functions)
$d$	thickness
$D$	coefficient (used in empirical correlations)
$D$	diffusion coefficient
$\mathbf{D}$	diffusion coefficient matrix
$E$	model constant (used in the SST $k-\omega$ model)
$\dot{e}$	emissive power
$E$	coefficient (used in empirical correlations)
$E$	emission

---

---

Symbol	Description
$E$	energy
$E$	model constant (used in wall functions)
$f$	auxiliary function (used for fall-off reaction rates or heterogeneous kinetics)
$f$	correction factor (used in heterogeneous kinetics)
$f$	empirical function (used in vapour pressure correlations)
$f$	factor (used in vaporisation models)
$f$	model parameter (used for fall-off reaction rates)
$f$	scattering factor
$F$	broadening/fall-off function (used for fall-off reaction rates)
$F$	coefficient (used in empirical correlations)
$F$	Fickian diffusion coefficient
$\mathbf{F}$	Fickian diffusion coefficient matrix
$\mathbf{F}$	force
$F$	model function (used in the SST $k$ - $\omega$ model)
$g$	acceleration due to gravity
$\mathbf{g}$	acceleration vector due to gravity
$g$	auxiliary function (used in physical property models)
$G$	coefficient (used in empirical correlations)
$G$	incident radiation
$h$	model parameter (used in the vaporisation model of Sazhin et al.)
$h$	heat transfer coefficient
$H$	coefficient (used in empirical correlations)
$H$	enthalpy
$\dot{H}$	enthalpy flow rate
$i$	general index (for example, for species)
$I$	intensity
$\mathbf{I}$	identity matrix
$\mathbf{j}$	diffusion flux
$j$	general index (for example, for species or for second-order groups)
$\mathbf{J}$	Jacobian matrix
$k$	absorption index
$k$	constant (for example, used for Boltzmann constant)
$k$	factor (used for reaction rates)
$k$	general index (for example, for first-order groups)
$k$	rate constant
$k$	shape parameter of the Weibull distribution

---

---

Symbol	Description
$k$	turbulent kinetic energy
$K$	absorption coefficient
$\mathbf{K}$	absorption coefficient vector
$K$	auxiliary parameter (used in heterogeneous kinetics)
$K$	equilibrium constant
$L$	length; length scale
$Le$	Lewis number
$m$	mass
$\dot{m}$	mass flow rate
$M$	molar mass
$n$	normal coordinate
$\mathbf{n}$	normal vector
$n$	reactant exponent
$n$	reaction order
$n$	refractive index
$N$	model parameter (used for fall-off reaction rates)
$N$	number
$Nu$	Nusselt number
$p$	coefficient (used in the vaporisation model of Sazhin et al.)
$p$	pressure
$P$	model function (used in wall functions)
$P$	model parameter (used for fall-off reaction rates)
$P$	thermal radiation power (distribution) (used in the intra-particle thermal radiation model)
$Pe$	Peclet number
$Pr$	Prandtl number
$q$	coefficient (used in the vaporisation model of Sazhin et al.)
$q$	probability density function
$\dot{q}$	heat flux
$Q$	coefficient (used in the intra-particle thermal radiation model)
$Q$	cumulative distribution function
$r$	radius
$r$	volume fraction
$\mathbf{r}$	volume fraction vector
$R$	gas constant
$R$	reaction rate
$R^2$	coefficient of determination
$Re$	Reynolds number

---

Symbol	Description
$s$	gap width
$\mathbf{s}$	radiation beam vector
$S$	entropy
$S$	source term
$\mathbf{S}$	source term vector
$S$	strain rate
$\mathbf{S}$	strain rate tensor
$Sc$	Schmidt number
$Sh$	Sherwood number
$t$	time
$T$	absolute temperature
$u$	velocity
$\mathbf{u}$	velocity vector
$v$	eigenfunction (used in the vaporisation model of Sazhin et al.)
$V$	volume
$\dot{V}$	volume flow rate
$w$	mass fraction
$\mathbf{w}$	mass fraction vector
$w$	weighting factor
$w$	weighting function
$x$	mole fraction
$\mathbf{x}$	mole fraction vector
$x$	position
$\mathbf{x}$	position vector
$X$	conversion
$y$	wall distance
$z$	auxiliary variable
$Z$	compressibility factor

---

## Greek symbols

Symbol	Description
$\alpha$	angle
$\alpha$	model function (used in the SST $k$ - $\omega$ model)
$\alpha$	shape parameter of the gamma distribution
$\beta$	model function (used in the SST $k$ - $\omega$ model)

---

---

Symbol	Description
$\beta$	shape parameter of the gamma distribution
$\gamma$	activity coefficient
$\gamma$	model function (used in the SST $k$ - $\omega$ model)
$\gamma$	model parameter (used in the intra-particle thermal radiation model)
$\gamma$	volume (used in the eddy-dissipation concept model)
$\Gamma$	gamma function
$\Gamma$	(generic) diffusion coefficient
$\delta$	Kronecker delta
$\Delta$	difference
$\epsilon$	efficiency (used for three-body reaction rates)
$\epsilon$	Lennard-Jones energy parameter
$\epsilon$	turbulent dissipation rate
$\varepsilon$	emissivity
$\varepsilon$	porosity
$\zeta$	distributed random number
$\eta$	dynamic viscosity
$\eta$	effectiveness factor
$\eta$	wavelength
$\vartheta$	Celsius temperature
$\Theta$	heaviside step function
$\kappa$	model constant (used in the SST $k$ - $\omega$ model)
$\kappa$	model parameter (in the vaporisation model of Sazhin et al.)
$\kappa$	van Kármán constant
$\lambda$	shape parameter of the Weibull distribution
$\lambda$	stoichiometric ratio
$\lambda$	thermal conductivity
$\Lambda$	eigenvalue
$\mathbf{\Lambda}$	eigenvalue vector
$\mu$	angle (used in the intra-particle thermal radiation model)
$\mu$	model parameter (used in the vaporisation model of Sazhin et al.)
$\mu$	second viscosity
$\nu$	kinematic viscosity
$\nu$	stoichiometric coefficient
$\xi$	model parameter (used in the intra-particle thermal radiation model)
$\pi$	pi
$\rho$	density
$\rho$	reflectivity
$\sigma$	Lennard-Jones diameter

---

Symbol	Description
$\sigma$	model constant (used in turbulence models)
$\sigma$	scattering coefficient
$\sigma$	Stefan-Boltzmann constant
$\tau$	characteristic time; characteristic time scale
$\tau$	optical thickness
$\tau$	shear stress
$\boldsymbol{\tau}$	shear stress tensor
$\tau$	tortuosity
$\varphi$	auxiliary coefficient
$\varphi$	(generic) scalar
$\varphi$	model parameter (used in vaporisation models)
$\Phi$	model parameter (used in the SST $k$ - $\omega$ model)
$\Phi$	scattering phase function
$\Phi$	Thiele modulus
$\chi$	factor accounting for the effect of internal recirculation (used in the vaporisation model of Sazhin et al.)
$\omega$	specific turbulent dissipation rate
$\Omega$	collision integral
$\Omega$	rotation rate
$\boldsymbol{\Omega}$	rotation rate tensor
$\Omega$	solid angle

---

## Diacritic symbols

Symbol	Description
—	molar
^	specific
·	flow rate or flux
~	dimensionless
~	slightly deviating
$\langle \rangle_{\text{F}}$	Favre averaged
$\langle \rangle_{\text{R}}$	Reynolds averaged
[ ]	molar concentration

---

---

## Indices

### Superscripts

---

Superscript	Description
*	auxiliary
+	dimensionless
/	fluctuating part
⊖	at standard condition; standard
E	of the reactant; reactant
P	of the product; product

---

### Subscripts

---

Subscript	Description
0	at the low-pressure limit (used for three-body reaction rates)
0	default
0	initial
0	number-based (used in combination with probability density functions or cumulative distributions functions)
0	pre-exponential (used for reaction rates)
3	mass-based (used in combination with probability density functions or cumulative distributions functions)
10,0	number-based 10th percentile value of (used in combination with probability density functions or cumulative distributions functions)
10,3	mass-based 10th percentile value of (used in combination with probability density functions or cumulative distributions functions)
50,0	number-based 50th percentile value of (used in combination with probability density functions or cumulative distributions functions)
50,3	mass-based 50th percentile value of (used in combination with probability density functions or cumulative distributions functions)
90,0	number-based 90th percentile value of (used in combination with probability density functions or cumulative distributions functions)
90,3	mass-based 90th percentile value of (used in combination with probability density functions or cumulative distributions functions)
*	characteristic
∞	at the high-pressure limit (used for three-body reaction rates)

---

---

Subscript	Description
a	activation
a	for the weights (used in the weighted-sum-of-grey-gas model)
a	of terms for the calculation of the weights (used in the weighted-sum-of-grey-gas model)
A	of species A
abs	absolute
abs	absorption
ad	adiabatic
air	of the air stream; air
ash	of ash; ash
at wall	due to air infiltration and supply of purge nitrogen near the wall (used with source terms)
ax	axial
b	backward
b	black body
B	Boltzmann
B	of species B
bal	balanced
bound	at boundary; of the boundary; boundary
c	at core; core
c	critical
c	of combustion
$c$	of (pseudo-)gas $c$
C	combinatorial
C	of carbon; carbon
C	of species C
calc	calculated
CH <sub>4</sub>	of methane
CH <sub>4</sub>	of the species balance equation of methane (used with source terms)
C <sub>2</sub> H <sub>6</sub> O <sub>2</sub>	of ethylene glycol
C <sub>2</sub> H <sub>6</sub> O <sub>2</sub>	of the species balance equation of ethylene glycol (used with source terms)
Cl	of (atomic) chlorine; (atomic) chlorine
CO	of carbon monoxide
CO	of the species balance equation of carbon monoxide (used with source terms)
CO <sub>2</sub>	of carbon dioxide

---

---

Subscript	Description
CO <sub>2</sub>	of the species balance equation of carbon dioxide (used with source terms)
cent	at centre
comb	of the combustibles; in the combustibles
cond	conductive
conv	convective
conv+cond	convective and conductive
cross	eddy crossing (used in the turbulent dispersion model)
d	drag
d	dry
D	of species D
daf	dry and ash-free
dev	after devolatilisation
dev	of devolatilisation; devolatilisation
dry gas	in the dry gas; dry gas
E	Einstein
E	energy (used in combination with source terms of the energy equation)
E	with respect to the particle energy equation
eddy	eddy; eddy life (used in the turbulent dispersion model)
eff	effective
eq	at equilibrium; equilibrium
eq	equivalent
est	estimated
f	final
f	forward
f	of formation
film	at film condition; film
fs	of the fine structure
fuel	of the fuel stream; fuel
g	gravity
g	of groups
G	Gaussian (used in the turbulent dispersion model)
gas	of the gas phase; gas
GGPD	generalised Gaussian probability density
GGPD/GMBS	combined generalised Gaussian probability density and generalised membership bell-shaped
GMBS	generalised membership bell-shaped function
H	of (atomic) hydrogen; (atomic) hydrogen

---

---

Subscript	Description
H <sub>2</sub>	of hydrogen
H <sub>2</sub>	of the species balance equation of hydrogen (used with source terms)
H <sub>2</sub> S	of hydrogen sulfide
H <sub>2</sub> O	of moisture; of water (vapour)
H <sub>2</sub> O	of the species balance equation of water (vapour) (used with source terms)
het	after heterogeneous gasification
het	of heterogeneous gasification; heterogeneous gasification
HCl	of hydrogen chloride
<i>i</i>	of parcel <i>i</i> ; of species <i>i</i>
I	in regime I
II	in regime II
<i>i,j</i>	of (species) <i>i</i> in (species) <i>j</i>
<i>j</i>	of species <i>j</i> ; of reaction <i>j</i> ; in reaction <i>j</i> ; of group <i>j</i>
in	entering a fluid cell
inf	of the infiltrated air stream; infiltrated air
inlet	at inlet; of the inlet stream
<i>k</i>	of group <i>k</i>
<i>k</i>	with respect to the turbulent kinetic energy equation (used in turbulence models)
K	Knudsen
K	for the absorption coefficients (used in the weighted-sum-of-grey-gas model)
L	Langrangian integral (used in the turbulent dispersion model)
l	lift
LHM	of/for the Langmuir-Hinshelwood model
liq	of the liquid phase; liquid
m	mass (used in combination with source terms of the continuity equation)
m	mass (used in combination with gas diffusion fluxes)
m	mixture (used in combination with liquid diffusion coefficients)
m	with respect to mass transfer (used in vaporisation models); mass transfer (used in heterogeneous gasification models)
m	with respect to the particle mass equation
M	of species M
macro	macro
max	maximum

---

---

Subscript	Description
mean,0	number-based mean value of
mean,3	mass-based mean value of
meas	measured
micro	micro
min	minimum
mod	modified
MYM	of/for the modified Yamamoto model
n	molar (used in gas diffusion fluxes)
N	of (atomic) nitrogen; (atomic) nitrogen
N <sub>2</sub>	of nitrogen
N <sub>2</sub>	of the purge nitrogen stream; purge nitrogen
N <sub>2</sub>	of the species balance equation of nitrogen (used with source terms)
NH <sub>3</sub>	of ammonia
nozzle	at nozzle; of the nozzle; nozzle
O	of (atomic) oxygen; (atomic) oxygen
O <sub>2</sub>	of oxygen
O <sub>2</sub>	of the oxygen stream; oxygen
obs	observed
outlet	at outlet; of the outlet stream
op	operating
<i>p</i>	at constant pressure; isobaric
p	projected
part	due to interaction with the dispersed phase (used with source terms)
ps	of (pseudo-)gases (used in the weighted-sum-of-grey-gas model)
PLM	of/for the power-law model
part	of the particle phase; particle
phys	physical
pore	pore
<i>r</i>	of reaction <i>r</i> ; in reaction <i>r</i>
r	of reaction
R	residual
R	Reynolds
rad	due to thermal radiation (used with source terms)
rad	radial
rad	radiative
rad	thermal radiation
reac	due to chemical reaction (used with source terms)

---

---

Subscript	Description
ref	at reference temperature
ref	reference; at reference condition
RPM	of/for the random pore model
s	at surface; surface
S	Sauter
S	of sulphur; sulphur
scat	scattering
SCM	of/for the shrinking core model
SFORALM	of/for the single first-order reaction Arrhenius law model
slurry	of the slurry stream; slurry
solid	of the solid phase; solid
sp	of species
spray	spray
STP	at standard conditions according to ISO 10780:1994 [133]
sur	of the surrounding
sw	swelling
T	of the thermal boundary layer
T	with respect to energy transfer (used in vaporisation models)
tech	technical
tot	total
trs	of transition
turb	turbulent
u	momentum (used in combination with source terms of the momentum equation)
u	of the hydrodynamic boundary layer
u	uniform (used in the turbulent dispersion model)
URM	of/for the uniform reaction model
vap	after vaporisation
vap	of vaporisation
vap	vapour
visc	viscous heating
vol	of the volatiles; in the volatiles
w	species (used in combination with source terms of the species balance equation)
w/ inf	accounting for infiltrated air and purge nitrogen
w/o inf	neglecting infiltrated air and purge nitrogen
wall	at wall; of wall; wall
water	of water

---

---

Subscript	Description
W	of the Weibull distribution
$\gamma$	of the gamma distribution
$\epsilon$	with respect to the turbulent dissipation rate equation (used in turbulence models)
$\eta$	spectral (used in thermal radiation models)
$\eta$	with respect to the turbulent viscosity (used in turbulence models)
$\varphi$	with respect to the generic scalar transport equation
$\omega$	with respect to the specific turbulent dissipation rate equation

---



# List of acronyms

---

Acronym	Description
ABB	measurements of dry gas species volume fractions using standard gas analysers
ARD	absolute relative deviation
ASM	model of Abramzon and Sirignano
ATMO	atmospheric spray test rig
B	Boudouard reaction
BET	Brunauer-Emmett-Teller
bioliq EFG	bioliq entrained flow gasifier
BtL	biomass-to-liquid
CDF	cumulative distribution function
CFD	computational fluid dynamics
CM	classical model
CMOS	complementary metal-oxide-semiconductor
CMR	cumulative mass flow rate
CPD	chemical percolation devolatilisation
CSP	computational singular perturbation
DIPPR	Design Institute for Physical Properties
DLR	German Aerospace Center
DLR2017/RM	DLR2017 reduced by Methling
DLR2017/RK	DLR2017 reduced by Kathrotia
DME	dimethylether
DNS	direct numerical simulation
DR	Dubinin-Radushkevich
DRG	direct relation graph method
DRGEP	direct relation graph method with error propagation
DTR	drop-tube reactor
DTU	Technical University of Denmark
EBI ceb	Engler-Bunte-Institute, Fuel Technology
eJL	extended Jones-Lindstedt
eJL/A	alternative extended Jones-Lindstedt

---

---

Acronym	Description
FBR	fluidised-bed reactor
FFBR	free-fall fixed bed reactor
FG-DVC	functional-group, depolymerisation, vaporisation, cross-linking
FZK	Forschungszentrum Karlsruhe; Karlsruhe Research Center
G	ethylene glycol
GC	gas chromatograph
GG	grey-gas
GGPD	generalised Gaussian probability density
GGPD/GMBS	combined generalised Gaussian probability density and generalised membership bell-shaped
GHKS10	90 % ethylene glycol + 10 % wood char HK01
GHKS30	70 % ethylene glycol + 30 % wood char HK07
GL	glycerine
GLR	gas-to-liquid ratio
GMBS	generalised membership bell-shaped
GRI	Gas Research Institute
HVI1	first HVIGasTech
HVIGasTech	Helmholtz Virtual Institute for Gasification Technology
IEVB	Institute for Energy Process Engineering and Fuel Technology
IGT	Institute of Gas Technology
ISAT	in-situ-adaptive-tabulation
ITC vgt	Institute for Technical Chemistry, Gasification Technology
JL	Jones-Lindstedt
JL/A	alternative Jones-Lindstedt
KIT	Karlsruhe Institute of Technology
LDA	laser-Doppler anemometry
LES	large eddy simulation
LHM	Langmuir-Hinshelwood model
MYM	modified Yamamoto model
NASA	National Aeronautics and Space Administration
NDIR	non-dispersive infrared sensor
pSPR	pressurised single-particle reactor
pTGA	pressurised thermogravimetric analyser
PCA	principal component analysis
PDA	phase-Doppler anemometry
PDF	probability density function
PFR	plug-flow reactor
PLM	power-law model

---

---

Acronym	Description
PO	pyrolysis oil
PPDS	Physical Property Data Services
PRESTO	pressure staggering option
PtX	power-to-X
PSTR	perfectly stirred tank reactor
QSSA	quasi-steady state approximation
RANS	Reynolds averaged Navier-Stokes
RD	relative deviation
REGA	atmospheric research entrained flow gasifier
RPM	random pore model
SCM	shrinking core model
SEM	scanning electron microscope
SFORALM	single first-order reaction Arrhenius law model
SIMPLEC	semi-implicit method for pressure linked equations-consistent
SM	model of Sazhin et al.
SMOD	specific minimum oxygen demand
SST	shear-stress transport
STP	at standard conditions according to ISO 10780:1994 [133]
TB	measurements of temperatures using double-bead type B thermocouples
TS	measurements of gas temperature using ceramic shielded type S thermocouples
TU Clausthal	Clausthal University of Technology
TU Wien	Vienna University of Technology
TUC	Clausthal University of Technology
URM	uniform reaction model
VDI	Verein Deutscher Ingenieure
W	water gas reaction
WD	Westbrook-Dryer
WSGG	weighted-sum-of-grey-gas
$\mu$ GC	micro gas chromatograph
$\mu$ GC	measurements of dry gas species volume fractions using micro gas chromatography

---



# 1 Introduction

Numerical modelling and simulation are important elements for design, optimisation and scale-up of high-temperature processes. Through better understanding of process steps, technology developments can be achieved faster with significantly reduced risks and costs, which is also crucial in the fight against climate change. The gasification research at Forschungszentrum Karlsruhe (FZK) / Karlsruhe Institute of Technology (KIT) in collaboration with Clausthal University of Technology (TU Clausthal) has consequently relied on numerical modelling and simulation to adapt existing entrained flow gasification technologies for coal to biogenic and anthropogenic feedstocks. In the early stages, sensitivity simulations with focus on geometry and model parameters were performed using simplified CFD models for the design of the high-pressure entrained flow gasifier of the bioliq pilot plant, the bioliq Entrained Flow Gasifier (bioliq EFG) [61, 87, 148]. At that time, two major limitations were identified for the numerical modelling of the entrained flow gasification of biomass [64, 65]:

- (i) Lack of experimental data on gas temperatures and gas species concentrations from entrained flow gasification processes with biogenic fuels.
- (ii) Lack of appropriate, sufficiently detailed and validated sub-models for the mathematical description of the physical and thermo-chemical conversion of biogenic fuels in entrained flow gasification processes.

To address these knowledge gaps, interdisciplinary research has been carried out in the frame of the Helmholtz Virtual Institute for Gasification Technology (HVIGasTech) [124, 154] and in further direct collaboration between (i) the Engler-Bunte-Institute, Fuel Technology (EBI ceb) of KIT, (ii) the Institute for Technical Chemistry, Gasification Technology (ITC vgt) of KIT and (iii) the Institute for Energy Process Engineering and Fuel Technology (IEVB) of TU Clausthal. The research has been focussed on the overall entrained flow gasification process and its physical and thermo-chemical sub-processes including atomisation, vaporisation, decomposition, devolatilisation and heterogeneous gasification.

Since not all sub-processes can be investigated inside pilot plants even in presence of excellent measurement techniques and possibilities, several atmospheric and pressurised

laboratory-scale plants have been established at KIT to investigate the sub-processes and to develop appropriate sub-models following a two-step approach [63]:

- (i) Experiments and numerical simulations at atmospheric conditions for the development and the validation of improved mathematical sub-models.
- (ii) Experiments and numerical simulations at high-pressure conditions for the development and validation of overall models and for design, operation, optimisation and scale-up.

The work presented in this thesis contributed to this research. Firstly, improved sub-models were developed, evaluated and integrated into overall entrained flow gasification models. Subsequently, the overall models were tested and validated for the atmospheric entrained flow gasification of surrogate fuels.

This chapter provides firstly the introductions to gasification, gasification technologies and the bioliq process in Section 1.1, Section 1.2 and Section 1.3, respectively. Subsequently, the laboratory-scale plants accounted for in this work are presented in Section 1.4. Then, the preceding works are described in Section 1.5. Finally, the objectives of this thesis are given in Section 1.6.

## 1.1 Gasification

Gasification is the conversion of carbonaceous fuels into a raw gas using gasification media under high-temperature and sub-stoichiometric conditions. Gasification media can be oxygen, oxygen enriched air and/or steam. The raw gas is called synthesis gas or syngas. Major components are hydrogen, carbon monoxide, carbon dioxide, water and nitrogen; minor components include methane, higher hydrocarbons, ammonia, hydrogen sulphide, hydrogen cyanide and hydrogen chloride. In addition to gas components, synthesis gas can contain solid or liquid residues such as tar, soot and ash. The exact composition of the synthesis gas depends on the fuel, the gasification technology and the operating conditions.

Gasification technologies have been developed and used for two centuries [125]. The history of gasification is particularly connected (i) with commercial coal gasification for illumination in England during the industrial revolution and (ii) with coal gasification for synthetic fuel production by Lurgi (now Air Liquide) in Germany between the 1920s and 1940s and by Sasol in South Africa since the 1950s [125]. Further gasification technologies were developed for oil gasification by Texaco (later Chevron and now GE Energy) and Shell. However, gasification technologies remained niche technologies until the 1980s despite steadily increasing research expenditures and number of plants [125]. Since then,

there has been an increased interest in these technologies which is partially related to the gasification of biomass and waste fuels [125].

Biomass and waste as feedstocks for gasification processes offer the possibility to close the anthropogenic carbon cycle which is one of the main challenges in the fight against climate change. In order to reduce carbon dioxide emissions, fossil energy carriers in the industrial and the transport sectors need to be replaced by renewable energy carriers. In this context, electricity from renewable sources is the best option for the short-distance transport sector (electric vehicles), while synthetic fuels for the long-distance transport sector (trucks, ships and aircrafts) and chemicals should be produced from renewable feedstocks in the medium term [87]. Therefore, both Power-to-X (PtX) technologies and Biomass-to-Liquid (BtL) technologies are under development [87]. PtX technologies typically rely on hydrogen from electrolysis and on carbon dioxide from industry and atmosphere, whereas BtL technologies are based on synthesis gas from the gasification of biomass.

## 1.2 Gasification technologies

Gasification technologies for biomass rely on the existing gasifier types: fixed bed, fluidised bed and entrained flow. Fixed bed gasifiers consists of moving fuel beds passed by the gas, while fluidised bed gasifiers are based on the suspension of fuel particles in the gas, and entrained flow gasifiers rely on the atomisation of the fuel and the entrainment of the recirculating gas. The technologies are described and discussed in detail elsewhere (for example, see [87, 125, 252]). However, some fundamentals are given below.

**Fixed bed gasifiers** are operated either in counter-current or in co-current mode and typically below the ash melting temperatures. Non-caking fuels with typically high mechanical strength are fed at the top of the gasifier. The gasification media enter the gasifier at the bottom in counter-current operating mode or at the centre in co-current operating mode. The synthesis gas leaves the gasifier at the top in counter-current operating mode or at the bottom in co-current operating mode. It is characterised by fluctuating compositions and high methane, tar or soot contents [87], which are typically lower in co-current than in counter-current mode. Build units of fixed bed gasifiers for biomass are operated at atmospheric conditions with thermal inputs below 1 MW [87]. The units are partially combined with co-generation and produce low-quality synthesis gas for combustion [87].

**Fluidised bed gasifiers** are operated either in stationary fluidised or in circulating mode typically below the ash melting temperatures. The fuels with typically higher corrosive ash contents are fluidised in gasification media. The gasification media enter the gasifier at the centre above the fuel inlet while solid residues and the synthesis gas leave the gasifier at the bottom and the top, respectively. The synthesis

gas can contain high methane, tar or soot contents [252]. Build units of fluidised bed gasifiers for wood developed at TU Wien are operated at atmospheric conditions with thermal inputs of up to 32 MW [87]. The units are combined with co-generation and produce synthesis gas for production of synthetic fuels such as natural gas [87].

**Entrained flow gasifiers** are operated with fuels from a wide range of feedstocks at high-temperature and high-pressure conditions (25-80 bar) either in one-stage or in two-stage mode [125]. In one-stage mode, fuels and gasification media are fed at the top; in two-stage mode, fuels are fed at the centre of both stages while gasification media are fed at the centre of the lower stage. Due to operating temperatures above the ash melting temperature, ash is typically deposited as slag at the cooled wall surfaces. Subsequently, the slag flows down the wall and exits the gasifier at the bottom through a quench. In one-stage mode, the synthesis gas also passes the quench while, in two-stage mode, the synthesis gas leaves the gasifier at the top. High-quality synthesis gas is produced since it is characterised by low methane and tar contents. Large-scale units of entrained flow gasifiers for coal have been constructed for decades while only pilot plants with thermal inputs of up to 15 MW have been developed yet for biomass [206, 239]. At Karlsruhe Research Center (FZK) (until 2009) and Campus North of Karlsruhe Institute of Technology (KIT) (since 2009), a one-stage entrained flow gasifier with a thermal input of approximately 5 MW has been developed as main component of the second stage of the bioliq pilot plant [61, 148].

In comparison with coal, biomass is characterised by lower heating values, by higher moisture and ash contents, by lower ash melting temperatures and by more fluctuating chemical and physical properties. The existing gasifier technologies have accordingly to be adapted to biomass using new concepts such as the bioliq process [87].

### 1.3 bioliq process

The bioliq process is a concept that relies on (i) regional biomass production and supply, (ii) regional energy densification and (iii) central, large-scale conversion to synthetic fuels [61, 148, 350]. The concept was implemented between 2005 and 2013 through the construction of the bioliq pilot plant, which was done in a collaboration between institutes of FZK/KIT, industrial partners<sup>1</sup> and public funding agencies<sup>2</sup> [148]. The bioliq pilot plant consists of four stages:

---

<sup>1</sup>Air Liquid Global Engineering & Construction Solutions Germany, Calida Cleantech, Chemieanlagenbau Chemnitz, MUT Advanced Heating, Bauer MAT Slurry Handling Systems

<sup>2</sup>Federal Ministry of Food and Agriculture (BMEL), Agency for Renewable Resources e.V. (FNR), European Union (EU), the European Regional Development Fund (ERDF), the Baden-Württemberg Ministry of the Environment, Climate Protection and the Energy Sector, Helmholtz Association of German Research Centres (HGF)

**bioliq I: fast pyrolysis and slurry production** Dried and crushed biomass mixed with hot fluidised sand is converted at 500 °C under inert and atmospheric conditions using a twin-screw mixing reactor to organic liquid (34 %), aqueous liquid (25 %), char (20 %) and non-condensable gas (21 %) [87]. The gas is used for providing combustion heat to the process, while the organic liquid (pyrolysis oil) and the char (pyrolysis char) are mixed to pumpable pyrolysis slurries containing up to 40 % char. The pyrolysis slurries from the bioliq pilot plant are called Biosyncrude [87].

**bioliq II: high-pressure gasification** Raw, tar-free synthesis gas is produced from pyrolysis slurries or surrogate slurries with high mineral contents using oxygen and steam as gasification media at high-temperature and high-pressure conditions (40 or 80 bar) enabled by two different burner and reactor configurations. [87] The gasifier is extensively equipped with instrumentation for pressure, temperature and concentration measurements, with optical access for non-intrusive (laser) diagnostics and camera visualisations and with sampling possibilities. The fuel is composed of slurry and natural gas. Natural gas is used for ignition and flame stabilisation. Due to operation in slagging mode, mineral residues leave the gasifier as slag via the segmental cooling screen and the water quench. The slag layer on the cooling screen serves also as protection of the refractory made of SiC. In addition to six water cooling circuits along the cooling screen, one water cooling circuit each is used for the cooling of slurry burner and natural gas burner. Characteristic parameters of the gasifier are given in Tables A.1-A.4.

**bioliq III: gas cleaning and gas conditioning** Raw synthesis gas must be purified after passing the quench in order to protect the catalysts in the gas synthesis [87]. Under high-pressure conditions of up to 80 bar, (i) particles, (ii) alkali salts, heavy metals, H<sub>2</sub>S, HCl and COS and (iii) NH<sub>3</sub> and HCN are removed from the raw synthesis gas using a particle separator at 700-800 °C, a fixed bed adsorber at 500-800 °C and a catalytic converter at 500-800 °C, respectively [61, 87].

**bioliq IV: gas synthesis** Purified synthesis gas is converted to dimethylether (DME) using a water-gas shift reactor, providing an equimolar H<sub>2</sub>/CO ratio, and a synthesis reactor operating at 250 °C and 55 bar [87]. Dimethylether serves as basis for the production of synthetic fuels in a further synthesis reactor at 350 °C and 25 bar [87].

Each stage of the bioliq pilot plant can be operated independently. However, a joint operation of bioliq II, bioliq III and bioliq IV has already been achieved in 2014 [61]. The bioliq pilot plant is used as a demonstration platform [350], as a data generation platform for process design, optimisation and scale-up of industrial size units [154] and as a research platform for KIT and its scientific and industrial partners [350].

## 1.4 Laboratory-scale plants

The experimental data that was used to develop and validate overall models and sub-models in this work was obtained at three laboratory-scale plants:

- (i) the atmospheric research entrained flow gasifier (REGA) at the Institute for Technical Chemistry, Gasification Technology,
- (ii) the atmospheric spray test rig (ATMO) at the Institute for Technical Chemistry, Gasification Technology and
- (iii) the drop-tube reactor (DTR) at Engler-Bunte-Institute, Fuel Technology.

The laboratory-scale plants are described in detail in Sections A.2, A.3 and A.4 and are briefly introduced below.

The **research entrained flow gasifier (REGA)** is used for stationary gasification of carbonaceous liquid and suspension fuels at atmospheric pressure. Surrogate fuels, including ethylene glycol and mixtures of ethylene glycol and wood char, and technical fuels based on biogenic or anthropogenic pyrolysis oils are converted to synthesis gas using oxygen-enriched air as gasification medium and external mixing nozzles. The gasifier is laterally heated up enabling near adiabatic operating conditions. Stoichiometry, process temperature and spray quality can be adjusted independently through changes of the fuel and gas flow rates and the nozzle configuration. Intrusive and non-intrusive measurements inside the gasifier at variable local positions are facilitated by a movable top and multiple lateral ports. The measurements enable the investigation of gas temperature, gas composition, carbon conversion, carbon morphology, droplet velocity distribution and droplet size distribution. Further information is given in Table A.5 and Section A.2.

The **atmospheric spray test rig (ATMO)** is applied for stationary atomisation of liquids and liquid suspensions in an atmospheric open surrounding using pressurised gas and external mixing nozzles and for spray characterisation using laser-based measurements and imaging at different local positions. The nozzle configuration, the operating conditions and the liquid medium are varied in order to investigate the effects of gas velocity, liquid velocity, gas-to-liquid ratio, liquid viscosity and liquid surface tension on spray quality. The spray quality is characterised, for example, by ligament lengths, spray angles, droplet velocity distributions and droplet size distributions. Further information is given in Table A.8 and Section A.3.

The **drop-tube reactor (DTR)** is used for stationary pyrolysis and gasification of solid fuels at atmospheric pressure. The reactor is laterally heated and enables approximately isothermal conditions for the conversion of solid fuels. In addition to fuel and

gas flow rates and gas compositions at the reactor inlets, gas temperatures inside the reactor are adjusted to investigate kinetics and morphology through analysis of the quenched product gas and the characterisation of solid residues. Further information is given in Table A.9 and Section A.4.

Furthermore, results from several internal and external analyses were used in this work including particle size distribution analyses of wood char particles. These analyses and the corresponding devices are introduced in the respective paragraphs.

## 1.5 Preceding works

The work presented in this thesis drew upon the experience which has been gained since 2008 through the constant development of overall models and sub-models for the atmospheric and the high-pressure entrained flow gasification of biogenic fuels. The models for atmospheric conditions were developed with emphasis on the REGA [63, 64, 185, 186, 187] while models for high-pressure conditions were established with focus on the bioliq EFG [65, 66, 135, 136, 186]. Furthermore, numerous CFD simulations have been performed for model validation and sensitivity analysis of the effects of turbulence, thermal radiation, turbulence-chemistry interaction, chemistry and slagging [63, 64, 65, 66, 135, 136, 185, 186, 187].

Since this work continued the research on atmospheric entrained flow gasification, the most important aspects and results from the preceding works [63, 64, 65, 66, 135, 136, 185, 186, 187] are summarised below.

### The preceding CFD models

The development of CFD models with focus on REGA experiments started in 2011 and has been carried out using ANSYS Fluent [9, 10, 11, 12, 13, 17], the RANS approach (see Section 2.2.2) and the Euler-Lagrange approach (see Sections 2.2, 2.2.1 and 2.2.5). The first CFD models applied the standard  $k-\epsilon$ , the realisable  $k-\epsilon$  model, the SST  $k-\omega$  model or the Reynolds stress equation model as turbulence model (see Section 2.2.2) and the discrete ordinates model as thermal radiation model (see Section 2.5). Thermodynamic and transport properties of the gas phase were described using ANSYS Fluent databases and polynomials, Sutherland laws, Chapman-Enskog equations, mass-weighted mixing rules and Wilke mixing rules. The gas absorption coefficient was estimated using the mean beam length model, where the gas emissivity was firstly [185] estimated using an exponential wide-band model [165] and later [187] using the improved emissivity charts of Alberti [8]. Droplet scattering and absorption were firstly [185] neglected and later [187]

approximated using the Mie theory. The physical properties required by the vaporisation model were based on constant values except for the vapour pressure and the effective diffusion coefficient of the fuel. The vapour pressure was approximated using linear splines, and the effective diffusion coefficient was described using an empirical polynomial. Two-dimensional axis-symmetric meshes of the complete REGA geometry with resolved nozzle geometry and approximately  $10^5$  triangular cells were generated [187]. Boundary conditions for the inlets were adopted from the REGA experiments but adjusted in two ways. Firstly, the streams of infiltrated air and purge nitrogen were added to the inlet gas stream. Secondly, the total gas stream was partially passed through the central orifice of the nozzle in order to stabilise the numerical gas flow (see Section 2.2.4.3) [187].

**Table 1.1:** Conditions of the REGA experiments: fuel, nozzle, gas-to-liquid ratio (GLR), technical stoichiometric ratio  $\lambda_{\text{tech}}$  and adiabatic temperature  $T_{\text{ad}}$  [63, 64, 98, 99, 100, 113, 114]. Acronyms: G: ethylene glycol; GHKS10: 90% ethylene glycol + 10% wood char HK01 (in mass fractions); GHKS30: 70% ethylene glycol + 30% wood char HK07 (in mass fractions). Further details about the external mixing nozzles D1, D2 and D1.1 and the wood chars HK01 and HK07 are given in Section C.1 and Sections 2.7.1 and I.1, respectively.

REGA experiment	Fuel	Nozzle	GLR	$\lambda_{\text{tech}}$	$\frac{T_{\text{ad}}}{\text{K}}$	Previously reported as
TUC2 V468	G	D1	1.965	0.750	2677	TUC2 [185]
TUC3 V479	G	D1	1.283	0.571	2282	TUC3 [185, 186] and rega-glycol-T1 [187]
TUC3 V786	G	D1	1.286	0.572	2284	rega-glycol-T1 [98]
TUC5 V1105	G	D2	0.830	0.466	1973	rega-glycol-T2 [64]
TUC5 V1374	G	D1.1	0.829	0.466	1974	—
TUC5 GHKS10 V1071	GHKS10	D2	0.855	0.453	2041	rega-slurry1-T2 [63, 64]
TUC5 GHKS30 V1284	GHKS30	D2	0.817	0.420	1971	rega-slurry2-T2 [64, 100]

## The earlier CFD studies

The earlier studies focused on the CFD simulations of the REGA experiments TUC2 V468 [185] and TUC3 V479 [185, 186, 187] with ethylene glycol (see Tables 1.1, B.1, B.2 and B.3). The CFD simulations were performed to identify the most appropriate model for the gas chemistry [185, 186, 187] (see Sections 2.3 and 2.4). Turbulence-chemistry interaction models and reaction mechanisms were tested with focus (i) on the prediction of the micro-mixing in the flame region, (ii) on the prediction of the gas composition outside the flame region and (iii) on the applicability to industrial entrained flow gasifiers [187]. Therefore, the gas chemistry was described using (i) the  $\beta$ -PDF model combined with the equilibrium approach, (ii) the  $\beta$ -PDF model combined with the flamelet approach or (iii) the eddy-dissipation-concept model combined with a global reaction mechanism [185,

186, 187]. For the latter approach, global reaction mechanisms were calibrated using one-dimensional PFR and PSTR simulations with Chemkin [253, 254] and using the DLR mechanism of Hafner et al. [115, 116] and the GRI mechanism [294] (see Section 2.3) as benchmark reaction mechanisms.

Preliminary and final results of the CFD simulations demonstrated that the  $\beta$ -PDF model provided superior predictions of gas temperatures and dry gas species concentrations for the REGA experiment TUC2 V468 and superior predictions of gas temperatures for the REGA experiment TUC3 V479, when the model was combined with the equilibrium approach and radicals were accounted for [185, 186, 187]. In contrast, the eddy-dissipation-concept model was superior for the predictions of the dry gas species concentrations with respect to the REGA experiment TUC3 V479 when applying an appropriate global reaction mechanism for the gasification of ethylene glycol [187].

Two reaction mechanisms were proposed [187]: the first HVI GasTech (HVI1) mechanism and the extended Jones-Lindstedt (eJL) mechanism (see Section 2.3.1). Both reaction mechanisms provided accurate dry gas species concentrations of CO, CO<sub>2</sub> and H<sub>2</sub> at two specific nozzle distances (300 mm and 680 mm). Dry gas species concentrations of CH<sub>4</sub> were slightly overpredicted by the HVI1 mechanism and underpredicted by the eJL mechanism [187]. Generally, the HVI1 mechanism was slightly superior since the correct CO/CO<sub>2</sub> ratios could be predicted in the near-axis region [187]. However, gas temperatures in the flame region were slightly overpredicted since radicals are not included in both reaction mechanisms [187].

Further sensitivity analyses were performed to investigate the effects of the turbulence model, the initial droplet diameter distribution, the thermal gas radiation property model and the thermal droplet radiation property model [187]. The results are described below.

**Turbulence model** Small sensitivities were found for the gas temperature and the dry gas species concentrations when the baseline SST  $k$ - $\omega$  model was replaced by the standard  $k$ - $\epsilon$  model, the realisable  $k$ - $\epsilon$  model or the Reynolds stress equation model [187]. Larger deviations were visible for the gas velocity and for the strength of the recirculation zone [187].

**Initial droplet diameter distribution** Effects on the radial profiles of gas temperature and dry gas species concentrations were found when particles were injected based on a broadened droplet size distribution (generated from the baseline droplet size distribution) since the vaporisation behaviour is directly affected by the initial droplet diameters [187]. Particles with larger diameters vaporised increasingly outside the flame region [187].

**Thermal gas radiation property model** Visible differences were found in the predictions of the wall temperatures as well as the total, the convection and the radiation wall heat fluxes, each in the upper region, when the constant gas absorption coefficient

based on the mean beam length model was replaced by a weighted-sum-of-grey-gas model generated using improved emissivity charts [187]. The wall temperatures increased slightly whereas the radiation and the total heat flow rates decreased [187]. The proportion of radiative heat transfer in the total heat flow rate increased from 77% to 93% [187].

**Thermal droplet radiation property model** Radiation source terms were strongly affected in the injection region when droplet scattering and absorption were described by improved correlations instead of by an isotropic phase function and constant values for droplet emissivity and droplet scattering factor [187]. The improved approximations were based on the Mie theory, the software of Maetzler [195], the refractive index measurements of Sani and Dell’Oro [266], the initial droplet size distribution and a reference source temperature of 1400 K. Outside the injection region, the radiation source terms were not affected due to the low proportion of thermal droplet radiation in thermal radiation [187].

### The later CFD studies

The later studies focussed on the CFD simulations of the REGA experiments TUC5 V1105, TUC5 GHKS10 V1071 and TUC5 GHKS30 V1284 [63, 64] (see Tables 1.1, B.1, B.2 and B.3) that are characterised by similar adiabatic temperatures. The REGA experiment TUC5 V1105 is another gasification experiment with ethylene glycol while the REGA experiments TUC5 GHKS10 V1071 and TUC5 GHKS30 V1284 are gasification experiments with mixtures of ethylene glycol and wood char.

The first CFD simulations of the REGA experiment TUC5 V1105 were challenged by species imbalances. Therefore, finer meshes of the upper part of the REGA were generated and subsequently applied for the CFD simulations. The improved meshes enabled a continuing good performance of the HVI1 mechanism and the eJL mechanism [63, 64]. Additionally, new modelling approaches for the supply of infiltrated air and purge nitrogen and for the droplet injection were initiated to comply with the momentum balance at nozzle inlet and to improve the predictions of the recirculation zone and the droplet dispersion [64] (see Section 2.2.4).

The first results of the CFD simulations of the REGA experiments TUC5 GHKS10 V1071 and TUC5 GHKS30 V1284 with the HVI1 mechanism demonstrated that the radial profiles of the gas temperature were in good agreement with the measurement data [63, 64]. However, this did not apply for the radial profiles of the dry gas species concentrations [63, 64]. The deviations were related to errors in the elemental balances. The errors increased with increasing wood char content and were probably induced by the coupling of the gas phase and the dispersed phase.

## 1.6 Objectives

This thesis is focussed on the development, implementation and evaluation of improved CFD sub-models for the atmospheric entrained flow gasification and has got five main objectives:

1. Improvement of the preceding overall model [187] for the atmospheric entrained flow gasification of ethylene glycol.
2. Application of the improved overall model to two atmospheric entrained flow gasification experiments with ethylene glycol (REGA experiments TUC3 V786 and TUC5 V1105).
3. Development and implementation of improved sub-models for the atmospheric entrained flow gasification of wood char.
4. Development of an overall model for the atmospheric entrained flow gasification of mixtures of ethylene glycol and wood char.
5. Application of the second overall model to two atmospheric entrained flow gasification experiments with mixtures of ethylene glycol and wood char (REGA experiments TUC5 GHKS10 V1071 and TUC5 GHKS30 V1284).

Improved sub-models were developed or tested for the supply of infiltrated air and purge nitrogen (see Section 2.2.3.3 and 4.2), the inlet conditions and the injection properties (see Section 2.2.4.4, 4.1, 4.2, 4.3 and 4.9), the vaporisation of ethylene glycol (see Section 2.6.4 and 4.6), the particle diameter changes during heterogeneous gasification (see Section 2.7.3.12), the devolatilisation of beech wood char (see [68] and Sections 2.7.4.3, 2.7.4.5 and 4.10) and the heterogeneous gasification of beech wood char (see Sections 2.7.5.4 and 4.10). This thesis presents (i) the model fundamentals for the atmospheric entrained flow gasification of ethylene glycol and mixtures of ethylene glycol and wood char, (ii) the methods used to perform and evaluate the CFD simulations and (iii) the results of the CFD simulations of the REGA experiments. The model fundamentals are described in Chapter 2. The methods are summarised in Chapter 3. The results are presented in Chapter 4. In comparison with previous publications [63, 64, 187], the results are based on revised models and methods especially to close the elemental and energy balances (see Section 1.5). The conclusions are finally given in Chapter 5.



## 2 Model fundamentals

This chapter describes the model fundamentals for the atmospheric entrained flow gasification of ethylene glycol and mixtures of ethylene glycol and wood char. Firstly, the general physical and thermo-chemical process steps of entrained flow gasification are summarised in Section 2.1. Then, the model fundamentals of multiphase flows, homogeneous reaction kinetics, turbulence-chemistry interactions and thermal radiation are presented in Section 2.2, Section 2.3, Section 2.4 and Section 2.5, respectively. Due to the application of widely established models in this work, the models are only briefly described. Detailed information about multiphase flows, turbulent flows, atomisation processes, turbulence-chemistry interaction, combustion and thermal radiation can be found elsewhere (for example, see [59], [245, 335], [170], [243] and [129, 209], respectively). Subsequently, overviews of the models for the vaporisation of ethylene glycol and the conversion of wood char are given in Section 2.6 and Section 2.7, respectively.

General reviews of entrained flow gasification and its sub-processes are not provided in this thesis since they can be found elsewhere. Specifically, Nikrityuk et al. [223] and Mularski et al. [214] recently reviewed the latest developments in CFD models for coal entrained flow gasification and discussed the improvements in sub-models for coal devolatilisation and coal char conversion.

### 2.1 Physical and thermo-chemical process steps

Physical and thermo-chemical process steps are used to simplify the mathematical description of more complex processes. For entrained flow gasification, numerous process steps have been identified, which are linked and influence each other in diverse ways. However, following Fig. 2.1, some major sub-processes can be used to describe the overall conversion [170, 187, 265]:

**Atomisation** is primarily the disintegration of the continuous slurry into a dispersed phase containing smaller discrete elements of different sizes, shapes and compositions using atomisation media. The elements include slurry fragments, slurry ligaments, slurry droplets and solid particles. Important process steps linked with atomisation are collision, coalescence, bouncing, near head-on separation and off-centre separation.

**Liquid conversion** describes the phase transition of liquid components from the dispersed into the gas phase through drying, vaporisation or boiling.

**Devolatilisation / secondary pyrolysis** is characterised by the release of secondary volatiles from the primary char into the gas phase. Important process steps connected with devolatilisation are swelling, fragmentation and thermal annealing.

**Homogeneous gasification** describes the conversion of gas components inside and outside the flame to synthesis gas through hydrogen oxidation, carbon monoxide oxidation, methane reforming reaction, water-gas shift reaction, secondary gas decomposition, soot formation and tar formation.

**Heterogeneous gasification** focusses on the conversion of secondary char with the gas species (for example, carbon dioxide and water vapour) and is linked with film diffusion, pore diffusion, adsorption, chemical reactions and desorption.

**Non-reactive gas heat and mass transfer** summarises the process steps associated with diffusion, convection and thermal radiation.

**Non-reactive particle heat and mass transfer** describes the motion, the collision and the heating and cooling of particles.

**Mineral matter transformation** summarises all process steps connected with the conversion of mineral components during fuel conversion, which includes vaporisation, homogeneous and heterogeneous condensation, chemical reactions, nucleation and sintering.

**Slagging** describes the impingement of particles containing mainly liquid mineral components on walls surfaces, the formation of the slag flow and the heat transfer in wall, slag and wall boundary layer.

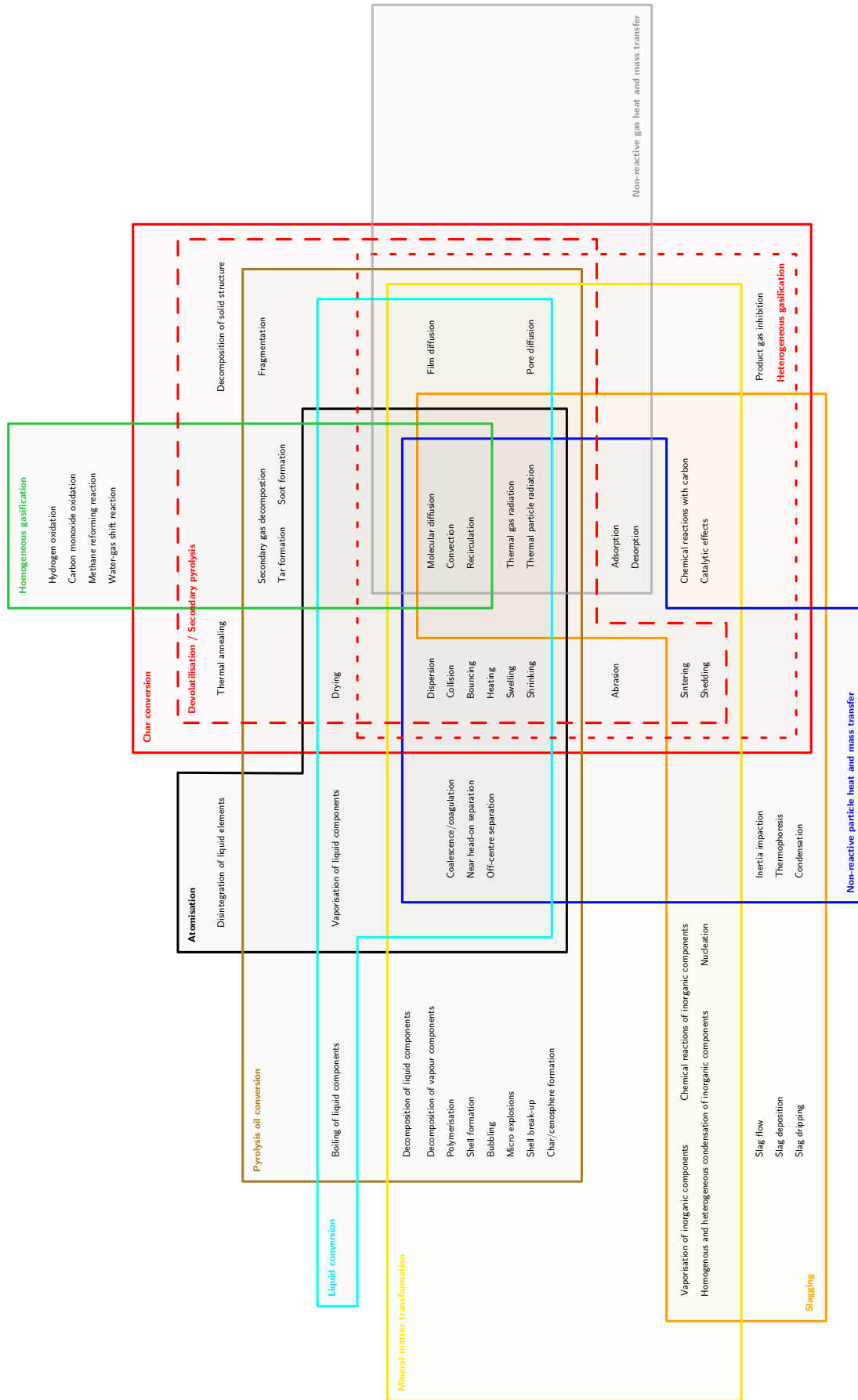
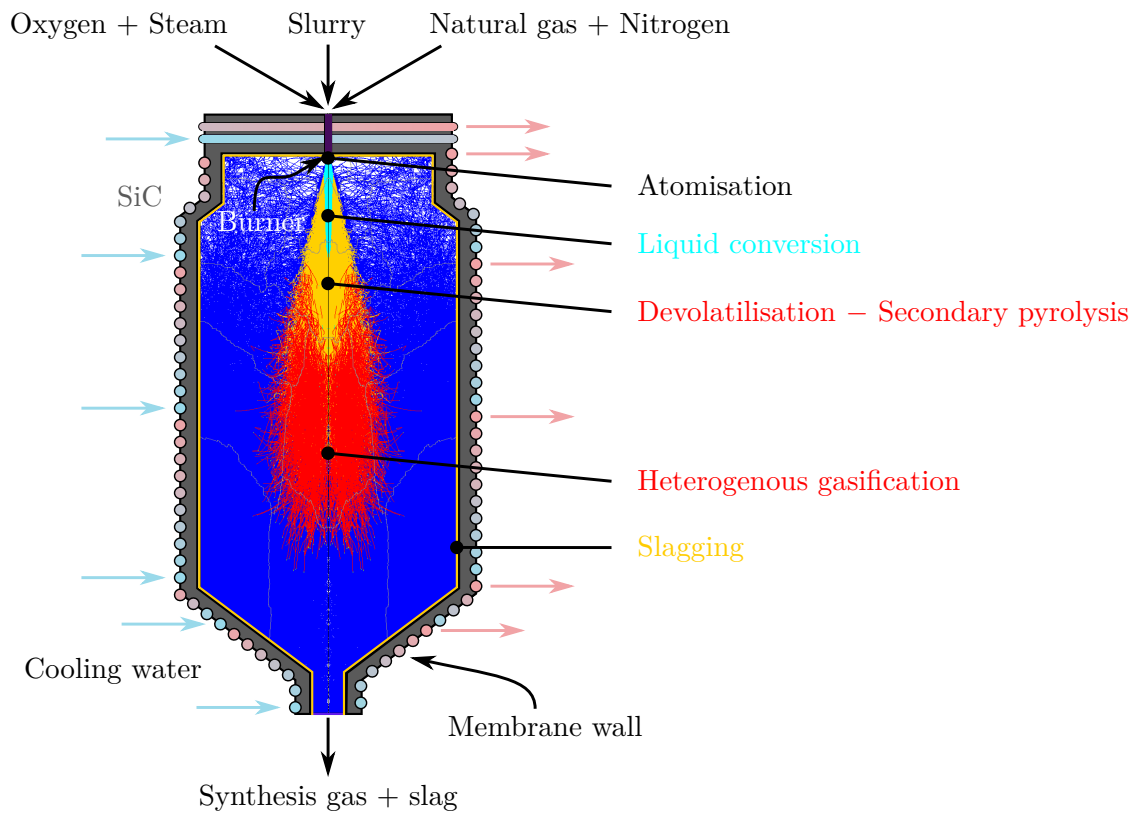


Figure 2.1: Physical and thermo-chemical process steps and sub-processes of entrained flow gasification.

Some sub-processes are schematically illustrated in Fig. 2.2 using the numerical trajectories of slurry particles inside the bioliq EFG. The slurry consisting of ethylene glycol and primary wood char is converted through atomisation, liquid conversion, devolatilisation/secondary pyrolysis and heterogeneous gasification to synthesis gas, which contains  $H_2$ ,  $CO$ ,  $CO_2$ ,  $H_2O$ ,  $N_2$ ,  $CH_4$ ,  $NH_3$ ,  $H_2S$ ,  $HCN$ ,  $HCl$ , higher hydrocarbons, tar, soot as well as char and ash residues. Further relevant sub-processes are slagging, homogeneous gasification and mineral matter transformation. Slagging takes place on the wall while homogeneous gasification and mineral matter transformation occur in almost the entire reactor.



**Figure 2.2:** Sub-processes of entrained flow gasification illustrated for the gasification of ethylene glycol and wood char in the bioliq EFG [64, 67]. For a visible distinction, the trajectories with regard to devolatilisation are marked in orange.

## 2.2 Multiphase flows

Multiphase flows are flows with at least two different phases and can be divided into separated flows and dispersed flows [59]. Separated flows contain continuous phases with interphases [59] and are typically described using the Euler-Euler approach, while dispersed flows consist of discrete elements in continuous phases including droplets and solid particles in gas flows [59] and are mainly modelled using the Euler-Lagrange approach.

The Euler-Euler approach applies the Eulerian specification for both the primary and the secondary phase and requires calibrated terms for the phase interactions. This approach is advantageous not only when higher volume fractions of the solid/liquid phase are expected but also when low computing times and parallelisation possibilities are regarded as beneficial.

The Euler-Lagrange approach describes the primary phase in the Eulerian specification and the secondary phase in the Lagrangian specification and is used in combination with both RANS based simulations and large eddy simulations (see Section 2.2.2). The injection properties for the dispersed phase are either assumed or derived from measured particle, droplet or bubble quantity distributions, while the particle, droplet or bubble trajectories are determined using steady-state tracking or transient tracking. Steady-state tracking is typically applied when performing steady-state RANS based simulations while transient tracking is usually combined with transient RANS based or large eddy simulations. Transient tracking enables to integrate break-up models but typically increases the computing time. This applies in particular when describing particles, droplets or bubbles with long residence times. In entrained flow gasification processes, either solid particles are mixed with gas or liquid/slurry droplets are generated through gas-assisted atomisation of continuous liquids/slurries. Therefore, the Euler-Lagrange approach was used in most of previous CFD studies on entrained flow gasification, while the Euler-Euler approach was only applied in a few CFD studies [101, 102, 326].

Vicente et al. [326] listed computing time and parallelisation as advantages of the Euler-Euler approach, while Fradet [102] pointed out high volume fractions of liquid or slurry in the near nozzle region and injection properties as challenges of the Euler-Lagrange approach. However, high droplet volume fractions are typically confined to the near-nozzle region. Furthermore, computing times nowadays only matter for large eddy simulations coupled with transient tracking of solid particles. Therefore, only the injection properties should be regarded as major challenge of the Euler-Lagrange approach. If computing times do not matter, appropriate injection properties can be generated for the gasification of liquids/slurries using large eddy simulations combined with the volume-of-fluid method as the transition from the continuous phase to the dispersed phase (i. e. from the Eulerian to the Lagrangian specification) can be completely described using numerical methods. However, this approach is currently not feasible for a substantial number of CFD simulations. Therefore, injection properties are typically calibrated using experiments. Such an approach was also used in this work and the preceding works [63, 64, 185, 186, 187]. The model equations for the continuous gas phase are presented in Sections 2.2.1 and 2.2.3, while the transport equations for the dispersed phase are described in Section 2.2.5. In addition, turbulent flows and atomisation processes are introduced in Section 2.2.2 and Section 2.2.4, respectively.

## 2.2.1 Continuous gas phases

Continuous gas phases are generally described using the transient transport equations for mass, species, momentum and energy in the Eulerian specification. The balance equations can be derived in differential or integral form assuming local thermal equilibrium and using the principles of conservation of mass, momentum and energy<sup>1</sup>. The equations for steady-state gas phases are given in Sections 2.2.1.1, 2.2.1.2, 2.2.1.3 and 2.2.1.4, while detailed derivations of the Navier-Stokes equations and the species balance equations are not be provided in this thesis.

### 2.2.1.1 Continuity equation

The continuity equation for steady-state gas phases is given by

$$\operatorname{div}(\rho \mathbf{u}_{\text{gas}}) = S_{\text{m,part}} + S_{\text{m,at wall}}, \quad (2.1)$$

where  $\rho_{\text{gas}}$  is the gas density,  $\mathbf{u}_{\text{gas}}$  is the gas velocity and  $S_{\text{m,part}}$  and  $S_{\text{m,at wall}}$  are the mass source terms due to interactions with the dispersed phase (see Section 2.2.5) and due to air infiltration and supply of purge nitrogen near the wall (see Section 2.2.3.3), respectively.

### 2.2.1.2 Species balance equation

The species balance equations for steady-state gas phases are given by

$$\operatorname{div}(\rho_{\text{gas}} \mathbf{u}_{\text{gas}} w_{i,\text{gas}}) = -\operatorname{div}(\mathbf{j}_{\text{m},i,\text{gas}}) + S_{\text{w,react},i} + S_{\text{w,part},i} + S_{\text{w,at wall},i} \quad (2.2)$$

for  $i = 1, \dots, N_{\text{sp}} - 1$ ,

$$w_{N_{\text{sp}},\text{gas}} = 1 - \sum_{i=1}^{N_{\text{sp}}-1} w_{i,\text{gas}}, \quad (2.3)$$

where  $w_{i,\text{gas}}$  is the gas species mass fraction of species  $i$ ,  $\mathbf{j}_{\text{m},i,\text{gas}}$  is the mass diffusion flux of species  $i$ ,  $S_{\text{w,react},i}$ ,  $S_{\text{w,part},i}$  and  $S_{\text{w,at wall},i}$  are the source terms of species  $i$  due to chemical reactions, due to interactions with the dispersed phase and due to air infiltration and supply of purge nitrogen near the wall, respectively, and  $N_{\text{sp}}$  is the number of species.

Neglecting the influence of thermal diffusion, the mass diffusion flux of species  $i$   $\mathbf{j}_{\text{m},i,\text{gas}}$  is defined by

$$\mathbf{j}_{\text{m},i,\text{gas}} = -\sum_{j=1}^{N_{\text{sp}}} \rho_{\text{gas}} F_{i,j,\text{gas}} \nabla w_{j,\text{gas}} + \rho_{\text{gas}} D_{\text{turb}} \nabla w_{i,\text{gas}} \quad \text{for } i = 1, \dots, N_{\text{sp}} - 1, \quad (2.4)$$

---

<sup>1</sup>Only the principles of conservation of momentum and energy are actually physical laws while the principle of conservation of mass is an approximation of the classical mechanics.

where  $F_{i,j,\text{gas}}$  is the Fickian gas diffusion coefficient of species  $i$  in  $j$ , which is not identical with the binary gas diffusion coefficient of species  $i$  in  $j$   $D_{i,j,\text{gas}}$  (see Section F.5.5). The turbulent diffusion coefficient  $D_{\text{turb}}$  is defined by

$$D_{\text{turb}} = \frac{\eta_{\text{turb}}}{\rho_{\text{gas}} Sc_{\text{turb}}}, \quad (2.5)$$

where  $\eta_{\text{turb}}$  is the turbulent viscosity and  $Sc_{\text{turb}} = 0.7$  is the turbulent Schmidt number. Since turbulent diffusion dominates in turbulent flows, the dilute approximation can be accepted to simplify the mathematical description of laminar diffusion. The mass diffusion flux of species  $i$   $\mathbf{j}_{m,i,\text{gas}}$  is given by

$$\mathbf{j}_{i,\text{gas}} = -(\rho_{\text{gas}} D_{i,\text{gas,eff}} + \rho_{\text{gas}} D_{\text{turb}}) \nabla w_{i,\text{gas}} \quad \text{for } i = 1, \dots, N_{\text{sp}} - 1, \quad (2.6)$$

where  $D_{i,\text{gas,eff}}$  is the effective laminar gas diffusion coefficient of species  $i$  (see Section F.5.5).

### 2.2.1.3 Momentum equation

The momentum equation can be derived from the second law of Newton. Neglecting external forces beyond gravity, the momentum equation for steady-state gas phase is given by

$$\text{div}(\rho_{\text{gas}} \mathbf{u}_{\text{gas}} \mathbf{u}_{\text{gas}}) = -\nabla p_{\text{gas}} + \text{div}(\boldsymbol{\tau}) + \text{div}(\boldsymbol{\tau}_{\text{R}}) + \rho_{\text{gas}} \mathbf{g} + \mathbf{S}_{\text{u,part}} + \mathbf{S}_{\text{u,at wall}}, \quad (2.7)$$

where  $p_{\text{gas}}$  is the (absolute) gas pressure,  $\boldsymbol{\tau}$  is the shear stress tensor,  $\boldsymbol{\tau}_{\text{R}}$  is the Reynolds shear stress tensor,  $\mathbf{g}$  is the acceleration due to gravity and  $\mathbf{S}_{\text{u,part}}$  and  $\mathbf{S}_{\text{u,at wall}}$  are the momentum source terms due to interactions with the dispersed phase and due to air infiltration and supply of purge nitrogen near the wall, respectively. The Reynolds shear stress tensor  $\boldsymbol{\tau}_{\text{R}}$  accounts for turbulence and is discussed in Section 2.2.2.3, while the shear stress tensor  $\boldsymbol{\tau} = (\tau_{i,j})$  is generally given for a Newtonian fluid by

$$\boldsymbol{\tau} = \mu_{\text{gas}} \text{div}(\mathbf{u}_{\text{gas}}) \mathbf{I} + 2\eta_{\text{gas}} \mathbf{S}, \quad (2.8)$$

where  $\mu_{\text{gas}}$  is the second gas viscosity and  $\mathbf{S}$  is the strain rate tensor. The strain rate tensor  $\mathbf{S} = (S_{i,j})$  is given by

$$S_{i,j} = \frac{1}{2} \left( \frac{\partial u_{\text{gas},i}}{\partial x_j} + \frac{\partial u_{\text{gas},j}}{\partial x_i} \right) \quad (2.9)$$

and is the symmetric part of the Jacobian matrix of the gas velocity  $\mathbf{J}_{\mathbf{u}_{\text{gas}}}$ , whereas the rotation rate tensor  $\boldsymbol{\Omega} = (\Omega_{i,j})$  is the antisymmetric part and is defined by

$$\Omega_{i,j} = \frac{1}{2} \left( \frac{\partial u_{\text{gas},i}}{\partial x_j} - \frac{\partial u_{\text{gas},j}}{\partial x_i} \right). \quad (2.10)$$

As the shear stress tensor  $\boldsymbol{\tau}$  is independent of the rotation rate tensor  $\boldsymbol{\Omega}$  and depends only on the strain rate tensor  $\boldsymbol{S}$ , the gas phase is isotropic. Furthermore, assuming the hypothesis of Stokes

$$\mu_{\text{gas}} + \frac{2}{3} \eta_{\text{gas}} = 0, \quad (2.11)$$

the shear stress tensor  $\boldsymbol{\tau} = (\tau_{i,j})$  can also be described by

$$\tau_{i,j} = 2 \eta_{\text{gas}} \left( S_{i,j} - \frac{1}{3} \frac{\partial u_{\text{gas},k}}{\partial x_k} \delta_{i,j} \right) = \eta_{\text{gas}} \left( \frac{\partial u_{\text{gas},i}}{\partial x_j} + \frac{\partial u_{\text{gas},j}}{\partial x_i} - \frac{2}{3} \frac{\partial u_{\text{gas},k}}{\partial x_k} \delta_{i,j} \right). \quad (2.12)$$

### 2.2.1.4 Energy equation

The energy equation was applied using the specific (total) gas energy  $\hat{E}_{\text{gas}}$  defined by

$$\hat{E}_{\text{gas}} = \hat{H}_{\text{phys,gas}} - \frac{p_{\text{gas}}}{\rho_{\text{gas}}} + \frac{1}{2} \|\mathbf{u}_{\text{gas}}\|^2, \quad (2.13)$$

where

$$\hat{H}_{\text{phys,gas}} = \sum_i w_{i,\text{gas}} \int_{T_{\text{ref}}}^{T_{\text{gas}}} \hat{C}_{p,i,\text{gas}} dT \quad (2.14)$$

is the specific physical gas enthalpy calculated using the gas temperature  $T_{\text{gas}}$ , the reference temperature  $T_{\text{ref}}$  and the specific gas heat capacity of species  $i$   $\hat{C}_{p,i,\text{gas}}$ . Based on the first law of thermodynamics, the energy equation for steady-state gas phases is given by

$$\begin{aligned} \text{div}(\mathbf{u}_{\text{gas}}(\rho_{\text{gas}} E_{\text{gas}} + p_{\text{gas}})) &= \text{div} \left( \lambda_{\text{eff}} \nabla T + \sum_i \hat{H}_{\text{phys},i,\text{gas}} \mathbf{j}_{i,\text{gas}} + \underbrace{\boldsymbol{\tau}_{\text{eff}} \mathbf{u}_{\text{gas}}}_{=0} \right) \\ &+ S_{\text{E,react}} + S_{\text{E,rad}} + S_{\text{E,part}} + S_{\text{E,at wall}}, \end{aligned} \quad (2.15)$$

where  $\lambda_{\text{eff}}$  is the effective thermal conductivity,  $\hat{H}_{\text{phys},i,\text{gas}}$  is the specific physical gas enthalpy of species  $i$ ,  $\boldsymbol{\tau}_{\text{eff}}$  is the effective shear stress tensor and  $S_{\text{E,react}}$ ,  $S_{\text{E,rad}}$ ,  $S_{\text{E,part}}$  and  $S_{\text{E,at wall}}$  are the energy source terms due to chemical reactions, due to thermal radiation, due to interactions with the dispersed phase and due to air infiltration and supply of purge nitrogen near the wall, respectively. The viscous dissipation term has been neglected in this work. The effective thermal conductivity  $\lambda_{\text{eff}}$  is given by

$$\lambda_{\text{eff}} = \lambda_{\text{gas}} + \lambda_{\text{turb}}, \quad (2.16)$$

where  $\lambda_{\text{gas}}$  is the gas thermal conductivity and  $\lambda_{\text{turb}}$  is the turbulent thermal conductivity. The turbulent thermal conductivity  $\lambda_{\text{turb}}$  is defined by

$$\lambda_{\text{turb}} = \frac{\hat{C}_{p,\text{gas}} \eta_{\text{turb}}}{Pr_{\text{turb}}}, \quad (2.17)$$

where  $\hat{C}_{p,\text{gas}}$  is the specific gas heat capacity and  $Pr_{\text{turb}} = 0.85$  is the turbulent Prandtl number.

## 2.2.2 Turbulent flows

Turbulent flows are unsteady, three-dimensional, irregular, seemingly random and chaotic flows [245] consisting of eddies with a wide range of time and length scales. As turbulent flows have been studied experimentally and theoretically for many decades, numerous mathematical approaches have been developed to describe the turbulence effects. Currently, direct numerical simulations, large eddy simulations, PDF based simulations and RANS based simulations are mainly used to compute turbulent flows.

**Direct numerical simulations** (DNS) are used to describe all turbulent scales through the numerical solution of the Navier-Stokes equations using appropriate fine resolutions for time and space. This can already be achieved for reactive flows in small domains (for example, see [2]), while simulations of reactive flows with atomisation processes in technical domains are currently not feasible even on high-performance computers.

**Large eddy simulations** (LES) rely on the separation of the larger and the smaller turbulent scales since the larger scales strongly depend on the domain and are not universal while the smaller scales have a more universal character [245, 264]. Therefore, filtered Navier-Stokes equations are solved using closure models for turbulence and chemistry to incorporate the effects of the smaller structures [245, 264]. Large eddy simulations can be performed for reactive flows in technical domains but only using additional simplifications in presence of dispersed phases (for example, see [88]). Simulations are typically carried out for selected operating conditions while extensive sensitivity analyses are not performed for computing time reasons.

**PDF based simulations** are based either on two transport equations for the dissipation and the probability density function of gas velocity or, superior to that, on a single transport equation for the joint probability density function of gas velocity and frequency [245]. Since the joint probability density function is a function of seven variables, the transport equation is solved using particle methods instead of finite methods. However, this still requires high computing times.

**RANS based simulations** rely on the Reynolds averaged Navier-Stokes (RANS) equations or the Favre averaged Navier-Stokes equations. Both approaches are based on averaged Navier-Stokes equations and on calibrated closure models for turbulence and chemistry. RANS based simulations are usually applied for technical domains and sensitivity analyses due to relatively short computing times compared to direct numerical simulations and large eddy simulations. However, the accuracy of the solutions strongly depends on the closure models.

In previous CFD studies on entrained flow gasification, RANS based simulations were strongly preferred over large eddy simulations. Although the requirements on computing time have significantly diminished for some time now, large eddy simulations were only applied in the studies of Abani and Ghoniem [1] and of Eckel et al. [88, 89]. Both studies have shown that large eddy simulations have advantages to describe mixing and particle dispersion but can obviously not solve deficiencies of homogeneous and heterogeneous reaction kinetics and incomplete information about boundary conditions.

Since large eddy simulations cannot be used for extensive sensitivity analyses, RANS based simulations using the Favre averaged Navier-Stokes equations were eventually applied in this work. Thus, simplified models were incorporated to describe turbulence and turbulence-related phenomena such as atomisation and turbulence-chemistry interaction. The Favre averaged Navier-Stokes equations are based on the concepts of Reynolds averaging and Favre averaging, which are described in Section 2.2.2.1 and Section 2.2.2.2, respectively. Subsequently, the Favre averaged Navier-Stokes equations are introduced in Section 2.2.2.3.

### 2.2.2.1 Reynolds averaging

Reynolds averaging is applied for constant density flows and is based on the decomposition of a transported quantity  $\varphi$  into an averaged part  $\langle \varphi \rangle_{\text{R}}$  and a fluctuating part  $\varphi'$  as given by

$$\varphi(\mathbf{x}, t) = \langle \varphi(\mathbf{x}, t) \rangle_{\text{R}} + \varphi'(\mathbf{x}, t) , \quad (2.18)$$

where

$$\langle \varphi(\mathbf{x}, t) \rangle_{\text{R}} = \frac{1}{\Delta t} \int_t^{t+\Delta t} \varphi(\mathbf{x}, \tilde{t}) \, d\tilde{t} . \quad (2.19)$$

Thus, Reynolds averaging is characterised by  $\langle \varphi'(\mathbf{x}, t) \rangle_{\text{R}} = 0$ .

### 2.2.2.2 Favre averaging

Favre averaging is used for compressible flows and is defined by

$$\langle \varphi(\mathbf{x}, t) \rangle_{\text{F}} = \frac{\langle \rho \varphi(\mathbf{x}, t) \rangle_{\text{R}}}{\langle \rho(\mathbf{x}, t) \rangle_{\text{R}}}, \quad (2.20)$$

where

$$\langle \rho \varphi(\mathbf{x}, t) \rangle_{\text{R}} = \frac{1}{\Delta t} \int_t^{t+\Delta t} \rho(\mathbf{x}, \tilde{t}) \varphi(\mathbf{x}, \tilde{t}) \, d\tilde{t}, \quad (2.21)$$

$$\langle \rho(\mathbf{x}, t) \rangle_{\text{R}} = \frac{1}{\Delta t} \int_t^{t+\Delta t} \rho(\mathbf{x}, \tilde{t}) \, d\tilde{t}. \quad (2.22)$$

Thus, Favre averaging is characterised by  $\langle \rho \varphi'(\mathbf{x}, t) \rangle_{\text{R}} = 0$  and  $\langle \varphi'(\mathbf{x}, t) \rangle_{\text{F}} \neq 0$ .

### 2.2.2.3 Favre averaged Navier-Stokes equations

In order to obtain the Favre averaged Navier-Stokes equations, Favre averaging is applied on the Navier-Stokes equations. In this thesis, this should be illustrated for the transport equation of a quantity  $\varphi$

$$\frac{\partial(\rho \varphi)}{\partial t} + \text{div}(\rho \varphi \mathbf{u}) = \text{div}(\Gamma_{\varphi} \nabla \varphi) + S_{\varphi}, \quad (2.23)$$

where  $\rho$  is the density,  $\mathbf{u}$  is the velocity,  $\Gamma_{\varphi}$  is the diffusion coefficient with respect to  $\varphi$  and  $S_{\varphi}$  is the source term with respect to  $\varphi$ .

Applying Favre averaging, the Favre averaged transport equation is given by

$$\frac{\partial(\langle \rho \rangle_{\text{R}} \langle \varphi \rangle_{\text{F}})}{\partial t} + \text{div}(\langle \rho \rangle_{\text{R}} \langle \varphi \rangle_{\text{F}} \langle \mathbf{u} \rangle_{\text{F}} + \langle \rho \varphi' \mathbf{u} \rangle_{\text{R}}) = \langle \text{div}(\Gamma_{\varphi} \nabla \varphi) \rangle_{\text{R}} + S_{\varphi}. \quad (2.24)$$

Since this equation still contains a fluctuating part, the averaged transport equation is not closed, which represents the *closure problem* of Favre averaged transport equations. Furthermore, this demonstrates that the closure problem is not restricted to one specific transport equation in view of the fact that the momentum equation and the corresponding fluctuating part, the Reynolds stress tensor, are the typical focus of the discussion of the closure problem. Other transport equations such as the energy equation and the species balance equations also require models for the unclosed terms.

In this work, the Reynolds stress tensor was described using the approximation of Boussinesq in combination with either the standard  $k$ - $\epsilon$  model [166, 167] or the shear-stress transport (SST)  $k$ - $\omega$  model [200] since the preceding work [187] demonstrated only small sensitivities with respect to the distributions of gas temperature and gas species

concentrations (see Section 1.5). The Reynolds stress tensor  $\boldsymbol{\tau}_R = (\tau_{R,i,j})$  is given by

$$\tau_{R,i,j} = -\langle \rho_{\text{gas}} u'_{\text{gas},i} u'_{\text{gas},j} \rangle = 2 \eta_{\text{turb}} S_{i,j} - \frac{2}{3} \left( \rho_{\text{gas}} k + \eta_{\text{turb}} \frac{\partial u_{\text{gas},k}}{\partial x_k} \right) \delta_{i,j}, \quad (2.25)$$

where  $\eta_{\text{turb}}$  is the turbulent dynamic viscosity and  $k$  is the turbulent kinetic energy. The latter is the first transported quantity of both the standard  $k$ - $\epsilon$  model and the shear-stress transport (SST)  $k$ - $\omega$  model and is defined by

$$k = \frac{1}{2} \langle u'_{\text{gas},i} u'_{\text{gas},i} \rangle. \quad (2.26)$$

Additionally, either the turbulent dissipation rate

$$\epsilon = \eta \left\langle \frac{\partial u'_{\text{gas},i}}{\partial x_k} \frac{\partial u'_{\text{gas},i}}{\partial x_k} \right\rangle \quad (2.27)$$

or the specific turbulent dissipation rate

$$\omega = \frac{\epsilon}{C_\eta k} \quad (2.28)$$

is the second transported quantity, where  $C_\eta = 0.09$  is a model constant. The respective transported quantities are used to approximate the turbulent dynamic viscosity  $\eta_{\text{turb}}$  (see Eqs. 2.31 and 2.37). The equations of the standard  $k$ - $\epsilon$  model are summarised in Section 2.2.2.4, and the equations of the shear-stress transport (SST)  $k$ - $\omega$  model are provided in Section 2.2.2.5.

### 2.2.2.4 Standard $k$ - $\epsilon$ model

The standard  $k$ - $\epsilon$  model [166, 167] is a two-equation turbulence model and consists of transport equations for the turbulent kinetic energy  $k$  and the turbulent dissipation rate  $\epsilon$ . For free shear flows at high Reynolds numbers, it provides a good compromise between computational efficiency, computational stability and accuracy. However, boundary layer flows and flow separation cannot be well described. The transport equations are given by [15]

$$\begin{aligned} \frac{\partial}{\partial x_i} (\rho_{\text{gas}} k u_{\text{gas},i}) &= \frac{\partial}{\partial x_j} \left( \left( \eta_{\text{gas}} + \frac{\eta_{\text{turb}}}{\sigma_k} \right) \frac{\partial k}{\partial x_j} \right) + \eta_{\text{turb}} S^2 \\ &\quad - g_i \frac{\eta_{\text{turb}}}{\rho_{\text{gas}} Pr_{\text{turb}}} \frac{\partial \rho_{\text{gas}}}{\partial x_i} - \rho_{\text{gas}} \epsilon, \end{aligned} \quad (2.29)$$

$$\begin{aligned} \frac{\partial}{\partial x_i} (\rho_{\text{gas}} \epsilon u_{\text{gas},i}) &= \frac{\partial}{\partial x_j} \left( \left( \eta_{\text{gas}} + \frac{\eta_{\text{turb}}}{\sigma_\epsilon} \right) \frac{\partial \epsilon}{\partial x_j} \right) + C_{\epsilon,1} \frac{\epsilon}{k} \left( \eta_{\text{turb}} S^2 \right. \\ &\quad \left. - C_{\epsilon,3} g_i \frac{\eta_{\text{turb}}}{\rho_{\text{gas}} Pr_{\text{turb}}} \frac{\partial \rho_{\text{gas}}}{\partial x_i} \right) - C_{\epsilon,2} \rho_{\text{gas}} \frac{\epsilon^2}{k}, \end{aligned} \quad (2.30)$$

where [15]

$$\eta_{\text{turb}} = \rho_{\text{gas}} C_{\eta} \frac{k^2}{\epsilon} \quad (2.31)$$

is the turbulent viscosity,  $S = \sqrt{2 S_{i,j} S_{i,j}}$  is the mean rate of the strain-rate tensor,  $\sigma_k = 1.0$ ,  $\sigma_{\epsilon} = 1.3$ ,  $C_{\epsilon,1} = 1.44$  and  $C_{\epsilon,2} = 1.92$  are model constants and  $C_{\epsilon,3} = \tanh(u_{\text{gas},1}/u_{\text{gas},2})$  is a model parameter.

### 2.2.2.5 Shear-stress transport (SST) $k$ - $\omega$ model

The shear-stress transport (SST)  $k$ - $\omega$  model [199, 200] is a two equation turbulence model and was developed by blending the standard  $k$ - $\epsilon$  model, transformed to a  $k$ - $\omega$  model, and the standard  $k$ - $\omega$  model [336] using the blending function  $F_1$  in order establish a model that is appropriate for both free shear flows and boundary layer flows. The transport equations for the turbulent kinetic energy  $k$  and the specific turbulent dissipation rate  $\omega$  are given by [15]

$$\frac{\partial}{\partial t} (\rho_{\text{gas}} k u_{\text{gas},i}) = \frac{\partial}{\partial x_j} \left( \left( \eta_{\text{gas}} + \frac{\eta_{\text{turb}}}{\sigma_k} \right) \frac{\partial k}{\partial x_j} \right) + \eta_{\text{turb}} S^2 - \rho_{\text{gas}} \beta^* \omega k, \quad (2.32)$$

$$\begin{aligned} \frac{\partial}{\partial t} (\rho_{\text{gas}} \omega u_{\text{gas},i}) &= \frac{\partial}{\partial x_j} \left( \left( \eta_{\text{gas}} + \frac{\eta_{\text{turb}}}{\sigma_{\omega}} \right) \frac{\partial \omega}{\partial x_j} \right) + \gamma \rho_{\text{gas}} S^2 - \rho_{\text{gas}} \beta \omega^2 \\ &+ 2 \rho_{\text{gas}} (1 - F_1) \frac{1}{\sigma_{\omega,2}} \frac{1}{\omega} \frac{\partial k}{\partial x_j} \frac{\partial \omega}{\partial x_j}. \end{aligned} \quad (2.33)$$

The model constants are given by [15]

$$\begin{aligned} \sigma_{k,1} &= 1.176, \quad \sigma_{k,2} = 1.0, \quad \sigma_k = \frac{1}{F_1/\sigma_{k,1} + (1 - F_1)/\sigma_{k,2}}, \\ \sigma_{\omega,1} &= 2.0, \quad \sigma_{\omega,2} = 1.168, \quad \sigma_{\omega} = \frac{1}{F_1/\sigma_{\omega,1} + (1 - F_1)/\sigma_{\omega,2}}, \\ \beta^* &= 0.09, \quad \beta_1 = 0.075, \quad \beta_2 = 0.0828, \quad \beta = F_1 \cdot \beta_1 + (1 - F_1) \cdot \beta_2, \\ \kappa &= 0.41, \quad \gamma_1 = \frac{\beta_1}{\beta^*} - \frac{1}{\sigma_{\omega,1}} \frac{\kappa^2}{\sqrt{\beta^*}}, \quad \gamma_2 = \frac{\beta_2}{\beta^*} - \frac{1}{\sigma_{\omega,2}} \frac{\kappa^2}{\sqrt{\beta^*}}, \\ \gamma &= F_1 \cdot \gamma_1 + (1 - F_1) \cdot \gamma_2. \end{aligned}$$

The blending function  $F_1$  is given by [15]

$$F_1 = \tanh(\Phi_1^4), \quad (2.34)$$

where [15]

$$\Phi_1 = \min \left( \max \left( \frac{\sqrt{k}}{\beta^* \omega y}, \frac{500 \eta_{\text{gas}}}{\rho_{\text{gas}} y^2 \omega} \right), \frac{4 \rho_{\text{gas}} k}{\sigma_{\omega,2} D y^2} \right), \quad (2.35)$$

$$D = \max \left( 2 \rho_{\text{gas}} \frac{1}{\sigma_{\omega,2}} \frac{1}{\omega} \frac{\partial k}{\partial x_j} \frac{\partial \omega}{\partial x_j}, 10^{-10} \right). \quad (2.36)$$

The turbulent viscosity  $\eta_{\text{turb}}$  is defined by [15]

$$\eta_{\text{turb}} = \frac{\rho_{\text{gas}} k / \omega}{\max \left( \frac{1}{\alpha^*}, \frac{S F_2}{0.31 \cdot \omega} \right)}, \quad (2.37)$$

where  $S$  is the mean rate of the strain-rate tensor (see Section 2.2.2.3) and [15]

$$\alpha^* = \left( \frac{0.024 + Re_{\text{turb}}/6}{1 + Re_{\text{turb}}/6} \right), \quad Re_{\text{turb}} = \frac{\rho_{\text{gas}} k}{\eta_{\text{gas}} \omega}, \quad \alpha_1 = 0.31,$$

$$F_2 = \tanh(\Phi_2^2), \quad \Phi_2 = \max \left( 2 \frac{\sqrt{k}}{\beta^* \omega y}, \frac{500 \eta_{\text{gas}}}{\rho_{\text{gas}} y^2 \omega} \right).$$

## 2.2.3 Boundary conditions

The transport equations of the gas phase are solved using boundary conditions for the inlet, the outlet and the walls. In this work, the boundary conditions have been defined using the available methods *mass-flow inlet*, *outflow* and *wall* in ANSYS Fluent [15, 17] and the experimental boundary conditions (see Section 1.5 and Chapter B).

### 2.2.3.1 Inlet

At the inlet, the gas temperature  $T_{\text{gas}}$  and the gas composition in mass fractions  $\mathbf{w}_{\text{gas}}$  are explicitly defined by

$$T_{\text{gas}}|_{\text{inlet}} = T_{\text{inlet}}, \quad (2.38)$$

$$w_{i,\text{gas}}|_{\text{inlet}} = w_{i,\text{inlet}}, \quad (2.39)$$

where  $T_{\text{inlet}}$  is the temperature at inlet and  $w_{i,\text{inlet}}$  is the mass fraction of species  $i$  at inlet. The magnitude of the gas velocity  $u_{\text{gas}}$  at inlet is determined by

$$u_{\text{gas}}|_{\text{inlet}} = \frac{\dot{m}_{\text{inlet}}}{\rho_{\text{gas}}|_{\text{inlet}} A_{\text{s,inlet}}} \quad (2.40)$$

using the mass flow rate at inlet  $\dot{m}_{\text{s,inlet}}$  and the surface area of the inlet  $A_{\text{s,inlet}}$  while the direction of the gas velocity  $u_{\text{gas}}$  is defined to be normal to the inlet surface.

The turbulent kinetic energy  $k$ , the turbulent dissipation rate  $\epsilon$  and the specific turbulent dissipation rate  $\omega$  at inlet are estimated by [16]

$$k|_{\text{inlet}} = \frac{3}{2} \left( u_{\text{gas}}|_{\text{inlet}} I_{\text{inlet}} \right)^2, \quad (2.41)$$

$$\epsilon|_{\text{inlet}} = \frac{C_\eta^{3/4} (k|_{\text{inlet}})^{3/2}}{0.07 L_{\text{inlet}}}, \quad (2.42)$$

$$\omega|_{\text{inlet}} = \frac{C_\eta^{-1/4} (k|_{\text{inlet}})^{1/2}}{0.07 L_{\text{inlet}}}, \quad (2.43)$$

where  $I_{\text{inlet}} = 10\%$  is an assumed intensity at inlet and  $L_{\text{inlet}}$  is the characteristic length scale of the inlet, i.e. the (equivalent) nozzle diameter  $d_{\text{nozzle,eq}}$  (see Sections 2.2.4.4 and 2.2.4.5).

### 2.2.3.2 Outlet

At the outlet, zero-gradient boundary conditions are assumed for the gas velocity  $\mathbf{u}_{\text{gas}}$ , the gas temperature  $T_{\text{gas}}$ , the gas pressure  $p_{\text{gas}}$ , the gas composition in mass fractions  $\mathbf{w}_{\text{gas}}$ , the turbulent kinetic energy  $k$  and the turbulent dissipation rate  $\epsilon$ .

### 2.2.3.3 Wall

At the walls, boundary conditions of first or second kind are combined with wall functions in order to avoid a fine resolution of the boundary layer. Wall functions are used to approximate the viscous hydrodynamic and thermal boundary layer effects in turbulent flows and in particular to estimate the gas velocity  $\mathbf{u}_{\text{gas}}$  and the gas temperature  $T_{\text{gas}}$  in the near-wall fluid cells. The distance of near-wall fluid cells is defined by  $y$ , while the dimensionless distance of the hydrodynamic boundary layer to the wall  $\tilde{y}_u$  is given by [15]

$$\tilde{y}_u = \frac{\rho_{\text{gas}} C_\eta^{1/4} k^{1/2} y}{\eta_{\text{gas}}}, \quad (2.44)$$

and the dimensionless distance of the thermal boundary layer to the wall  $\tilde{y}_T$  is defined as intersection of the linear temperature wall function and the logarithmic temperature wall function.

Due to sufficiently small dimensionless distances to the wall  $\tilde{y}_u$  for the fluid cells in this work, the linear velocity wall function was applied for the gas velocity. This function is defined by [15]

$$\tilde{u} \equiv \frac{u_{\text{gas}} C_\eta^{1/4} k^{1/2}}{\tau_{\text{wall}}/\rho_{\text{gas}}} = \tilde{y}_u, \quad (2.45)$$

where  $\tilde{u}$  is the dimensionless gas velocity and [15]

$$\tau_{\text{wall}} = \eta_{\text{gas}} \left. \frac{\partial u_{\text{gas}}}{\partial n} \right|_{\text{wall}} \quad (2.46)$$

is the shear stress at the wall. The gas velocity at the wall is defined by the no-slip condition [15]

$$u_{\text{gas}}|_{\text{wall}} = 0. \quad (2.47)$$

The temperature wall function is defined by [15]

$$\tilde{T} \equiv \frac{(T_{\text{gas}}|_{\text{wall}} - T_{\text{gas}}) \rho_{\text{gas}} \hat{C}_{p,\text{gas}} C_{\eta}^{1/4} k^{1/2}}{\dot{q}_{\text{wall}}} = \tilde{T}_{\text{conv+cond}} + \tilde{T}_{\text{visc}}, \quad (2.48)$$

where [15]

$$\tilde{T}_{\text{conv+cond}} = \begin{cases} Pr \tilde{y}_u, & \text{if } \tilde{y}_u < \tilde{y}_T \\ Pr_{\text{turb}} \left( \frac{1}{\kappa} \ln(E \tilde{y}_u) + P \right), & \text{else} \end{cases} \quad (2.49)$$

is the dimensionless convective-conductive part while the dimensionless viscous heating part  $\tilde{T}_{\text{visc}}$  is neglected.  $\dot{q}_{\text{wall}}$  is the heat flux at the wall,  $\kappa = 0.4187$  is the van Kármán constant and  $E = 9.793$  is an empirical constant [15].

$$P = 9.24 \left( \left( \frac{Pr}{Pr_{\text{turb}}} \right)^{3/4} - 1 \right) \left( 1 + 0.28 \exp \left( -0.007 \frac{Pr}{Pr_{\text{turb}}} \right) \right) \quad (2.50)$$

is an auxiliary function for smooth walls. Assuming a thin wall, the gas temperature at the wall is determined by [16]

$$T_{\text{gas}}|_{\text{wall}} = T_{\text{wall}} + \dot{q}_{\text{wall}} \frac{d_{\text{wall}}}{\lambda_{\text{wall}}}, \quad (2.51)$$

where  $T_{\text{wall}}$  is the wall temperature,  $d_{\text{wall}}$  is the wall thickness and  $\lambda_{\text{wall}}$  is the wall thermal conductivity. The wall temperature  $T_{\text{wall}}$  of approximately 1473.15 K is measured using thermocouples, which are located approximately 50 mm below the surface of the refractory concrete. The refractory concrete is made of 94 %  $\text{Al}_2\text{O}_3$ , 0.1 %  $\text{SiO}_2$ , 0.1 %  $\text{Fe}_2\text{O}_3$  and 4.6 %  $\text{CaO}$  [134]. The wall thermal conductivity  $\lambda_{\text{wall}}$  was determined as 2.240 W/(m K) at 1273.15 K and 2.220 W/(m K) at 1473.15 K based on DIN 51046 [73] according to the manufacturer's information [134]. However, this work applied the slightly larger value of 2.3 W/(m K) in agreement with the preceding works [63, 64, 185, 186, 187] (see Section 3.1).

Wall functions are not required for the species balance equations and the turbulent kinetic energy equation as zero-gradient boundary conditions are applied for the gas species mass fraction of each species  $i$  and for the turbulent kinetic energy. The boundary conditions are given by [15]

$$\left. \frac{\partial w_{i,\text{gas}}}{\partial n} \right|_{\text{wall}} = 0, \quad (2.52)$$

$$\left. \frac{\partial k}{\partial n} \right|_{\text{wall}} = 0. \quad (2.53)$$

Further equations are used depending on the turbulence model. For the standard  $k$ - $\epsilon$  model, the turbulent dissipation rate  $\epsilon$  in the near-wall cells and the turbulent production term are approximated by [15]

$$\epsilon = \frac{C_\eta^{3/4} k^{3/2}}{\kappa y}, \quad (2.54)$$

$$\eta_{\text{turb}} S^2 \approx \tau_{\text{wall}} \frac{\tau_{\text{wall}}}{\kappa \rho_{\text{gas}} C_\eta^{1/4} k^{1/2} y}. \quad (2.55)$$

For the SST  $k$ - $\omega$  model, the specific turbulent dissipation rate  $\omega$  in the near-wall cells is described using the linear function and is given by [15]

$$\omega|_{\text{wall}} = \frac{\rho_{\text{gas}} (\tilde{u})^2}{\eta_{\text{gas}}} \frac{6}{\beta (y^+)^2}, \quad (2.56)$$

where [15]

$$y^+ = \frac{\rho_{\text{gas}} \sqrt{\tau_{\text{wall}} / \rho_{\text{gas}}} y}{\eta_{\text{turb}}}. \quad (2.57)$$

In addition to the boundary conditions described above, source terms have been defined near the wall between the points (0 mm | 140 mm) and (300 mm | 140 mm) for the continuity equation, the oxygen balance equation and the energy equation in order to account for infiltrated air and purge nitrogen. The source terms eventually replace lateral inlets to decrease the computing time and increase the numerical stability. The source terms are defined by

$$S_{\text{m,at wall}} = \left( \dot{m}_{\text{inf}} + \dot{m}_{\text{N}_2} \right) \frac{V_{\text{gas}}}{\sum_{\text{at wall}} V_{\text{gas}}}, \quad (2.58)$$

$$S_{\text{w,at wall,O}_2} = \frac{w_{\text{O}_2,\text{inf}} \dot{m}_{\text{inf}}}{\dot{m}_{\text{inf}} + \dot{m}_{\text{N}_2}} S_{\text{m,at wall}}, \quad (2.59)$$

$$S_{\text{u,at wall}} = 0, \quad (2.60)$$

$$S_{\text{E,at wall}} = \left( \dot{H}_{\text{inf}} + \dot{H}_{\text{N}_2} \right) \frac{V_{\text{gas}}}{\sum_{\text{at wall}} V_{\text{gas}}}, \quad (2.61)$$

where  $\dot{m}_{\text{inf}}$  is the mass flow rate of infiltrated air,  $\dot{m}_{\text{N}_2}$  is the mass flow rate of purge nitrogen,  $V_{\text{gas}}$  is the gas volume of the wall-adjacent cell,  $\sum_{\text{at wall}} V_{\text{gas}}$  is the gas volume of all wall-adjacent cells between the points (0 mm | 140 mm) and (300 mm | 140 mm),  $w_{\text{O}_2,\text{inf}}$  is the mass fraction of oxygen in the infiltrated air,  $\dot{H}_{\text{inf}}$  is the enthalpy flow rate of infiltrated air and  $\dot{H}_{\text{N}_2}$  is the enthalpy flow rate of purge nitrogen.

## 2.2.4 Atomisation

Atomisation is a process in which a continuous liquid based phase is disintegrated to smaller discrete elements of different sizes and shapes in a surrounding gas phase using an atomiser [170]. The process is primarily characterised by the interaction of stabilising and destabilising forces [170, 265]. The stabilising forces include surface tension and viscosity forces, while the destabilising forces comprise normal, shear and gravity forces [170, 265]. The increase of destabilising forces leads to the primary break-up after exiting the atomiser [170, 265]. Liquid fragments, ligaments and larger droplets can be observed. Since the liquid elements move forwards to reach new equilibrium states, secondary break-up to smaller droplets and relaxation to spherical and distorted droplets happen [170, 265]. In addition, phase transition by vaporisation and interactions such as coalescence, bouncing, off-centre separation and near head-on separation are possible phenomena [265]. The liquid elements stop to break up when reaching new equilibrium states [170, 265].

The break-up based on various break-up regimes occurs in both quiescent and moving gas phases and depends on the physical properties of the liquid based phase, on the geometry of the atomiser and on the operating conditions [170, 265]. The obtained collective of liquid elements is called spray and can be characterised by spray angles and droplet velocity and droplet size distributions. Such data is typically obtained through high-speed camera images and anemometry techniques such as Laser-Doppler Anemometry (LDA) and Phase-Doppler Anemometry (PDA) [265].

Results from spray characterisation experiments are used to develop empirical spray correlations (for example, see [138, 171, 176, 177, 189, 215, 265, 328, 329]) or to validate numerical interphase tracking methods such as the volume-of-fluid method (for example, see [86, 216, 217, 290, 330, 347]), the level-set method (for example, see [236]), the front-tracking method (for example, see [319]) or the smoothed particle hydrodynamics method (for example, see [45, 46, 47, 48]). In addition, if atomisation itself should not be described for computing time reasons, droplet velocity, droplet size and droplet mass flux distributions and the spray angle at atomiser exit can be used to estimate the initial particle state properties of simplified multi-phase simulations (see Section 2.2.5.6). Following the discussion in Section 2.2, this approach was used in this work. Initial particle state properties and equivalent nozzle diameters  $d_{\text{nozzle,eq}}$  were determined from atmospheric spray experiments [98, 113, 114, 137].

The experiments were carried out by Sanger and Jakobs [98, 137] and by Haas [113, 114] at ATMO (see Sections 1.4 and A.3) using ethylene glycol (G) and pressurised air. The experiments are directly linked to the REGA experiments TUC3 V479, TUC3 V786, TUC5 V1105 and TUC5 V1374, i. e. the input conditions of the atmospheric spray experiments were defined using the input conditions of the gasification experiments [98, 113, 114, 137]. Furthermore, atmospheric spray experiments with glycerine (GL) were

performed that are linked to the REGA experiment TUC5 GHKS30 V1284 [113], whereas atmospheric spray experiments with char slurries have been not performed yet since laser-based measurements are challenged by safety requirements [113, 137].

The conditions of the ATMO experiments are summarised in Table 2.1 while some characteristic results are given in Table 2.2. Further information about the experiments of Sanger and Jakobs [98, 137] and of Haas [113, 114] are provided in Section 2.2.4.1 and Section 2.2.4.2, respectively. The (new) approaches to obtain simplified initial particle state properties and equivalent nozzle diameters  $d_{\text{nozzle,eq}}$  are described in Sections 2.2.4.4 and 2.2.4.5, while the previous approach is discussed in Section 2.2.4.3.

**Table 2.1:** Conditions of the ATMO experiments [98, 113, 114, 137]: liquid mass flow rates  $\dot{m}_{\text{liq}}$ , gas mass flow rates  $\dot{m}_{\text{gas}}$ , liquid velocities  $u_{\text{liq}}$ , gas velocities  $u_{\text{gas}}$ , gas-to-liquid ratios GLR, operating temperatures  $T_{\text{op}}$  and operating pressures  $p_{\text{op}}$ . Acronyms: G: ethylene glycol; GL: glycerine. Further details about the external mixing nozzles D1, D2, D1.1 and D2.1 are given in Section C.1.

ATMO experiment	Fuel	Nozzle	$\frac{\dot{m}_{\text{liq}}}{\text{kg/h}}$	$\frac{\dot{m}_{\text{gas}}}{\text{kg/h}}$	$\frac{u_{\text{liq}}}{\text{m/s}}$	$\frac{u_{\text{gas}}}{\text{m/s}}$	GLR	$\frac{T_{\text{op}}}{\text{K}}$	$\frac{p_{\text{op}}}{\text{bar}}$
TUC3 D1 [98]	G	D1	12.526	16.079	1.00	111.7	1.284	293.15	1
TUC5 D2 [137]	G	D2	12.419	10.295	0.99	165.1	0.829	293.15	1
TUC5 D1.1 [113]	G	D1.1	11.690	9.690	0.93	67.3	0.829	293.15	1
TUC5 D2.1 [113]	G	D2.1	11.690	9.690	0.93	155.4	0.829	293.15	1
TUC5 PO D2.1 [113]	GL	D2.1	11.690	9.690	0.82	155.4	0.829	293.15	1

**Table 2.2:** Characteristic results from the ATMO experiments [98, 113, 114, 137]: spray angles  $\alpha_{\text{spray}}$ , Sauter diameters  $d_{\text{S}}$  at centre position and axial gas velocities  $u_{\text{gas}}$  at centre position.

ATMO experiment	$\alpha_{\text{spray}}$	$\frac{d_{\text{S}} _{r=0}}{\mu\text{m}}$	$\frac{u_{\text{gas}} _{r=0}}{\text{m/s}}$
TUC3 D1 [98]	22.4°	62.1	62.4
TUC5 D2 [137]	18.8°	65.8	65.7
TUC5 D1.1 [113]	60.2°	106.4	28.2
TUC5 D2.1 [113]	20.0°	72.9	52.0
TUC5 PO D2.1 [113]	58.8°	82.8	17.9

### 2.2.4.1 Experiments of Sanger and Jakobs

In the ATMO experiments TUC3 D1 and TUC3 D2 of Sanger and Jakobs, ethylene glycol was atomised using pressurised air with gas and liquid mass flow rates quite similar to the mass flow rates used in the REGA experiments TUC3 V479/TUC3 V786 and TUC5 V1105 [98, 137]. Measurements using two-dimensional Phase-Doppler Anemometry were performed at nozzle distances of 50 mm and at seven radial positions between

–15 mm and 15 mm with a radial step size of 5 mm since the spray break-up was approximately completed after 50 mm in each experiment [98, 137]. Subsequently, droplet velocity, droplet size and droplet mass flux distributions were estimated from the measurement data using limit droplet sizes of 220  $\mu\text{m}$  (TUC3 D1) and 200  $\mu\text{m}$  (TUC3 D2) [98, 137]. In addition, high-speed camera images were generated to derive the image based spray angle of each experiment [98, 137].

The characteristic droplet diameters, the characteristic axial droplet velocities and the characteristic radial droplet velocities are shown in Figs. D.6 and D.7 demonstrating that the droplet size and droplet velocity measurement data is characterised by a high degree of axial symmetry and that the characteristic droplet diameters slightly increase with increasing centre distance [98, 137].

The axial and radial gas velocity distributions were estimated from the axial and radial droplet velocity distributions of droplets with diameters less than than 0.5  $\mu\text{m}$  assuming that such droplets follow the gas flow. The characteristic values are shown in Figs. D.6 and D.7 and indicate that the axial gas velocities in the ATMO experiment TUC5 D2 could be similar to the droplet velocities and that the axial gas velocities in the ATMO experiment TUC3 D1 could be higher than the axial droplet velocities. Furthermore, the image based spray angles spray angles were determined to be 22.4° and 18.8° [137] and were thus significantly greater than the usual free jet angle of 9.5° [110].

### 2.2.4.2 Experiments of Haas

In the ATMO experiments TUC5 D2.1 and TUC5 D1.1 of Haas, ethylene glycol was atomised using pressurised air with the gas-to-liquid mass flow rate ratios of the REGA experiments TUC5 V1105 and TUC5 V1374 [113, 114]. PDA measurements were performed in line with the methods described in Section 2.2.4.1 but at nozzle distances of 50 mm, 100 mm, 150 mm, 200 mm and 250 mm and at radial positions between –40 mm and 40 mm with a radial step size of 4 mm [113, 114]. Limit droplet sizes above 425  $\mu\text{m}$  were applied for the evaluation of the measurement data [113]. Furthermore, patternator measurements using a radial step size of 6.35 mm were carried out to derive mass flux distributions [113]. The number-based cumulative distribution functions  $Q_0$  and the mass-based cumulative distribution functions  $Q_3$  are shown in Fig. D.4 demonstrating that the droplet break-up is approximately completed after 50 mm. Furthermore, Fig. D.5 shows that the ATMO experiment TUC5 D2.1 is characterised by clearly deviating spray properties compared to the ATMO experiment TUC5 D2. This can mainly be attributed to the different input conditions and to the different limit droplet sizes for the evaluation of the measurement data.

Furthermore, glycerine was atomised using pressurised air at conditions similar to those of the REGA experiment TUC5 GHKS30 V1284 [113]. PDA measurements were only carried

out at 200 mm since the spray break-up was not finished before that distance. Patternator measurement data was not performed since the measurements were completely impeded by glycerine foaming [113]. The number-based cumulative distribution function  $Q_0$  and the mass-based cumulative distribution function  $Q_3$  are shown in Fig. D.5. The number-based cumulative distribution function  $Q_0$  is accordingly quite similar to the distribution functions based on the ATMO experiments TUC5 D2 and TUC5 D2.1, while the mass-based cumulative distribution function  $Q_3$  is significantly affected by a few larger droplets.

### 2.2.4.3 Previous initial particle state properties for liquid gasification

In the preceding works [63, 64, 187], the initial particle state properties for the CFD simulations of the REGA experiments TUC3 V479, TUC3 V786 and TUC5 V1105 were defined using the measurement data from the ATMO experiments TUC3 D1 and TUC5 D2 [98, 137]. Global droplet diameter distributions were obtained using area and mass flux weighted summation of the data from all measurement points since similar droplet diameter distributions were obtained at each measurement point [137]. The method is described in detail by Sanger [265] while the local and global droplet diameter distributions are compared in Figs. D.1 and D.2.

The global number-based and mass-based droplet diameter distributions were approximated using gamma ( $\gamma$ ) and Weibull (W) distributions (see Section E.2), respectively. The number-based probability density function  $q_0$ , the number-based cumulative distribution function  $Q_0$ , the mass-based probability density function  $q_3$  and the mass-based cumulative distribution function  $Q_3$  are shown in Fig. D.3.

The preceding works [63, 64, 187] additionally relied on estimates for the initial axial and radial droplet velocities. The initial axial droplet velocities were estimated with 20 m/s, while the initial radial droplet velocities were defined by values evenly distributed between 0 and 4 m/s. However, considering the atomiser nozzles D1 and D2, this approach has deficiencies since (i) the nozzle momentum balance is not satisfied and (ii) the spray dispersion is not well described in the RANS based simulations of the REGA experiments. The last point needs to be explained further. If the details of the atomisation process are not retained in the model, no continuous liquid enters the domain through the inner duct. Therefore, the zones, that are actually filled with liquid, contain gas. A tiny recirculation zone establishes in the near nozzle region which impedes appropriate droplet injections and decreases the numerical stability. Therefore, the total gas stream at inlet was split in the preceding works [63, 64, 187]. Some gas was allowed to enter through the central duct (see Section 1.5). This obviously stabilised the numerical gas flow but also affected the predictions of the droplet dispersion and the droplet velocities as the tracked droplets typically passed through the flame in the near-axis region. Since vaporisation and decomposition of ethylene glycol are endothermic processes, this also affected the

predictions of gas temperature and gas species concentrations in the flame region. Instead of possible V-shaped flames, W-shaped flames with lower gas temperatures in the near axis region were always formed and stabilised by the combustion of the recirculated synthesis gas (see Fig. 2.3 and [63, 64, 187]).

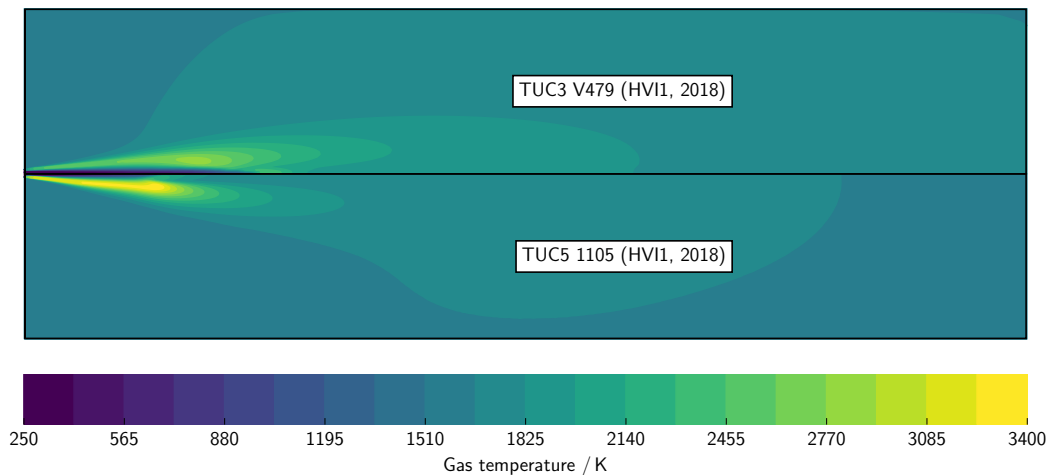


**Figure 2.3:** Predicted gas temperature distributions. TUC3 V479 (2018): results for the REGA experiment TUC3 V479 obtained in the preceding work [187]; TUC5 V1105 (HVI1, 2018): results for the REGA experiment TUC5 V1105 obtained in the preceding work [63].

#### 2.2.4.4 Improved initial particle state properties for liquid gasification

Due to the large impact of the droplet dispersion on the flame predictions, the previous injection approach was not adopted in this work. Instead, the gas stream was fed through a cylindrical nozzle with an equivalent diameter  $d_{\text{nozzle,eq}}$ . In addition, the droplets were injected with velocities, diameters and mass flow rates that enabled a sufficient description of the spray dispersion. The initial particle state properties and the equivalent nozzle diameter  $d_{\text{nozzle,eq}}$  were determined complying with the nozzle momentum balance and using the steps described below.

1. Interpolation of the experimental global droplet diameter distribution with cubic smoothing splines to 50 diameter bins evenly distributed between the minimum and the limit droplet diameter.
2. Normalisation of the experimental droplet velocity, axial droplet velocity and droplet mass flux distributions using the maximum values.
3. Approximation of the normalised distributions using generalised membership bell-shaped (GMBS) functions, generalised Gaussian probability density (GGPD) functions and combinations thereof, GGPD/GMBS functions (see Section E.1).
4. Centring of the normalised distributions.

5. Narrowing of the normalised and centred approximations using the equivalent nozzle diameter  $d_{\text{nozzle,eq}}$ .
6. Definition of 13 uniform distributed injection positions using the equivalent nozzle diameter  $d_{\text{nozzle,eq}}$  at a nozzle distance of 5 mm.
7. Calculation of the initial droplet momentum flow rates and the initial droplet mass flow rates for each injection position complying (i) with the normalised, centred and narrowed approximations and (ii) with the mass and momentum flow rates at nozzle inlet.
8. Definition of the spray angles for each injection position using spray angles evenly distributed between zero and the image based spray angle.
9. Calculation of the initial axial and radial droplet velocities using the discrete spray angles and the initial droplet momentum flow rates.
10. Definition of the initial droplet properties using the interpolated global droplet diameter distribution, the 13 discrete initial droplet mass flow rates, the 13 discrete initial axial droplet velocities and the 13 discrete initial radial droplet velocities.

The approximations of the normalised distributions are shown in Figs. E.1-E.4. Accordingly, different bell functions need to be applied for the approximations of the measurement data. In the case of the ATMO experiments TUC3 D1 and TUC5 D2, GMBS functions were used for the velocity distribution, and GGPD/GMBS functions were applied for the mass flux distribution. In the case of the ATMO experiments TUC5 D2.1 and TUC5 D1.1, GGPD functions were used for the velocity distribution, and GMBS functions were applied for the mass flux distribution. The final approximations of the injection properties are shown in Figs. E.5-E.9 while the equivalent nozzle diameters  $d_{\text{nozzle,eq}}$  are given in Table 2.3.

**Table 2.3:** Equivalent nozzle diameters  $d_{\text{nozzle,eq}}$  based on the ATMO experiments and applied for the CFD simulations of the REGA experiments TUC3 V479/TUC3 V786, TUC5 V1105 and TUC5 V1374.

ATMO experiment	REGA experiment	$\frac{d_{\text{nozzle,eq}}}{\text{mm}}$
TUC3 D1	TUC3 V479/TUC3 V786	7.150
TUC5 D2	TUC5 V1105	5.093
TUC5 D1.1	TUC5 V1374	4.646
TUC5 D2.1	TUC5 V1105	4.895

### 2.2.4.5 Initial particle state properties for slurry gasification

The methods described in Section 2.2.4.4 could only be used in this work to generate the initial particle state properties for the CFD simulations of the REGA experiments TUC3 V479, TUC3 V786, TUC5 V1105 and TUC5 V1374 as spray characterisation experiments could not be performed yet for mixtures of ethylene glycol and wood char. Therefore, in spite of the fact that the initial particle state distributions and the particle dispersion in the flame region are sensitive aspects in RANS based simulations (see Section 2.2.4.3), assumptions were used to define the initial particle state properties for the CFD simulations of the REGA experiments TUC5 GHKS10 V1071 and TUC5 GHKS30 V1284.

Since it is generally expected that slurry atomisation generates droplets that contain both liquid and solid fractions, the initial particle state properties need to reflect the droplet velocity, droplet diameter, droplet mass flux and droplet solid fraction distributions. This is aggravated by the facts (i) that the original wood char particles can form agglomerates during atomisation and flame crossing and (ii) that the agglomerates and particles can break up again during devolatilisation (see Section 2.7.3). In view of the uncertainties and in view of the particle morphology changes observed in the REGA experiments (see Section 2.7.3.2), the initial particle state properties were defined with major simplifications:

1. Ethylene glycol droplets and wood char particles were injected separately.
2. Normalised, centred and shifted axial particle velocity and particle mass flux distributions of the ATMO experiments TUC5 D1.1 were used for the calculation of the initial particle velocity and particle mass flow rate distributions of both the ethylene glycol droplets and the wood char particles.
3. Assumed Weibull parameters were used for the definition of the droplet diameter distribution with 50 diameter bins.
4. Measured particle size distributions of the wood char particles (see Section 2.7.3.1) were interpolated using cubic smoothing splines and were subsequently used for the particle diameter distribution with 50 diameter bins.

The equivalent nozzle diameters  $d_{\text{nozzle,eq}}$  are given in Table 2.4 while the final approximations of the injection properties are shown in Figs. E.10-E.13. Accordingly, the droplet diameter distributions were defined using shapes similar to the global droplet diameter distributions from the ATMO experiments TUC3 D1 and TUC5 D2. In contrast, the global droplet diameter distribution from the ATMO experiments TUC5 PO D2.1 is characterised by significant larger droplets, which demonstrates the need of future experimental and numerical research (see Chapter 5).

**Table 2.4:** Equivalent nozzle diameters  $d_{\text{nozzle,eq}}$  applied for the CFD simulations of the REGA experiments TUC5 GHKS10 V1071 and TUC5 GHKS30 V1284.

REGA experiment	Nozzle	$\frac{d_{\text{nozzle,eq}}}{\text{mm}}$
TUC5 GHKS10 V1071	D2	4.856
TUC5 GHKS30 V1284	D2	4.895

## 2.2.5 Dispersed phases

Dispersed phases are typically described using the transient differential transport equations in the Lagrangian specification. Accordingly, numerous particles are injected with well-defined injection properties and are subsequently tracked while heat and mass transfer including thermal radiation and particle-gas interaction are accounted for. The particle-particle interactions are usually neglected when the particle volume fractions are small, whereas the mass flow rate of the dispersed phase can still be higher than the mass flow rate of the gas phase [15].

In this work, spherical particles were injected in the near-nozzle region. Subsequently, the particle trajectories were determined using simplified particle motion equations for the particle position  $\mathbf{x}_{\text{part}}$  and the particle velocity  $\mathbf{u}_{\text{part}}$  [15, 33, 34, 332]. The particle position  $\mathbf{x}_{\text{part}}$  and the particle velocity  $\mathbf{u}_{\text{part}}$  (based on the second law of Newton) are described by [15]

$$\frac{d\mathbf{x}_{\text{part}}}{dt} = \mathbf{u}_{\text{part}}, \quad (2.62)$$

$$\mathbf{x}_{\text{part}}|_{t=0} = \mathbf{x}_{\text{part},0}, \quad (2.63)$$

$$m_{\text{part}} \frac{d\mathbf{u}_{\text{part}}}{dt} = \mathbf{F}_d + \mathbf{F}_g + \mathbf{F}_l, \quad (2.64)$$

$$\mathbf{u}_{\text{part}}|_{t=0} = \mathbf{u}_{\text{part},0}, \quad (2.65)$$

where  $\mathbf{x}_{\text{part},0}$  is the initial particle position,  $\mathbf{u}_{\text{part},0}$  is the initial particle velocity,  $m_{\text{part}}$  is the particle mass,  $\mathbf{F}_d$  is the drag force,  $\mathbf{F}_g$  is the gravity force and  $\mathbf{F}_l$  is the lift force. Further forces such as the virtual mass force, the thermophoretic force, the Brownian force and the Saffman's lift force have been neglected due to small gas phase/dispersed phase density ratios, due to small temperature gradients near surfaces, due to the presence of turbulence and due to super-micron particles, respectively.

The drag force  $\mathbf{F}_d$ , the gravity force  $\mathbf{F}_g$  and the lift force  $\mathbf{F}_l$  are given by [15]

$$\mathbf{F}_d = \frac{\rho_{\text{part}}}{2} \|\mathbf{u}_{\text{gas}} - \mathbf{u}_{\text{part}}\| (\mathbf{u}_{\text{gas}} - \mathbf{u}_{\text{part}}) \frac{\pi}{4} d_{\text{part}}^2 C_d, \quad (2.66)$$

$$\mathbf{F}_g = \rho_{\text{part}} \frac{\pi}{6} d_{\text{part}}^3 \mathbf{g}, \quad (2.67)$$

$$\mathbf{F}_1 = -\rho_{\text{gas}} \frac{\pi}{6} d_{\text{part}}^3 \mathbf{g}, \quad (2.68)$$

where  $\rho_{\text{part}}$  is the particle density,  $d_{\text{part}}$  is the particle diameter,  $\mathbf{g}$  is the earth acceleration and  $C_d$  is the drag coefficient. Inserting Eqs. (2.66), (2.67) and (2.68) into Eq. (2.64), the time derivative of the particle velocity is given by [15]

$$\frac{d\mathbf{u}_{\text{part}}}{dt} = \frac{1}{\tau_{\text{part}}} (\mathbf{u}_{\text{gas}} - \mathbf{u}_{\text{part}}) + \frac{(\rho_{\text{part}} - \rho_{\text{gas}})}{\rho_{\text{part}}} \mathbf{g} \quad (2.69)$$

where [15]

$$\tau_{\text{part}} = \frac{\rho_{\text{part}} d_{\text{part}}^2}{18 \eta_{\text{gas}}} \frac{24}{C_d Re_{\text{part}}} \quad (2.70)$$

is the particle relaxation time and  $Re_{\text{part}}$  is the particle Reynolds number. The particle Reynolds number  $Re_{\text{part}}$  is defined by

$$Re_{\text{part}} = \frac{\rho_{\text{part}} d_{\text{part}} \|\mathbf{u}_{\text{part}} - \mathbf{u}_{\text{gas}}\|}{\eta_{\text{gas}}}. \quad (2.71)$$

### 2.2.5.1 Drag coefficient

The drag coefficient  $C_d$  depends on the particle Reynolds number  $Re_{\text{part}}$  and the particle shape. For spheres, several relationships have been derived (see [55]) including the Stokes equation [302]

$$C_d = \frac{24}{Re_{\text{part}}}, \quad \text{if } 0 < Re_{\text{part}} < 0.25, \quad (2.72)$$

the Schiller-Naumann equation [274]

$$C_d = \frac{24}{Re_{\text{part}}} (1 + 0.15 Re_{\text{part}}), \quad \text{if } 0 < Re_{\text{part}} < 800, \quad (2.73)$$

and the Morsi-Alexander equation [212]

$$C_d = C_1 + \frac{C_2}{Re_{\text{part}}} + \frac{C_3}{Re_{\text{part}}^2}, \quad (2.74)$$

where  $C_1$ ,  $C_2$  and  $C_3$  are coefficients, which are given for several ranges of the particle Reynolds number  $Re_{\text{part}}$  in Table 2.5.

Within the respective limits, the three approximations provide similar accurate predictions and are in good agreement with the most recent findings (for example, see [223, 258]). This work eventually adopted the Morsi-Alexander equation.

**Table 2.5:** Coefficients  $C_1$ ,  $C_2$  and  $C_3$  for the calculation of the drag coefficient  $C_d$  using the Morsi-Alexander equation [212].

Range	$C_1$	$C_2$	$C_3$
$0 < Re_{\text{part}} \leq 0.1$	0	24	0
$0.1 < Re_{\text{part}} \leq 1$	3.69	22.73	0.0903
$1 < Re_{\text{part}} \leq 10$	1.222	29.1667	-3.8889
$10 < Re_{\text{part}} \leq 100$	0.6167	46.5	-116.67
$100 < Re_{\text{part}} \leq 1000$	0.3644	98.33	-2778
$1000 < Re_{\text{part}} \leq 5000$	0.357	148.62	-47500
$5000 < Re_{\text{part}} \leq 10000$	0.46	-490.546	578700
$10000 < Re_{\text{part}} \leq 50000$	0.5191	-1662.5	5416700

### 2.2.5.2 Turbulent dispersion

The turbulent dispersion of the particles is described using the discrete random walk model. In the case of two-equation turbulence models, this model modifies the gas velocity  $\mathbf{u}_{\text{gas}}$  using random gas velocity fluctuations  $\mathbf{u}'_{\text{gas}} = (u'_{\text{gas},i})$  with [15]

$$u'_{\text{gas},i} = \zeta_G \sqrt{\frac{2}{3} k}, \quad (2.75)$$

where  $\zeta_G$  is a Gaussian distributed random number and  $k$  is the turbulent kinetic energy. The random particle velocity fluctuation is preserved over the minimum of two time scales: the characteristic eddy lifetime  $\tau_{\text{eddy}}$  and the particle eddy crossing time  $\tau_{\text{cross}}$  [15]. The characteristic eddy lifetime  $\tau_{\text{eddy}}$  is defined by [15]

$$\tau_{\text{eddy}} = -\tau_L \ln(\zeta_u), \quad (2.76)$$

where  $0 < \zeta_u < 1$  is a uniform random number and  $\tau_L = C_L k/\varepsilon$  is the Lagrangian integral time scale.  $C_L$  is typically approximated with 0.15 in the case of two-equation turbulence models [15] while a modification of this value to 0.6 following the studies of Kumar and Ghoniem [161, 162] was not accounted for in this work.

The particle eddy crossing time  $\tau_{\text{cross}}$  is given by [15]

$$\tau_{\text{cross}} = \left( 1 - \left( \frac{L_{\text{eddy}}}{\tau_{\text{part}} \|\mathbf{u}_{\text{part}} - \mathbf{u}_{\text{gas}}\|} \right) \right), \quad (2.77)$$

where  $\tau_{\text{part}}$  is the particle relaxation time (see Eq. (2.70)) and  $L_{\text{eddy}}$  is the eddy length scale, which is defined by [15]

$$L_{\text{eddy}} = C_\eta^{3/4} \frac{k^{3/2}}{\epsilon} \quad (2.78)$$

or [15]

$$L_{\text{eddy}} = C_{\eta}^{-1/4} \frac{k^{1/2}}{\omega}. \quad (2.79)$$

### 2.2.5.3 Heat and mass transfer

The heat and mass transfer between the dispersed phase and the gas phase depends on the particle type. While vaporisation only is accounted for liquid droplets, consecutive processes are assumed for solid char particles and slurry droplets. The processes are summarised in Table 2.6 while the conditions of the processes are specified in Table 2.7, where  $m_{\text{part}}$  is the particle mass,  $T_{\text{part}}$  is the particle temperature (assumed to be uniform at each time step for computing time reasons),  $T_{\text{vap, min}}$  is the minimum vaporisation temperature (assumed to be the reference temperature  $T_{\text{ref}}$ ) and  $m_{\text{part, min, vap}}$ ,  $m_{\text{part, min, dev}}$  and  $m_{\text{part, min, het}}$  are auxiliary minimum masses. The latter are defined by

$$m_{\text{part, min, vap}} = (1 - w_{\text{liq}, 0}) m_{\text{part}, 0}, \quad (2.80)$$

$$m_{\text{part, min, dev}} = (1 - w_{\text{vol, solid}, 0}) (1 - w_{\text{liq}, 0}) m_{\text{part}, 0}, \quad (2.81)$$

$$m_{\text{part, min, het}} = (1 - w_{\text{vol, solid}, 0} - w_{\text{comb, solid}, 0}) (1 - w_{\text{liq}, 0}) m_{\text{part}, 0}, \quad (2.82)$$

where  $w_{\text{liq, part}, 0}$  is the initial particle mass fraction of the liquid phase,  $w_{\text{vol, solid}, 0}$  is the initial solid mass fraction of the volatiles and  $w_{\text{comb, solid}, 0}$  is the initial solid mass fraction of the combustibles and  $m_{\text{part}, 0}$  is the initial particle mass. The initial particle mass fraction of the liquid phase  $w_{\text{liq, part}, 0}$  is one in the case of liquid droplets and is zero in the case of solid particles.

**Table 2.6:** Particle conversion processes for the different particle types.

Particle	Processes
Inert particle	Inert heating or cooling
Solid particle	Devolatilisation, heterogeneous gasification and inert heating or cooling
Liquid droplet	Vaporisation
Slurry droplet	Vaporisation, devolatilisation, heterogeneous gasification and inert heating or cooling

**Table 2.7:** Conditions for the particle conversion processes.

Process	Conditions
Inert heating or cooling	$T_{\text{part}} < T_{\text{vap, min}}$ OR $m_{\text{part}} < m_{\text{part, min, het}}$
Vaporisation	$T_{\text{part}} \geq T_{\text{vap, min}}$ and $m_{\text{part}} \geq m_{\text{part, min, vap}}$
Devolatilisation	$T_{\text{part}} \geq T_{\text{vap, min}}$ and $m_{\text{part, min, dev}} \leq m_{\text{part}} < m_{\text{part, min, vap}}$
Heterogeneous gasification	$T_{\text{part}} \geq T_{\text{vap, min}}$ and $m_{\text{part, min, het}} \leq m_{\text{part}} < m_{\text{part, min, dev}}$

Since vaporisation is discussed in Section 2.6 and wood char conversion is described in Section 2.7, the overall heat and mass transfer equations for the calculation of particle mass  $m_{\text{part}}$  and particle temperature  $T_{\text{part}}$  are focussed here. The particle mass  $m_{\text{part}}$  is obtained by [15]

$$\frac{dm_{\text{part}}}{dt} = -R_{\text{m, part}}, \quad (2.83)$$

$$m_{\text{part}}|_{t=0} = m_{\text{part, 0}}, \quad (2.84)$$

where  $R_{\text{m, part}}$  is the particle mass transfer rate which depends on the particle conversion process.

The particle temperature  $T_{\text{part}}$  changes due to convective and radiative heat transfer and due to transition enthalpies. Since, as mentioned above, uniform particle temperatures are assumed and small temperature gradients are neglected, the particle temperature  $T_{\text{part}}$  is determined by [15]

$$m_{\text{part}} \hat{C}_{p, \text{part}} \frac{dT_{\text{part}}}{dt} = A_{\text{s, part}} h_{\text{conv, part}} (T_{\text{gas}} - T_{\text{part}}) + A_{\text{s, part}} \varepsilon_{\text{part}} \sigma (T_{\text{rad}}^4 - T_{\text{part}}^4) + R_{\text{E, part}}, \quad (2.85)$$

$$T_{\text{part}}|_{t=0} = T_{\text{part, 0}}, \quad (2.86)$$

where  $\hat{C}_{p, \text{part}}$  is the specific particle heat capacity,  $A_{\text{s, part}}$  is the particle surface area,  $\varepsilon_{\text{part}}$  is the particle emissivity,  $\sigma$  is the Stefan-Boltzmann constant,  $T_{\text{rad}}$  is the thermal radiation temperature,  $R_{\text{E, part}}$  is the particle energy transfer rate depending on the particle conversion process. The thermal radiation temperature  $T_{\text{rad}}$  is estimated by [15]

$$T_{\text{rad}} = \left( \frac{G}{4\sigma} \right)^{1/4}, \quad (2.87)$$

where  $G$  is the incident radiation (see Eqs. (2.131), (2.132) and (2.135)). The convective particle heat transfer coefficient  $h_{\text{conv, part}}$  is determined by

$$h_{\text{conv, part}} = \frac{Nu_{\text{film}} \lambda_{\text{gas, film}}}{d_{\text{part}}}, \quad (2.88)$$

where  $Nu_{\text{film}}$  is the Nusselt number at film condition and  $\lambda_{\text{gas,film}}$  is the gas thermal conductivity at film condition. Except for vaporisation (see Section 2.6), the film condition is identical to the gas condition.

The Nusselt number at film condition  $Nu_{\text{film}}$  is determined using the Ranz-Marshall equation [248, 249]

$$Nu_{\text{film}} = 2 + 0.6 Re_{\text{film}}^{1/2} Pr_{\text{film}}^{1/3}, \quad (2.89)$$

where  $Re_{\text{film}}$  is the Reynolds number and  $Pr_{\text{film}}$  is the Prandtl number, each at film condition. Since recent studies [90, 258] showed that the Ranz-Marshall equation is still an accurate approximation for spherical particles, no adjustments have been made in this work, even in view of possible effects connected with vaporisation (for example, see [139]). This also applies for the calculation of the Sherwood number at film condition  $Sh_{\text{film}}$  which is obtained using the Ranz-Marshall equation [248, 249]

$$Sh_{\text{film}} = 2 + 0.6 Re_{\text{film}}^{1/2} Sc_{\text{film}}^{1/3}, \quad (2.90)$$

where  $Sc_{\text{film}}$  is the Schmidt number at film condition.

The Reynolds number at film condition  $Re_{\text{film}}$ , the Prandtl number at film condition  $Pr_{\text{film}}$  and the Schmidt number at film condition  $Sc_{\text{film}}$  are defined by

$$Re_{\text{film}} = \frac{\rho_{\text{gas,film}} d_{\text{part}} \|\mathbf{u}_{\text{part}} - \mathbf{u}_{\text{gas}}\|}{\eta_{\text{gas,film}}}, \quad (2.91)$$

$$Pr_{\text{film}} = \frac{\eta_{\text{gas,film}} \hat{C}_{p,\text{gas,film}}}{\lambda_{\text{gas,film}}}, \quad (2.92)$$

$$Sc_{\text{film}} = \frac{\eta_{\text{gas,film}}}{\rho_{\text{gas,film}} D_{\text{gas,film}}}. \quad (2.93)$$

In addition to the convective particle heat transfer coefficient  $h_{\text{conv,part}}$ , a radiative particle heat transfer coefficient  $h_{\text{rad,part}}$  and a (total) particle heat transfer coefficient  $h_{\text{part}}$  are given by

$$h_{\text{rad,part}} = \varepsilon_{\text{part}} \sigma \left( T_{\text{rad}}^2 + T_{\text{part}}^2 \right) (T_{\text{rad}} + T_{\text{part}}), \quad (2.94)$$

$$h_{\text{part}} = h_{\text{conv,part}} + h_{\text{rad,part}}. \quad (2.95)$$

#### 2.2.5.4 Source terms

The interaction between the continuous gas phase and the dispersed phase is accounted for using source terms in the continuity equation (see Section 2.2.1.1), the species balance equations (see Section 2.2.1.2), the momentum equation (see Section 2.2.1.3) and the energy equation (see Section 2.2.1.4). These terms are determined by accounting for all

particles entering or leaving each gas cell. Particles entering a gas cell are characterised by the particle time  $t_{\text{part,in}}$ , the particle position  $\mathbf{x}_{\text{part,in}}$ , the particle velocity  $\mathbf{u}_{\text{part,in}}$ , the particle mass  $m_{\text{part,in}}$  and the particle temperature  $T_{\text{part,in}}$  [15]. In contrast, particles leaving the gas cell are characterised by the particle time  $t_{\text{part}}$ , the particle position  $\mathbf{x}_{\text{part}}$ , the particle velocity  $\mathbf{u}_{\text{part}}$ , the particle mass  $m_{\text{part}}$  and the particle temperature  $T_{\text{part}}$  as determined by the differential transport equations [15].

Practically, instead of particles, parcels are defined consisting of numerous particles. The number flow rate of particles  $N_{\text{part}}$  of a parcel  $i$  is defined by [15]

$$\dot{N}_{\text{part},i} = \frac{\dot{m}_{\text{part},0,i}}{m_{\text{part},0,i}}, \quad (2.96)$$

where  $\dot{m}_{\text{part},0,i}$  is the initial particle mass flow rate of parcel  $i$  and  $m_{\text{part},0,i}$  is the initial particle mass of parcel  $i$ . Applying this definition, the source terms for the continuity equation  $S_{\text{m,part}}$ , the momentum equation  $S_{\text{u,part}}$  and the energy equation  $S_{\text{E,part}}$  are given by [15]

$$S_{\text{m,part}} = \frac{1}{V_{\text{gas}}} \sum_i (m_{\text{part,in},i} - m_{\text{part},i}) \dot{N}_{\text{part},i}, \quad (2.97)$$

$$S_{\text{u,part}} = \frac{1}{V_{\text{gas}}} \sum_i \left( \frac{1}{\tau_{\text{part},i}} (\mathbf{u}_{\text{part},i} - \mathbf{u}_{\text{gas}}) \right) \frac{dm_{\text{part},i}}{dt} (t_{\text{part,in},i} - t_{\text{part},i}), \quad (2.98)$$

$$S_{\text{E,part}} = \frac{1}{V_{\text{gas}}} \sum_i \left( \dot{N}_{\text{part},i} \left( (m_{\text{part,in},i} - m_{\text{part},i}) \Delta_{\text{trs}} \hat{H}_i - m_{\text{part},i} \int_{T_{\text{ref}}}^{T_{\text{part},i}} \hat{C}_{p,\text{part},i} dT + m_{\text{part,in},i} \int_{T_{\text{ref}}}^{T_{\text{part,in},i}} \hat{C}_{p,\text{part,in},i} dT \right) \right). \quad (2.99)$$

In addition, source terms for the species balance equations  $S_{\text{w,part},i}$ ,  $i = 1, \dots, N_{\text{sp}} - 1$ , are used to describe the mass transfer during vaporisation, devolatilisation and heterogeneous gasification. The source terms for the species balance equations  $S_{\text{w,part},i}$ ,  $i = 1, \dots, N_{\text{sp}} - 1$ , are zero except for

- (i) the species balance equation of ethylene glycol  $S_{\text{w,part},\text{C}_2\text{H}_6\text{O}_2}$  during vaporisation (see Section 2.6),
- (ii) the species balance equations of methane  $S_{\text{w,part},\text{CH}_4}$ , carbon monoxide  $S_{\text{w,part},\text{CO}}$ , carbon dioxide  $S_{\text{w,part},\text{CO}_2}$ , hydrogen  $S_{\text{w,part},\text{H}_2}$  and water vapour  $S_{\text{w,part},\text{H}_2\text{O}}$  during devolatilisation (see Section 2.7.4) and
- (ii) the species balance equations of carbon monoxide  $S_{\text{w,part},\text{CO}}$ , carbon dioxide  $S_{\text{w,part},\text{CO}_2}$ , hydrogen  $S_{\text{w,part},\text{H}_2}$  and water vapour  $S_{\text{w,part},\text{H}_2\text{O}}$  during heterogeneous gasification (see Section 2.7.5).

The source term of the species balance equation of ethylene glycol during vaporisation is given by the source term for the continuity equation  $S_{m,\text{part}}$ , while the source terms of the species balance equations during devolatilisation are described by the source term for the continuity equation  $S_{m,\text{part}}$  and the volatiles composition in mass fractions  $\mathbf{w}_{\text{vol}}$  (see Section 2.7.4). Finally, the source terms for the species balance equations during heterogeneous gasification are defined by the source term for the continuity equation  $S_{m,\text{part}}$  and the reaction rates of the Boudouard reaction and the water-gas reaction (see Section 2.7.5).

### 2.2.5.5 Physical properties

The physical particle properties depend on the particle composition and the particle type. In the case of liquid droplets, the physical particle properties are given by the physical properties of the liquid phase (see Section F.6). In the case of solid particles, the physical particle properties are given by the physical properties of the solid phase (see Section F.7). In the case of slurry droplets, the specific particle heat capacity and the specific physical particle enthalpy are described using the mass-weighted mixing rule and the correlations for the liquid phase and the solid phase, while the particle density  $\rho_{\text{part}}$  is determined using the volume-weighted mixing rule and the correlations for the liquid phase and the solid phase. Furthermore, the particle emissivity  $\varepsilon_{\text{part}}$  is specified following Section 2.5.3.

### 2.2.5.6 Initial particle state properties

The initial particle state properties are defined according to the particle type and the experiment (see Section 2.2.5.3). First of all, the initial particle position  $\mathbf{x}_{\text{part},0}$ , the initial particle velocity  $\mathbf{u}_{\text{part},0}$ , the initial particle temperature  $T_{\text{part},0}$ , the initial particle mass flow rate  $\dot{m}_{\text{part},0}$  and the initial particle diameter  $d_{\text{part},0}$  are given. Furthermore, the initial particle composition is defined by the initial particle mass fraction of the liquid phase  $w_{\text{liq,part},0}$ , the initial particle mass fraction of the volatiles in the solid phase  $w_{\text{vol,solid,part},0}$  and the initial particle mass fraction of the combustibles in the solid phase  $w_{\text{comb,solid,part},0}$ .

## 2.3 Homogeneous reaction kinetics

Homogeneous reaction kinetics are used to describe the chemical reactions in the gas phase and are typically based on detailed, reduced or global reaction mechanisms. Such mechanisms differ in the number of species, the number of chemical reactions, the computational requirements and the transferability to different conditions. However, the same models are applied to describe the reaction rates of the chemical reactions. Some details of the

mechanisms used in this work are given in Section 2.3.1 while the models for the reaction rates are described in Section 2.3.2.

### 2.3.1 Detailed, reduced and global reaction mechanisms

Detailed reaction mechanisms take into account all potential species and all possible reactions and have thus high computational requirements on spatial and temporal resolutions. This still restricts the broad application for technical domains and has led to the development of global and reduced reaction mechanisms. Global reaction mechanisms typically account for a few major species and reactions and provide a sufficiently accurate and computationally efficient basis for selected operating conditions in technical domains. However, the transfer of global reaction mechanisms to deviating operating conditions is limited. Furthermore, gas temperatures and gas species concentrations in the flame region are seldom predicted concurrently with sufficient accuracy. Erroneous flame gas temperatures and gas species concentrations are usually accepted. In order to overcome these limitations, reduced reaction mechanisms, that can provide lower and more reasonable flame temperatures, are developed from detailed mechanisms, for example, using graph-based methods (DRG and DRGEP) or timescale separation methods (QSSA, CSP and PCA) [320]. Unfortunately, reduced and global reaction mechanisms are typically characterised by higher stiffness due to a wide range of chemical times scales [89].

Numerous reaction mechanisms have been developed so far. Some of them are introduced in the paragraphs below.

**Detailed reaction mechanisms** are, for example, the GRI mechanism (version 3.0) [294] and the DLR mechanism for ethylene glycol [115, 116, 149].

The GRI mechanism (version 3.0) [294] was developed for the combustion of natural gas accounting for 53 species and 325 reactions. The mechanism was optimised using shock-tube, laminar flame and flow reactor experiments at fuel-rich and fuel-lean conditions, partially at very high temperatures up to 2800 K and high pressures above 80 bar [294]. However, the mechanism has been recommended for temperatures between 1000 K and 2500 K and pressures between 10 Torr and 10 atm [294].

The DLR mechanism for ethylene glycol was originally developed by Hafner et al. [115, 116] and is based on the C<sub>1</sub>-C<sub>4</sub> hydrocarbon oxidation mechanism of Hedges [122] and the ethanol mechanism of Marinov et al. [190]. Further reactions related to ethylene glycol and its products have been included using experiments, similarity methods and analogy methods [115]. Kathrotia et al. [149] recently revised the thermodynamic database and the reaction parameters to reduce numerical instabilities and validated the updated mechanism (DLR2017/DK; 78 species, 574 reactions) using ignition delay times from shock-tube

experiments and using species profiles from flow reactor experiments [149]. The shock-tube experiments were performed at equivalence ratios of 0.5, 1.0 and 2.0 between 800 K and 1500 K and at 16 bar, while the flow reactor experiments were carried out at equivalence ratios of 1.0 and 2.0 between 700 K and 1200 K [149]. The experimental results were mainly in good agreement with the numerical results except for some species profiles.

**Reduced reaction mechanisms** have been generated by numerous research groups. For example, Kazakov and Frenklach [150] and Lu and Law [178] developed reduced mechanisms based on the GRI mechanism (version 1.2) and the GRI mechanism (version 3.0), respectively. Furthermore, Kathrotia et al. [149] and Methling et al. [204] proposed reduced mechanisms for ethylene glycol using the directed relation graph method (DLR2017/RK mechanism; 43 species, 270 reactions) and the rapid reduction method (DLR2017/RM mechanism; 24 species, 87 reactions), respectively.

Previous CFD studies on entrained flow gasification have seldom used reduced and detailed reaction mechanism. Variants based on the GRI mechanism [150, 255, 294, 345] were applied for RANS based simulations of coal gasification at TU Freiberg [259, 263, 322, 323, 324]. Variants of the DLR mechanism for ethylene glycol [115, 116, 149, 204] were used by Rashidi et al. [250, 251] and Fradet et al. [101, 102] for RANS based simulations and by Eckel et al. [88, 89] for a large eddy simulation. The experimental results were mainly in good agreement with the numerical results in the studies of TU Freiberg and in good to sufficient agreement with the numerical results in the studies of Rashidi et al. [250, 251], Eckel et al. [88, 89] and Fradet et al. [101, 102]. However, note that these conclusions assume accurate turbulence-chemistry interaction models and heterogeneous reaction kinetics.

**Global reaction mechanisms** are, for example, the four-step mechanisms of Jones and Lindstedt (JL and JL/A) [144] and the two-step mechanism of Westbrook and Dryer (WD) [333, 334]. The JL mechanism and the JL/A mechanism consist of the oxidation reactions of methane and hydrogen, the methane reforming reaction and the water-gas shift reaction while the WD mechanism contains the oxidation reactions of methane and carbon monoxide. Chemical equations and reaction parameters of the WD mechanism, the JL mechanism and the JL/A mechanism are given in Sections G.1, G.2 and G.3.

Previous CFD studies on entrained flow gasification typically adopted the chemical equations of the WD mechanism, the JL mechanism and the JL/A mechanism and combined them with reaction parameters that were either taken from literature [26, 41, 42, 144, 181, 333, 334] or adapted to the prevailing operating conditions in order to reduce the discrepancies between the numerical and the experimental results. Mularski et al. [214] recently compiled detailed overviews of the chemical equations and the reaction parameters used in previous studies and concluded that reaction rates from literature

might only be reasonable as initial guess and should be adjusted for the respective specific gasifier condition. Eventually, global reaction mechanisms have typically been preferred to reduce the computing times, to calibrate the reaction rates and to understand the overall phenomena, considering that reduced and detailed reaction mechanisms should not be further optimised for single operating conditions and may also provide imperfect predictions.

For the gasification of ethylene glycol, Mancini et al. [187] proposed two global reaction mechanisms, the first mechanism of HVIGasTech (HVI1; 8 species, 6 reactions) and the extended mechanism of Jones and Lindstedt (eJL; 8 species, 6 reactions). Both mechanisms consist of an ethylene glycol decomposition reaction, the methane reforming reaction, the methane and hydrogen oxidation reactions and the water-gas shift reaction. The HVI1 mechanism and the eJL mechanism also include the oxidation reaction of carbon monoxide and ethylene glycol, respectively. Chemical equations and reactions parameters of the HVI1 mechanism and the eJL mechanism are given in Section G.4 and Section G.5, respectively. The HVI1 mechanism and the eJL mechanism were applied in the preceding works of Mancini et al. [187] and Dammann et al. [63, 64] providing a good agreement between experimental and numerical results (see Section 1.5).

In summary, detailed, reduced and global reaction mechanisms were established for the gasification of ethylene glycol and were already tested in several studies [63, 64, 89, 101, 102, 187, 250, 251]. However, none of these studies investigated whether global or reduced reaction mechanisms should be preferred for technical domains and whether the efforts for the calibration of the reaction rates of global reaction mechanisms are justified. Therefore, CFD simulations performed in this work were based on both global and reduced reaction mechanisms.

The global reaction mechanisms applied in this work were the HVI1 mechanism and the eJL mechanism of Mancini et al. [187]. Furthermore, an alternative eJL mechanism (eJL/A) was defined corresponding to the JL/A mechanism with the alternative reaction rate for the hydrogen oxidation. Chemical equations and reaction parameters are presented in Section G.6.

The detailed reaction mechanisms used in this work were the reduced DLR2017 mechanism of Kathrotia et al. [149] (DLR2017/RK) and the reduced DLR2017 mechanism of Methling et al. [204] (DLR2017/RM). However, single highly stiff backward reactions were removed from both mechanisms to enable the application in ANSYS Fluent [17] without any integration failures [205]. Details are given in Sections G.7 and G.8.

### 2.3.2 Reaction rates

Reactions in detailed, reduced or global reaction mechanisms are elementary reactions, adapted elementary reactions, three-body reactions or fall-off reactions.

**Elementary reactions** are the basic chemical reactions between two species A and B and can be described by



The forward reaction rate of an elementary reaction  $j$  is

$$R_{f,j} = k_{f,j} c_{A,\text{gas}}^{\nu_A} c_{B,\text{gas}}^{\nu_B}, \quad (2.101)$$

where  $c_{A,\text{gas}}$  and  $c_{B,\text{gas}}$  are the molar gas species concentrations of A and B, respectively.  $k_{f,j}$  is the forward rate constant of reaction  $j$  which is defined by

$$k_{f,j} = k_{0,j} T^{b_j} \exp\left(-\frac{\bar{E}_{a,j}}{RT}\right), \quad (2.102)$$

where  $k_{0,j}$  is the pre-exponential factor of reaction  $j$ ,  $b_j$  is the temperature exponent of reaction  $j$  and  $\bar{E}_{a,j}$  is the molar activation energy of reaction  $j$ .

**Adapted elementary reactions** are elementary reactions with non-default reaction orders and are common in global reaction mechanisms. The forward reaction rate of an adapted elementary reaction  $j$  is

$$R_{f,j} = k_{f,j} c_{A,\text{gas}}^{n_{A,j}} c_{B,\text{gas}}^{n_{B,j}}, \quad (2.103)$$

where  $n_{A,j}$  and  $n_{B,j}$  are the reaction orders with respect to A and B, respectively.

**Three-body reactions** include unspecified collision partners M in elementary reactions and are described by



The forward reaction rate of a three-body reaction  $j$  is

$$R_{f,j} = k_{f,j} c_{A,\text{gas}} c_{B,\text{gas}} c_{M_j,\text{gas}}, \quad (2.105)$$

where  $k_{f,j}$  is the forward rate constant of reaction  $j$  as defined by Eq. (2.102) and

$$c_{M_j,\text{gas}} = \sum_k \epsilon_{k,j} c_{k,\text{gas}} \quad (2.106)$$

is the molar gas species concentration of M for reaction  $j$  calculated using the efficiencies  $\epsilon$  and the molar gas species concentrations of selected species.

**Fall-off reactions** changes the reaction order for the collision partner M from first order at low-pressures to zero order at high pressures and applies the forward rate constants  $k_{0,j}$

and  $k_{\infty,j}$  at the low-pressure limit and the high-pressure limit, respectively. The forward rate constant of reaction  $j$  is given by

$$k_{f,j} = k_{\infty,j} \left( \frac{P_j}{1 + P_j} \right) F_j(T, P_j), \quad (2.107)$$

where

$$P_j = \frac{k_{0,j} c_{M_j, \text{gas}}}{k_{\infty,j}} \quad (2.108)$$

is a dimensionless reduced pressure and  $F_j(T, P_j)$  is the broadening/fall-off function. Detailed and reduced reaction mechanisms used in this work applied the Troe fall-off function [105] based on the relationships [105]

$$\begin{aligned} \lg(F_j(T, P_j)) &= \frac{\lg(F_{\text{cent},j}(T))}{1 + f_{1,j}^2}, \\ F_{\text{cent},j}(T) &= (1 - k_{0,j}) \exp\left(-\frac{T}{T_{3,j}}\right) + k_{0,j} \exp\left(-\frac{T}{T_{1,j}}\right) + \exp\left(-\frac{T_{2,j}}{T}\right), \\ f_{1,j} &= \frac{\lg(P_j) + C_j}{N_j - 0.14(\lg(P_j) + C_j)}, \\ C_j &= -0.4 - 0.67 \lg(F_{\text{cent},j}), \\ N_j &= 0.75 - 1.27 \lg(F_{\text{cent},j}). \end{aligned} \quad (2.109)$$

## 2.4 Turbulence-chemistry interactions

Turbulence-chemistry interactions describe the influence of turbulence on the homogeneous reactions and vice versa. Following Mancini [188], turbulence-chemistry interaction models are typically focussed on the first aspect while turbulence models are expected to appropriately describe the latter aspect.

In previous CFD studies on entrained flow gasification, typical turbulence-chemistry interaction models were the eddy-dissipation model, the finite-rate/eddy-dissipation model, the eddy-dissipation-concept model, the assumed probability-density function model using a flamelet or an equilibrium approach and the transported probability-density function model. Since the eddy-dissipation-concept model has been proven superior to  $\beta$ -PDF models in the preceding works on entrained flow gasification of ethylene glycol of Rashidi et al. [250, 251] and Mancini et al. [185, 187], the eddy-dissipation-concept model was the only model applied in this work.

The eddy-dissipation-concept model was originally developed by Magnussen [184] and is based on the eddy-break up model of Spalding [296] and the eddy-dissipation model of Magnussen and Hjertager [183]. The eddy-break up model and the eddy-dissipation model

assume infinitely fast chemical reactions leading to reaction rates controlled by turbulence. In addition, the eddy-break up model differentiates between burnt and unburnt zones and depends on the mass fraction of the fuel, while the eddy-dissipation model assumes lean and rich zones and depends on the minimum mass fraction of the reactants and on the total mass fraction of the products.

The eddy-dissipation-concept model is a more sophisticated approach and divides each gas cell into the *fine structure* and the surrounding, which is illustrated in Fig. 2.4.

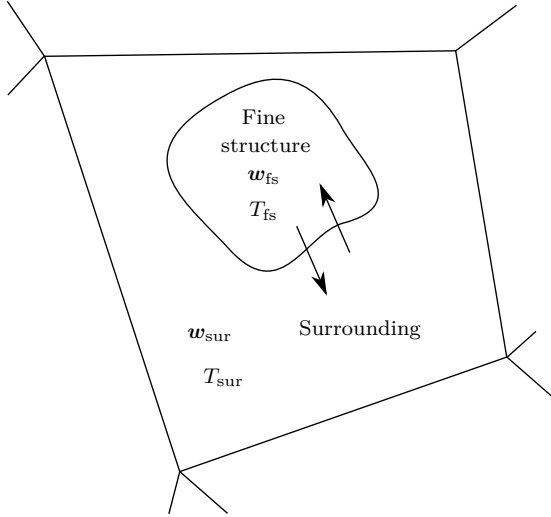


**Figure 2.4:** Fluid zones assumed by the eddy-dissipation-concept model: fine structure with the composition in mass fractions  $w_{fs}$  and the temperature  $T_{fs}$  and the surrounding with the composition in mass fractions  $w_{sur}$  and the temperature  $T_{sur}$ .

The volume of the fine structure  $\gamma_{fs}$  is defined by [184]

$$\gamma_{fs} = \left( \frac{3 C_2}{4 C_1^2} \right)^{1/4} \left( \frac{\nu_{gas} \varepsilon}{k^2} \right)^{1/4}, \quad (2.110)$$

where  $C_1 = 0.135$  and  $C_2 = 0.5$  are model constants and  $\nu_{gas} = \eta_{gas}/\rho_{gas}$  is the kinematic gas viscosity. Inside the fine structure, the gas phase is well mixed at the molecular level and can be described using a perfectly stirred reactor, a plug-flow reactor or an equilibrium reactor. In this work, the reaction rates were determined using a plug-flow reactor at constant pressure over the timescale [184]

$$\tau_{fs} = \left( \frac{C_2}{3} \right)^{1/2} \sqrt{\frac{\nu_{gas}}{\varepsilon}}. \quad (2.111)$$

The mass fraction of species  $i$  in the fine structure  $w_{i,fs}$  and the temperature in the fine structure  $T_{fs}$  are calculated by

$$\frac{dw_{i,fs}}{dt} = \frac{R_{i,fs}}{\rho_{fs}}, \quad (2.112)$$

$$w_{i,\text{fs}}|_{t=0} = w_{i,\text{gas}}, \quad (2.113)$$

$$\frac{dT_{\text{fs}}}{dt} = -\frac{1}{\hat{C}_{p,\text{fs}} \rho_{\text{fs}}} \sum_i R_{i,\text{fs}} \bar{H}_{i,\text{fs}}, \quad (2.114)$$

$$T_{\text{fs}}|_{t=0} = T_{\text{gas}}, \quad (2.115)$$

where  $\rho_{\text{fs}}$  is the density,  $\hat{C}_{p,\text{fs}}$  is the specific heat capacity and  $\bar{H}_{i,\text{fs}}$  is the molar enthalpy of species  $i$ , each in the fine structure. The gas phase reaction rate for a species  $i$  in the fine structures  $R_{i,\text{fs}}$  is defined by [15]

$$R_{i,\text{fs}} = M_i \sum_r (\nu_{i,r}^{\text{P}} - \nu_{i,r}^{\text{E}}) \left( k_{\text{f},r} \prod_j c_{j,\text{gas}}^{n_{j,r}} - k_{\text{b},r} \prod_j c_{j,\text{gas}}^{\nu_{j,r}^{\text{P}}} \right), \quad (2.116)$$

where  $k_{\text{f},r}$  is the forward rate constant of reaction  $r$ ,  $k_{\text{b},r}$  is the backward rate constant of reaction  $r$ ,  $c_{j,\text{gas}}$  is the molar gas species concentration of species  $j$ ,  $\nu_{i,r}^{\text{P}}$  is the product stoichiometric coefficient of species  $j$  for reaction  $r$ ,  $\nu_{i,r}^{\text{E}}$  is the reactant stoichiometric coefficient of species  $j$  for reaction  $r$  and  $n_{j,r}$  is the reactant exponent of species  $j$ , which can be but does not have necessarily to be the reactant stoichiometric coefficient of species  $j$  (see Section 2.3). The backward rate constant of reaction  $r$  is defined by [15]

$$k_{\text{b},r} = \begin{cases} \frac{k_{\text{f},r}}{\left( \frac{p^\ominus}{RT_{\text{fs}}} \right)^{\sum_i (\nu_{i,r}^{\text{P}} - \nu_{i,r}^{\text{E}})}}, & \text{if } r \text{ is reversible} \\ 0, & \text{otherwise} \end{cases}, \quad (2.117)$$

where

$$K_r^\ominus = \exp \left( \frac{\Delta_r \bar{S}_r^\ominus}{R} - \frac{\Delta_r \bar{H}_r^\ominus}{RT_{\text{gas}}} \right), \quad (2.118)$$

$$\Delta_r \bar{H}_r^\ominus = \sum_i (\nu_{i,r}^{\text{P}} - \nu_{i,r}^{\text{E}}) \bar{H}_i^\ominus, \quad (2.119)$$

$$\Delta_r \bar{S}_r^\ominus = \sum_i (\nu_{i,r}^{\text{P}} - \nu_{i,r}^{\text{E}}) \bar{S}_i^\ominus. \quad (2.120)$$

$p^\ominus$  is the standard pressure,  $K_r^\ominus$  is the standard equilibrium constant of reaction  $r$ ,  $\Delta_r \bar{H}_r^\ominus$  is the molar standard enthalpy of reaction of reaction  $r$ ,  $\Delta_r \bar{S}_r^\ominus$  is the molar standard entropy of reaction of reaction  $r$ ,  $\bar{H}_i^\ominus$  is the molar standard enthalpy of species  $i$  and  $\bar{S}_i^\ominus$  is the molar standard entropy of species  $i$ .

The gas phase reaction rate for a species  $i$  in the fluid cell  $R_i$  is defined by [15, 184]

$$R_i = \frac{\rho_{\text{gas}} \gamma_{\text{fs}}^3}{\tau_{\text{fs}}} (w_{i,\text{fs}} - w_{i,\text{sur}}), \quad (2.121)$$

where  $w_{i,\text{fs}}$  is the (final) mass fraction of species  $i$  in the fine structure and  $w_{i,\text{sur}}$  is the

mass fraction of species  $i$  in the surrounding. Both mass fractions are linked by [15, 184]

$$w_{i,\text{gas}} = \gamma_{\text{fs}}^3 w_{i,\text{fs}} + (1 - \gamma_{\text{fs}}^3) w_{i,\text{sur}}. \quad (2.122)$$

The reaction rate of species  $i$  in the gas cell  $R_i$  is finally expressed by [15, 184]

$$R_i = \frac{\rho_{\text{gas}} \gamma_{\text{fs}}^3}{\tau_{\text{fs}} (1 - \gamma_{\text{fs}}^3)} (w_{i,\text{fs}} - w_{i,\text{gas}}) \quad (2.123)$$

and is used as source term of species  $i$  due to the chemical reactions  $S_{\text{w, reac}, i}$ .

The model parameters of the eddy-dissipation-concept model have been adjusted in some previous CFD studies on gasification. For example, Rehm et al. [255] derived model parameters for the flame zone and the reforming zone from the analysis of conditions prevailing in a high-pressure partial oxidation gasifier used for reforming of natural gas and high-pressure partial oxidation of liquid hydrocarbons [260]. In this work, however, the eddy-dissipation-concept model was applied without any changes.

## 2.5 Thermal radiation

Thermal radiation describes the heat transfer between gas molecules, particles and boundaries through electromagnetic waves with wavelength between 0.1  $\mu\text{m}$  and 1000  $\mu\text{m}$  or through corresponding photons [209]. Similar to conduction, thermal radiation is taken into account as source term in the energy equation (see Section 2.2.1.4). However, the different nature of thermal radiation requires an advanced calculation approach, for which several mathematical models and numerous physical property models have been developed using different assumptions and simplifications.

Possible mathematical models are the discrete ordinates model, the P-1 model, the discrete transfer radiation model and the Monte Carlo model while the physical property models can be divided into grey-gas, spectral and band models. Grey-gas models are based on non-spectral physical properties, which, however, can be temperature or composition dependent. Spectral models are identical to line-by-line models, and band models can be divided into narrow-band models, wide-band models, weighted-sum-of-grey-gas models, spectral-line-weighted-sum-of-grey-gas models or full-spectrum- $k$  distribution models.

In previous CFD studies on entrained flow gasification, thermal radiation has always been accounted for, except for the CFD study of Eckel et al. [88, 89], since thermal radiation significantly contributes to the energy transfer at high temperature and high pressure conditions. However, the vast majority of CFD studies was contented to include (i) the

discrete ordinates, the P-1 or the discrete transfer radiation model, (ii) the weighted-sum-of-grey-gas model of Smith et al. [293] and (iii) the mean beam length model [128] into their CFD models. Only Lu and Wang [179] and Park et al. [238] investigated the effect of the thermal radiation model while the influence of the thermal radiation property model was discussed briefly by Marklund et al. [193] and extensively by Mancini et al. [187] and Dammann et al. [66, 67].

The scarce focus on thermal radiation is probably due to the fact that even larger errors in the thermal radiation model or in the thermal radiation property model do not significantly affect the overall results, as long as thermal radiation is accounted for in some way. The recent results of Mancini et al. [187] and Dammann et al. [66, 67] confirm this observation. Furthermore, improved thermal radiation property models and implementations have not been made available in popular CFD software. Nikrityuk et al. [223] also emphasised this aspect and the need for further research.

This work drew on the experience and the software from the preceding works of Mancini et al. [187] and Alberti [8] in order to describe thermal radiation based on the most recent knowledge. Hence, the discrete ordinates model was used as thermal radiation model and combined with simplified thermal gas and particle radiation property models. The discrete ordinates model is introduced in Section 2.5.1 while the assumptions and models for the thermal gas, thermal particle and thermal wall radiation properties are described in Section 2.5.2, Section 2.5.3 and Section 2.5.4, respectively.

### 2.5.1 Discrete ordinates model

The discrete ordinates model determines the energy source terms due to thermal radiation  $S_{E,\text{rad}}$  by solving the radiative transfer equation for an absorbing, emitting and scattering medium using the discrete ordinates or the finite volume method. In this work, the model was based on the finite volume method [54, 218] as incorporated in ANSYS Fluent [15]. Furthermore, the model was combined either with a grey-gas model or a weighted-sum-of-grey-gas model, i. e. the radiative transfer equation was solved either for a single grey gas or for a gas consisting of five grey gases and one clear gas. Furthermore, the numerical integration was carried out using  $4 \times 8 \times 8$  discrete solid angles, i. e. each quadrant was divided into 8 polar and 8 azimuthal angles. Due to the use of unstructured meshes, pixelation of  $4 \times 4$  was additionally applied to minimise the influence of the control-angle overhang.

If the discrete ordinates model is combined with the grey-gas model, the radiative transfer equation is given by [15]

$$\text{div}(I) + (K_{\text{gas}} + K_{\text{part}} + \sigma_{\text{part}}) I = K_{\text{gas}} I_{\text{b}} + E_{\text{part}} + \frac{\sigma_{\text{part}}}{4\pi} \int_0^{4\pi} I \Phi_{\text{part}} d\Omega, \quad (2.124)$$

where  $I$  is the intensity,  $K_{\text{gas}}$  is the (mean) gas absorption coefficient,  $K_{\text{part}}$  is the (mean) particle absorption coefficient,  $\sigma_{\text{part}}$  is the (mean) particle scattering coefficient,  $I_{\text{b}}$  is the black body intensity,  $E_{\text{part}}$  is the particle emission,  $\Phi_{\text{part}}$  is the particle scattering phase function and  $\Omega$  is the solid angle. The black body intensity  $I_{\text{b}}$  is defined by [15]

$$I_{\text{b}} = n_{\text{gas}}^2 \frac{\sigma T_{\text{gas}}^4}{\pi}, \quad (2.125)$$

where  $n_{\text{gas}}$  is the gas refractive index and is assumed to be one.

If the discrete ordinates model is combined with the weighted-sum-of-grey-gas model, the radiative transfer equation is solved for each pseudo-gas  $c$  and is defined by

$$\begin{aligned} \text{div}(I_c) + (K_{\text{gas},c} + K_{\text{part}} + \sigma_{\text{part}}) I_c = & K_{\text{gas},c} I_{\text{b},c} \\ & + a_c E_{\text{part}} + \frac{\sigma_{\text{part}}}{4\pi} \int_0^{4\pi} I_c \Phi_{\text{part}} d\Omega. \end{aligned} \quad (2.126)$$

where  $I_c$  is the intensity,  $K_{\text{gas},c}$  is the gas absorption coefficient,  $a_c$  is the weight and  $I_{\text{b},c} = a_c I_{\text{b}}$  is the black body intensity, each of pseudo-gas  $c$ . Details on the gas absorption coefficients  $\mathbf{K}_{\text{gas}} = (K_{\text{gas},c})$  and the weights  $\mathbf{a} = (a_c)$  are given in Section 2.5.2.

Solving the radiative transfer equations requires boundary conditions for the inlet, the outlet and the walls. For reflecting and emitting boundaries, the boundary conditions are defined by [15]

$$I_{\text{bound}} = \varepsilon_{\text{bound}} n_{\text{gas}}^2 \frac{\sigma T_{\text{bound}}^4}{\pi} + \frac{\rho_{\text{bound}}}{\pi} \int_{\langle \mathbf{n}, \mathbf{s} \rangle < 0} I_{\text{bound}} |\langle \mathbf{n}, \mathbf{s} \rangle| d\Omega \quad (2.127)$$

or

$$I_{\text{bound},c} = a_{\text{bound},c} \varepsilon_{\text{bound},c} n_{\text{gas}}^2 \frac{\sigma T_{\text{bound}}^4}{\pi} + \frac{\rho_{\text{bound},c}}{\pi} \int_{\langle \mathbf{n}, \mathbf{s} \rangle < 0} I_{\text{bound},c} |\langle \mathbf{n}, \mathbf{s} \rangle| d\Omega, \quad (2.128)$$

where  $\varepsilon_{\text{bound}}$  is the boundary emissivity,  $T_{\text{bound}}$  is the boundary temperature,  $\rho_{\text{bound}}$  is the boundary reflectivity,  $\mathbf{n}$  is the normal vector,  $\mathbf{s}$  is the radiation beam vector,  $I_{\text{bound}}$  is the intensity at the boundary,  $a_{\text{bound},c}$  is the weight of pseudo-gas  $c$  at the boundary temperature,  $\varepsilon_{\text{bound},c}$  is the boundary emissivity for pseudo-gas  $c$ ,  $\rho_{\text{bound},c}$  is the boundary reflectivity for pseudo-gas  $c$  and  $I_{\text{bound},c}$  is the intensity at the boundary for pseudo-gas  $c$ . The boundary emissivity  $\varepsilon_{\text{bound}}$  and the boundary reflectivity  $\rho_{\text{bound}}$  are linked by

$$\rho_{\text{bound}} + \varepsilon_{\text{bound}} = 1, \quad (2.129)$$

while the boundary emissivity  $\varepsilon_{\text{bound},c}$  and the boundary reflectivity  $\rho_{\text{bound},c}$  are connected through

$$\rho_{\text{bound},c} + \varepsilon_{\text{bound},c} = 1. \quad (2.130)$$

The boundary emissivities and the boundary reflectivities are defined according to the boundary type; the inlet and the outlet are treated as black bodies while the walls are described as grey with application of both grey-gas and weighted-sum-of-grey-gas models. The intensities  $I$  and  $I_c$  are used to determine the incident radiations  $G$  and  $G_c$ , respectively. The incident radiations  $G$  and  $G_c$  are given by

$$G = \int_0^{4\pi} I \, d\Omega, \quad (2.131)$$

$$G_c = \int_0^{4\pi} I_c \, d\Omega \quad (2.132)$$

and are used to determine the energy source term due to thermal radiation  $S_{E,\text{rad}}$  (see Section 2.2.1.4). When applying the grey-gas model, the source term due to thermal radiation  $S_{E,\text{rad}}$  is defined by

$$S_{E,\text{rad}} = -\text{div}(\dot{q}_{\text{rad}}) = (K_{\text{gas}} + K_{\text{part}}) G - 4\pi (K_{\text{gas}} I_b + E_{\text{part}}), \quad (2.133)$$

where  $\dot{q}_{\text{rad}}$  is the heat flux due to thermal radiation. When using the weighted-sum-of-grey-gas model, the source term due to thermal radiation  $S_{E,\text{rad}}$  is given by [15]

$$S_{E,\text{rad}} = -\text{div}\left(\sum_c \dot{q}_{\text{rad},c}\right) = \sum_{c=1}^{N_{\text{ps}}} (K_{\text{gas},c} + K_{\text{part}}) G_c - 4\pi (K_{\text{gas},c} I_{b,c}) + a_c E_{\text{part},c}, \quad (2.134)$$

where  $\dot{q}_{\text{rad},c}$  is the heat flux due to thermal radiation of pseudo-gas  $c$ . Furthermore, the incident radiations  $\mathbf{G} = (G_c)$  are summed up using the number of pseudo-gases  $N_{\text{ps}}$  for the calculation of the thermal radiation temperature  $T_{\text{rad}}$  (see Eq. (2.87)). The (total) incident radiation  $G$  is given by

$$G = \sum_{c=1}^{N_{\text{ps}}} G_c. \quad (2.135)$$

## 2.5.2 Thermal gas radiation property models

The thermal gas radiation properties were described according to Section 2.5 either using a grey-gas model or a weighted-sum-of-grey-gas model.

### 2.5.2.1 Grey-gas model

Grey-gas models assume non-spectral gas absorption coefficients  $K_{\text{gas}}$ . In this work, a constant value of  $0.53 \text{ m}^{-1}$  was applied following the preceding work [187], which demonstrated that similar predictions of gas temperature and gas species concentration

distributions can be obtained with this value and with a customised weighted-sum-of-grey-gas model (see Section 1.5).

### 2.5.2.2 Weighted-sum-of-grey-gas model

Weighted-sum-of-grey-gas models are described using weights  $\mathbf{a} = (a_c)$  and gas absorption coefficients  $\mathbf{K}_{\text{gas}} = (K_{\text{gas},c})$  for pseudo-gases and are generally defined by

$$\varepsilon_{\text{gas,tot}} = \sum_{c=1}^{N_{\text{ps}}} a_c(T) (1 - \exp(-K_{\text{gas},c} L)) , \quad (2.136)$$

where  $\varepsilon_{\text{gas,tot}}$  is the total gas emissivity and  $L$  is the path length. The gas absorption coefficient  $K_{\text{gas},c}$  and the weight  $a_c$  are given by

$$K_{\text{gas},c} = C_{K,c} (x_{\text{H}_2\text{O,gas}} + x_{\text{CO}_2,\text{gas}} + x_{\text{CO,gas}}) p_{\text{gas}} , \quad (2.137)$$

$$a_c = \sum_{i=1}^{N_a} C_{a,c,i} \left( \frac{T}{1200 \text{ K}} \right)^{i-1} , \quad (2.138)$$

where  $C_{K,c}$  is a (pressure-based gas absorption) coefficient of pseudo-gas  $c$ ,  $N_a$  is the number of terms for the calculation of the weights and  $C_{a,c,1}, \dots, C_{a,c,N_a}$  are polynomial coefficients for pseudo-gas  $c$ .

The weighted-sum-of-grey-gas model used in this work was adopted from the preceding work [187] and actually consists of several individual weighted-sum-of-grey-gas models. The latter were generated using emissivity charts for atmospheric gasification conditions corresponding to 13 mole fraction ratios of water vapour and carbon dioxide between 1.5 and 3.3 and corresponding to constant mole fractions of carbon monoxide. Accordingly, only water vapour, carbon dioxide and carbon monoxide were assumed to be radiating gases; absorption and emission contributions of other gases such as methane were neglected. Typical gas species mole fractions of carbon monoxide, carbon dioxide and water vapour are summarised for the REGA experiments TUC3 V786 and TUC5 V1105 in Table 2.8.

**Table 2.8:** Typical gas species mole fractions of carbon monoxide  $x_{\text{CO,gas}}$ , carbon dioxide  $x_{\text{CO}_2,\text{gas}}$  and water vapour  $x_{\text{H}_2\text{O,gas}}$  in the CFD simulations of the REGA experiments TUC3 V786 and TUC5 V1105.

REGA experiment	$x_{\text{CO,gas}}$	$x_{\text{CO}_2,\text{gas}}$	$x_{\text{H}_2\text{O,gas}}$
TUC3 V786	0.08-0.17	0.13-0.20	0.24-0.37
TUC5 V1105	0.19-0.24	0.11-0.15	0.31-0.37

Each emissivity chart was obtained using (i) line-by-line calculations with the cut-off criteria and the software of Alberti et al. [5, 6, 7, 8] at 51 temperatures between 450 K

and 2950 K and (ii) using 30 discrete pressure path lengths based on logarithmic spacing between 0.001 bar cm and 6000 bar cm. The emissivity charts were fitted using non-linear optimisation with the *fmincon* method of Matlab [194] and using a pre-defined number of pseudo-gases  $N_{ps} = 6$ , a pre-defined number of terms for the calculation of the weights  $N_a = 7$  and Eqs. (2.136)-(2.138) [67]. However, since setting the mole fraction of carbon dioxide  $x_{CO_2, gas}$  in Eq. (2.137) to zero improved the numerical approximations, Eq. (2.137) was replaced by

$$K_{gas,c} = C_{K,c} \left( x_{H_2O, gas} + x_{CO_2, gas} \right) p_{gas} . \quad (2.139)$$

This finding was actually not reported in the preceding work [187] but can be explained by the overlapping of the 4.67  $\mu\text{m}$ -absorption band of carbon monoxide with the 6.3  $\mu\text{m}$ -absorption band of water vapour and the 4.3  $\mu\text{m}$ -absorption band of carbon dioxide [66, 67]. Compared to the preceding work [187], improvements were focussed on the previously erroneous implementation (see Section 3.1).

### 2.5.3 Thermal particle radiation property models

The thermal particle radiation properties introduced in Section 2.5 are the (mean) particle absorption coefficient  $K_{part}$ , the (mean) particle scattering coefficient  $\sigma_{part}$ , the particle emission  $E_{part}$  and the particle scattering phase function  $\Phi_{part}$ . In ANSYS Fluent [17], the former are defined by [15]

$$K_{part} = \frac{1}{V_{gas}} \sum_i \varepsilon_{part,i} A_{p,part,i} , \quad (2.140)$$

$$\sigma_{part} = \frac{1}{V_{gas}} \sum_i (1 - f_{part,i}) (1 - \varepsilon_{part,i}) A_{part,i} , \quad (2.141)$$

$$E_{part} = \frac{1}{V_{gas}} \sum_i \varepsilon_{part,i} A_{p,part,i} \frac{\sigma T_{part,i}^4}{\pi} , \quad (2.142)$$

where  $\varepsilon_{part,i}$  is the particle emissivity,  $A_{p,part,i}$  is the projected particle area,  $T_{part,i}$  is the particle temperature and  $f_{part,i}$  is the particle scattering factor, each of parcel  $i$ . The projected particle area  $A_{p,part}$  is given by [15]

$$A_{p,part} = \frac{\pi}{4} d_{part}^2 . \quad (2.143)$$

In ANSYS Fluent [17], approximations have thus to be provided for the particle emissivity  $\varepsilon_{part}$ , the particle scattering factor  $f_{part}$  and the particle scattering phase function  $\Phi_{part}$ . These quantities can be obtained, for example, using Mie theory, which provides spectral particle absorption coefficients  $Q_{abs,part,\eta}$ , spectral particle scattering coefficients  $Q_{scat,part,\eta}$  and spectral particle scattering phase function values  $\Phi_{part,\eta}$ . Subsequently, the spectral

averaged particle absorption coefficient  $Q_{\text{abs,part}}$ , the spectral averaged particle scattering coefficient  $Q_{\text{scat,part}}$  and the spectral averaged particle scattering phase function value  $\Phi_{\text{part}}$  can be determined by

$$Q_{\text{abs,part}} = \frac{\int_0^\infty Q_{\text{abs,part},\eta} \dot{e}_{\text{b},\eta} d\eta}{\int_0^\infty \dot{e}_{\text{b},\eta} d\eta}, \quad (2.144)$$

$$Q_{\text{scat,part}} = \frac{\int_0^\infty Q_{\text{scat,part},\eta} \dot{e}_{\text{b},\eta} d\eta}{\int_0^\infty \dot{e}_{\text{b},\eta} d\eta}, \quad (2.145)$$

$$\Phi_{\text{part}} = \frac{\int_0^\infty Q_{\text{scat,part},\eta} \Phi_{\text{part},\eta} \dot{e}_{\text{b},\eta} d\eta}{\int_0^\infty Q_{\text{scat,part},\eta} \dot{e}_{\text{b},\eta} d\eta}. \quad (2.146)$$

Here,  $\dot{e}_{\eta,\text{b}}$  is the spectral emissive power of a black body and is defined by

$$\dot{e}_{\eta,\text{b}} = \frac{C_1 \eta^3}{\exp(C_2 \eta/T) - 1}, \quad (2.147)$$

where  $C_1 = 3.7417... \cdot 10^{-12} \text{ W cm}^2$  and  $C_2 = 1.4387... \text{ cm K}$  are the common radiation constants.

The diameter dependent particle emissivity  $\varepsilon_{\text{part}}$  and the diameter dependent particle scattering  $f_{\text{part}}$  factor can finally be obtained by

$$\varepsilon_{\text{part}} = Q_{\text{abs,part}}, \quad (2.148)$$

$$f_{\text{part}} = 1 - \frac{Q_{\text{scat,part}} (1 - g)}{1 - \varepsilon_{\text{part}}}, \quad (2.149)$$

where  $g$  is the asymmetric factor determined by Mie theory. Concerning the particle scattering phase function value  $\Phi_{\text{part}}$ , additional diameter averaging needs to be applied due to interface restrictions of ANSYS Fluent [14, 17]. The diameter averaged approximation is defined by

$$\Phi_{\text{part}} := \frac{\int_{d_{\text{part,min}}}^{d_{\text{part,max}}} q_\gamma d_{\text{part}}^2 Q_{\text{scat,part}} \Phi_{\text{part}} dd_{\text{part}}}{\int_{d_{\text{part,min}}}^{d_{\text{part,max}}} q_\gamma d_{\text{part}}^2 Q_{\text{scat,part}} dd_{\text{part}}}, \quad (2.150)$$

where  $q_\gamma$  is the probability density function of the gamma distribution (see Section E.2). The preceding work of Mancini et al. [187] already established approximations for ethylene glycol using the Mie software of Mätzler [195] and the measurement data of Sani and Dell'Oro [266]. The particle emissivity  $\varepsilon_{\text{part}}$  was approximated by

$$\varepsilon_{\text{part}} = 0.0129977 \left( \lg \left( \frac{d_{\text{part}}}{\mu\text{m}} \right) \right)^2 + 0.231115 \lg \left( \frac{d_{\text{part}}}{\mu\text{m}} \right) + 0.007101. \quad (2.151)$$

In this work, this approximation was adopted for the CFD simulations while particle scattering of ethylene glycol was described based on previous results (see Section 1.5), i. e. assuming isotropic scattering with a zero particle scattering factor  $f_{\text{part}}$ . However, for

sensitivity analyses, more accurate emissivity values were tabulated using Mie calculations and using interpolated and extrapolated data for the spectral refractive index  $n_{\text{part},\eta}$  and the spectral absorption index  $k_{\text{part},\eta}$ . The interpolated and extrapolated data for the spectral refractive index  $n_{\text{part},\eta}$  and the spectral absorption index  $k_{\text{part},\eta}$  is compared with the measurement data [266] in Fig. 2.5. The tabulated values of the absorption efficiency  $Q_{\text{abs,part}}$  and the particle scattering efficiency  $Q_{\text{scat,part}}$  are shown for four different thermal radiation temperatures  $T_{\text{rad}}$  in Fig. 2.6.

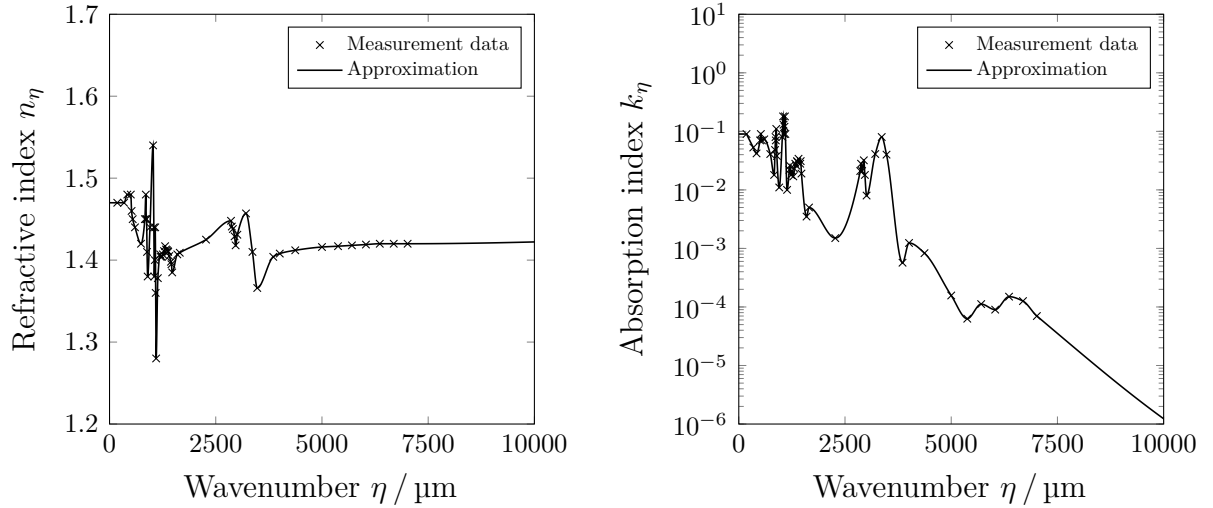


**Figure 2.5:** Spectral refractive index  $n_\eta$  and spectral absorption index  $k_\eta$  of ethylene glycol based on measurements [266] and piecewise cubic hermite interpolation and extrapolation.

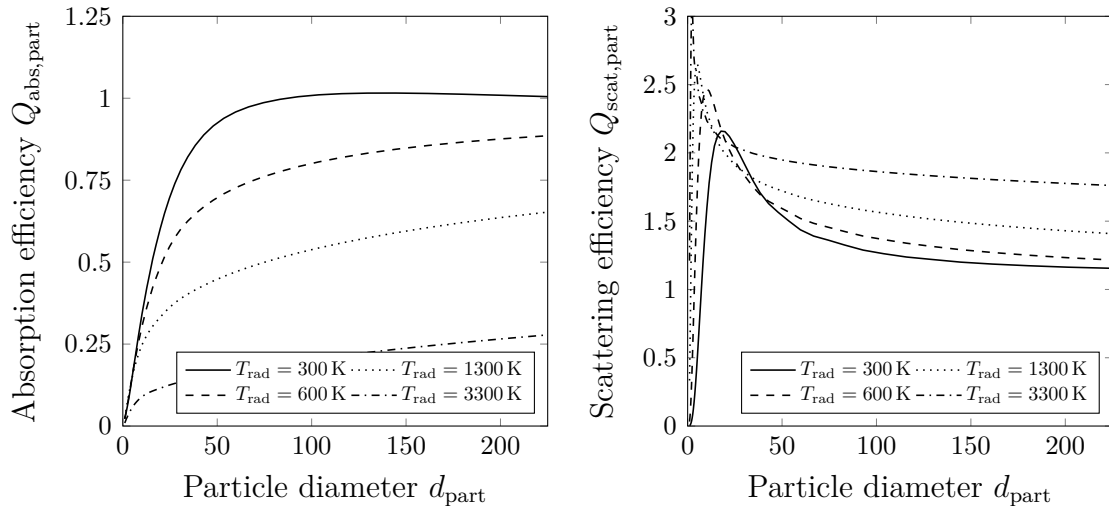


**Figure 2.6:** Particle absorption efficiency  $Q_{\text{abs,part}}$  and the particle scattering efficiency  $Q_{\text{scat,part}}$  of ethylene glycol for four different thermal radiation temperatures  $T_{\text{rad}}$  based on measurements [266] and Mie theory.

Mie calculations can also be applied for wood char or slurry particles. However, in view of the significant uncertainties related to atomisation and conversion of solids and slurries (see Sections 2.2.4.5 and 2.7), detailed a-priori calculations were not performed in this work.

For wood char particles, isotropic scattering was assumed while the particle emissivity  $\varepsilon_{\text{part}}$  and the particle scattering factor  $f_{\text{scat,part}}$  were given by a value of 0.8. The particle emissivity  $\varepsilon_{\text{part}}$  was thus not described as function of temperature or conversion (for example, see [180, 273]). For slurry particles, the properties were approximated using the properties of ethylene glycol during vaporisation while the properties of wood char were used during devolatilisation and heterogeneous gasification.

### 2.5.4 Thermal wall radiation property models

The thermal wall radiation properties are assumed to be grey. The emissivity values reported for  $\text{Al}_2\text{O}_3$  rich materials and temperatures above 1473.15 K are typically between 0.4 and 0.8 [24, 325]. In this work, the wall emissivity  $\varepsilon_{\text{wall}}$  was approximated with 0.8 in agreement with the preceding works [63, 64, 185, 186, 187] (see Section 3.1).

## 2.6 Ethylene glycol vaporisation

Distilled ethylene glycol of high purity ( $> 99.5\%$ ) was used in the REGA experiments as liquid surrogate fuel for pyrolysis oil [98, 99] since ethylene glycol is characterised by chemical properties similar to those of biogenic pyrolysis oils and enables a simplified mathematical description of the entrained flow gasification process [98]. While the conversion of pyrolysis oils needs to be modelled through combined vaporisation, decomposition and heterogeneous gasification models, the vaporisation of ethylene glycol can be accounted for using a single-component vaporisation model.

Numerous vaporisation models have been developed so far. Following Sirignano [292], they can be classified into six types. The simplest model assumes a constant particle temperature and is not sufficiently accurate for CFD simulations while the most detailed model relies on the Navier-Stokes equations and requires high computing times in CFD simulations. Good compromises are infinite thermal conductivity models and effective thermal conductivity models.

**Infinite thermal conductivity models** assume uniform temperature distributions inside the droplet, that only change with time. Internal heat transfer is accordingly neglected.

**Effective thermal conductivity models** assume one-dimensional temperature distributions inside the droplet and rely on an algebraic function for the effective liquid thermal conductivity. Appropriate approximations for the algebraic function have been derived from detailed CFD predictions (for example, see [3]).

Due to the assumption of uniform particle temperatures at each time step, the infinite thermal conductivity model in form of the classical vaporisation model was applied in this work. Additionally, the model of Abramzon and Sirignano [3] and the model of Sazhin et al. [270] were used for comparative calculations. The model of Abramzon and Sirignano [3] is an infinite thermal conductivity model while the model of Sazhin et al. [270] belongs to the effective thermal conductivity models.

Infinite thermal conductivity models and effective thermal conductivity models have in common that they do not resolve the film boundary layer and rely on the definition of a film condition. This condition is used for the calculation of most of the physical properties in each vaporisation model and is defined for single-component droplets using the film temperature [3]

$$T_{\text{film}} = T_{\text{part,s}} + f_{\text{film}} (T_{\text{gas}} - T_{\text{part,s}}) , \quad (2.152)$$

where  $T_{\text{part,s}}$  is the particle surface temperature and  $f_{\text{film}}$  is the film factor and is usually assumed to be 1/3 due to the good agreement between experimental and numerical results (for example, see [3, 301, 343]). Note that the particle surface temperature  $T_{\text{part,s}}$  is identical to the particle temperature  $T_{\text{part}}$  used in the classical vaporisation model and the model of Abramzon and Sirignano [3].

The classical vaporisation model, the vaporisation model of Abramzon and Sirignano [3] and the vaporisation model of Sazhin et al. [270] are described in Section 2.6.1, Section 2.6.2 and Section 2.6.3, respectively, and are compared in Section 2.6.4.

### 2.6.1 Classical model

The classical vaporisation model for single-component droplets assumes a spherical droplet with a uniform temperature distribution and a film boundary layer. The mass transfer rate between droplet and gas is given by

$$R_{\text{m,part}} = \frac{A_{\text{s,part}} \rho_{\text{gas,film}} D_{\text{C}_2\text{H}_6\text{O}_2,\text{gas,eff,film}}}{d_{\text{part}}} Sh_{\text{mod,film}} \ln(1 + B_{\text{m}}) , \quad (2.153)$$

where  $A_{\text{s,part}}$  is the particle surface area,  $\rho_{\text{gas,film}}$  is the gas density at film condition,  $D_{\text{C}_2\text{H}_6\text{O}_2,\text{gas,eff,film}}$  is an effective gas diffusion coefficient of ethylene glycol evaluated at film condition,  $Sh_{\text{mod,film}}$  is a modified Sherwood number at film condition and  $B_{\text{m}}$  is the Spalding mass transfer number.

The modified Sherwood number at film condition  $Sh_{\text{mod,film}}$  as well as the corresponding modified Nusselt number at film condition  $Nu_{\text{mod,film}}$  are calculated using the Ranz-Marshall correlations (see Section 2.2.5.3). The actual Sherwood number at film condition  $Sh_{\text{film}}$  is defined by

$$Sh_{\text{film}} = \begin{cases} Sh_{\text{mod,film}} , & \text{if } B_m = 0 \\ Sh_{\text{mod,film}} \ln \left( \frac{1+B_m}{B_m} \right) , & \text{else} \end{cases} , \quad (2.154)$$

and the actual Nusselt number at film condition  $Nu_{\text{film}}$  is obtained by

$$Nu_{\text{film}} = \begin{cases} Nu_{\text{mod,film}} , & \text{if } B_T = 0 \\ Nu_{\text{mod,film}} \ln \left( \frac{1+B_T}{B_T} \right) , & \text{else} \end{cases} , \quad (2.155)$$

where  $B_T$  is the Spalding heat transfer number. The Spalding mass transfer number  $B_m$  and the Spalding heat transfer number  $B_T$  are defined by

$$B_m = \frac{w_{\text{C}_2\text{H}_6\text{O}_2,\text{gas,s}} - w_{\text{C}_2\text{H}_6\text{O}_2,\text{gas}}}{1 + w_{\text{C}_2\text{H}_6\text{O}_2,\text{gas,s}}} , \quad (2.156)$$

$$B_T = (1 + B_m)^\varphi - 1 , \quad (2.157)$$

where  $w_{\text{C}_2\text{H}_6\text{O}_2,\text{gas,s}}$  and  $w_{\text{C}_2\text{H}_6\text{O}_2,\text{gas}}$  are the gas mass fractions of ethylene glycol at the surface and in the bulk, respectively. The model parameter  $\varphi$  is given by

$$\varphi = \frac{1}{Le_{\text{film}}} \frac{Sh_{\text{mod,film}}}{Nu_{\text{mod,film}}} \frac{\hat{C}_{p,\text{C}_2\text{H}_6\text{O}_2,\text{gas,film}}}{\hat{C}_{p,\text{gas,film}}} , \quad (2.158)$$

where  $Le_{\text{film}}$  is the Lewis number at film condition,  $\hat{C}_{p,\text{C}_2\text{H}_6\text{O}_2,\text{gas,film}}$  is the specific gas heat capacity of ethylene glycol at film condition and  $\hat{C}_{p,\text{gas,film}}$  is the specific gas heat capacity at film condition. The Lewis number at film condition  $Le_{\text{film}}$  is defined by

$$Le_{\text{film}} = \frac{\lambda_{\text{gas,film}}}{\rho_{\text{gas,film}} \hat{C}_{p,\text{gas,film}} D_{\text{C}_2\text{H}_6\text{O}_2,\text{gas,eff,film}}} , \quad (2.159)$$

where  $\lambda_{\text{gas,film}}$  is the gas thermal conductivity at film condition.

The heat transfer between droplet and gas neglects the pressure change work and the pressure dependency of enthalpy. The energy transfer rate  $R_{\text{E,part}}$  and the specific enthalpy of transition  $\Delta_{\text{trs}}\hat{H}$  are given by

$$R_{\text{E,part}} = -R_{\text{m,part}} \Delta_{\text{vap}}\hat{H}_{\text{C}_2\text{H}_6\text{O}_2} , \quad (2.160)$$

$$\Delta_{\text{trs}}\hat{H} = \Delta_{\text{vap}}\hat{H}_{\text{C}_2\text{H}_6\text{O}_2,\text{ref}} , \quad (2.161)$$

where  $\Delta_{\text{vap}}\hat{H}_{\text{C}_2\text{H}_6\text{O}_2}$  and  $\Delta_{\text{vap}}\hat{H}_{\text{C}_2\text{H}_6\text{O}_2,\text{ref}}$  are the specific enthalpies of vaporisation of ethylene glycol at particle temperature and reference temperature, respectively.

### 2.6.2 Model of Abramzon and Sirignano

In contrast to the classical vaporisation model, the vaporisation model of Abramzon and Sirignano [3] takes into account the thickening of the laminar boundary layer due to Stefan flow [3] and relies on a modified Sherwood number at film condition [3]

$$Sh_{\text{mod, film}} = 2 + \frac{Sh_{0, \text{film}} - 2}{F_m} \quad (2.162)$$

and a modified Nusselt number at film condition [3]

$$Nu_{\text{mod, film}} = 2 + \frac{Nu_{0, \text{film}} - 2}{F_T}. \quad (2.163)$$

Here,  $Sh_{0, \text{film}}$  is the default Sherwood number and  $Nu_{0, \text{film}}$  is the default Nusselt number, each at film condition; both numbers are calculated using the Ranz-Marshall correlations (see Section 2.2.5.3).  $F_m$  and  $F_T$  are the correction factors for mass transfer and heat transfer and are defined by [3]

$$F_m = \begin{cases} (1 + B_m)^{0.7}, & \text{if } B_m = 0 \\ (1 + B_m)^{0.7} \ln\left(\frac{1+B_m}{B_m}\right), & \text{else} \end{cases}, \quad (2.164)$$

and [3]

$$F_T = \begin{cases} (1 + B_T)^{0.7}, & \text{if } B_T = 0 \\ (1 + B_T)^{0.7} \ln\left(\frac{1+B_T}{B_T}\right), & \text{else} \end{cases}. \quad (2.165)$$

### 2.6.3 Model of Sazhin

The vaporisation model of Sazhin et al. [270] adopts most parts of the model of Abramzon and Sirignano [3] but relies on the analytical solution of the heat conduction equation to describe the temperature distribution inside a droplet [270]. Adaptions have been made to account for a non-uniform initial (or temporary) temperature distribution and intra-droplet radiative heat transfer [270]. Accordingly, Eq. (2.85) corresponding to the calculation of the uniform particle temperature  $T_{\text{part}}$  is replaced by a series formula that assumes or neglects intra-droplet radiative heat transfer. The initial condition given by Eq. (2.86) is used for the initial particle temperature distribution.

The series formulae accounting for or neglecting the intra-droplet radiative heat transfer are given in Section 2.6.3.1 and Section 2.6.3.2, respectively. Absorption and emission are accounted for using a thermal radiation power distribution, which is described in Section 2.6.3.3.

### 2.6.3.1 Temperature distribution in presence of intra-droplet radiation

If absorption and emission inside the droplet are accounted for using a thermal radiation power distribution  $P$ , the particle temperature  $T_{\text{part}}$  at an inner radius  $r$  after a small time step  $\Delta t$  is given by [270]

$$\begin{aligned}
 T_{\text{part}} = & \frac{1}{\tilde{r}} \sum_{n=1}^{\infty} \left( \frac{p_n}{\kappa_{\text{T}} \Lambda_{\text{T},n}^2} + \exp(-\kappa_{\text{T}} \Lambda_{\text{T},n}^2 \Delta t) \left( q_{\text{T},n} - \frac{p_n}{\kappa_{\text{T}} \Lambda_{\text{T},n}^2} \right) \right. \\
 & - \frac{\sin(\Lambda_{\text{T},n})}{\|v_{\text{T},n}\|^2 \Lambda_{\text{T},n}^2} \mu_0 \exp(-\kappa_{\text{T}} \Lambda_{\text{T},n}^2 \Delta t) \\
 & \left. - \frac{\sin(\Lambda_{\text{T},n})}{\|v_{\text{T},n}\|^2 \Lambda_{\text{T},n}^2} \frac{d\mu_0}{dt} \frac{(1 - \exp(-\kappa_{\text{T}} \Lambda_{\text{T},n}^2 \Delta t))}{\kappa_{\text{T}} \Lambda_{\text{T},n}^2} \right) \sin(\Lambda_{\text{T},n} \tilde{r}) + T_{\text{eff}}, \tag{2.166}
 \end{aligned}$$

where [270]

$$\begin{aligned}
 \tilde{r} &= \frac{r}{r_{\text{part}}}, \quad \kappa_{\text{T}} = \frac{\lambda_{\text{eff}}}{\rho_{\text{liq}} \hat{C}_{p,\text{liq}} r_{\text{part}}^2}, \quad q_{\text{T},n} = \frac{1}{\|v_{\text{T},n}\|^2} \int_0^1 \tilde{r} T \sin(\Lambda_{\text{T},n} \tilde{r}) d\tilde{r}, \\
 p_n &= \frac{1}{\rho_{\text{liq}} \hat{C}_{p,\text{liq}}} \frac{1}{\|v_{\text{T},n}\|^2} \int_0^1 \tilde{r} P \sin(\Lambda_{\text{T},n} \tilde{r}) d\tilde{r}, \\
 \|v_{\text{T},n}\| &= \frac{1}{2} \left( 1 + \frac{h_{0,\text{T}}}{h_{0,\text{T}}^2 + \Lambda_{\text{T},n}^2} \right), \quad h_{0,\text{T}} = \frac{h_{\text{conv,part}} r_{\text{part}}}{\lambda_{\text{eff}}} - 1, \\
 \mu_0(t) &= \frac{h_{\text{conv,part}} T_{\text{eff}}(t) r_{\text{part}}}{\lambda_{\text{eff}}}, \quad T_{\text{eff}} = T_{\text{gas}} - \frac{\rho_{\text{part}} \Delta_{\text{vap}} \hat{H}}{h_{\text{conv,part}}} \frac{1}{4 \pi r_{\text{part}}^2 \rho_{\text{liq}}} \frac{dm_{\text{part}}}{dt}.
 \end{aligned}$$

$\Lambda_{\text{T}} = (\Lambda_{\text{T},n})$  are eigenvalues for the calculation of the temperature distribution inside the droplet and are obtained from [270]

$$\Lambda_{\text{T},n} \cos(\Lambda_{\text{T},n}) + h_{0,\text{T}} \sin(\Lambda_{\text{T},n}) = 0. \tag{2.167}$$

Furthermore,  $r_{\text{part}}$  is the particle radius,  $\rho_{\text{liq}}$  is the liquid density,  $\hat{C}_{p,\text{liq}}$  is the specific liquid heat capacity and  $\lambda_{\text{eff}}$  is the effective thermal conductivity. The latter is defined by [3]

$$\lambda_{\text{eff}} = \chi \lambda_{\text{liq}}, \tag{2.168}$$

where  $\lambda_{\text{liq}}$  is the liquid thermal conductivity and  $\chi_{\text{T}}$  is a factor accounting for the effect of internal recirculation. Abramzon and Sirignano [3] fitted this factor as

$$\chi_{\text{T}} = \begin{cases} 1.86 + 0.86 \tanh\left(2.225 \lg\left(\frac{Pe_{\text{liq}}}{30}\right)\right), & \text{if } Pe_{\text{liq}} > 0 \\ 1, & \text{else} \end{cases}, \tag{2.169}$$

where  $Pe_{\text{liq}}$  is the liquid Peclet number which is the product of the liquid Reynolds number

$$Re_{\text{liq}} = \frac{\rho_{\text{liq}} u_{\text{liq,max}} d_{\text{part}}}{\eta_{\text{liq}}} \quad (2.170)$$

and the liquid Prandtl number

$$Pr_{\text{liq}} = \frac{\eta_{\text{liq}} \hat{C}_{p,\text{liq}}}{\lambda_{\text{liq}}}. \quad (2.171)$$

The maximum liquid velocity  $u_{\text{liq,max}}$  at the particle surface is given by [3]

$$u_{\text{liq,max}} = \frac{1}{32} \|\mathbf{u}_{\text{part}} - \mathbf{u}_{\text{gas}}\| \left( \frac{\eta_{\text{gas,film}}}{\eta_{\text{liq}}} \right) Re_{\text{part,film}} C_d, \quad (2.172)$$

where  $Re_{\text{part,film}}$  is the particle Reynolds number at film condition and  $\eta_{\text{liq}}$  is the liquid dynamic viscosity.

The calculation using Eq. (2.166) should generally be performed twice for each time step [271]. Firstly, a temporary new particle temperature distribution should be obtained using the particle radius  $r_{\text{part}}$  from the previous time step [271]. Subsequently, the particle radius  $r_{\text{part}}$  should be updated, and the particle temperature distribution should be recalculated using the new particle radius  $r_{\text{part}}$  [271]. However, the recalculation has not always been accounted for in previous works (for example, see [262]) since the double amount of computing time restricts the application in CFD simulations. Corresponding to that, baseline calculations were performed in this work without recalculation. Furthermore, previous works (for example, see [262]) have mainly neglected the time derivative of  $\mu_0$  in Eq. (2.166) in presence of constant gas temperatures  $T_{\text{gas}}$ , which is not valid anymore for gasification or combustion conditions. However, the successful implementation of the time derivative of  $\mu_0$  based on

$$\frac{d\mu_0}{dt} \approx \frac{T_{\text{eff}}(t) - T_{\text{eff}}(t - \Delta t)}{\Delta t} \frac{h_{\text{conv,part}} r_{\text{part}}}{\lambda_{\text{eff}}} \quad (2.173)$$

could not be achieved for the conditions assumed in this work. Therefore, the time derivative of  $\mu_0$  was not accounted for in the simulations.

### 2.6.3.2 Temperature distribution in absence of intra-droplet radiation

If absorption and emission inside the droplet are neglected, the Fourier series for the temperature distribution inside the particle  $T_{\text{part}}$  after a small time step  $\Delta t$  reduces to [271]

$$T_{\text{part}} = \frac{1}{\tilde{r}} \sum_{n=1}^{\infty} \left( q_{\text{T},n} \exp(-\kappa_{\text{T}} \Lambda_{\text{T},n}^2 \Delta t) - \frac{\sin(\Lambda_{\text{T},n})}{\|v_{\text{T},n}\|^2 \Lambda_{\text{T},n}^2} \mu_0 \exp(-\kappa_{\text{T}} \Lambda_{\text{T},n}^2 \Delta t) - \frac{\sin(\Lambda_{\text{T},n})}{\|v_{\text{T},n}\|^2 \Lambda_{\text{T},n}^2} \frac{d\mu_0}{dt} \frac{(1 - \exp(-\kappa_{\text{T}} \Lambda_{\text{T},n}^2 t))}{\kappa \Lambda_{\text{T},n}^2} \right) \sin(\Lambda_{\text{T},n} \tilde{r}) + T_{\text{eff}}. \quad (2.174)$$

### 2.6.3.3 Thermal radiation power distribution

The thermal radiation power distribution is calculated by [78, 270]

$$P = \frac{6}{\pi d_{\text{part}}} \int_{\eta_1}^{\eta_2} w Q_{\text{abs,part},\eta} \dot{e}_{\eta,\text{b}} d\eta, \quad (2.175)$$

where  $w$  is the weighing function and  $Q_{\text{abs,part},\eta}$  is the spectral absorption efficiency. The weighting function  $w$  is given by [78, 270]

$$w = \begin{cases} \frac{(1 - \mu_* \Theta(\tilde{r} - 1/n_{\text{part},\eta})) (\tilde{r}^2 + \gamma_{\eta})}{0.6 (1 - \mu_c^5) - \mu_c^3/n_{\text{part},\eta}^2 (1 - \mu_c^3)}, & \text{if } \tau_{\eta,0} < n_{\text{part},\eta} \sqrt{2.5} \\ \frac{\xi^2 \tau_{\eta,0}^2 \exp(-\xi (\tau_{\eta,0} - \tau_{\eta}))}{3 \tau_{\eta,0} (\xi \tau_{\eta,0} - 2) + 2/\xi (1 - \exp(-\xi \tau_{\eta,0}))}, & \text{else} \end{cases}, \quad (2.176)$$

where [78, 270]

$$\mu_* = \sqrt{1 - \left(\frac{1}{n_{\text{part},\eta} \tilde{r}}\right)^2}, \quad \mu_c = \sqrt{1 - \left(\frac{1}{n_{\text{part},\eta}}\right)^2}, \quad \tau_{\eta,0} = 4 \pi k_{\text{part},\eta} \eta r_{\text{part}},$$

$$\Theta(x) = \begin{cases} 0, & \text{if } x < 0 \\ 1 & \text{else} \end{cases}, \quad \gamma_{\eta} = \frac{1.5}{\tau_{\eta,0}^2} - \frac{0.6}{n_{\text{part},\eta}^2}, \quad \tau_{\eta} = 4 \pi k_{\text{part},\eta} \eta \tilde{r} r_{\text{part}},$$

$$\xi = \frac{2}{(1 + \mu_c)}.$$

The exact spectral particle absorption efficiency  $Q_{\text{abs,part},\eta}$  can be obtained using Mie theory (see Section 2.5.3). However, since this is time consuming for single-droplet vaporisation simulations, Dombrovsky et al. [78, 270] developed an approximation, which is given by [78, 270]

$$Q_{\text{abs,part},\eta} = \frac{4 n_{\text{part},\eta}}{(n_{\text{part},\eta} + 1)^2} (1 - \exp(-2 \pi k_{\text{part},\eta} \eta r_{\text{part}})). \quad (2.177)$$

## 2.6.4 Comparisons and conclusions

### 2.6.4.1 Thermal radiation power distribution

The spectral particle absorption efficiencies  $Q_{\text{abs,part},\eta}$  based on Mie theory or Dombrovsky approximation (see Eq. (2.177)) are shown for ethylene glycol and several particle diameters  $d_{\text{part}}$  in Fig. 2.7. The comparison demonstrates that the Dombrovsky approximation mainly provides similar predictions for the spectral particle absorption efficiency  $Q_{\text{abs,part},\eta}$  compared to Mie theory. Smaller deviations can typically be found for wavenumbers below  $1800 \text{ cm}^{-1}$ .

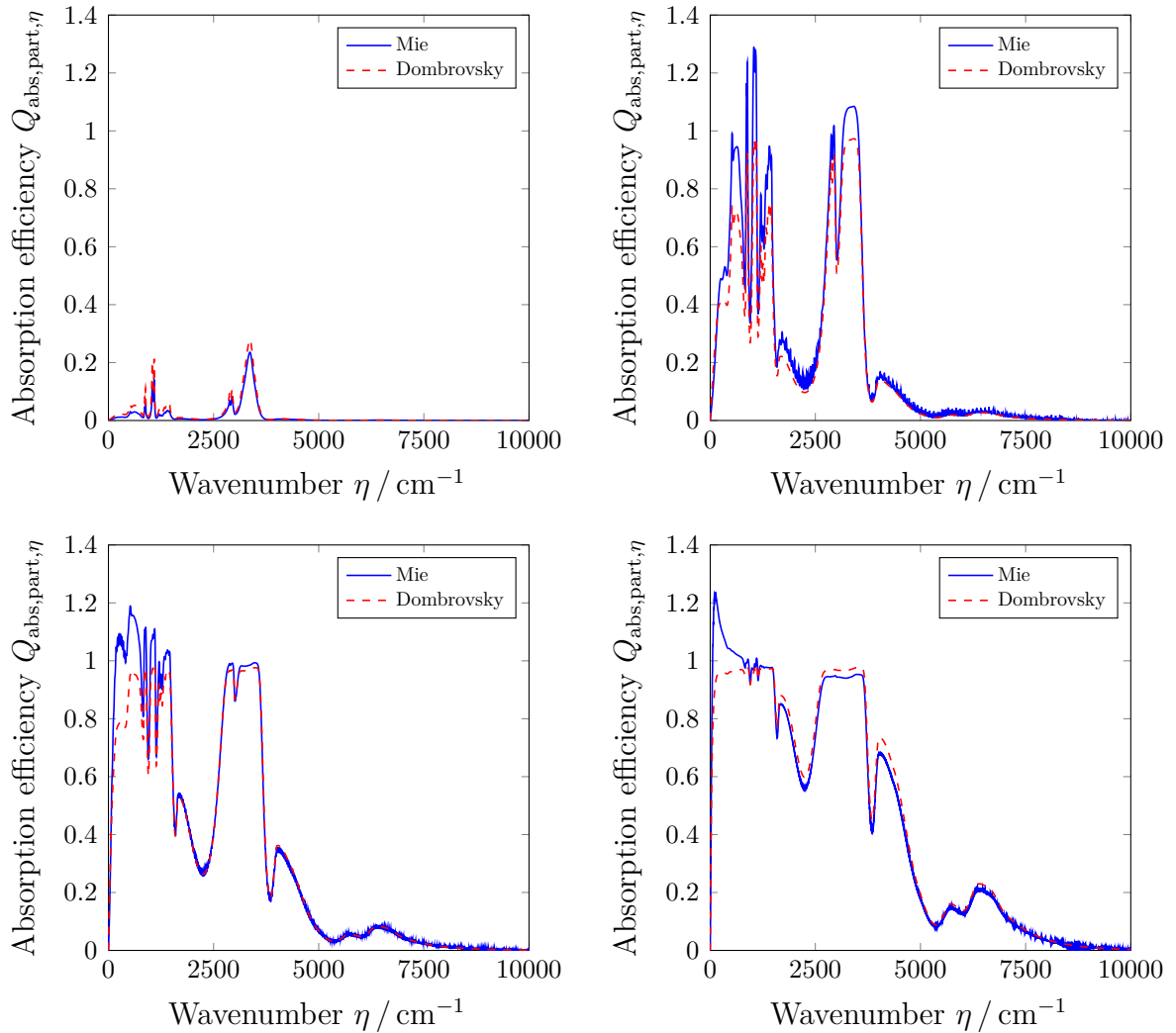


**Figure 2.7:** Spectral particle absorption efficiencies  $Q_{\text{abs,part},\eta}$  based on Mie theory or Dombrovsky approximation for particle diameters of  $1 \mu\text{m}$  (top left),  $25 \mu\text{m}$  (top right),  $75 \mu\text{m}$  (bottom left) and  $225 \mu\text{m}$  (bottom right).

The radial profiles of the thermal radiation power  $P$  for several thermal radiation temperatures  $T_{\text{rad}}$  are illustrated for ethylene glycol in Fig. 2.8. The comparison shows that

the predicted thermal radiation powers for ethylene glycol based on Dombrovsky approximation are quite similar to values based on Mie theory. This applies particular for larger particle diameters. Therefore, the Dombrovsky approximation was regarded as accurate in this work and was coupled with the vaporisation model of Sazhin et al. [270] for the single-droplet vaporisation simulations described in Section 2.6.4.2.

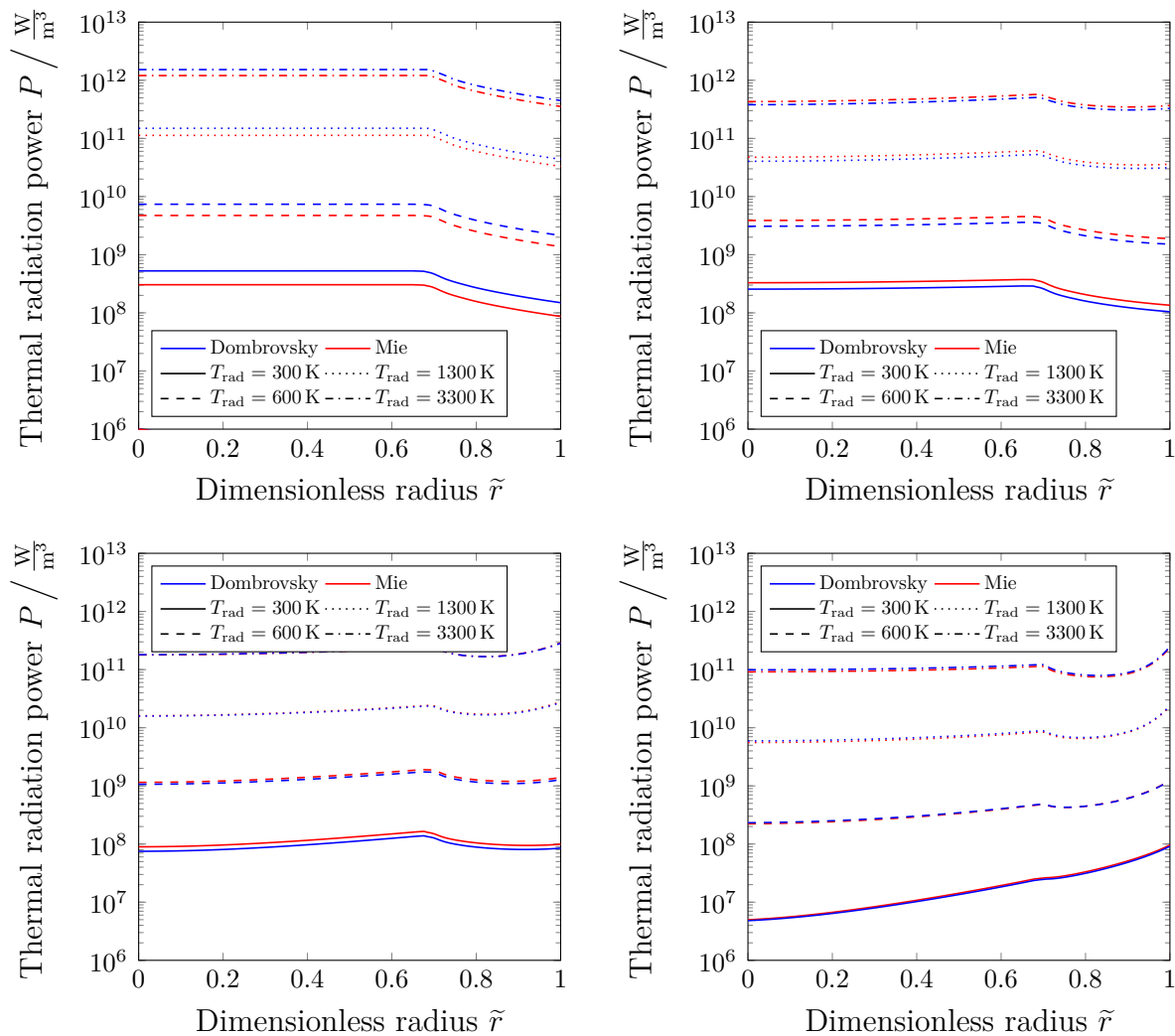


**Figure 2.8:** Thermal radiation powers  $P$  (based on Mie theory or Dombrovsky approximation) for thermal radiation temperatures  $T_{\text{rad}}$  of 300 K, 600 K, 1300 K and 3300 K and for particle diameters of  $1\ \mu\text{m}$  (top left),  $25\ \mu\text{m}$  (top right),  $75\ \mu\text{m}$  (bottom left) and  $225\ \mu\text{m}$  (bottom right).

### 2.6.4.2 Single-droplet vaporisation

Preceding works [63, 64, 88, 89, 187] relied either on the classical vaporisation model or on the vaporisation model of Abramzon and Sirignano [3]. In order to verify the rather minor influence for the vaporisation of ethylene glycol, comparative single-particle vaporisation simulations were carried out using the classical vaporisation model, the vaporisation model of Abramzon and Sirignano [3] and the vaporisation model of Sazhin et al. [270].

For two prescribed trajectories shown in Fig. 2.9, profiles of gas temperature, thermal radiation temperature and gas composition were extracted from the CFD simulation of the REGA experiment TUC3 V786 (see Chapter 4). The first trajectory is defined along the *axis*, between the points (5 mm | 0 mm) and (1100 mm | 0 mm). The second trajectory is defined along a *diagonal*, between the points (5 mm | 0 mm) and (1100 mm | 140 mm). The profiles of gas temperature  $T_{\text{gas}}$  and gas velocity  $u_{\text{gas}}$  are shown in Fig. 2.10. Accordingly, both trajectories are characterised by non-constant gas conditions in contrast to the conditions regarded in typical comparisons (for example, see [262, 271]).

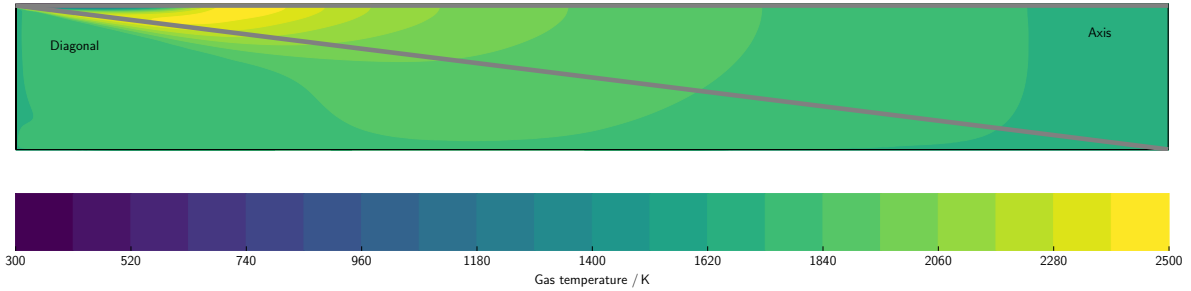


**Figure 2.9:** Predicted gas temperature distribution for the REGA experiment TUC3 V789 obtained using the DLR2017/RM mechanism. Axis: trajectory along the *axis*; Diagonal: trajectory along the *diagonal*.

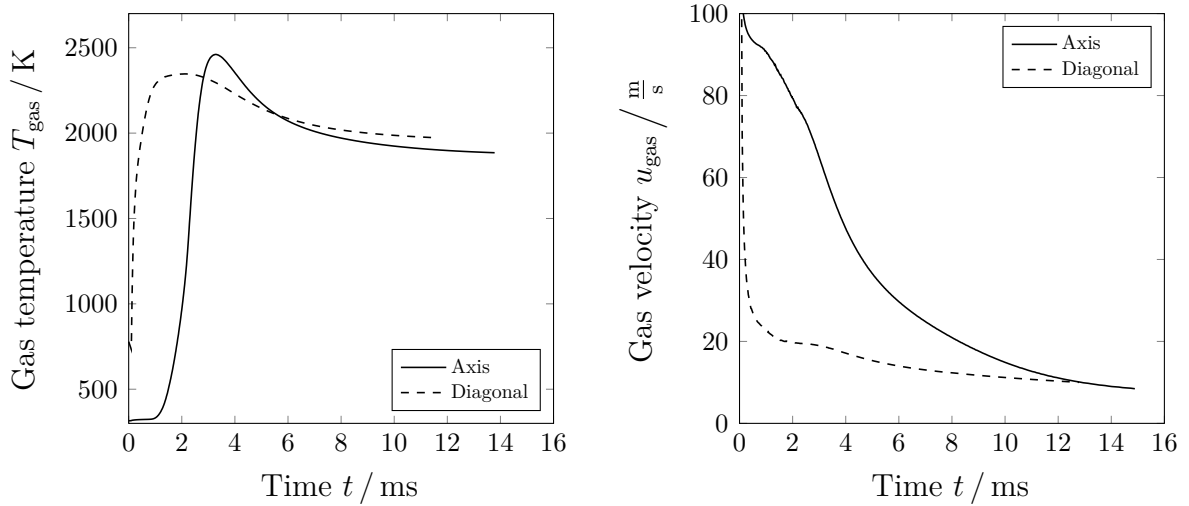


**Figure 2.10:** Predicted gas temperatures  $T_{\text{gas}}$  and predicted gas velocities  $u_{\text{gas}}$  along the reactor axis and the reactor diagonal for the REGA experiment TUC3 V786.

The single-particle vaporisation simulations subsequently accounted for or neglected thermal radiation and were performed using non-constant time steps  $\Delta t$  estimated by

$$\Delta t|_t = \Delta t|_{t-\Delta t} \left( \frac{d_{\text{part}}|_t}{d_{\text{part}}|_{t-\Delta t}} \right)^2, \quad (2.178)$$

where  $\Delta t|_{t=0}$  was given through values between  $10^{-5}$  s and  $10^{-6}$  s. The emissivity was

described using the polynomial approximation (see Section 2.5.3 and Eq. (2.151)), and the vapour film diffusion coefficient was accounted for using the Fickian approximation (see Section F.6.6 and Eq. (F.50)). Furthermore, the simulations with the model of Sazhin et al. were carried out without recalculation (see Section 2.6.3.1), with a wavenumber discretisation of  $25 \text{ cm}^{-1}$ , with 1001 equidistant radial nodes and 200 sum terms. Such settings ensured numerically stable simulations and provided accurate results (see Chapter H). The results of the simulations that neglected thermal radiation are shown in Figs. 2.11, while the results of the simulations that accounted for thermal radiation are depicted in Fig. 2.12. Accordingly, all three vaporisation models predict similar vaporisation times in both absence and presence of thermal radiation (see Fig. 2.11 (right) and Fig. 2.12 (right)). However, the results also show that non-uniform temperature heating is very likely and that thermal intra-droplet radiation significantly changes the heating process (see Fig. 2.11 (left) and Fig. 2.12 (left)).

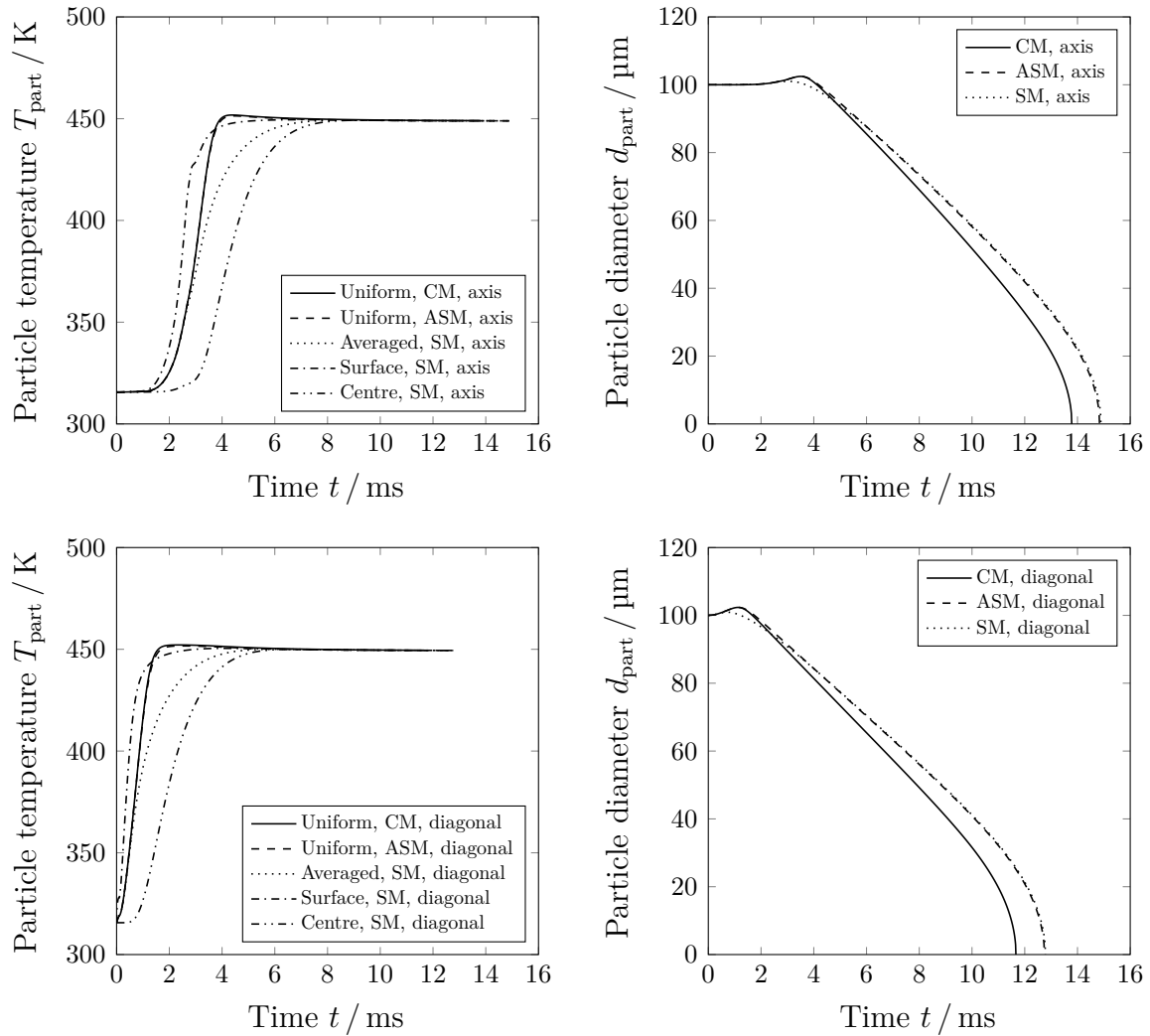


**Figure 2.11:** Simulated particle temperatures  $T_{\text{part}}$  and simulated particle diameters  $d_{\text{part}}$  along the reactor axis (top) and the reactor diagonal (bottom) based on the classical model (CM), the model of Abramzon and Sirignano (ASM) or the model of Sazhin et al. (SM) in absence of thermal radiation.

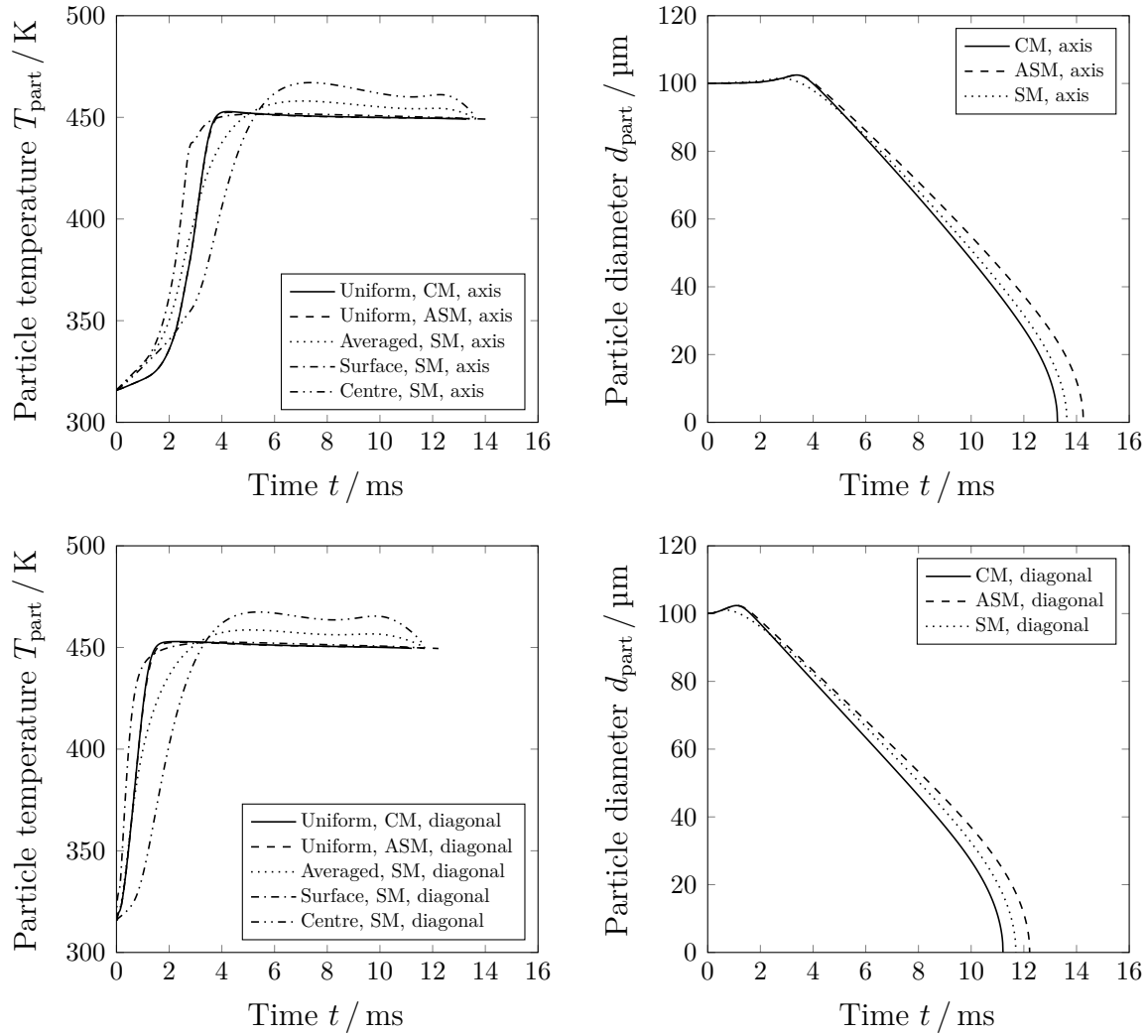


**Figure 2.12:** Simulated particle temperatures  $T_{\text{part}}$  and simulated particle diameters  $d_{\text{part}}$  along the reactor axis (top) and the reactor diagonal (bottom) based on the classical model (CM), the model of Abramzon and Sirignano (ASM) or the model of Sazhin et al. (SM) in presence of thermal radiation.

## 2.7 Wood char conversion

Wood char is the solid product of the fast pyrolysis of wood at moderate temperatures ( $\sim 900$  K) using high heating rates ( $\sim 10^4$ - $10^5$  K/s) and short residence times ( $< 2$  s) [210]. Its properties are influenced by the properties of the original wood and by the pyrolysis operating conditions. Increasing residence times or increasing operating temperatures typically decrease the hydrogen and oxygen contents and increase the carbon content. Wood chars become increasingly similar to graphite [220]. Furthermore, wood chars are characterised by high porosities and large pore sizes [72] and are assumed to be phenomenologically similar to coal chars. According to that, the compositions of both chars are determined using elemental and proximate analyses. Furthermore, the conversion of both chars are typically defined using two consecutive processes: devolatilisation and heterogeneous gasification (for example, see [72]).

Devolatilisation reflects the decomposition of the solid phase into volatiles (vol), fixed combustible substances (comb) and fixed residual substances (ash) according to



while heterogeneous gasification describes the chemical reactions of the fixed combustible substances with the major gas species (i. e. carbon monoxide, carbon dioxide, hydrogen, water vapour and oxygen). In previous CFD studies on entrained flow gasification, devolatilisation and heterogeneous gasification kinetics have usually been adopted from literature (for example, see [214]), whereas customised kinetics were seldom applied in spite of the fact that devolatilisation and heterogeneous gasification kinetics should be developed for the specific gasifier conditions. Exemplary exceptions are the studies of Watanabe and Otaka [331], Vascellari et al. [322, 323, 324], Halama and Spliethoff [117] and Steibel et al. [299]. Watanabe and Otaka [331] used the kinetics of Kajitani et al. [146] developed for high-temperature and high-pressure conditions. Vascellari et al. [322, 323, 324] used detailed char devolatilisation and gasification models and laboratory-scale experiments to calibrate devolatilisation and heterogeneous gasification rates and showed that the agreement between numerical and experimental results was good for lower-rank coals and sufficient for higher-rank coals. Halama and Spliethoff [117] and Steibel et al. [299] also used models for char devolatilisation and gasification based on laboratory-scale experiments and accounting for the effect of thermal annealing.

In this work, devolatilisation and heterogeneous gasification kinetics were adopted from HVIGasTech works and were combined with assumptions and models for the chemical and physical properties and the morphology changes during both devolatilisation and heterogeneous gasification. The chemical and physical properties are presented in Sections 2.7.1 and 2.7.2, the morphology changes are discussed in Section 2.7.3, and the devolatilisation and heterogeneous gasification kinetics are finally focussed in Sections 2.7.4 and 2.7.5.

### 2.7.1 Chemical properties

Wood char characterisation and gasification experiments at the laboratory-scale and pilot-scale plants that were carried out in the frame of HVIGasTech [124] have relied on commercial wood chars produced by Chemviron [49] or Holzkohlenverarbeitung Schütte [126]. Furthermore, several characterisation experiments [155, 156, 157, 275, 300, 303] were conducted using wood char that was produced in a bench-scale intermediate screw pyrolysis reactor with integrated hot gas filtration, the STYX reactor of the Institute for Technical Chemistry [211]. The origins and applications of the wood chars applied at KIT are summarised in Table I.1 while the elemental and proximate compositions are reported in Table I.2. The compositions in mass fractions  $\boldsymbol{w}_{\text{solid}}$  are based on proximate and ultimate

analyses of the laboratories of Eurofins (EF) [94] and Engler-Bunte-Institute (EBI). The elemental compositions given in Table I.2 are commented below.

1. The wood chars HK01, HK02, HK04, HK06 and HK07 differ in the compositions. The deviations in the elemental contents can be attributed to different natural origins, different pyrolysis conditions or different sampling and analysis methods. As the experimental conditions restricted the use of a wood char with constant material properties, the deviations have to be accepted from the modelling point of view.
2. The wood chars HK06 and HK07 differ in carbon, hydrogen and oxygen contents in spite of the fact that the batches originated from the same charge. The deviations in the elemental contents thus demonstrate the challenges in the use of a wood char with constant material properties.
3. The wood chars HK01, HK04, HK06 and HK07 have a significantly lower volatiles content than the wood char HK02. Since this indicates different physical and chemical properties, available physical property data and devolatilisation and heterogeneous gasification kinetics for the fir char HK02 [156, 275, 303] could not be appropriate for the beech wood chars HK01, HK04, HK06 and HK07.
4. The wood chars HK02-1600, HK06-1400-200 and HK06-1600-200 have high carbon and low hydrogen and oxygen contents since they were produced from the (primary) wood chars HK02 and HK06, respectively, in the drop-tube reactor at Engler-Bunte-Institute, Fuel Technology. These secondary wood chars should represent intermediate chars in entrained flow gasification processes.

### 2.7.1.1 Simplified elemental and proximate compositions

Simplified elemental and proximate compositions have been defined for the CFD simulations using the original analyses of Eurofins (EF simple) [94] and Engler-Bunte-Institute (EBI simple) under the assumption that the simplified wood chars do not contain sulphur (S), chlorine (Cl) and moisture (H<sub>2</sub>O). The mass fraction of moisture  $w_{\text{H}_2\text{O},\text{solid},0}$ , the mass fraction of sulphur  $w_{\text{S},\text{solid},0}$  and the mass fraction of chlorine  $w_{\text{Cl},\text{solid},0}$  were added to the mass fractions of (atomic) hydrogen  $w_{\text{H},\text{solid},0}$ , (atomic) oxygen  $w_{\text{O},\text{solid},0}$  and nitrogen  $w_{\text{N},\text{solid},0}$  using the equations

$$w_{\text{H},\text{solid},0} := w_{\text{H},\text{solid},0} + 2 \cdot \frac{M_{\text{H}}}{M_{\text{H}_2\text{O}}} w_{\text{H}_2\text{O},\text{solid},0} , \quad (2.180)$$

$$w_{\text{O},\text{solid},0} := w_{\text{O},\text{solid},0} + \frac{M_{\text{O}}}{M_{\text{H}_2\text{O}}} w_{\text{H}_2\text{O},\text{solid},0} , \quad (2.181)$$

$$w_{\text{N},\text{solid},0} := w_{\text{N},\text{solid},0} + w_{\text{S},\text{solid},0} + w_{\text{Cl},\text{solid},0} , \quad (2.182)$$

where  $M_{\text{H}}$ ,  $M_{\text{H}_2\text{O}}$  and  $M_{\text{O}}$  are the molar masses of (atomic) hydrogen, water and (atomic) oxygen.

### 2.7.1.2 Equilibrium contents and equilibrium volatiles compositions

Equilibrium calculations were performed to determine the equilibrium mass fraction of the volatiles  $w_{\text{vol,solid,eq}}$ , the equilibrium mass fraction of the combustibles  $w_{\text{comb,solid,eq}}$  and the equilibrium composition of the volatiles in mass fractions  $\mathbf{w}_{\text{vol,eq}}$ . The calculations were carried out with Python [261] and Cantera [106] using the minimisation of the Gibbs energy at 1 bar and assuming  $\text{C}_{(\text{gr})}$ ,  $\text{CH}_4$ ,  $\text{CO}$ ,  $\text{CO}_2$ ,  $\text{H}_2$ ,  $\text{H}_2\text{O}$ ,  $\text{O}_2$  and  $\text{N}_2$  as possible species. The changes of the equilibrium mass fraction of the volatiles  $w_{\text{vol,solid,eq}}$  and of the equilibrium composition of the volatiles in mass fractions  $\mathbf{w}_{\text{vol,eq}}$  with the equilibrium temperature  $T_{\text{eq}}$  are shown for several wood chars in Fig. 2.13.

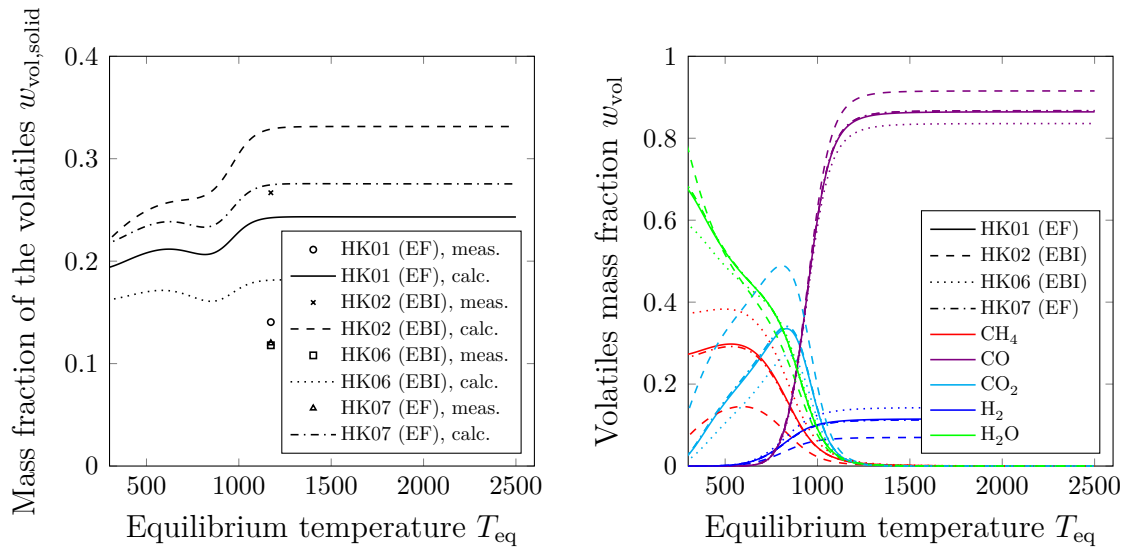


**Figure 2.13:** Mass fractions of the volatiles  $w_{\text{vol,solid}}$  measured at 1173.15 K or calculated for 1 bar (left) and equilibrium volatiles composition in mass fractions  $w_{\text{vol,eq}}$  (right).

Only minor changes of both the equilibrium mass fraction of the volatiles  $w_{\text{vol,solid,eq}}$  and the equilibrium volatiles composition in mass fractions  $\mathbf{w}_{\text{vol,eq}}$  can accordingly be expected for equilibrium temperatures  $T_{\text{eq}}$  above 1473.15 K. At such temperatures, the volatiles mainly consist of carbon monoxide, hydrogen and nitrogen, while the composition shifts to methane, carbon dioxide and water with decreasing equilibrium temperature  $T_{\text{eq}}$ . Therefore, the equilibrium temperature  $T_{\text{eq}}$  of 1473.15 K was selected to obtain appropriate and consistent model estimates for both the mass fraction of the volatiles  $w_{\text{vol,solid}}$  and the composition of the volatiles at atmospheric entrained flow gasification conditions with temperatures typically above 1473.15 K (see Section 2.7.4.5). The equilibrium mass fraction of the volatiles  $w_{\text{vol,solid,eq}}$  and the equilibrium mass fraction of the combustibles  $w_{\text{comb,solid,eq}}$

are given in Table I.2, alongside the mass fraction of the volatiles  $w_{\text{vol,solid}}$  according to DIN 51720:2001 [75] and the mass fraction of the combustibles  $w_{\text{comb,solid}}$  according to DIN 51734:2008 [76]. Significant deviations can be found between the mass fraction of the volatiles  $w_{\text{vol,solid}}$  and the equilibrium mass fraction of the volatiles  $w_{\text{vol,solid,eq}}$ , as some volatiles are not released during the analyses due to a lower temperature of 1173.15 K and too short residence times.

### 2.7.1.3 Compositions during devolatilisation and heterogeneous gasification

An averaged composition of the volatiles which obeys the elemental balances enables to describe the solid composition during devolatilisation and heterogeneous gasification. The solid composition during devolatilisation in mass fractions  $\mathbf{w}_{\text{solid}} = (w_{i,\text{solid}})$  is given by

$$w_{i,\text{solid}} = \begin{cases} 1 - w_{\text{vol,solid}} - w_{\text{ash,solid}}, & \text{if } i = \text{comb} \\ \frac{w_{\text{vol,solid},0} (1 - X_{\text{dev,part}})}{\sum_{j \neq \text{vol,comb}} w_{j,\text{solid},0} - w_{j,\text{vol}} w_{\text{vol,solid},0} X_{\text{dev,part}}}, & \text{if } i = \text{vol} \\ \frac{w_{i,\text{solid},0} - w_{i,\text{vol}} w_{\text{vol,solid},0} X_{\text{dev,part}}}{\sum_{j \neq \text{vol,comb}} w_{j,\text{solid},0} - w_{j,\text{vol}} w_{\text{vol,solid},0} X_{\text{dev,part}}}, & \text{else} \end{cases}, \quad (2.183)$$

where  $w_{i,\text{vol}}$  and  $w_{j,\text{vol}}$  are the volatiles mass fractions of *element*  $i$  and  $j$ , respectively,  $w_{i,\text{solid},0}$ ,  $w_{j,\text{solid},0}$  and  $w_{\text{vol,solid},0}$  are the initial mass fractions of component  $i$ , component  $j$  and the volatiles, respectively, in the solid phase and  $X_{\text{dev,part}}$  is the particle devolatilisation conversion. The elemental volatiles composition in mass fractions  $\mathbf{w}_{\text{vol}} = (w_{i,\text{vol}})$  is defined by

$$w_{\text{C,vol}} = M_{\text{C}} \left( \frac{w_{\text{CH}_4,\text{vol}}}{M_{\text{CH}_4}} + \frac{w_{\text{CO,vol}}}{M_{\text{CO}}} + \frac{w_{\text{CO}_2,\text{vol}}}{M_{\text{CO}_2}} \right), \quad (2.184)$$

$$w_{\text{H,vol}} = M_{\text{H}} \left( 4 \cdot \frac{w_{\text{CH}_4,\text{vol}}}{M_{\text{CH}_4}} + 2 \cdot \frac{w_{\text{H}_2,\text{vol}}}{M_{\text{H}_2}} + 2 \cdot \frac{w_{\text{H}_2\text{O,vol}}}{M_{\text{H}_2\text{O}}} + \frac{w_{\text{HCl,vol}}}{M_{\text{HCl}}} + 2 \cdot \frac{w_{\text{H}_2\text{S,vol}}}{M_{\text{H}_2\text{S}}} + 3 \cdot \frac{w_{\text{NH}_3,\text{vol}}}{M_{\text{NH}_3}} \right), \quad (2.185)$$

$$w_{\text{O,vol}} = M_{\text{O}} \left( \frac{w_{\text{CO,vol}}}{M_{\text{CO}}} + 2 \cdot \frac{w_{\text{CO}_2,\text{vol}}}{M_{\text{CO}_2}} + \frac{w_{\text{H}_2\text{O,vol}}}{M_{\text{H}_2\text{O}}} \right), \quad (2.186)$$

$$w_{\text{N,vol}} = M_{\text{N}} \left( 2 \cdot \frac{w_{\text{N}_2,\text{vol}}}{M_{\text{N}_2}} + \frac{w_{\text{NH}_3,\text{vol}}}{M_{\text{NH}_3}} \right), \quad (2.187)$$

$$w_{\text{S,vol}} = M_{\text{S}} \frac{w_{\text{H}_2\text{S,vol}}}{M_{\text{H}_2\text{S}}}, \quad (2.188)$$

$$w_{\text{Cl,vol}} = M_{\text{Cl}} \frac{w_{\text{HCl,vol}}}{M_{\text{HCl}}}, \quad (2.189)$$

where  $M_{\text{C}}$ ,  $M_{\text{CH}_4}$ ,  $M_{\text{CO}}$ ,  $M_{\text{CO}_2}$ ,  $M_{\text{H}}$ ,  $M_{\text{H}_2}$ ,  $M_{\text{H}_2\text{O}}$ ,  $M_{\text{HCl}}$ ,  $M_{\text{H}_2\text{S}}$ ,  $M_{\text{NH}_3}$ ,  $M_{\text{O}}$ ,  $M_{\text{N}}$ ,  $M_{\text{N}_2}$ ,  $M_{\text{S}}$  and  $M_{\text{Cl}}$  are molar masses. After complete devolatilisation, the solid composition in mass fractions  $\mathbf{w}_{\text{solid,dev}} = (w_{i,\text{solid,dev}})$  is given by

$$w_{i,\text{solid,dev}} = \begin{cases} 1 - \frac{w_{\text{ash,solid},0}}{1 - w_{\text{vol,solid},0}}, & \text{if } i = \text{C} \\ \frac{w_{\text{ash,solid},0}}{1 - w_{\text{vol,solid},0}}, & \text{if } i = \text{ash} \\ 0, & \text{else} \end{cases} . \quad (2.190)$$

During the heterogeneous gasification, the solid composition in mass fractions  $\mathbf{w}_{\text{solid}} = (w_{i,\text{solid}})$  changes again according to

$$w_{i,\text{solid}} = \begin{cases} \frac{w_{\text{C,solid,dev}} (1 - X_{\text{het,part}})}{(1 - X_{\text{het,part}})}, & \text{if } i = \text{C} \\ \frac{w_{\text{ash,solid,dev}}}{(1 - X_{\text{het,part}})}, & \text{if } i = \text{ash} \\ 0, & \text{else} \end{cases} , \quad (2.191)$$

where  $X_{\text{het,part}}$  is the particle gasification conversion. The particle devolatilisation conversion  $X_{\text{dev,part}}$  and the particle gasification conversion  $X_{\text{het,part}}$  are defined by

$$X_{\text{dev,part}} = \frac{m_{\text{part,min,vap}} - m_{\text{part}}}{m_{\text{part,min,vap}} - m_{\text{part,min,dev}}} , \quad (2.192)$$

$$X_{\text{het,part}} = \frac{m_{\text{part,min,dev}} - m_{\text{part}}}{m_{\text{part,min,dev}} - m_{\text{part,min,het}}} . \quad (2.193)$$

In addition, the carbon conversions  $X_{\text{C,fuel,gas}}$ ,  $X_{\text{C,solid,gas}}$  and  $X_{\text{C,part}}$  are used in this thesis following preceding studies [98, 99, 100]. The carbon conversions  $X_{\text{C,fuel,gas}}$  and  $X_{\text{C,solid,gas}}$  are based on the gas composition and are given by [98, 99, 100]

$$X_{\text{C,fuel,gas}} = 1 - \frac{\dot{m}_{\text{C,gas}}}{\dot{m}_{\text{C,fuel}}} , \quad (2.194)$$

$$X_{\text{C,solid,gas}} = 1 - \frac{1 - X_{\text{C,fuel,gas}}}{\dot{m}_{\text{C,solid,fuel}}/\dot{m}_{\text{C,fuel}}} , \quad (2.195)$$

where  $\dot{m}_{\text{C,gas}}$  is the carbon mass flow rate in the gas,  $\dot{m}_{\text{C,fuel}}$  is the carbon mass flow rate in the fuel and  $\dot{m}_{\text{C,solid,fuel}}$  is the carbon mass flow rate in the solid. The carbon conversion  $X_{\text{C,part}}$  is based on the solid composition and is defined by [99, 100]

$$X_{\text{C,part}} = 1 - \frac{m_{\text{C,part}}}{m_{\text{C,part,min,vap}}} , \quad (2.196)$$

where  $m_{\text{C,part}}$  is the carbon mass in the particle and  $m_{\text{C,part,min,vap}}$  is the remaining carbon mass in the particle after vaporisation.

## 2.7.2 Physical properties

Physical solid property models are used to describe the (true) solid density  $\rho_{\text{solid}}$ , the effective solid density  $\rho_{\text{solid,eff}}$  (see Sections 2.7.3.10, 2.7.3.11 and 2.7.3.12), the (true) solid

thermal conductivity  $\lambda_{\text{solid}}$ , the effective solid thermal conductivity  $\lambda_{\text{solid,eff}}$ , the specific solid heat capacity  $\hat{C}_{p,\text{solid}}$  and the solid emissivity  $\varepsilon_{\text{solid}}$  (see Section 2.5.3) during wood char conversion. Models for the effective solid density  $\rho_{\text{solid,eff}}$ , the specific solid heat capacity  $\hat{C}_{p,\text{solid}}$  and the solid emissivity  $\varepsilon_{\text{solid}}$  are required to describe the heat and mass transfer in simplified particle models (see Section 2.2.5.3) while correlations for the true solid density  $\rho_{\text{solid}}$ , the true solid thermal conductivity  $\lambda_{\text{solid}}$  and the effective solid thermal conductivity  $\lambda_{\text{solid,eff}}$  are useful to estimate the effective solid porosity  $\varepsilon_{\text{solid,eff}}$  and the influence of temperature gradients, respectively. However, such relationships have not been developed yet for wood chars since the physical properties of wood char (i) strongly depend on the natural origin and the pyrolysis and conversion conditions and (ii) can hardly be accessed at intermediated states. Fortunately, several experimental and modelling studies [4, 23, 43, 56, 69, 119, 131, 152, 169, 172, 182, 197, 198, 202, 203, 313] already focussed on the physical properties of graphite, coal and coke. Specifically, Kirov [152] and Merrick et al. [202] suggested models for the heat capacity (see Section F.7.2). The model of Kirov [152] describes the heat capacity only as function of temperature, while the model of Merrick et al. [202] relies on both elemental composition and temperature. Consequently, previous numerical studies with focus on the conversion of wood or wood char used existing approaches. For example, Ragland et al. [247] and Fradet [102] applied the heat capacity correlations of graphite and of Merrick et al. [202], respectively. Furthermore, constant values were used. For example, DiBlasi [71] applied a specific heat capacity of 1100 J/(kg K) and a thermal conductivity of 0.1 W/(m K).

Eventually, some physical property data was measured for biogenic fuels. Most of the data is for raw biomasses at ambient conditions (see [85]), while the studies of Gupta et al. [112], Dupont et al. [85], Brewer et al. [36], Dubil [80] and Arnold et al. [20] investigated the physical properties of biomass chars at moderate temperatures.

### 2.7.2.1 Experiments of Gupta et al.

Gupta et al. [112] measured the thermal conductivity of softwood char between 310 K and 713 K and the specific heat capacity of softwood char between 313 K and 713 K. While the specific heat capacity of softwood char increased from 768 J/(kg K) to 1506 J/(kg K), the thermal conductivity of softwood char only slightly increased and can approximately be described by a value of 0.1 W/(m K) [112]. In addition, Gupta et al. [112] measured thermal conductivities and specific heat capacities of both softwood and softwood bark. The thermal conductivities and specific heat capacities of softwood and softwood bark were up to twice as large compared to the respective properties of softwood char [112].

### 2.7.2.2 Experiments of Dupont et al.

Dupont et al. [85] measured the specific heat capacities of several biomasses between 313 K and 353 K including woods and crops and two beech wood chars, produced at pyrolysis temperatures of 773 K and 1073 K. The biomasses showed similar, approximately linear relationships between temperature and specific heat capacity while the values were between 1300 J/(kg K) and 1850 J/(kg K). In contrast, the specific heat capacities of the beech wood chars were above 1127 J/(kg K) and less than those of beech wood [85]. Furthermore, the measured specific heat capacities of the wood chars were interfered with exothermic phenomena at higher temperatures such as atomic recombination [85].

### 2.7.2.3 Experiments of Brewer et al.

Brewer et al. [36] measured true solid densities of grass and mesquite wood chars obtained from pyrolysis at several temperatures. The true density was increasing with increasing pyrolysis temperature from 1300 kg/m<sup>3</sup> to 1700 kg/m<sup>3</sup> for both grass chars and mesquite wood chars [36].

### 2.7.2.4 Experiments of Dubil

Dubil [80] measured solid densities  $\rho_{\text{solid}}$  of devolatilised and gasified wood chars using helium pycnometry (Micromeritics AccuPyc 1330). The measured solid densities  $\rho_{\text{solid}}$  are reproduced in Table 2.9.

**Table 2.9:** Solid densities of wood char HK02-1600 based on measurements [80] and predictions using the model of Merrick et al. [203], the model of IGT for coals [131] and the model of IGT for coal chars [131].

Material	$\frac{\rho_{\text{solid}}}{\text{m}^3/\text{kg}}$			
	Exp.	Merrick	IGT   coal	IGT   char
HK02-1600 ( $X_{\text{C,part}} = 0\%$ )	2187.8	2297.3	2284.7	2288.7
HK02-1600 ( $X_{\text{C,part}} = 9.1\%$ )	2288.5	2298.7	2285.7	2290.1
HK02-1600 ( $X_{\text{C,part}} = 21.2\%$ )	2321.8	2301.0	2287.4	2292.5
HK02-1600 ( $X_{\text{C,part}} = 31.9\%$ )	2315.1	2303.8	2289.4	2295.2
HK02-1600 ( $X_{\text{C,part}} = 40.7\%$ )	2343.8	2306.8	2291.5	2298.2
HK02-1600 ( $X_{\text{C,part}} = 56.0\%$ )	2347.6	2314.7	2297.3	2306.2
HK02-1600 ( $X_{\text{C,part}} = 68.2\%$ )	2298.6	2326.1	2305.5	2317.7
HK02-1600 ( $X_{\text{C,part}} = 78.0\%$ )	2203.1	2343.6	2318.1	2335.4

### 2.7.2.5 Experiments of Arnold et al.

Arnold et al. [20] characterised several bio-oil chars, that were obtained in a tube oven at 873.15 K and 1173.15 K for 30 min and 60 min, and measured thermal conductivities between 0.238 W/(m K) and 0.285 W/(m K) and volumetric heat capacities between 2.5 J/(m<sup>3</sup> K) and 3.24 J/(m<sup>3</sup> K).

### 2.7.2.6 Conclusions

Valuable data was obtained in the studies of Gupta et al. [112], Dupont et al. [85], Brewer et al. [36], Dubil [80] and Arnold et al. [20] while further data is not available to the best knowledge of the author. The conclusions based on the scarce data (see [85]) are summarised below.

1. The measured solid densities  $\rho_{\text{solid}}$  are compared with the solid densities calculated using the model of Merrick et al. [203], the model of IGT for coals [131] and the model of IGT for coal chars [131] (see Section F.7) in Table 2.9. Except for the particle carbon conversions  $X_{\text{C,part}}$  of 0% and 78%, the predictions are in very good agreement with the measurement results; the relative errors are smaller than 2.5%. Thus, all three correlations originally developed using densities of coals, coking coals or coal chars can be accepted for devolatilised and gasified wood chars.
2. The measured specific solid heat capacities  $\hat{C}_{p,\text{solid}}$  reported by Gupta et al. [112] are in a basic agreement with the measurement data of Dupont et al. [85]. However, future studies should provide additional measurement data and should focus on the development of models reflecting the deviating data.

In view of the lack of appropriate data and customised models for wood chars, this work used the models of Merrick et al. [202, 203] for the true solid density  $\rho_{\text{solid}}$  and the specific solid heat capacity  $\hat{C}_{p,\text{solid}}$  (see Section F.7), while the effective solid thermal conductivity  $\lambda_{\text{solid,eff}}$  was approximated with 0.1-0.3 W/(m K).

## 2.7.3 Morphology

Devolatilisation and heterogeneous gasification are not only affected by changes of chemical and physical properties but also by changes of particle morphology, i. e. internal particle surface area, particle pore diameter distribution, particle shape distribution and particle size distribution.

In entrained flow gasification processes, the first minor changes of the particle morphologies occur during the fuel preparation due to collision and abrasion, while significant changes

are likely during the heat-up and the release of secondary volatiles. Since mechanical and thermal stresses are induced, particle break-ups according to different fragmentation modes (exfoliation, fragmentation at the particle centre, fragmentation at an internal radial position, exfoliation and fragmentation) are generally likely following Senneca et al. [284]. At least several new particles with different particles sizes and shapes emerge from each particle. The release of the volatiles also increases the internal particle surface area and changes the particle pore size distribution of each particle. In addition, the particle morphology can be affected by shrinking, swelling and mineral matter transformation such as fusion. After devolatilisation, heterogeneous gasification can further increase the internal particle surface area and accordingly change the particle pore size distribution of each particle in the initial stages. However, this can reverse in the final stages. Due to hollow solid matrices with reduced stabilities, particles can collapse which obviously affects the particle morphology. Furthermore, the particle morphology properties can change due to abrasion induced by particle and wall collisions.

Although the qualitative changes of the particle morphology are known, the mathematical description of the changes is challenged by variable fuel properties and operating conditions. In order to give an insight into the changes, numerous experimental and modelling studies [25, 53, 57, 58, 60, 62, 82, 83, 123, 147, 158, 246, 267, 268, 269, 272, 281, 282, 283, 284, 285, 286, 287, 289, 297, 298, 304, 308, 337] have contributed to fragmentation only. Several coal/ash fragmentation models [25, 53, 82, 83, 151, 158, 208, 284, 285, 286, 287, 298, 308] have been proposed, mainly for combustion conditions and using the percolation theory or using the population balance method. Recently, Syred et al. [308] and Kreutzkam et al. [158] showed feasible fragmentation implementations for ANSYS Fluent and large-scale simulations. Furthermore, Simone et al. [291] and Costa et al. [57, 58] investigated experimentally the fragmentation of biomass. Simone et al. [291] performed drop-tube reactor devolatilisation experiments with cacao shells at 873.15 K and 1073.15 K while Costa et al. [57, 58] carried out drop-tube reactor combustion experiments with olive stones, pine shells and wheat straw between 1173.15 K and 1373.15 K. The results showed that fragmentation of biomass particles is likely to occur. However, some results of Costa et al. [57, 58] also indicated no (significant) fragmentation as raw biomass particles can be more affected by shrinking during pyrolysis or devolatilisation (see [40, 44, 51, 70, 160, 174, 237]).

Previous studies clearly show the range of possible changes of particle morphology and indicate that detailed experimental and theoretical investigations of the particle morphology are required for the slurry entrained flow gasification with wood char. However, such investigations were beyond the objectives of this work. Only first experimental results obtained in the frame of HVI GasTech [124] were used to draw conclusions concerning the changes of particle morphology during devolatilisation and heterogeneous gasification. Five analyses or measurements were accounted for:

1. Particle size distribution analyses of wood char HK06 and wood char HK06-1400-200 from the DTR experiments of Schneider et al. [68, 276, 279].
2. Scanning electron microscope analyses from wood char particles used and collected in the REGA experiments TUC5 GHKS10 V1071 and TUC5 GHKS30 V1284 of Fleck et al. [97, 99, 100].
3. Mineral matter analyses from wood char particles collected in the REGA experiment TUC5 GHKS30 V1284 of Fleck et al. [99, 100].
4. Particle temperature and particle diameter measurements of Kreitzberg et al. [157] using 3CCD camera images in the course of heterogeneous gasification experiments with single particles of wood char HK02.
5. Particle micropore surface area measurements of Müller et al. [213], Dubil [80], Stösser [303] and Schneider et al. [276] with focus on several wood chars.

The analyses, measurements or experiments are described in Sections 2.7.3.1, 2.7.3.2, 2.7.3.3 and 2.7.3.4 while conclusions concerning fragmentation, particle shape, particle shrinking and particle pore structures are drawn in Sections 2.7.3.5, 2.7.3.6, 2.7.3.7 and 2.7.3.8. Sections 2.7.3.9, 2.7.3.10, 2.7.3.11 and 2.7.3.12 finally describe the model equations that were used in this work to describe the particle pore diameter, the initial effective particle density and the particle diameter.

### **2.7.3.1 DTR experiments of Schneider et al.**

In the DTR experiments of Schneider et al. [68, 276, 279], sieved samples of wood char HK06 were devolatilised at several operating temperatures and residence times. Most of the devolatilised particles were collected using a cyclone separator while some particles could only be trapped in the subsequent candle filter (see Section A.4). Particle size distributions were determined for a sieved sample of wood char HK06 and for the collected sample of wood char HK06-1400-200 with laser diffraction (Sympatec HELOS H0309) at the Institute of Mechanical Process Engineering and Mechanics of Karlsruhe Institute of Technology [68]. The cumulative distribution functions  $Q_3$  are shown in Figure 2.14 (left) and demonstrate a shift of the particle size distribution to smaller particles.

### **2.7.3.2 REGA experiments of Fleck et al.**

In the REGA experiments TUC5 GHKS10 V1071 and TUC5 GHKS30 V1284 of Fleck et al. [97, 99, 100], the wood chars HK01 and HK07 were gasified in suspensions with ethylene glycol. The particle size distributions of the original wood chars were determined

with laser-diffraction (Fritsch Analysette 22 NanoTec plus) at Fritsch [103] or with laser diffraction (Sympatec HELOS H0309) at the Institute of Mechanical Process Engineering and Mechanics of Karlsruhe Institute of Technology [97, 99, 100]. The cumulative distribution functions  $Q_3$  are shown in Figure 2.14 (left) demonstrating the strong reduced particle sizes of wood char HK01 due to grinding.

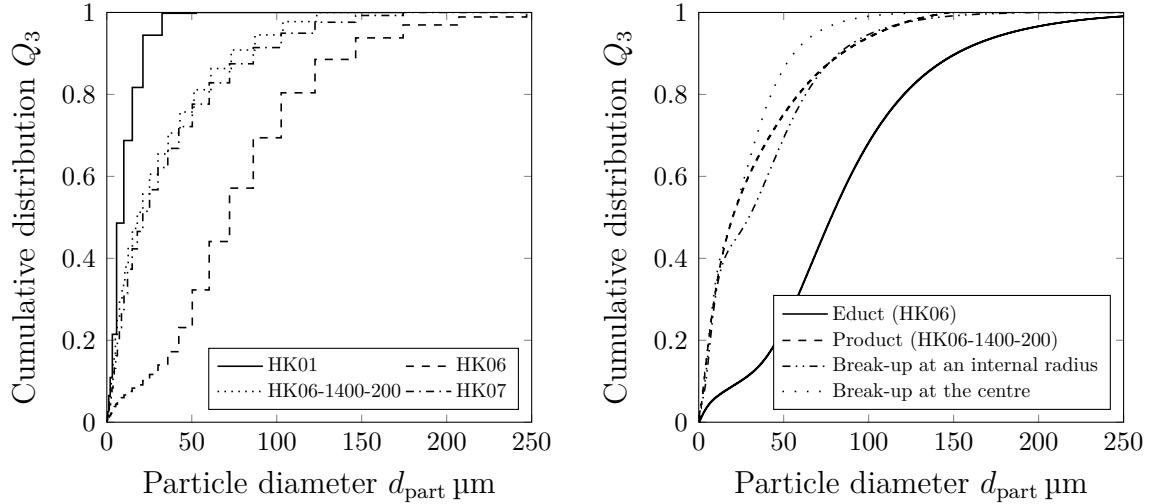


**Figure 2.14:** Cumulative particle size distributions  $Q_3$  of the wood chars HK01, HK06, HK06-1400-200 and HK07 based on laser diffraction measurements (left), interpolated cumulative particle size distributions  $Q_3$  of the wood chars HK06 and HK06-1400-200 (right) and calculated cumulative particle size distributions  $Q_3$  based on simplified break-up approaches (right). The primary wood chars HK01 and HK07 were applied in the REGA experiments while the primary wood char HK06 was used in the DTR experiments and the secondary wood char HK06-1400-200 was obtained in the DTR experiments.

**Table 2.10:** Carbon conversions  $X_C$  in the REGA experiment TUC5 GHKS30 V1284 [99, 100]. The carbon conversions  $X_{C,part}$  were determined using the Ca tracer method and the Mg tracer method [99, 100] while the carbon conversions  $X_{C,solid,gas}$  were calculated using the balancing method [98].

Sample	$X_{C,part} / \%$		$X_{C,solid,gas} / \%$
	Ca tracer method	Mg tracer method	
Particles sucked at 680 mm	77.2	71.0	79.7
Particles sucked at exit	89.0	87.4	85.4

Furthermore, in both REGA experiments, solid particles were collected at the exit of the reactor and were extracted from the reactor using a ceramic suction probe and using a high-separation, high-temperature candle filter [99]. The non-isokinetic particle suction were carried out for 60-90 minutes in the REGA experiment TUC5 GHKS10 V1071 and for 30-60 minutes in the REGA experiment TUC5 GHKS30 V1284 [99]. The long suction times and the non-isokinetic conditions were essential in order to collect at least enough sample material for scanning electron microscope (SEM) and mineral matter analyses [99]. The images of the SEM analyses of the original wood char samples and of the collected samples

are reproduced from Fleck et al. [97, 100] in Fig. 2.15 and indicate that particles partially retain their size and their non-spherical shape during devolatilisation and heterogeneous gasification [97, 100]. The mineral matter analyses were performed to estimate the carbon conversions  $X_{C,part}$  using the Ca tracer method and the Mg tracer method [99, 100].

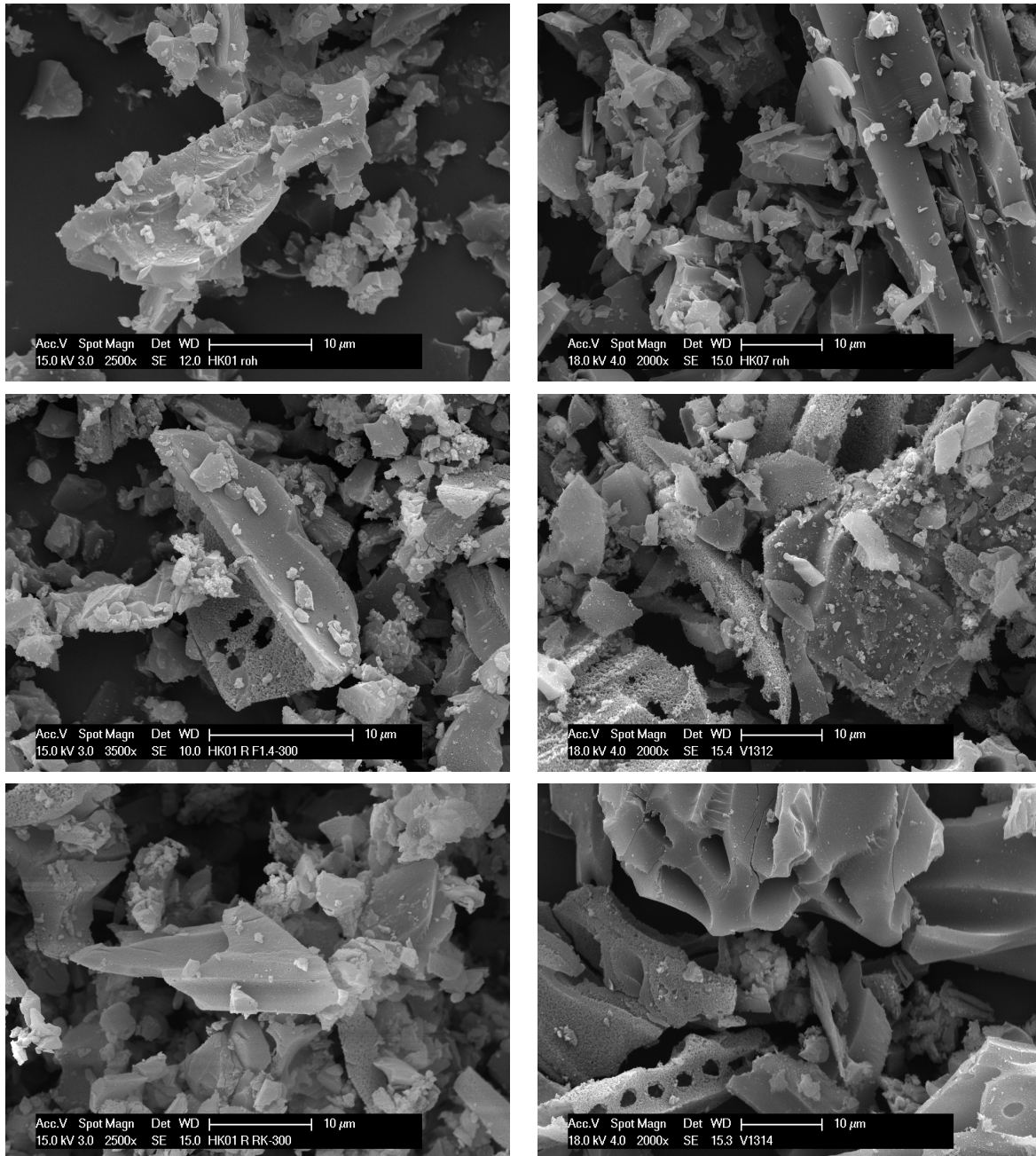


**Figure 2.15:** SEM images of particles of wood char HK01 (top left), of particles collected in the REGA experiment TUC5 GHKS10 V1071 at 300 mm (centre left) and at the outlet (bottom left), of particles of wood char HK07 (top right) and of particles collected in the REGA experiment TUC5 GHKS30 V1284 at 680 mm (centre right) and at the outlet (bottom right) [97, 99, 100].

However, since the sample material from the REGA experiment TUC5 GHKS10 V1071 was not sufficiently large, this could only be done for the collected samples of the REGA

experiment TUC5 GHKS30 V1284 [99, 100]. For the sample collected at 680 mm and for the sample obtained at the outlet [99, 100], the carbon conversions  $X_{C,\text{part}}$  based on both tracer methods are given in Table 2.10 and are in good agreement with each other. The experimental carbon conversions  $X_{C,\text{part}}$  of the sample collected at the outlet are also in good agreement with the balanced carbon conversions  $X_{C,\text{solid,gas}}$  [99, 100].

### 2.7.3.3 Experiments of Kreitzberg et al.

In the experiments of Kreitzberg et al. [157], single particles of wood char HK02 with initial equivalent particle diameters of 1061  $\mu\text{m}$ , 1622  $\mu\text{m}$  and 2135  $\mu\text{m}$  were converted in an optically accessible reaction chamber with a McKenna type flat flame burner. The chamber was applied to establish combustion or gasification conditions at high heating rates. Images recorded with a 3CCD camera were used to determine a particle surface temperature and a normalised equivalent particle diameter

$$\tilde{d}_{\text{part}} = \frac{d_{\text{part}} - d_{\text{part,het,f}}}{d_{\text{part,het,0}} - d_{\text{part,het,f}}} \quad (2.197)$$

as function of a normalised time

$$\tilde{t} = \frac{t - t_{\text{het,f}}}{t_{\text{het,0}} - t_{\text{het,f}}}, \quad (2.198)$$

where  $d_{\text{part,het,0}}$  is the initial particle diameter before gasification,  $d_{\text{part,het,f}}$  is the final particle diameter after gasification,  $t_{\text{part,het,0}}$  is the initial gasification time and  $t_{\text{part,het,f}}$  is the final gasification time. The initial and the final gasification times were defined using visual observations, i. e. using the end of particle swelling (and thus devolatilisation) and the end of particle diameter changes (and thus conversion). Fragmentation was not observed in spite of the fact that the experiments were carried out with relatively large particles. The experiments also showed (i) that the particle surface temperature was approximately constant during the conversion, except for the final stages, and (ii) that the particle diameter slowly decreases until a normalised conversion time of 70-90%. The experimental results for the normalised particle diameter are reproduced in Figure 2.16.

### 2.7.3.4 Experiments of Müller et al., Dubil, Stösser and Schneider et al.

In the experiments of Müller et al. [213], Dubil [80], Stösser [303] and Schneider et al. [276], specific particle pore surface areas  $\hat{A}_{\text{pore,part}}$  were determined in a physisorption analyser (Micromeritics ASAP 2020) either using nitrogen adsorption at 77 K and the Brunauer-Emmett-Teller (BET) method [38] following DIN ISO 9722:2014 [77] or using carbon dioxide adsorption at 273.15 K and the Dubinin-Radushkevich (DR) method [81]. Before

each analysis, the samples were firstly degassed over a longer period (12-24 h) at high vacuum and moderate temperatures (378.15-453.15 K) and were subsequently flushed with nitrogen [80, 276, 303]. The specific particle pore surface area measurement results are summarised in Table I.4. The results indicate that the specific surface area increases (i) during devolatilisation until fusion of mineral matter compounds and (ii) during heterogeneous gasification until a specific carbon conversion (certainly above 50%). Specifically, Schneider et al. [276] observed that the surface area of wood char HK06 increased with increasing pyrolysis temperature (from 1273.15 K to 1673.15 K) and significantly decreased at a pyrolysis temperature of 1873.15 K. The surface area also decreased with increasing residence times [276]. Furthermore, the values reported by Schneider et al. [276] are in terms of magnitude in good agreement with the values that were determined by Stösser [303] in connection with the pyrolysis of wood char HK02.

In addition to surface areas, Dubil [80] and Stösser [303] determined particle pore volumes and particle porosities of both macro pores and micro pores. Macro pore volumes and macro porosities  $\varepsilon_{\text{solid,macro}}$  were obtained using mercury porosimetry (Micromeritics AutoPore III 9420 / AutoPore IV 9420) following DIN 66133:1993 [74], while micro pore volumes and micro porosities  $\varepsilon_{\text{solid,micro}}$  were determined using carbon dioxide adsorption at 273.15 K up to a relative pressure of 0.35 and using the Dubinin-Radushkevich method [81]. However, pore volumes and porosities based on both approaches should be regarded carefully since, for example, macro pore volumes are generally overestimated due to inter-particle voids [80].

### 2.7.3.5 Conclusions concerning fragmentation

The results of the REGA experiments of Fleck et al. [97, 99, 100] (see Section 2.7.3.2) and the experiments of Kreitzberg et al. [157] (see Section 2.7.3.3) indicate that wood char particles were not subject to fragmentation and approximately retained their sizes during conversion.

In contrast, the results of the DTR experiments [68] (see Section 2.7.3.1) indicate changes of the particle size distribution, which can be caused by fragmentation. However, since the particles passed several pipes after the outlet of the DTR [68], abrasion and similar effects cannot be ruled out. Therefore, particle break-up calculations were performed to test possible fragmentation modes (exfoliation, fragmentation at the centre, fragmentation at an internal radial position and combinations thereof). The calculations were carried out assuming (i) that the particle samples obtained at the cyclone separator were not affected by abrasion and (ii) that the particles can be described with equivalent diameters and with uniform material properties. The calculated cumulative distributions  $Q_3$  for fragmentation at an internal radial position of  $0.6 r_{\text{part}}$  with numerous small particles or fragmentation at the particle centre are shown in Figure 2.14 (right). Accordingly, both

fragmentation modes can reflect the results of the DTR experiments, while abrasion or exfoliation may only lead to modestly changed particle sizes. Therefore, changes of the particle size distribution in the DTR experiments were most likely caused by internal fragmentation, while different explanations as abrasion or exfoliation can be discarded under the assumptions chosen for the calculations.

Eventually, due to the good agreement of the observations of Fleck et al. [97, 99, 100] with the results of Kreitzberg et al. [157] in spite of the fundamentally different set-ups, fragmentation of wood char particles was not accounted for in this work. Modifications are left for future works when particle size distribution measurements of samples collected in both REGA and DTR experiments provide further information.

### **2.7.3.6 Conclusions concerning particle shape**

The results of the SEM analyses (see Section 2.7.3.2) demonstrate that the wood char particles have non-spherical shapes, which is in agreement with previous observations (for example, see [51]) and can affect CFD predictions. Recently, Zhang et al. [348] accounted for non-spherical shapes in the CFD simulations of the laboratory-scale DTU entrained flow gasifier in order to investigate the influence of the aspect ratio and of the particle shape factor on the particle predictions. In their simulations, prolate particles were more scattered to the heated wall and showed faster heat-up and higher carbon conversion [348]. Such effects are of course unlikely for the REGA experiments due to quite similar wall and gas temperatures. Possible effects could be rather changes of the particles trajectories and the particle conversion. However, in view of the uncertainties related to kinetics and fragmentation, such investigations were not accounted for in this work. Thus, spherical particles were assumed in this work (see Section 2.2.5.6) following most of the preceding CFD studies on entrained flow gasification (for example, see [223]), while future works may focus on the the implementation of particle shape models and the investigation of possible effects.

### **2.7.3.7 Conclusions concerning particle shrinking**

The results of the experiments of Kreitzberg et al. [157] indicate a significant effect of shrinking during heterogeneous gasification above a carbon conversion of 70-90%. Therefore, shrinking was reflected in this work (see Section 2.7.3.12).

### **2.7.3.8 Conclusions concerning particle pore structures**

The internal particle pore structures are significantly affected by devolatilisation, heterogeneous gasification, fragmentation, shrinking, abrasion and mineral matter transformation.

This obviously challenges predictions of particle quantities such as particle surface area and particle pore size distribution. Thus, common particle pore structure models, such as isolated pore models [311] and random pore models [28, 29], cannot simply be adopted but need to be calibrated using measurement data. For coal entrained flow gasification, calibrated models were developed by the group of Spliethoff [117, 118, 299, 316, 314, 315]. The proposed models relied on uniform cylindrical pores with a mean particle pore diameter and a mean particle pore length, while reflecting the impact of thermal annealing and neglecting fragmentation and swelling. However, similar investigations were beyond the objectives of this work. Therefore, the effective solid density and the particle diameter were approximated using simplified approaches (see Sections 2.7.3.10 and 2.7.3.12).

Furthermore, as *one* mean particle pore diameter is required for the heterogeneous gasification kinetics (see Section 2.7.5.1), the measured mean particle pore diameters  $d_{\text{pore,part,meas}}$  (based on nitrogen adsorption at 77 K [303]) and estimated mean particle pore diameters  $d_{\text{pore,part,est}}$  (see Section 2.7.3.9) were compared with the fitted particle pore diameters  $d_{\text{pore,part}}$  of Kreitzberg et al. [156], that were derived from measured apparent reaction rates assuming constant solid porosities  $\varepsilon_{\text{solid}}$  and constant carbon densities  $\rho_{\text{C}}$  and should be considered as fitted parameters. The data is summarised in Table I.3. The fitted diameters are accordingly in the range of the measured mean particle pore diameters  $d_{\text{pore,part,meas}}$  and estimated mean particle pore diameters  $d_{\text{pore,part,est}}$  (between 1 nm and 30 nm). Thus, the fitted parameters could be appropriate estimates.

Finally, the results of the particle surface area measurements of Müller et al. [213], Dubil [80], Stösser [303] and Schneider et al. [276] were reviewed demonstrating that the measurement results are in agreement with the findings of Di Blasi [72], Fleck et al. [99, 100] and Kreitzberg et al. [157]. Thus, the effect of higher flame temperatures on the specific surface area and the wood char kinetics should be focussed in future works.

### 2.7.3.9 Particle pore diameter

The mean particle pore diameter  $d_{\text{pore,part,est}}$  can be estimated assuming particles with a uniform distribution of cylindrical pores and can be determined by

$$d_{\text{pore,part,est}} = \frac{4}{\rho_{\text{solid,eff}} \hat{A}_{\text{pore,part}}} \varepsilon_{\text{solid,eff}} = \frac{4}{\rho_{\text{solid}} \hat{A}_{\text{pore,part}}} \frac{\varepsilon_{\text{solid,eff}}}{1 - \varepsilon_{\text{solid,eff}}}, \quad (2.199)$$

where  $\hat{A}_{\text{pore,part}}$  is the specific particle pore area,  $\rho_{\text{solid,eff}}$  is the effective solid density,  $\rho_{\text{solid}}$  is the true solid density and  $\varepsilon_{\text{solid,eff}}$  is the effective solid porosity. The specific particle pore area  $\hat{A}_{\text{pore,part}}$ , the effective solid density  $\rho_{\text{solid,eff}}$  and the effective solid porosity  $\varepsilon_{\text{solid,eff}}$  are defined by

$$\hat{A}_{\text{pore,part}} = \frac{A_{\text{pore,part}}}{m_{\text{part}}} = \frac{4}{\rho_{\text{solid,eff}} d_{\text{pore,part}}} \frac{V_{\text{pore,part}}}{V_{\text{part}}} = \frac{4 \varepsilon_{\text{solid,eff}}}{\rho_{\text{solid,eff}} d_{\text{pore,part}}}, \quad (2.200)$$

$$\rho_{\text{solid,eff}} = (1 - \varepsilon_{\text{solid,eff}}) \rho_{\text{solid}} , \quad (2.201)$$

$$\varepsilon_{\text{solid,eff}} = 1 - \frac{\rho_{\text{solid,eff}}}{\rho_{\text{solid}}} , \quad (2.202)$$

where  $A_{\text{pore,part}}$  is the particle pore area and  $V_{\text{pore,part}}$  is the particle pore volume. The particle pore area  $A_{\text{pore,part}}$  and the particle pore volume  $V_{\text{pore,part}}$  are given by

$$A_{\text{pore,part}} = \pi d_{\text{pore,part}} L_{\text{pore,part}} , \quad (2.203)$$

$$V_{\text{pore,part}} = \pi \frac{d_{\text{pore,part}}^2}{4} L_{\text{pore,part}} , \quad (2.204)$$

where  $d_{\text{pore,part}}$  is the mean particle pore diameter and the  $L_{\text{pore,part}}$  is the mean particle pore length. The estimated mean particle pore diameters  $d_{\text{pore,part,est}}$  are given in Table I.3.

### 2.7.3.10 Initial effective solid density

The initial effective solid density  $\rho_{\text{solid,eff},0}$  can be determined using the initial true particle density  $\rho_{\text{solid},0}$  and the initial effective solid porosity  $\varepsilon_{\text{solid,eff},0}$ . However, firstly, the effective solid density  $\rho_{\text{solid,eff}}$  and the effective solid porosity  $\varepsilon_{\text{solid,eff}}$  depend on the natural origin and the pyrolysis condition. For example, Brewer et al. [36] determined a wide range of effective solid densities for wood chars (475-600 kg/m<sup>3</sup>) and for grass chars (200-300 kg/m<sup>3</sup>). Secondly, the experiments of Dubil [80] and Stösser [303] only provided the macro solid porosity  $\varepsilon_{\text{solid,macro}}$  and the micro solid porosity  $\varepsilon_{\text{solid,micro}}$ , which both cannot be used to approximate the effective solid porosity  $\varepsilon_{\text{solid,eff}}$ . Therefore, the initial effective solid densities  $\rho_{\text{solid,eff},0}$  were obtained in this work from the mass flow controller measurements in the REGA experiments. Measured fuel densities  $\rho_{\text{fuel}}$  at inlet were used to determine the initial effective solid densities  $\rho_{\text{solid,eff},0}$  for the REGA experiments TUC5 GHKS10 V1071 and TUC5 GHKS30 V1284. The initial effective solid densities  $\rho_{\text{solid,eff}}$  were calculated by

$$\rho_{\text{solid,eff},0} = \frac{\dot{m}_{\text{solid}}|_{\text{inlet}}}{\frac{\dot{m}_{\text{fuel}}|_{\text{inlet}}}{\rho_{\text{fuel}}|_{\text{inlet}} - \frac{\dot{m}_{\text{C}_2\text{H}_6\text{O}_2}|_{\text{inlet}}}{\rho_{\text{C}_2\text{H}_6\text{O}_2}|_{\text{inlet}}}} , \quad (2.205)$$

where  $\dot{m}_{\text{solid}}|_{\text{inlet}} = w_{\text{solid,fuel}}|_{\text{inlet}} \dot{m}_{\text{fuel}}|_{\text{inlet}}$  is the solid mass flow rate at inlet,  $\dot{m}_{\text{fuel}}$  is the measured fuel mass flow rate,  $\rho_{\text{fuel}}$  is the measured fuel density,  $\dot{m}_{\text{C}_2\text{H}_6\text{O}_2}|_{\text{inlet}} = w_{\text{C}_2\text{H}_6\text{O}_2,\text{fuel}}|_{\text{inlet}} \dot{m}_{\text{fuel}}|_{\text{inlet}}$  is the ethylene glycol mass flow rate at inlet,  $\rho_{\text{C}_2\text{H}_6\text{O}_2}$  is the density of ethylene glycol,  $w_{\text{C}_2\text{H}_6\text{O}_2,\text{fuel}}$  is the mass fraction of ethylene glycol at inlet and  $w_{\text{solid,fuel}}$  is the mass fraction of wood char at inlet. The initial effective solid densities  $\rho_{\text{solid,eff},0}$  as well as the calculated initial effective solid porosities  $\varepsilon_{\text{solid,eff},0}$  and the calculated initial solid densities  $\rho_{\text{solid},0}$  for the REGA experiments TUC5 GHKS10 V1071 and TUC5 GHKS30 V1284 are given in Table 2.11.

**Table 2.11:** Initial effective solid densities  $\rho_{\text{solid,eff},0}$ , initial effective solid porosities  $\varepsilon_{\text{solid,eff},0}$  and initial solid densities  $\rho_{\text{solid},0}$  based on the REGA experiments TUC5 GHKS10 V1071 and TUC5 GHKS30 V1284.

REGA experiment	$\frac{\rho_{\text{solid,eff},0}}{\text{kg/m}^3}$	$\varepsilon_{\text{solid,eff},0}$	$\frac{\rho_{\text{solid},0}}{\text{kg/m}^3}$
TUC5 GHKS10 V1071	1448.5	0.158	1719.3
TUC5 GHKS30 V1284	1460.3	0.132	1682.6

### 2.7.3.11 Initial particle diameter

The initial particle diameter  $d_{\text{solid},0}$  is correlated with the initial effective solid density  $\rho_{\text{solid,eff},0}$  by

$$d_{\text{solid},0} = \sqrt[3]{\frac{6}{\pi} \frac{m_{\text{solid},0}}{\rho_{\text{solid,eff},0}}}. \quad (2.206)$$

### 2.7.3.12 Particle diameter

The particle diameter  $d_{\text{part}}$  changes during devolatilisation and heterogeneous gasification. Four approaches for the particle diameter were focussed in this work.

The **first approach** assumes a constant particle diameter  $d_{\text{part}}$  during devolatilisation and heterogeneous gasification. The effective solid density  $\rho_{\text{solid,eff}}$  changes according to

$$\rho_{\text{solid,eff}} = \frac{m_{\text{part}}}{\frac{\pi}{6} d_{\text{part}}^3}. \quad (2.207)$$

Such an assumption leads to a sharp increase of the effective solid porosity  $\varepsilon_{\text{solid,eff}}$  in the final stages of the heterogeneous gasification. Thus, a highly porous solid particle is left behind.

The **second approach** is based on a constant particle diameter during devolatilisation and on a constant effective solid density  $\rho_{\text{solid,eff}}$  during heterogeneous gasification; the corresponding particle diameter  $d_{\text{part}}$  is given by

$$d_{\text{part}} = \sqrt[3]{\frac{6}{\pi} \frac{m_{\text{solid}}}{\rho_{\text{solid,eff}}}}. \quad (2.208)$$

The **third approach** and the **fourth approach** are based on a constant particle diameter during devolatilisation and on a changing particle diameter during heterogeneous gasification, where the relationships for the particle diameter were derived using the experimental results of Kreitzberg et al. [157] (see Section 2.7.3.3). Firstly, the experimental data was approximated by

$$\tilde{d}_{\text{part}} = \begin{cases} 1 - \sum_{i=1}^3 C_i \tilde{t}^i, & \text{if } 0 \leq \tilde{t} \leq C_9 \\ C_6 \left(1 - |\tilde{t}|^{C_7}\right)^{1/C_8}, & \text{else} \end{cases}, \quad (2.209)$$

where  $C_1, \dots, C_9$  are coefficients, which were determined using the *least\_squares* method of SciPy [280, 327]. The approximations are shown in Fig. 2.16. Subsequently, since the fragmentation probability (for coal particles) increases with increasing particle diameter at constant temperature [284], it was assumed that small wood char particles do not show fragmentation just as the large wood char particles applied in the experiments of Kreitzberg et al. [157]. Based on the approximations for the large particles, a relationship was derived for small particles; the normalised particle diameter of small particles has been determined by

$$\tilde{d}_{\text{part}} = 1 - |\tilde{t}|^{14}. \quad (2.210)$$

This relationship is shown in Fig. 2.16. Accordingly, the particle diameter of small particles is retained in the initial conversion stages and rapidly decreases in the final conversion stages.

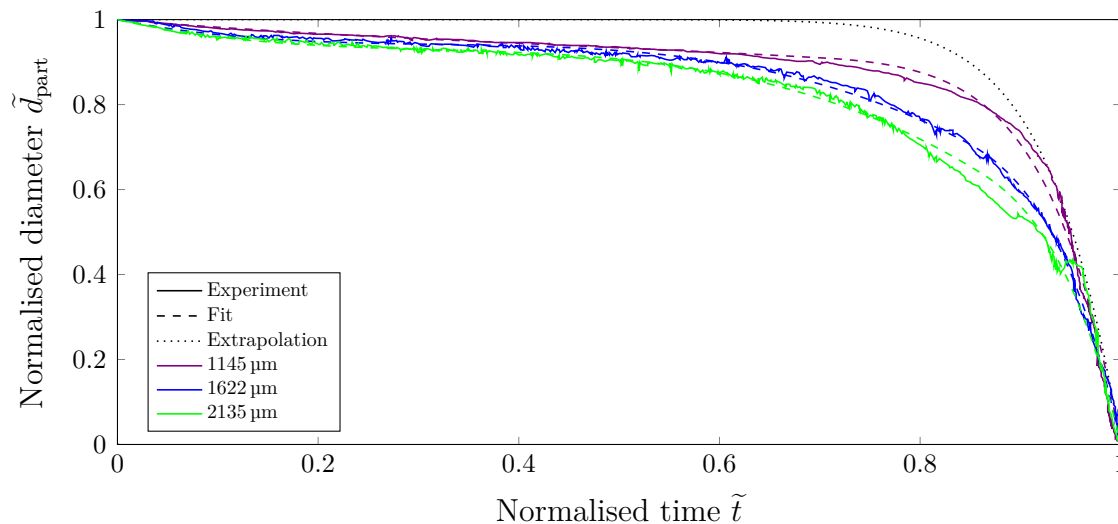


**Figure 2.16:** Normalised particle diameters during heterogeneous gasification based on measurements [157], fitting and extrapolation.

Finally, several attempts were made in order to correlate this relationship with the particle gasification conversion  $X_{\text{het,part}}$ . Two empirical approaches were eventually developed, which are referred as the third approach and the fourth approach in this work. In the **third approach**, a linear correlation between the particle gasification conversion  $X_{\text{het,part}}$  and the normalised time  $\tilde{t}$  is assumed. The particle diameter  $d_{\text{part}}$  is defined by

$$d_{\text{part}} = d_{\text{part},0} \left( (1 - C_{\text{sw}}) (1 - |X_{\text{het,part}}|^C) + C_{\text{sw}} \right), \quad (2.211)$$

where  $C = 14$  is the exponent already used in Eq. (2.210) and  $C_{\text{sw}} = 0.3$  is an (estimated) swelling/shrinking coefficient. In the **fourth approach**, the exponent  $C$  in Eq. (2.211) is described by

$$C = \begin{cases} \max \left( 200 + \operatorname{arctanh} (X_{\text{het,part}})^{5.4}, 10^5 \right), & \text{if } X_{\text{het,part}} < 1 \\ 10^5, & \text{else} \end{cases}. \quad (2.212)$$

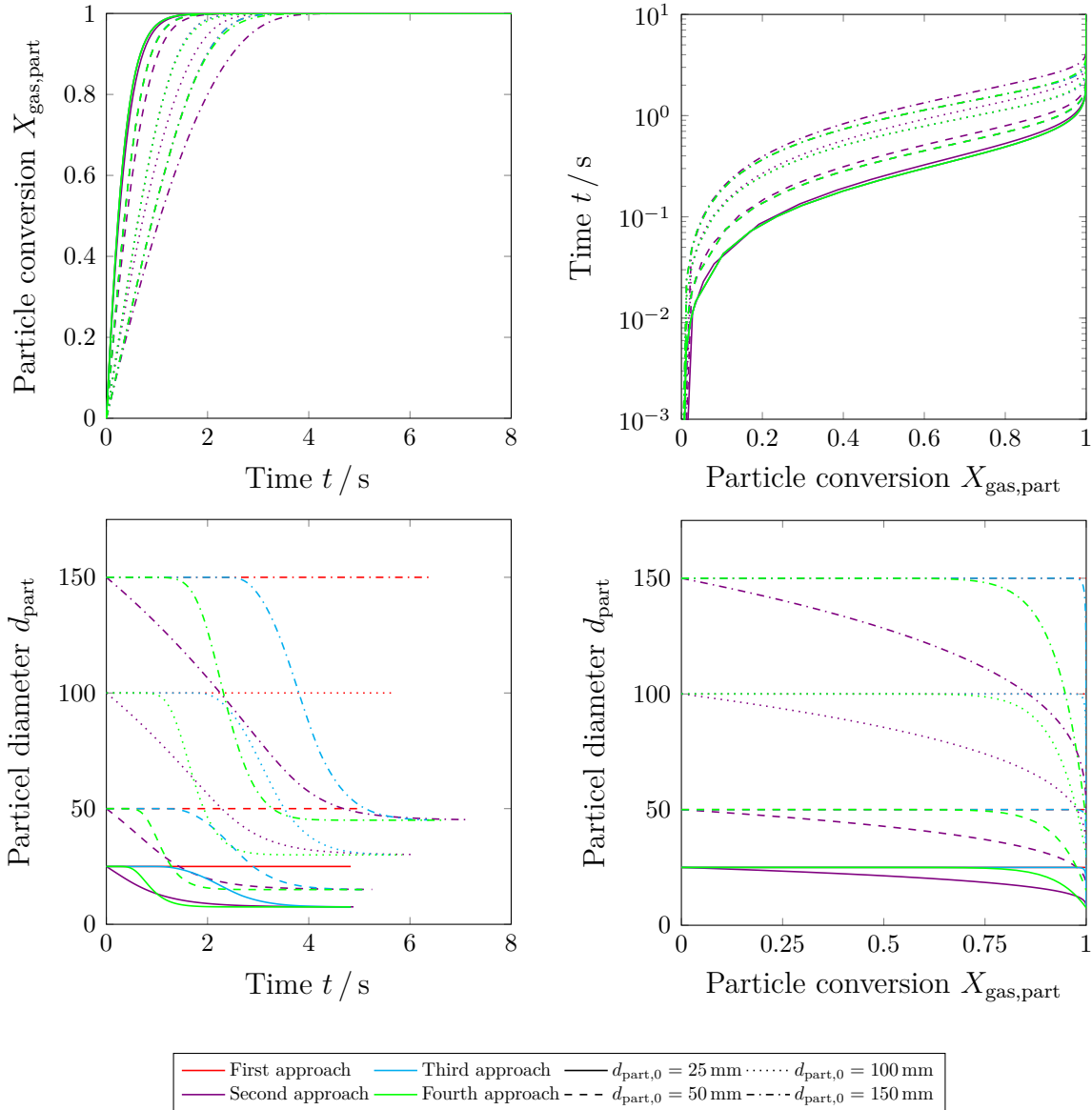


**Figure 2.17:** Simulated particle diameters  $d_{\text{part}}$  during heterogeneous gasification  $X_{\text{het,part}}$  at constant gas condition ( $T_{\text{gas}} = 1673.15$  K,  $x_{\text{CO}_2,\text{gas}} = 0.16$ ,  $x_{\text{H}_2\text{O},\text{gas}} = 0.38$ ,  $x_{\text{N}_2,\text{gas}} = 0.46$ ) and based on different approaches.

Assuming heterogeneous gasification kinetics for the Boudouard and the water gas reaction (see Section 2.7.5) and a constant gas condition, the four approaches are compared in

Fig. 2.17. Accordingly, the curves for the particle diameter  $d_{\text{part}}$  strongly differ. While the particle diameter  $d_{\text{part}}$  remains constant using the first approach, the particle shrinks either continuously when using the second approach or in short periods of time when applying the third or the fourth approach. As the short periods of time are typically at particle gasification conversions  $X_{\text{het,part}}$  above 75 %, similar curves were determined for the particle gasification conversion  $X_{\text{het,part}}$  using the first approach, the third approach and the fourth approach. In contrast, the second approach for the particle diameter  $d_{\text{part}}$  significantly affects the prediction of the particle gasification conversion  $X_{\text{het,part}}$ . Furthermore, none of the approaches can reflect the experimental observations of Kreitzberg et al. [157] for the particle diameter  $d_{\text{part}}$  during heterogeneous gasification. This is because of the experimental approach for the definition of the initial and final gasification times. Therefore, detailed evaluations of both the third approach and the fourth approach (or similar approaches) are hardly possible, and only the first approach was applied in the CFD simulations carried out in this work.

## 2.7.4 Devolatilisation

Devolatilisation describes the decomposition of the solid char matrix, the transport of the volatiles through the pores and the secondary reactions of the volatiles inside and outside the pores (for example, see [188]) and usually occurs during the heat-up of the solid particles in both solid and slurry entrained flow gasification. Thus, devolatilisation depends on the fuel properties and the operating conditions and is a strong non-isothermal process. The heat transfer Biot numbers  $Bi_T = h_{\text{part}} r_{\text{part}} / (3 \lambda_{\text{solid,eff}})$  are typically greater than 0.1. This is usually accounted for in single-particle simulations [39, 50, 104, 108, 116, 141, 175, 256] while non-uniform temperature distributions are generally not regarded in CFD simulations of combustion or gasification processes due to computing time reasons. Uniform temperature distributions are assumed even if this can require corrections of the actual reaction rates (for example, see [141]).

### 2.7.4.1 Detailed network models and global models

Detailed network models and global models are typically used to describe devolatilisation.

**Detailed network models** have been developed for coal pyrolysis (FG-DVC [295], Flashchain [225, 226, 227, 228, 229, 230, 235], CPD [107]) or for biomass and torrefied biomass (bioFlashchain [231, 232, 233, 234], bio-CPD [30], bio-FG DVC [52], FG-BioMass [145]). These models account for the influence of the solid char matrix and predict both devolatilisation kinetics and products using the chemical composition and the conversion conditions (temperature history and operating pressure).

**Global devolatilisation models** are based on pseudo-chemical equations and have been developed and applied numerous times for single-particle and multiphase simulations of combustion or gasification processes (for example, see [121, 214]). Various models exist including the single first-order reaction Arrhenius law model, the multi-reaction Arrhenius law model, the Kobayashi model [153], the single-reaction distributed activation energy model [19], the multi-reaction distributed activation energy model [321], the Yamamoto model [342], the Biagini and Tognotti model [31] and the Richards and Fletcher model (a modified Kobayashi model) [257]. For example, the reaction rate of a single first-order reaction Arrhenius law model (SFORALM)  $R_{\text{SFORALM}}$  is given by

$$R_{\text{SFORALM}} = k_0 \exp\left(-\frac{\bar{E}_a}{R T_{\text{part}}}\right) (m_{\text{part}} - m_{\text{part,min,dev}}), \quad (2.213)$$

and the reaction rate of a modified Yamamoto model (MYM)  $R_{\text{MYM}}$  is defined by

$$R_{\text{MYM}} = \sum_{i=1}^3 C_i X_{\text{dev,part}}^{i-1} k_0 \exp\left(-\frac{\bar{E}_a}{R T_{\text{part}}}\right) (m_{\text{part}} - m_{\text{part,min,dev}}), \quad (2.214)$$

where  $k_0$  is the pre-exponential factor,  $\bar{E}_a$  is the molar activation energy and  $C_1$ ,  $C_2$  and  $C_3$  are coefficients.

The global models can be calibrated using data from experimental measurements or detailed network simulations (for example, see [120, 173, 224, 257, 322]). However, uncertainties in the approximations can be significant if a wide range of temperature or heating rate conditions needs to be considered. Then, global models with a large number of parameters such as the multi-reaction distributed activation energy model or the Richards and Fletcher model are superior to other models (see [257]).

Coal, petroleum coke, biomass and torrefied biomass differ in chemical properties from pyrolysed wood char. Thus, detailed network models cannot be adopted to derive reliable devolatilisation kinetics and products for wood chars. Therefore, global devolatilisation kinetics and products were obtained in this work either from previous works or from experiments.

#### 2.7.4.2 Previous studies and HVIGasTech kinetics

Previous experimental studies on devolatilisation experiments with biomass [27, 35, 37, 51, 84, 95, 109, 111, 140, 142, 145, 221, 222, 240, 241, 242, 288, 291, 303, 305, 310, 312, 317, 318, 339, 344, 346, 349] applied thermogravimetric analysers, drop-tube reactors, wire mesh reactors, fluidised bed reactors and entrained flow reactors. However, while most of these studies analysed raw biomasses, only the studies of Branca and Di Blasi [35] and of Stösser [303] investigated the devolatilisation of wood char.

Branca and Di Blasi [35] performed thermogravimetric analyses with beech, chestnut, Douglas fir, redwood and pine chars in air up to 873 K (i. e. at combustion conditions) and developed multi-reaction Arrhenius law models. Stösser [303] carried out drop-tube reactor experiments with the fir char HK02, which contains significantly more volatiles than the beech wood chars HK01, HK06 or HK07 (see Section 2.7.1), and proposed a single first-order reaction Arrhenius law model.

### 2.7.4.3 New HVIGasTech kinetics, comparisons and conclusions

The kinetics of Branca and Di Blasi [35] and of Stösser [303] can be adopted with major uncertainties only [68]. Therefore, in the frame of an experimental and numerical collaboration [68, 276, 279], new devolatilisation experiments with the wood char HK06 were carried out in the DTR at Engler-Bunte-Institute, Fuel Technology. Contrary to the preceding work [303], the DTR experiments were combined with CFD simulations in order to reflect the strongly changing gas conditions and the initial particle size distribution and to develop devolatilisation kinetics based on a single first-order reaction Arrhenius law model and a modified Yamamoto model [68]. While the experimental and numerical methods and the results are reported in detail elsewhere [68], the parameters and the coefficients of determination  $R^2$  for the single first-order reaction Arrhenius law model and the modified Yamamoto model are reproduced alongside the parameters for the devolatilisation kinetics of Stoesser [303] in Table 2.12.

**Table 2.12:** Parameters for the devolatilisation kinetics of Stösser [303] based on a single first-order reaction Arrhenius law model (SFORALM) and of Dammann et al. [68] based on a single first-order reaction Arrhenius law model (SFORALM) or a modified Yamamoto model (MYM), coefficients of determination  $R^2$  and ranges of relative deviations (RD) between balanced and simulated particle devolatilisation conversions  $X_{\text{dev,part}}$  for various DTR experiments [68].

Model	$k_0$ 1/s	$\bar{E}_a$ J/mol	$C_1$	$C_2$	$C_3$	$R^2$	RD %
SFORALM [303]	6400	72000	–	–	–	–	+13.5 ... + 76.6
SFORALM [68]	266	48232	–	–	–	0.891	–30.2 ... + 10.9
MYM [68]	4511	64724	1.010	–10.623	9.065	0.939	–11.2 ... + 10.4

For the DTR experiments [68], the simulated devolatilisation conversions based on the devolatilisation kinetics of Dammann et al. [68] and Stösser [303] are compared with the balanced devolatilisation conversions in Fig. 2.18. The ranges of relative deviations are given in Table 2.12. The particle devolatilisation conversion in the DTR experiments can be well described using both devolatilisation kinetics of Dammann et al. [68] while the devolatilisation kinetics of Stösser [303] provide higher particle devolatilisation conversions  $X_{\text{dev,part}}$  and are thus characterised by higher reaction rates. This is also evident from

the comparison in Fig. 2.19. The predicted particle devolatilisation conversions  $X_{\text{dev,part}}$  at a constant heating rate of  $10^4$  K/s or at a constant temperature of 1673.15 K demonstrate that the complete conversion is achieved faster using the devolatilisation kinetics of Stösser [303] than using the devolatilisation kinetics of Dammann et al. [68]. However, the rates based on the devolatilisation kinetics of Stösser [303] are not significantly faster (see the predictions using the devolatilisation kinetics of Dammann et al. [68] with pre-exponential factors increased by a factor of 10 in Fig. 2.19).

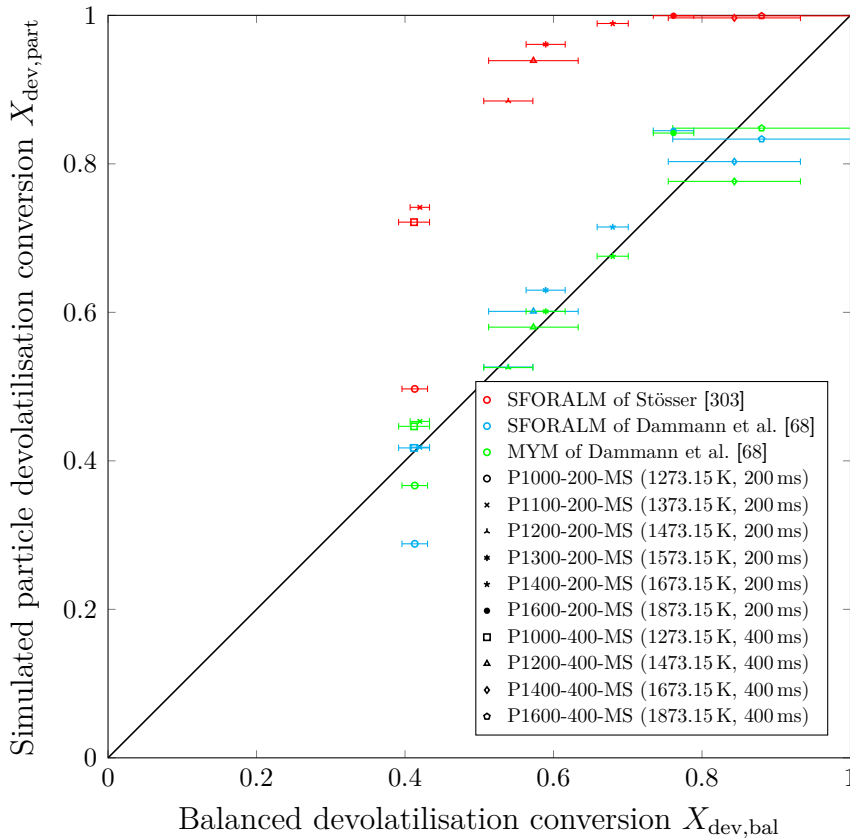


**Figure 2.18:** Mean particle devolatilisation conversions  $X_{\text{dev,part}}$  simulated for various DTR experiments [68] using the single first-order reaction Arrhenius law model of Stösser [303], the single first-order reaction Arrhenius law model of Dammann et al. [68] and the modified Yamamoto model of Dammann et al. [68] in comparison with balanced devolatilisation conversions  $X_{\text{dev,bal}}$  of various DTR experiments [68].

Furthermore, at low temperatures and short residence times, the predictions based on the single first-order reaction Arrhenius law model of Dammann et al. [68] strongly deviate from the predictions based on the modified Yamamoto model in absence of experimental data for these conditions [68]. Eventually, the single first-order reaction Arrhenius law model of Dammann et al. [68] was applied for the CFD simulations in this work.

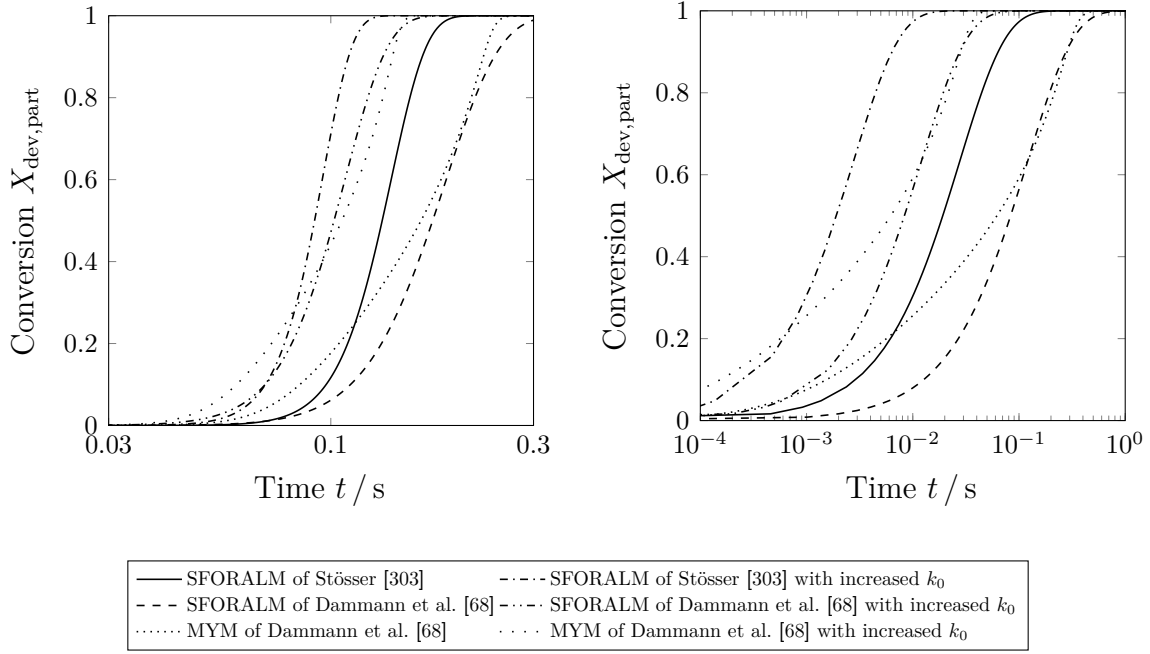


**Figure 2.19:** Simulated particle devolatilisation conversions  $X_{\text{dev,part}}$  at a constant heating rate of  $10^4$  K/s (left) and at a constant temperature of 1673.15 K (right) based on the devolatilisation kinetics of Stösser [303] and Dammann et al. [68]. Kinetics were applied with the original or with modified pre-exponential factors (increased by a factor of 10).

#### 2.7.4.4 Heat and mass transfer

The particle mass transfer rate  $R_{\text{m,part}}$ , the particle energy transfer rate  $R_{\text{E,part}}$  and the specific enthalpy of transition  $\Delta_{\text{trs}}\hat{H}$  are given by

$$R_{\text{m,part}} \equiv R_{\text{m,part,dev}} = R_{\text{SFORALM}}, \quad (2.215)$$

$$R_{\text{E,part}} = R_{\text{m,part}} \Delta_{\text{dev}}\hat{H}^\ominus, \quad (2.216)$$

$$\Delta_{\text{trs}}\hat{H} = \Delta_{\text{dev}}\hat{H}^\ominus, \quad (2.217)$$

where  $\Delta_{\text{dev}}\hat{H}^\ominus$  is the measured specific standard enthalpy of devolatilisation. In contrast to previous works (for example, see [331]), the energy release during devolatilisation was not neglected and described complying with the energy balance. The specific standard enthalpy of devolatilisation  $\Delta_{\text{dev}}\hat{H}^\ominus$  is defined by

$$\Delta_{\text{dev}}\hat{H}^\ominus = \Delta_{\text{c}}\hat{H}_{\text{vol}}^\ominus - \frac{1}{M_{\text{vol}}} \sum_i x_{i,\text{vol}} \Delta_{\text{c}}\bar{H}_{i,\text{ref}}^\ominus, \quad (2.218)$$

where  $\Delta_{\text{c}}\hat{H}_{\text{vol}}^\ominus$  is the specific standard combustion enthalpy of the volatiles,  $M_{\text{vol}}$  is the molar mass of the volatiles and  $\Delta_{\text{c}}\bar{H}_{i,\text{ref}}^\ominus$  is the molar standard combustion enthalpy of species  $i$  at the reference temperature  $T_{\text{ref}}$ . Assuming that the combustibles can be described using

the physical properties of graphite, the specific standard combustion enthalpy of the volatiles  $\Delta_c \hat{H}_{\text{vol}}^\ominus$  is given by

$$\Delta_c \hat{H}_{\text{vol}}^\ominus = \frac{1}{w_{\text{vol,solid}}} \left( \Delta_c \hat{H}_{\text{solid}}^\ominus - \Delta_c \hat{H}_{\text{C}_{(\text{gr})},\text{ref}}^\ominus w_{\text{comb,solid}} \right), \quad (2.219)$$

where  $\Delta_c \hat{H}_{\text{solid}}^\ominus$  is the (experimental) specific standard combustion enthalpy of wood char and  $\Delta_c \hat{H}_{\text{C}_{(\text{gr})},\text{ref}}^\ominus$  is the specific standard combustion enthalpy of graphite at the reference temperature  $T_{\text{ref}}$ .

Values for the specific standard combustion enthalpy of the wood char  $\Delta_c \hat{H}_{\text{solid}}^\ominus$ , the specific standard combustion enthalpy of the volatiles  $\Delta_c \hat{H}_{\text{vol}}^\ominus$  and the specific standard enthalpy of devolatilisation  $\Delta_{\text{dev}} \hat{H}^\ominus$  are given for the wood chars HK01 (EF simple) and HK07 (EF simple) in Table 2.13. Approximately 20% of the combustion enthalpy of wood char is released during devolatilisation under the model assumptions chosen in this work.

**Table 2.13:** Specific standard combustion enthalpies  $\Delta_c \hat{H}_{\text{solid}}^\ominus$  of wood chars HK01 (EF simple) and HK07 (EF simple) based on heating value analyses [94] and corresponding specific standard combustion enthalpies of the volatiles  $\Delta_c \hat{H}_{\text{vol}}^\ominus$  and specific standard enthalpies of devolatilisation  $\Delta_{\text{dev}} \hat{H}^\ominus$  based on calculations.

Wood char	$\frac{\Delta_c \hat{H}_{\text{solid}}^\ominus}{\text{kJ/kg}}$	$\frac{\Delta_c \hat{H}_{\text{vol}}^\ominus}{\text{kJ/kg}}$	$\frac{\Delta_{\text{dev}} \hat{H}^\ominus}{\text{kJ/kg}}$
HK01 (EF simple)	-31153	-28730	-6168
HK07 (EF simple)	-28400	-34859	-12325

#### 2.7.4.5 Volatiles compositions

The devolatilisation products are oxygenated and nitrogenated hydrocarbons which typically decompose or react with oxygen or water vapour to methane, carbon monoxide, carbon dioxide, hydrogen, water vapour and nitrogen in accordance with the elemental balance. Such assumptions were used, for example, by Kumar and Ghoniem [162], Vascellari et al. [322] and Halama and Spliethoff [117]. Ma and Zitney [181] also accounted for benzene, hydrogen sulfide, carbonyl sulfide and hydrogen chloride. However, the methods to determine the volatiles composition have rather seldom been reported in detail in previous studies. For example, Watanabe and Otaka [331] and Ku et al. [159] used not further specified equilibrium calculations. More detailed approaches were suggested, for example, by Marklund et al. [191, 192, 193] for black liquor decomposition and by Syamlal and Bissett [307], Nakod [219] and Kumar and Paul [163, 164] for coal decomposition [68]. The compositions of the devolatilisation products were derived in this work using equilibrium calculations (see Section 2.7.1) and are given in Table 2.14.

**Table 2.14:** Volatiles compositions in mass fractions  $w_{\text{vol}}$  based on equilibrium calculations at 1473.15 K and based on measurements and reactive plug-flow reactor simulations combined with numerical optimisation [68].

$i$	$w_{i,\text{vol}}$		
	Equilibrium calculation results		Estimates [68]
	HK01 (EF simple)	HK07 (EF simple)	
CH <sub>4</sub>	0.001713	0.001673	0-0.02
CO	0.862164	0.865036	0.75-0.81
CO <sub>2</sub>	0.000394	0.000400	0-0.06
H <sub>2</sub>	0.114523	0.112589	0.14-0.15
H <sub>2</sub> O	0.000736	0.000734	0
N <sub>2</sub>	0.020470	0.019568	0.02

The equilibrium compositions of the volatiles are characterised by high contents of carbon monoxide and hydrogen and low contents of methane and carbon dioxide. Table 2.14 also lists estimated ranges for the mass fractions of the devolatilisation products, that were determined (i) using the dry gas species concentrations measured in the DTR experiments and (ii) using one-dimensional reactive plug-flow reactor simulations with the GRI mechanism (version 3.0) [294] (see [68]). Accordingly, the equilibrium concentrations are in a reasonable agreement with the estimated concentrations but may underestimate the concentrations of methane and carbon dioxide. Thus, an estimated composition may provide better predictions. However, in view of the methodological uncertainties [68], the estimates were not applied in this work.

### 2.7.5 Heterogeneous gasification

Heterogeneous gasification describes the conversion of the solid char matrix with gaseous reactants. Several sub-processes are involved including (i) the diffusion of the gaseous reactants from the bulk through the boundary layer and the pores to the surface, (ii) the adsorption of the gaseous reactants at active sites of the solid char matrix, (iii) the reaction of the gaseous reactants with the solid matrix, (iv) the desorption of the gaseous products from the active sites of the solid matrix and (v) the diffusion of the gaseous products through the pores and boundary layer back into the bulk (see [188]). The reaction rates are influenced by graphitisation, ash dispersion, morphology, pore diffusion, film diffusion and the reactants (for example, see [188, 277]). Possible reactants in slurry entrained flow gasification processes are carbon dioxide, hydrogen, water vapour and oxygen. However, since reactions with both hydrogen and oxygen are relatively unlikely due to low reaction rates and flame stoichiometry, respectively, [303], reactions with carbon dioxide and water vapour only were accounted for in this work. Both reactions can either be described

using detailed reaction mechanisms [32, 130, 143, 168, 201] or global approaches for the Boudouard reaction



and the water-gas reaction



### 2.7.5.1 Reaction regimes

Char conversion can be divided into three regimes (see Fig. 2.20): regime I, which is controlled by adsorption, reaction and desorption; regime II, which is controlled by diffusion through the pores; regime III, which is controlled by diffusion through the film layer. Kinetics are usually determined for the intrinsic regime (regime I), while kinetics for the pore diffusion regime (regime II) and the film diffusion regime (regime III) are investigated less frequently since the experimental apparatus strongly affects pore and film diffusion; only elaborative drop-tube reactor experiments are typically appropriate to derive kinetics for the regimes II and III.

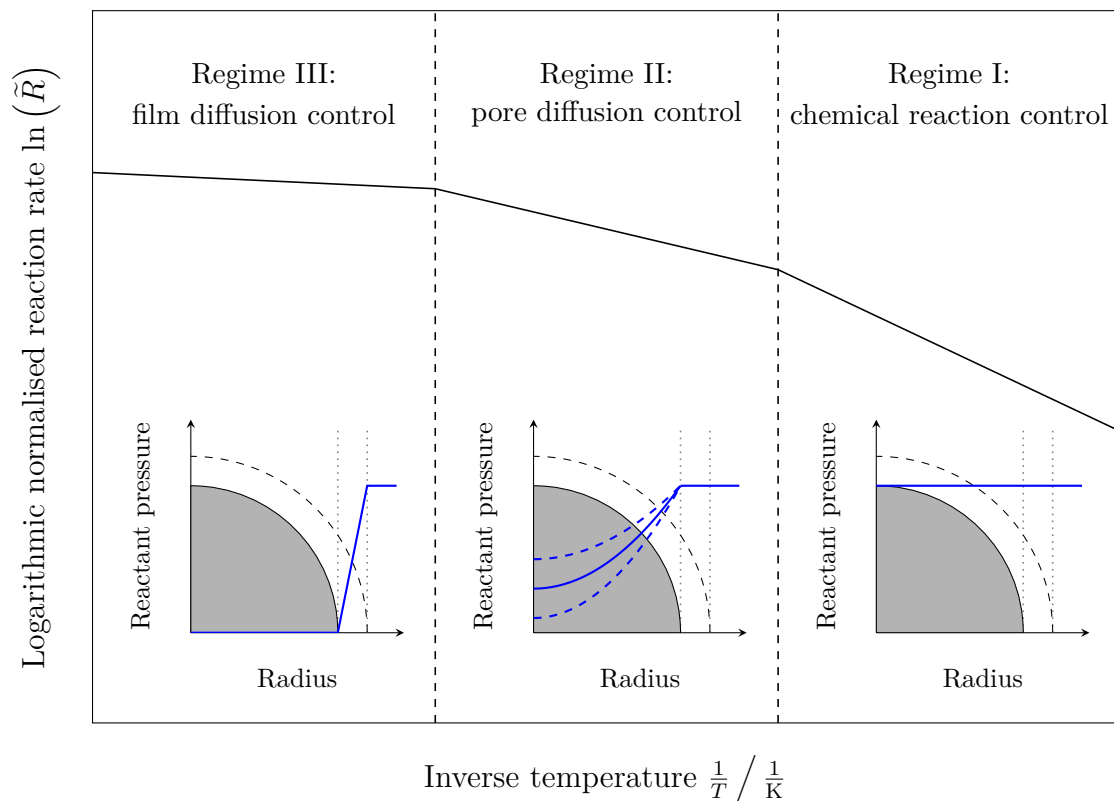


**Figure 2.20:** Kinetic regimes for the heterogeneous gasification of porous carbonaceous particles [276, 303].

**Reaction rates in regime I** are usually described either using the power-law model (PLM)

$$R_{i,\text{PLM,I}} = k_{0,i} \exp\left(-\frac{\bar{E}_{a,i}}{RT}\right) \tilde{p}_i^{n_i} \quad (2.222)$$

or the Langmuir-Hinshelwood model (LHM)

$$R_{i,\text{LHM,I}} = \frac{k_{1,i} \tilde{p}_i}{1 + K_i \tilde{p}_i}, \quad (2.223)$$

where

$$\tilde{p}_i = \left(\frac{p_{i,\text{gas,s}}}{\text{bar}}\right), \quad (2.224)$$

$$K_i = \frac{k_{1,i}}{k_{3,i}}, \quad (2.225)$$

$$k_{1,i} = k_{0,1,i} \exp\left(-\frac{\bar{E}_{a,1,i}}{RT}\right), \quad (2.226)$$

$$k_{3,i} = k_{0,3,i} \exp\left(-\frac{\bar{E}_{a,3,i}}{RT}\right). \quad (2.227)$$

Here,  $k_{0,i}$ ,  $k_{0,1,i}$  and  $k_{0,3,i}$  are the pre-exponential factors of reaction  $i$ ,  $\bar{E}_{a,i}$ ,  $\bar{E}_{a,1,i}$  and  $\bar{E}_{a,3,i}$  are the molar activation energies of reaction  $i$ ,  $n_i$  is the reaction order of reaction  $i$  and  $p_{i,\text{gas,s}}$  is the partial pressure of species  $i$  at the particle surface. Since the diffusion time scale through the particle boundary layer is much smaller than the reaction time scale, the pressure of species  $i$  at the particle surface  $p_{i,\text{gas,s}}$  can be approximated with the partial pressure of species  $i$  in the bulk  $p_{i,\text{gas}} = x_{i,\text{gas}} p_{\text{gas}}$ .

**Reaction rates in regime II** are generally determined using the intrinsic reaction rates and effectiveness factors according to

$$R_{i,j,\text{II}} = \eta_{i,j} R_{i,j,\text{I}}, \quad (2.228)$$

where  $j = \text{PLM, LHM}$  and [127]

$$\eta_{i,j} = \frac{f_{i,j}}{\Phi_{i,j}} \left( \frac{1}{\tanh(3\Phi_{i,j})} - \frac{1}{3\Phi_{i,j}} \right) \quad (2.229)$$

is the effectiveness factor,  $\Phi_{i,j}$  is the Thiele modulus [311] and  $f_{i,j}$  is a correction function [127], each for reaction  $i$  and model  $j$ . The latter is given by [127]

$$f_{i,j} = \left( 1 + \frac{\sqrt{1/2}}{\frac{1}{2\Phi_{i,j}^2} + 2\Phi_{i,j}} \right)^{1/2(1-n_{\text{obs},i,j})^2}, \quad (2.230)$$

where [127]

$$n_{\text{obs},i,j} = \begin{cases} \frac{1}{1 + K_i \tilde{p}_i}, & \text{if } j = \text{LHM} \\ n_i, & \text{if } j = \text{PLM} \end{cases}. \quad (2.231)$$

The Thiele modulus for reaction  $i$  and the power-law model  $\Phi_{i,\text{PLM}}$  is defined by [127]

$$\Phi_{i,\text{PLM}} = \frac{d_{\text{part}}}{6} \sqrt{\frac{(n_i + 1) k_1 \tilde{p}_i^{n_i}}{2 D_{\text{eff}}} \frac{\rho_C}{M_C} \frac{\bar{R} T_{\text{part}}}{p_{i,\text{gas,s}}}}, \quad (2.232)$$

and the Thiele modulus for reaction  $i$  and the Langmuir-Hinshelwood model  $\Phi_{i,\text{LHM}}$  is given by [127]

$$\Phi_{i,\text{LHM}} = \begin{cases} \frac{d_{\text{part}}}{6} \sqrt{\frac{k_1 \tilde{p}_i}{2 D_{i,\text{eff}}} \frac{\rho_C}{M_C} \frac{\bar{R} T_{\text{part}}}{p_{\text{gas}}}} \frac{K_i \tilde{p}_i}{1 + K_i \tilde{p}_i} \frac{1}{\sqrt{K_i \tilde{p}_i - \ln(1 + K_i \tilde{p}_i)}}, & \text{if } K_i \tilde{p}_i > 0 \\ \frac{d_{\text{part}}}{6} \sqrt{\frac{k_1 \tilde{p}_i}{D_{i,\text{eff}}} \frac{\rho_C}{M_C} \frac{\bar{R} T_{\text{part}}}{p_{\text{gas}}}}, & \text{else} \end{cases}, \quad (2.233)$$

where  $D_{i,\text{eff}}$  is the effective diffusion coefficient for reaction  $i$ ,  $\rho_C$  is the density of carbon and  $M_C$  is the molar mass of carbon.

The effective diffusion coefficient for reaction  $i$  is given by

$$D_{i,\text{eff}} = \frac{\varepsilon_{\text{part}}}{\tau_{\text{part}}} \left( \frac{1}{D_{i,\text{gas,eff}}} + \frac{1}{D_{i,\text{K}}} \right)^{-1}, \quad (2.234)$$

where  $\varepsilon_{\text{part}}$  is the particle porosity,  $\tau_{\text{part}}$  is the particle tortuosity,  $D_{i,\text{gas,eff}}$  is the effective gas diffusion coefficient of species  $i$  and  $D_{i,\text{K}}$  is the Knudsen diffusion coefficient of species  $i$ . The latter is determined by

$$D_{i,\text{K}} = \frac{d_{\text{pore,part},i}}{3} \sqrt{\frac{8 \bar{R} T_{\text{part}}}{\pi M_i}}, \quad (2.235)$$

where  $d_{\text{pore,part},i}$  is the mean particle pore diameter for reaction  $i$ .

The density of carbon  $\rho_C$  is defined by [207]

$$\rho_C = \frac{w_{\text{C,solid}}}{\frac{1}{\rho_{\text{solid,eff}}} - \frac{w_{\text{ash,solid}}}{\rho_{\text{ash}}}}, \quad (2.236)$$

where  $w_{\text{C,solid}}$  is the carbon mass fraction and  $w_{\text{ash,solid}}$  is the ash mass fraction, each during heterogeneous gasification, and  $\rho_{\text{ash}}$  is the density of ash.

In addition to the intrinsic reaction parameters, the particle porosity  $\varepsilon_{\text{part}}$ , the particle tortuosity  $\tau_{\text{part}}$  and the mean particle pore diameters  $d_{\text{pore,part,CO}_2}$  and  $d_{\text{pore,part,H}_2\text{O}}$  can be assumed as model parameters and are typically determined from the observed reaction rates in combination with assumptions and density or porosity measurements.

**Reaction rates in regime III** are derived from the reaction rates in regime II using the partial pressures at the particle surface, i. e. the partial pressure of each species  $i$  at the particle surface  $p_{i,\text{gas,s}}$  is determined using the mass transfer rate rate due to film diffusion

$$k_{\text{m},i} A_{\text{s,part}} M_{\text{C}} \left( \frac{x_{i,\text{gas}} p_{\text{gas}}}{\bar{R} T_{\text{gas}}} - \frac{x_{i,\text{gas,s}} p_{\text{gas}}}{\bar{R} T_{\text{part,s}}} \right) \quad (2.237)$$

and the mass transfer rate due to intrinsic reaction and pore diffusion. Here,  $k_{\text{m},i}$  is the mass transfer coefficient of species  $i$  defined by

$$k_{\text{m},i} = \frac{Sh_{i,\text{film}} D_{i,\text{gas,film}}}{d_{\text{part}}}, \quad (2.238)$$

where  $Sh_{i,\text{film}}$  is the Sherwood number for species  $i$  at film condition and  $D_{i,\text{gas,film}}$  is the gas diffusion coefficient of species  $i$  at film condition.

### 2.7.5.2 Previous studies and HVIGasTech kinetics

Numerous global heterogeneous gasification kinetics have been developed for coal (see [132]) and biomass (see [72]). However, the kinetics could not be adopted in this work since (i) the kinetics are mainly intrinsic kinetics, whereas kinetics for the pore diffusion regime at low-partial pressure and high-temperature conditions are required for the conditions focussed in this work, and (ii) the reaction rates of the intrinsic kinetics already vary several orders of magnitude due to differences in fuel and char properties and in the experimental apparatus [277].

In order to incorporate appropriate kinetics for the Boudouard reaction and the water-gas reaction, experimental studies [155, 156, 275, 277, 303] have been carried out in the frame of HVIGasTech [124]. The first studies [155, 156, 275, 303] focussed on the fir chars HK02 and HK02-1600 while the most recent study of Schneider et al. [277] investigated the beech wood chars HK06-1400-200 and HK06-1600-200. The kinetics developed so far are summarised in Tables I.5-I.7.

Two kinetics sets were developed by Kreitzberg et al. [156] using fluidised bed reactor (FBR) experiments with the wood char HK02 at regime I and regime II conditions. The

kinetics were obtained assuming constant values<sup>2</sup> for the density of carbon  $\rho_C$ , the particle pore diameters  $d_{\text{pore,part,CO}_2}$  and  $d_{\text{pore,part,H}_2\text{O}}$ , the particle porosity  $\varepsilon_{\text{part}}$  and the particle tortuosity  $\tau_{\text{part}}$ ; the values are given in Table I.7. Two further kinetics sets were established by Schneider et al. [277] using pressurised single-particle reactor (pSPR) experiments with the wood char HK06-1400-200 at high-pressure regime I conditions.

The kinetics sets of Kreitzberg et al. [156] and Schneider et al. [277] rely on the power-law model or the Langmuir-Hinshelwood model and on the uniform reaction model  $f_{\text{URM}}$  as dimensionless surface model. The uniform reaction model  $f_{\text{URM}}$  is defined by

$$f_{\text{URM}}(X) = (1 - X) \quad (2.239)$$

and was superior to the shrinking core model  $f_{\text{SCM}}$  [340, 341] or the random pore model  $f_{\text{RPM}}$  [28, 29] in the approximation of the experimental reaction rates [156].

### 2.7.5.3 Heat and mass transfer

The particle mass transfer rate  $R_{\text{m,part}}$ , the particle energy transfer rate  $R_{\text{E,part}}$  and the specific enthalpy of transition  $\Delta_{\text{trs}}\hat{H}$  during heterogeneous gasification are given for the kinetics of Kreitzberg et al. [156] and Schneider et al. [277] by

$$R_{\text{m,part}} \equiv R_{\text{m,part,het}} = \sum_{i=\text{CO}_2, \text{H}_2\text{O}} R_{\text{m,part},i}, \quad (2.240)$$

$$R_{\text{E,part}} = 0, \quad (2.241)$$

$$\Delta_{\text{trs}}\hat{H} = \frac{1}{R_{\text{m,part}}} \sum_{i=\text{CO}_2, \text{H}_2\text{O}} R_{\text{m,part},i} \Delta_{\text{r}}\hat{H}_{i,\text{ref}}^\ominus, \quad (2.242)$$

where

$$R_{\text{m,part},i} = R_{i,j,\text{II}} f_{\text{URM}}(X_{\text{het,part}}) (m_{\text{part,min,dev}} - m_{\text{part,het,min,het}}) \quad (2.243)$$

is the particle mass transfer rate for reaction  $i$  and model  $j$  and  $\Delta_{\text{r}}\hat{H}_{i,\text{ref}}^\ominus$  is the specific standard enthalpy of reaction of reaction  $i$  at the reference temperature  $T_{\text{ref}}$ . The latter is defined for the Boudouard reaction by

$$\Delta_{\text{r}}\hat{H}_{\text{CO}_2,\text{ref}}^\ominus = \frac{1}{M_C} (2 \bar{H}_{\text{CO,ref}}^\ominus - \bar{H}_{\text{CO}_2,\text{ref}}^\ominus) \quad (2.244)$$

and for the water-gas reaction by

$$\Delta_{\text{r}}\hat{H}_{\text{H}_2\text{O,ref}}^\ominus = \frac{1}{M_C} (\bar{H}_{\text{CO,ref}}^\ominus - \bar{H}_{\text{H}_2\text{O,ref}}^\ominus), \quad (2.245)$$

---

<sup>2</sup>The values were adopted in this work for all calculations except for the comparisons in Figs. 2.21 and 2.22.

where  $\overline{H}_{\text{CO,ref}}^\ominus$  is the molar standard enthalpy of carbon monoxide,  $\overline{H}_{\text{CO}_2,\text{ref}}^\ominus$  is the molar standard enthalpy of carbon dioxide and  $\overline{H}_{\text{H}_2\text{O,ref}}^\ominus$  is the molar standard enthalpy of water vapour, each at the reference temperature  $T_{\text{ref}}$ . Thus, carbon used in Eqs. (2.220) and (2.221) is assumed to be graphite corresponding to the assumptions in Sections 2.7.1 and 2.7.4.

#### 2.7.5.4 Comparisons and conclusions

The kinetics of Kreitzberg et al. [156] have two deficiencies. Firstly, the reaction rates are affected by response control at regime II conditions (for example, see [300]) and do not actually reflect regime II conditions. Secondly, the kinetics were developed for the fir char HK02 which is characterised by different graphitisation, ash dispersion or pore structures in comparison with the beech wood chars HK01 and HK07. In contrast, the kinetics of Schneider et al. [277] were developed for beech wood char. However, to apply the kinetics at low-partial-pressure and high-temperature conditions, assumptions are needed for the particle porosity  $\varepsilon_{\text{part}}$ , the particle tortuosity  $\tau_{\text{part}}$  and the mean particle pore diameters  $d_{\text{pore,part,CO}_2}$  and  $d_{\text{pore,part,H}_2\text{O}}$ . Therefore, previous HVIGasTech studies have not established yet appropriate heterogeneous gasification kinetics for beech wood char at atmospheric entrained flow gasification conditions. However, in absence of appropriate alternatives, the kinetics sets of Kreitzberg et al. [156] and Schneider et al. [277] were examined in this work.

The particle gasification conversions  $X_{\text{het,part}}$  and the effectiveness factors  $\eta$  based on the kinetics are compared (i) for constant gas conditions and for various particle pore diameters  $d_{\text{pore,part}}$  in Fig. 2.21 and (ii) for constant gas conditions and for various initial particle diameters  $d_{\text{part},0}$  in Fig. 2.22. Accordingly, faster particle gasification conversion  $X_{\text{het,part}}$  can be expected for smaller initial particle diameters  $d_{\text{part},0}$  and larger particle pore diameters  $d_{\text{pore,part}}$ . The progress of the particle gasification conversion  $X_{\text{het,part}}$  thus shifts as expected but strongly differs for each kinetics set. The deviations are due to both effectiveness factors and intrinsic reaction rates. Furthermore, Figs. 2.21 and 2.22 show that the reaction rate of the water-gas reaction is typically higher than the rate of the Boudouard reaction and that the kinetics of Kreitzberg et al. [156] based on the Langmuir-Hinshelwood model typically provide the highest reaction rates.

Eventually, the kinetics of Kreitzberg et al. [156] based on the Langmuir-Hinshelwood model were chosen for the CFD simulations in this work (i) since these kinetics were calibrated to a certain extent at pore diffusion conditions (see Section 2.7.3.8) and (ii) since Langmuir-Hinshelwood models are slightly superior to power-law models concerning extrapolation. However, further experimental research is needed to validate the existing wood char kinetics at high-temperature conditions (see Chapter 5).

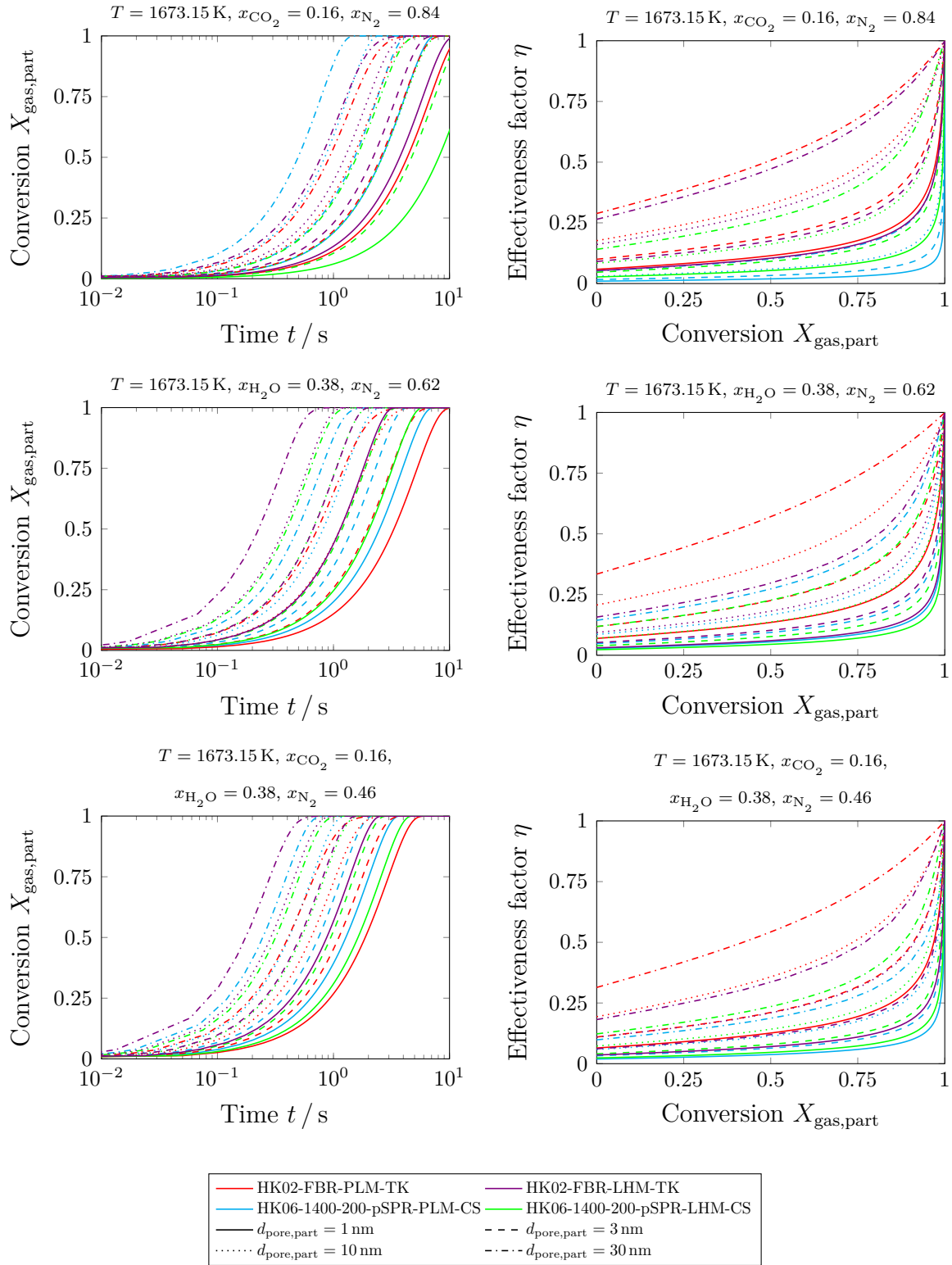


**Figure 2.21:** Simulated particle gasification conversions  $X_{\text{het,part}}$  and effectiveness factors  $\eta$  at constant gas condition and various constant particle pore diameters  $d_{\text{pore,part}}$  based on the heterogeneous gasification kinetics of Kreitzberg et al. [156] and Schneider et al. [277]: only the Boudouard reaction (top), only the water-gas reaction (centre) and Boudouard reaction and water-gas reaction (bottom).

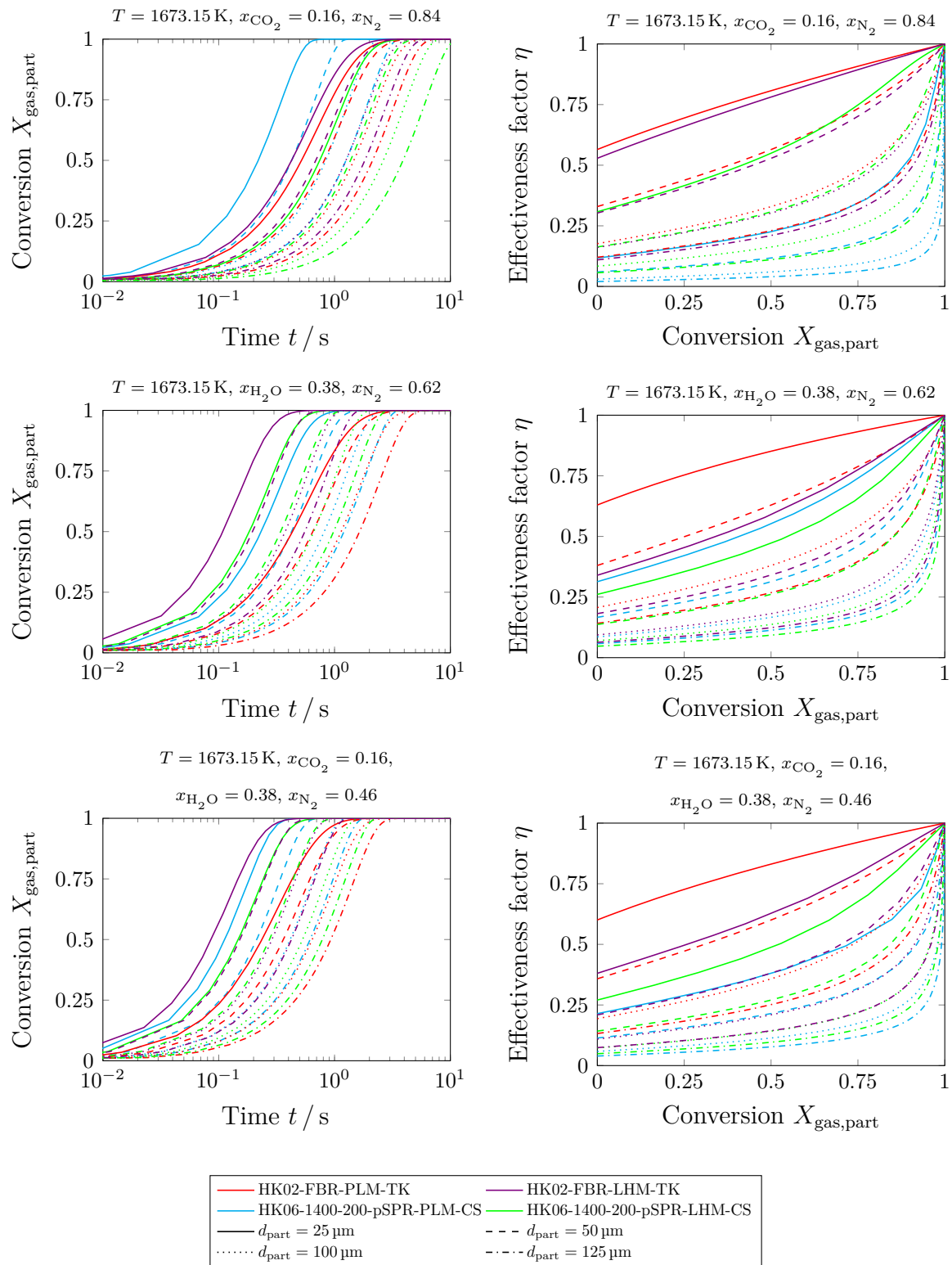


**Figure 2.22:** Simulated particle gasification conversions  $X_{\text{het,part}}$  and effectiveness factors  $\eta$  at constant gas condition and various constant particle diameters  $d_{\text{part}}$  based on the heterogeneous gasification kinetics of Kreitzberg et al. [156] and Schneider et al. [277]: only the Boudouard reaction (top), only the water-gas reaction (centre) and Boudouard reaction and water-gas reaction (bottom).

## 3 Simulation and evaluation methods

This chapter summarises the simulation and evaluation methods applied for the CFD simulations of the REGA experiments. The set-ups of the CFD simulations including the sub-models and solver settings are presented in Section 3.1. The experimental and numerical data used for comparison with the CFD predictions are introduced in Sections 3.2 and 3.3. The approaches to determine recirculation strengths, recirculation lengths, relative deviations, absolute relative deviations, cumulative mass flow rates and solid conversions are described in Sections 3.4, 3.5, 3.6 and 3.7.

### 3.1 Settings

The overall models for the atmospheric entrained flow gasification of ethylene glycol and of mixtures of ethylene glycol and wood char were compiled using the models presented in Chapter 2 and implemented using the software ANSYS Fluent [17] and user-defined functions (DEFINE macros). The main sub-models of the baseline overall models are summarised in Table 3.1. The reaction mechanism of the baseline overall models was thus either the DLR2017/RM mechanism or the HVI1 mechanism. The DLR2017/RM mechanism was applied to predict reasonable flame temperatures, whereas the HVI1 mechanism was used to enable fast computing times and fair comparisons with previous numerical predictions [63, 64, 187] that were obtained using the HVI1 mechanism only. In this sense, previous assumptions for the wall boundary conditions including wall temperature  $T_{\text{wall}}$ , wall thermal conductivity  $\lambda_{\text{wall}}$  and wall emissivity  $\varepsilon_{\text{wall}}$  have also not been modified (see Sections 2.2.3.3 and 2.5.4); minor changes are left for future works.

The DEFINE macros used in this work are given in Table 3.2. Compared to preceding works [63, 64, 187] (see Section 1.5), the implementations have been improved and extended. For example, the macro DEFINE\_WSGGM\_ABS\_COEFF has been proven erroneous for non-grey gases and was therefore replaced by the macro DEFINE\_GRAY\_BAND\_ABS\_COEFF.

**Table 3.1:** Baseline sub-models used for the CFD simulations.

Property	Model	Section
Turbulence	SST $k-\omega$ model	2.2.2.5
Turbulence-chemistry interaction	EDC model	2.4
Drag coefficient	Morsi-Alexander equation	2.2.5.1
Homogeneous reaction kinetics	HV11 mechanism or DLR2017/RM mechanism	2.3
Thermal radiation	Discrete ordinates model	2.5.1
Gas absorption/emission properties	Grey-gas model	2.5.2
Droplet absorption/emission properties	Diameter polynomial	2.5.2
Droplet scattering properties	None	2.5.3
Solid particle absorption/emission properties	Constant	2.5.2
Solid particle scattering properties	Isotropic and constant	2.5.3
Ethylene glycol injection properties	Mainly measurement based distributions	2.2.4.4
Solid particle injection properties	Assumed and measurement based distributions	2.2.4.5
Vaporisation	Classical model	2.6.1
Devolatilisation kinetics	Arrhenius law model of Dammann et al.	2.7.4.3
Devolatilisation morphology changes	Constant particle diameter	2.7.3
Devolatilisation products	Equilibrium composition at 1473.15 K	2.7.4.5
Heterogeneous gasification kinetics	Langmuir-Hinshelwood kinetics of Kreitzberg et al.	2.7.5.4
Heterogeneous gasification morphology changes	Constant particle diameter	2.7.3

**Table 3.2:** User-defined functions used for the CFD simulations.

Property	Macro
Miscellaneous	DEFINE_ADJUST
Method to supply infiltrated air and purge nitrogen	DEFINE_ON_DEMAND and DEFINE_SOURCE
Particle vapour pressure	DEFINE_DPM_PROPERTY
Particle density	DEFINE_DPM_PROPERTY
Particle heat capacity and enthalpy	DEFINE_DPM_PROPERTY
Particle diffusion coefficient	DEFINE_DPM_PROPERTY
Particle emissivity	DEFINE_DPM_PROPERTY
Miscellaneous	DEFINE_DPM_SCALAR_UPDATE
Miscellaneous	DEFINE_DPM_OUTPUT
Particle vaporisation	DEFINE_ON_DEMAND and DEFINE_DPM_HEAT_MASS
Particle decomposition	DEFINE_DPM_HEAT_MASS
Particle time step	DEFINE_DPM_TIMESTEP
Miscellaneous	DEFINE_DPM_SCALAR_UPDATE
Particle source	DEFINE_DPM_SOURCE
Particle devolatilisation	DEFINE_DPM_LAW
Particle surface reaction	DEFINE_DPM_LAW
Particle surface reaction rates	DEFINE_PR_RATE
Scattering phase function	DEFINE_SCAT_PHASE_FUNC
Grey-gas absorption coefficient based on WSGG model and mean beam length model	DEFINE_WSGGM_ABS_COEFF
Non-grey-gas absorption coefficients based on WSGG model	DEFINE_GRAY_BAND_ABS_COEFF
Non-grey-gas weight factors based on WSGG model	DEFINE_EMISSIVITY_WEIGHTING_FACTOR

Furthermore, new two-dimensional axis-symmetrical unstructured meshes with approximately  $2 \cdot 10^5$  cells were generated using ANSYS Meshing [18] for the numerical solution of the gas transport equations with the finite volume method. Compared to the preceding works [63, 64, 187], the number of cells was significantly increased inside and outside the flame to close the elemental and energy balances (see Section 1.5). The SIMPLEC algorithm [79] was used for the coupling of gas pressure and gas velocity while spatial discretisations were incorporated using the schemes given in Table 3.3. Multi-grid methods and linear equation solvers were applied using the default settings in ANSYS Fluent [17] while under-relaxation was used corresponding to Table 3.4. Specifically, slight under-

relaxation was applied for the species balance and energy equations in order to improve the numerical stability of some CFD simulations.

**Table 3.3:** Spatial discretisation schemes used for the CFD simulations.

Equation	Scheme
Pressure	PRESTO!
Momentum	Second-order upwind
Energy	Second-order upwind
Species balance	Second-order upwind
Turbulent kinetic energy	First-order upwind
Turbulent dissipation rate	First-order upwind
Radiation intensity	First-order upwind

**Table 3.4:** Under-relaxation factors used for the CFD simulations.

Equation	Under-relaxation factor
Pressure	0.2
Momentum	0.5
Density	1
Body forces	1
Energy	0.98 or 1
Species	0.98 or 1
Turbulent kinetic energy	0.7
Turbulent dissipation rate (standard $k$ - $\epsilon$ model)	0.7
Turbulent dissipation rate (SST $k$ - $\omega$ model)	0.8
Turbulent viscosity	1
Radiation intensity	1

## 3.2 Experimental data for comparison

The experimental data of Fleck et al. [63, 64, 98, 99, 100, 113, 114] from REGA experiments with ethylene glycol and from REGA experiments with mixtures of ethylene glycol and wood char (see Tables 1.1, B.1, B.2 and B.3) is used for the validation of the numerical predictions. The data originates from both intrusive and laser-based measurements and includes radial profiles of gas temperatures and dry gas species volume fractions ( $\text{CH}_4$ ,  $\text{CO}$ ,  $\text{CO}_2$ ,  $\text{H}_2$ ) at two nozzle distances (300 mm and 680 mm), axial droplet velocities, OH-LIF images and particle carbon conversions. Most of the data is tabulated in Section D.2. The

methods that were applied to obtain this data are briefly described in Section A.2, while detailed information can be found elsewhere [98, 100, 114].

### 3.3 Numerical data for comparison

The numerical predictions of the preceding works [63, 64, 187] are used for comparison with the numerical results obtained in this work. However, it should be emphasised (i) that previous overall models differ from each other and from the models used in this work and (ii) that previous inlet boundary conditions are not entirely consistent with the inlet boundary conditions applied in this work<sup>1</sup>. For example, this work typically applied the DLR2017/RM mechanism and a film factor  $f_{\text{film}} = 1/3$  while the preceding works [63, 64, 187] used the HVI1 mechanism and a film factor  $f_{\text{film}} = 1$ .

### 3.4 Recirculation strengths and lengths

Recirculation strengths and lengths were calculated using different approaches compared to the preceding work [187]. The recirculation strength was determined as the gas mass flow rate through an annular reactor cross-section. The inner radius of this cross-section was defined by the centre of the two-dimensional cross-sectional recirculation zone with the maximum streamline function value. The recirculation length was calculated as minimum nozzle distance to the reactor cross-section with exclusively positive axial gas velocities.

### 3.5 Relative deviations

Relative deviations were used to compare the predicted and measured profiles of gas temperature and gas species concentrations. The relative deviations  $RD_T$ ,  $RD_{\text{CH}_4}$ ,  $RD_{\text{CO}}$ ,  $RD_{\text{CO}_2}$  and  $RD_{\text{H}_2}$  are defined by

$$RD_T = \frac{1}{\sum_i i} \sum_i \frac{T_{\text{gas}}|_{\text{CFD},i} - T_{\text{gas}}|_{\text{TB},i}}{T_{\text{gas}}|_{\text{TB},i}}, \quad (3.1)$$

$$RD_{\text{CH}_4} = \frac{1}{\sum_i i} \sum_i \frac{r_{\text{CH}_4, \text{dry gas}}|_{\text{CFD},i} - r_{\text{CH}_4, \text{dry gas}}|_{\text{ABB},i}}{r_{\text{CH}_4, \text{dry gas}}|_{\text{ABB},i}}, \quad (3.2)$$

<sup>1</sup>The focus of the preceding works [63, 187] was on the REGA experiment TUC3 V479 which differs from the REGA experiment TUC3 V786 in the amount of infiltrated air (see Tables 1.1, B.1, B.2 and B.3). In this work, CFD simulations of both REGA experiments were performed to obtain quantitative comparisons. The results shown in Figs. J.1 and J.2 demonstrate only minor differences in the far-flame predictions. Therefore, CFD predictions are focussed on the REGA experiment TUC3 V786 in this work.

$$RD_{CO} = \frac{1}{\sum_i i} \sum_i \frac{r_{CO,dry\ gas}|_{CFD,i} - r_{CO,dry\ gas}|_{ABB,i}}{r_{CO,dry\ gas}|_{ABB,i}}, \quad (3.3)$$

$$RD_{CO_2} = \frac{1}{\sum_i i} \sum_i \frac{r_{CO_2,dry\ gas}|_{CFD,i} - r_{CO_2,dry\ gas}|_{ABB,i}}{r_{CO_2,dry\ gas}|_{ABB,i}}, \quad (3.4)$$

$$RD_{H_2} = \frac{1}{\sum_i i} \sum_i \frac{r_{H_2,dry\ gas}|_{CFD,i} - r_{H_2,dry\ gas}|_{ABB,i}}{r_{H_2,dry\ gas}|_{ABB,i}}, \quad (3.5)$$

where CFD refers to the CFD results, TB refers to the measurements of temperatures using double-bead type B thermocouples, ABB refers to the measurements of dry gas species volume fractions using standard gas analysers,  $T_{gas}$  is the gas temperature,  $r_{CH_4,dry\ gas}$  is the dry gas species volume fraction of methane,  $r_{CO,dry\ gas}$  is the dry gas species volume fraction of carbon monoxide,  $r_{CO_2,dry\ gas}$  is the dry gas species volume fraction of carbon dioxide and  $r_{H_2,dry\ gas}$  is the dry gas species volume fraction of hydrogen. Furthermore, absolute relative deviations ARD were determined using the relative deviations  $RD_T$ ,  $RD_{CO}$ ,  $RD_{CO_2}$  and  $RD_{H_2}$  and are defined by

$$ARD = \frac{1}{4} \left( |RD_T| + |RD_{CO}| + |RD_{CO_2}| + |RD_{H_2}| \right). \quad (3.6)$$

The relative deviation  $RD_{CH_4}$  is not accounted for in Eq. (3.6) as it is typically significantly larger than the other relative deviations and thereby affects the meaningfulness of the absolute relative deviation ARD.

### 3.6 Cumulative mass flow rates

Cumulative mass flow rates of vaporised ethylene glycol  $CMR_{C_2H_6O_2}$  were determined as function of the nozzle distance using integration of the source terms of ethylene glycol. The cumulative mass flow rate of vaporised ethylene glycol  $CMR_{C_2H_6O_2}$  is given by

$$CMR_{C_2H_6O_2}(z) = \int_A S_{w,part,C_2H_6O_2} dV, \quad (3.7)$$

where  $A$  is the set of all cell volumes with (centroid) nozzle distances  $0 \leq z' \leq z$ .

### 3.7 Solid conversions

Simulated solid devolatilisation conversions  $X_{dev,solid}$ , simulated solid gasification conversions  $X_{het,solid}$  and simulated solid carbon conversions  $X_{C,solid}$  were determined by

$$X_{\text{dev,solid}} = \frac{\sum_{i \in I} \dot{N}_{\text{part},i} (m_{\text{part,min,vap}} - m_{\text{part,dev}})}{\sum_{i \in I} \dot{N}_{\text{part},i} (m_{\text{part,min,vap}} - m_{\text{part,min,dev}})}, \quad (3.8)$$

$$X_{\text{het,solid}} = \frac{\sum_{i \in I} \dot{N}_{\text{part},i} (m_{\text{part,min,dev}} - m_{\text{part,het}})}{\sum_{i \in I} \dot{N}_{\text{part},i} (m_{\text{part,min,dev}} - m_{\text{part,min,het}})}, \quad (3.9)$$

$$X_{\text{C,solid}} = \frac{\sum_{i \in I} \dot{N}_{\text{part},i} (m_{\text{C,solid},0} - m_{\text{C,solid}})}{\sum_{i \in I} \dot{N}_{\text{part},i} m_{\text{C,solid},0}}, \quad (3.10)$$

where  $m_{\text{part,dev}}$  and  $m_{\text{part,het}}$  are auxiliary particle masses,  $I$  is the set of all parcels with  $w_{\text{vol,solid},0} \geq 0$  entering a gas cell and  $m_{\text{C,solid},0}$  is the initial carbon mass of the solid phase and  $m_{\text{C,solid}}$  is the carbon mass in the solid phase. The auxiliary particle masses  $m_{\text{part,dev}}$  and  $m_{\text{part,het}}$  are given by

$$m_{\text{part,dev}} = \min(m_{\text{part,min,vap}}, \max(m_{\text{part}}, m_{\text{part,min,dev}})), \quad (3.11)$$

$$m_{\text{part,het}} = \min(m_{\text{part,min,dev}}, \max(m_{\text{part}}, m_{\text{part,min,het}})). \quad (3.12)$$

For comparison with balanced data, simulated solid devolatilisation conversions  $X_{\text{dev,solid}}$ , simulated solid gasification conversions  $X_{\text{het,solid}}$  and simulated solid carbon conversions  $X_{\text{C,solid}}$  at the reactor axis and a nozzle distance of 680 mm are required. However, the simulated data along the reactor axis strongly scatters due to the particle dispersion model. Therefore, face-averaged values at the nozzle distance of 680 mm were determined using a cross-section with a radius of 20 mm.



## 4 Results

This chapter presents the results of the CFD simulations of the REGA experiments with ethylene glycol (TUC3 V786, TUC5 V1105 and TUC5 V1374) and the REGA experiments with mixtures of ethylene glycol and wood char (TUC5 GHKS10 V1071 and TUC5 GHKS30 V1284). The preceding works [63, 64, 101, 102, 187] already provided comparisons of far-flame predictions of gas temperatures and gas species concentrations with experimental observations. Furthermore, predictions of reaction, recirculation and vaporisation zones were extensively discussed for the REGA experiments TUC3 V479 [187] and TUC3 V786 [101, 102]. However, flame predictions are strongly affected by inlet conditions, injection properties, turbulence-chemistry interactions and homogeneous reaction kinetics. Furthermore, previous CFD simulations of the REGA experiments TUC5 GHKS10 V1071 and TUC5 GHKS30 V1284 were affected by elemental imbalances [64] or were based on assumed wood char kinetics [101, 102]. Therefore, new baseline CFD simulations were carried out for both the REGA experiments with ethylene glycol and the REGA experiments with mixtures of ethylene glycol and wood char. Subsequently, sensitivity analyses were performed considering the impact of the homogeneous reaction kinetics, the vaporisation model, the turbulence model, the thermal gas radiation property model, the inlet conditions, the injection properties and the wood char kinetics.

Sections 4.1, 4.2, 4.3 and 4.4 focus on the flame shapes, the recirculation zones, the droplet dispersions and the droplet velocities of the baseline predictions. Sections 4.5 and 4.6 describe the effects of various homogeneous reaction kinetics and of the mass transfer of ethylene glycol into the gas phase. Then, Sections 4.7 and 4.8 show the sensitivities of the turbulence model and the thermal gas radiation property model. Finally, Sections 4.9 and 4.10 demonstrate the effects of the injection properties and the wood char kinetics.

### 4.1 Flame shapes

The gas temperature distributions obtained in this work and the preceding works [63, 64, 187] are compared for the REGA experiment TUC3 V479/V786 in Fig. 4.1 and for the REGA experiment TUC5 V1105 in Fig. 4.2. First of all, it needs to be recalled (see Section 2.2.4.3) that OH-LIF measurements [113, 114] have indicated a V-shaped flame for

the REGA experiments TUC3 V479 and TUC3 V786 and a W-shaped flame for the REGA experiment TUC5 V1105. Such flames were reproduced in this work, whereas W-shaped flames were predicted in the preceding works [63, 64, 187]. Thus, the new approach for the inlet conditions and injection properties considerably improved the mathematical description of the flame zone.

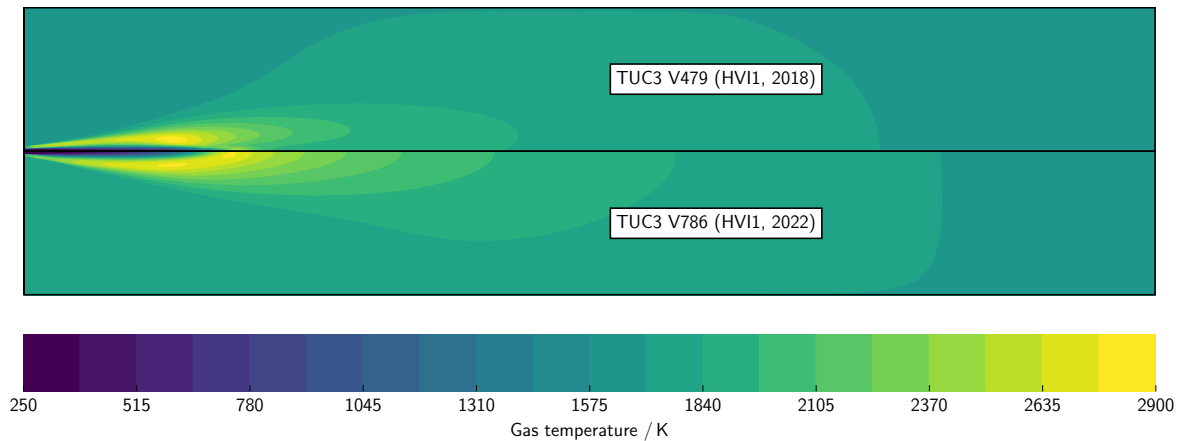


**Figure 4.1:** Predicted gas temperature distributions. TUC3 V479 (HVI1, 2018): results for the REGA experiment TUC3 V479 obtained using the HVI1 mechanism in the preceding work [187]; TUC3 V786 (HVI1, 2022): results for the REGA experiment TUC3 V786 obtained using the HVI1 mechanism in this work.

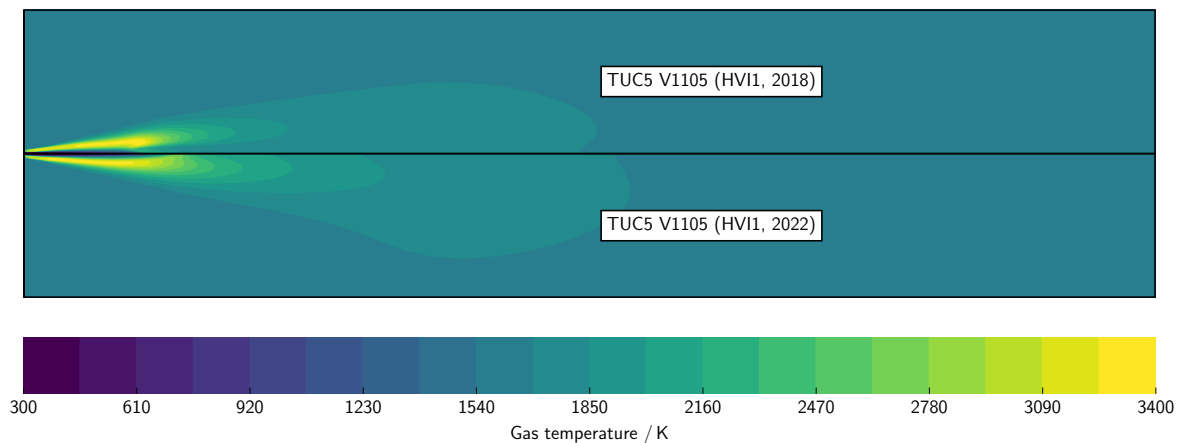


**Figure 4.2:** Predicted gas temperature distributions. TUC5 V1105 (HVI1, 2018): results for the REGA experiment TUC5 V1105 obtained using the HVI1 mechanism in the preceding work [63]; TUC5 V1105 (HVI1, 2022): results for the REGA experiment TUC5 V1105 obtained using the HVI1 mechanism in this work.

Furthermore, in the near-axis region, the improved inlet conditions and injection properties reduced the impact of the endothermic vaporisation and decomposition processes (see Section 2.2.4.3) and prevented strong changes of flame temperatures and concentrations compared to the preceding works [63, 187]. However, the predicted cold core zones in the near-axis region are still significantly longer than observed in OH-LIF measurements [113,

114] and LES predictions of the REGA experiment TUC3 [88, 89]. Thus, the mixing of gasification medium and recirculating gas is slower in the RANS based simulations using the common turbulence and turbulence-chemistry interaction approaches. Compared to the preceding works [63, 187], the cold zones are slightly longer due to the missing angle of attack. Future works may improve the mathematical description of the turbulence and turbulence-chemistry interaction approaches.

The maximum gas temperatures are given in Table 4.1. Similar maximum gas temperature were accordingly obtained in this work and the preceding works [63, 187]. Thus, the strong changes of the inlet conditions and the injection properties only slightly affected the predictions. The maximum gas temperatures have rather been determined by the rates of the gas phase reactions (see Section 4.5).

**Table 4.1:** Predicted maximum gas temperatures  $T_{\text{gas,max}}$  for the REGA experiments TUC3 V479, TUC3 V786 and TUC5 V1105: comparison of results from the preceding works [63, 187] and this work. Compared to the preceding work [187], deviating data is given for the REGA experiment TUC3 V479 due to the use of different evaluation methods.

REGA experiment	$T_{\text{gas,max}} / \text{K}$	
	Previous work	This work
TUC3 V479	2853	2815
TUC3 V786	–	2786
TUC5 V1105	3355	3305

## 4.2 Recirculation zones

The changes of the inlet conditions were accompanied by changes of the supply of infiltrated air and purge nitrogen. In the preceding works [63, 187], infiltrated air and purge nitrogen were fed through the inner duct of the external mixing nozzle leading to increased gas and droplet velocities in the near-nozzle region. The impact of the changes on the recirculation zones is shown in Table 4.2 and in Figs. 4.3 and 4.4. For the REGA experiment TUC3 V479, both the strength and the length of the recirculation zone are reduced by approximately 10 % when less gas is fed through the nozzle. For the REGA experiment TUC5 V1105, the strength of the recirculation zone has changed similarly despite less air infiltration and no supply of purge nitrogen, whereas the length of the recirculation zone has slightly increased. Furthermore, the new method for the supply of infiltrated air and purge nitrogen did not decrease the numerical stability or increased the computing time and is therefore recommended for future works.

**Table 4.2:** Predicted strengths and lengths of the recirculation zones for the REGA experiments TUC3 V479, TUC3 V786 and TUC5 V1105: comparison of results from the preceding works [63, 187] and this work. Compared to the preceding work [187], deviating data is given for the REGA experiment TUC3 V479 due to the use of different evaluation methods.

REGA experiment	Strength / kg/h		Length / mm	
	Previous work	This work	Previous work	This work
TUC3 V479	91	81	841	791
TUC3 V786	–	81	–	787
TUC5 V1105	95	79	772	797

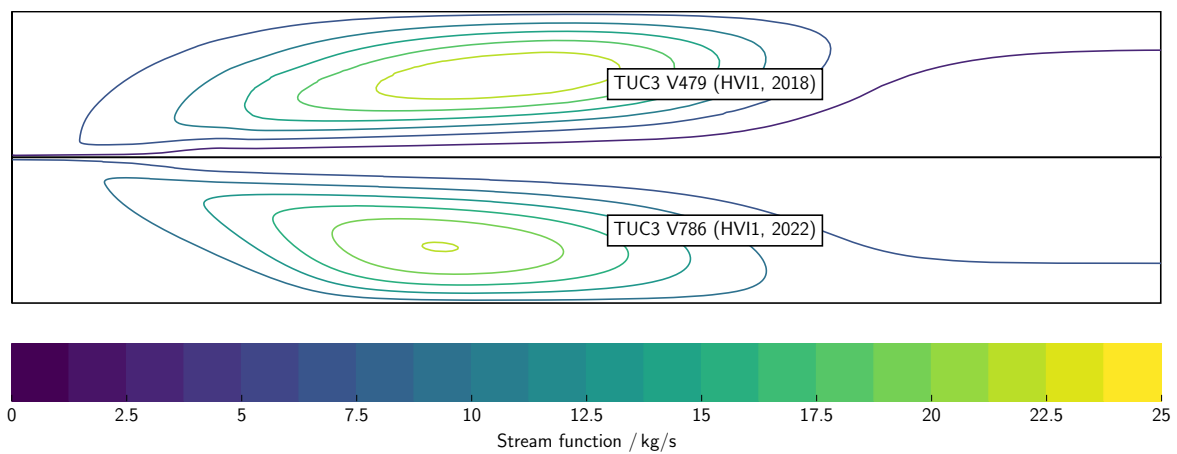


**Figure 4.3:** Predicted stream function distributions. TUC3 V479 (HVI1, 2018): results for the REGA experiment TUC3 V479 obtained using the HVI1 mechanism in the preceding work [187]; TUC3 V786 (HVI1, 2022): results for the REGA experiment TUC3 V786 obtained using the HVI1 mechanism in this work.

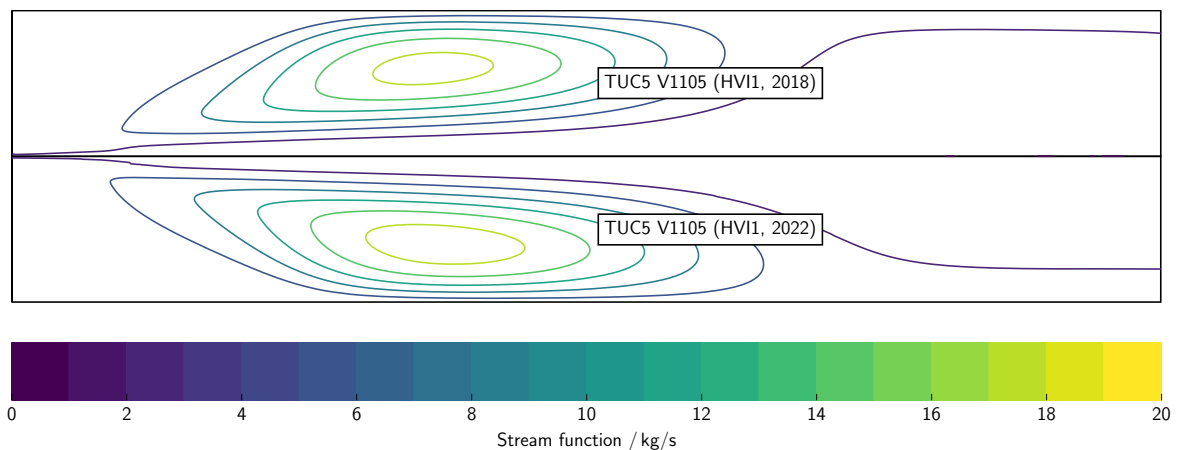


**Figure 4.4:** Predicted stream function distributions. TUC5 V1105 (HVI1, 2018): results for the REGA experiment TUC5 V1105 obtained using the HVI1 mechanism in the preceding work [63]; TUC5 V1105 (HVI1, 2022): results for the REGA experiment TUC5 V1105 obtained using the HVI1 mechanism in this work.

### 4.3 Droplet dispersions

The impact of the injection properties and the film factor  $f_{\text{film}}$  on the droplet dispersion is shown for the REGA experiment TUC3 V479/V786 in Figs. 4.5 and 4.7 and for the REGA experiment TUC5 V1105 in Figs. 4.6 and 4.8. The droplet dispersion accordingly narrows if the physical properties in the vaporisation model are determined using the gas condition ( $f_{\text{film}} = 1$ ) instead of the film condition ( $f_{\text{film}} = 1/3$ ) (see Figs. 4.7 and 4.8). Furthermore, the droplet dispersion reflects the spray angle at nozzle exit, specified by the initial droplet velocities, if the gas enters the domain through a cylindrical nozzle instead of an external mixing nozzle (see Figs. 4.5-4.8 and Section 2.2.4.3). Thus, inlet conditions, injection properties and film factor  $f_{\text{film}}$  strongly determine the droplet dispersion.

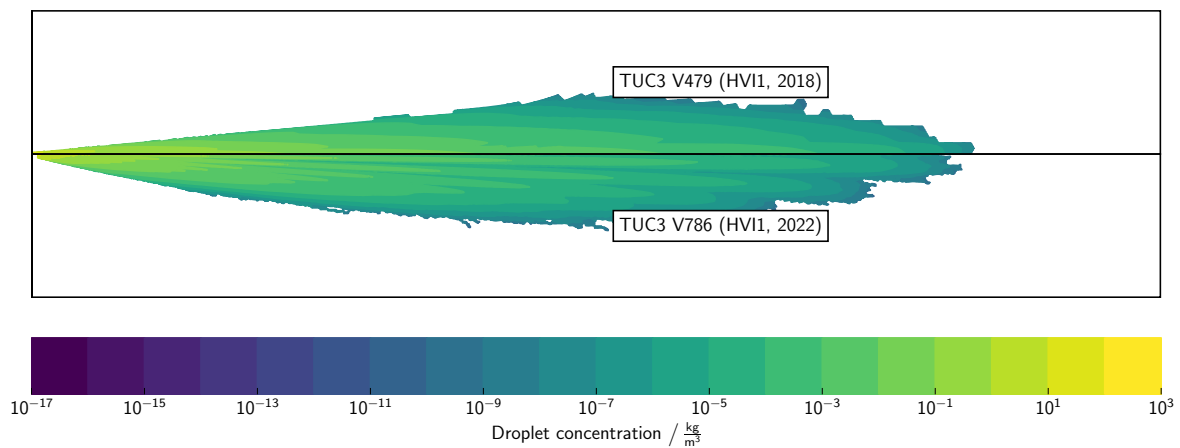


**Figure 4.5:** Predicted droplet concentration distributions. TUC3 V479 (HVI1, 2018): results for the REGA experiment TUC3 V479 obtained using the HVI1 mechanism and a film factor  $f_{\text{film}} = 1$  in the preceding work [187]; TUC3 V786 (HVI1, 2022): results for the REGA experiment TUC3 V786 obtained using the HVI1 mechanism and a film factor  $f_{\text{film}} = 1$  in this work.

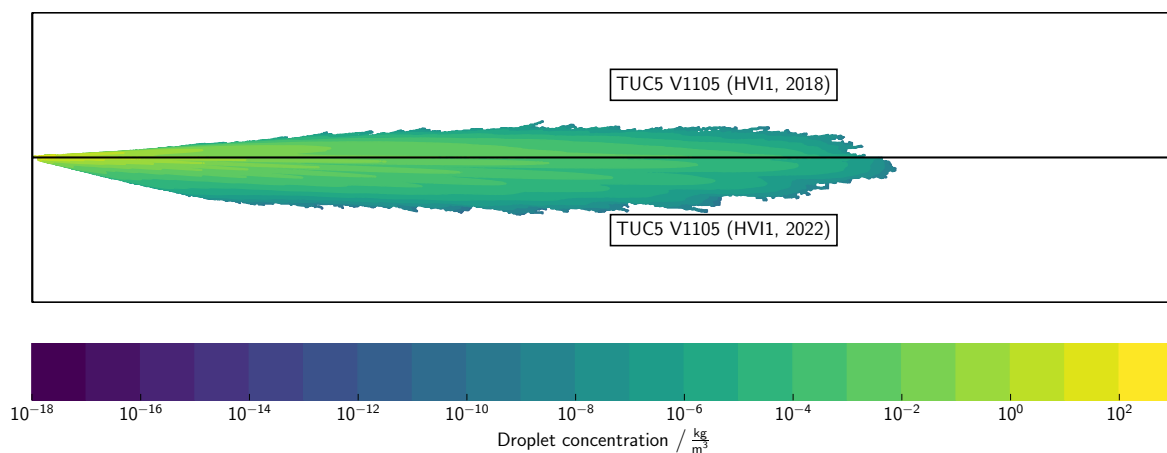


**Figure 4.6:** Predicted droplet concentration distributions. TUC5 V1105 (HVI1, 2018): results for the REGA experiment TUC5 V1105 obtained using the HVI1 mechanism and a film factor  $f_{\text{film}} = 1$  in the preceding work [63]; TUC5 V1105 (HVI1, 2022): results for the REGA experiment TUC5 V1105 obtained using the HVI1 mechanism and a film factor  $f_{\text{film}} = 1$  in this work.

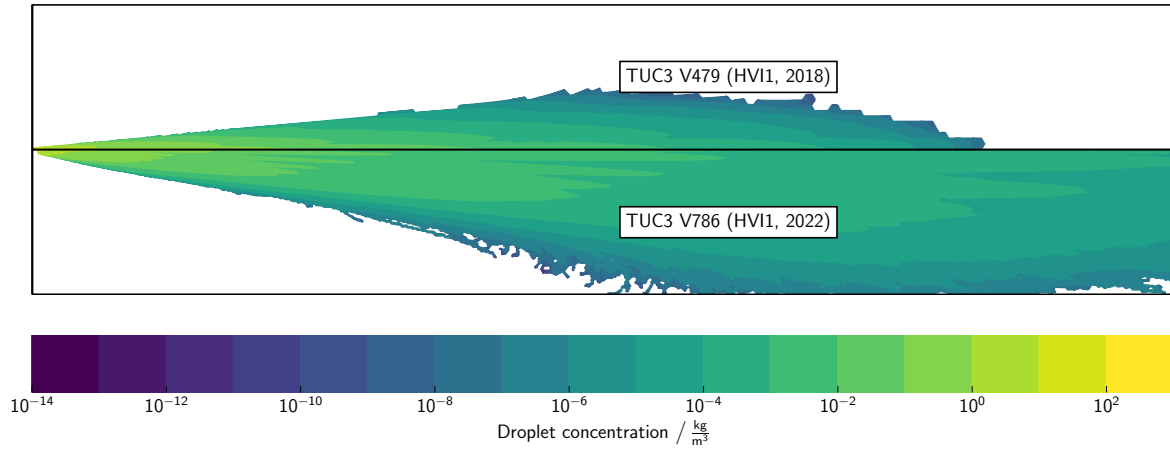


**Figure 4.7:** Predicted droplet concentration distributions. TUC3 V479 (HVI1, 2018): results for the REGA experiment TUC3 V479 obtained using the HVI1 mechanism and a film factor  $f_{\text{film}} = 1$  in the preceding work [187]; TUC3 V786 (HVI1, 2022): results for the REGA experiment TUC3 V786 obtained using the HVI1 mechanism and a film factor  $f_{\text{film}} = 1/3$  in this work.

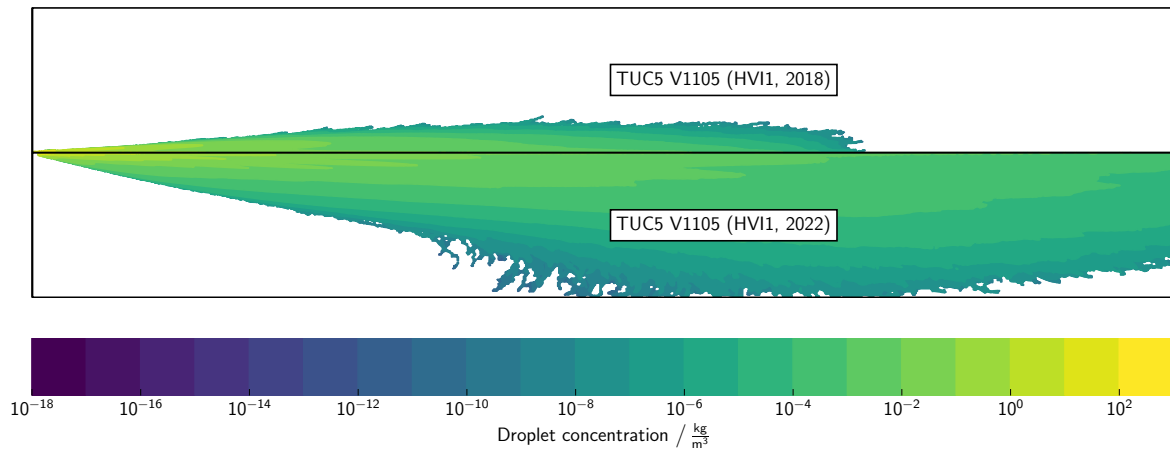


**Figure 4.8:** Predicted droplet concentration distributions. TUC5 V1105 (HVI1, 2018): results for the REGA experiment TUC5 V1105 obtained using the HVI1 mechanism and a film factor  $f_{\text{film}} = 1$  in the preceding work [187]; TUC5 V1105 (HVI1, 2022): results for the REGA experiment TUC5 V1105 obtained using the HVI1 mechanism and a film factor  $f_{\text{film}} = 1/3$  in this work.

In anemometry measurements, the droplet detection rates significantly reduce at larger nozzle distances [99]. This suggest that a film factor  $f_{\text{film}} = 1$  should be preferred over a film factor  $f_{\text{film}} = 1/3$ . However, the LES results for the REGA experiment TUC3 that were obtained using the 1/3 rule have shown that the vaporisation of ethylene glycol droplets mainly occurs in the centred area [88, 89] due to the strong instantaneous fluctuations in the flame zone. Furthermore, even the latest studies on vaporisation of single droplets (for example, see [301]) have indicated that the 1/3 rule is appropriate for simplified vaporisation predictions. Therefore, this work applied the 1/3 rule in the baseline CFD simulations and accepted that the simplified models for turbulence, turbulence dispersion and turbulence-chemistry interaction shift the vaporisation of the ethylene glycol droplets downwards, i. e.

away from the nozzle. Future large eddy simulations combined with the volume-of-fluid method or improved measurement devices may reduce this knowledge gap.

## 4.4 Droplet velocities

The predicted axial droplet velocities near the axis are compared with axial droplet velocities that were obtained using LDA measurements [98, 99] for the REGA experiment TUC3 V786 in Fig. 4.9 and for the REGA experiment TUC5 V1105 in Fig. 4.10. The predicted axial droplet velocities are accordingly in sufficient to good agreement with the measured values.

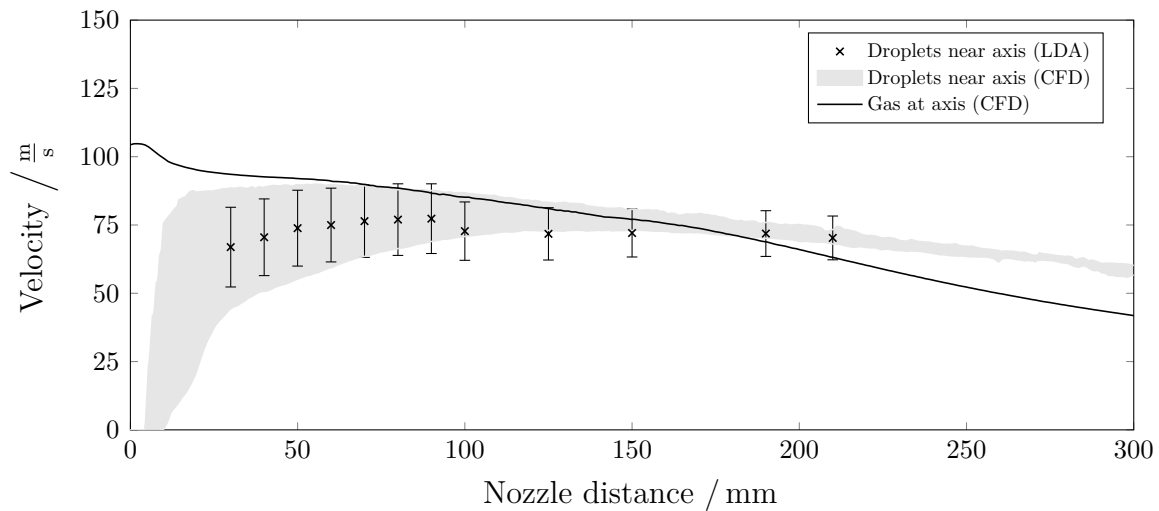


**Figure 4.9:** Measured axial droplet velocities, predicted axial droplet velocities and predicted axial gas velocities for the REGA experiment TUC3 V786.

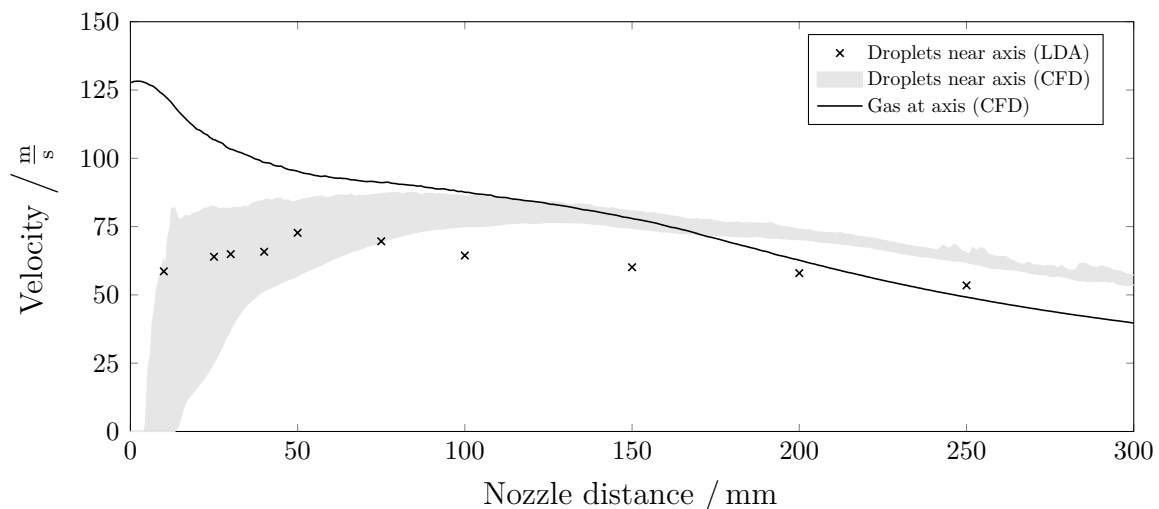


**Figure 4.10:** Measured axial droplet velocities, predicted axial droplet velocities and predicted axial gas velocities for the REGA experiment TUC5 V1105.

## 4.5 Homogeneous reaction kinetics

The results presented in Sections 4.1 and 4.2 were generated using the HVI1 mechanism. Additionally, the eJL mechanism, the eJL/A mechanism, the DLR2017/RK mechanism and the DLR2017/RM mechanism were applied in this work (see Section 2.3.1). The predicted gas temperature distributions are shown in Figs. 4.11-4.18. The maximum gas temperatures are listed in Table 4.3. As expected, the DLR2017/RM mechanism and the DLR2017/RK mechanism provide quite similar flame temperatures and lower flame temperatures than the HVI1 mechanism and the eJL mechanism. The flame temperatures based on the eJL/A mechanism are also significantly lower than flame temperatures based on the HVI1 mechanism or the eJL mechanism. This demonstrates the impact of single reaction rates in global reaction mechanisms.

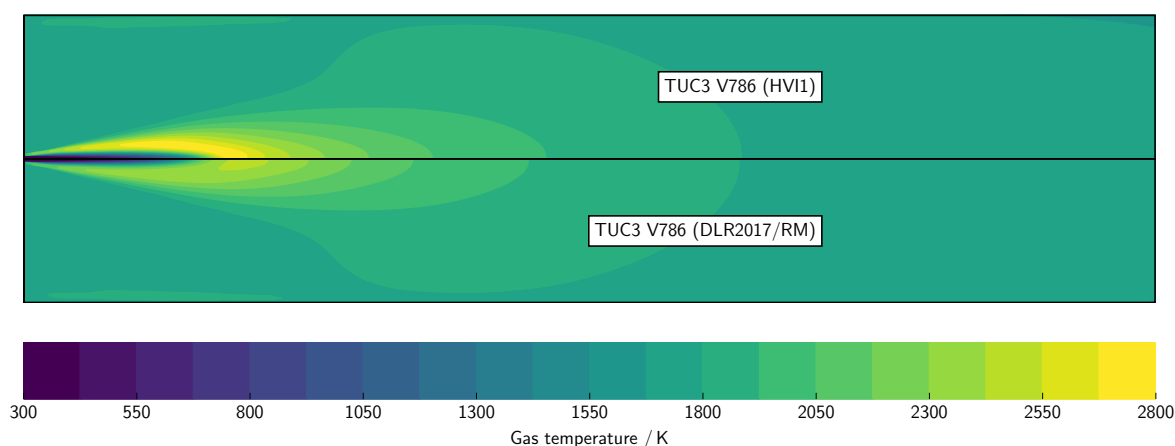


**Figure 4.11:** Predicted gas temperature distributions. TUC3 V786 (HVI1): results for the REGA experiment TUC3 V786 obtained using the HVI1 mechanism; TUC3 V786 (DLR2017/RM): results for the REGA experiment TUC3 V786 obtained using the DLR2017/RM mechanism.

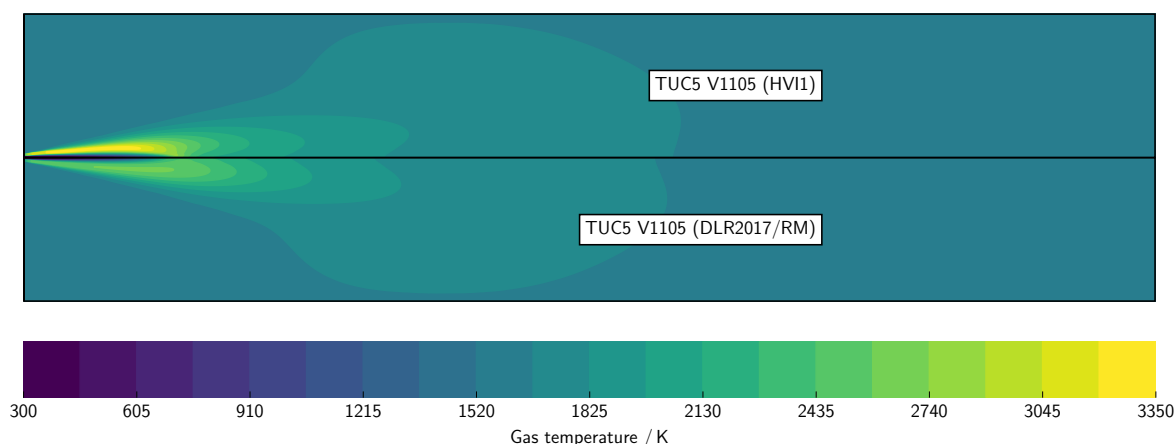


**Figure 4.12:** Predicted gas temperature distributions. TUC5 V1105 (HVI1): results for the REGA experiment TUC5 V1105 obtained using the HVI1 mechanism; TUC5 V1105 (DLR2017/RM): results for the REGA experiment TUC5 V1105 obtained using the DLR2017/RM mechanism.

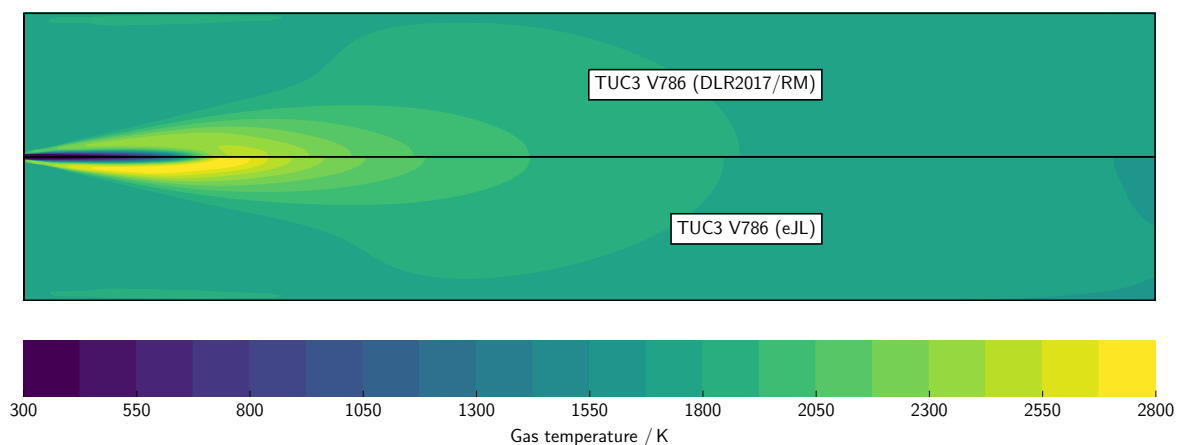


**Figure 4.13:** Predicted gas temperature distributions. TUC3 V786 (DLR2017/RM): results for the REGA experiment TUC3 V786 obtained using the DLR2017/RM mechanism; TUC3 V786 (eJL): results for the REGA experiment TUC3 V786 obtained using the eJL mechanism.

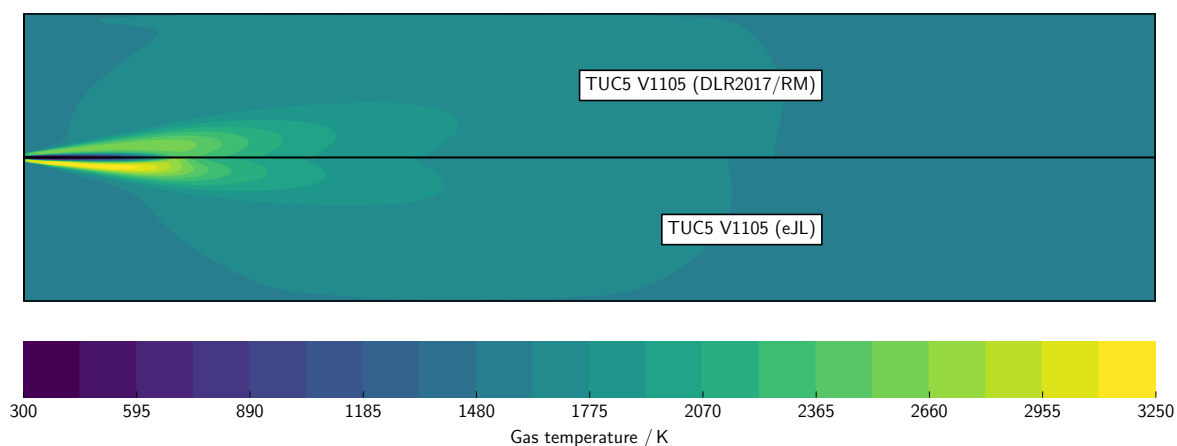


**Figure 4.14:** Predicted gas temperature distributions. TUC5 V1105 (DLR2017/RM): results for the REGA experiment TUC5 V1105 obtained using the DLR2017/RM mechanism; TUC5 V1105 (eJL): results for the REGA experiment TUC5 V1105 obtained using the eJL mechanism.

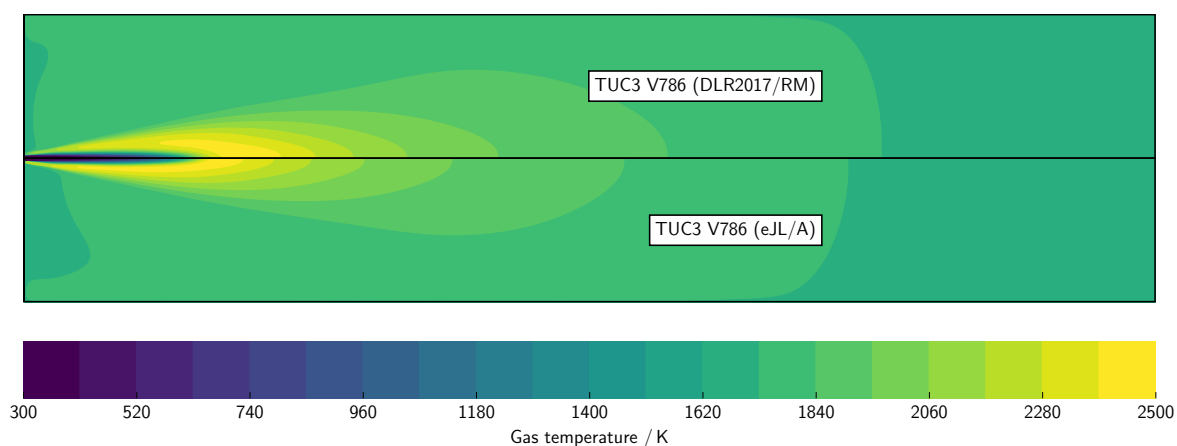


**Figure 4.15:** Predicted gas temperature distributions. TUC3 V786 (DLR2017/RM): results for the REGA experiment TUC3 V786 obtained using the DLR2017/RM mechanism; TUC3 V786 (eJL/A): results for the REGA experiment TUC3 V786 obtained using the eJL/A mechanism.

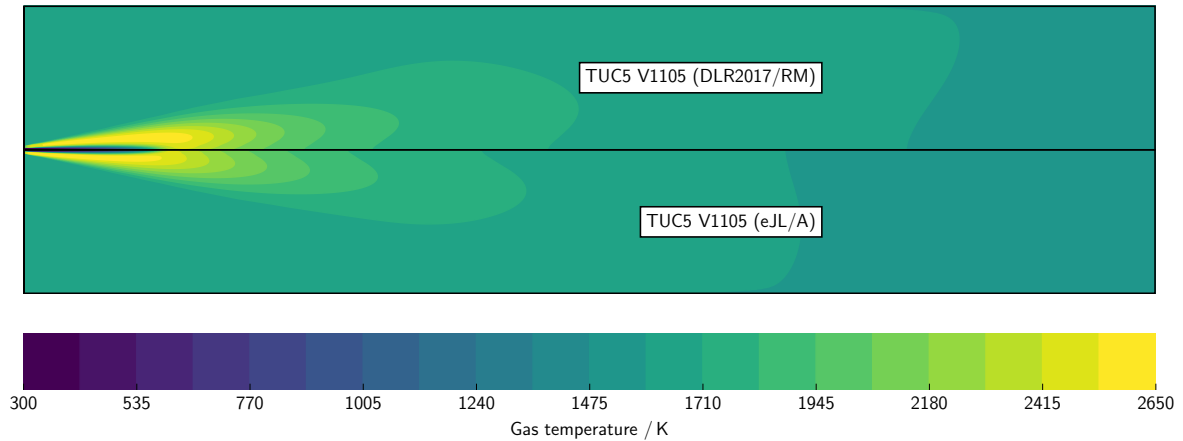


**Figure 4.16:** Predicted gas temperature distributions. TUC5 V1105 (DLR2017/RM): results for the REGA experiment TUC5 V1105 obtained using the DLR2017/RM mechanism; TUC5 V1105 (eJL/A): results for the REGA experiment TUC5 V1105 obtained using the eJL/A mechanism.

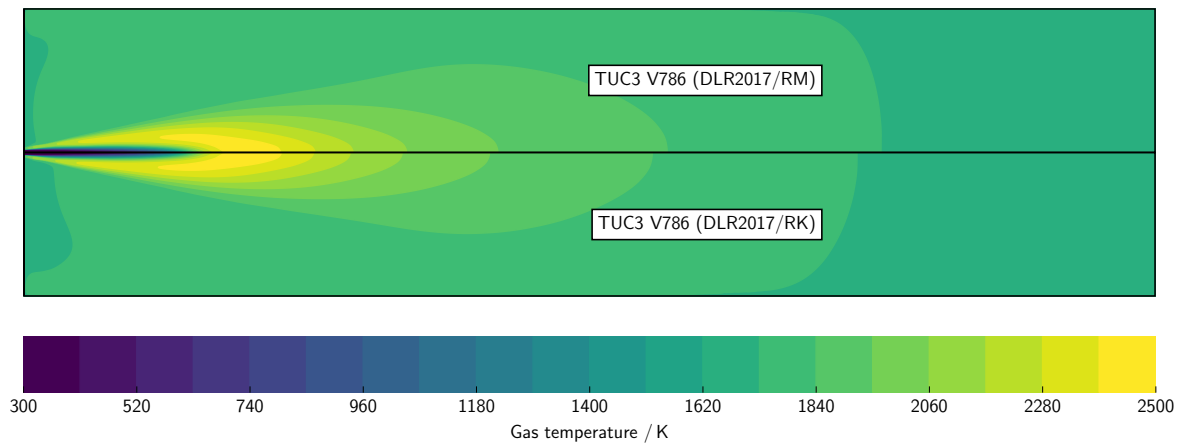


**Figure 4.17:** Predicted gas temperature distributions. TUC3 V786 (DLR2017/RM): results for the REGA experiment TUC3 V786 obtained using the DLR2017/RM mechanism; TUC3 V786 (DLR2017/RK): results for the REGA experiment TUC3 V786 obtained using the DLR2017/RK mechanism.

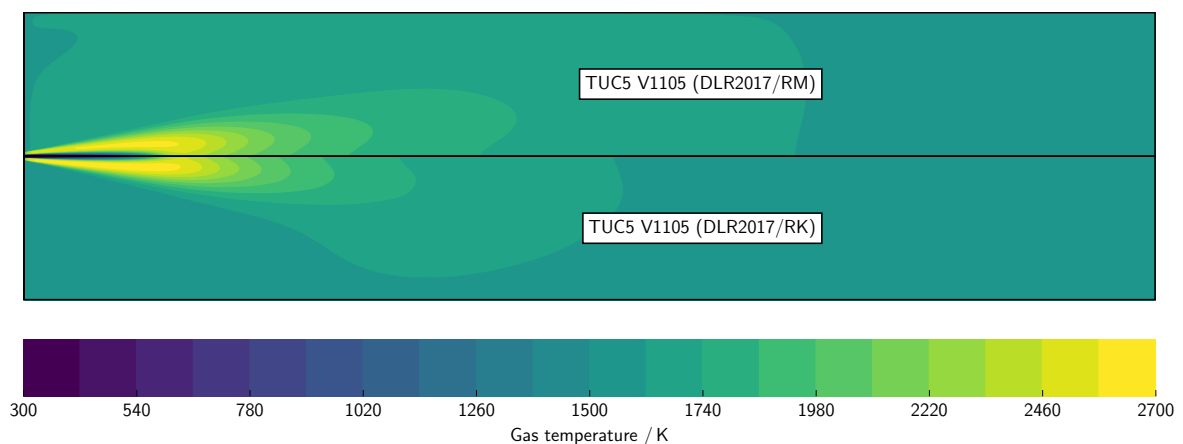


**Figure 4.18:** Predicted gas temperature distributions. TUC5 V1105 (DLR2017/RM): results for the REGA experiment TUC5 V1105 obtained using the DLR2017/RM mechanism; TUC5 V1105 (DLR2017/RK): results for the REGA experiment TUC5 V1105 obtained using the DLR2017/RK mechanism.

Furthermore, all reaction mechanisms have provided V-shaped flames for the REGA experiment TUC3 V786 and W-shaped flames for the REGA experiment TUC5 V1105. This demonstrates that the flame shape is less affected by the reaction mechanism while it is primarily determined by the injection properties, the turbulence-chemistry interaction and the droplet dispersion.

**Table 4.3:** Predicted maximum gas temperatures for the REGA experiments TUC3 V786 and TUC5 V1105: comparison of results based on various reaction mechanisms.

Reaction mechanism	$T_{\text{gas,max}} / \text{K}$	
	REGA TUC3 V786	REGA TUC5 V1105
HVI1	2786	3305
DLR2017/RM	2458	2604
eJL	2791	3207
eJL/A	2449	2642
DLR2017/RK	2462	2654

The predicted profiles of gas temperature and dry gas species concentrations at nozzle distances of 300 mm and at 680 mm are shown in Figs. 4.19-4.26 and are typically in good agreement with the measured profiles for carbon monoxide, carbon dioxide and hydrogen, while larger deviations are found for methane at both nozzle distances. This is also evident from the relative deviations given in Tables 4.4-4.7. The dry gas species concentrations of methane are typically underpredicted by the eJL mechanism and the eJL/A mechanism and significantly overpredicted by the HVI1 mechanism, the DLR2017/RM mechanism and the DLR2017/RK mechanism. Larger deviations are also found for carbon monoxide, carbon dioxide and hydrogen in the near-axis region at the nozzle distance of 300 mm due to effects of the mass transfer of ethylene glycol into the gas phase (see Section 4.6) and, in the case of global reaction mechanisms, due to simplified decomposition kinetics.

**Table 4.4:** Relative deviations  $RD_T$ ,  $RD_{\text{CH}_4}$ ,  $RD_{\text{CO}}$ ,  $RD_{\text{CO}_2}$  and  $RD_{\text{H}_2}$  concerning the profiles of gas temperature and dry gas species volume fractions and absolute relative deviations ARD at the nozzle distance of 300 mm for the REGA experiment TUC3 V786.

Reaction mechanism	$\frac{RD_T}{\%}$	$\frac{RD_{\text{CH}_4}}{\%}$	$\frac{RD_{\text{CO}}}{\%}$	$\frac{RD_{\text{CO}_2}}{\%}$	$\frac{RD_{\text{H}_2}}{\%}$	ARD
HVI1	12.91	509.52	-5.73	7.94	-22.49	12.27
DLR2017/RM	12.44	132.86	-0.47	2.83	-21.74	9.37
eJL	12.04	-78.78	2.46	0.47	-17.69	8.17
eJL/A	10.37	-100	2.45	3.79	-15.66	8.07
DLR2017/RK	12.04	99.52	1.60	0.47	-18.23	8.09

**Table 4.5:** Relative deviations  $RD_T$ ,  $RD_{CH_4}$ ,  $RD_{CO}$ ,  $RD_{CO_2}$  and  $RD_{H_2}$  concerning the profiles of gas temperature and dry gas species volume fractions and absolute relative deviations ARD at the nozzle distance of 680 mm for the REGA experiment TUC3 V786.

Reaction mechanism	$\frac{RD_T}{\%}$	$\frac{RD_{CH_4}}{\%}$	$\frac{RD_{CO}}{\%}$	$\frac{RD_{CO_2}}{\%}$	$\frac{RD_{H_2}}{\%}$	ARD %
HVI1	5.51	1271.70	-1.56	1.20	-9.06	4.33
DLR2017/RM	5.49	834.14	1.31	-1.73	-7.32	3.96
eJL	4.87	101.12	4.29	-5.02	-1.27	3.86
eJL/A	4.59	-100.00	5.29	-7.63	1.13	4.66
DLR2017/RK	4.94	776.19	2.95	4.18	-3.39	3.86

**Table 4.6:** Relative deviations  $RD_T$ ,  $RD_{CH_4}$ ,  $RD_{CO}$ ,  $RD_{CO_2}$  and  $RD_{H_2}$  concerning the profiles of gas temperature and dry gas species volume fractions and absolute relative deviations ARD at the nozzle distance of 300 mm for the REGA experiment TUC5 V1105.

Reaction mechanism	$\frac{RD_T}{\%}$	$\frac{RD_{CH_4}}{\%}$	$\frac{RD_{CO}}{\%}$	$\frac{RD_{CO_2}}{\%}$	$\frac{RD_{H_2}}{\%}$	ARD %
HVI1	4.92	142.43	0.09	6.50	-10.70	5.55
DLR2017/RM	1.76	99.15	1.90	5.21	-12.51	6.28
eJL	4.00	-79.67	5.03	-3.05	-3.84	3.98
eJL/A	4.28	-100.00	4.97	-4.00	-4.01	4.31
DLR2017/RK	5.49	116.31	6.76	-16.17	3.38	7.02

**Table 4.7:** Relative deviations  $RD_T$ ,  $RD_{CH_4}$ ,  $RD_{CO}$ ,  $RD_{CO_2}$  and  $RD_{H_2}$  concerning the profiles of gas temperature and dry gas species volume fractions and absolute relative deviations ARD at the nozzle distance of 680 mm for the REGA experiment TUC5 V1105.

Reaction mechanism	$\frac{RD_T}{\%}$	$\frac{RD_{CH_4}}{\%}$	$\frac{RD_{CO}}{\%}$	$\frac{RD_{CO_2}}{\%}$	$\frac{RD_{H_2}}{\%}$	ARD %
HVI1	0.45	156.45	0.56	0.86	-5.70	1.89
DLR2017/RM	0.34	154.72	0.95	0.30	-6.17	1.94
eJL	-0.90	-62.79	2.88	-6.63	3.66	3.52
eJL/A	-1.41	-99.89	3.41	-8.77	5.79	4.84
DLR2017/RK	-3.83	158.79	5.44	-21.19	9.32	9.94

Based on the absolute relative deviations in Tables 4.4-4.7, the best predictions are provided by the eJL/A mechanism, closely followed by the DLR2017/RM mechanism, the eJL mechanism, the HVI1 mechanism and the DLR2017/RK mechanism. Thus, under the same test conditions, both reduced and global reaction mechanisms provide accurate far-flame predictions for the gasification of ethylene glycol. However, due to the use of radicals, reduced mechanisms predict more reasonable flame temperatures than global mechanisms.

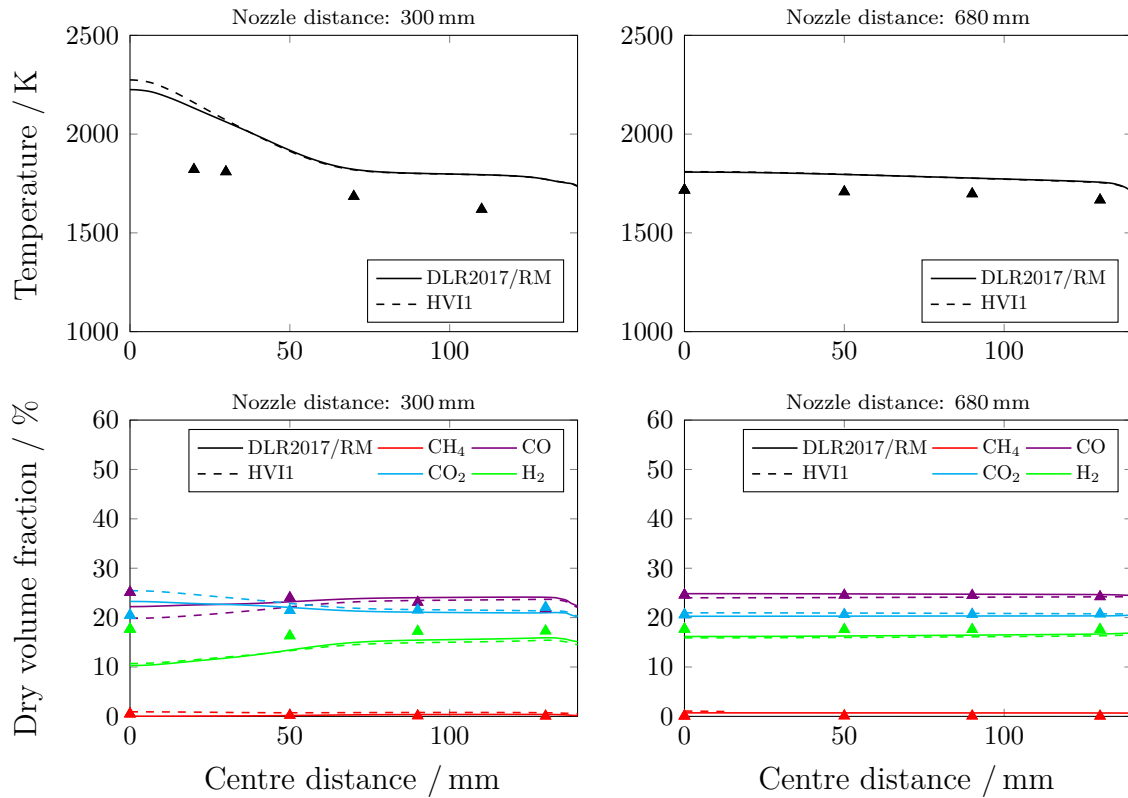


**Figure 4.19:** Predicted profiles of gas temperature and dry gas species volume fractions for the REGA experiment TUC3 V786 in comparison with measured profiles. DLR2017/RM: results obtained using the DLR2017/RM mechanism; HVI1: results obtained using the HVI1 mechanism.

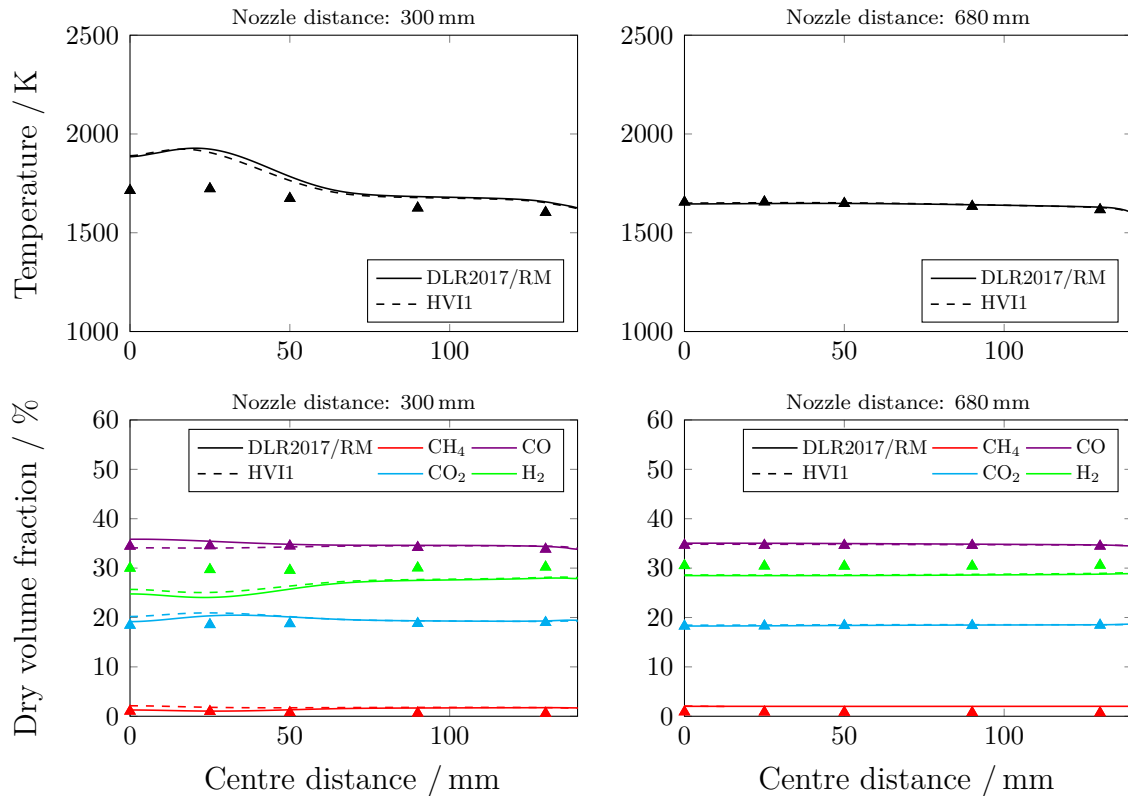


**Figure 4.20:** Predicted profiles of gas temperature and dry gas species volume fractions for the REGA experiment TUC5 V1105 in comparison with measured profiles. DLR2017/RM: results obtained using the DLR2017/RM mechanism; HVI1: results obtained using the HVI1 mechanism.

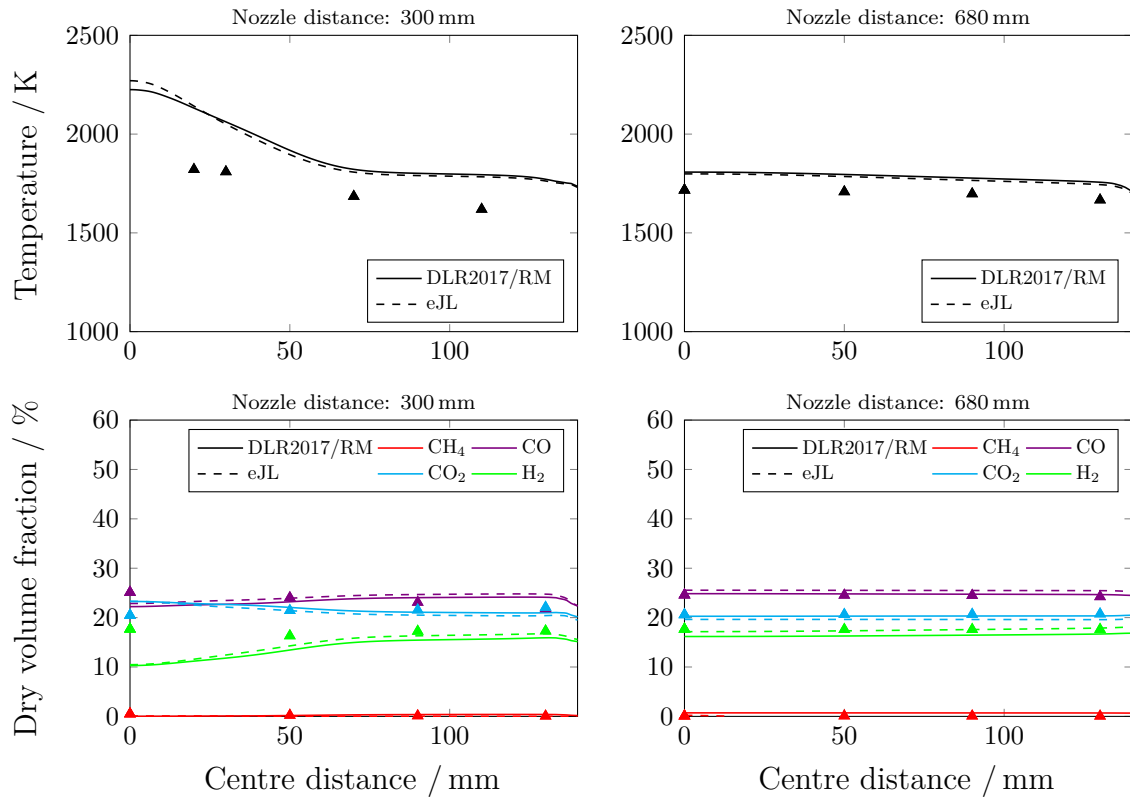


**Figure 4.21:** Predicted profiles of gas temperature and dry gas species volume fractions for the REGA experiment TUC3 V786 in comparison with measured profiles. DLR2017/RM: results obtained using the DLR2017/RM mechanism; eJL: results obtained using the eJL mechanism.

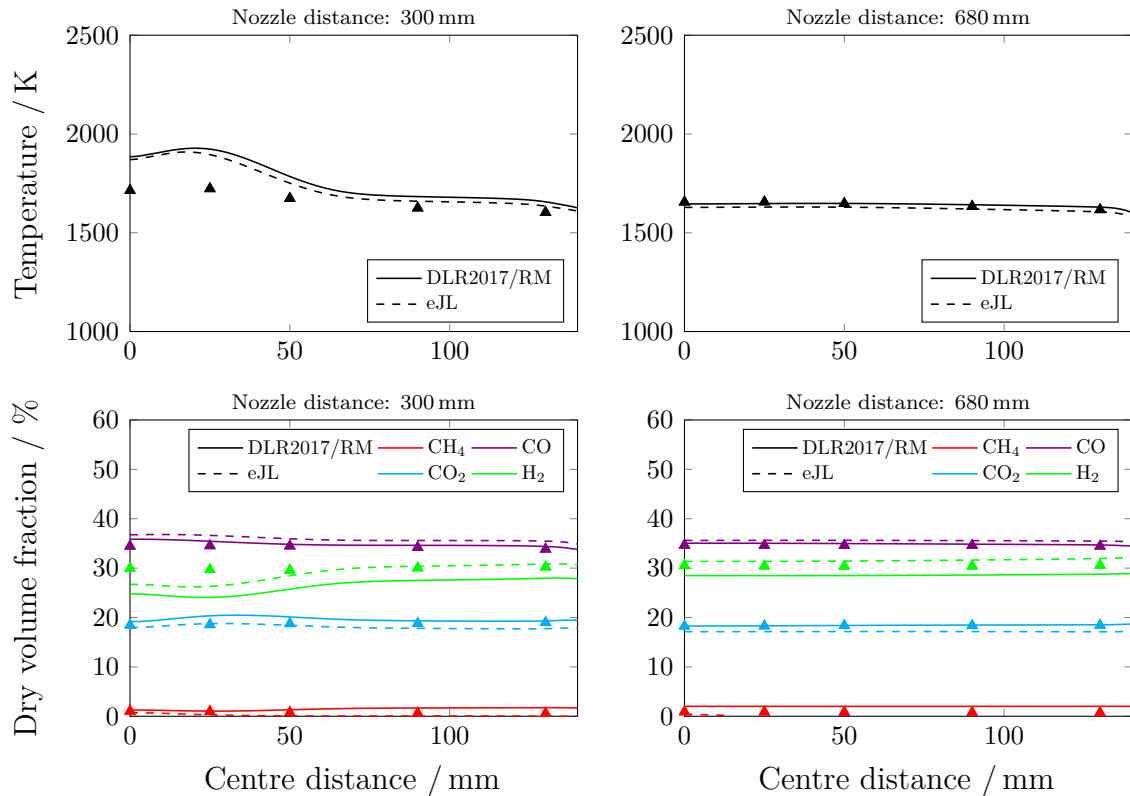


**Figure 4.22:** Predicted profiles of gas temperature and dry gas species volume fractions for the REGA experiment TUC5 V1105 in comparison with measured profiles. DLR2017/RM: results obtained using the DLR2017/RM mechanism; eJL: results obtained using the eJL mechanism.

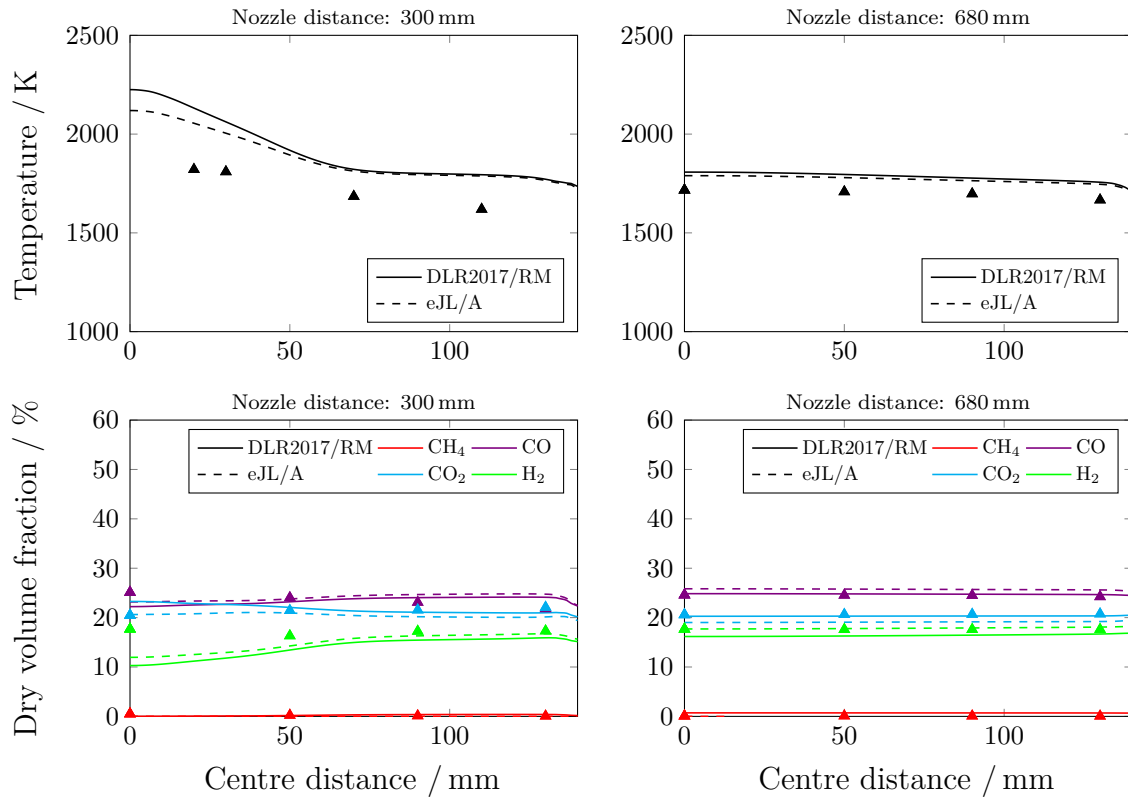


**Figure 4.23:** Predicted profiles of gas temperature and dry gas species volume fractions for the REGA experiment TUC3 V786 in comparison with measured profiles. DLR2017/RM: results obtained using the DLR2017/RM mechanism; eJL/A: results obtained using the eJL/A mechanism.

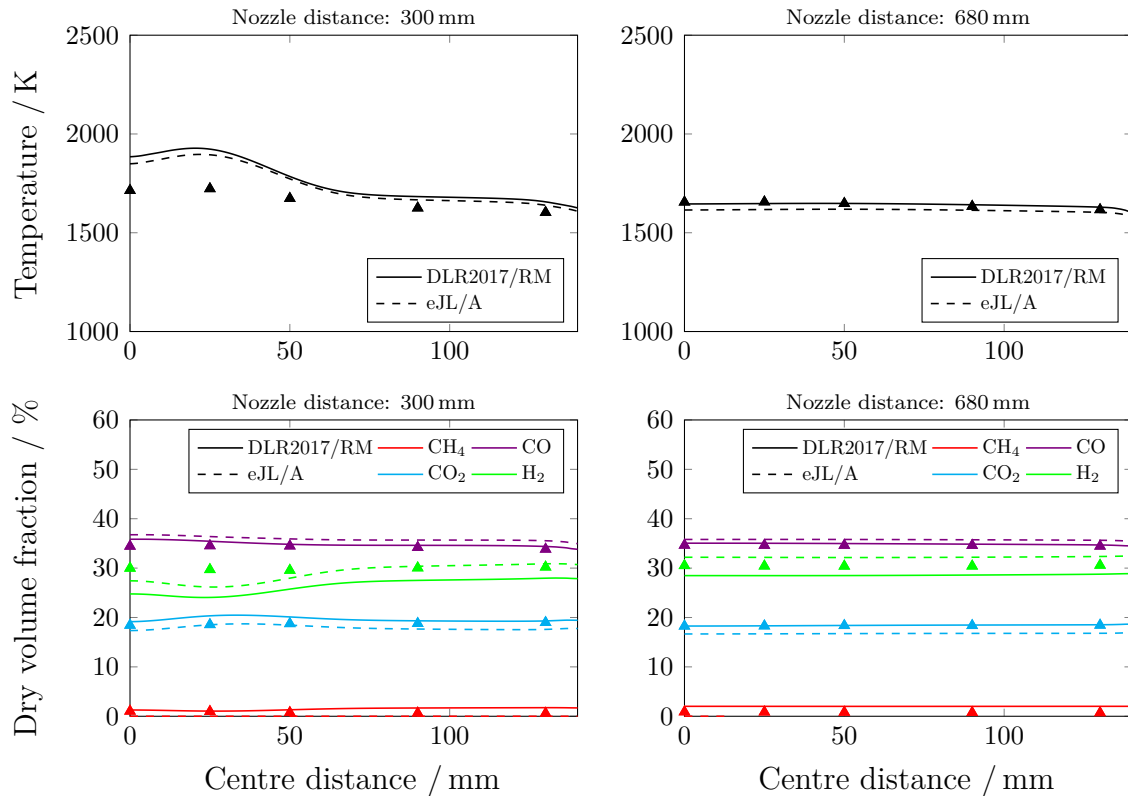


**Figure 4.24:** Predicted profiles of gas temperature and dry gas species volume fractions for the REGA experiment TUC5 V1105 in comparison with measured profiles. DLR2017/RM: results obtained using the DLR2017/RM mechanism; eJL/A: results obtained using the eJL/A mechanism.

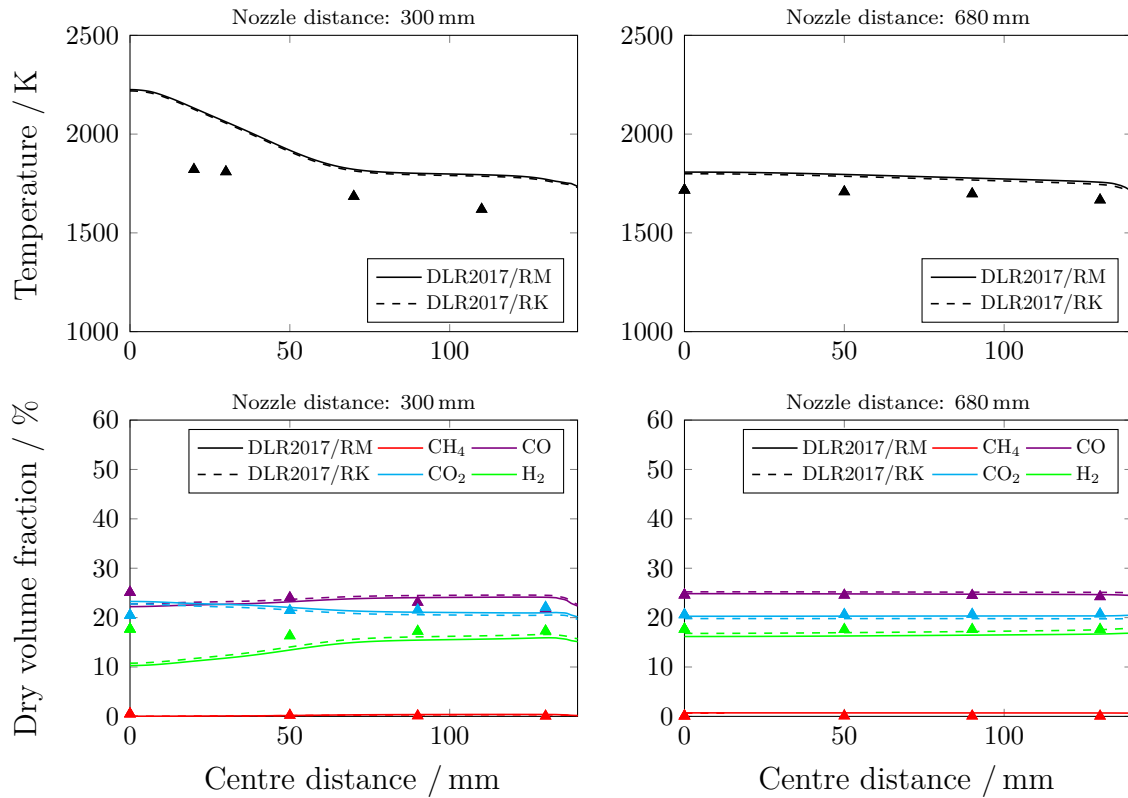


**Figure 4.25:** Predicted profiles of gas temperature and dry gas species volume fractions for the REGA experiment TUC3 V786 in comparison with measured profiles. DLR2017/RM: results obtained using the DLR2017/RM mechanism; DLR2017/RK: results obtained using the DLR2017/RK mechanism.

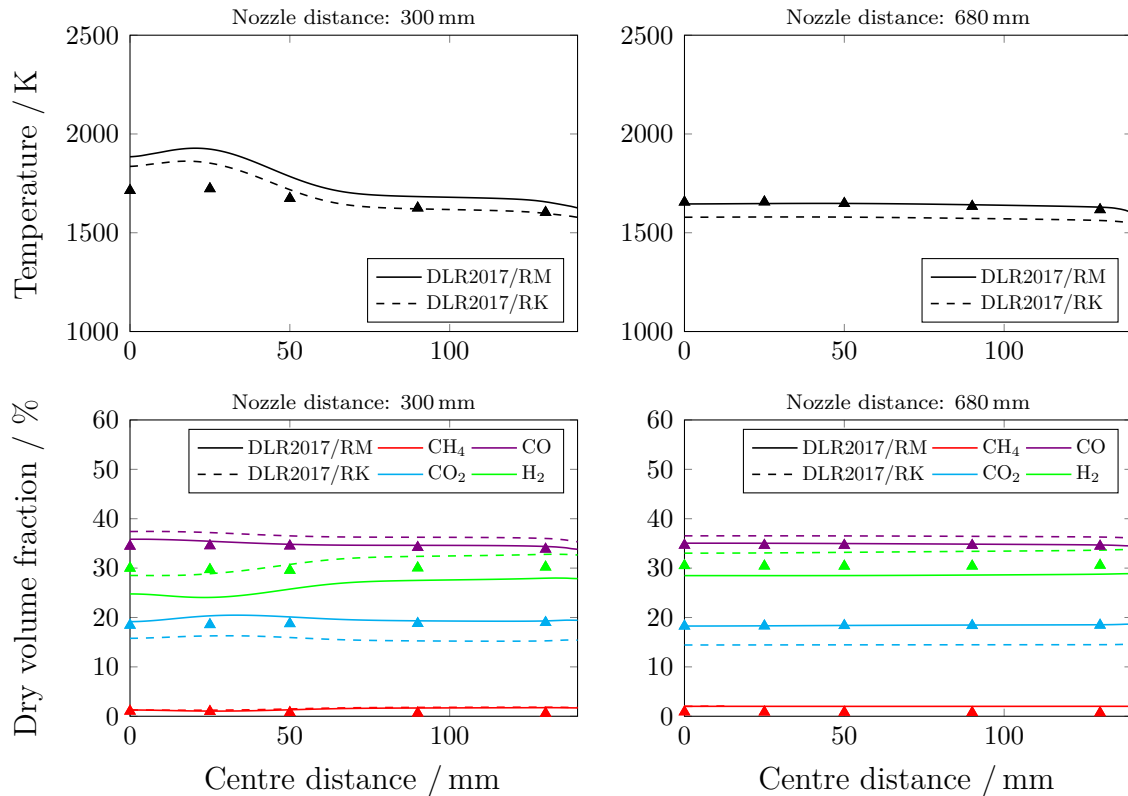


**Figure 4.26:** Predicted profiles of gas temperature and dry gas species volume fractions for the REGA experiment TUC5 V1105 in comparison with measured profiles. DLR2017/RM: results obtained using the DLR2017/RM mechanism; DLR2017/RK: results obtained using the DLR2017/RK mechanism.

The rates of the gas phase reactions are determined by solving the concentrations and energy equations for the fine structures in which the gas is well mixed at molecular level (see Section 2.4). However, solving these equations required different computing times in the CFD simulations due to different stiffnesses of the various reaction mechanisms. This was also true when the numerical integration was applied with the in-situ-adaptive-tabulation (ISAT) algorithm. In order to provide a fair quantitative comparison of the computing times, 100 additional flow iterations were performed for the REGA experiments TUC3 V786 and TUC5 V1105 after already achieving final numerical results. The CFD simulations were carried out using direct integration and 48 computing nodes. The normalised computing times are given in Table 4.8 and confirm the qualitative impression. CFD simulations with the HVI1 mechanism are characterised by the lowest computing times while CFD simulations using the DLR2017/RK mechanism and the DLR2017/RM mechanism already require more resources. The DLR2017/RK mechanism outperforms the DLR2017/RM mechanism in this comparison, whereas CFD simulations with the ISAT algorithm were faster when applying the DLR2017/RM mechanism. This is certainly related to the number of species. 24 species are accounted for in the DLR2017/RM mechanism while 43 species are used in the DLR2017/RK mechanism. CFD simulations using the eJL mechanism and the eJL/A mechanism are finally characterised by very high computing times due to high stiffness, which was not observed in the preceding work [187] using coarser meshes. In summary, the HVI1 mechanism and the DLR2017/RM mechanism are recommended for future works. The HVI1 mechanism should be used for first CFD simulations while the DLR2017/RM mechanism should be applied to obtain reasonable flame predictions of gas temperature and gas species concentrations.

**Table 4.8:** Normalised computing times for the CFD simulations of the REGA experiments TUC3 V786 and TUC5 V1105: comparison of results for various reaction mechanisms.

Reaction mechanism	Normalised computing time	
	REGA TUC3 V786	REGA TUC5 V1105
HVI1	1	1
DLR2017/RM	8.0	8.6
eJL	22.9	18.7
eJL/A	14.0	13.8
DLR2017/RK	3.5	7

## 4.6 Vaporisation

The predicted profiles in the near-axis region have been in worse agreement with the measured profiles compared to the preceding works [63, 64, 187]. However, this work and

the preceding works [63, 64, 187] relied on different assumptions for the film factor  $f_{\text{film}}$ , which particularly determines the mass transfer of ethylene glycol into the gas phase. The impact of the film factor is demonstrated in Figs. 4.27-4.30, accounting for either the HVI1 mechanism or the DLR2017/RM mechanism. The deviations between measured and predicted profiles of gas temperature and gas species concentrations are accordingly smaller using a film factor  $f_{\text{film}} = 1$  than using a film factor  $f_{\text{film}} = 1/3$ . Thus, the mass transfer of ethylene glycol into the gas phase is faster in the experiments than in RANS based simulations with a film factor  $f_{\text{film}} = 1/3$ . This is likely due to longer droplet residence times in the flame region and a better mixing of ethylene glycol, recirculating gas and gasification medium. In contrast to the film factor, the reaction mechanism only slightly affects the vaporisation behaviour, where the impact is larger for lower film factors.

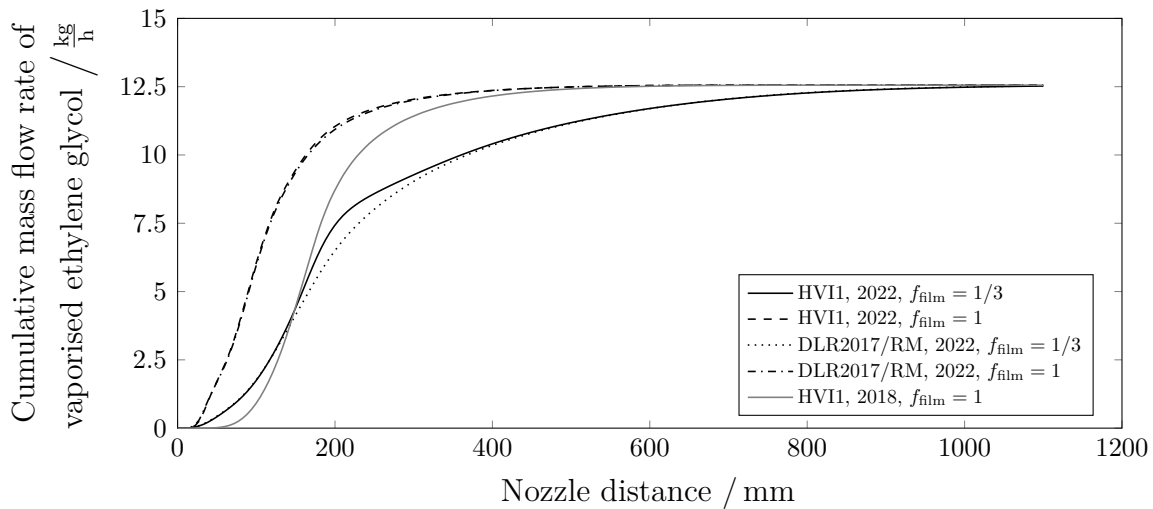


**Figure 4.27:** Predicted cumulative mass flow rates of vaporised ethylene glycol for the REGA experiment TUC3 V786: comparison of results based on various reaction mechanisms and film factors.

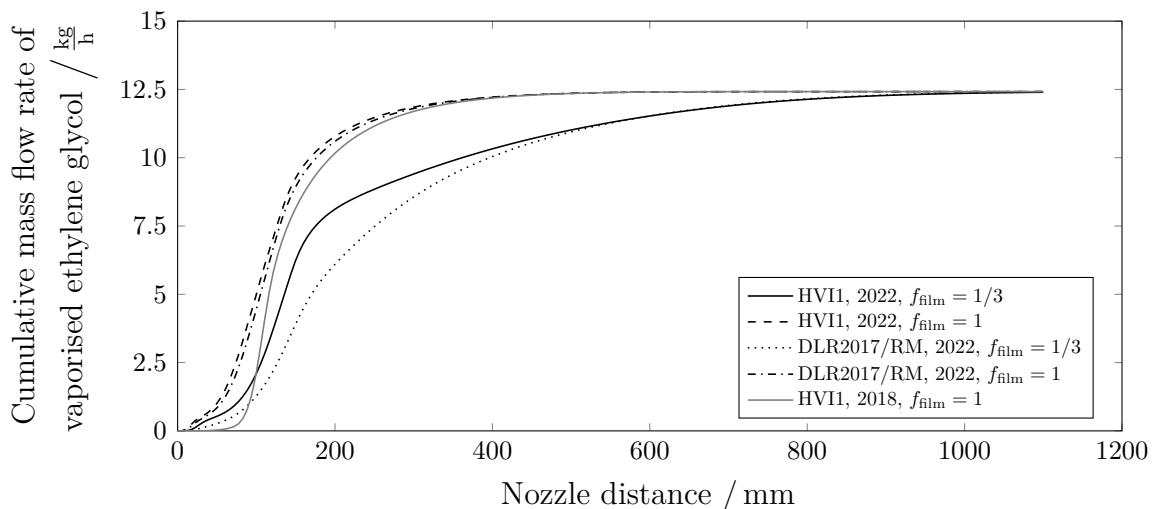


**Figure 4.28:** Predicted cumulative mass flow rates of vaporised ethylene glycol for the REGA experiment TUC5 V1105: comparison of results based on various reaction mechanisms and film factors.

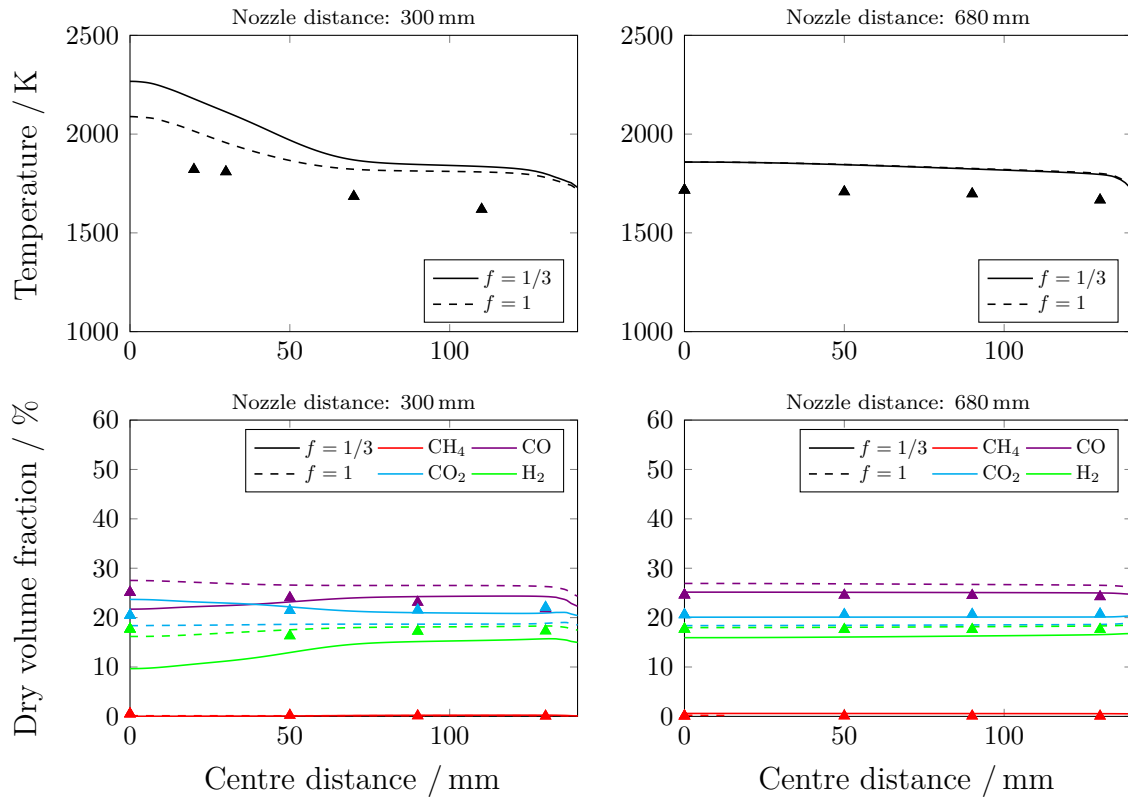


**Figure 4.29:** Predicted profiles of gas temperature and dry gas species volume fractions for the REGA experiment TUC3 V786 in comparison with measured profiles.  $f_{\text{film}} = 1/3$ : results obtained using the DLR2017/RM mechanism and the 1/3 rule for the film condition;  $f_{\text{film}} = 1$ : results obtained using the DLR2017/RM mechanism and the gas condition for the film condition.

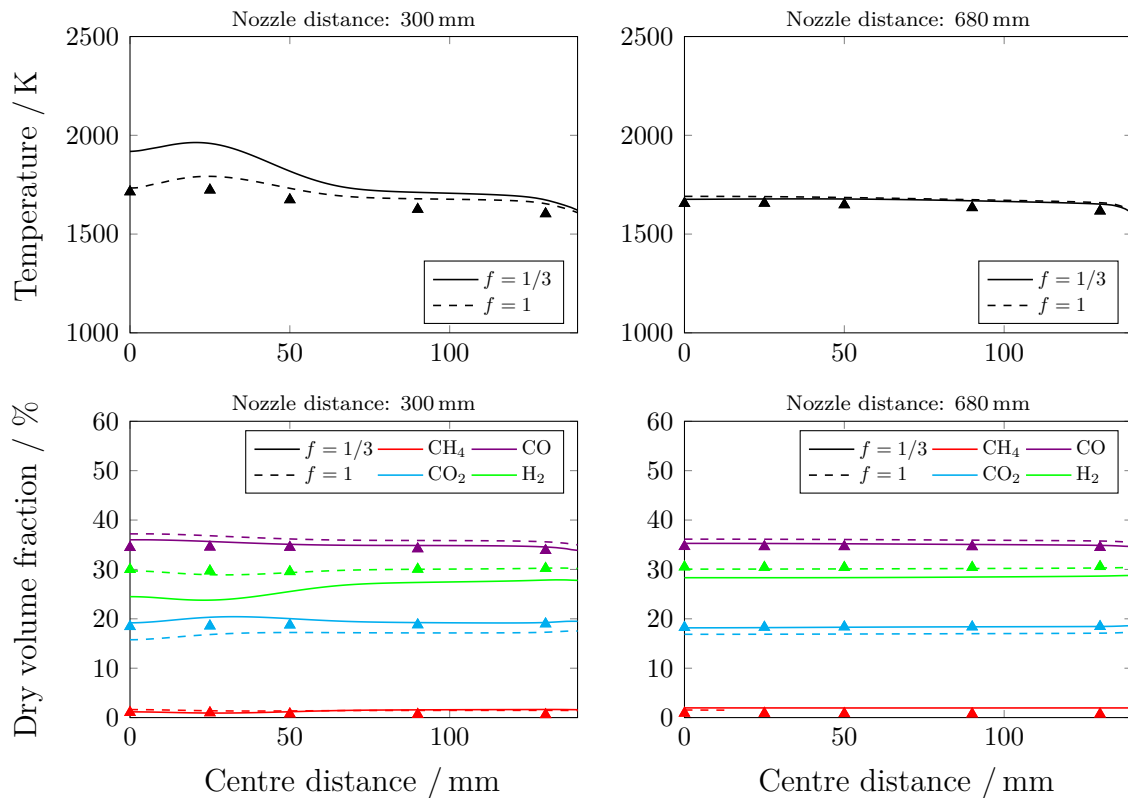


**Figure 4.30:** Predicted profiles of gas temperature and dry gas species volume fractions for the REGA experiment TUC5 V1105 in comparison with measured profiles.  $f_{\text{film}} = 1/3$ : results obtained using the DLR2017/RM mechanism and the 1/3 rule for the film condition;  $f_{\text{film}} = 1$ : results obtained using the DLR2017/RM mechanism and the gas condition for the film condition.

## 4.7 Turbulence

The impact of the turbulence model was already analysed in the preceding work [187]. Similar predictions of gas temperature and dry gas species concentrations were obtained using various turbulence models due to similar predictions of turbulent kinetic energy  $k$  and turbulent dissipation rate  $\epsilon$  [187]. However, the inlet conditions were significantly changed in this work. Therefore, the sensitivity analysis was repeated accounting for the standard  $k$ - $\epsilon$  model and the SST  $k$ - $\omega$  model. The results are shown in Figs. 4.31 and 4.32 and in Table 4.9. Thus, the standard  $k$ - $\epsilon$  model and the SST  $k$ - $\omega$  model provided almost identical predictions of gas temperature and dry gas species concentrations, while predictions of recirculation strength and length strongly differ. This confirms previous conclusions [187].

**Table 4.9:** Predicted strengths and lengths of the recirculation zones for the REGA experiments TUC3 V479, TUC3 V786 and TUC5 V1105: comparison of results based on various turbulence models.

REGA experiment	Strength / kg/h		Length / mm	
	$k$ - $\epsilon$ model	SST $k$ - $\omega$ model	$k$ - $\epsilon$ model	SST $k$ - $\omega$ model
TUC3 V479	76	81	824	789
TUC3 V786	76	81	824	787
TUC5 V1105	74	79	836	795

## 4.8 Thermal gas radiation properties

The impact of the thermal gas radiation model was already examined in the preceding work [187]. However, non-grey-gas absorption coefficients were incorporated using the macro `DEFINE_WSGGM_ABS_COEFF` that is restricted for WSGG models combined with mean beam length model (see Section 3.1). Therefore, the sensitivity analysis was repeated using improved implementations. The results are shown in Figs. 4.33-4.36 and in Table 4.10. Thus, the grey-gas model and the non-grey-gas model provided almost identical predictions of dry gas species concentrations and total heat flow rate and similar predictions of gas temperature and radiation heat flow rate. When using the WSGG model, the gas temperatures are mainly higher, while less heat is removed through thermal radiation in the upper reactor part. In comparison with previous results [187], the deviations between predictions using grey-gas model and non-grey-gas model remain small as the high wall temperatures minimise the impact of the thermal gas radiation property model. Furthermore, the radiation heat fluxes shown in Figs. 4.35 and 4.36 strongly changed below 300 mm as they were interfered by the supply of infiltrated air and purge nitrogen. However, the total heat fluxes changed less due to the high wall temperatures.

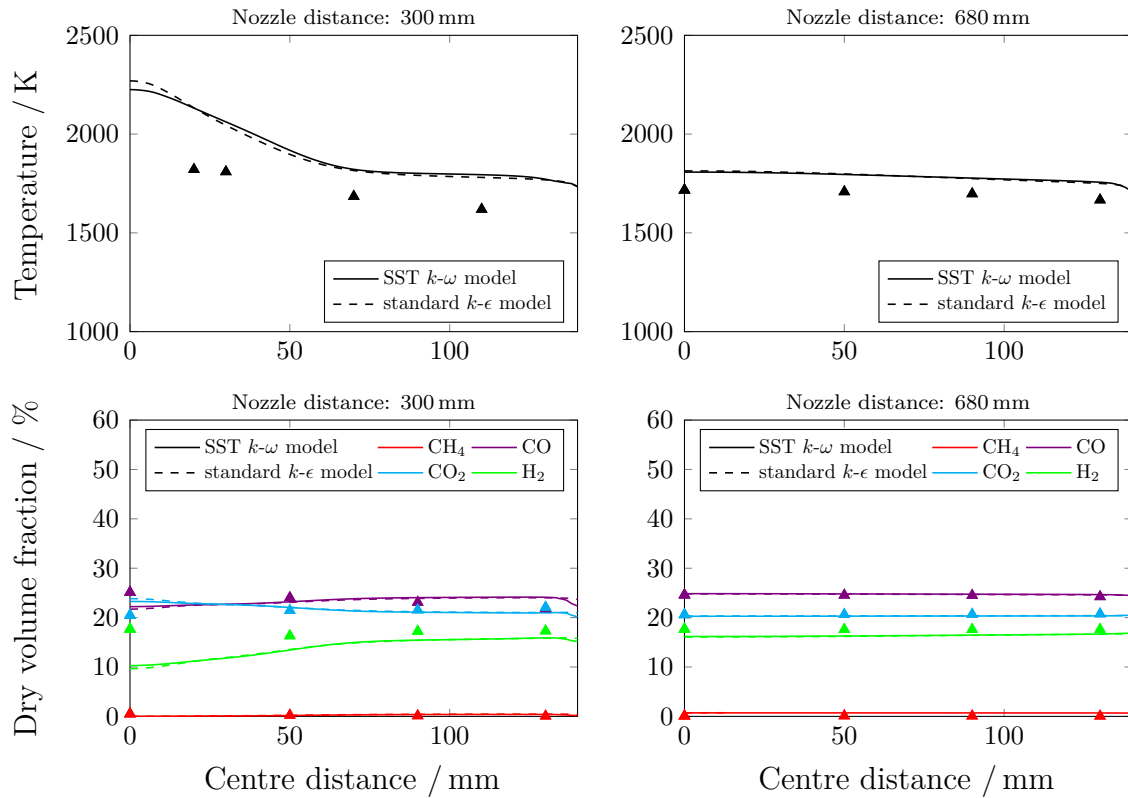


**Figure 4.31:** Predicted profiles of gas temperature and dry gas species volume fractions for the REGA experiment TUC3 V786 in comparison with measured profiles. SST  $k-\omega$  model: results obtained using the DLR2017/RM mechanism and the SST  $k-\omega$  model; standard  $k-\epsilon$  model: results obtained using the DLR2017/RM mechanism and the standard  $k-\epsilon$  model.

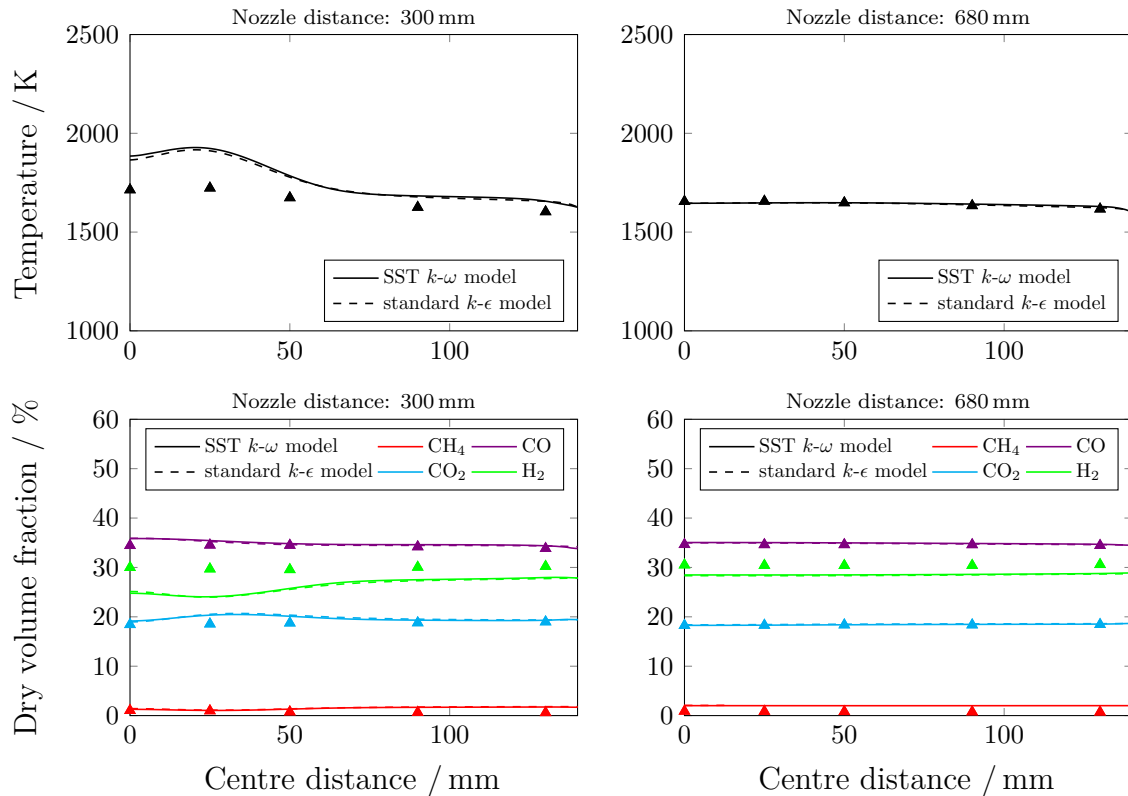


**Figure 4.32:** Predicted profiles of gas temperature and dry gas species volume fractions for the REGA experiment TUC5 V1105 in comparison with measured profiles. SST  $k-\omega$  model: results obtained using the DLR2017/RM mechanism and the SST  $k-\omega$  model; standard  $k-\epsilon$  model: results obtained using the DLR2017/RM mechanism and the standard  $k-\epsilon$  model.

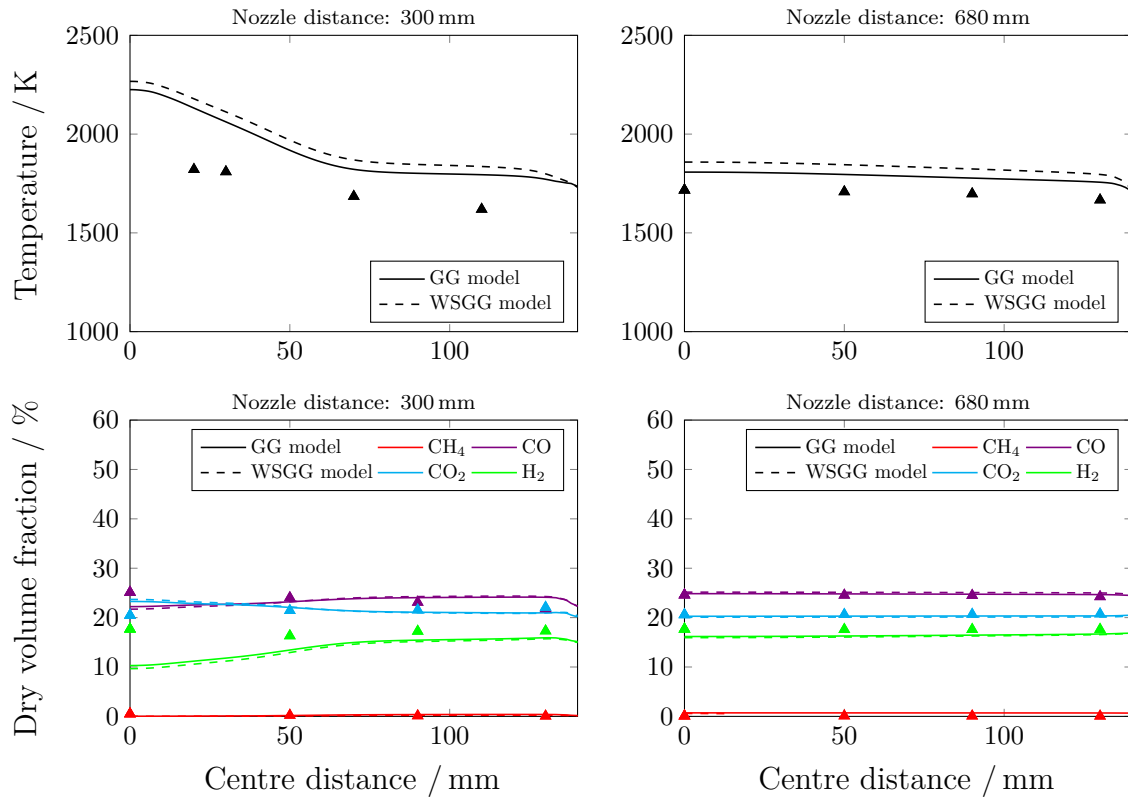


**Figure 4.33:** Predicted profiles of gas temperature and dry gas species volume fractions for the REGA experiment TUC3 V786 in comparison with measured profiles. GG model: results obtained using the DLR2017/RM mechanism and the grey-gas model; WSGG model: results obtained using the DLR2017/RM mechanism and the weighted-sum-of-grey-gas model.

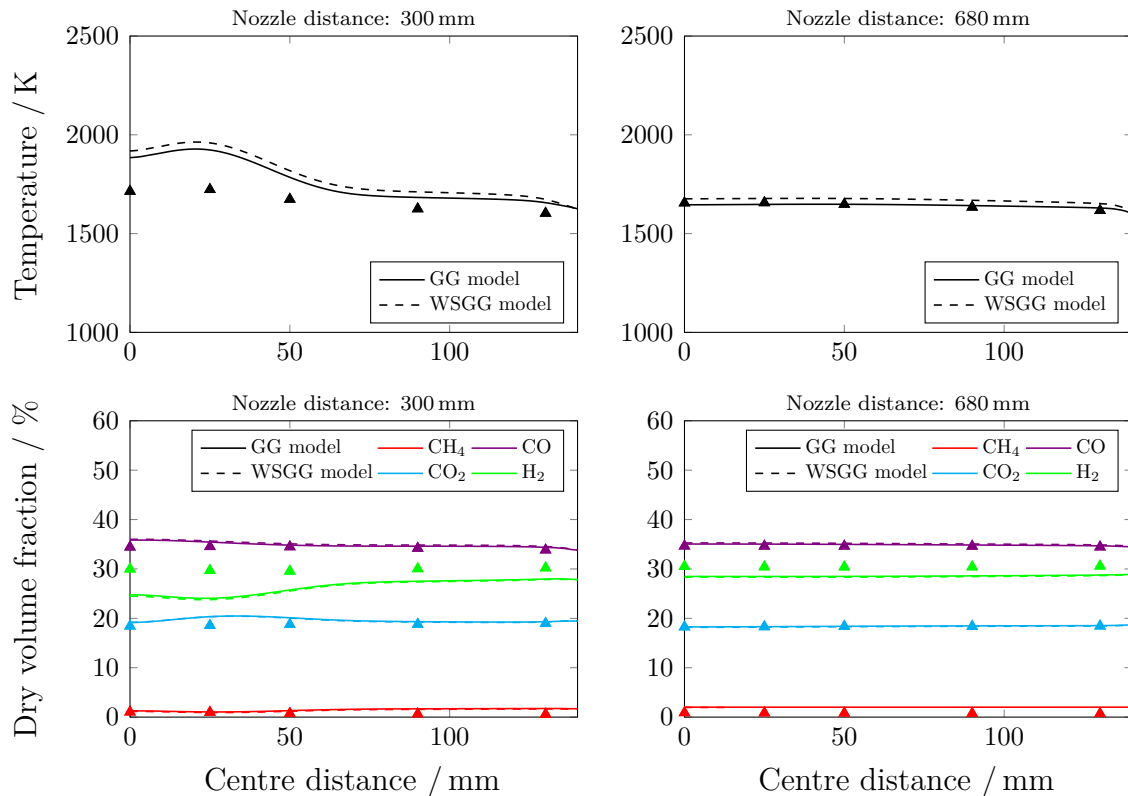


**Figure 4.34:** Predicted profiles of gas temperature and dry gas species volume fractions for the REGA experiment TUC5 V1105 in comparison with measured profiles. GG model: results obtained using the DLR2017/RM mechanism and the grey-gas model; WSGG model: results obtained using the DLR2017/RM mechanism and the weighted-sum-of-grey-gas model.

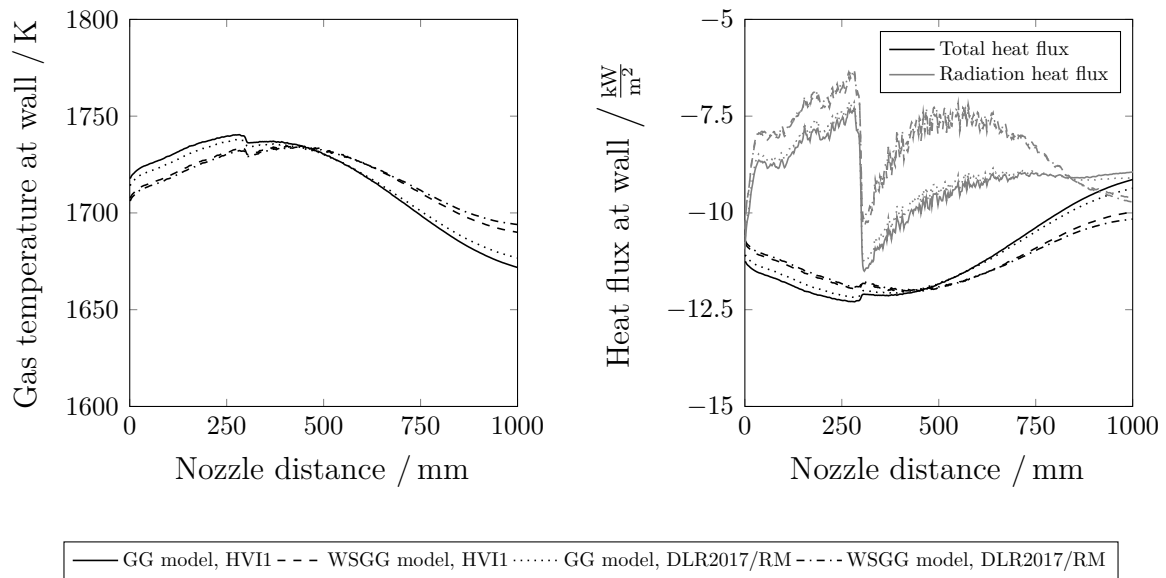


**Figure 4.35:** Predicted gas temperatures and heat fluxes at wall for the REGA experiment TUC3 V786: comparison of results based on various thermal gas radiation property models and various reaction mechanisms.

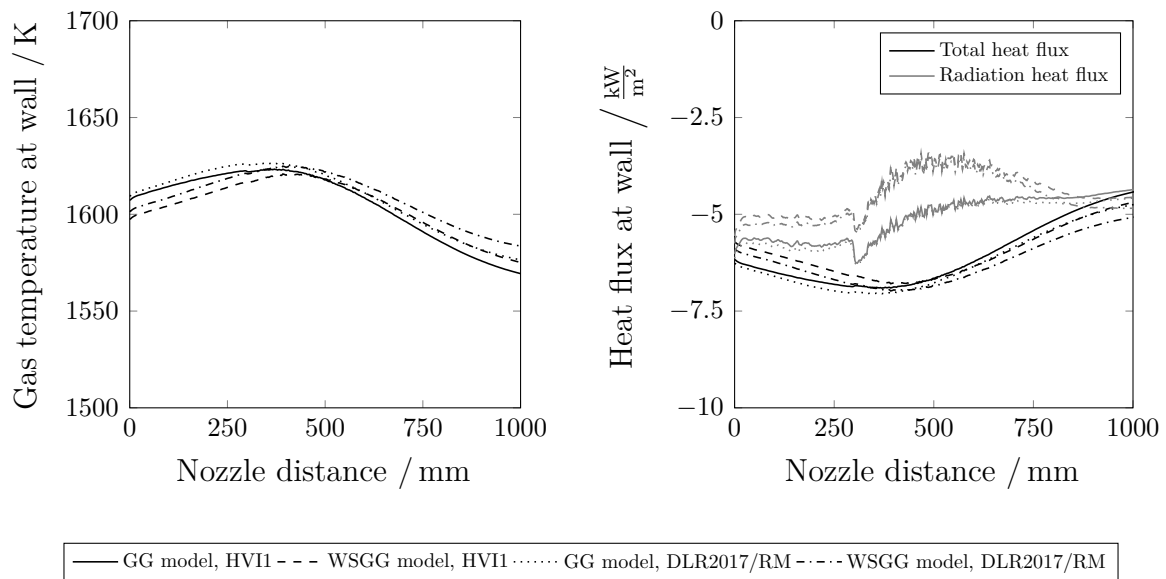


**Figure 4.36:** Predicted gas temperatures and heat fluxes at wall for the REGA experiment TUC5 V1105: comparison of results based on various thermal gas radiation property models and various reaction mechanisms.

**Table 4.10:** Predicted total and radiation heat flow rates at wall for the REGA experiments TUC3 V786 and TUC5 V1105: comparison of results based on various thermal gas radiation property models. The data was obtained using the DLR2017/RM mechanism.

REGA experiment	Total heat flow rate / kW		Radiation heat flow rate / kW	
	GG model	WSGG model	GG model	WSGG model
TUC3 V786	-11.36	-11.52	-9.39	-8.67
TUC5 V1105	-6.30	-6.32	-5.36	-4.82

## 4.9 Inlet conditions and injection properties

The ATMO experiments TUC5 D2.1 and TUC5 D1.1 were performed using different experimental conditions compared to the ATMO experiments TUC3 D1 and TUC5 D2 (see Section 2.2.4.2). It was thus interesting to describe the REGA experiment TUC5 V1105 and the REGA experiment TUC5 V1374 using inlet conditions and injection properties based on the ATMO experiment TUC5 D2.1 and the ATMO experiment TUC5 D1.1, respectively.

For the REGA experiment TUC5 V1105, the results based on the adapted model are compared with the baseline results in Figs. 4.37 and 4.38. Thus, the inlet conditions and injection properties based on the ATMO experiments TUC5 D2.1 changed the flame shape from W-shaped to V-shaped but had less impact on the far-flame predictions of gas temperature and dry gas species concentrations.

For the REGA experiment TUC5 V1374, the predicted gas temperature distribution is shown in Fig. 4.39. The injection properties based on the ATMO experiment TUC5 D1.1 thus provided a W-shaped flame which is not in agreement with the OH-LIF measurement results [113, 114] indicating a V-shaped flame.

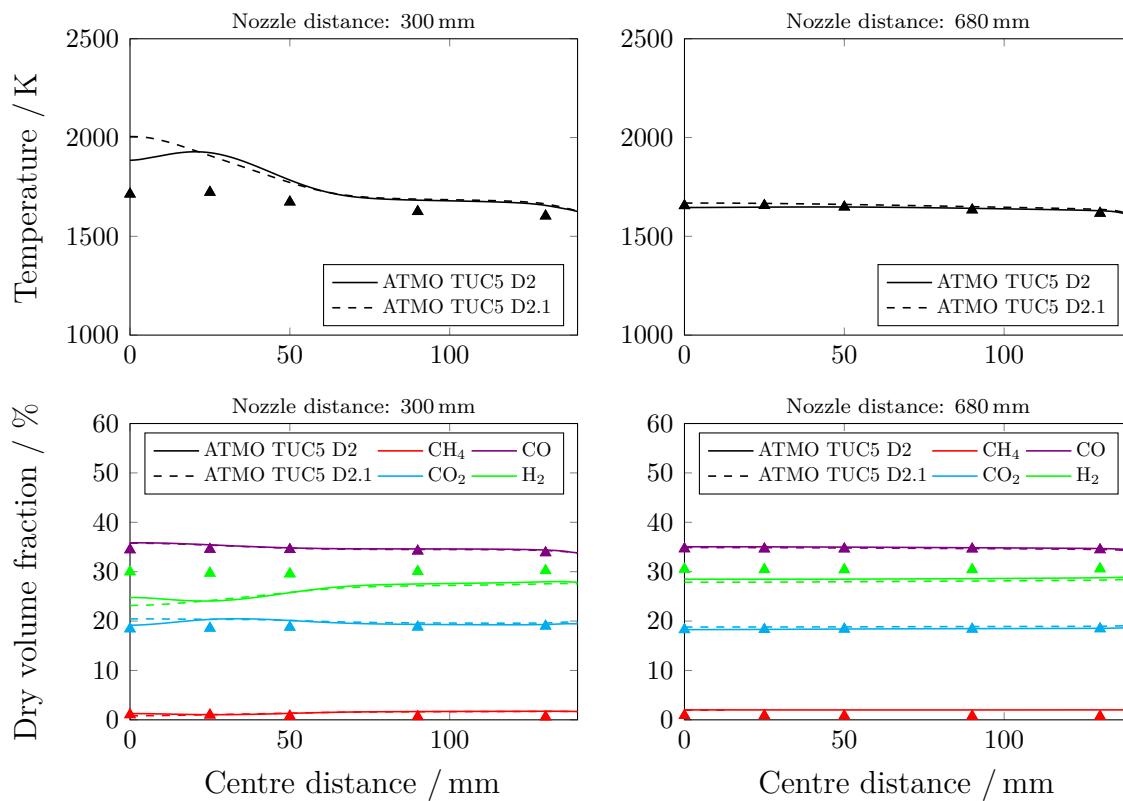


**Figure 4.37:** Predicted profiles of gas temperature and dry gas species volume fractions for the REGA experiment TUC5 V1105 in comparison with measured profiles. ATMO TUC5 D2: results obtained using the DLR2017/RM mechanism and the injection properties based on the ATMO experiment TUC5 D2; ATMO TUC5 D2.1: results obtained using the DLR2017/RM mechanism and the injection properties based on the ATMO experiment TUC5 D2.1.

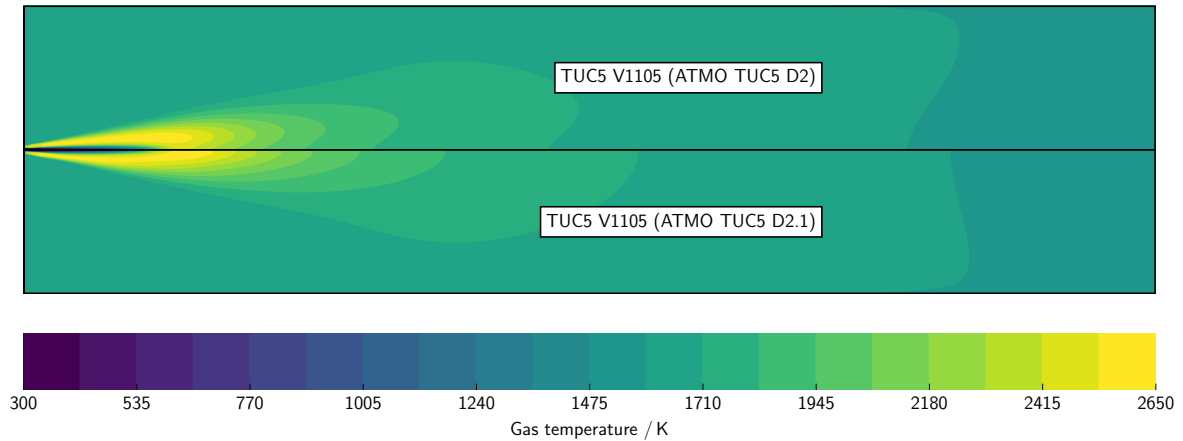


**Figure 4.38:** Predicted gas temperature distributions. TUC5 V1105 (ATMO TUC5 D2): results obtained for the REGA experiment TUC5 V1105 using the DLR2017/RM mechanism and the injection properties based on the ATMO experiment TUC5 D2; TUC5 V1105 (ATMO TUC5 D2.1): results obtained for the REGA experiment TUC5 V1105 using the DLR2017/RM mechanism and the injection properties based on the ATMO experiment TUC5 D2.1.

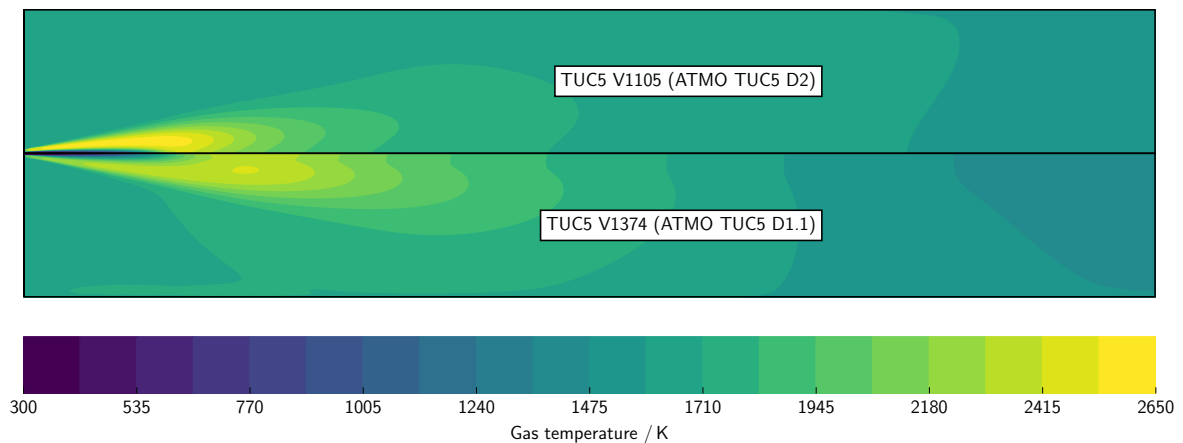


**Figure 4.39:** Predicted gas temperature distributions. TUC5 V1105 (ATMO TUC5 D2): results for the REGA experiment TUC5 V1105 obtained using the DLR2017/RM mechanism and the injection properties based on the ATMO experiment TUC5 D2; TUC5 V1374 (ATMO TUC5 D1.1): results for the REGA experiment TUC5 V1374 obtained using the DLR2017/RM mechanism and the injection properties based on the ATMO experiment TUC5 D1.1.

In summary, the injection properties based on the ATMO experiments TUC3 D1 and TUC5 D2 provided more reasonable flame shapes than the injection properties based on the ATMO experiments TUC5 D2.1 and TUC5 D1.1. Therefore, the injection properties based on the ATMO experiment TUC5 D2.1 and TUC5 D1.1 cannot be recommended for future works. Furthermore, the numerical results show that injection properties for RANS based simulations should be derived from appropriate experimental data and may be verified using different approaches such as large eddy simulations combined with the volume-of-fluid method. Through improved approaches for the injections properties, subsequent works [114] were eventually able to provide superior numerical results for the

REGA experiments TUC5 V1105 and TUC5 V1374 using data from the ATMO experiment TUC5 D2.1 and the ATMO experiment TUC5 D1.1, respectively.

## 4.10 Wood char kinetics

Appropriate inlet conditions and injection properties are essential for accurate predictions of gas temperatures, gas species concentrations and droplet velocities in the flame region (see Sections 4.1, 4.4 and 4.9). Since such inlet conditions and injection properties have been derived in this work for the atmospheric entrained flow gasification of ethylene glycol only, the REGA experiments TUC5 GHKS10 V1071 and TUC5 GHKS30 V1284 have not been focussed in Sections 4.1-4.9. Furthermore, adjustments of devolatilisation kinetics, heterogeneous gasification kinetics and morphology changes are computationally time-consuming. Therefore, CFD simulations of the REGA experiments TUC5 GHKS10 V1071 and TUC5 GHKS30 V1284 were performed only to investigate the impact of the devolatilisation and heterogeneous gasification kinetics on the predictions of gas temperature, gas species concentrations and wood char conversion, while using the SST  $k$ - $\omega$  model as turbulence model, the HVI1 mechanism as reaction mechanism and the grey-gas model as thermal gas radiation property model. The cases that were studied in this work are summarised in Table 4.11.

**Table 4.11:** CFD simulations of the REGA experiments TUC5 GHKS10 V1071 and TUC5 GHKS30 V1284.

REGA experiment	Case	$R_{m,part,dev}$	$R_{m,part,het}$
TUC5 GHKS10 V1071	S1	$\times 1$	$\times 1$
	S2	$\times 2$	$\times 1$
	S4	$\times 1$	$\times 2$
	S5	$\times 2$	$\times 2$
TUC5 GHKS30 V1284	S1	$\times 1$	$\times 1$
	S2	$\times 2$	$\times 1$
	S3	$\times 5$	$\times 1$
	S4	$\times 1$	$\times 2$
	S5	$\times 2$	$\times 2$
	S6	$\times 5$	$\times 2$
	S7	$\times 1$	$\times 10$
	S8	$\times 2$	$\times 10$
	S9	$\times 5$	$\times 10$

The reaction rates during devolatilisation  $R_{m,\text{part,dev}}$  based on the Arrhenius law model of Dammann et al. [68] and the reaction rates of the Boudouard reaction and the water gas reaction  $R_{m,\text{part,het}}$  based on the Langmuir-Hinshelwood models (regime II) of Kreitzberg et al. [156] were thus adapted using factors of 1, 2, 5 and 10 in various combinations.

The predicted baseline profiles are compared with the measured profiles in Figs. 4.40 and 4.41. The predictions of gas temperature and dry gas species concentrations are accordingly in good to excellent agreement with the measured data for both REGA experiments. Excellent agreement between the predicted and measured profiles is found at 680 mm for the REGA experiment TUC5 GHKS10 V1071, whereas larger deviations are observed at 300 mm in the near-axis region for both REGA experiments. This is likely due to slower mass transfer of ethylene glycol into the gas phase (see Section 4.6). Larger deviations are also found between predicted and measured gas temperature profiles at 680 mm for the REGA experiment TUC5 GHKS30 V1284. This indicates erroneous flame predictions. Furthermore, Figs. 4.40 and 4.41 demonstrate that the deviations between the measured and predicted profiles have only been slightly reduced assuming devolatilisation rates increased by a factor of 2. Similarly, Figs. 4.42 and 4.43 show that heterogeneous gasification rates increased by a factor of 2 combined with the baseline devolatilisation rates or devolatilisation rates increased by a factor of 2 have only marginally changed the predictions of gas temperature and dry gas species volume fractions. Even devolatilisation rates increased by a factor of 5 combined with heterogeneous gasification rates increased by a factor of 10 or strong changes of the volatiles compositions or the particle diameter have only some impact on the predictions for the REGA experiment TUC5 GHKS30 V1284. As shown in Fig. 4.44, the gas temperatures can decrease due to higher conversion while the dry gas species volume fractions hardly change. Thus, the predictions of gas temperature and dry gas species volume fractions for the atmospheric entrained flow gasification of mixtures with wood char contents of up to 30% are more strongly determined by the conversion of ethylene glycol than by the conversion of wood char. Within certain limits, the accuracy of the devolatilisation kinetics and the heterogeneous gasification kinetics is not decisive for the predictions of gas temperature and gas species concentrations. This is also clear from the gas temperature distributions shown in Figs. 4.45 and 4.46.

For further analysis of the wood char conversion and for comparison with the balanced carbon conversions  $X_{C,\text{solid}}$  (see Section 2.7.3.2), simulated solid devolatilisation conversions  $X_{\text{dev,solid}}$ , simulated solid gasification conversions  $X_{\text{het,solid}}$  and simulated solid carbon conversions  $X_{C,\text{solid}}$  were calculated at the nozzle distance of 680 mm. The averaged data is given in Table 4.12. First of all, this data demonstrates that the solid conversions typically increase with both increasing devolatilisation rates and increasing heterogeneous gasification rates (apart from stochastic fluctuations and endothermic temperature effects). Furthermore, for the REGA experiment TUC5 GHKS10 V1071, the averaged solid devolatilisation conversion  $X_{\text{dev,solid}}$  is 85%, the averaged solid gasification conversion  $X_{\text{het,solid}}$

is 70% and the averaged solid carbon conversion  $X_{C,\text{solid}}$  is 72% if the devolatilisation and heterogeneous gasification rates are described by the baseline kinetics. The averaged solid carbon conversions can be increased up to 80% when both the devolatilisation rates and the heterogeneous gasification rates are increased by a factor of 2. In contrast, for the REGA experiment TUC5 GHKS30 V1284, the averaged solid devolatilisation conversion  $X_{\text{dev},\text{solid}}$  is 67%, the averaged solid gasification conversion  $X_{\text{het},\text{solid}}$  is 48% and the averaged solid carbon conversion  $X_{C,\text{solid}}$  is 50% if the devolatilisation and heterogeneous gasification rates are described by the baseline kinetics. Thus, the predicted solid conversions are lower for the REGA experiment TUC5 GHKS30 V1284 than for the REGA experiment TUC5 GHKS10 V1071. This is likely due to the larger particle sizes assumed for the CFD simulations of the REGA experiment TUC5 GHKS30 V1284 (see Fig. 2.14).

The predicted solid carbon conversion  $X_{C,\text{solid}}$  at 680 mm for the REGA experiment TUC5 GHKS30 V1284 is also significantly below the experimental estimates of 71% and 77% (see Table 2.10). Even if the devolatilisation rates are increased by a factor of 2 and the heterogeneous gasification rates are increased by a factor of 10, the averaged solid carbon conversion  $X_{C,\text{solid}}$  only increases to 70%. Since a factor of 2 likely exceeds the uncertainty factor of the devolatilisation kinetics of Dammann et al. [68] and a factor of 10 is likely an appropriate upper uncertainty bound for the heterogeneous gasification kinetics of Kreitzberg et al. [156], other effects have caused the erroneous prediction of the solid carbon conversion  $X_{C,\text{solid}}$  for the REGA experiment TUC5 GHKS30 V1284.

**Table 4.12:** Predicted solid devolatilisation conversions  $X_{\text{dev},\text{solid}}$ , predicted solid gasification conversions  $X_{\text{het},\text{solid}}$  and predicted solid carbon conversions  $X_{C,\text{solid}}$  for the REGA experiments TUC5 GHKS10 V1071 and TUC5 GHKS30 V1284 at a nozzle distance of 680 mm and near axis.

REGA experiment	Case	$\frac{X_{\text{dev},\text{solid}}}{\%}$	$\frac{X_{\text{het},\text{solid}}}{\%}$	$\frac{X_{C,\text{solid}}}{\%}$
TUC5 GHKS10 V1071	S1	$\approx 85.4$	$\approx 70.1$	$\approx 71.8$
	S2	$\approx 91.7$	$\approx 78.0$	$\approx 79.5$
	S4	$\approx 83.1$	$\approx 64.4$	$\approx 66.4$
	S5	$\approx 90.2$	$\approx 77.9$	$\approx 79.3$
TUC5 GHKS30 V1284	S1	$\approx 66.7$	$\approx 47.5$	$\approx 50.0$
	S2	$\approx 76.5$	$\approx 56.0$	$\approx 58.6$
	S3	$\approx 83.9$	$\approx 57.6$	$\approx 61.1$
	S4	$\approx 69.9$	$\approx 52.4$	$\approx 54.6$
	S5	$\approx 74.0$	$\approx 55.5$	$\approx 57.9$
	S6	$\approx 83.3$	$\approx 59.5$	$\approx 62.6$
	S7	$\approx 68.2$	$\approx 51.8$	$\approx 54.0$
	S8	$\approx 78.1$	$\approx 69.2$	$\approx 70.3$
	S9	$\approx 84.1$	$\approx 64.4$	$\approx 67.0$

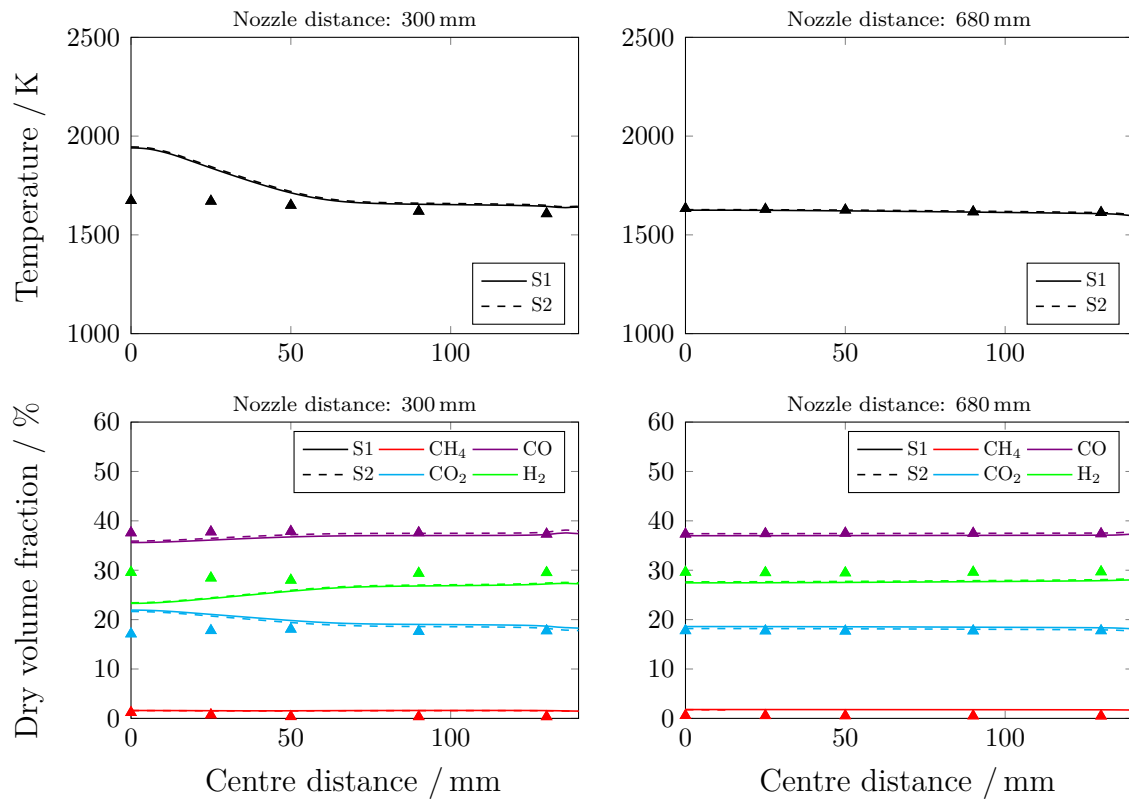


**Figure 4.40:** Predicted profiles of gas temperature and dry gas species volume fractions for the REGA experiment TUC5 GHKS10 V1071 in comparison with measured profiles. S1: baseline results; S2: results obtained using devolatilisation rates increased by a factor of 2.

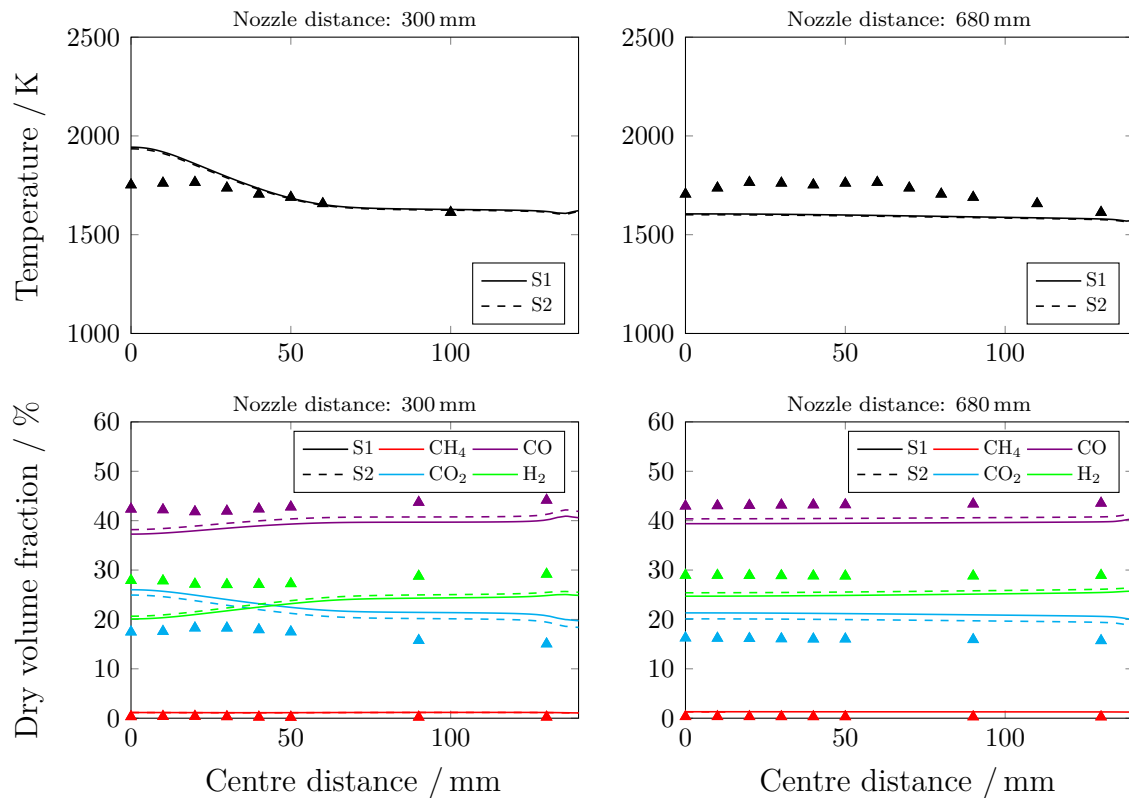


**Figure 4.41:** Predicted profiles of gas temperature and dry gas species volume fractions for the REGA experiment TUC5 GHKS30 V1284 in comparison with measured profiles. S1: baseline results; S2: results obtained using devolatilisation rates increased by a factor of 2.

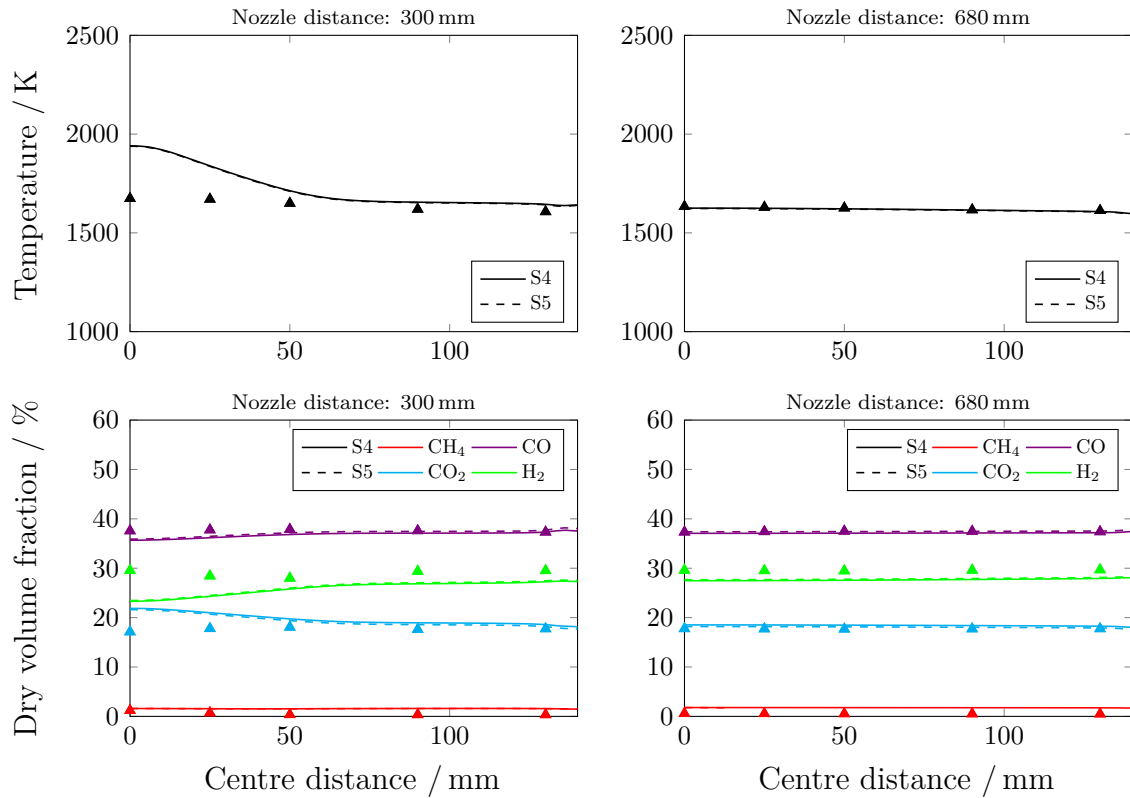


**Figure 4.42:** Predicted profiles of gas temperature and dry gas species volume fractions for the REGA experiment TUC5 GHKS10 V1071 in comparison with measured profiles. S4: results obtained using heterogeneous gasification rates increased by a factor of 2; S5: results obtained using devolatilisation rates and heterogeneous gasification rates increased both by a factor of 2.

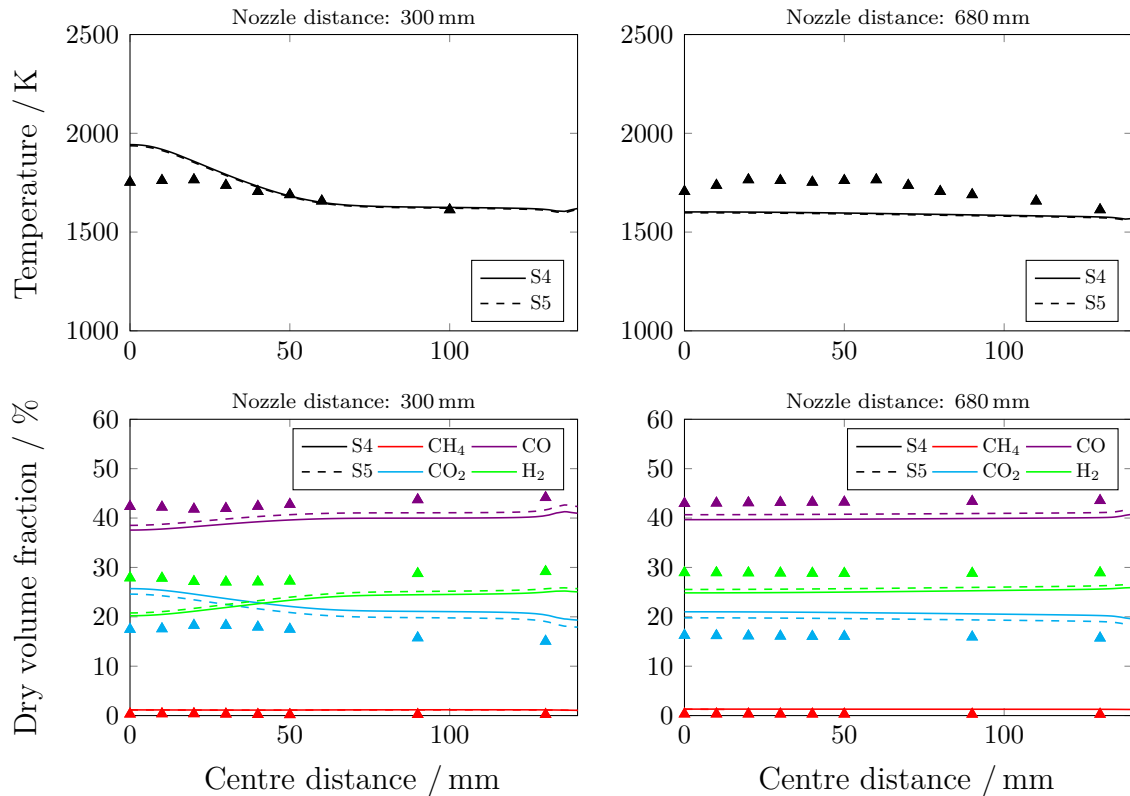


**Figure 4.43:** Predicted profiles of gas temperature and dry gas species volume fractions for the REGA experiment TUC5 GHKS30 V1284 in comparison with measured profiles. S4: results obtained using heterogeneous gasification rates increased by a factor of 2; S5: results obtained using devolatilisation rates and heterogeneous gasification rates increased both by a factor of 2.

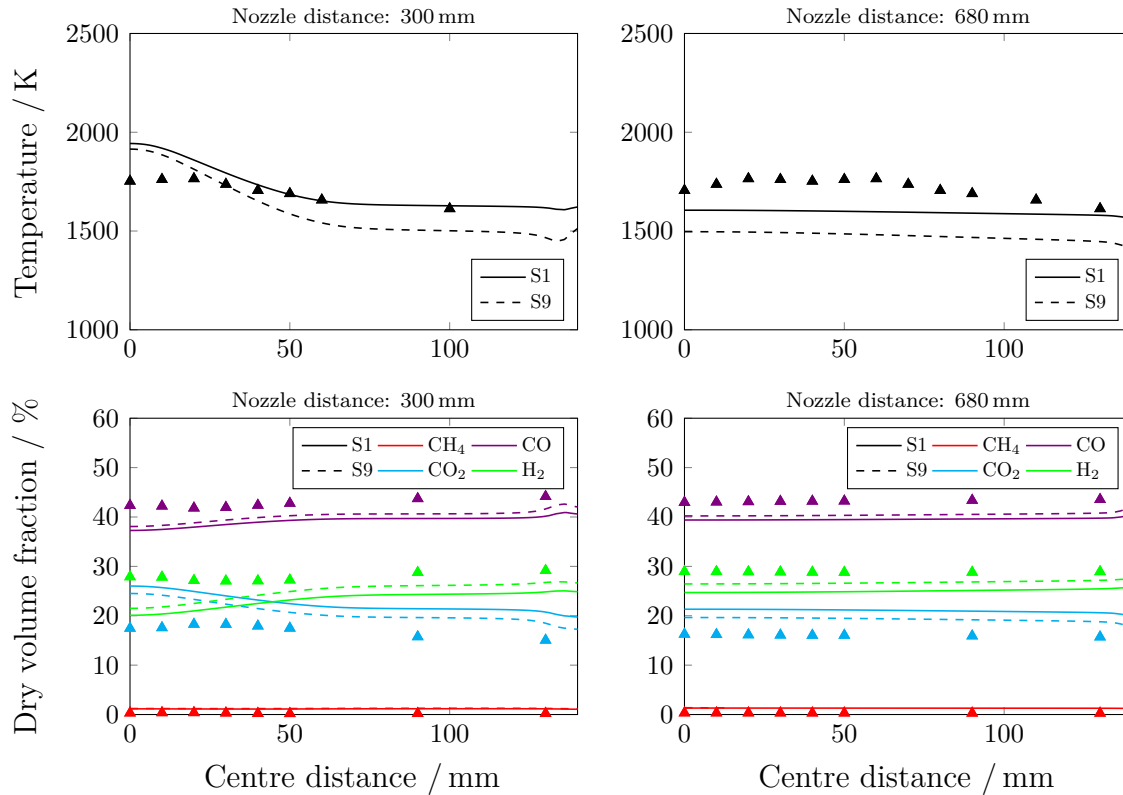


**Figure 4.44:** Predicted profiles of gas temperature and dry gas species volume fractions for the REGA experiment TUC5 GHKS30 V1284 in comparison with measured profiles. S1: baseline results; S9: results obtained using devolatilisation rates increased by a factor of 5 and heterogeneous gasification rates increased by a factor of 10.

**Table 4.13:** Balanced solid gasification conversions  $X_{\text{het,solid}}$  of particles collected in the REGA experiment TUC5 GHKS30 V1284 corresponding to the balanced solid carbon conversions  $X_{\text{C,solid}}$  given in Table 2.10.

Sample	$X_{\text{het,solid}} / \%$		
	Ca tracer method	Mg tracer method	balancing method
Particles sucked at 680 mm	73.8	66.6	76.7
Particles sucked at exit	87.4	85.5	83.2

Specifically, too large wood char particles (as fragmentation due to atomisation and devolatilisation was neglected) and too short residence times of wood char particles in the flame region could have led to a lower solid devolatilisation conversion  $X_{\text{dev,solid}}$  and a lower solid carbon conversion  $X_{\text{C,solid}}$ . This observation is confirmed by the balanced solid gasification conversions  $X_{\text{het,solid}}$  that are given in Table 4.13 and were derived from the balanced carbon conversions  $X_{\text{C,solid}}$  assuming balanced solid devolatilisation conversions  $X_{\text{dev,solid}} = 1$  and using the model equations described in Section 2.7.1. The balanced solid gasification conversions  $X_{\text{het,solid}}$  of 66-77 % are already close to the predicted gasification conversions  $X_{\text{het,solid}}$  when using heterogeneous gasification rates increased by a factor of 10. Thus, the predicted solid devolatilisation conversions  $X_{\text{dev,solid}}$  could be too low.

Furthermore, the predicted gas temperature distributions are shown for the REGA experiment TUC5 GHKS10 V1071 in Fig. 4.45 and for the REGA experiment TUC5 GHKS30 V1284 in Fig. 4.46. The flames are thus characterised by irregular, stretched V-shapes with quite high temperatures. In contrast, OH-LIF measurements indicated W-shapes for the REGA experiments TUC5 V1105 and TUC5 GHKS30 V1284 [113, 114] and are also expected by analogy for the REGA experiment TUC5 GHKS10 V1071. Therefore, the injection properties combined with the turbulence-chemistry interaction model and the HVI1 mechanism are likely inappropriate for the REGA experiments TUC5 GHKS10 V1071 and TUC5 GHKS30 V1284.

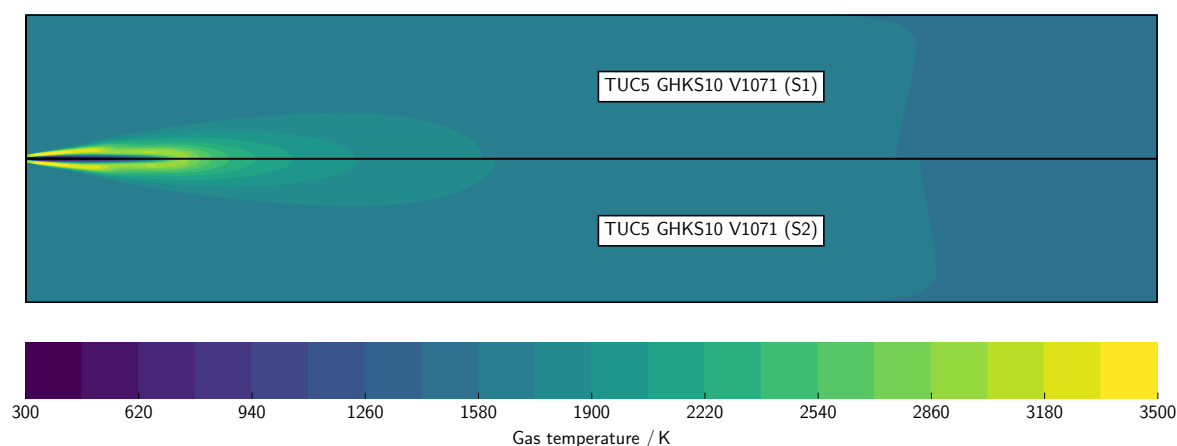


**Figure 4.45:** Predicted gas temperature distributions. TUC5 GHKS10 V1071 (S1): baseline results for the REGA experiment TUC5 GHKS10 V1071; TUC5 GHKS10 V1071 (S2): results for the REGA experiment TUC5 GHKS10 V1071 obtained using devolatilisation rates increased by a factor of 2.

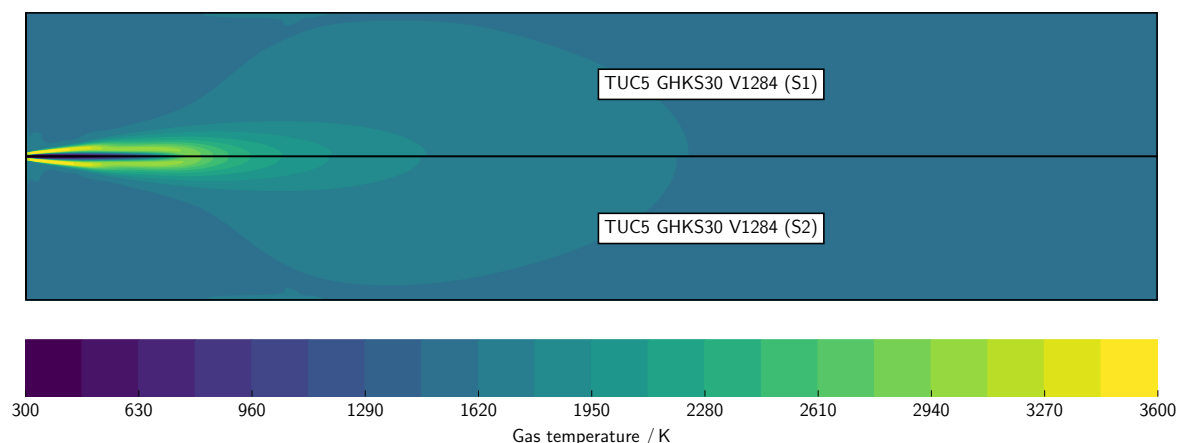


**Figure 4.46:** Predicted gas temperature distributions. TUC5 GHKS30 V1284 (S1): baseline results for the REGA experiment TUC5 GHKS30 V1284; TUC5 GHKS30 V1284 (S2): results for the REGA experiment TUC5 GHKS30 V1284 obtained using devolatilisation rates increased by a factor of 2.

## 5 Conclusions

This thesis has been focussed on the numerical modelling and simulation of the atmospheric entrained flow gasification of ethylene glycol and of mixtures of ethylene glycol and wood char. Firstly, sub-models used for RANS based simulations of atmospheric entrained flow gasification experiments have been described in Chapter 2. Specifically, improved approaches have been presented for the inlet conditions and the injection properties (see Section 2.2.4.4), the supply of infiltrated air and purge nitrogen (see Section 2.2.3.3) and the devolatilisation kinetics (see Section 2.7.4.3). Subsequently, the simulation and evaluation methods have been introduced in Chapter 3. In comparison with preceding works [63, 64, 187], improved implementations and meshes were used to close the elemental and energy balances (see Section 3.1). Finally, the numerical results have been presented and compared with experimental flame shape observations [113, 114], experimental axial droplet velocities [99, 100] and experimental radial profiles of gas temperature and dry gas species concentrations [63, 64, 98, 99, 100] in Chapter 4. The conclusions based on the comparisons and on further analysis of the numerical results are summarised below.

**Sections 2.2.4.4, 4.1 and 4.9** The inlet conditions and the injection properties are decisive for accurate flame predictions of atmospheric entrained flow gasification experiments using RANS based simulations. In comparison with preceding works [63, 64, 187], the flame shapes have been well described for the gasification of ethylene glycol due to appropriate injection properties derived from spray data of atomisation experiments with ethylene glycol. Furthermore, injection properties based on deviating data or deviating methods already altered the flame shape predictions. Injection properties are thus very sensitive for such RANS based simulations. For the gasification of mixtures of ethylene glycol and wood char, adequate injection properties have not been generated in this work as atomisation experiments with ethylene glycol and wood char have been restricted by safety requirements.

**Sections 2.2.3.3, 4.2, 4.8 and 4.9** The infiltrated air and the purge nitrogen were supplied using source terms in the lateral wall boundary layer, whereas preceding works [63, 101, 102, 187] supplied the infiltrated air and the purge nitrogen through the nozzle. With the new approach, the uncertainties in the predictions of the recirculation strength and length can be reduced without decreasing the numerical stability. However, the predictions of the convection and radiation wall heat fluxes

have been interfered at high flow rates of infiltrated air and purge nitrogen, while the prediction of the total heat flux changed less due to the high wall temperatures.

**Sections 4.5 and 4.6** The improved inlet conditions and injection properties slightly changed the far-flame predictions of gas temperature and dry gas species concentrations for the gasification of ethylene glycol compared to the preceding works [63, 64, 187]. The far-flame predictions at nozzle distances of 300 mm and 680 mm were in good agreement with the experimental results. Larger deviations were found in the near-axis region at 300 mm as a result of a too slow mass transfer of ethylene glycol into the gas phase. Compared to the experiments and previous large eddy simulations, the RANS based simulations using the common turbulence, turbulence dispersion, turbulence-chemistry interaction models predicted shorter droplet residence times in the flame region and a significantly weaker mixing of ethylene glycol, recirculating gas and gasification medium.

**Section 4.7** The modified inlet conditions and injection properties did not change the sensitivity of the turbulence model on the overall model predictions. Similar to the preceding works [63, 187], the predictions of gas velocity, recirculation strength and recirculation length clearly changed when using the standard  $k-\epsilon$  model instead of the SST  $k-\omega$  model, while the far-flame predictions of gas temperature and dry gas species concentrations were slightly affected only.

**Sections 4.3 and 4.6** The revised implementations for the vaporisation model significantly changed the mass transfer of ethylene glycol into the gas phase. Specifically, the application of the 1/3 rule for the film factor shifted the mass transfer of ethylene glycol into the gas phase to positions with larger nozzle distances compared to the preceding works [63, 187].

**Sections 3.1 and 4.8** The corrected implementations for the weighted-sum-of-grey-gas model provided numerical results that can confirm previous conclusions concerning the impact of the thermal gas radiation property model. Similar to the preceding work [187], the gas and wall temperatures and the wall radiation heat fluxes were only slightly changed when using a customised weighted-sum-of-grey-gas model instead of a customised grey-gas model for the gasification of ethylene glycol.

**Section 4.5** Three global reaction mechanisms (HVI1, eJL and eJL/A) and two reduced reaction mechanisms (DLR2017/RK and DLR2017/RM) for ethylene glycol were tested using the same numerical set-ups, as different entrained flow gasification models and different solvers were applied in the preceding works [63, 101, 102, 187]. The HVI1 mechanism ensured accurate far-flame predictions of dry gas species concentrations at low stiffness and is therefore recommended for preliminary simulations. In contrast, the eJL mechanism and the eJL/A mechanism are not

---

recommended for future simulations as both mechanisms are characterised by high stiffness. Instead, the DLR2017/RM mechanism should be incorporated since it guarantees reasonable flame and accurate far-flame predictions and is significantly superior to the eJL mechanism and the eJL/A mechanism with respect to computing time and to the DLR2017/RK mechanism with respect to accuracy.

**Section 2.7.4.3** The reaction rates of the devolatilisation kinetics developed for beech wood char are lower than the reaction rates of previous devolatilisation kinetics for fir char [303]. This indicates that customised devolatilisation kinetics should be derived for each wood char to reflect deviating devolatilisation behaviour due to different chemical and physical properties.

**Section 4.10** The far-flame predictions of gas temperature and dry gas species concentrations at nozzle distances of 300 mm and 680 mm for the gasification of mixtures of ethylene glycol and wood char were in good to excellent agreement with the experimental results. While the preceding works were challenged by elemental imbalances [63, 64] or relied on estimated kinetics [101, 102], this work developed a model for the atmospheric gasification of mixtures of ethylene glycol and wood char using particle size distributions, devolatilisation kinetics and heterogeneous gasification kinetics based on experiments. However, the model provided clearly lower predictions for the solid carbon conversion at the nozzle distance of 680 mm compared to the experimental results. This cannot be explained even by significantly increased reaction rates for both devolatilisation and heterogeneous gasification. Therefore, other effects have caused the erroneous predictions. Higher solid carbon conversions can be expected when the wood char particles break up due to both atomisation and devolatilisation and stay longer in the flame region. Furthermore, both the devolatilisation and heterogeneous gasification kinetics only slightly affected the far-flame predictions of gas temperature and dry gas species concentrations at nozzle distances of 300 mm and 680 mm. Accurate far-flame predictions for the atmospheric gasification of mixtures with wood char contents of up to 30 % are thus possible within certain uncertainty limits of the wood char kinetics.

Thus, the improved inlet conditions and injection properties have provided superior flame shape predictions of the gasification experiments with ethylene glycol. Furthermore, the new devolatilisation kinetics combined with heterogeneous gasification kinetics developed in parallel works [156] have been appropriate for far-flame predictions of gasification experiments with mixtures of ethylene glycol and wood char. However, the accuracy of some other models was not sufficient in this work. Specifically, the adopted common models for turbulent mixing and turbulent dispersion led to erroneous predictions of fuel conversion. Furthermore, the incomplete experimental basis for the injection properties was detrimental for appropriate flame shape predictions of the gasification experiments

with mixtures of ethylene glycol and wood char. In summary, RANS based models for the atmospheric entrained flow gasification of surrogate fuels were developed and validated for the far-flame region but may be revised in future studies to improve the mathematical description of the flame region.

Future experimental research should focus on atmospheric atomisation experiments with mixtures of ethylene glycol and wood char and on atmospheric drop-tube reactor experiments with wood char:

1. The atomisation experiments should provide data for the droplet size, droplet velocity and droplet composition distributions.
2. The atmospheric drop-tube reactor experiments with wood char should provide data to improve or validate the heterogeneous gasification kinetics at high-temperature conditions.

Future numerical research should focus on both large eddy simulations and RANS based simulations:

1. Large eddy simulations combined with the volume-of-fluid method should be applied to previous and future atomisation experiments for model validation and verification of the experimental and numerical findings.
2. Large eddy simulations combined with the DLR2017/RM mechanism and the volume-of-fluid method should be applied to the gasification experiments with ethylene glycol. Infiltrated air and purge nitrogen should be provided as source terms in the near boundary layer. However, to reduce the impact on the lateral wall radiation heat flux, the source terms may be defined at the top wall instead of the lateral wall.
3. RANS based simulations of the gasification experiments with mixtures of ethylene glycol and wood char should be continued as soon as spray experiments or large eddy simulations can provide appropriate data for the injection properties. Then, the wood char kinetics compiled in this work can be tested further. If the numerical results are in good agreement with the experimental results, large eddy simulations should be applied to the gasification experiments with mixtures of ethylene glycol and wood char.

# A Plant descriptions

This chapters provides additional information on the bioliq EFG plant in Section A.1 as well as detailed information on the REGA plant in Section A.2, on the ATMO plant in Section A.3 and on the DTR plant in Section A.4.

## A.1 bioliq entrained flow gasifier (bioliq EFG)

**Table A.1:** Characteristic plant properties of the bioliq EFG reactor [87]

Quantity	Value
Operating pressure	40/80 bar
Fuel	slurry and natural gas
Thermal input of slurry	3.5-4.5 MW
Thermal input of natural gas	0-1 MW
Gasifier temperature	1300-2000 K
Adiabatic temperature	1900-2550 K
Residence time	10-15 s
Gas-to-liquid ratio	1-1.8
Stoichiometric ratio	0.45-0.63
Cold gas efficiency	53-72 %
Slurry mass flow rate	650-900 kg/h
Synthesis gas mass flow rate	1200-1800 kg/h
Slag mass flow rate	30-90 kg/h

**Table A.2:** Characteristic properties of slurries applied in the bioliq EFG reactor [87].

Quantity	Value
Lower heating value	14-22 MJ/kg
Solid content	< 30 %
Ash content	3-10 %
Particle sizes	up to 1 mm, usually < 100 $\mu\text{m}$
Viscosity	up to 1 Pa at 70 °C
Pre-heat temperature	40-120 °C

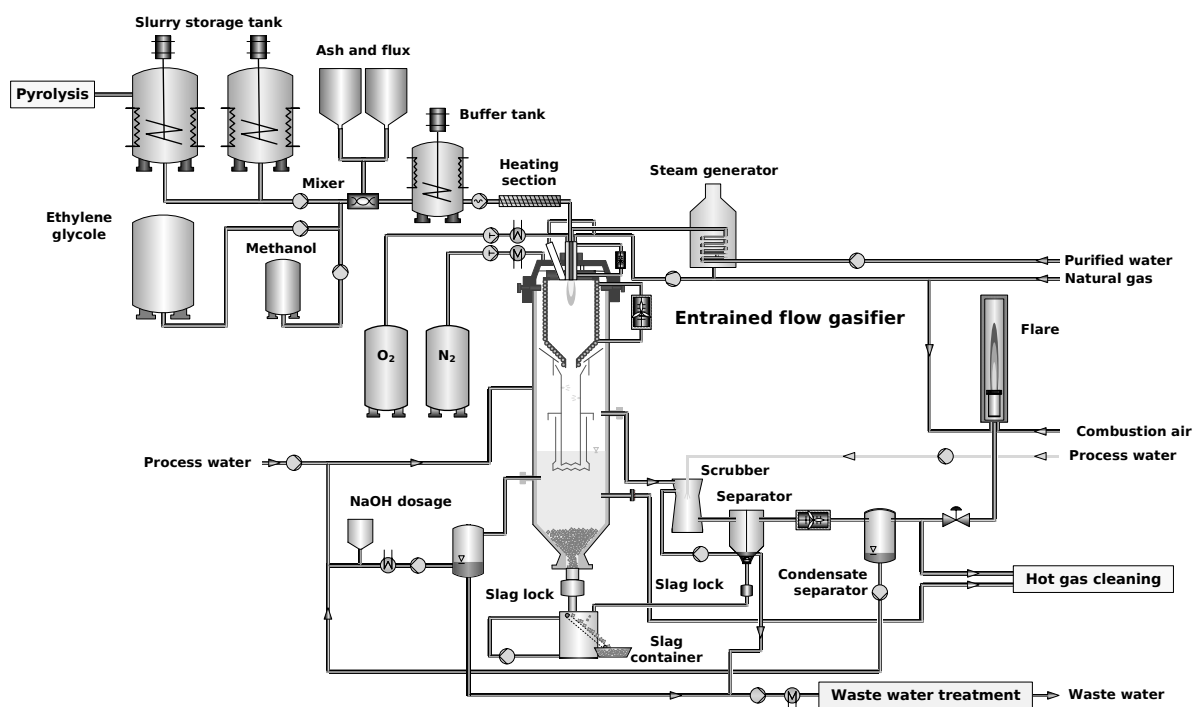


**Figure A.1:** Sketch of the bioliq EFG plant [87].

**Table A.3:** Characteristic properties of synthesis gas produced in the bioliq EFG reactor [87].

Quantity	Value
H <sub>2</sub> volume fraction	26-34 %
CO volume fraction	27-39 %
CO <sub>2</sub> volume fraction	14-28 %
CH <sub>4</sub> volume fraction	< 0.1 %
N <sub>2</sub> volume fraction	12-15 %
H <sub>2</sub> /CO volume fraction ratio	0.75-1.1
Lower heating value	5.5-8.5 MJ/kg
H <sub>2</sub> S and COS volume fraction	50-100 mg/m <sup>3</sup> (STP)
HCl volume fraction	0-300 mg/m <sup>3</sup> (STP)
NH <sub>3</sub> and HCN volume fraction	200-2000 mg/m <sup>3</sup> (STP)
Tar concentration	0-20000 mg/m <sup>3</sup> (STP)
Particle concentration	103-105 mg/m <sup>3</sup> (STP)

**Table A.4:** Characteristic properties of slags discharged from the bioliq EFG reactor [87].

Quantity	Value
Si mass fraction	20-32 %
K mass fraction	10-25 %
Ca mass fraction	5-10 %
Mg mass fraction	1-2 %
P mass fraction	0.7-1.6 %

## A.2 Atmospheric research entrained flow gasifier (REGA)

The atmospheric research entrained flow gasifier (REGA) is used for atmospheric gasification experiments with surrogate and technical fuels and is shown in Figs. A.2 and A.3. The plant consists of five major parts: the fuel and gasification medium supply, the reactor with measurement equipment, the synthesis gas cooler, the quench and the flare for the combustion of the exhaust gas [98].

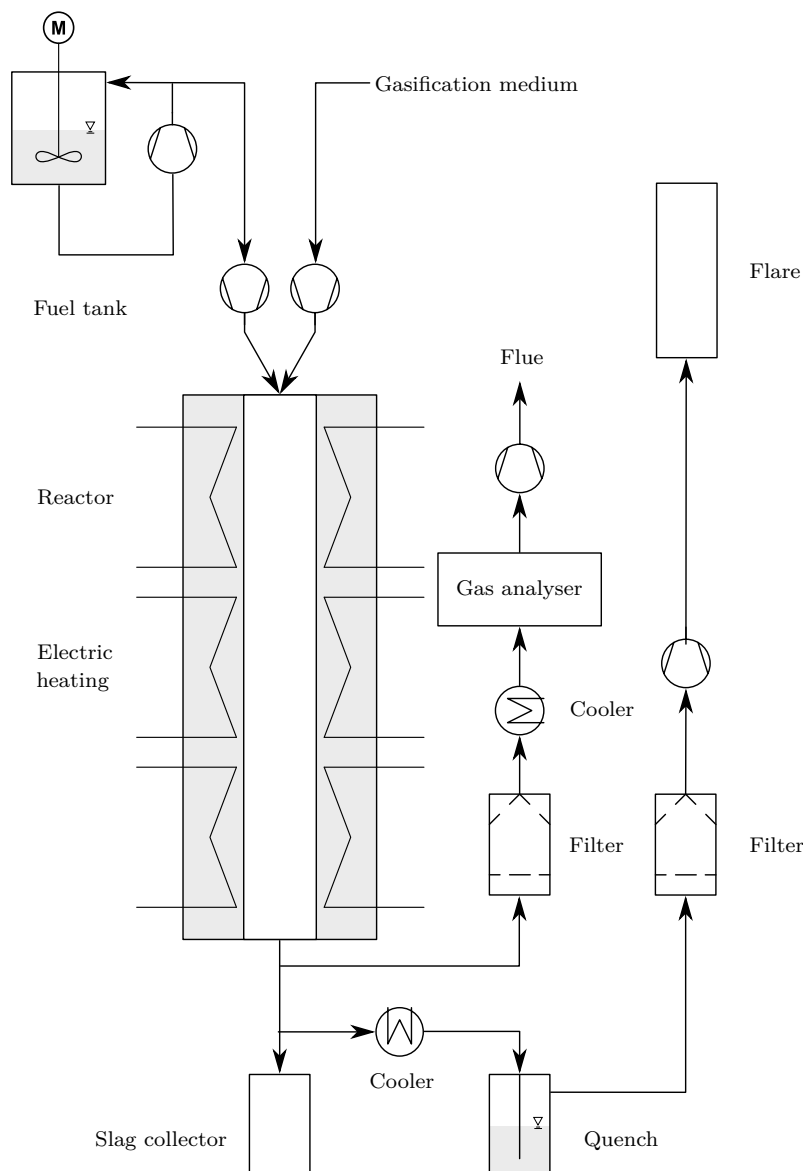


**Figure A.2:** Sketch of the REGA plant [98].

In the fuel and gasification medium supply, the fuel can be heated up to a temperature of 80 °C ensuring the pumpability while the dry air can be enriched with oxygen; the oxygen content in volume fraction is limited to 70 % for safety reasons [98]. Furthermore, nitrogen is provided for purging of the reactor and for purging of the sight glasses which

are used for laser-based measurements. The mass flow rate of the fuel stream is adjusted using a Coriolis mass flow controller while the volume flow rates of the gas streams are determined by thermal flow controllers based on hot wire anemometry [98]. Table A.6 summarises the measurement ranges and the measurement accuracies.

**Table A.5:** Characteristic plant properties of the REGA reactor [98].

Quantity	Value
Operating pressure	atmospheric
Synthesis gas temperature	up to 1600 °C
Wall temperature	up to 1195 °C
Thermal heating power	up to 60 kW
Synthesis gas volume flow rates	up to 80 m <sup>3</sup> /h

**Table A.6:** Measurement ranges and measurement accuracies for the flow rates at the REGA plant [98].

Stream	Measurement range	Measurement accuracy
Fuel	0-20 kg/h	± 0.04 kg/h
Air	0-20 m <sup>3</sup> /h (STP)	± 0.04 m <sup>3</sup> /h (STP)
O <sub>2</sub>	0-20 m <sup>3</sup> /h (STP)	± 0.04 m <sup>3</sup> /h (STP)
N <sub>2</sub>	0-4.2 m <sup>3</sup> /h (STP)	± 0.004 m <sup>3</sup> /h (STP)

The reactor consists of a cylindrical ceramic tube with multiple lateral ports and of a vertically movable top [136]. This enables measurements at a large continuous range of nozzle distances [136]. The insulated tube has got an inner diameter of 280 mm and a length of 2772 mm (see Fig. C.3) and can be heated up to a maximum temperature of 1195 °C using three lateral electric heating zones [136]. The heat loss of the gasifier is consequently minimised enabling near-adiabatic operating conditions [136]. The top is insulated and has a round opening for the burner nozzle [136]. The nozzle configuration can be adapted with respect to dimension, angle of attack and fluid arrangement. The reactor operates under slightly sub-atmospheric pressure for safety reasons and for minimising air infiltration. The mean gas residence times are approximately 1-10 s [98, 136].

In addition to laser-based measurements, intrusive measurements are carried out:

- Gas temperatures are measured using ceramic shielded type S thermocouples at fixed axial positions and using type B double bead thermocouples with bead diameters of 300 µm and 1500 µm at variable positions. Temperatures of the bead thermocouples are corrected by accounting for radiation and assuming a wall temperature of 1200 °C [96, 98].
- Gas species concentrations are determined at outlet and at variable positions. For this purpose, gas samples are extracted from the reactor using cooled steel probes with a

ceramic tip, then quenched by thermal oil at 80 °C and filtered [98]. After further cooling to 3 °C, gas sub-samples are analysed based on standard measurement principles (ABB) and micro gas chromatography (Agilent Technologies 490 Micro GC); concentrations of CH<sub>4</sub>, CO, CO<sub>2</sub>, H<sub>2</sub>, O<sub>2</sub> and N<sub>2</sub> are determined as dry volume fractions [98, 99, 100]. In addition, the concentration of organic carbon is measured as (wet) mass concentration [98]. In order to reduce measurement uncertainties including uncertainties due to cross sensitivities of CO and CO<sub>2</sub> in NDIR sensors, the gas analysers are calibrated using reference gases with compositions comparable to synthesis gas [98, 99, 100]. Table A.7 lists the measurement principles applied and the measurement ranges (in volume fractions). Standard measurement methods (ABB) are usually applied for the major species and are affected by relative maximum uncertainties of ± 2 % [98, 99, 100].

**Table A.7:** Measurement principles and measurement ranges (in volume fractions) for gas species concentrations at the REGA plant [98].

Species	Measurement principle	Measurement range
CH <sub>4</sub>	NDIR (ABB)	0-0.10
CO	NDIR (ABB)	0-0.50
CO <sub>2</sub>	NDIR (ABB)	0-0.30
H <sub>2</sub>	Thermal conductivity (ABB)	0-0.50
O <sub>2</sub>	Paramagnetism (ABB)	0-0.15
CH <sub>4</sub>	μGC (Agilent Technologies)	0-10 %
CO	μGC (Agilent Technologies)	0-50 %
CO <sub>2</sub>	μGC (Agilent Technologies)	0-30 %
H <sub>2</sub>	μGC (Agilent Technologies)	0-50 %

- Particles are extracted from the reactor using a ceramic suction probe and a high-separation, high-temperature candle filter operating at a temperature of 300 °C and a volume flow rate of 2 m<sup>3</sup>/h (STP) [99]. In order to obtain a sufficient amount of particles, suction is carried out for up to 2 h [99].
- Droplet velocities and droplet diameters are determined using a two-dimensional Phase-Doppler Anemometry (PDA) system operating in backward scattering mode due to the limited optical access into the reactor and applying a lens with 1000 mm focal length [98].
- OH-LIF images are determined using an image intensifier (LaVision IRO), using a CMOS-camera (LaVision Imager M-Lite 2M) and using a bandpass filter (LaVision, λ = 320 nm, FWHM = 40 nm) [114]. Images are recorded in 20 mm steps with 500 images at each position and are subsequently averaged and corrected [114].

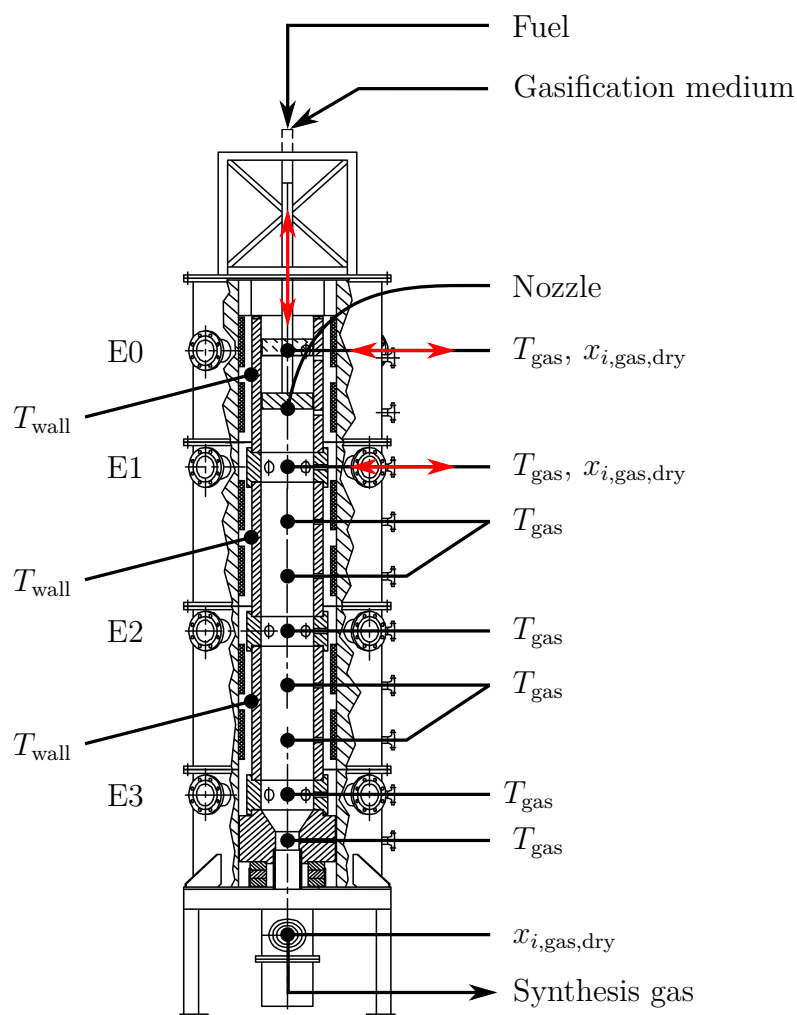


**Figure A.3:** Sketch of the REGA reactor [98].

### A.3 Atmospheric spray test rig (ATMO)

The atmospheric spray test rig (ATMO) is used for atmospheric atomisation experiments and is shown in Fig. A.4. It is composed of four parts: the liquid and compressed air supply, the atomiser mounted on a lance and positioned in an open surrounding, the measurement equipment and a collecting tank.

**Table A.8:** Characteristic plant properties of the ATMO plant [265].

Quantity	Value
Operating pressure	atmospheric
Operating temperature	10-50 °C
Liquid mass flow rate	5-50 kg/h
Air mass flow rate	0-20 kg/h
Liquid viscosity	1-1000 mPa s

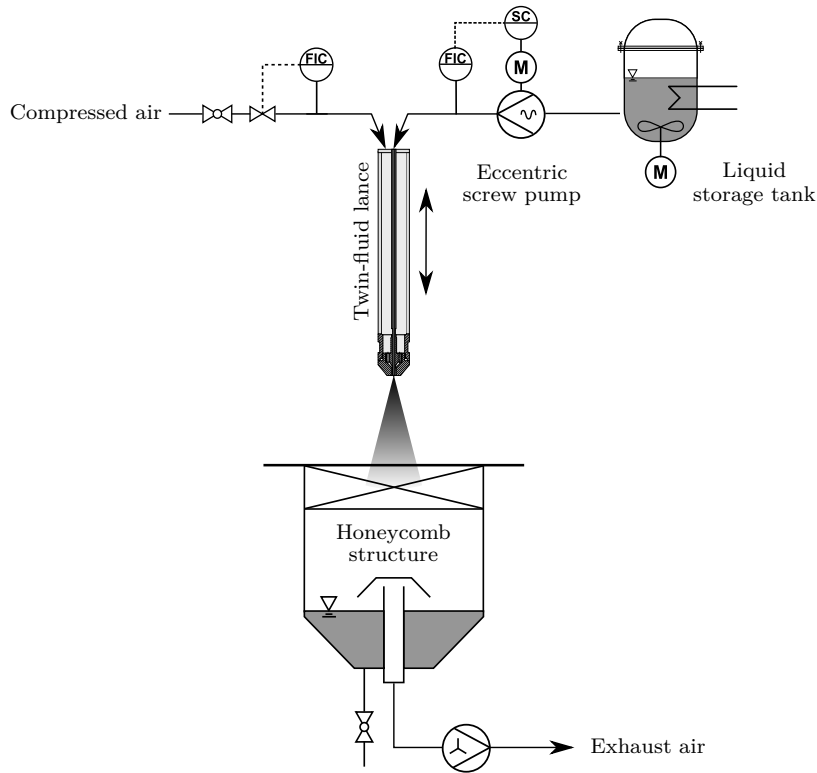


**Figure A.4:** Sketch of the ATMO plant [265].

The compressed air is provided from an internal network to the lance with a pressure up to 5 bar while the liquid is transported from an atmospheric stirred tank to the lance using an eccentric screw pump [265]. The tank can be heated up to a temperature of 80 °C in order to enable the use of liquids with viscosities between 1 mPa s and 1000 mPa s [265]. Mass flow rates of liquid are determined by a Coriolis mass flow controller, and the mass flow rates of air are measured by a volume flow controller based on the principle of electromagnetic induction [265].

After atomisation and passing the measurement plane, the liquid enters the collecting tank via a honeycomb structure [265]. The honeycomb structure straightens the flow and avoids recirculation of droplets [265]. In the collecting tank, the liquid is separated from the air using an impact plane [265].

In addition to two-dimensional Phase-Doppler Anemometry measurements for droplet size and droplet velocity distributions, high-speed camera and shadow-sizer imaging are carried out. All measurements are evaluated using the spray characterisation toolbox *SprayCat* [265]. Detailed description of the measurement and evaluation techniques applied can be found elsewhere [265].

## A.4 Drop-tube reactor (DTR)

The drop-tube reactor (DTR) is applied for atmospheric, high-temperature experiments with solid fuels and is shown in Fig. A.5. It consists of the fuel and gas supply, the reactor, the gas phase measurement unit and the particle extraction unit.

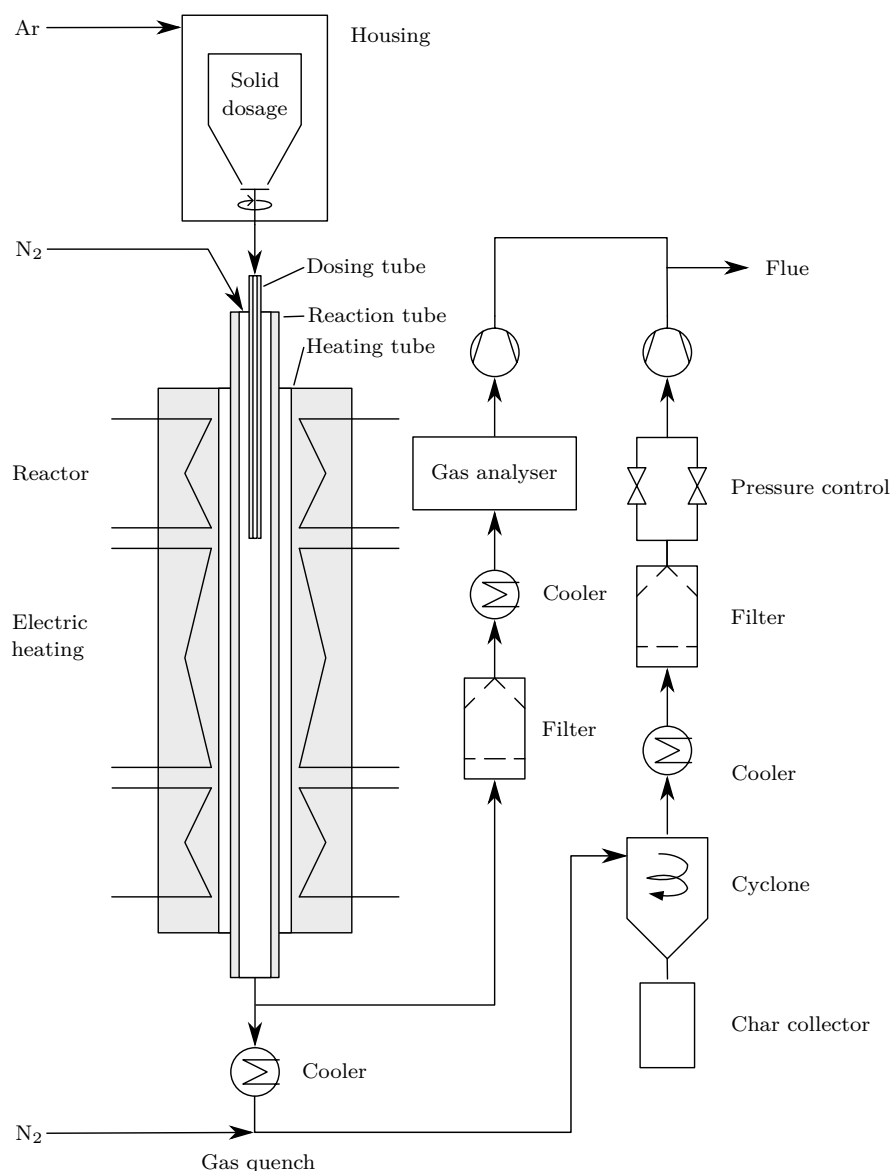


**Figure A.5:** Sketch of the DTR plant [279].

The reactor, which is based on a commercial oven (HTM Reetz LORA1700-70-30), consists of an outer enclosure with insulation and heating and of three ceramic tubes made of  $\text{Al}_2\text{O}_3$  (see also Fig. C.4): a heating tube, a reaction tube and a dosing tube [68]. The heating tube (length: 1800 mm, inner diameter: 70.5 mm, thickness: 6.25 mm) is wrapped with W-Mo heating coils [68]. The heating coils, flushed with Ar and combined with a control system (HTM Reetz), provide three heating zones with lengths of 200 mm,

920 mm and 200 mm [68]. The upper heating zone is used for heating-up of both gas and solid [68] up to maximum temperatures of 1650 °C for long-term operation and of 1700 °C for short-term operation. The centre heating zone is assumed to be isothermal, and the lower heating zone is used to reduce the heat loss at outlet [68]. The reaction tube (length: 2100 mm, inner diameter: 20 mm), thickness: 2.5 mm) is positioned axially inside the heating tube, while the dosing tube (length: 810 mm, inner diameter: 4 mm, thickness: 1 mm) is inserted into the reaction tube in such a way that the lower end is located at the beginning of the second heating zone [68]. At the upper end of the dosing tube, a powder disperser (Schenck Process PureFeed DP-4) is mounted [68]. Solid particles filled in the disperser are fed to a gas stream, that enters the dosing tube, using a speed-controlled scale and a hopper [68]. Another gas stream enters the reactor through the annular gap between the dosing and the working tube [68]. Both gas streams are controlled using pre-calibrated mass flow controllers (Bronkhorst EL-Flow) [68]. The dosing stream contains Ar while N<sub>2</sub> or CO<sub>2</sub> may be used for the annular gap stream [68]. The reactor is operated under slightly super-atmospheric pressure [68]. The pressure is measured at the reaction tube inlet and is controlled using two valves and a vacuum pump located after the particle extraction unit [68].

**Table A.9:** Characteristic plant properties of the DTR plant [303].

Quantity	Value
Operating pressure	atmospheric
Gas temperature	up to 1700 °C
N <sub>2</sub> volume flow rates	0-40 l/min
CO <sub>2</sub> volume flow rates	0-40 l/min
Ar volume flow rates	0-10 l/min
Solid mass flow rates	1-10 g/min
Residence times in isothermal zone	≈ 0.1-1 s
Solid particle diameters	3-200 μm

At the outlet of the reaction tube, gas samples are extracted from the gas stream and are subsequently filtered, quenched and transferred to a micro gas chromatograph (Agilent Technologies 490 Micro GC), which is calibrated using reference gases [68]. After the sample extraction, the gas stream is quenched by a cooler and N<sub>2</sub> and enters a cyclone separator [68]. After separation of most of the particles, the remaining particles are collected using a candle filter (HEPA) [68].

In addition to continuous gas species concentration measurements, single temperature measurements using a type B thermocouple are performed at the outer surfaces of the reaction tube and the dosing tube while temperature measurements inside the reactor are carried out by introducing the type B thermocouple through the inlet of the reactor [68]. The latter measurements are used for the calibration of the heating zones [68].



## **B Gasification experiments**

**Table B.1:** Inlet conditions of the REGA experiments [63, 64, 98, 99, 100, 113, 187].  $\dot{m}_{\text{fuel}}$ : fuel mass flow rate,  $\dot{V}_{\text{air,STP}}$ : air volume flow rate (STP),  $\dot{V}_{\text{O}_2,\text{STP}}$ : oxygen volume flow rate (STP),  $\dot{V}_{\text{N}_2,\text{STP}}$ : nitrogen volume flow rate (STP),  $\dot{V}_{\text{inf,STP}}$ : infiltrated air volume flow rate (STP),  $\vartheta_{\text{nozzle}}$ : Celsius temperature at nozzle,  $T_{\text{nozzle}}$ : absolute temperature at nozzle,  $u_{\text{gas,nozzle}}$ : gas velocity at nozzle,  $p_{\text{op}}$ : operating pressure. Acronyms: G: ethylene glycol; GHKS10: 90% ethylene glycol + 10% wood char HK01; GHKS30: 70% ethylene glycol + 30% wood char HK07; STP: standard conditions according to ISO 10780:1994 [133]. Further details about the external mixing nozzles D1, D1.1 and D2 and the wood chars HK01 and HK07 are given in Section C.1 and Sections 2.7.1 and I.1, respectively.

REGA experiment	Fuel	Nozzle	$\dot{m}_{\text{fuel}}$ kg/h	$\dot{V}_{\text{air,STP}}$ m <sup>3</sup> /h	$\dot{V}_{\text{O}_2,\text{STP}}$ m <sup>3</sup> /h	$\dot{V}_{\text{N}_2,\text{STP}}$ m <sup>3</sup> /h	$\dot{V}_{\text{inf,STP}}$ m <sup>3</sup> /h	$\vartheta_{\text{nozzle}}$ °C	$T_{\text{nozzle}}$ K	$u_{\text{gas,nozzle}}$ m/s	$p_{\text{op}}$ Pa
TUC2 V468	G	D1	8.1289	8.2656	3.7370	0.5137	1.1323	38.00	311.15	112.88	99920
TUC3 V479	G	D1	12.5560	7.0030	4.9710	0.5132	1.2390	38.03	311.17	112.62	99920
TUC3 V786	G	D1	12.5612	7.0259	4.9787	0.5132	1.5030	42.51	315.66	114.53	99914
TUC5 V1105	G	D2	12.4192	2.9215	4.5823	0.0000	0.2595	36.69	309.84	162.18	99900
TUC5 V1374	G	D1.1	12.4182	2.9178	4.5840	0.0000	0.9607	34.47	307.62	160.97	99852
TUC5 GHKS10 V1071	GHKS10	D2	12.4533	2.8404	4.8934	0.0000	0.2674	36.20	309.35	166.89	99800
TUC5 GHKS30 V1284	GHKS30	D2	12.7594	2.0597	5.4429	0.0000	0.4988	42.24	315.39	165.06	99851

**Table B.2:** Characteristic parameters of the REGA experiments [63, 64, 98, 99, 100, 113, 187].  $\text{SMOD}_{\text{STP}}$ : specific minimum oxygen demand (STP),  $\lambda_{\text{tech}}$ : technical stoichiometric ratio,  $\lambda_{\text{abs,w/o inf}}$ : absolute stoichiometric ratio neglecting infiltrated air and purge nitrogen,  $\lambda_{\text{abs,w/inf}}$ : absolute stoichiometric ratio accounting for infiltrated air and purge nitrogen,  $\vartheta_{\text{ad}}$ : adiabatic Celsius temperature,  $T_{\text{ad}}$ : adiabatic absolute temperature, GLR: gas-to-liquid ratio.

REGA experiment	$\frac{\text{SMOD}_{\text{STP}}}{\text{m}^3/\text{kg}}$	$\lambda_{\text{tech}}$	$\lambda_{\text{abs,w/o inf, air}}$	$\lambda_{\text{abs,w/inf, air}}$	$\frac{\vartheta_{\text{ad}}}{\text{°C}}$	$\frac{T_{\text{ad}}}{\text{K}}$	GLR
TUC2 V468	0.8982	0.750	0.822	0.845	2403.53	2676.68	1.965
TUC3 V479	0.8983	0.571	0.692	0.708	2008.56	2281.71	1.283
TUC3 V786	0.8983	0.572	0.692	0.712	2011.24	2284.39	1.286
TUC5 V1105	0.8983	0.466	0.619	0.622	1699.78	1972.93	0.830
TUC5 V1374	0.8983	0.466	0.619	0.631	1700.49	1973.64	0.829
TUC5 GHKS10 V1071	0.9740	0.453	0.592	0.596	1767.38	2040.53	0.855
TUC5 GHKS30 V1284	1.0958	0.420	0.539	0.543	1698.21	1971.36	0.817

**Table B.3:** Inlet conditions applied for the REGA simulations [63, 64, 98, 99, 100, 113, 187].  $\dot{m}_{\text{air}}$ : air mass flow rate,  $\dot{m}_{\text{O}_2}$ : oxygen mass flow rate,  $\dot{m}_{\text{N}_2}$ : nitrogen mass flow rate,  $\dot{m}_{\text{inf, air}}$ : infiltrated air mass flow rate,  $\dot{m}_{\text{inlet}}$ : inlet mass flow rate,  $w_{\text{O}_2, \text{inlet}}$ : oxygen mass fraction at inlet,  $w_{\text{N}_2, \text{inlet}}$ : nitrogen mass fraction at inlet,  $\dot{m}_{\text{at wall}}$ : mass flow rate at wall,  $w_{\text{O}_2, \text{at wall}}$ : oxygen mass fraction at wall,  $w_{\text{N}_2, \text{at wall}}$ : nitrogen mass fraction at wall.

REGA experiment	$\frac{\dot{m}_{\text{fuel}}}{\text{kg/h}}$	$\frac{\dot{m}_{\text{air}}}{\text{kg/h}}$	$\frac{\dot{m}_{\text{O}_2}}{\text{kg/h}}$	$\frac{\dot{m}_{\text{N}_2}}{\text{kg/h}}$	$\frac{\dot{m}_{\text{inf, air}}}{\text{kg/h}}$	$\frac{\dot{m}_{\text{inlet}}}{\text{kg/h}}$	$\frac{\dot{m}_{\text{at wall}}}{\text{kg/h}}$	$w_{\text{O}_2, \text{at wall}}$	$w_{\text{N}_2, \text{at wall}}$
TUC2 V468	8.1289	10.6392	5.3351	0.6420	1.4574	15.9743	2.0995	0.1617	0.8383
TUC3 V479	12.5560	9.0140	7.0967	0.6412	1.5948	16.1107	2.2359	0.1661	0.8339
TUC3 V786	12.5612	9.0435	7.1077	0.6412	1.9346	16.1512	2.5758	0.1749	0.8251
TUC5 V1105	12.4192	3.7604	6.5418	0.0000	0.3340	10.3023	0.3340	0.2329	0.7671
TUC5 V1374	12.4182	3.7557	6.5443	0.0000	1.2366	10.3000	1.2366	0.2329	0.7671
TUC5 GHKS10 V1071	12.4533	3.6561	6.9859	0.0000	0.3442	10.6420	0.3442	0.2329	0.7671
TUC5 GHKS30 V1284	12.7594	2.6511	7.7704	0.0000	0.6421	10.4215	0.6421	0.2329	0.7671



# C Technical drawings

This chapter provides the simplified technical drawings for the CFD geometries. The drawings of the nozzles are summarised in Section C.1 while the drawings of the reactors are given in Section C.2.

## C.1 Nozzles

In the ATMO and REGA experiments, four different twin fluid external mixing nozzles were applied for atomisation: D1, D2, D1.1 and D2.1. The cross-sections of the lower parts of the nozzles D1 and D2 are shown in Fig. C.1 while the cross-sections of the lower parts of the nozzles D1.1 and D2.1 are depicted in Fig. C.2. All nozzles are characterised by central ducts and first cylindrical and then concentric annuli. The continuous liquid or slurry is typically fed through the central ducts while the gas is supplied through the annuli. The nozzle D1 was used in the ATMO experiment TUC3 D1 and in the REGA experiments TUC3 V479 and TUC3 V786 while the nozzle D2 was applied in the ATMO experiment TUC5 D2 and in the REGA experiments TUC5 V1105, TUC5 GHKS10 V1071 and TUC5 GHKS30 V1284. The nozzles D1.1 and D2.1 are modified versions of the original nozzles and were used in the ATMO experiments TUC5 D1.1 and TUC5 D2.1 and in the REGA experiment V1374. The cross-sections of the nozzles D1 and D2 were only accounted for in the preceding works [63, 64, 185, 186, 187].

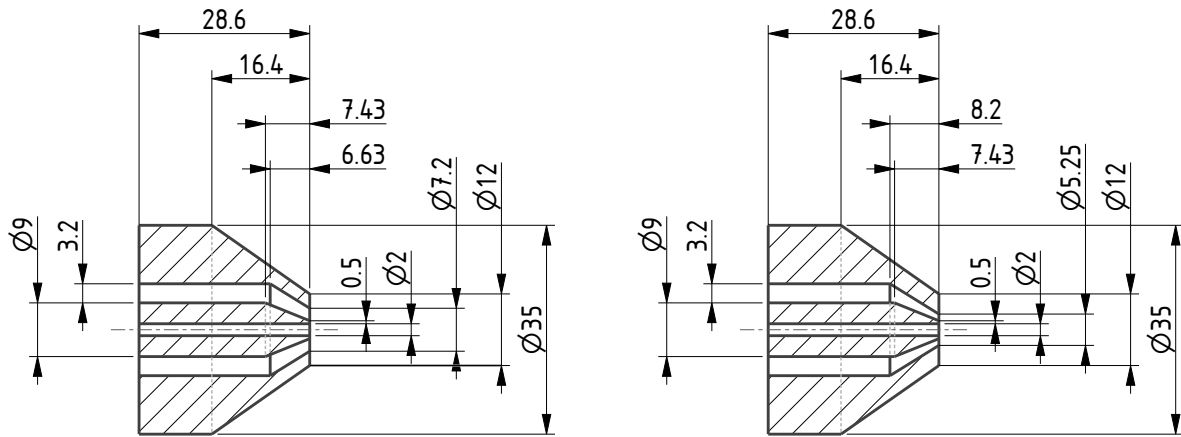


Figure C.1: Cross-sections of nozzle D1 (left) and nozzle D2 (right) [98, 99]. Dimensions are given in mm.

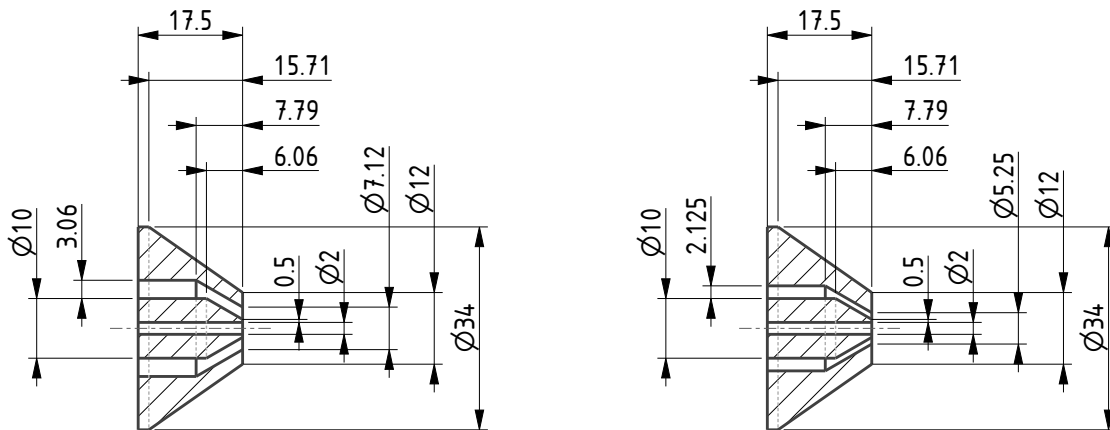


Figure C.2: Cross-sections of nozzle D1.1 (left) and nozzle D2.1 (right) [113]. Dimensions are given in mm.

## C.2 Reactors

The cross-sections of the REGA reactor and the DTR reactor are shown in Fig. C.3 and in Fig. C.4, respectively.

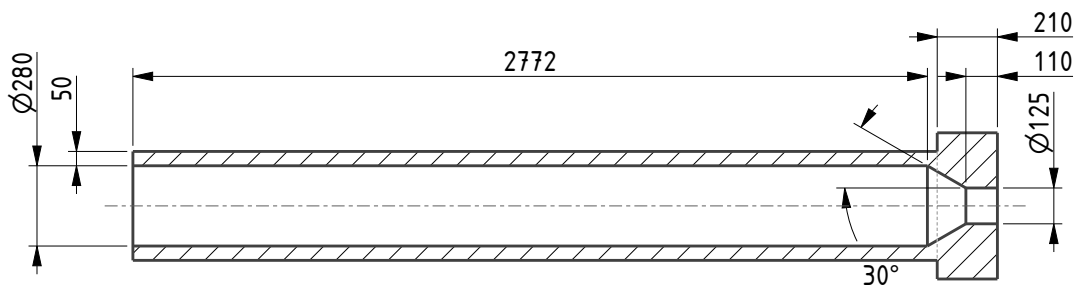
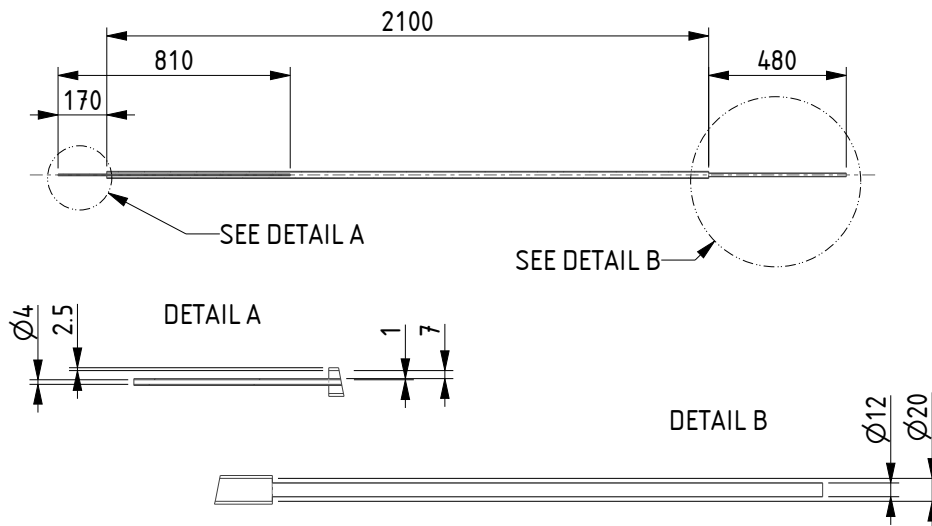


Figure C.3: Cross-section of the REGA reactor. Dimensions are given in mm.



**Figure C.4:** Cross-section of the DTR reactor. Dimensions are given in mm.



# D Experimental results

This chapter summarises some experimental results of the ATMO experiments and the REGA experiments. Section D.1 provides the droplet diameter distributions of the ATMO experiments TUC3 D1, TUC5 D2, TUC5 D2.1 and TUC5 D2.1 and the characteristic values of the ATMO experiments TUC3 D1 and TUC5 D2. Section D.2 lists the data from the REGA experiments.

## D.1 ATMO experiments

The droplet diameter distributions of the ATMO experiments TUC3 D1, TUC5 D2, TUC5 D2.1 and TUC5 D2.1 are depicted in Section D.1.1. The characteristic values of the ATMO experiments TUC3 D1 and TUC5 D2 are shown in Section D.1.2.

### D.1.1 Droplet diameter distributions

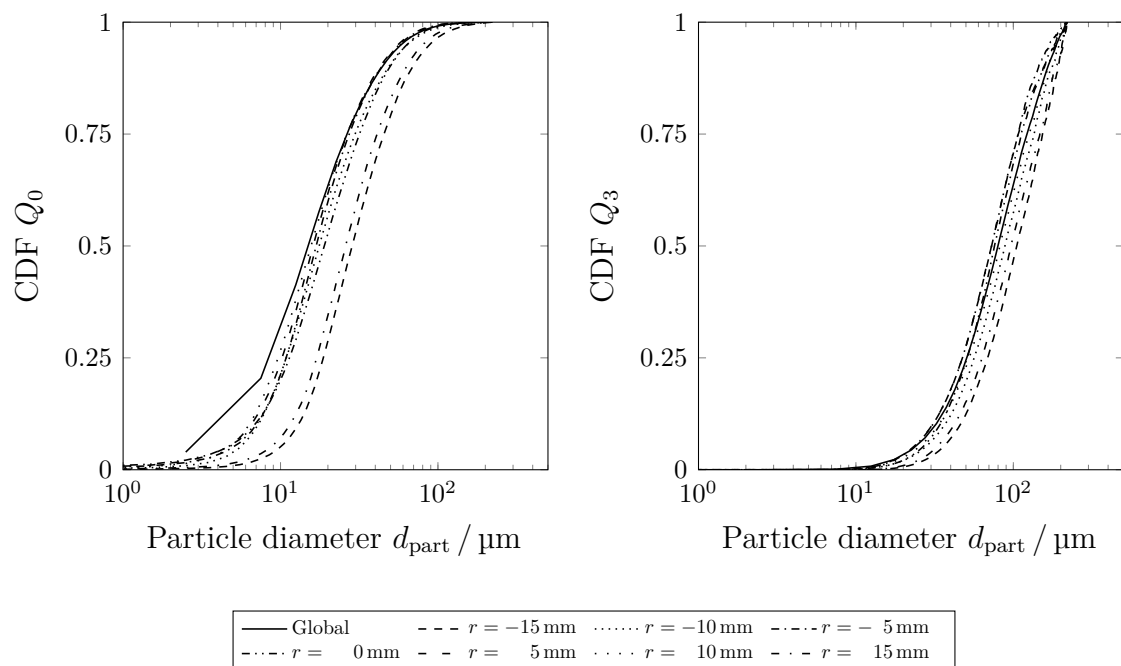


**Figure D.1:** Number-based cumulative distributions  $Q_0$  and mass-based cumulative distributions  $Q_3$  of the particle diameters at various radial positions based on the ATMO experiment TUC3 D1 [98, 137].

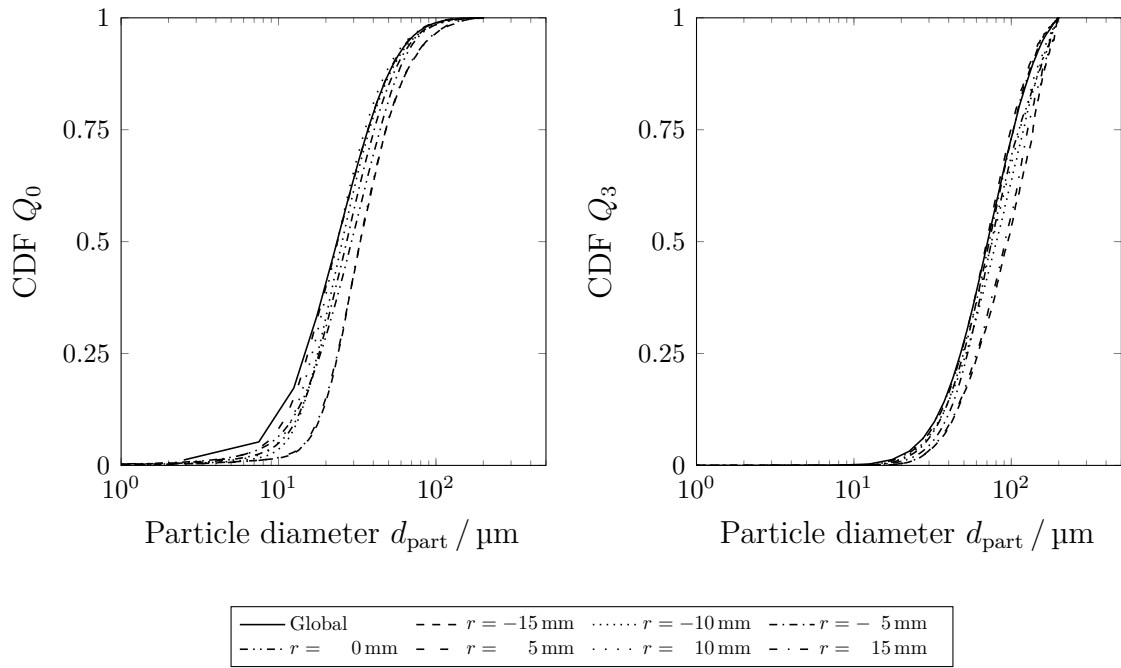


**Figure D.2:** Number-based cumulative distributions  $Q_0$  and mass-based cumulative distributions  $Q_3$  of the particle diameters at various radial positions based on the ATMO experiment TUC5 D2 [137].

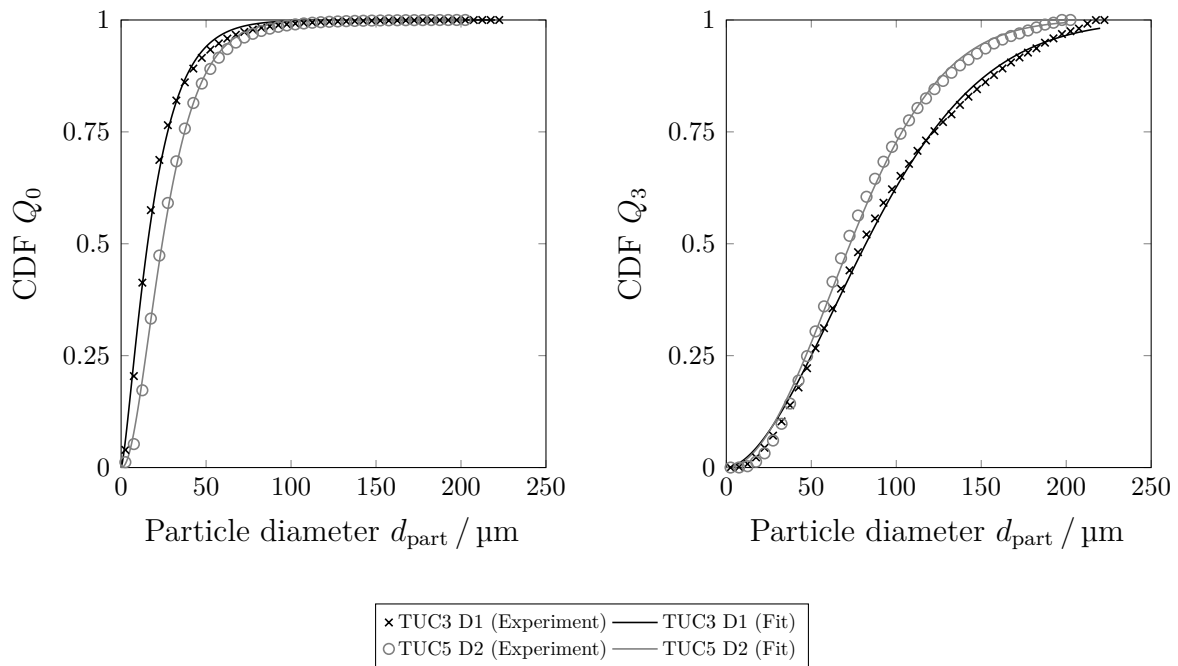


**Figure D.3:** Global number-based cumulative distributions  $Q_0$  and global mass-based cumulative distributions  $Q_3$  of the particle diameters based on the ATMO experiments TUC3 D1 and TUC5 D2 [98, 137]. Fits for the global number-based cumulative distributions  $Q_0$  were obtained using gamma distribution while fits for the global mass-based cumulative distributions  $Q_3$  were determined using Weibull distributions.

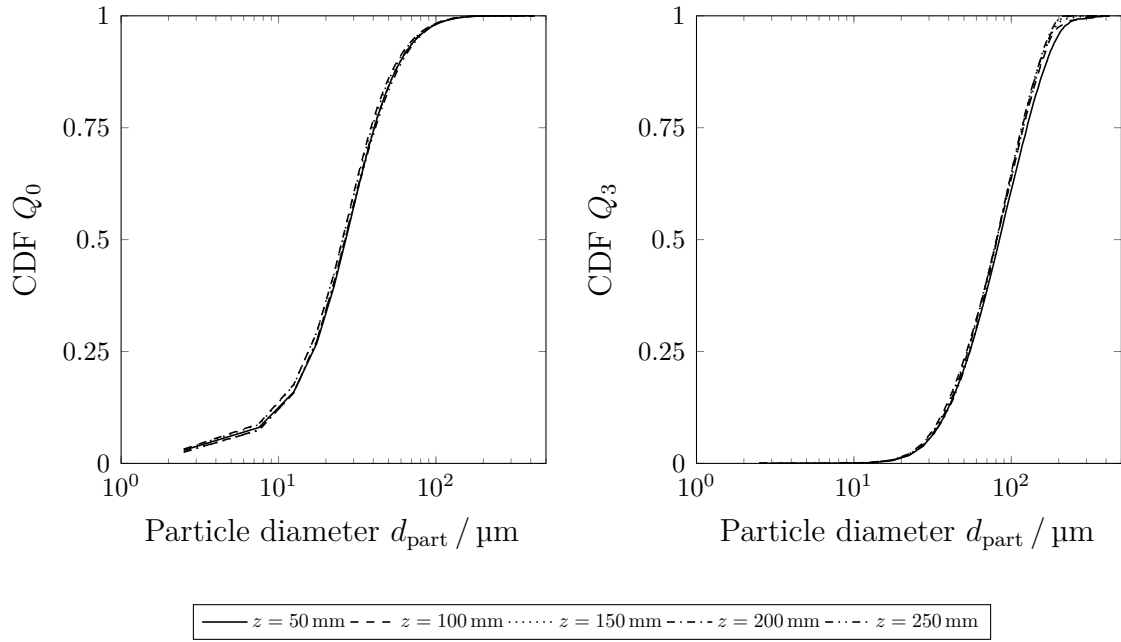


**Figure D.4:** Number-based cumulative distributions  $Q_0$  and mass-based cumulative distributions  $Q_3$  of the particle diameters at various axial positions based on the ATMO experiment TUC5 D2.1 [98, 137, 113].

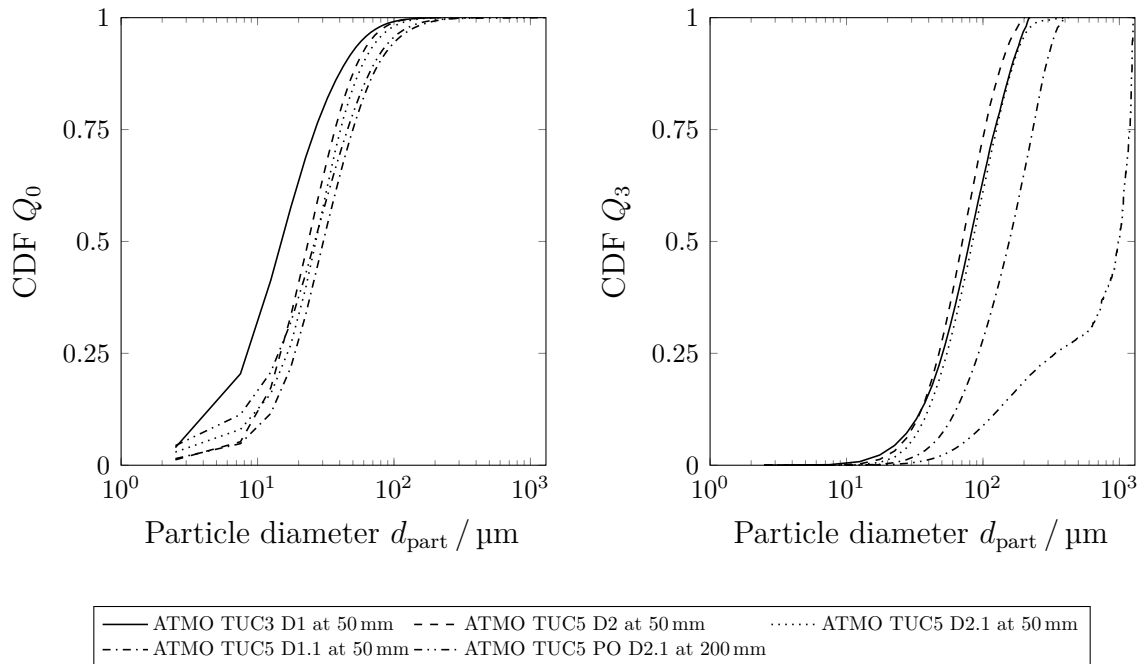


**Figure D.5:** Number-based cumulative distributions  $Q_0$  and mass-based cumulative distributions  $Q_3$  of the particle diameters based on the ATMO experiments TUC3 D1, TUC5 D2, TUC5 D1.1, TUC5 D2.1 and TUC5 PO D2.1 [113].

## D.1.2 Characteristic values

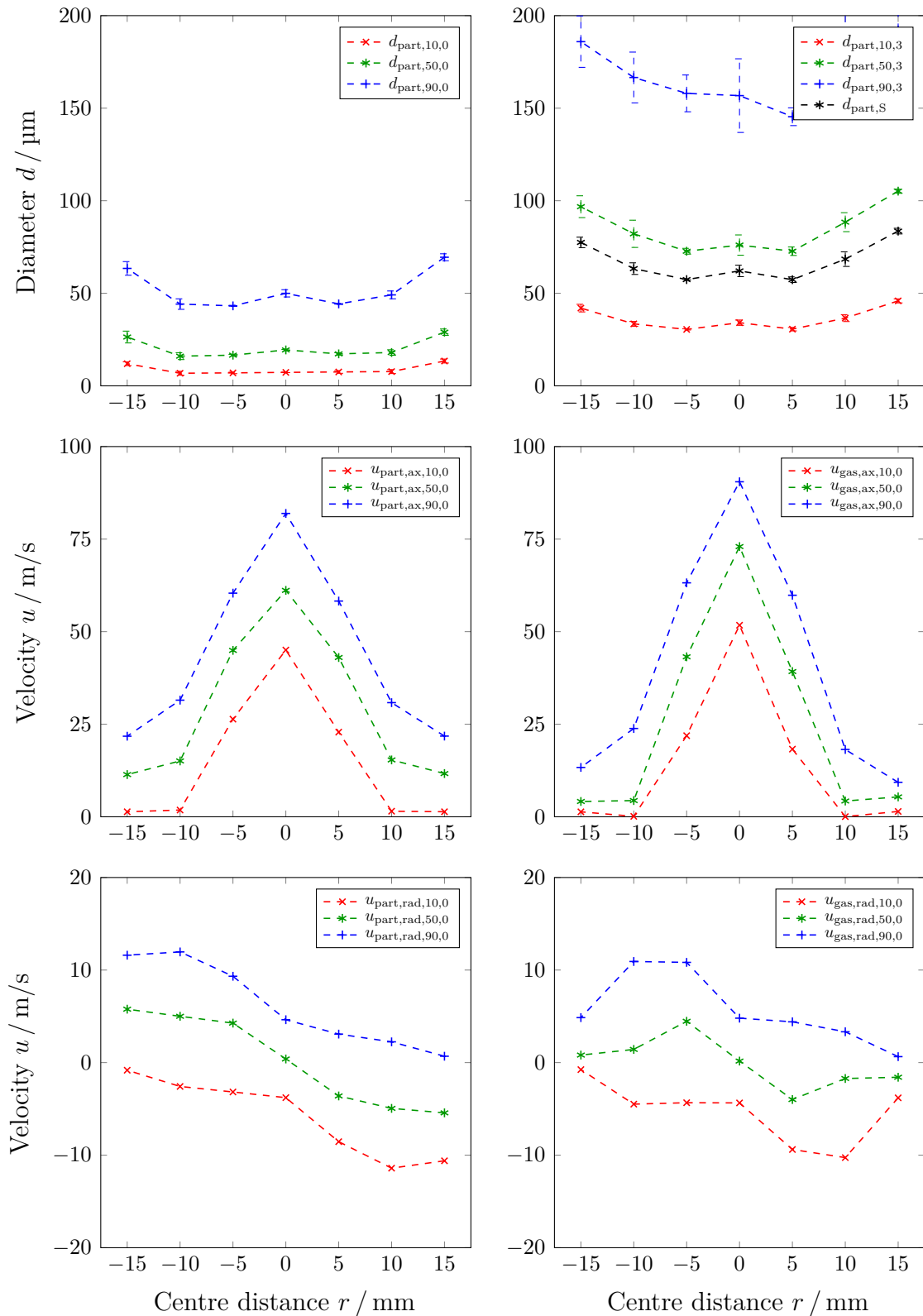


**Figure D.6:** Characteristic particle diameters  $d_{\text{part}}$ , characteristic axial particle velocities  $u_{\text{part,ax}}$ , characteristic radial particle velocities  $u_{\text{part,rad}}$ , characteristic axial gas velocities  $u_{\text{gas,ax}}$  and characteristic radial gas velocities  $u_{\text{gas,rad}}$  based on the ATMO experiment TUC3 D1 [98, 137]. Subscripts: 10,0: number-based 10th percentile value; 10,3: mass-based 10th percentile value; 50,0: number-based 50th percentile value; 50,3: mass-based 50th percentile value; 90,0: number-based 90th percentile value; 90,3: mass-based 90th percentile value; S: Sauter.

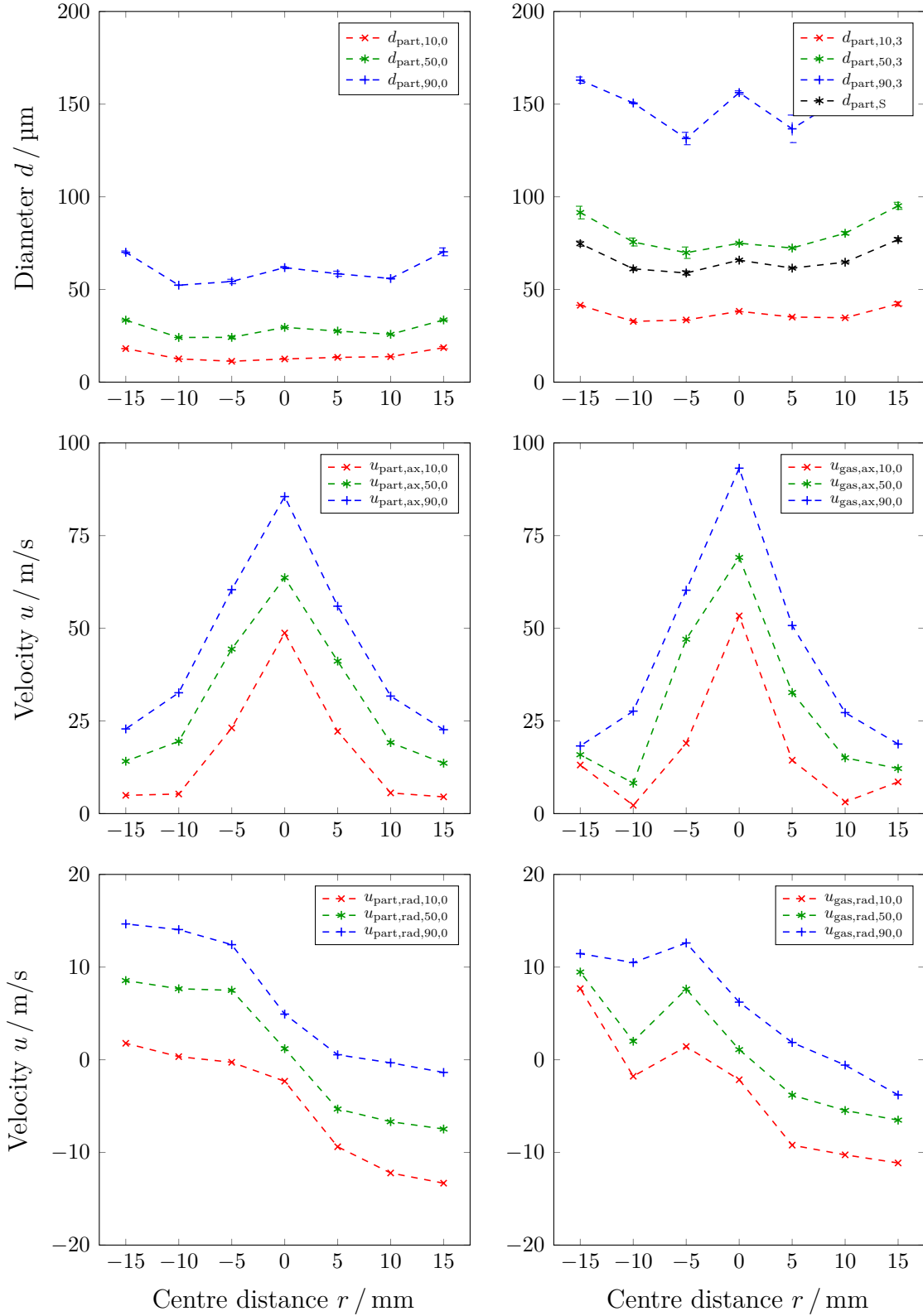


**Figure D.7:** Characteristic particle diameters  $d_{\text{part}}$ , characteristic axial particle velocities  $u_{\text{part,ax}}$ , characteristic radial particle velocities  $u_{\text{part,rad}}$ , characteristic axial gas velocities  $u_{\text{gas,ax}}$  and characteristic radial gas velocities  $u_{\text{gas,rad}}$  based on the ATMO experiment TUC5 D2 [98, 137]. Subscripts: 10,0: number-based 10th percentile value; 10,3: mass-based 10th percentile value; 50,0: number-based 50th percentile value; 50,3: mass-based 50th percentile value; 90,0: number-based 90th percentile value; 90,3: mass-based 90th percentile value; S: Sauter.

## D.2 REGA experiments

The measured profiles of gas temperature, dry gas species volume fraction and axial droplet velocity, used in Chapters 4 and J, are given in Tables D.1 and D.2. Note that the undisturbed sections of the radial profiles of gas temperatures and dry gas species volume fractions were mirrored for each experiment (see [98, 99, 100]).

**Table D.1:** Measured axial droplet velocities  $u_{\text{part,ax}}$  from the REGA experiments [98, 99].

REGA experiment	$\frac{x_1}{\text{mm}}$	$\frac{x_2}{\text{mm}}$	$\frac{u_{\text{part,ax}}}{\text{m/s}}$
TUC3 V479 / TUC3 V786	30	0	66.8
	40	0	70.1
	50	0	73.8
	60	0	75.0
	70	0	76.4
	80	0	77.0
	90	0	77.3
	100	0	72.8
	125	0	71.8
	150	0	72.1
	190	0	71.9
210	0	70.3	
TUC5 V1105	10	0	58.6
	25	0	64.0
	30	0	64.9
	40	0	65.8
	50	0	72.7
	75	0	69.6
	100	0	64.4
	150	0	60.1
	200	0	58.0
250	0	53.5	

**Table D.2:** Measured gas temperatures  $T_{\text{gas}}$  and dry gas species volume fractions  $r_{\text{dry gas}}$  from the REGA experiments [63, 64, 98, 99, 100]. Acronyms: TS: measurements of gas temperature using ceramic shielded type S thermocouples; TB: measurements of gas temperature using double-bead type B thermocouples; ABB: measurements of dry gas species volume fractions using standard gas analysers (ABB);  $\mu\text{GC}$ : measurements of dry gas species volume fractions using micro gas chromatography (Agilent Technologies 490 Micro GC).

REGA experiment	$x_1$ mm	$x_2$ mm	$T_{\text{gas}}$ K	$r_{\text{CH}_4, \text{dry gas}}$ %	$r_{\text{CO, dry gas}}$ %	$r_{\text{CO}_2, \text{dry gas}}$ %	$r_{\text{H}_2, \text{dry gas}}$ %	$r_{\text{N}_2, \text{dry gas}}$ %	Method
TUC3 V479	300	$\pm 130$	1527	—	—	—	—	—	TS
	300	$\pm 90$	1612	—	—	—	—	—	TS
	300	$\pm 50$	1791	—	—	—	—	—	TS
	300	0	1933	—	—	—	—	—	TS
	500	$\pm 130$	1657	0.0981	24.42	20.95	17.36	37.17	TB, ABB
	500	$\pm 90$	1684	0.1389	24.67	20.85	17.11	37.23	TB, ABB
	500	$\pm 50$	1696	0.2090	24.96	20.75	16.66	37.42	TB, ABB
	500	0	1716	0.3547	25.58	20.39	16.66	37.02	TB, ABB
	682	$\pm 130$	1671	0.0839	25.06	20.78	17.63	36.45	TB, ABB
	682	$\pm 90$	1706	0.0853	25.10	20.75	17.64	36.42	TB, ABB
	682	$\pm 50$	1733	0.1048	25.31	20.65	17.54	36.40	TB, ABB
	682	0	1754	0.1520	25.60	20.49	17.43	36.33	TB, ABB
	682	0	1682	—	—	—	—	—	TS
	1348	0	1602	—	—	—	—	—	TS
	1682	0	1560	—	—	—	—	—	TS
	2015	0	1535	—	—	—	—	—	TS
2682	0	1464	—	—	—	—	—	TS	
2962	0	1383	—	—	—	—	—	TS	

REGA experiment	$x_1$ mm	$x_2$ mm	$T_{\text{gas}}$ K	$r_{\text{CH}_4,\text{dry gas}}$ %	$r_{\text{CO}_2,\text{dry gas}}$ %	$r_{\text{CO}_2,\text{dry gas}}$ %	$r_{\text{H}_2,\text{dry gas}}$ %	$r_{\text{N}_2,\text{dry gas}}$ %	Method
	3260	0	—	0.0115	22.11	21.90	18.73	37.25	ABB
TUC3 V786	300	$\pm 130$	—	0.0634	21.81	22.09	17.31	38.70	ABB
	300	$\pm 110$	1619	—	—	—	—	—	TB
	300	$\pm 90$	—	0.1164	23.11	21.55	17.24	37.95	ABB
	300	$\pm 70$	1685	—	—	—	—	—	TB
	300	$\pm 50$	—	0.2251	24.04	21.43	16.32	37.85	ABB
	300	$\pm 30$	1809	—	—	—	—	—	TB
	300	$\pm 20$	1821	—	—	—	—	—	TB
	300	0	—	0.5132	25.11	20.47	17.68	35.93	ABB
	682	$\pm 130$	—	0.0557	24.24	20.75	17.61	37.35	ABB
	682	$\pm 110$	1667	—	—	—	—	—	TB
	682	$\pm 90$	—	0.0758	24.50	20.66	17.60	37.16	ABB
	682	$\pm 70$	1698	—	—	—	—	—	TB
	682	$\pm 50$	—	0.0959	24.54	20.63	17.60	37.12	ABB
	682	$\pm 30$	1708	—	—	—	—	—	TB
	682	$\pm 20$	1717	—	—	—	—	—	TB
	682	0	—	0.0876	24.60	20.59	17.68	37.04	ABB
	682	0	1677	—	—	—	—	—	TS
	1348	0	1618	—	—	—	—	—	TS
	1682	0	1548	—	—	—	—	—	TS
	2015	0	1523	—	—	—	—	—	TS
	2682	0	1450	—	—	—	—	—	TS

REGA experiment	$x_1$ mm	$x_2$ mm	$T_{\text{gas}}$ K	$r_{\text{CH}_4,\text{dry gas}}$ %	$r_{\text{CO}_2,\text{dry gas}}$ %	$r_{\text{CO}_2,\text{dry gas}}$ %	$r_{\text{H}_2,\text{dry gas}}$ %	$r_{\text{N}_2,\text{dry gas}}$ %	Method
	2962	0	1369	—	—	—	—	—	TS
	3260	0	—	0.0133	21.86	22.05	19.11	36.96	ABB
TUC5 V1105	300	$\pm 130$	1599	0.5971	33.83	18.98	30.21	16.26	TB, ABB
	300	$\pm 90$	1638	0.6476	34.18	18.79	30.04	16.29	TB, ABB
	300	$\pm 50$	1724	0.7447	34.48	18.75	29.55	16.37	TB, ABB
	300	$\pm 25$	1747	0.9693	34.52	18.55	29.70	16.10	TB, ABB
	300	0	1714	1.0291	34.43	18.43	29.98	15.96	TB, ABB
	682	$\pm 130$	1613	0.7129	34.44	18.44	30.58	15.78	TB, ABB
	682	$\pm 90$	1630	0.7489	34.60	18.36	30.41	15.81	TB, ABB
	682	$\pm 50$	1642	0.8078	34.61	18.36	30.40	15.73	TB, ABB
	682	$\pm 25$	1651	0.8567	34.61	18.29	30.42	15.73	TB, ABB
	682	0	1655	0.8856	34.63	18.25	30.50	15.62	TB, ABB
	682	0	1609	—	—	—	—	—	TS
	1015	0	1562	—	—	—	—	—	TS
	1682	0	1502	—	—	—	—	—	TS
	2015	0	1485	—	—	—	—	—	TS
	2962	0	1340	—	—	—	—	—	TS
	3260	0	—	0.4912	32.31	19.44	32.41	15.35	ABB
TUC5 GHKS10 V1071	300	$\pm 130$	1589	0.3415	37.32	17.74	29.52	15.07	TB, ABB
	300	$\pm 90$	1620	0.3459	37.60	17.61	29.38	15.05	TB, ABB
	300	$\pm 50$	1693	0.3598	37.86	18.07	27.99	15.69	TB, ABB
	300	$\pm 25$	1710	0.7203	37.76	17.78	28.43	15.19	TB, ABB

REGA experiment		$x_1$ mm	$x_2$ mm	$T_{\text{gas}}$ K	$r_{\text{CH}_4, \text{dry gas}}$ %	$r_{\text{CO}_2, \text{dry gas}}$ %	$r_{\text{CO}_2, \text{dry gas}}$ %	$r_{\text{H}_2, \text{dry gas}}$ %	$r_{\text{N}_2, \text{dry gas}}$ %	Method
		300	0	1674	1.1846	37.58	17.12	29.57	14.39	TB, ABB
		682	$\pm 130$	1604	0.4885	37.39	17.75	29.68	14.66	TB, ABB
		682	$\pm 90$	1622	0.5120	37.48	17.72	29.61	14.64	TB, ABB
		682	$\pm 50$	1635	0.5369	37.50	17.68	29.47	14.76	TB, ABB
		682	$\pm 25$	1636	0.5644	37.41	17.72	29.51	14.75	TB, ABB
		682	0	1633	0.5813	37.33	17.76	29.60	14.69	TB, ABB
		300	0	1636	—	—	—	—	—	TS
		633	0	1579	—	—	—	—	—	TS
		682	0	1509	—	—	—	—	—	TS
		1015	0	1490	—	—	—	—	—	TS
		1300	0	1351	—	—	—	—	—	TS
		3260	0	—	0.3791	35.41	18.48	31.36	14.38	ABB
TUC5 GHKS30 V1284										
		300	$\pm 130$	—	0.2236	44.15	15.05	29.16	11.42	TB, ABB
		300	$\pm 100$	1613	—	—	—	—	—	TB
		300	$\pm 90$	—	0.2157	43.71	15.75	28.75	11.57	TB, ABB
		300	$\pm 60$	1657	—	—	—	—	—	TB
		300	$\pm 50$	1689	0.1841	42.77	17.48	27.24	12.32	TB, ABB
		300	$\pm 40$	1706	0.2182	42.38	17.92	27.08	12.41	TB, ABB
		300	$\pm 30$	1737	0.3038	41.94	18.26	27.05	12.45	TB, ABB
		300	$\pm 20$	1765	0.3722	41.81	18.27	27.14	12.40	TB, ABB
		300	$\pm 10$	1761	0.3619	42.21	17.58	27.82	12.03	TB, ABB
		300	0	1752	0.3103	42.34	17.46	27.89	12.00	TB, ABB

REGA experiment	$x_1$ mm	$x_2$ mm	$T_{\text{gas}}$ K	$r_{\text{CH}_4,\text{dry gas}}$ %	$r_{\text{CO}_2,\text{dry gas}}$ %	$r_{\text{CO}_2,\text{dry gas}}$ %	$r_{\text{H}_2,\text{dry gas}}$ %	$r_{\text{N}_2,\text{dry gas}}$ %	Method
	682	$\pm 130$	1613	0.2673	43.54	15.70	28.92	11.57	TB, ABB
	682	$\pm 110$	1657	—	—	—	—	—	TB
	682	$\pm 90$	1689	0.2792	43.38	15.92	28.81	11.62	TB, ABB
	682	$\pm 80$	1706	—	—	—	—	—	TB
	682	$\pm 70$	1737	—	—	—	—	—	TB
	682	$\pm 60$	1765	—	—	—	—	—	TB
	682	$\pm 50$	1761	0.3018	43.23	16.05	28.79	11.63	TB, ABB
	682	$\pm 40$	1752	0.3070	43.20	16.04	28.82	11.64	TB, ABB
	682	$\pm 30$	1761	0.3125	43.17	16.09	28.87	11.57	TB, ABB
	682	$\pm 20$	1765	0.3205	43.10	16.14	28.90	11.54	TB, ABB
	682	$\pm 10$	1737	0.3231	43.03	16.19	28.93	11.52	TB, ABB
	682	0	1706	0.3229	42.96	16.25	28.94	11.52	TB, ABB
	682	0	1659	—	—	—	—	—	TS
	1015	0	1565	—	—	—	—	—	TS
	1682	0	1485	—	—	—	—	—	TS
	2015	0	1468	—	—	—	—	—	TS
	2962	0	1328	—	—	—	—	—	TS
	3260	0	—	0.2169	41.56	16.56	30.80	10.86	ABB



# E Injection properties

## E.1 Mathematical methods

The approximations described in Sections 2.2.4.4 and 2.2.4.5 were performed using cubic smoothing spline interpolations, minimisation methods, bell-shaped functions and distribution functions.

Cubic smoothing spline interpolations were applied using the *csaps* method of *csaps* [91] with a smoothing factor of 0.02 while the minimisations were performed using the *least\_squares* method of SciPy [280, 327] based on the Trust Region Reflective method. From various bell-shaped functions, only the generalised Gaussian probability density (GGPD) function  $q_{\text{GGPD}}$  and the generalised membership bell-shaped (GMBS) function  $q_{\text{GMBS}}$  were eventually used in this work. The GGPD function  $q_{\text{GGPD}}$  is given by

$$q_{\text{GGPD}} = a \exp\left(-\frac{1}{2} \left(\frac{x-b}{c}\right)^2\right), \quad (\text{E.1})$$

where  $a = 1$ ,  $b$  and  $c$  are the shape parameters. The GMBS function  $q_{\text{GMBS}}$  is defined by

$$q_{\text{GMBS}} = \frac{1}{1 + \left|\frac{x-b}{c}\right|^{2|d|}}, \quad (\text{E.2})$$

where  $b$ ,  $c$  and  $d$  are the shape parameters. Additionally, the GGPD function  $q_{\text{GGPD}}$  and the GMBS function  $q_{\text{GMBS}}$  were combined using a weighting factor  $w$ . The combined function  $q_{\text{GGPD/GMBS}}$  is given by

$$q_{\text{GGPD/GMBS}} = w q_{\text{GGPD}} + (1 - w) q_{\text{GMBS}}. \quad (\text{E.3})$$

## E.2 Gamma and Weibull distributions

Two distribution functions were applied for the droplet diameter approximations in the preceding works [63, 64, 187], the gamma ( $\gamma$ ) distribution and the Weibull (W)

distribution. For the gamma distribution, the probability density function  $q_\gamma$  and the cumulative distribution function  $Q_\gamma$  are defined by

$$q_\gamma = \frac{1}{\Gamma(\alpha)} \left( \frac{d_{\text{part}}/\mu\text{m}}{\beta} \right)^{\alpha-1} \exp\left(-\frac{d_{\text{part}}/\mu\text{m}}{\beta}\right) \quad (\text{E.4})$$

$$Q_\gamma = \frac{1}{\Gamma(\alpha)} \gamma(\alpha, d_{\text{part}}), \quad (\text{E.5})$$

where  $\alpha$  and  $\beta$  are the shape parameters of the gamma distribution,  $\Gamma(\alpha)$  is the gamma function and  $\gamma(\alpha, d_{\text{part}})$  is the lower incomplete gamma function.

For the Weibull distribution, the probability density function  $q_W$  and the cumulative distribution function  $Q_W$  are defined by

$$q_W = \frac{k}{\lambda} \left( \frac{d_{\text{part}}/\mu\text{m}}{\lambda} \right)^{k-1} \exp\left(-\left(\frac{d_{\text{part}}/\mu\text{m}}{\lambda}\right)^k\right), \quad (\text{E.6})$$

$$Q_W = 1 - \exp\left(-\left(\frac{d_{\text{part}}/\mu\text{m}}{\lambda}\right)^k\right), \quad (\text{E.7})$$

where  $k$  and  $\lambda$  are the shape parameters of the Weibull distribution.

**Table E.1:** Shape parameters  $\alpha$  and  $\beta$  for the gamma distributions used to approximate the number-based droplet diameter distributions.

ATMO experiment	$\alpha$	$\beta$
TUC3 D1	1.442	13.847
TUC5 D2	2.328	12.057
TUC5 D1.1	2.265	13.783
TUC5 D2.1	1.863	20.442

**Table E.2:** Shape parameters  $k$  and  $\lambda$  for the Weibull distributions used to approximate the mass-based droplet diameter distributions.

ATMO experiment	$k$	$\lambda$
TUC3 D1	1.776	100.893
TUC5 D2	1.987	87.686
TUC5 D1.1	1.868	105.217
TUC5 D2.1	1.855	189.669

### E.3 Normalised distributions

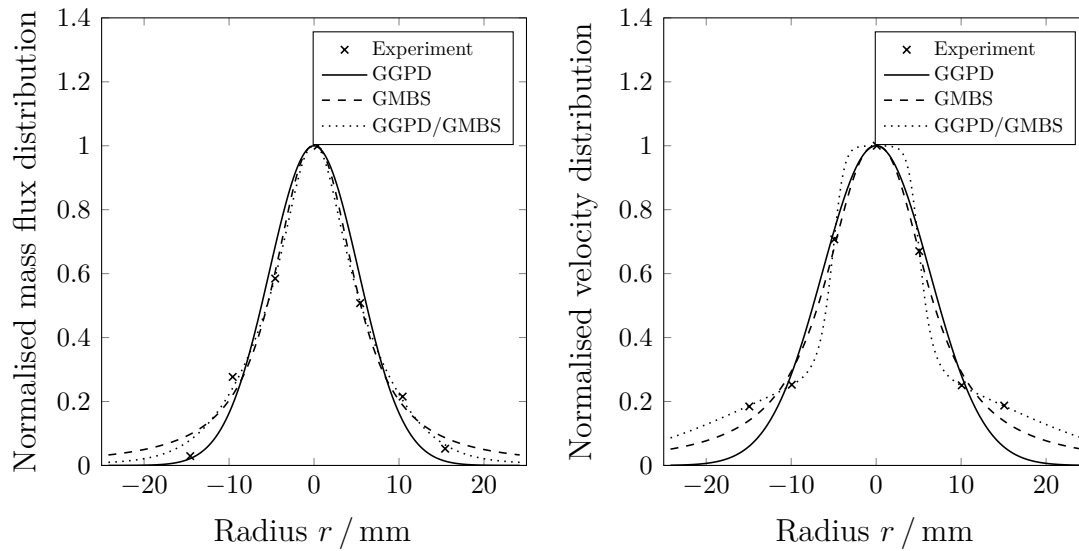


**Figure E.1:** Normalised mass flux and velocity distributions based on the ATMO experiment TUC3 D1 and applied to derive the injection properties for the CFD simulations of the REGA experiments TUC3 V479 and TUC3 V786.

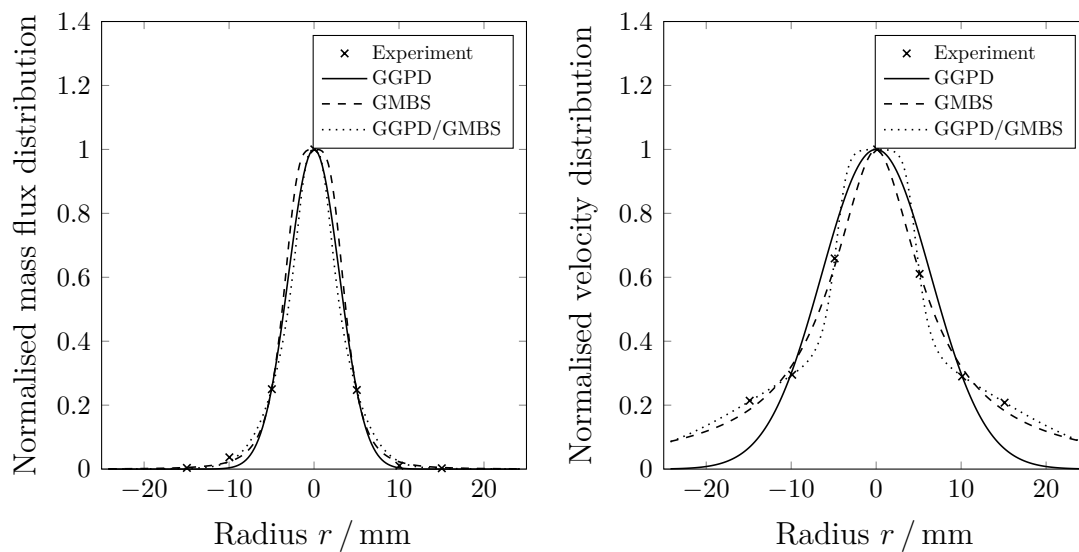


**Figure E.2:** Normalised mass flux and velocity distributions based on the ATMO experiment TUC5 D2 and applied to derive the injection properties for the CFD simulations of the REGA experiment TUC5 V1105.

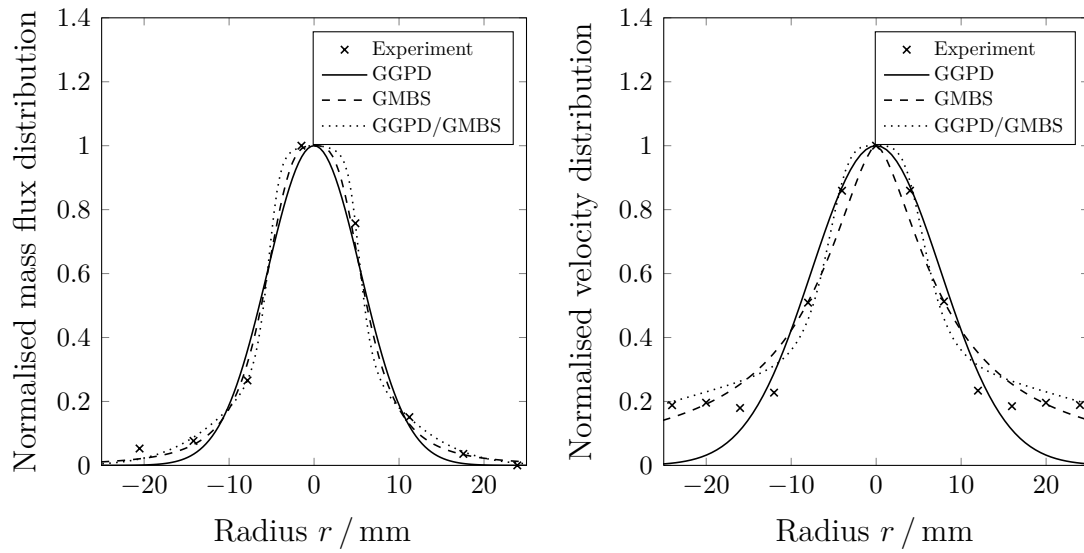


**Figure E.3:** Normalised mass flux and velocity distributions based on the ATMO experiment TUC5 D2.1 and applied to derive the injection properties for the CFD simulations of the REGA experiment TUC5 V1105.

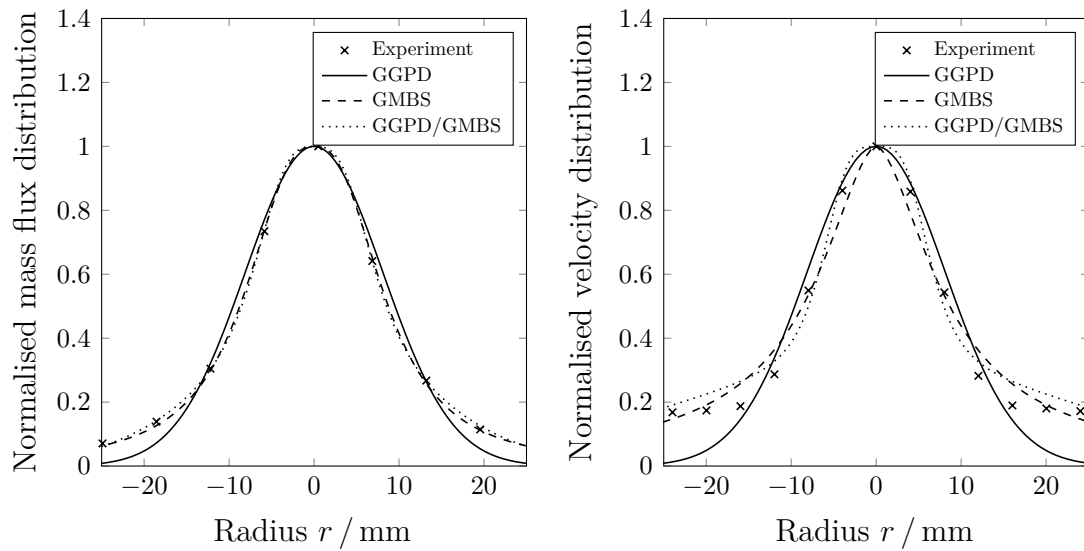


**Figure E.4:** Normalised mass flux and velocity distributions based on the ATMO experiment TUC5 D1.1 and applied to derive the injection properties for the CFD simulations of the REGA experiment TUC5 V1374.

## E.4 Injection distributions

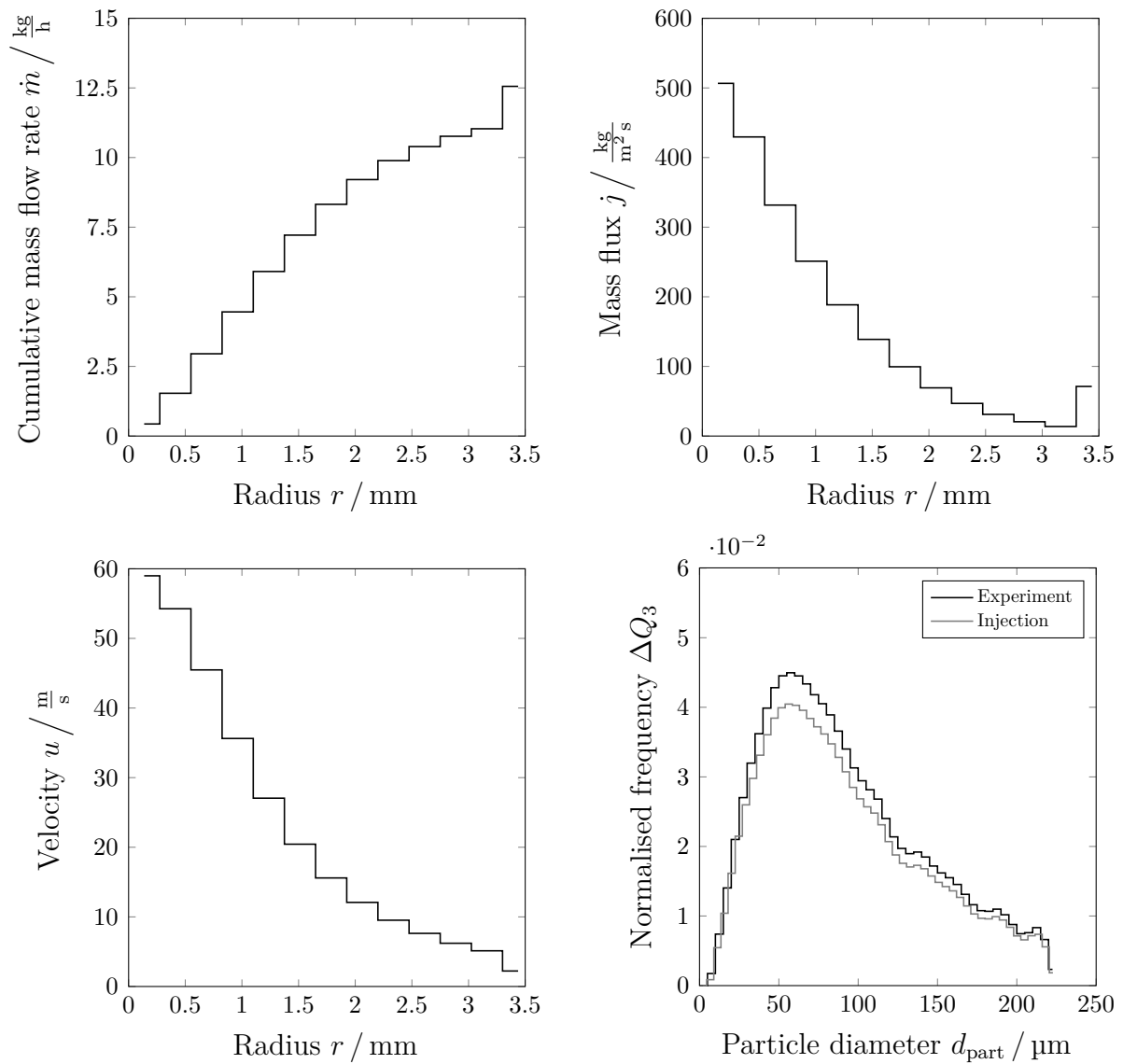


**Figure E.5:** Injection distributions of the ethylene glycol droplets based on the ATMO experiment TUC3 D1 and used for the CFD simulations of the REGA experiment TUC3 V479.

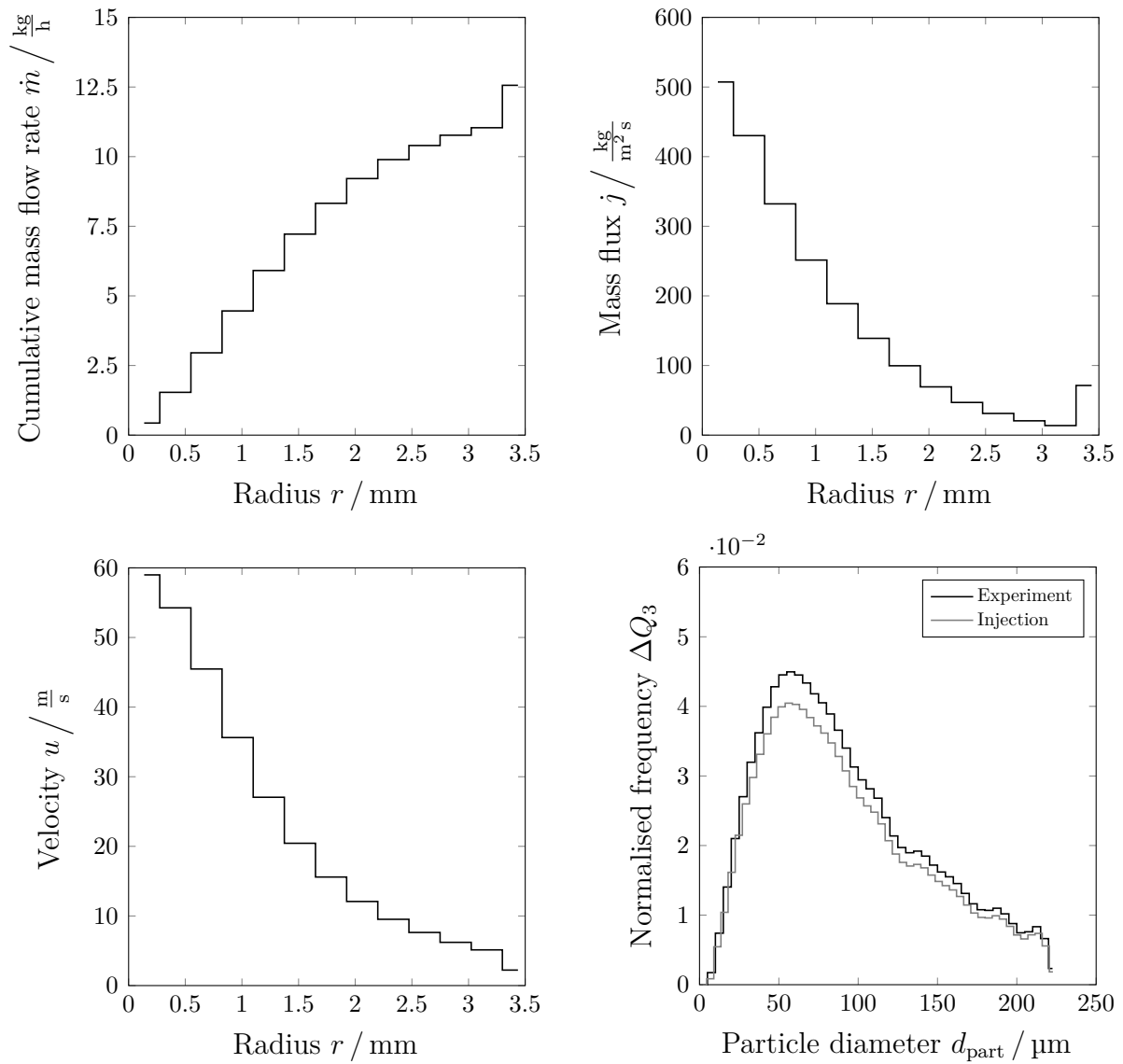


**Figure E.6:** Injection distributions of the ethylene glycol droplets based on the ATMO experiment TUC3 D1 and used for the CFD simulations of the REGA experiment TUC3 V786.

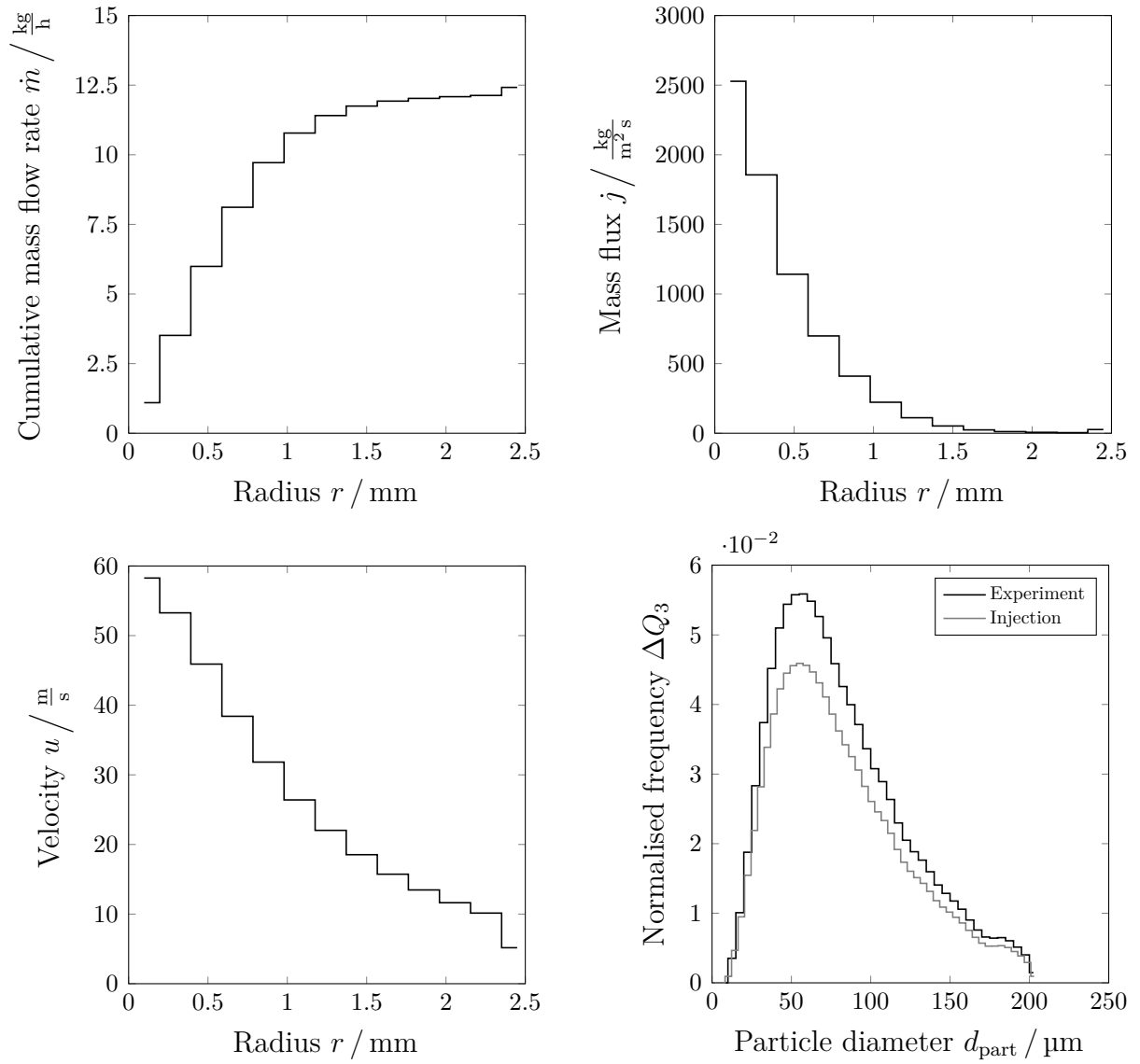


**Figure E.7:** Injection distributions of the ethylene glycol droplets based on the ATMO experiment TUC5 D2 and used for the CFD simulations of the REGA experiment TUC5 V1105.

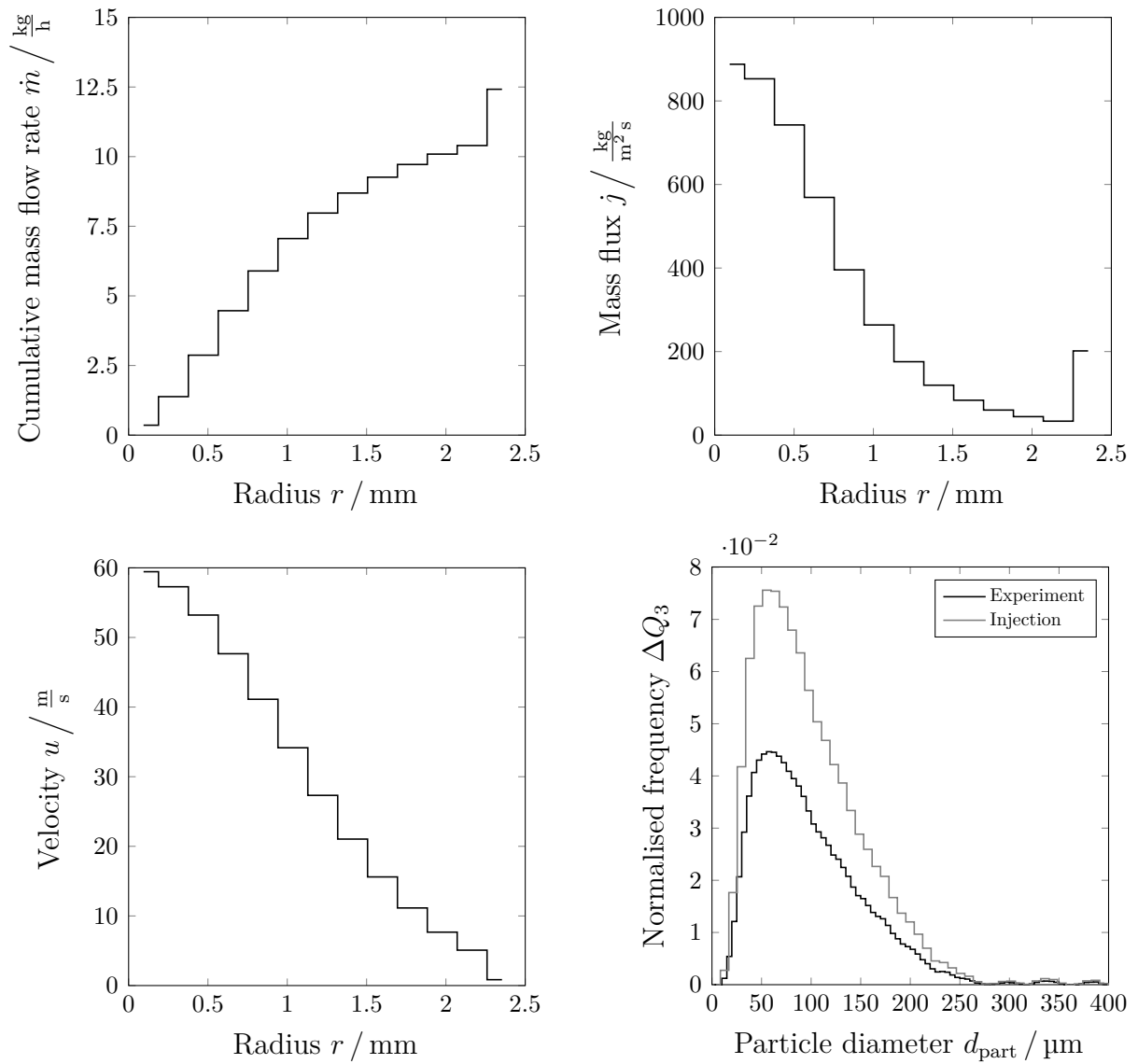


**Figure E.8:** Injection distributions of the ethylene glycol droplets based on the ATMO experiment TUC5 D2.1 and used for the CFD simulations of the REGA experiment TUC5 V1105.

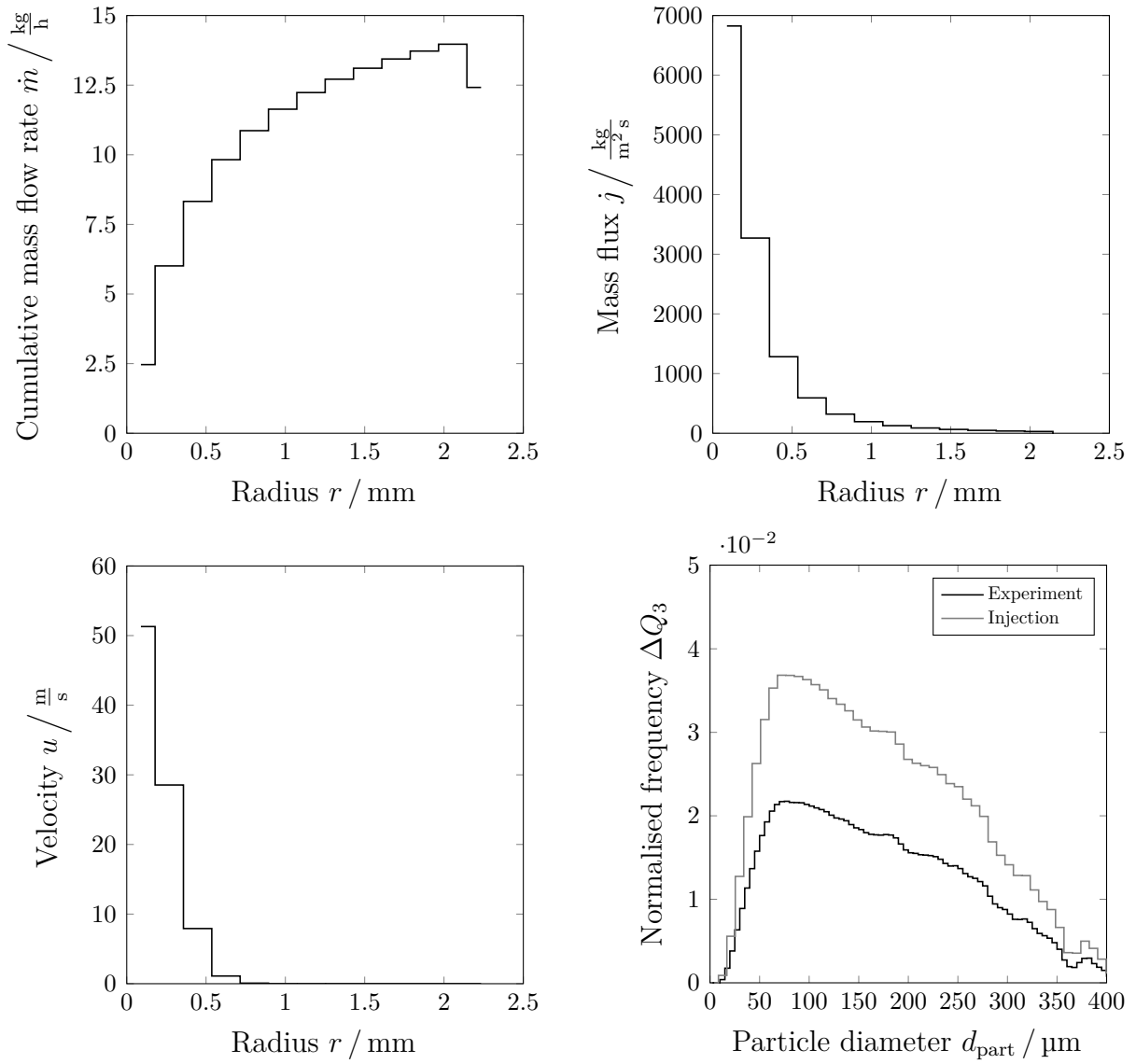


**Figure E.9:** Injection distributions of the ethylene glycol droplets based on the ATMO experiment TUC5 D1.1 and used for the CFD simulations of the REGA experiment TUC5 V1374.

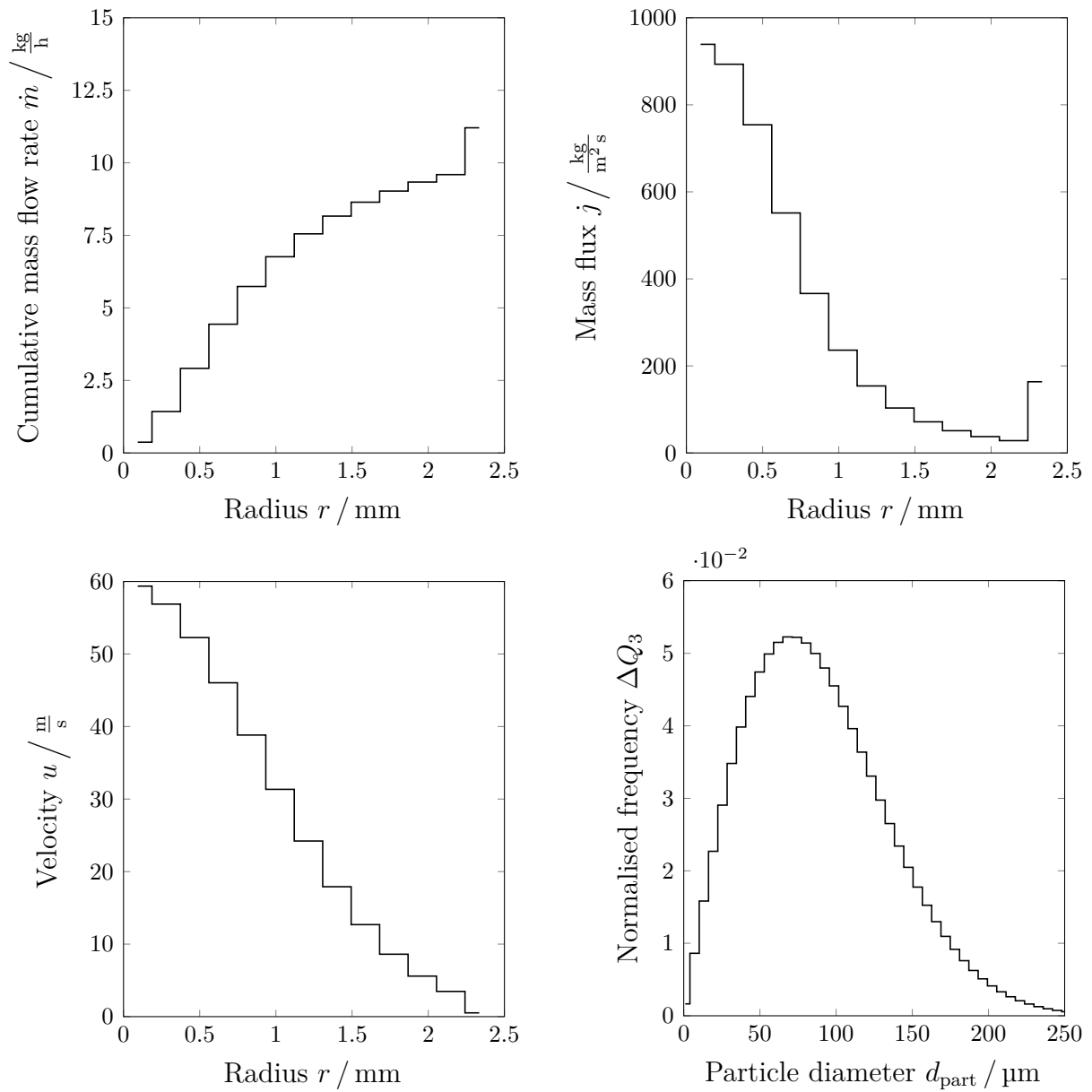


**Figure E.10:** Injection distributions of the ethylene glycol droplets used for the CFD simulations of the REGA experiment TUC5 GHKS10 V1071.

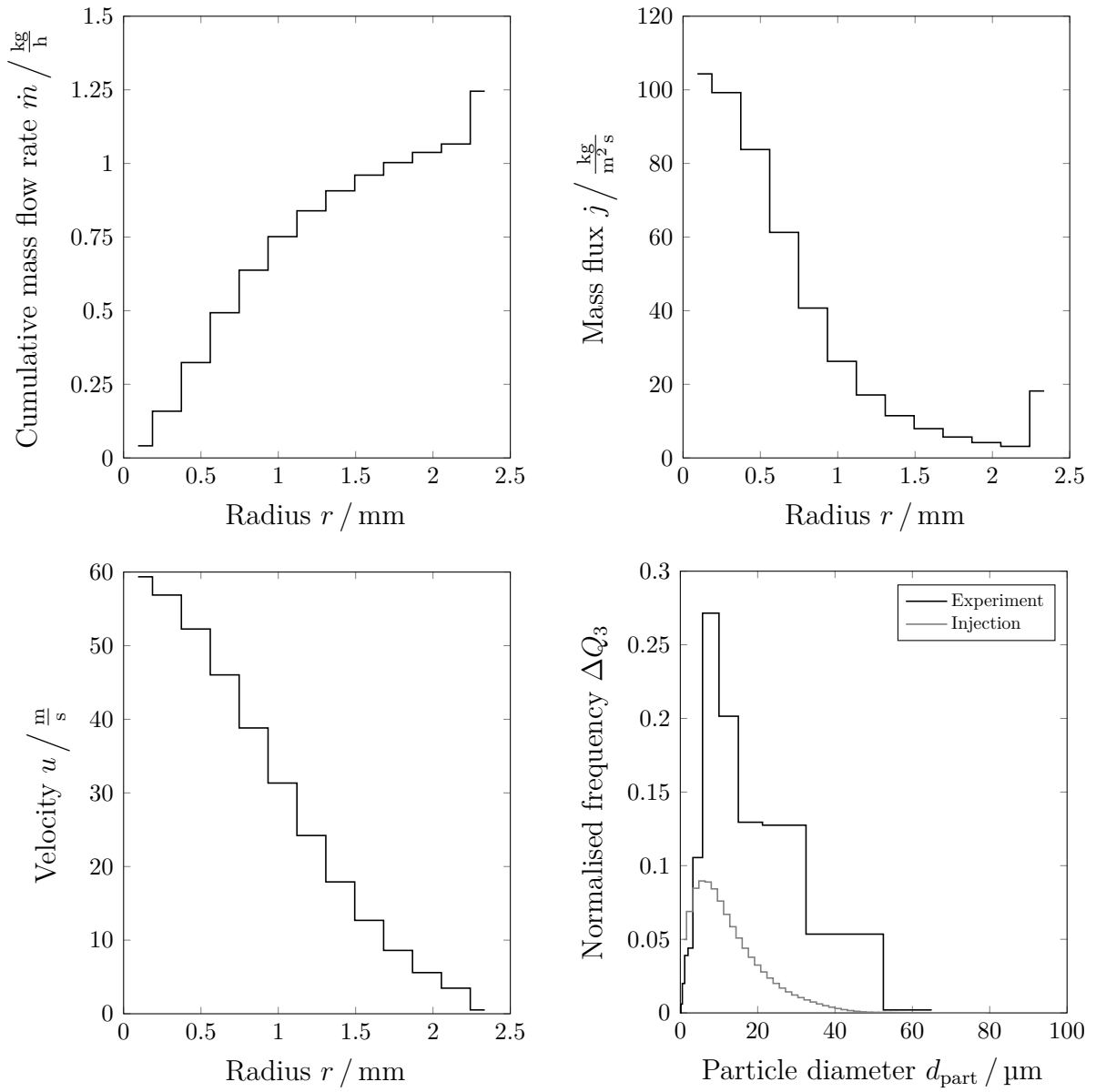


**Figure E.11:** Injection distributions of the wood char particles used for the CFD simulations of the REGA experiment TUC5 GHKS10 V1071.

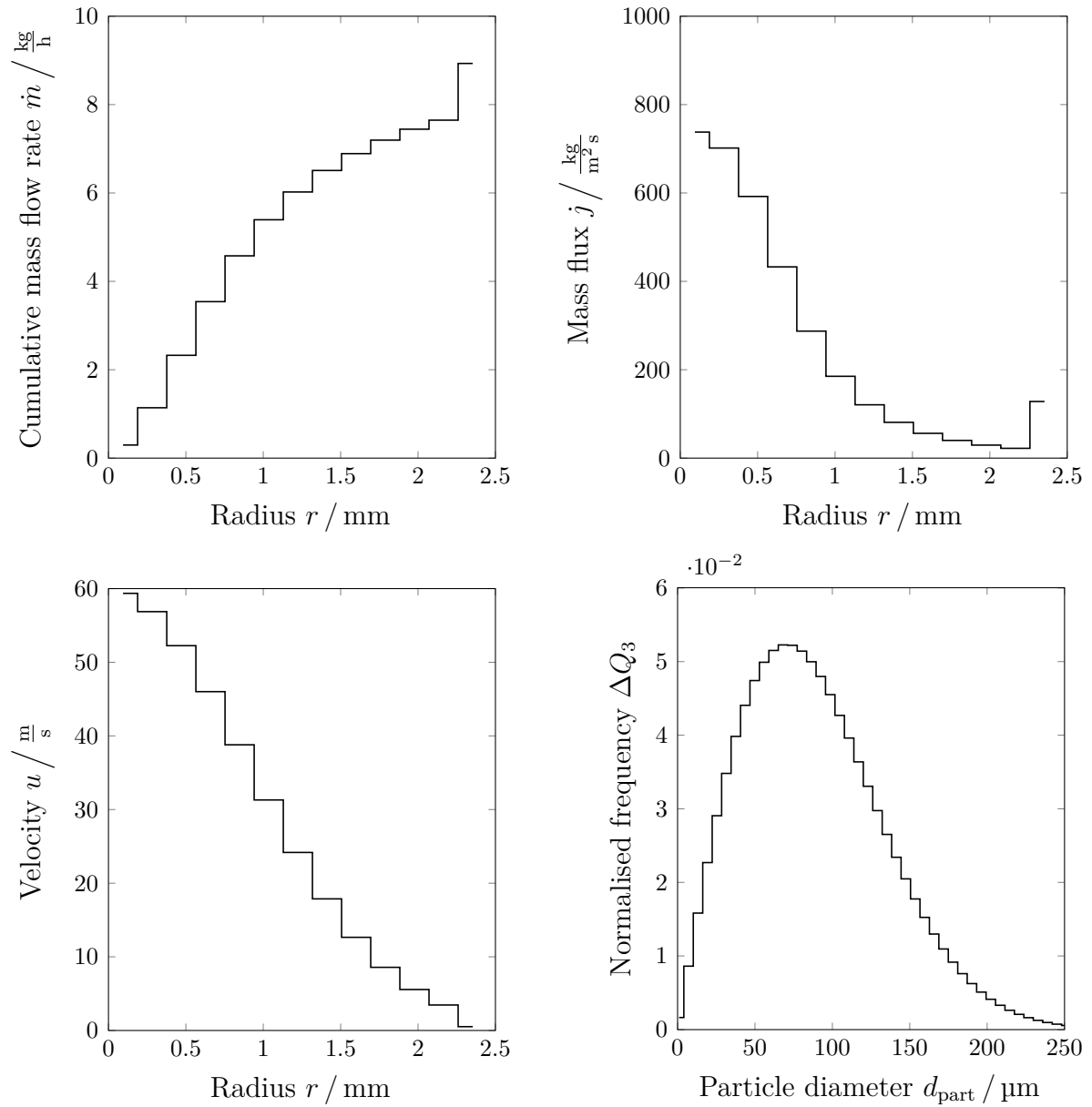


**Figure E.12:** Injection distributions of the ethylene glycol droplets used for the CFD simulations of the REGA experiment TUC5 GHKS30 V1284.

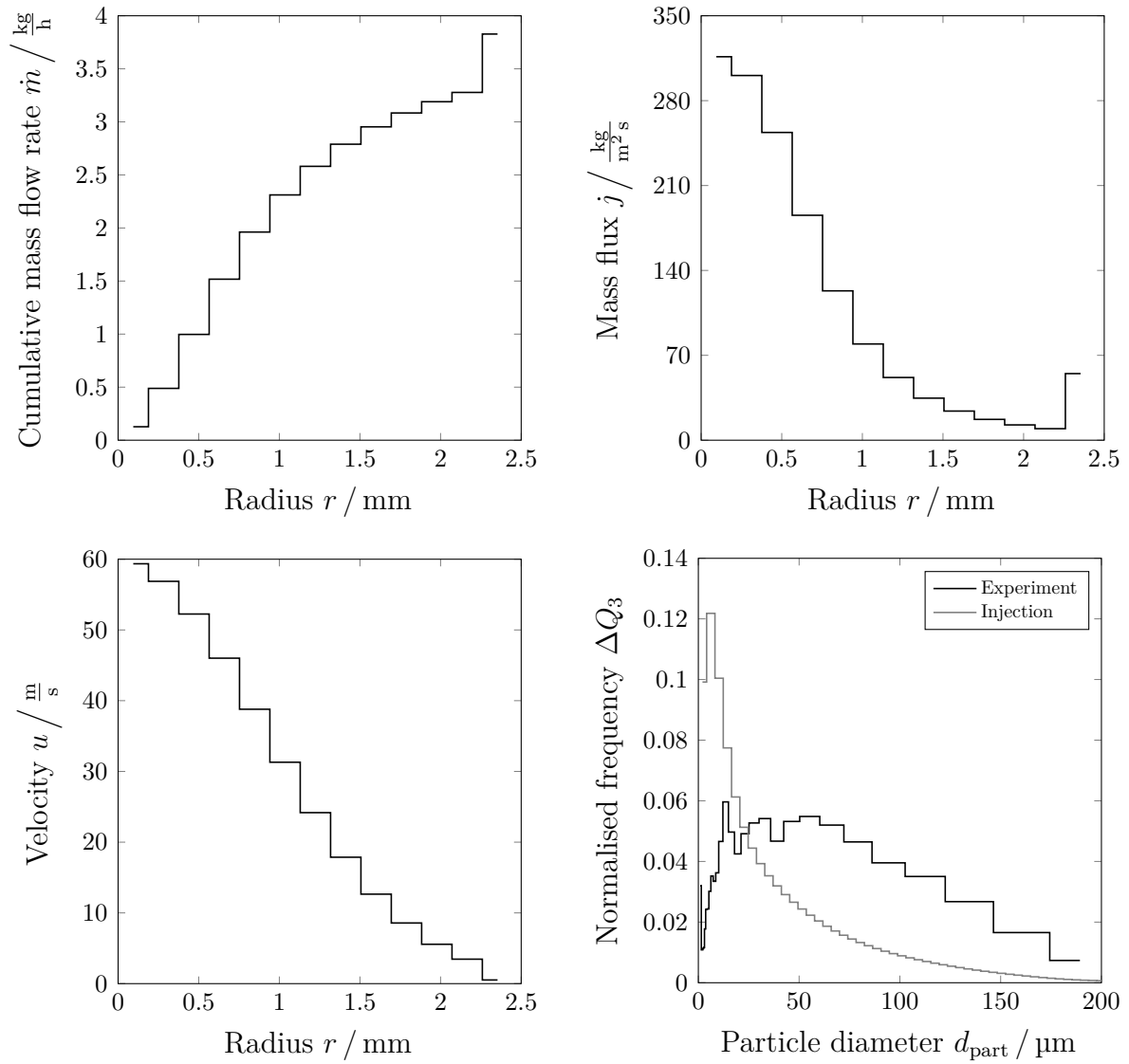


**Figure E.13:** Injection distributions of the wood char particles used for the CFD simulations of the REGA experiment TUC5 GHKS30 V1284.



# F Physical properties

This chapter provides the model equations for the physical properties of the gas phase, the liquid phase and the solid phase. Firstly, the approaches for the molar masses, the molar and specific standard enthalpies, the molar and specific standard entropies and the Lennard-Jones diameters and energy parameters are presented in Sections F.1-F.4. Subsequently, the physical properties of the gas phase, the liquid phase and the solid phase are focussed in Sections F.5-F.7.

## F.1 Molar masses

The molar masses  $M$  were mainly obtained from the thermodynamic data of the reaction mechanisms and from the databases of NASA [196]. Furthermore, the molar mass of the volatiles  $M_{\text{vol}}$  was calculated by

$$M_{\text{vol}} = \sum_{\substack{k=\text{CH}_4, \text{CO}, \\ \text{CO}_2, \text{H}_2, \text{H}_2\text{O}, \text{N}_2}} x_{k,\text{vol}} M_k , \quad (\text{F.1})$$

where  $x_{k,\text{vol}}$  is the volatiles species mole fraction of species  $k$  and  $M_k$  is the molar mass of species  $k$ .

## F.2 Molar standard enthalpies and molar standard entropies

The molar standard gas enthalpies at reference temperature  $\overline{H}_{\text{gas,ref}}^\circ$  and the molar standard gas entropies at reference temperature  $\overline{S}_{\text{gas,ref}}^\circ$  were obtained from the thermodynamic data of the reaction mechanisms and from the databases of NASA [196]. Furthermore, the molar standard gas enthalpy of the volatiles at reference temperature  $\overline{H}_{\text{vol,gas,ref}}^\circ$  and the molar standard gas entropy of the volatiles at reference temperature  $\overline{S}_{\text{vol,gas,ref}}^\circ$  were determined by

$$\overline{H}_{\text{vol,gas,ref}}^\circ = \sum x_{k,\text{vol}} \overline{H}_{k,\text{gas,ref}}^\circ \quad \text{where } k = \text{CH}_4, \text{CO}, \text{CO}_2, \text{H}_2, \text{H}_2\text{O} , \quad (\text{F.2})$$

$$\bar{S}_{\text{vol,gas,ref}}^{\ominus} = \sum x_{k,\text{vol}} \bar{S}_{k,\text{gas,ref}}^{\ominus} \quad \text{where } k = \text{CH}_4, \text{CO}, \text{CO}_2, \text{H}_2, \text{H}_2\text{O}, \quad (\text{F.3})$$

where  $x_{k,\text{vol}}$  is the volatiles species mole fraction of species  $k$ ,  $\bar{H}_{k,\text{gas,ref}}$  is the molar standard gas enthalpy at reference temperature and  $\bar{S}_{k,\text{gas,ref}}$  is the molar standard gas entropy of species  $k$  at reference temperature.

### F.3 Specific standard enthalpies and specific standard entropies

The specific standard gas enthalpies at reference temperature  $\hat{H}_{\text{gas,ref}}^{\ominus}$  and the specific standard gas entropies at reference temperature  $\hat{S}_{\text{gas,ref}}^{\ominus}$  were calculated from the molar standard gas enthalpies at reference temperature  $\bar{H}_{\text{gas,ref}}^{\ominus}$  and the molar standard gas entropies at reference temperature  $\bar{S}_{\text{gas,ref}}^{\ominus}$ . The specific standard gas enthalpy of species  $i$  at reference temperature  $\hat{H}_{i,\text{gas,ref}}^{\ominus}$  and the specific standard gas entropy of species  $i$  at reference temperature  $\hat{S}_{i,\text{gas,ref}}^{\ominus}$  is given by

$$\hat{H}_{i,\text{gas,ref}}^{\ominus} = \frac{\bar{H}_{i,\text{gas,ref}}^{\ominus}}{M_i}, \quad (\text{F.4})$$

$$\hat{S}_{i,\text{gas,ref}}^{\ominus} = \frac{\bar{S}_{i,\text{gas,ref}}^{\ominus}}{M_i}, \quad (\text{F.5})$$

where  $\bar{H}_{i,\text{gas,ref}}^{\ominus}$  is the molar standard gas enthalpy of species  $i$  at reference temperature,  $M_i$  is the molar mass of species  $i$  and  $\bar{S}_{i,\text{gas,ref}}^{\ominus}$  is the molar standard gas entropy of species  $i$  at reference temperature.

### F.4 Lennard-Jones diameters and Lennard-Jones energy parameters

The Lennard-Jones diameters  $\sigma$  and the Lennard-Jones energy parameters  $\epsilon$  were obtained from the transport data of the reaction mechanisms.

### F.5 Gas phase

The physical properties of the gas phase include the molar mass  $M_{\text{gas}}$ , the density  $\rho_{\text{gas}}$ , the dynamic viscosity  $\eta_{\text{gas}}$ , the thermal conductivity  $\lambda_{\text{gas}}$ , diffusion coefficients  $D_{\text{gas}}$ , the specific

heat capacity  $\hat{C}_{p,\text{gas}}$ , the specific physical enthalpy  $\hat{H}_{\text{phys,gas}}$  and the specific entropy  $\hat{S}_{\text{gas}}$ . The model equations used in this work are given in Sections F.5.1-F.5.8.

### F.5.1 Molar mass

The molar mass of the gas phase  $M_{\text{gas}}$  was determined by

$$M_{\text{gas}} = \sum_i x_{i,\text{gas}} M_i = \left( \sum_i \frac{w_{i,\text{gas}}}{M_i} \right)^{-1}, \quad (\text{F.6})$$

where  $x_{i,\text{gas}}$  is the gas species mole fraction of species  $i$ ,  $w_{i,\text{gas}}$  is the gas species mass fraction of species  $i$  and  $M_i$  is the molar mass of species  $i$ .

### F.5.2 Density

The gas density  $\rho_{\text{gas}}$  was calculated by

$$\rho_{\text{gas}} = \frac{M_{\text{gas}}}{\bar{V}_{\text{gas}}}, \quad (\text{F.7})$$

where  $M_{\text{gas}}$  is the molar mass of the gas phase and  $\bar{V}_{\text{gas}}$  is the molar gas volume. The latter was determined using the incompressible ideal gas equation of state by

$$\bar{V}_{\text{gas}} = \frac{\bar{R} T_{\text{gas}}}{p_{\text{op}}}, \quad (\text{F.8})$$

where  $\bar{R}$  is the molar gas constant,  $T_{\text{gas}}$  is the gas temperature and  $p_{\text{op}}$  is the operating pressure.

### F.5.3 Dynamic viscosity

The dynamic gas viscosity  $\eta_{\text{gas}}$  was calculated using the Wilke mixing rule by [338]

$$\eta_{\text{gas}} = \sum_i \left( \frac{\eta_i}{1 + \frac{1}{x_{i,\text{gas}}} \sum_{j \neq i} (x_{j,\text{gas}} \varphi_{i,j})} \right), \quad (\text{F.9})$$

where

$$\varphi_{i,j} = \frac{\left( 1 + (\eta_{i,\text{gas}}/\eta_{j,\text{gas}})^{1/2} (M_j/M_i)^{1/4} \right)^2}{\sqrt{8} (1 + M_i/M_j)} \quad \text{for } i \neq j \quad (\text{F.10})$$

and [16, 244]

$$\eta_{i,\text{gas}} = 2.669 \cdot 10^{-6} \frac{\sqrt{\frac{M_i}{\text{g/mol}} \frac{T_{\text{gas}}}{\text{K}}}}{\left(\frac{\sigma_i}{\text{\AA}}\right)^2} \Omega_{\eta_{i,\text{gas}}} \text{ Pa s} \quad (\text{F.11})$$

is the dynamic gas viscosity of species  $i$ . The collision integral for the dynamic gas viscosity of species  $i$  is given by

$$\Omega_{\eta_{i,\text{gas}}} = \frac{A}{\tilde{T}_{i,\text{gas}}^B} + \frac{C}{\exp(D \tilde{T}_{i,\text{gas}})} + \frac{E}{\exp(F \tilde{T}_{i,\text{gas}})}, \quad (\text{F.12})$$

where

$$\tilde{T}_{i,\text{gas}} = \frac{k_B T_{\text{gas}}}{\varepsilon_i} \quad (\text{F.13})$$

is a dimensionless temperature and  $A, B, C, D, E$  and  $F$  are coefficients, which are given in Table F.1.

**Table F.1:** Coefficients  $A, B, C, D, E$  and  $F$  for the calculation of the collision integral for the dynamic gas viscosity of species  $i$   $\Omega_{\eta_{i,\text{gas}}}$  [244].

$A$	$B$	$C$	$D$	$E$	$F$
1.161 45	0.148 74	0.524 87	0.773 20	2.161 78	2.437 87

### F.5.4 Thermal conductivity

The thermal gas conductivity  $\lambda_{\text{gas}}$  was determined using the Wilke mixing rule by [338]

$$\lambda_{\text{gas}} = \sum_i \left( \frac{\lambda_{i,\text{gas}}}{1 + \frac{1}{x_{i,\text{gas}}} \sum_{j \neq i} (x_{j,\text{gas}} \varphi_{i,j})} \right) \quad (\text{F.14})$$

where

$$\varphi_{i,j} = \frac{(1 + (\eta_{i,\text{gas}}/\eta_{j,\text{gas}})^{1/2} (M_j/M_i)^{1/4})^2}{\sqrt{8 (1 + M_i/M_j)}} \quad \text{for } i \neq j \quad (\text{F.15})$$

and [16, 92, 93, 244]

$$\lambda_{i,\text{gas}} = \frac{15}{4} \frac{\eta_{i,\text{gas}} \bar{R}}{M_i} \left( \frac{4}{15} \frac{\hat{C}_{p,i,\text{gas}} M_i}{\bar{R}} + \frac{1}{3} \right), \quad (\text{F.16})$$

is the thermal gas conductivity of species  $i$ .  $\hat{C}_{p,i,\text{gas}}$  is the specific gas heat capacity of species  $i$ .

### F.5.5 Diffusion coefficients

The gas diffusion in an ideal multi-component mixture at constant pressure is described by the Stefan-Maxwell equation [306, 309]

$$c_{\text{gas}} \nabla x_{i,\text{gas}} = - \sum_{j=1}^{N_{\text{sp}}} \frac{x_{j,\text{gas}} \mathbf{j}_{n,i,\text{gas}} - x_{i,\text{gas}} \mathbf{j}_{n,j,\text{gas}}}{D_{i,j,\text{gas}}}, \quad (\text{F.17})$$

where  $c_{\text{gas}} = p_{\text{gas}} / (\bar{R} T_{\text{gas}})$  is the molar gas concentration,  $\mathbf{j}_{n,i,\text{gas}}$  and  $\mathbf{j}_{n,j,\text{gas}}$  are molar fluxes of species  $i$  and  $j$  in the gas phase, respectively, and  $D_{i,j,\text{gas}}$  is the binary gas diffusion coefficient of species  $i$  in species  $j$ . The molar flux of species  $i$  in the gas phase  $\mathbf{j}_{n,i,\text{gas}}$  is described by [306, 309]

$$\mathbf{j}_{n,i,\text{gas}} = c_{\text{gas}} x_{i,\text{gas}} (\mathbf{u}_{i,\text{gas}} - \mathbf{u}_{\text{gas}}), \quad (\text{F.18})$$

where  $\mathbf{u}_{i,\text{gas}}$  is the gas velocity of species  $i$  and  $\mathbf{u}_{\text{gas}}$  is the gas velocity. By combining this equation with

$$\mathbf{j}_{n,i,\text{gas}} = -c_{\text{gas}} D_{i,\text{gas,eff}} \nabla x_{i,\text{gas}}, \quad (\text{F.19})$$

the effective gas diffusion coefficient for species  $i$   $D_{i,\text{gas,eff}}$  is obtained as [306, 309]

$$D_{i,\text{gas,eff}} = \left( c_{\text{gas}} x_{i,\text{gas}} \mathbf{u}_{i,\text{gas}} - x_i \sum_{j=1}^{N_{\text{sp}}} c_{\text{gas}} x_{j,\text{gas}} \mathbf{u}_{j,\text{gas}} \right) \left( c_{\text{gas}} x_{i,\text{gas}} \mathbf{u}_{i,\text{gas}} \sum_{\substack{j=1 \\ j \neq i}}^{N_{\text{sp}}} \frac{x_{j,\text{gas}}}{D_{i,j,\text{gas}}} - x_i \sum_{\substack{j=1 \\ j \neq i}}^{N_{\text{sp}}} \frac{c_{\text{gas}} x_{j,\text{gas}} \mathbf{u}_{j,\text{gas}}}{D_{i,j,\text{gas}}} \right)^{-1}. \quad (\text{F.20})$$

Assuming a stagnant mixture, further simplification leads to [306, 309]

$$D_{i,\text{gas,eff}} = \frac{1 - x_{i,\text{gas}}}{\sum_{\substack{j=1 \\ j \neq i}}^{N_{\text{sp}}} \frac{x_{j,\text{gas}}}{D_{i,j}}}. \quad (\text{F.21})$$

This equation is valid for a stagnant mixture only but is typically used for all mixtures [306]. It is a compromise between assuming a constant gas diffusion coefficient for all species and calculating the Fickian diffusion coefficients  $\mathbf{F}_{\text{gas}} = (F_{i,j,\text{gas}})$ . In the latter case, the

gas species mass flux of species  $i$

$$J_{m,i,\text{gas}} = \rho_{\text{gas}} w_{i,\text{gas}} \mathbf{u}_{i,\text{gas}} - w_{i,\text{gas}} \dot{m}_{\text{gas}} \quad (\text{F.22})$$

is accounted for, and the Stefan-Maxwell equation is transformed to [306, 309]

$$\rho_{\text{gas}} \nabla x_{i,\text{gas}} = - \sum_{\substack{j=1 \\ j \neq i}}^{N_{\text{sp}}} \frac{M_{\text{gas}}^2}{M_i M_j} \frac{1}{D_{i,j,\text{gas}}} (w_{j,\text{gas}} \mathbf{j}_{m,i,\text{gas}} - w_{i,\text{gas}} \mathbf{j}_{m,j,\text{gas}}) \quad (\text{F.23})$$

by employing the gas species mass fluxes  $\mathbf{j}_{m,i,\text{gas}}$  and  $\mathbf{j}_{m,j,\text{gas}}$  and substituting the gas species mole fractions  $x_{i,\text{gas}}$  and  $x_{j,\text{gas}}$  on the right hand side by the gas species mass fractions  $w_{i,\text{gas}}$  and  $w_{j,\text{gas}}$ . Due to the relationship

$$J_{m,N,\text{gas}} = - \sum_{\substack{j=1 \\ j \neq i}}^{N_{\text{sp}}-1} J_{m,i,\text{gas}} \quad (\text{F.24})$$

between the gas species mass fluxes, further transformation of the right hand side leads to [306, 309]

$$\rho_{\text{gas}} \nabla x_{i,\text{gas}} = L_{i,i} J_{m,i,\text{gas}} + \sum_{\substack{j=1 \\ j \neq i}}^{N_{\text{sp}}-1} L_{i,j} J_{m,j,\text{gas}}, \quad (\text{F.25})$$

where  $\mathbf{L} = (L_{i,j})$  is a matrix with the coefficients [306, 309]

$$L_{i,i} = - \left( \frac{w_{i,\text{gas}} M_{\text{gas}}^2}{M_i M_{N_{\text{sp}}} G_{i,N_{\text{sp}}}} + \sum_{\substack{j=1 \\ j \neq i}}^{N_{\text{sp}}} \frac{w_{j,\text{gas}} M_{\text{gas}}^2}{G_{i,j} M_i C M_j} \right), \quad (\text{F.26})$$

$$L_{i,j} = - \frac{w_{i,\text{gas}} M_{\text{gas}}^2}{M_i} \left( \frac{1}{G_{i,j} M_j} - \frac{1}{G_{i,N_{\text{sp}}} M_{N_{\text{sp}}}} \right). \quad (\text{F.27})$$

As the species balance equation is typically written using the mass fraction gradient of species  $i$   $\nabla w_{i,\text{gas}}$ , the left hand side of the Stefan-Maxwell equation needs to be rearranged by a transformation matrix [306, 309]

$$\mathbf{T} = (T_{i,j}) = - (\mathbf{I} \mathbf{x}_{\text{gas}}) (\mathbf{I} \mathbf{w}_{\text{gas}})^{-1} \mathbf{P}, \quad (\text{F.28})$$

where [306, 309]

$$\begin{aligned} T_{i,j} &= - \frac{x_{i,\text{gas}}}{w_{i,\text{gas}}} \left( \delta_{i,j} - w_{i,\text{gas}} \left( \frac{M_{\text{gas}}}{M_j} - \frac{M}{M_{N_{\text{sp}}}} \right) \right) \\ &= - \frac{M_{\text{gas}}}{M_i} (\delta_{i,j} - x_{i,\text{gas}}) - x_{i,\text{gas}} \frac{M_{\text{gas}}}{M_{N_{\text{sp}}}} \end{aligned} \quad (\text{F.29})$$

and  $\mathbf{P}$  is a further transformation matrix [306, 309]. By comparing the final transformed Stefan-Maxwell equation [306, 309]

$$-\rho_{\text{gas}} \mathbf{T} \nabla \mathbf{w}_{\text{gas}} = \mathbf{L} \mathbf{j}_m \quad (\text{F.30})$$

with the species balance equation, the relationship for the Fickian matrix is found as [306, 309]

$$\mathbf{F}_{\text{gas}} = \mathbf{L}^{-1} \mathbf{T}. \quad (\text{F.31})$$

The binary gas diffusion coefficient of species  $i$  in species  $j$   $D_{i,j,\text{gas}}$  can be described by the Chapman-Enskog equation. Assuming ideal gas behaviour, the equation is given by [244]

$$D_{i,j,\text{gas}} = \frac{3}{16} \left( \frac{4\pi k_B T_{\text{gas}}}{M_{i,j}} \right)^{1/2} \frac{k_B T_{\text{gas}}}{p_{\text{gas}} \pi \sigma_{i,j}^2 \Omega_{D_{i,j,\text{gas}}}} f_D, \quad (\text{F.32})$$

where

$$M_{i,j} = 2 \frac{M_i M_j}{M_i + M_j}, \quad (\text{F.33})$$

$$\sigma_{i,j} = \frac{\sigma_i + \sigma_j}{2} \quad (\text{F.34})$$

are the mean molar mass of species  $i$  and  $j$  and the mean Lennard-Jones diameter of species  $i$  and  $j$ , respectively,  $f_D$  is a correction term with values between 1.0 and 1.1 [244] and  $\Omega_{D_{i,j,\text{gas}}}$  is the collision integral for the gas diffusion of species  $i$  in species  $j$ . The latter is defined by [244]

$$\Omega_{D_{i,j,\text{gas}}} = \frac{A}{(\tilde{T}_{i,j,\text{gas}})^B} + \frac{C}{\exp(D \tilde{T}_{i,j,\text{gas}})} + \frac{E}{\exp(F \tilde{T}_{i,j,\text{gas}})} + \frac{G}{\exp(H \tilde{T}_{i,j,\text{gas}})}, \quad (\text{F.35})$$

where  $A$ ,  $B$ ,  $C$ ,  $D$ ,  $E$ ,  $F$ ,  $G$  and  $H$  are coefficients, which are given in Table F.2, and

$$\tilde{T}_{i,j,\text{gas}} = \frac{k_B T_{\text{gas}}}{\epsilon_{i,j}} \quad (\text{F.36})$$

is a dimensionless temperature [244] with  $\epsilon_{i,j} = \sqrt{\epsilon_i \epsilon_j}$  as a mean Lennard-Jones energy parameter of species  $i$  and  $j$ . Inserting the mathematical and physical constants and adapting the units, the Chapman-Enskog equation is given by [244]

$$D_{i,j,\text{gas}} = 2.663528769 \cdot 10^{-7} \frac{\left(\frac{T_{\text{gas}}}{\text{K}}\right)^{3/2}}{\left(\frac{p}{\text{bar}}\right) \left(\frac{M_{i,j}}{\text{g/mol}}\right)^{1/2} \left(\frac{\sigma_{i,j}}{\text{\AA}}\right)^2 \Omega_{\Omega_{D_{i,j,\text{gas}}}}} \frac{\text{m}^2}{\text{s}}. \quad (\text{F.37})$$

**Table F.2:** Coefficients  $A$ ,  $B$ ,  $C$ ,  $D$ ,  $E$ ,  $F$ ,  $G$  and  $H$  for the calculation of the collision integral for the gas diffusion coefficients of species  $i$  in species  $j$   $\Omega_{D_{i,j,\text{gas}}}$  [244].

$A$	$B$	$C$	$D$	$E$	$F$	$G$	$H$
1.060 36	0.156 10	0.193 00	0.476 35	1.035 87	1.529 96	1.764 74	3.894 11

### F.5.6 Specific heat capacity

The specific gas heat capacity  $\hat{C}_{p,\text{gas}}$  was calculated using the mass-weighted mixing rule by

$$\hat{C}_{p,\text{gas}} = \sum_i w_{i,\text{gas}} \hat{C}_{p,i,\text{gas}}, \quad (\text{F.38})$$

where  $\hat{C}_{p,i,\text{gas}}$  is the specific gas heat capacity of species  $i$ . The latter was determined by

$$\hat{C}_{p,i,\text{gas}} = \begin{cases} \sum_{j=1}^5 C_{1,j,i} \left( \frac{T_{\text{gas}}}{\text{K}} \right)^{j-1} \left( \frac{\bar{R}}{M_i} \right), & T_{\min,1,C_{p,\text{gas}},i} \leq T_{\text{gas}} \leq T_{\max,1,C_{p,\text{gas}},i} \\ \sum_{j=1}^5 C_{2,j,i} \left( \frac{T_{\text{gas}}}{\text{K}} \right)^{j-1} \left( \frac{\bar{R}}{M_i} \right), & T_{\min,2,C_{p,\text{gas}},i} \leq T_{\text{gas}} \leq T_{\max,2,C_{p,\text{gas}},i} \end{cases}, \quad (\text{F.39})$$

where  $C_{1,1,i}$ ,  $C_{1,2,i}$ ,  $C_{1,3,i}$ ,  $C_{1,4,i}$  and  $C_{1,5,i}$  as well as  $C_{2,1,i}$ ,  $C_{2,2,i}$ ,  $C_{2,3,i}$ ,  $C_{2,4,i}$  and  $C_{2,5,i}$  are coefficients that were taken from the thermodynamic data of the reaction mechanisms,  $\bar{R}$  is the molar gas constant and  $M_i$  is the molar mass of species  $i$ .

### F.5.7 Specific physical enthalpy

The specific physical gas enthalpy  $\hat{H}_{\text{phys,gas}}$  was calculated using the mass-weighted mixing rule by

$$\hat{H}_{\text{phys,gas}} = \sum_i w_{i,\text{gas}} \hat{H}_{\text{phys},i,\text{gas}} = \sum_i w_{i,\text{gas}} \left( \hat{H}_{i,\text{gas}}^\circ - \hat{H}_{i,\text{gas,ref}}^\circ \right), \quad (\text{F.40})$$

where  $\hat{H}_{\text{phys},i,\text{gas}}$  is the specific physical gas enthalpy of species  $i$ . The latter was obtained by

$$\hat{H}_{\text{phys},i,\text{gas}} = \hat{H}_{i,\text{gas}}^\circ - \hat{H}_{i,\text{gas,ref}}^\circ, \quad (\text{F.41})$$

where

$$\hat{H}_{i,\text{gas}}^\ominus = \begin{cases} \left( \sum_{j=1}^5 \frac{C_{1,j,i}}{j} \left( \frac{T_{\text{gas}}}{\text{K}} \right)^j + C_{1,6,i} \right) \left( \frac{\bar{R}}{M_i} \right), \\ T_{\min,1,C_{p,\text{gas},i}} \leq T_{\text{gas}} \leq T_{\max,1,C_{p,\text{gas},i}} \\ \left( \sum_{j=1}^5 \frac{C_{2,j,i}}{j} \left( \frac{T_{\text{gas}}}{\text{K}} \right)^j + C_{2,6,i} \right) \left( \frac{\bar{R}}{M_i} \right), \\ T_{\min,2,C_{p,\text{gas},i}} \leq T_{\text{gas}} \leq T_{\max,2,C_{p,\text{gas},i}} \end{cases} \quad (\text{F.42})$$

is the specific standard gas enthalpy of species  $i$ .  $C_{1,1,i}$ ,  $C_{1,2,i}$ ,  $C_{1,3,i}$ ,  $C_{1,4,i}$  and  $C_{1,5,i}$  as well as  $C_{2,1,i}$ ,  $C_{2,2,i}$ ,  $C_{2,3,i}$ ,  $C_{2,4,i}$  and  $C_{2,5,i}$  are coefficients that were taken from the thermodynamic data of the reaction mechanisms,  $\bar{R}$  is the molar gas constant and  $M_i$  is the molar mass of species  $i$ .

### F.5.8 Specific entropy

The specific gas entropy  $\hat{S}_{\text{gas}}$  is identical to the specific standard gas entropy  $\hat{S}_{\text{gas}}^\ominus$  when assuming ideal gas behaviour and was calculated using the mass-weighted mixing rule by

$$\hat{S}_{\text{gas}} = \hat{S}_{\text{gas}}^\ominus = \sum_i w_{i,\text{gas}} \hat{S}_{i,\text{gas}}^\ominus, \quad (\text{F.43})$$

where

$$\hat{S}_{i,\text{gas}}^\ominus = \begin{cases} \left( C_{1,1,i} \ln \left( \frac{T_{\text{gas}}}{\text{K}} \right) + \sum_{j=2}^5 C_{1,j,i} \left( \frac{T_{\text{gas}}}{\text{K}} \right)^{j-1} + C_{1,7,i} \right) \left( \frac{\bar{R}}{M_i} \right), \\ T_{\min,1,C_{p,\text{gas},i}} \leq T_{\text{gas}} \leq T_{\max,1,C_{p,\text{gas},i}} \\ \left( C_{2,1,i} \ln \left( \frac{T_{\text{gas}}}{\text{K}} \right) + \sum_{j=2}^5 C_{2,j,i} \left( \frac{T_{\text{gas}}}{\text{K}} \right)^{j-1} + C_{2,7,i} \right) \left( \frac{\bar{R}}{M_i} \right), \\ T_{\min,2,C_{p,\text{gas},i}} \leq T_{\text{gas}} \leq T_{\max,2,C_{p,\text{gas},i}} \end{cases} \quad (\text{F.44})$$

is the specific standard gas entropy of species  $i$ .  $C_{1,1,i}$ ,  $C_{1,2,i}$ ,  $C_{1,3,i}$ ,  $C_{1,4,i}$  and  $C_{1,5,i}$  as well as  $C_{2,1,i}$ ,  $C_{2,2,i}$ ,  $C_{2,3,i}$ ,  $C_{2,4,i}$  and  $C_{2,5,i}$  are coefficients that were taken from the thermodynamic data of the reaction mechanisms,  $\bar{R}$  is the molar gas constant and  $M_i$  is the molar mass of species  $i$ .

## F.6 Liquid phase

The physical properties of the liquid phase include the vapour pressure  $p_{\text{vap}}$ , the specific enthalpy of vaporisation  $\Delta_{\text{vap}}\hat{H}$ , the density  $\rho_{\text{liq}}$ , the dynamic viscosity  $\eta_{\text{liq}}$ , the thermal conductivity  $\lambda_{\text{liq}}$ , the specific heat capacity  $\hat{C}_{p,\text{liq}}$  and the specific physical enthalpy  $\hat{H}_{\text{phys,liq}}$ . The model equations used in this work are given in Sections F.6.1-F.6.8.

### F.6.1 Vapour pressure

The vapour pressure  $p_{\text{vap}}$  was calculated using a Wagner equation by [325]

$$p_{\text{vap}} = p_{c,\text{C}_2\text{H}_6\text{O}_2} \exp\left(\frac{T_{c,\text{C}_2\text{H}_6\text{O}_2}}{T} \left(A\tilde{T} + B\tilde{T}^{1.5} + C\tilde{T}^{2.5} + D\tilde{T}^5\right)\right), \quad (\text{F.45})$$

where  $p_{c,\text{C}_2\text{H}_6\text{O}_2}$  is the critical pressure of ethylene glycol,  $T_{c,\text{C}_2\text{H}_6\text{O}_2}$  is the critical temperature of ethylene glycol,  $\tilde{T} = 1 - T/T_{c,\text{C}_2\text{H}_6\text{O}_2}$  is a dimensionless temperature and  $A$ ,  $B$ ,  $C$  and  $D$  are coefficients that were taken from the databases of the VDI Warmeatlas [325].

### F.6.2 Specific enthalpy of vaporisation

The specific enthalpy of vaporisation  $\Delta_{\text{vap}}\hat{H}$  was determined using a PPDS equation by [325]

$$\Delta_{\text{vap}}\hat{H} = \frac{\bar{R}}{M_{\text{C}_2\text{H}_6\text{O}_2}} T_{c,\text{C}_2\text{H}_6\text{O}_2} \left(A\tilde{T}^{1/3} + B\tilde{T}^{2/3} + C\tilde{T} + D\tilde{T}^2 + E\tilde{T}^3\right), \quad (\text{F.46})$$

where  $M_{\text{C}_2\text{H}_6\text{O}_2}$  is the molar mass of ethylene glycol,  $T_{c,\text{C}_2\text{H}_6\text{O}_2}$  is the critical temperature of ethylene glycol,  $\tilde{T} = 1 - T/T_{c,\text{C}_2\text{H}_6\text{O}_2}$  is a dimensionless temperature and  $A$ ,  $B$ ,  $C$ ,  $D$  and  $E$  are coefficients that were taken from the databases of the VDI Warmeatlas [325].

### F.6.3 Density

The liquid density  $\rho_{\text{liq}}$  was calculated using a PPDS equation by [325]

$$\rho_{\text{liq}} = \rho_{c,\text{C}_2\text{H}_6\text{O}_2} + \left(A\tilde{T}^{0.35} + B\tilde{T}^{2/3} + C\tilde{T} + D\tilde{T}^{4/3}\right) \frac{\text{kg}}{\text{m}^3}, \quad (\text{F.47})$$

where  $\rho_{c,\text{C}_2\text{H}_6\text{O}_2}$  is the critical density of ethylene glycol,  $\tilde{T} = 1 - T/T_{c,\text{C}_2\text{H}_6\text{O}_2}$  is a dimensionless temperature,  $T_{c,\text{C}_2\text{H}_6\text{O}_2}$  is the critical temperature of ethylene glycol and  $A$ ,  $B$ ,  $C$  and  $D$  are coefficients that were taken from the databases of the VDI Warmeatlas [325].

### F.6.4 Dynamic viscosity

The dynamic liquid viscosity  $\eta_{\text{liq}}$  was determined using a DIPPR equation by [22]

$$\eta_{\text{liq}} = \exp \left( C_1 + C_2 \left( \frac{\text{K}}{T} \right) + C_3 \ln \left( \frac{T}{\text{K}} \right) + C_4 \left( \frac{T}{\text{K}} \right)^{C_5} \right) \text{ Pa.s}, \quad (\text{F.48})$$

where  $C_1$ ,  $C_2$ ,  $C_3$ ,  $C_4$  and  $C_5$  are coefficients that were taken from the databases of ASPEN Properties [22]. The equation was applied between the temperatures  $T_{\text{min},\eta_{\text{liq}}}$  and  $T_{\text{max},\eta_{\text{liq}}}$ , as defined by the databases of ASPEN Properties [22], whereas linear extrapolation was used outside the temperatures  $T_{\text{min},\lambda_{\text{liq}}}$  and  $T_{\text{max},\lambda_{\text{liq}}}$  [22].

### F.6.5 Thermal conductivity

The liquid thermal conductivity  $\lambda_{\text{liq}}$  was calculated using a DIPPR equation by [22]

$$\lambda_{\text{liq}} = \left( \sum_j^5 C_j \left( \frac{T}{\text{K}} \right)^{j-1} \right) \frac{\text{W}}{\text{m K}} \quad (\text{F.49})$$

where  $C_1$ ,  $C_2$ ,  $C_3$ ,  $C_4$  and  $C_5$  are coefficients that were taken from the databases of ASPEN Properties [22]. The equation was applied between the temperatures  $T_{\text{min},\lambda_{\text{liq}}}$  and  $T_{\text{max},\lambda_{\text{liq}}}$ , as defined by the databases of ASPEN Properties [22], whereas linear extrapolation was used outside the temperatures  $T_{\text{min},\lambda_{\text{liq}}}$  and  $T_{\text{max},\lambda_{\text{liq}}}$  [22].

### F.6.6 Vapour diffusion coefficient

The vapour diffusion coefficient  $D_{\text{vap}}$  is a simplified diffusion coefficient for vaporisation simulations and was determined by (see Section F.5.5)

$$D_{\text{vap}} = D_{\text{C}_2\text{H}_6\text{O}_2,\text{gas,eff}} = \frac{1 - x_{\text{C}_2\text{H}_6\text{O}_2,\text{gas}}}{\sum_{i \neq \text{C}_2\text{H}_6\text{O}_2} \frac{x_{i,\text{gas}}}{D_{\text{C}_2\text{H}_6\text{O}_2,j,\text{gas}}}} \quad (\text{F.50})$$

where  $D_{\text{C}_2\text{H}_6\text{O}_2,j,\text{gas}}$  is the binary gas diffusion coefficient of ethylene glycol in species  $j$  and was calculated using the adapted Chapman-Enskog equation. In contrast, Mancini et al. [187] applied a polynomial to determine the vapour diffusion coefficient  $D_{\text{vap}}$ . The polynomial was obtained from effective diffusion coefficients of ethylene glycol  $D_{\text{C}_2\text{H}_6\text{O}_2,\text{eff}}$  at pre-scribed gas conditions and is given by

$$D_{\text{vap}} = D_{\text{C}_2\text{H}_6\text{O}_2, \text{gas, eff}} = \left( -1.34316 \cdot 10^{-5} + 5.27316 \cdot 10^{-8} \left( \frac{T}{\text{K}} \right) + 7.26287 \cdot 10^{-11} \left( \frac{T}{\text{K}} \right)^2 - 8.73484 \cdot 10^{-15} \left( \frac{T}{\text{K}} \right)^3 \right) \frac{\text{m}^2}{\text{s}}. \quad (\text{F.51})$$

### F.6.7 Specific heat capacity

The specific liquid heat capacity  $\hat{C}_{p, \text{liq}}$  was determined using a PPDS equation by [325]

$$\hat{C}_{p, \text{liq}} = \frac{\bar{R}}{M_{\text{C}_2\text{H}_6\text{O}_2}} \left( A \tilde{T}^{-1} + B + C \tilde{T} + D \tilde{T}^2 + E \tilde{T}^3 + F \tilde{T}^4 \right), \quad (\text{F.52})$$

where  $M_{\text{C}_2\text{H}_6\text{O}_2}$  is the molar mass of ethylene glycol,  $\tilde{T} = 1 - T/T_{\text{c}, \text{C}_2\text{H}_6\text{O}_2}$  is a dimensionless temperature,  $T_{\text{c}, \text{C}_2\text{H}_6\text{O}_2}$  is the critical temperature of ethylene glycol and  $A, B, C, D, E$  and  $F$  are coefficients that were taken from the databases of the VDI Warmeatlas [325].

### F.6.8 Specific physical enthalpy

The specific physical liquid enthalpy  $\hat{H}_{\text{phys, liq}}$  was determined using the integral of the PPDS equation by

$$\hat{H}_{\text{phys, liq}} = -\frac{\bar{R}}{M_{\text{C}_2\text{H}_6\text{O}_2}} T_{\text{c}, \text{C}_2\text{H}_6\text{O}_2} \left( A \ln \left( \frac{\tilde{T}}{\tilde{T}_{\text{ref}}} \right) + B (\tilde{T} - \tilde{T}_{\text{ref}}) + \left( C \frac{\tilde{T}_i^2 - \tilde{T}_{i, \text{ref}}^2}{2} + D \left( \frac{\tilde{T}_i^3 - \tilde{T}_{i, \text{ref}}^3}{3} \right) + E \left( \frac{\tilde{T}_i^4 - \tilde{T}_{i, \text{ref}}^4}{4} \right) + F \left( \frac{\tilde{T}_i^5 - \tilde{T}_{i, \text{ref}}^5}{5} \right) \right), \quad (\text{F.53})$$

where  $M_{\text{C}_2\text{H}_6\text{O}_2}$  is the molar mass of ethylene glycol,  $T_{\text{c}, \text{C}_2\text{H}_6\text{O}_2}$  is the critical temperature of ethylene glycol,  $\tilde{T} = 1 - T/T_{\text{c}, \text{C}_2\text{H}_6\text{O}_2}$  and  $\tilde{T}_{\text{ref}} = 1 - T_{\text{ref}}/T_{\text{c}, \text{C}_2\text{H}_6\text{O}_2}$  are dimensionless temperatures,  $T_{\text{ref}}$  is the reference temperature and  $A, B, C, D, E$  and  $F$  are coefficients that were taken from the databases of the VDI Warmeatlas [325].

## F.7 Solid phase

The physical properties of the solid phase include density  $\rho_{\text{solid}}$ , specific heat capacity  $\hat{C}_{p,\text{solid}}$  and specific physical enthalpy  $\hat{H}_{\text{phys},\text{solid}}$ . The model equations used in this work are given in Sections F.7.1-F.7.3.

### F.7.1 Density

The (true) solid density  $\rho_{\text{solid}}$  (which should not be confused with the effective solid density  $\rho_{\text{solid,eff}}$ ) can be estimated for coking coals using the model of Merrick et al. [203] and for coals and coal chars using the models of IGT [21, 131]. The model of Merrick et al. [203] is based on previous works of Franklin, van Krevelen, and Ergun and numerous measured densities of hard coals, semi-cokes and cokes. It is assumed that (i) the solid volume can be determined using the atomic volumes of carbon, hydrogen, oxygen, nitrogen and sulphur and (ii) the density of pure carbon can be described using the density of graphite. The (true) solid density  $\rho_{\text{solid}}$  is given by [203]

$$\rho_{\text{solid}} = \left( \frac{1 - w_{\text{ash,solid}}}{\rho_{\text{solid,daf}}} + \frac{w_{\text{ash,solid}}}{\rho_{\text{ash}}} \right)^{-1}, \quad (\text{F.54})$$

where [203]

$$\rho_{\text{solid,daf}} = 10^3 \left( \sum_{j=\text{C,H,O,N,S}} \gamma_j \frac{w_{j,\text{solid,daf}}}{M_j / (\text{kg/mol})} \right)^{-1} \frac{\text{kg}}{\text{m}^3}, \quad (\text{F.55})$$

is the (true) solid (daf) density and  $\rho_{\text{ash}}$  is the ash density. The coefficients  $\gamma_{\text{C}}$ ,  $\gamma_{\text{H}}$ ,  $\gamma_{\text{O}}$ ,  $\gamma_{\text{N}}$  and  $\gamma_{\text{S}}$  were determined using linear regression and are reproduced in Table F.3.

**Table F.3:** Coefficients  $\gamma_{\text{C}}$ ,  $\gamma_{\text{H}}$ ,  $\gamma_{\text{O}}$ ,  $\gamma_{\text{N}}$  and  $\gamma_{\text{S}}$  for the calculation of the solid density  $\rho_{\text{solid}}$  using the model of Merrick et al. [203].

$j$	$\frac{\gamma_j}{\text{kg/m}^3}$
C	0.00530
H	0.00577
O	0.00346
N	0.06690
S	0.03840

The models of IGT [21, 131] are similar to the model of Merrick et al. [203] and are based on measured densities of coals, cokes, coking coals, chars and graphite. The model of IGT

for coals is applicable for coals with a wide range of hydrogen contents and is based on the equations [21]

$$\rho_{\text{solid,daf}} = \frac{1000 \text{ kg}}{A \text{ m}^3}, \quad (\text{F.56})$$

$$\rho_{\text{solid,d}} = \frac{1000 \rho_{\text{solid,daf}}}{B + C}, \quad (\text{F.57})$$

where

$$A = C_1 + C_2 (w_{\text{H,solid,d}} \cdot 100) + C_3 (w_{\text{H,solid,d}} \cdot D) + C_4 (w_{\text{H,solid,d}} \cdot 100)^3, \quad (\text{F.58})$$

$$B = \rho_{\text{solid,daf}} (0.42 w_{\text{ash,solid,d}} - 0.15 w_{\text{S,solid,d}}), \quad (\text{F.59})$$

$$C = (1 - 1.13 w_{\text{ash,solid,d}} - 0.5475 w_{\text{S,solid,d}}) \quad (\text{F.60})$$

with the coefficients  $C_1$ ,  $C_2$ ,  $C_3$  and  $C_4$  given in Table F.4 and with

$$D = 100 \cdot \frac{w_{\text{H,solid,d}} - 0.013 w_{\text{ash,solid,d}} + 0.020 w_{\text{S,solid,d}}}{1 - 1.130 w_{\text{ash,solid,d}} - 0.475 w_{\text{S,solid,d}}}. \quad (\text{F.61})$$

The model of IGT for coal chars should be used for carbonised coking coals and is based on the equations [21]

$$\rho_{\text{solid,daf}} = \frac{1000 \text{ kg}}{\sum_{i=1}^4 C_i (w_{\text{H,solid,daf}} \cdot 100)^{i-1} \text{ m}^3}, \quad (\text{F.62})$$

$$\rho_{\text{solid,d}} = \frac{\rho_{\text{ash}} \rho_{\text{solid,daf}}}{w_{\text{ash,solid,d}} \rho_{\text{solid,daf}} + (1 - w_{\text{ash,solid,d}}) \rho_{\text{ash}}}. \quad (\text{F.63})$$

**Table F.4:** Coefficients  $C_1$ ,  $C_2$ ,  $C_3$  and  $C_4$  for the calculation of the solid density  $\rho_{\text{solid}}$  using the models of IGT [21].

$i$	$C_i$
1	$4.397 \cdot 10^{-1}$
2	$1.223 \cdot 10^{-1}$
3	$-1.715 \cdot 10^{-2}$
4	$1.077 \cdot 10^{-3}$

The solid densities  $\rho_{\text{solid}}$  during the devolatilisation simulated using the three models are compared in Fig. F.1, assuming a constant heating rate of  $10^4 \frac{\text{K}}{\text{s}}$  (left) or a constant temperature of 1673.15 K (right). The (true) solid density  $\rho_{\text{solid}}$  accordingly changes during devolatilisation although a temperature dependence is not assumed in the three density models. This is due to changes of the composition and can also be observed during heterogeneous gasification. Furthermore, the models provide significant deviating predictions at low particle devolatilisation conversions.

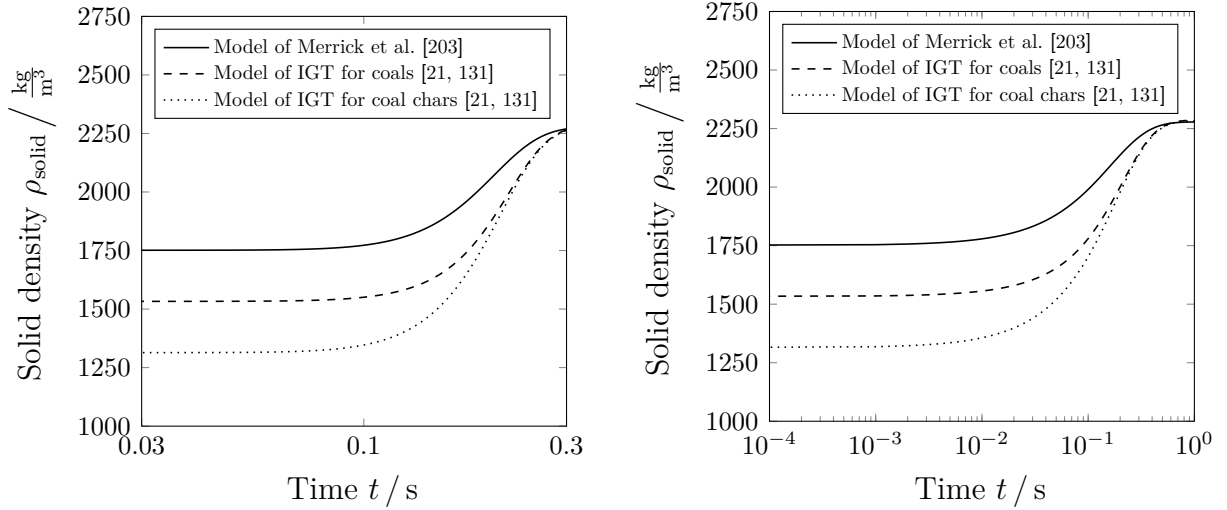


**Figure F.1:** Comparison of simulated solid densities  $\rho_{\text{solid}}$  during devolatilisation at a constant heating rate of  $10^4$  K/s (left) or at a constant temperature of 1673.15 K (right) based on various models. Devolatilisation is based on the single first-order reaction Arrhenius law model of Dammann et al [68].

## F.7.2 Specific heat capacity

The specific solid heat capacity  $\hat{C}_{p,\text{solid}}$  can be determined, for example, by the models of Kirov [152] and Merrick et al. [202]. The model of Kirov [152] is given by [152]

$$\hat{C}_{p,\text{solid}} = \begin{cases} w_{\text{H}_2\text{O, char}} \hat{C}_{p,\text{H}_2\text{O}} + w_{\text{comb, char}} \hat{C}_{p,\text{comb}} + w_{\text{ash, char}} \hat{C}_{p,\text{ash}} \\ \quad + 0.1 (1 - w_{\text{H}_2\text{O, char}} - w_{\text{ash, char}}) \hat{C}_{p,\text{vol},1} \\ \quad + (w_{\text{vol, char, daf}} - 0.1) (1 - w_{\text{H}_2\text{O, char}} - w_{\text{ash, char}}) \hat{C}_{p,\text{vol},2}, & \text{if } w_{\text{vol, char, daf}} > 0.1 \\ w_{\text{H}_2\text{O, char}} \hat{C}_{p,\text{H}_2\text{O}} + w_{\text{comb, char}} \hat{C}_{p,\text{comb}} + w_{\text{vol, char}} \hat{C}_{p,\text{vol},2} \\ \quad + w_{\text{ash, char}} \hat{C}_{p,\text{ash}}, & \text{else} \end{cases} \quad (\text{F.64})$$

where [152]

$$\hat{C}_{p,\text{H}_2\text{O}} = 4184 \frac{\text{J}}{\text{kg K}}, \quad (\text{F.65})$$

$$\hat{C}_{p,\text{comb}} = \left( 1.65 \cdot 10^{-1} + 6.8 \cdot 10^{-4} \tilde{T} - 4.2 \cdot 10^{-7} \tilde{T}^2 \right) 4184 \frac{\text{J}}{\text{kg K}}, \quad (\text{F.66})$$

$$\hat{C}_{p,\text{vol},1} = \left( 7.1 \cdot 10^{-1} + 6.1 \cdot 10^{-4} \tilde{T} \right) 4184 \frac{\text{J}}{\text{kg K}}, \quad (\text{F.67})$$

$$\hat{C}_{p,\text{vol},2} = \left( 3.95 \cdot 10^{-1} + 8.1 \cdot 10^{-4} \tilde{T} \right) 4184 \frac{\text{J}}{\text{kg K}}, \quad (\text{F.68})$$

$$\hat{C}_{p,\text{ash}} = \left( 1.8 \cdot 10^{-1} + 1.4 \cdot 10^{-4} \tilde{T} \right) 4184 \frac{\text{J}}{\text{kg K}}, \quad (\text{F.69})$$

$$\tilde{T} = \frac{T}{\text{K}} - 273.15. \quad (\text{F.70})$$

The model of Merrick et al. [202] has both a theoretical and an empirical basis and is defined by [202]

$$\begin{aligned} \hat{C}_{p,\text{solid}} = & w_{\text{H}_2\text{O},\text{solid}} \hat{C}_{p,\text{H}_2\text{O}} + \left(1 - w_{\text{H}_2\text{O},\text{solid}} - w_{\text{ash},\text{solid}}\right) \hat{C}_{p,\text{solid,daf}} \\ & + w_{\text{ash},\text{solid}} \hat{C}_{p,\text{ash}}, \end{aligned} \quad (\text{F.71})$$

where [202]

$$\hat{C}_{p,\text{H}_2\text{O}} = 4187 \frac{\text{J}}{\text{kg K}}, \quad (\text{F.72})$$

$$\hat{C}_{p,\text{solid,daf}} = \frac{\bar{R}}{M_{\text{solid,daf}}} \left( g\left(\frac{T_{\text{E},1}}{T}\right) + 2g\left(\frac{T_{\text{E},2}}{T}\right) \right), \quad (\text{F.73})$$

$$\hat{C}_{p,\text{ash}} = \left( 754 + 0.586 \left( \frac{T}{\text{K}} - 273.15 \right) \right) \frac{\text{J}}{\text{kg K}}. \quad (\text{F.74})$$

$T_{\text{E},1} = 380 \text{ K}$  and  $T_{\text{E},2} = 1800 \text{ K}$  are Einstein temperatures [202], while  $g$  is an auxiliary function and is given by [202]

$$g(z) = \frac{\exp(z)}{((\exp(z) - 1)/z)^2}. \quad (\text{F.75})$$

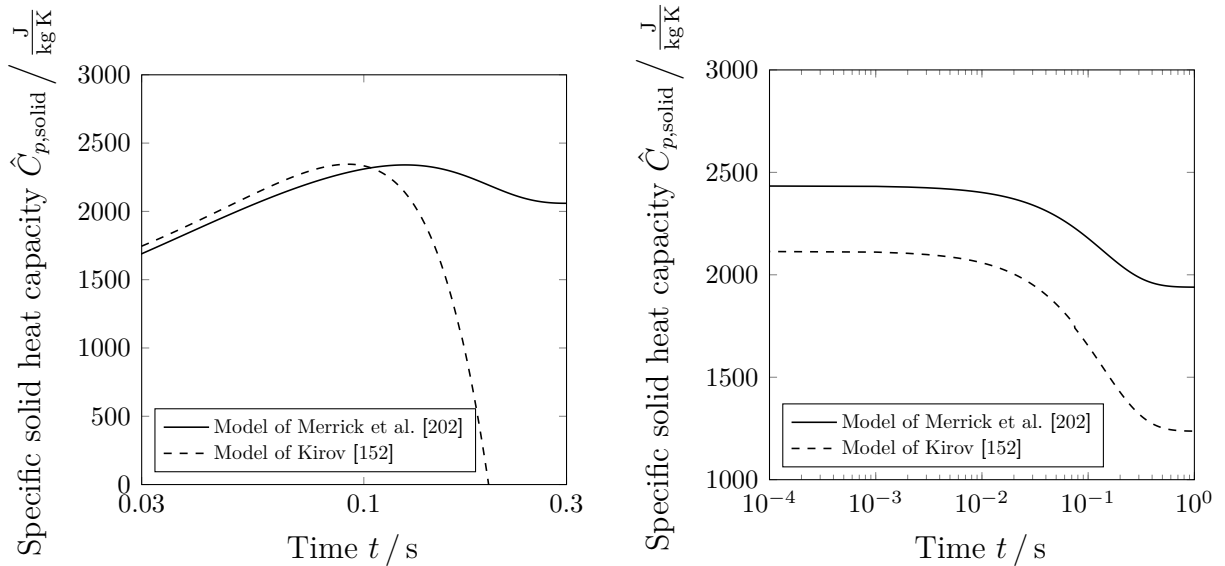


**Figure F.2:** Comparison of simulated specific solid heat capacities  $\hat{C}_{p,\text{solid}}$  during devolatilisation at a constant heating rate of  $10^4 \text{ K/s}$  (left) or at a constant temperature of  $1673.15 \text{ K}$  (right) based on various models. Devolatilisation is based on the single first-order reaction Arrhenius law model of Dammann et al [68].

The specific solid heat capacities  $\hat{C}_{p,\text{solid}}$  during the devolatilisation simulated using both models are compared in Fig. F.2, assuming a constant heating rate of  $10^4 \frac{\text{K}}{\text{s}}$  (left) or a constant temperature of 1673.15 K (right). The predictions based on the model of Merrick et al. accordingly provide reasonable results at elevated temperatures, while the predictions based on the model of Kirov are erroneous at such conditions.

### F.7.3 Specific physical enthalpy

The specific physical solid enthalpy  $\hat{H}_{\text{phys},\text{solid}}$  based on the model of Merrick et al. [202] is given by

$$\begin{aligned} \hat{H}_{\text{phys},\text{solid}} = & w_{\text{H}_2\text{O},\text{solid}} \hat{H}_{\text{phys},\text{H}_2\text{O}} + \left(1 - w_{\text{H}_2\text{O},\text{solid}} - w_{\text{ash},\text{solid}}\right) \hat{H}_{\text{phys},\text{solid},\text{daf}} \\ & + w_{\text{ash},\text{solid}} \hat{H}_{\text{phys},\text{ash}}, \end{aligned} \quad (\text{F.76})$$

where

$$\hat{C}_{p,\text{H}_2\text{O}} = 4187 (T - T_{\text{ref}}) \frac{\text{J}}{\text{kg K}}, \quad (\text{F.77})$$

$$\hat{C}_{p,\text{solid},\text{daf}} = \frac{\bar{R}}{M_{\text{solid},\text{daf}}} \left( T_{\text{E},1} g\left(\frac{T_{\text{E},1}}{T}, \frac{T_{\text{E},1}}{T_{\text{ref}}}\right) + 2 T_{\text{E},2} g\left(\frac{T_{\text{E},2}}{T}, \frac{T_{\text{E},2}}{T_{\text{ref}}}\right) \right), \quad (\text{F.78})$$

$$\begin{aligned} \hat{C}_{p,\text{ash}} = & \left( 754 (T - T_{\text{ref}}) + 0.586 \left( \left( \frac{T}{\text{K}} - 273.15 \right) - \left( \frac{T_{\text{ref}}}{\text{K}} - 273.15 \right)^2 \right) \right) \\ & \cdot \frac{\text{J}}{\text{kg K}}. \end{aligned} \quad (\text{F.79})$$

$T_{\text{E},1} = 380 \text{ K}$  and  $T_{\text{E},2} = 1800 \text{ K}$  are Einstein temperatures, while  $g$  is an auxiliary function and is given by [202]

$$g(z, z_{\text{ref}}) = \frac{1}{\exp(z) - 1} - \frac{1}{\exp(z_{\text{ref}}) - 1}. \quad (\text{F.80})$$



# G Reaction mechanisms

## G.1 The WD mechanism

**Table G.1:** Chemical equations of the reaction mechanism of Westbrook and Dryer [333].

$r$	Chemical equation of reaction $r$
R1	$\text{CH}_4 + \frac{3}{2}\text{O}_2 \longrightarrow \text{CO} + 2\text{H}_2\text{O}$
R2	$\text{CO} + \frac{1}{2}\text{O}_2 \longrightarrow \text{CO}_2$
R3	$\text{CO}_2 \longrightarrow \text{CO} + \frac{1}{2}\text{O}_2$

**Table G.2:** Parameters of the reaction mechanism of Westbrook and Dryer [333].

$r$	$\frac{k_{0,r}}{1/\text{s}}$	$\frac{\bar{E}_{a,r}}{10^8 \text{ cal/kmol}}$	$b_r$	Concentrations product for reaction $r$
R1	$1.59 \cdot 10^{13} \frac{\text{m}^{1.5}}{\text{kmol}^{0.5}}$	47.8	0	$[\text{CH}_4]^{0.7} [\text{O}_2]^{0.8}$
R2	$3.98 \cdot 10^{14} \frac{\text{m}^{2.25}}{\text{kmol}^{0.75}}$	40.7	0	$[\text{CO}] [\text{O}_2]^{0.25} [\text{H}_2\text{O}]^{0.5}$
R3	$5.00 \cdot 10^8$	40.7	0	$[\text{CO}_2]$

## G.2 The JL mechanism

**Table G.3:** Chemical equations of the reaction mechanism of Jones and Lindstedt [144].

$r$	Chemical equation of reaction $r$
R1	$\text{CH}_4 + \text{O}_2 \longrightarrow \text{CO} + 2\text{H}_2$
R2	$\text{CH}_4 + \text{H}_2\text{O} \longrightarrow \text{CO} + 3\text{H}_2$
R3	$\text{H}_2 + \frac{1}{2}\text{O}_2 + \theta\text{H}_2\text{O} \rightleftharpoons \text{H}_2\text{O}$
R4	$\text{CO} + \text{H}_2\text{O} \rightleftharpoons \text{CO}_2 + \text{H}_2$

**Table G.4:** Parameters of the reaction mechanism of Jones and Lindstedt [144].

$r$	$\frac{k_{0,r}}{1/\text{s}}$	$\frac{\bar{E}_{a,r}}{10^8 \text{ cal/kmol}}$	$b_r$	Concentrations product for reaction $r$
R1	$7.82 \cdot 10^{13} \frac{\text{m}^{2.25}}{\text{kmol}^{0.75}}$	30	0	$[\text{CH}_4]^{0.5} [\text{O}_2]^{1.25}$
R2	$0.30 \cdot 10^{12} \frac{\text{m}^3}{\text{kmol}}$	30	0	$[\text{CH}_4] [\text{H}_2\text{O}]$
R3	$4.45 \cdot 10^{18} \frac{\text{m}^{2.25}}{\text{kmol}^{0.75}}$	40	-1	$[\text{H}_2]^{0.5} [\text{O}_2]^{2.25} [\text{H}_2\text{O}]^{-1}$
R4	$2.75 \cdot 10^{12} \frac{\text{m}^3}{\text{kmol}}$	20	0	$[\text{CO}] [\text{H}_2\text{O}]$

### G.3 The JL/A mechanism

**Table G.5:** Chemical equations of the alternative reaction mechanism of Jones and Lindstedt [144].

$r$	Chemical equation of reaction $r$
R1	$\text{CH}_4 + \text{O}_2 \longrightarrow \text{CO} + 2 \text{H}_2$
R2	$\text{CH}_4 + \text{H}_2\text{O} \longrightarrow \text{CO} + 3 \text{H}_2$
R3	$\text{H}_2 + \frac{1}{2} \text{O}_2 + 0 \text{H}_2\text{O} \rightleftharpoons \text{H}_2\text{O}$
R4	$\text{CO} + \text{H}_2\text{O} \rightleftharpoons \text{CO}_2 + \text{H}_2$

**Table G.6:** Parameters of the alternative reaction mechanism of Jones and Lindstedt [144].

$r$	$\frac{k_{0,r}}{1/\text{s}}$	$\frac{\overline{E}_{a,r}}{10^8 \text{ cal/kmol}}$	$b_r$	Concentration product for reaction $r$
R1	$7.82 \cdot 10^{13} \frac{\text{m}^{2.25}}{\text{kmol}^{0.75}}$	30	0	$[\text{CH}_4]^{0.5} [\text{O}_2]^{1.25}$
R2	$0.30 \cdot 10^{12} \frac{\text{m}^3}{\text{kmol}}$	30	0	$[\text{CH}_4] [\text{H}_2\text{O}]$
R3	$1.21 \cdot 10^{18} \frac{\text{m}^{2.25}}{\text{kmol}^{0.75}}$	40	-1	$[\text{H}_2]^{0.25} [\text{O}_2]^{1.5}$
R4	$2.75 \cdot 10^{12} \frac{\text{m}^3}{\text{kmol}}$	20	0	$[\text{CO}] [\text{H}_2\text{O}]$

### G.4 The HVI1 mechanism

**Table G.7:** Chemical equations of the first reaction mechanism of HVIGasTech for the gasification of ethylene glycol [187].

$r$	Chemical equation of reaction $r$
R1	$4 \text{C}_2\text{H}_6\text{O}_2 \longrightarrow 9 \text{H}_2 + 7 \text{CO} + \text{H}_2\text{O} + \text{CH}_4$
R2	$\text{CO} + \frac{1}{2} \text{O}_2 + \text{H}_2\text{O} \longrightarrow \text{CO}_2 + \text{H}_2\text{O}$
R3	$\text{CH}_4 + \text{H}_2\text{O} \rightleftharpoons \text{CO} + 3 \text{H}_2$
R4	$\text{CH}_4 + \frac{1}{2} \text{O}_2 \longrightarrow \text{CO} + 2 \text{H}_2$
R5	$\text{CO} + \text{H}_2\text{O} \rightleftharpoons \text{CO}_2 + \text{H}_2$
R6	$\text{H}_2 + \frac{1}{2} \text{O}_2 \longrightarrow \text{H}_2\text{O}$

**Table G.8:** Parameters of the first reaction mechanism of HVIGasTech for the gasification of ethylene glycol [187].

$r$	$\frac{k_{0,r}}{1/\text{s}}$	$\frac{\overline{E}_{a,r}}{10^8 \text{ J/kmol}}$	$b_r$	Concentrations product for reaction $r$
R1	$9.31 \cdot 10^{13}$	2.684	0	$[\text{C}_2\text{H}_6\text{O}_2]$
R2	$3.1623 \cdot 10^{11} \frac{\text{m}^6}{\text{kmol}^3}$	1.256	0	$[\text{CO}] [\text{O}_2] [\text{H}_2\text{O}]$
R3	$1.7 \cdot 10^{10} \frac{\text{m}^{1.5}}{\text{kmol}^{0.5}}$	2.300	0	$[\text{CH}_4] [\text{H}_2\text{O}]$
R4	$1.5811 \cdot 10^{14}$	2.512	0	$[\text{CH}_4] [\text{O}_2]^{0.5}$
R5	$8.5 \cdot 10^9$	2.040	0	$[\text{CO}] [\text{H}_2\text{O}]$
R6	$2.8464 \cdot 10^{14} \frac{\text{m}^{1.5}}{\text{kmol}^{0.5}}$	2.592	0	$[\text{H}_2] [\text{O}_2]^{0.5}$

## G.5 The eJL mechanism

**Table G.9:** Chemical equations of the extended reaction mechanism of Jones and Lindstedt for the gasification of ethylene glycol [187].

$r$	Chemical equation of reaction $r$
R1	$4 \text{C}_2\text{H}_6\text{O}_2 \longrightarrow \text{CH}_4 + 7 \text{CO} + 9 \text{H}_2 + \text{H}_2\text{O}$
R2	$\text{C}_2\text{H}_6\text{O}_2 + \text{O}_2 \longrightarrow 2 \text{CO} + 2 \text{H}_2\text{O} + \text{H}_2$
R3	$\text{CH}_4 + \text{H}_2\text{O} \longrightarrow \text{CO} + 3 \text{H}_2$
R4	$\text{CH}_4 + \frac{1}{2} \text{O}_2 \longrightarrow \text{CO} + 2 \text{H}_2$
R5	$\text{CO} + \text{H}_2\text{O} \rightleftharpoons \text{CO}_2 + \text{H}_2$
R6	$2 \text{H}_2 + \text{O}_2 + 0 \text{H}_2\text{O} \rightleftharpoons 2 \text{H}_2\text{O}$

**Table G.10:** Parameters of the extended reaction mechanism of Jones and Lindstedt for the gasification of ethylene glycol [187].

$r$	$\frac{k_{0,r}}{1/\text{s}}$	$\frac{\bar{E}_{a,r}}{10^8 \text{ J/kmol}}$	$b_r$	Concentrations product for reaction $r$
R1	$9.31 \cdot 10^{13}$	2.684	0	$[\text{C}_2\text{H}_6\text{O}_2]$
R2	$4.4 \cdot 10^{11} \frac{\text{m}^{2.25}}{\text{kmol}^{0.75}}$	1.256	0	$[\text{C}_2\text{H}_6\text{O}_2]^{0.5} [\text{O}_2]^{1.25}$
R3	$3 \cdot 10^8 \frac{\text{m}^3}{\text{kmol}}$	1.256	0	$[\text{CH}_4] [\text{H}_2\text{O}]$
R4	$4.4 \cdot 10^{11} \frac{\text{m}^{2.25}}{\text{kmol}^{0.75}}$	1.256	0	$[\text{CH}_4]^{0.5} [\text{O}_2]^{1.25}$
R5	$2.75 \cdot 10^9 \frac{\text{m}^3}{\text{kmol}}$	0.8381	0	$[\text{CO}] [\text{H}_2\text{O}]$
R6	$2.5 \cdot 10^{16} \frac{\text{m}^{2.25}}{\text{kmol}^{0.75}}$	1.6747	-1	$[\text{H}_2]^{0.5} [\text{O}_2]^{2.25} [\text{H}_2\text{O}]^{-1}$

## G.6 The eJL/A mechanism

**Table G.11:** Chemical equations of the alternative extended reaction mechanism of Jones and Lindstedt for the gasification of ethylene glycol [187].

$r$	Chemical equation of reaction $r$
R1	$4 \text{C}_2\text{H}_6\text{O}_2 \longrightarrow \text{CH}_4 + 7 \text{CO} + 9 \text{H}_2 + \text{H}_2\text{O}$
R2	$\text{C}_2\text{H}_6\text{O}_2 + \text{O}_2 \longrightarrow 2 \text{CO} + 2 \text{H}_2\text{O} + \text{H}_2$
R3	$\text{CH}_4 + \text{H}_2\text{O} \longrightarrow \text{CO} + 3 \text{H}_2$
R4	$\text{CH}_4 + \frac{1}{2} \text{O}_2 \longrightarrow \text{CO} + 2 \text{H}_2$
R5	$\text{CO} + \text{H}_2\text{O} \rightleftharpoons \text{CO}_2 + \text{H}_2$
R6	$\text{H}_2 + 0.5 \text{O}_2 \rightleftharpoons \text{H}_2\text{O}$

**Table G.12:** Parameters of the alternative extended reaction mechanism of Jones and Lindstedt for the gasification of ethylene glycol [187].

$r$	$\frac{k_{0,r}}{1/\text{s}}$	$\frac{\bar{E}_{a,r}}{10^8 \text{ J/kmol}}$	$b_r$	Exponents for reaction $r$
R1	$9.31 \cdot 10^{13}$	2.684	0	$[\text{C}_2\text{H}_6\text{O}_2]$
R2	$4.4 \cdot 10^{11} \frac{\text{m}^{2.25}}{\text{kmol}^{0.75}}$	1.256	0	$[\text{C}_2\text{H}_6\text{O}_2]^{0.5} [\text{O}_2]^{1.25}$
R3	$3 \cdot 10^8 \frac{\text{m}^3}{\text{kmol}}$	1.256	0	$[\text{CH}_4] [\text{H}_2\text{O}]$
R4	$4.4 \cdot 10^{11} \frac{\text{m}^{2.25}}{\text{kmol}^{0.75}}$	1.256	0	$[\text{CH}_4]^{0.5} [\text{O}_2]^{1.25}$
R5	$2.75 \cdot 10^9 \frac{\text{m}^3}{\text{kmol}}$	0.8381	0	$[\text{CO}] [\text{H}_2\text{O}]$
R6	$6.8043 \cdot 10^{15} \frac{\text{m}^{2.25}}{\text{kmol}^{0.75}}$	1.6736	-1	$[\text{H}_2]^{0.25} [\text{O}_2]^{1.5}$

## G.7 The DLR2017/RK mechanism

**Table G.13:** Adapted chemical equations of the reduced DLR2017 mechanism of Kathrotia et al. for the gasification of ethylene glycol [149].

$r$	Chemical equation of reaction $r$
R58	$\text{HOCHCHO} + \text{M} \longrightarrow \text{CHOCHO} + \text{H} + \text{M}$
R117	$\text{CH} + \text{H}_2\text{O} \longrightarrow \text{Th-CH}_2 + \text{OH}$
R149	$\text{CH}_3 + \text{M} \longrightarrow \text{Th-CH}_2 + \text{H} + \text{M}$
R150	$\text{CH}_3 + \text{M} \longrightarrow \text{CH} + \text{H}_2 + \text{M}$
R198	$\text{CH}_2\text{CO} + \text{M} \longrightarrow \text{Th-CH}_2 + \text{CO} + \text{M}$

## G.8 The DLR2017/RM mechanism

**Table G.14:** Adapted chemical equations of the reduced DLR2017 mechanism of Methling et al. for the gasification of ethylene glycol [204].

$r$	Chemical equation of reaction $r$
R62	$\text{CH}_3 + \text{M} \longrightarrow \text{Th-CH}_2 + \text{H} + \text{M}$
R80	$\text{CH}_2\text{CO} + \text{M} \longrightarrow \text{Th-CH}_2 + \text{CO} + \text{M}$

# H Vaporisation simulation results

Single-droplet vaporisation simulations were also carried out (i) using a wavenumber discretisation of  $10 \text{ cm}^{-1}$ , (ii) using recalculation, (iii) using the tabulated values for the emissivity (see Section 2.5.3) and (iv) using the previous polynomial approximation for the film diffusion coefficient (see Section F.6.6). The results are shown in Figs. H.1, H.2 and H.3.

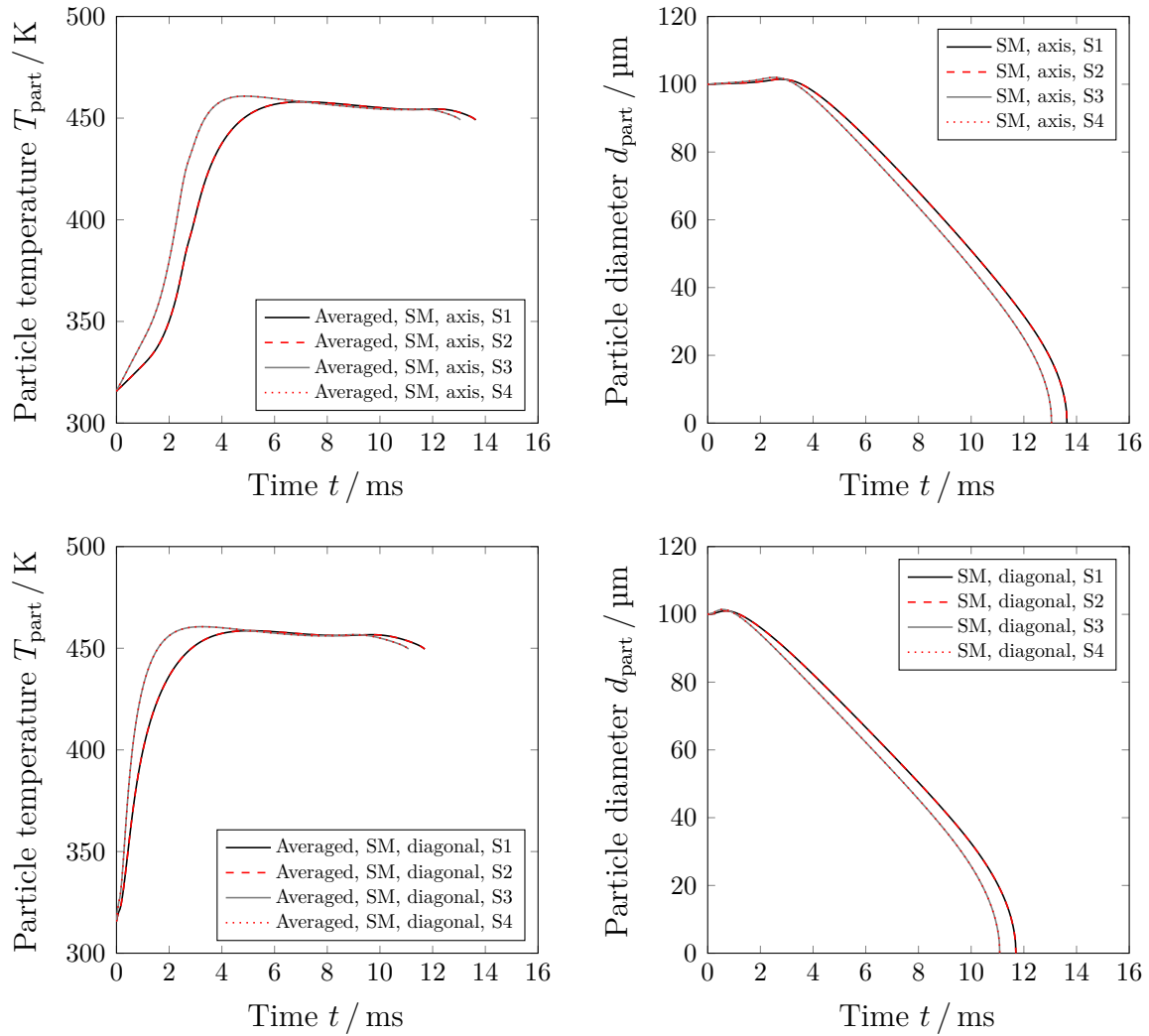


**Figure H.1:** Simulated particle temperatures  $T_{\text{part}}$  and simulated particle diameters  $d_{\text{part}}$  along the reactor axis (top) and the reactor diagonal (bottom) based on the model of Sazhin et al. (SM) in presence of thermal radiation. S1: w/o recalculation,  $\Delta\eta = 25 \text{ cm}^{-1}$ ; S2: w/o recalculation,  $\Delta\eta = 10 \text{ cm}^{-1}$ ; S3: w/ recalculation,  $\Delta\eta = 25 \text{ cm}^{-1}$ ; S4: w/ recalculation,  $\Delta\eta = 10 \text{ cm}^{-1}$ .

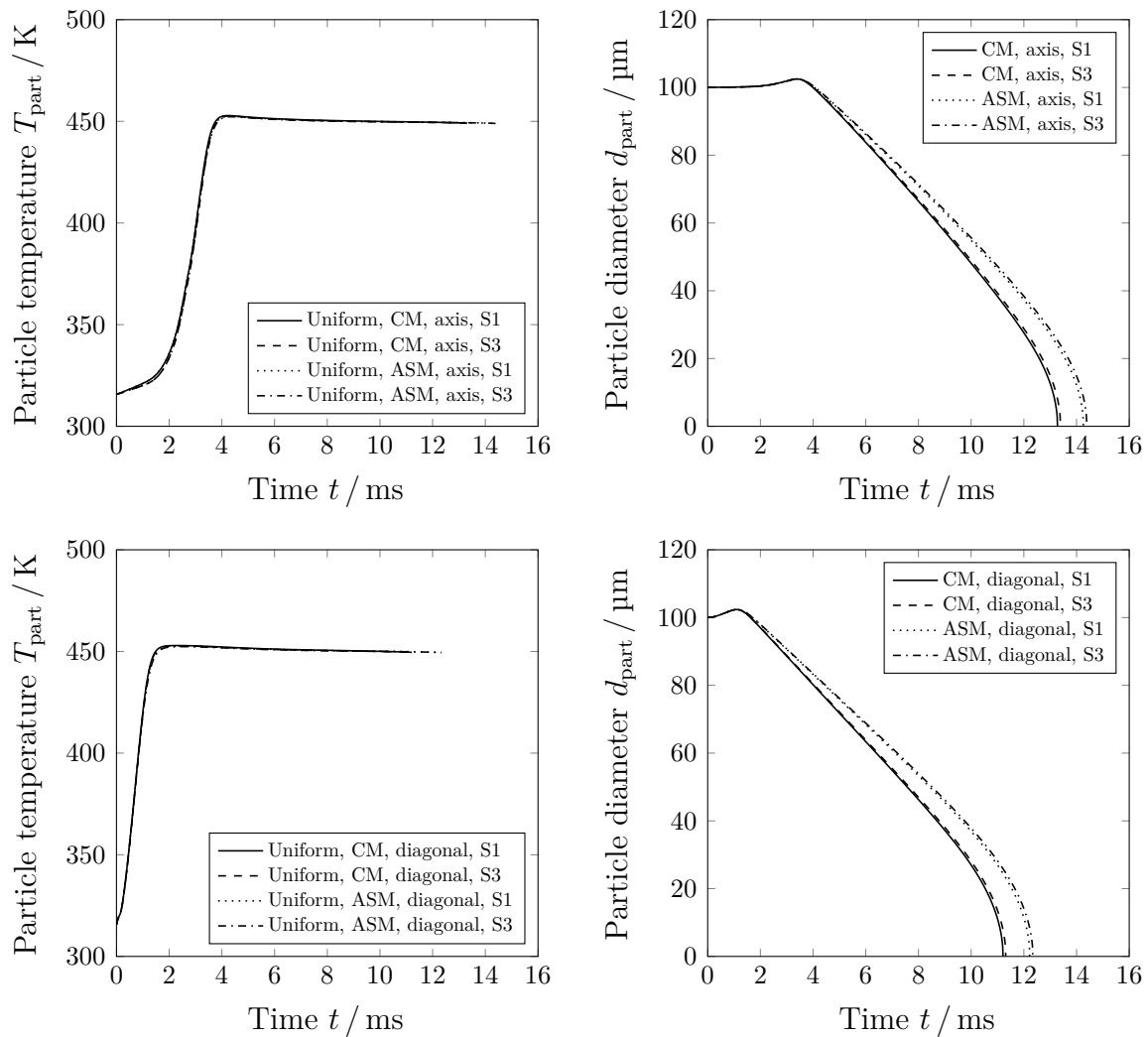


**Figure H.2:** Simulated particle temperatures  $T_{\text{part}}$  and simulated particle diameters  $d_{\text{part}}$  along the reactor axis (top) and the reactor diagonal (bottom) based on the classical model (CM) and the model of Abramzon and Sirignano (ASM) in presence of thermal radiation and with two different approaches for the emissivity. S1: polynomial approximation; S3: tabulation.

Accordingly, a wavenumber discretisation of  $10 \text{ cm}^{-1}$  provides almost identical results compared to a wavenumber discretisation of  $25 \text{ cm}^{-1}$  for predictions using the model of Sazhin et al. [270]. Furthermore, small deviations for the vaporisation time can be found when the particle temperature distribution is recalculated at each time step, the emissivity is described using (more accurate) tabulated values or the film diffusion coefficient is described following the preceding work [187]. Thus, single-droplet vaporisation simulations with the model of Sazhin et al. [270] using a wavenumber discretisation of  $25 \text{ cm}^{-1}$  and without recalculation provide sufficiently accurate predictions for ethylene glycol droplets, and single-droplet vaporisation simulations can be performed using simplifications for the emissivity and the film diffusion coefficient.

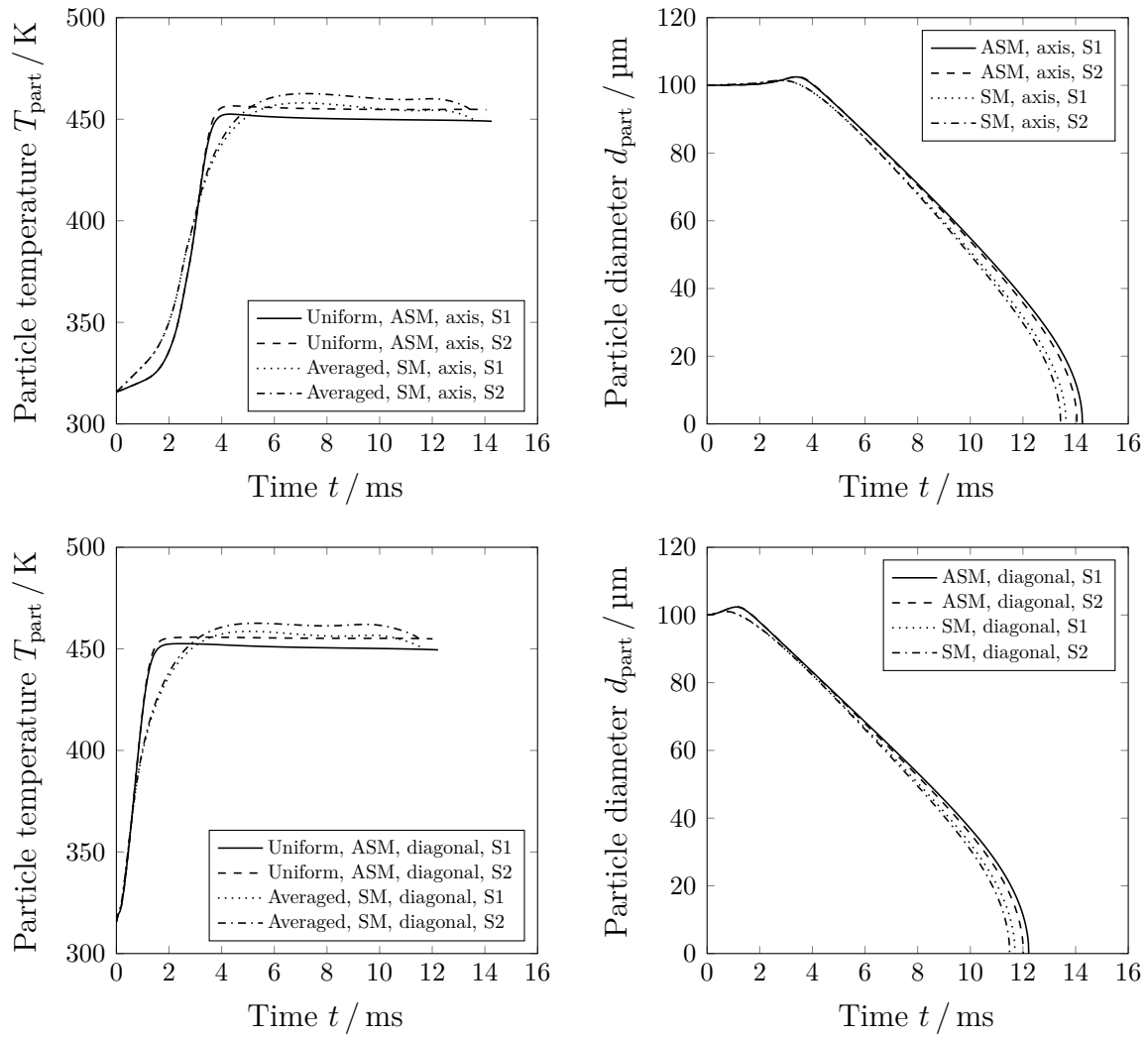


**Figure H.3:** Simulated particle temperatures  $T_{\text{part}}$  and simulated particle diameters  $d_{\text{part}}$  along the reactor axis (top) and the reactor diagonal (bottom) based on the model of Abramzon and Sirignano (ASM) and the model of Sazhin et al. (SM) in presence of thermal radiation and with two different approaches for the vapour film diffusion coefficient. S1: effective Fickian diffusion; S2: polynomial approximation.



# **I Wood char properties**

## **I.1 Chemical properties**

**Table I.1:** Origins and applications of wood chars focussed in the characterisation and gasification experiments and in the numerical simulations.

Wood char	Origin	Application
HK01	Beech wood, Chemviron [49]	REGA experiment TUC5 GHKS10 [63, 64, 97]
HK02	Fir wood, STYX [303]	Characterisation experiments [155, 156, 157, 300, 300]
HK02-1600	HK02 + DTR (1600 °C, 200 ms) [275, 303]	Characterisation experiments [156, 275, 300, 303]
HK04	Beech wood, Schütte [126]	bioliq EFG experiments; REGA experiments
HK06	Beech wood, Schütte [126]	Characterisation experiments [276, 277, 278]
HK06-1400-200	HK06 + DTR (1400 °C, 200 ms) [276, 278]	Characterisation experiments [276, 277, 278]
HK06-1600-200	HK06 + DTR (1600 °C, 200 ms) [276, 278]	Characterisation experiments [276, 277, 278]
HK07	Beech wood, Schütte [126]	REGA experiment TUC5 GHKS30 [64, 100]

**Table I.2:** Proximate and ultimate compositions of wood chars focussed in the characterisation and gasification experiments and in the numerical simulations.

Wood char	Analysis	$w_{\text{solid},0}$										
		C	H	O	N	H <sub>2</sub> O	ash	comb	vol	comb,eq	vol,eq	
HK01	EF	0.828	0.023	0.080	0.004	0.045	0.019	0.795	0.141	0.738	0.243	
HK01	EF simple	0.828	0.028	0.120	0.005	0	0.019	–	–	0.738	0.243	
HK02	EBI	0.766	0.022	0.164	0.004	0.011	0.033	0.689	0.267	0.636	0.331	
HK02	EBI simple	0.766	0.023	0.173	0.005	0	0.033	–	–	0.636	0.331	
HK02-1600	EBI	0.937	0.000	0.005	0.007	0	0.052	0.948	0.000	0.933	0.015	
HK02-1600	EBI simple	0.937	0.000	0.005	0.007	0	0.052	–	–	0.933	0.015	
HK04	EF	0.804	0.021	0.063	0.005	0.041	0.066	0.790	0.103	0.712	0.245	
HK06	EF	0.845	0.024	0.056	0.004	0.054	0.018	0.822	0.106	0.766	0.216	
HK06	EF simple	0.845	0.030	0.104	0.005	0	0.018	–	–	0.766	0.216	
HK06	EBI	0.866	0.025	0.078	0.004	0.009	0.018	0.855	0.118	0.801	0.182	
HK06	EBI simple	0.866	0.026	0.087	0.004	0	0.018	–	–	0.801	0.182	
HK07	EF	0.787	0.023	0.072	0.004	0.073	0.040	0.767	0.120	0.685	0.275	
HK06-1400-200	EBI	0.954	0.002	0.018	0.007	0.002	0.019	0.954	0.025	0.937	0.044	
HK06-1600-200	EBI	0.974	0.002	0.003	0.005	0.000	0.016	0.971	0.013	0.972	0.011	

## **I.2 Morphology measurements**

**Table I.3:** Mean particle pore diameters obtained by measurements [80, 303], numerical regressions [156] or estimations. Note: HK02 was reported as wood char in [303]; HK02-1000 was reported as HK1000 in [303]; HK02-1600 was reported as HK1600 in [303] and as WC1600 in [80].

Wood char	$\frac{\rho_{\text{solid}}}{\text{m}^3/\text{kg}}$	$\frac{\rho_{\text{solid,eff}}}{\text{m}^3/\text{kg}}$	$\epsilon_{\text{solid,macro}}$	$\epsilon_{\text{solid,micro}}$	$\hat{A}_{\text{pore,part}}$ $\text{m}^2/\text{g}$	$\frac{d_{\text{pore,part,meas}}}{\text{nm}}$	$\frac{d_{\text{pore,part,est}}}{\text{nm}}$	Source
HK02	1510	850	0.54	—	$\approx 247$	2.6	$\approx 12.6$	[303]
HK02-1000	1950	860	0.56	—	$\approx 610$	2.4	$\approx 4.3$	[303]
HK02-1000 ( $X_{\text{C,solid}} = 30\%$ )	1990	880	0.56	—	$\approx 690$	2.4	$\approx 3.7$	[303]
HK02-1600	2030	910	0.55	—	$\approx 80$	2.2	$\approx 30.1$	[303]
HK02-1600 ( $X_{\text{C,solid}} = 30\%$ )	2110	900	0.57	—	$\approx 280$	2.2	$\approx 9.0$	[303]
HK02-1600	2178.8	—	0.500	—	231.7	—	$\approx 7.9$	[80]
HK02-1600 ( $X_{\text{C,solid}} = 9.1\%$ )	2288.5	—	0.565	—	—	—	—	[80]
HK02-1600 ( $X_{\text{C,solid}} = 21.2\%$ )	2321.8	—	0.598	—	471.1	—	$\approx 5.9$	[80]
HK02-1600 ( $X_{\text{C,solid}} = 31.9\%$ )	2315.1	—	0.606	—	—	—	—	[80]
HK02-1600 ( $X_{\text{C,solid}} = 40.7\%$ )	2343.8	—	0.621	—	500.9	—	$\approx 5.6$	[80]
HK02-1600 ( $X_{\text{C,solid}} = 56.0\%$ )	2347.6	$\approx 1626.9$	0.623	0.307	544.3	—	$\approx 1.4\text{-}5.2$	[80]
HK02-1600 ( $X_{\text{C,solid}} = 68.2\%$ )	2298.6	—	0.659	—	550.4	—	$\approx 6.1$	[80]
HK02-1600 ( $X_{\text{C,solid}} = 78.0\%$ )	2203.1	$\approx 1401.2$	0.682	0.364	571.1	—	$\approx 1.8\text{-}6.8$	[80]
HK02 (B, PLM)	—	—	0.691	—	—	—	3.9	[156]
HK02 (B, LHM)	—	—	0.691	—	—	—	10.5	[156]
HK02-1600 (B, PLM)	—	—	0.262	—	—	—	16.0	[156]
HK02 (W, PLM)	—	—	0.691	—	—	—	4.8	[156]
HK02 (W, LHM)	—	—	0.691	—	—	—	3.3	[156]
HK02-1600 (W, PLM)	—	—	0.262	—	—	—	20.5	[156]

**Table 1.4:** Measured specific surface areas  $\hat{A}_{\text{int,part}}$  obtained in the frame of HVI GasTech [124]. Note: The BET method provides good estimates of the surface area for substances with mesopores and macropores while estimates for substances with micropores are affected by capillary condensation. The measurements with Ar generally provide results superior to  $\text{N}_2$  due to spherical charge distribution. The DR method is used to estimate the volume and the surface area in presence of micropores.

Wood char	Apparatus	Method	$\frac{S_{\text{BET}}}{\text{m}^2/\text{g}}$	$\frac{S_{\text{DR}}}{\text{m}^2/\text{g}}$	Source
HK02	Micromeritics, ASAP 2020	BET, $\text{N}_2$ at 77 K	6	–	[213]
HK02-900	Micromeritics, ASAP 2020	BET, $\text{N}_2$ at 77 K	254.6	–	[213]
HK06	Micromeritics, ASAP 2020	DR, $\text{CO}_2$ at 273.15 K	–	394.6	[276, 279]
HK06-1000-200	Micromeritics, ASAP 2020	DR, $\text{CO}_2$ at 273.15 K	–	529.7	[276, 279]
HK06-1000-400	Micromeritics, ASAP 2020	DR, $\text{CO}_2$ at 273.15 K	–	562.0	[279]
HK06-1100-200	Micromeritics, ASAP 2020	DR, $\text{CO}_2$ at 273.15 K	–	564.6	[279]
HK06-1200-200	Micromeritics, ASAP 2020	DR, $\text{CO}_2$ at 273.15 K	–	552.7	[276, 279]
HK06-1200-400	Micromeritics, ASAP 2020	DR, $\text{CO}_2$ at 273.15 K	–	555.0	[279]
HK06-1300-200	Micromeritics, ASAP 2020	DR, $\text{CO}_2$ at 273.15 K	–	541.1	[279]
HK06-1400-200	Micromeritics, ASAP 2020	DR, $\text{CO}_2$ at 273.15 K	–	660.0	[276, 279]
HK06-1400-400	Micromeritics, ASAP 2020	DR, $\text{CO}_2$ at 273.15 K	–	854.2	[279]
HK06-1600-200	Micromeritics, ASAP 2020	DR, $\text{CO}_2$ at 273.15 K	–	126.4	[276, 279]
HK06-1600-400	Micromeritics, ASAP 2020	DR, $\text{CO}_2$ at 273.15 K	–	95.6	[279]
HK02-1600	Micromeritics, ASAP 2020	BET, $\text{N}_2$ at 77 K	78	–	[80]
HK02-1600 ( $X_{\text{C,solid}} = 56.0\%$ )	Micromeritics, ASAP 2020	BET, Ar at X K	492.2	–	[80]
HK02-1600 ( $X_{\text{C,solid}} = 78.0\%$ )	Micromeritics, ASAP 2020	BET, Ar at X K	581.9	–	[80]
HK02-1600	Micromeritics, ASAP 2020	DR, $\text{CO}_2$ at 273.15 K	–	231.7	[80]
HK02-1600 ( $X_{\text{C,solid}} = 21.2\%$ )	Micromeritics, ASAP 2020	DR, $\text{CO}_2$ at 273.15 K	–	471.1	[80]
HK02-1600 ( $X_{\text{C,solid}} = 40.7\%$ )	Micromeritics, ASAP 2020	DR, $\text{CO}_2$ at 273.15 K	–	500.9	[80]

Wood char	Apparatus	Method	$\frac{S_{\text{BET}}}{\text{m}^2/\text{g}}$	$\frac{S_{\text{DR}}}{\text{m}^2/\text{g}}$	Source
HK02-1600 ( $X_{\text{C,solid}} = 56.0\%$ )	Micromeritics, ASAP 2020	DR, CO <sub>2</sub> at 273.15 K	—	544.3	[80]
HK02-1600 ( $X_{\text{C,solid}} = 68.2\%$ )	Micromeritics, ASAP 2020	DR, CO <sub>2</sub> at 273.15 K	—	550.4	[80]
HK02-1600 ( $X_{\text{C,solid}} = 78.0\%$ )	Micromeritics, ASAP 2020	DR, CO <sub>2</sub> at 273.15 K	—	571.1	[80]
HK02	Micromeritics, ASAP 2020	DR, CO <sub>2</sub> at 273.15 K	—	24	[303]
HK02	Micromeritics, ASAP 2020	DR, CO <sub>2</sub> at 273.15 K	—	247	[303]
HK02-800-100	Micromeritics, ASAP 2020	DR, CO <sub>2</sub> at 273.15 K	—	310	[303]
HK02-800-200	Micromeritics, ASAP 2020	DR, CO <sub>2</sub> at 273.15 K	—	342	[303]
HK02-800-1000	Micromeritics, ASAP 2020	DR, CO <sub>2</sub> at 273.15 K	—	481	[303]
HK02-1000-200	Micromeritics, ASAP 2020	DR, CO <sub>2</sub> at 273.15 K	—	425	[303]
HK02-1000-1000	Micromeritics, ASAP 2020	DR, CO <sub>2</sub> at 273.15 K	—	480	[303]
HK02-1200-100	Micromeritics, ASAP 2020	DR, CO <sub>2</sub> at 273.15 K	—	455	[303]
HK02-1200-200	Micromeritics, ASAP 2020	DR, CO <sub>2</sub> at 273.15 K	—	467	[303]
HK02-1400-200	Micromeritics, ASAP 2020	DR, CO <sub>2</sub> at 273.15 K	—	431	[303]
HK02-1600-100	Micromeritics, ASAP 2020	DR, CO <sub>2</sub> at 273.15 K	—	87	[303]
HK02-1600-200	Micromeritics, ASAP 2020	DR, CO <sub>2</sub> at 273.15 K	—	254	[303]
HK02-1000 ( $X_{\text{C,solid}} = 0\%$ )	Micromeritics, ASAP 2020	DR, CO <sub>2</sub> at 273.15 K	—	611	[303]
HK02-1000 ( $X_{\text{C,solid}} = 10\%$ )	Micromeritics, ASAP 2020	DR, CO <sub>2</sub> at 273.15 K	—	620	[303]
HK02-1000 ( $X_{\text{C,solid}} = 30\%$ )	Micromeritics, ASAP 2020	DR, CO <sub>2</sub> at 273.15 K	—	678	[303]
HK02-1000 ( $X_{\text{C,solid}} = 50\%$ )	Micromeritics, ASAP 2020	DR, CO <sub>2</sub> at 273.15 K	—	751	[303]
HK02-1600-200 ( $X_{\text{C,solid}} = 0\%$ )	Micromeritics, ASAP 2020	DR, CO <sub>2</sub> at 273.15 K	—	87	[303]
HK02-1600-200 ( $X_{\text{C,solid}} = 0.5\%$ )	Micromeritics, ASAP 2020	DR, CO <sub>2</sub> at 273.15 K	—	156	[303]
HK02-1600-200 ( $X_{\text{C,solid}} = 1.4\%$ )	Micromeritics, ASAP 2020	DR, CO <sub>2</sub> at 273.15 K	—	214	[303]

Wood char	Apparatus	Method	$\frac{S_{\text{BET}}}{\text{m}^2/\text{g}}$	$\frac{S_{\text{DR}}}{\text{m}^2/\text{g}}$	Source
HK02-1600-200 ( $X_{\text{C,solid}} = 8.5\%$ )	Micromeritics, ASAP 2020	DR, CO <sub>2</sub> at 273.15 K	—	230	[303]
HK02-1600-200 ( $X_{\text{C,solid}} = 30.7\%$ )	Micromeritics, ASAP 2020	DR, CO <sub>2</sub> at 273.15 K	—	279	[303]
HK02-1600-200 ( $X_{\text{C,solid}} = 67.7\%$ )	Micromeritics, ASAP 2020	DR, CO <sub>2</sub> at 273.15 K	—	136	[303]

## **I.3 Heterogeneous gasification kinetics**

**Table 1.5:** Heterogeneous gasification kinetics developed in the frame of HVI GasTech [124]. Acronyms: FFBR: free-fall fixed bed reactor, FBR: fluidised bed reactor, LHM: Langmuir-Hinshelwood model, PLM: power-law model, pTGA: pressurised thermogravimetric analyser, pSPR: pressurised single particle reactor.

Kinetics	Wood char	Reactor	Temperature range	Pressure range	Model	Regime	Source
HK02-1600-FFBR-PLM-PS	CO <sub>2</sub> H <sub>2</sub> O	FFBR	800-1000 °C	$p_{\text{CO}_2}$ : 0.05-0.8 bar $p_{\text{H}_2\text{O}}$ : 0.05-0.8 bar	PLM	I	[303]
HK02-FBR-PLM-TK	CO <sub>2</sub> H <sub>2</sub> O	FBR	800-1200 °C	$p_{\text{CO}_2}$ : 0.1-0.8 bar $p_{\text{H}_2\text{O}}$ : 0.1-0.8 bar	PLM	I+II <sup>a</sup>	[156]
HK02-FBR-LHM-TK	CO <sub>2</sub> H <sub>2</sub> O	FBR	800-1200 °C	$p_{\text{CO}_2}$ : 0.1-0.8 bar $p_{\text{H}_2\text{O}}$ : 0.1-0.8 bar	LHM	I+II <sup>a</sup>	[156]
HK02-1600-FBR-PLM-TK	CO <sub>2</sub> H <sub>2</sub> O	FBR	800-1200 °C	$p_{\text{CO}_2}$ : 0.1-0.8 bar $p_{\text{H}_2\text{O}}$ : 0.1-0.8 bar	PLM	I+II <sup>a</sup>	[156]
HK02-1600-pTGA-PLM-CS	CO <sub>2</sub>	pTGA	750-850 °C	$p_{\text{CO}_2}$ : 0.2-5 bar	PLM	I	[275]
HK06-1400-200-pSPR-PLM-CS	CO <sub>2</sub> H <sub>2</sub> O	pSPR	830-870 °C	$p_{\text{CO}_2}$ : 1-20 bar $p_{\text{H}_2\text{O}}$ : 0.2-5 bar	PLM	I	[277]
HK06-1400-200-pSPR-LHM-CS	CO <sub>2</sub> H <sub>2</sub> O	pSPR	830-870 °C	$p_{\text{CO}_2}$ : 1-20 bar $p_{\text{H}_2\text{O}}$ : 0.2-5 bar	LHM	I	[277]
HK06-1600-200-pSPR-PLM-CS	CO <sub>2</sub> H <sub>2</sub> O	pSPR	830-870 °C	$p_{\text{CO}_2}$ : 1-20 bar $p_{\text{H}_2\text{O}}$ : 0.2-5 bar	PLM	I	[277]
HK06-1600-200-pSPR-LHM-CS	CO <sub>2</sub> H <sub>2</sub> O	pSPR	830-870 °C	$p_{\text{CO}_2}$ : 1-20 bar $p_{\text{H}_2\text{O}}$ : 0.2-5 bar	LHM	I	[277]

<sup>a</sup>Observed reactions rates at regime II conditions were limited by response control.

**Table I.6:** Parameters of heterogeneous gasification kinetics developed in the frame of HVI GasTech [124] for regime I.

Kinetics		$\frac{k_0}{1/s}$	$\frac{k_{0,1}}{1/(\text{bar s})}$	$\frac{k_{0,3}}{1/s}$	$\frac{\bar{E}_a}{\text{kJ/mol}}$	$\frac{\bar{E}_{a,1}}{\text{kJ/mol}}$	$\frac{\bar{E}_{a,3}}{\text{kJ/mol}}$	$n$	Source
HK02-1600-FFBR-PLM-PS	CO <sub>2</sub>	$2.28 \cdot 10^8$	—	—	236.0	—	—	0.520	[303]
	H <sub>2</sub> O	$1.23 \cdot 10^9$	—	—	242.0	—	—	0.430	[303]
HK02-FBR-PLM-TK	CO <sub>2</sub>	$2.39 \cdot 10^6$	—	—	185.3	—	—	0.314	[156]
	H <sub>2</sub> O	$6.40 \cdot 10^7$	—	—	211.0	—	—	0.475	[156]
HK02-FBR-LHM-TK	CO <sub>2</sub>	—	$6.58 \cdot 10^6$	$1.86 \cdot 10^8$	—	177.9	227.6	—	[156]
	H <sub>2</sub> O	—	$2.39 \cdot 10^6$	$3.33 \cdot 10^9$	—	144.0	259.4	—	[156]
HK02-1600-FBR-PLM-TK	CO <sub>2</sub>	$4.69 \cdot 10^8$	—	—	238.7	—	—	0.566	[156]
	H <sub>2</sub> O	$8.19 \cdot 10^8$	—	—	248.3	—	—	0.499	[156]
HK02-1600-pTGA-PLM-CS	CO <sub>2</sub>	$8.97 \cdot 10^6$	—	—	248.7	—	—	0.35	[275]
HK06-1400-200-pSPR-PLM-CS	CO <sub>2</sub>	$1.22 \cdot 10^{11}$	—	—	308.7	—	—	0.214	[277]
	H <sub>2</sub> O	$1.85 \cdot 10^{90}$	—	—	263.6	—	—	0.467	[277]
HK06-1400-200-pSPR-LHM-CS	CO <sub>2</sub>	—	$2.45 \cdot 10^9$	$4.23 \cdot 10^{11}$	—	265.8	314.9	—	[277]
	H <sub>2</sub> O	—	$4.02 \cdot 10^7$	$3.96 \cdot 10^{11}$	—	219.4	306.6	—	[277]
HK06-1600-200-pSPR-PLM-CS	CO <sub>2</sub>	$6.81 \cdot 10^{10}$	—	—	300.7	—	—	0.186	[277]
	H <sub>2</sub> O	$6.86 \cdot 10^7$	—	—	234.8	—	—	0.445	[277]
HK06-1600-200-pSPR-LHM-CS	CO <sub>2</sub>	—	$2.68 \cdot 10^8$	$3.01 \cdot 10^{11}$	—	241.5	309.6	—	[277]
	H <sub>2</sub> O	—	$3.66 \cdot 10^6$	$2.59 \cdot 10^9$	—	198.4	262.3	—	[277]

**Table I.7:** Parameters of heterogeneous gasification kinetics developed in the frame of HVI GasTech [124] for regime II.

Kinetics		$\frac{\rho_C}{\text{kg/m}^3}$	$\frac{d_{\text{pore,part}}}{\text{nm}}$	$\varepsilon_{\text{part}}$	$\tau_{\text{part}}$	Source
HK02-FBR-PLM-TK	CO <sub>2</sub>	680	3.9	0.691	3	[156]
	H <sub>2</sub> O	680	4.8	0.691	3	[156]
HK02-FBR-LHM-TK	CO <sub>2</sub>	680	10.5	0.691	3	[156]
	H <sub>2</sub> O	680	3.3	0.691	3	[156]
HK02-1600-FBR-PLM-TK	CO <sub>2</sub>	1496	16.0	0.262	3	[156]
	H <sub>2</sub> O	1496	20.5	0.262	3	[156]

## J CFD simulation results

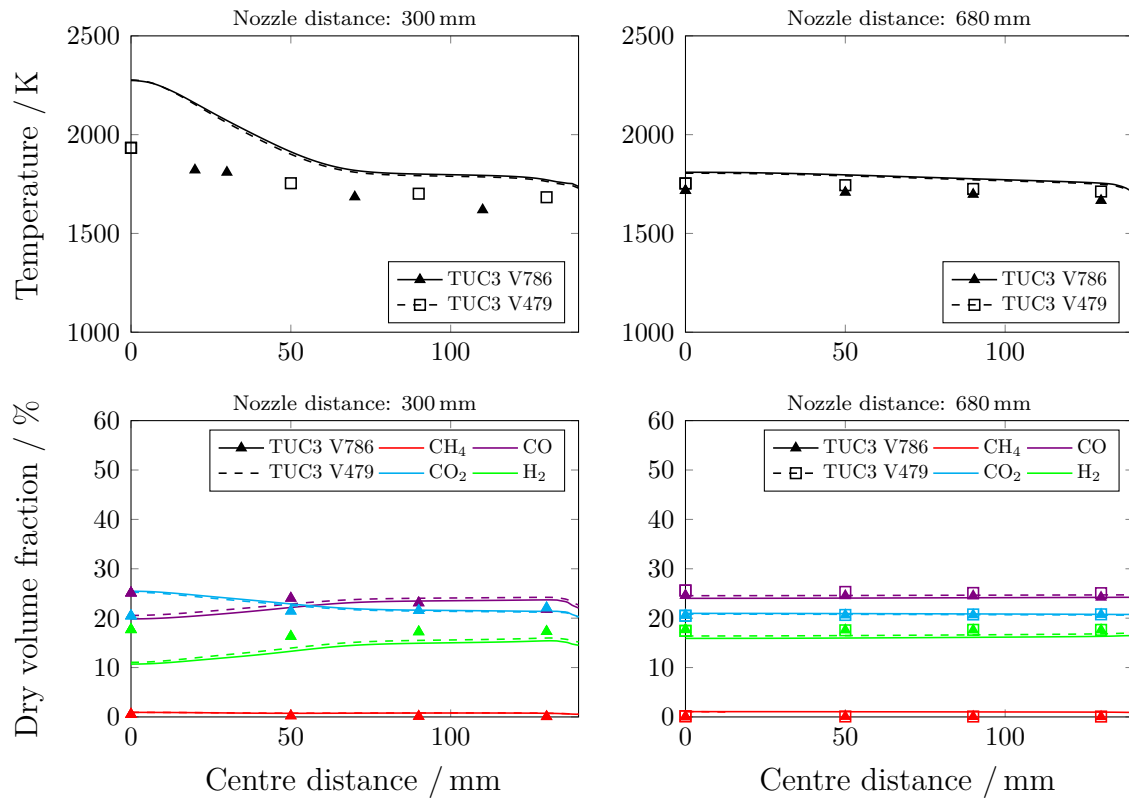


**Figure J.1:** Predicted profiles of gas temperature and dry gas species volume fractions in comparison with measured profiles. TUC3 V479: results for the REGA experiment TUC3 V479 obtained using the DLR2017/RM mechanism; TUC3 V786: results for the REGA experiment TUC3 V786 obtained using the DLR2017/RM mechanism.

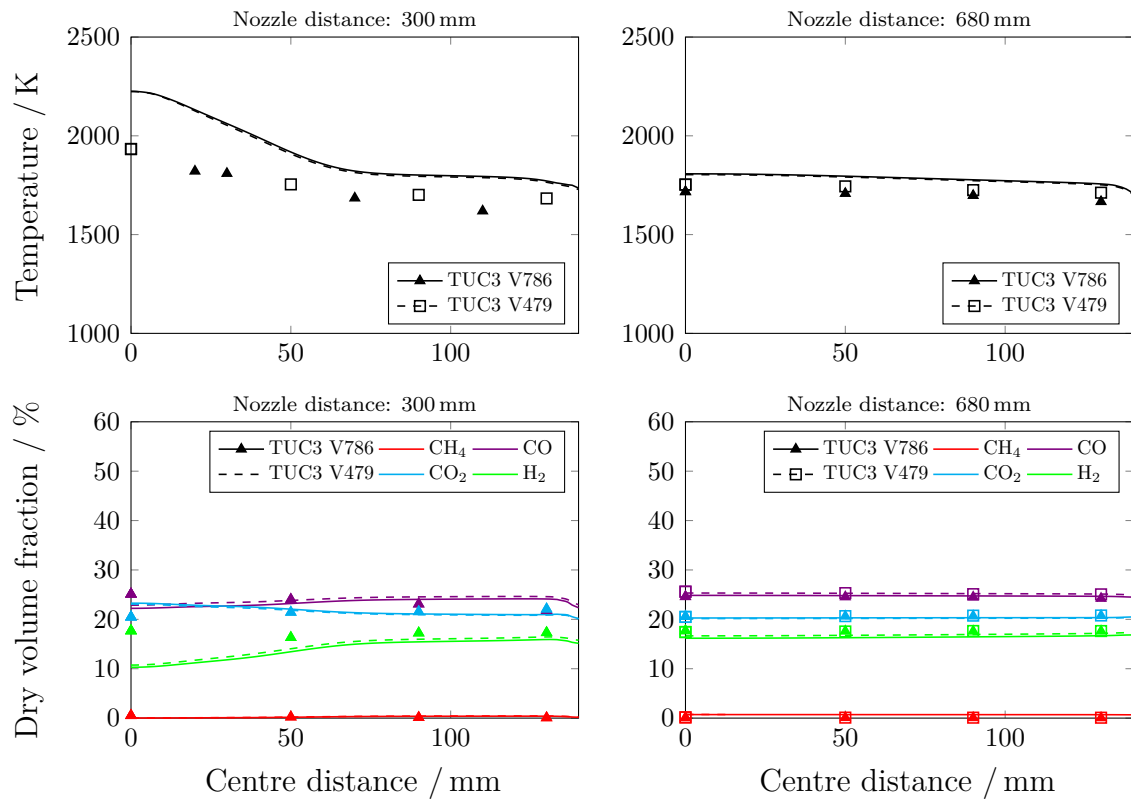


**Figure J.2:** Predicted profiles of gas temperature and dry gas species volume fractions using the DLR2017/RM mechanism in comparison with measured profiles. TUC3 V479: results for the REGA experiment TUC3 V479 obtained using the DLR2017/RM mechanism; TUC3 V786: results for the REGA experiment TUC3 V786 obtained using the DLR2017/RM mechanism.

# Bibliography

- [1] ABANI, N.; GHONIEM, A. F. Large eddy simulations of coal gasification in an entrained flow gasifier. *Fuel*. 2013, vol. 104, pp. 664–680. issn 0016-2361. Available from doi: 10.1016/j.fuel.2012.06.006.
- [2] ABDELSAMIE, A.; CHI, C.; NANJAIH, M.; SKENDEROVIĆ, I.; SULEIMAN, S.; THÉVENIN, D. Direct numerical simulation of turbulent spray combustion in the SpraySyn burner: impact of injector geometry. *Flow, Turbulence and Combustion*. 2021, vol. 106, no. 2, pp. 453–469. issn 1386-6184. Available from doi: 10.1007/s10494-020-00183-5.
- [3] ABRAMZON, B.; SIRIGNANO, W. A. Droplet vaporization model for spray combustion calculations. *International Journal of Heat and Mass Transfer*. 1989, vol. 32, no. 9, pp. 1605–1618. issn 0017-9310. Available from doi: 10.1016/0017-9310(89)90043-4.
- [4] AGROSKIN, A. A. The thermophysical properties of coke. *Coke and Chemistry*. 1980, no. 2, pp. 14–25. issn 0010-0501.
- [5] ALBERTI, M.; WEBER, R.; MANCINI, M. Re-creating Hottel’s emissivity charts for carbon dioxide and extending them to 40 bar pressure using HITEMP-2010 data base. *Combustion and Flame*. 2015, vol. 162, no. 3, pp. 597–612. issn 0010-2180. Available from doi: 10.1016/j.combustflame.2014.09.005.
- [6] ALBERTI, M.; WEBER, R.; MANCINI, M. Re-creating Hottel’s emissivity charts for water vapor and extending them to 40 bar pressure using HITEMP-2010 data base. *Combustion and Flame*. 2016, vol. 169, pp. 141–153. issn 0010-2180. Available from doi: 10.1016/j.combustflame.2016.04.013.
- [7] ALBERTI, M.; WEBER, R.; MANCINI, M. Gray gas emissivities for H<sub>2</sub>O-CO<sub>2</sub>-CO-N<sub>2</sub> mixtures. *Journal of Quantitative Spectroscopy and Radiative Transfer*. 2018, vol. 219, pp. 274–291. issn 0022-4073. Available from doi: 10.1016/j.jqsrt.2018.08.008.
- [8] ALBERTI, M. *Total emissivity charts for H<sub>2</sub>O, CO<sub>2</sub> and CO from low to high pressures*. Clausthal-Zellerfeld, Germany: Papierflieger, 2018. isbn 978-3-86948-648-2. Ph.D. Thesis. Fakultät für Energie- und Wirtschaftswissenschaften, Technische Universität Clausthal.

- 
- [9] ANSYS. *ANSYS Fluent. Release 12.0*. 2009. Available also from: <https://www.ansys.com/products/fluids/ansys-fluent>.
- [10] ANSYS. *ANSYS Fluent. Release 14.5*. 2013. Available also from: <https://www.ansys.com/products/fluids/ansys-fluent>.
- [11] ANSYS. *ANSYS Fluent. Release 15.0*. 2014. Available also from: <https://www.ansys.com/products/fluids/ansys-fluent>.
- [12] ANSYS. *ANSYS Fluent. Release 16.0*. 2015. Available also from: <https://www.ansys.com/products/fluids/ansys-fluent>.
- [13] ANSYS. *ANSYS Fluent. Release 17.1*. 2016. Available also from: <https://www.ansys.com/products/fluids/ansys-fluent>.
- [14] ANSYS. *ANSYS Fluent customization manual. Release 2020 R2*. Canonsburg, PA, USA: SAS IP, 2020.
- [15] ANSYS. *ANSYS Fluent theory guide. Release 2020 R2*. Canonsburg, PA, USA: SAS IP, 2020.
- [16] ANSYS. *ANSYS Fluent user's guide. Release 2020 R2*. Canonsburg, PA, USA: SAS IP, 2020.
- [17] ANSYS. *ANSYS Fluent. Release 2020 R2*. 2020. Available also from: <https://www.ansys.com/products/fluids/ansys-fluent>.
- [18] ANSYS. *ANSYS Meshing. Release 2020 R2*. 2020. Available also from: <https://www.ansys.com/products/platform/ansys-meshing>.
- [19] ANTHONY, D. B.; HOWARD, J. B.; HOTTEL, H. C.; MEISSNER, H. P. Rapid devolatilization of pulverized coal. *Symposium (International) on Combustion*. 1975, vol. 15, no. 1, pp. 1303–1317. issn 0082-0784. Available from doi: 10.1016/s0082-0784(75)80392-4.
- [20] ARNOLD, S.; RODRIGUEZ-URIBE, A.; MISRA, M.; MOHANTY, A. K. Slow pyrolysis of bio-oil and studies on chemical and physical properties of the resulting new bio-carbon. *Journal of Cleaner Production*. 2018, vol. 172, pp. 2748–2758. issn 0959-6526. Available from doi: 10.1016/j.jclepro.2017.11.137.
- [21] ASPEN TECHNOLOGY. *Aspen Physical Property System: physical property models V7.3*. Burlington, MA, USA, 2011.
- [22] ASPEN TECHNOLOGY (ed.). *Aspen Properties. Release V12*. 2022. Available also from: <https://www.aspentech.com/products/aspen-properties.aspx>.
- [23] BADZIOCH, S. Thermo-physical properties of coals and cokes. *BCURA Monthly Bulletin*. 1960, vol. 24, no. 11, pp. 485–520. issn 0365-9461.
- [24] BAUER, W.; STEINHARDT, R. Emissionsgrade feuerfester Baustoffe. *Gaswärme international*. 1990, vol. 39, no. 9, pp. 388–391. issn 0020-9384.

- 
- [25] BAXTER, L. L. Char fragmentation and fly ash formation during pulverized-coal combustion. *Combustion and Flame*. 1992, vol. 90, no. 2, pp. 174–184. issn 0010-2180. Available from doi: 10.1016/0010-2180(92)90118-9.
- [26] BENYON, P. J. *Computational modelling of entrained flow slagging gasifiers*. Sydney, NSW, Australia, 2002. Available also from: <http://hdl.handle.net/2123/1276>. Ph.D. Thesis. School of Aerospace, Mechanical & Mechatronic Engineering, University of New South Wales.
- [27] BHARADWAJ, A.; BAXTER, L. L.; ROBINSON, A. L. Effects of intraparticle heat and mass transfer on biomass devolatilization: experimental results and model predictions. *Energy & Fuels*. 2004, vol. 18, no. 4, pp. 1021–1031. issn 0887-0624. Available from doi: 10.1021/ef0340357.
- [28] BHATIA, S. K.; PERLMUTTER, D. D. A random pore model for fluid-solid reactions. I. Isothermal, kinetic control. *AIChE Journal*. 1980, vol. 26, no. 3, pp. 379–386. issn 0001-1541. Available from doi: 10.1002/aic.690260308.
- [29] BHATIA, S. K.; PERLMUTTER, D. D. A random pore model for fluid-solid reactions. II. Diffusion and transport effects. *AIChE Journal*. 1981, vol. 27, no. 2, pp. 247–254. issn 0001-1541. Available from doi: 10.1002/aic.690270211.
- [30] BIAGINI, E.; FALCITELLI, M.; TOGNOTTI, L. Devolatilisation and pyrolysis of biomasses: development and validation of structural models. In: *Proceedings of the XXIX Meeting of the Italian Section of the Combustion Institute, 14-17 June 2006, Pisa, Italy*. Pisa, Italy: Italian Section of the Combustion Institute, 2006.
- [31] BIAGINI, E.; TOGNOTTI, L. A generalized correlation for coal devolatilization kinetics at high temperature. *Fuel Processing Technology*. 2014, vol. 126, pp. 513–520. issn 0378-3820. Available from doi: 10.1016/j.fuproc.2014.06.008.
- [32] BLACKWOOD, J. D.; INGEME, A. J. The reaction of carbon with carbon dioxide at high pressure. *Australian Journal of Chemistry*. 1960, vol. 13, no. 2, p. 194. issn 0004-9425. Available from doi: 10.1071/ch9600194.
- [33] BOYSAN, F.; AYERS, W.; SWITENBANK, J. A fundamental mathematical modelling approach to cyclone design. *Transactions of the Institution of Chemical Engineers. A. Chemical engineering research & design*. 1982, vol. 60, pp. 220–230.
- [34] BOYSAN, F.; WEBER, R.; SWITENBANK, J.; LAWN, C. J. Modeling coal-fired cyclone combustors. *Combustion and Flame*. 1986, vol. 63, no. 1–2, pp. 73–86. issn 0010-2180. Available from doi: 10.1016/0010-2180(86)90112-4.
- [35] BRANCA, C.; DI BLASI, C. Global kinetics of wood char devolatilization and combustion. *Energy & Fuels*. 2003, vol. 17, no. 6, pp. 1609–1615. issn 0887-0624. Available from doi: 10.1021/ef030033a.
-

- 
- [36] BREWER, C. E.; CHUANG, V. J.; MASIELLO, C. A.; GONNERMANN, H.; GAO, X.; DUGAN, B.; DRIVER, L. E.; PANZACCHI, P.; ZYGOURAKIS, K.; DAVIES, C. A. New approaches to measuring biochar density and porosity. *Biomass and Bioenergy*. 2014, vol. 66, pp. 176–185. issn 0961-9534. Available from doi: 10.1016/j.biombioe.2014.03.059.
- [37] BROSTRÖM, M.; NORDIN, A.; POMMER, L.; BRANCA, C.; DI BLASI, C. Influence of torrefaction on the devolatilization and oxidation kinetics of wood. *Journal of Analytical and Applied Pyrolysis*. 2012, vol. 96, pp. 100–109. issn 0165-2370. Available from doi: 10.1016/j.jaap.2012.03.011.
- [38] BRUNAUER, S.; EMMETT, P. H.; TELLER, E. Adsorption of gases in multimolecular layers. *Journal of the American Chemical Society*. 1938, vol. 60, no. 2, pp. 309–319. issn 0002-7863. Available from doi: 10.1021/ja01269a023.
- [39] BRYDEN, K. M.; RAGLAND, K. W.; RUTLAND, C. J. Modeling thermally thick pyrolysis of wood. *Biomass and Bioenergy*. 2002, vol. 22, no. 1, pp. 41–53. issn 0961-9534. Available from doi: 10.1016/s0961-9534(01)00060-5.
- [40] BRYDEN, K. M.; HAGGE, M. J. Modeling the combined impact of moisture and char shrinkage on the pyrolysis of a biomass particle. *Fuel*. 2003, vol. 82, no. 13, pp. 1633–1644. issn 0016-2361. Available from doi: 10.1016/s0016-2361(03)00108-x.
- [41] BUSTAMANTE, F.; ENICK, R. M.; CUGINI, A. V.; KILLMEYER, R. P.; HOWARD, B. H.; ROTHENBERGER, K. S.; CIOCCO, M. V.; MORREALE, B. D.; CHATTOPADHYAY, S.; SHI, S. High-temperature kinetics of the homogeneous reverse water-gas shift reaction. *AIChE Journal*. 2004, vol. 50, no. 5, pp. 1028–1041. issn 0001-1541. Available from doi: 10.1002/aic.10099.
- [42] BUSTAMANTE, F.; ENICK, R. M.; KILLMEYER, R. P.; HOWARD, B. H.; ROTHENBERGER, K. S.; CUGINI, A. V.; MORREALE, B. D.; CIOCCO, M. V. Uncatalyzed and wall-catalyzed forward water-gas shift reaction kinetics. *AIChE Journal*. 2005, vol. 51, no. 5, pp. 1440–1454. issn 0001-1541. Available from doi: 10.1002/aic.10396.
- [43] BUTLAND, A. T. D.; MADDISON, R. J. The specific heat of graphite: an evaluation of measurements. *Journal of Nuclear Materials*. 1973, vol. 49, no. 1, pp. 45–56. issn 0022-3115. Available from doi: 10.1016/0022-3115(73)90060-3.
- [44] CAPOSCIUTTI, G.; ALMUINA-VILLAR, H.; DIEGUEZ-ALONSO, A.; GRUBER, T.; KELZ, J.; DESIDERI, U.; HOCHENAUER, C.; SCHARLER, R.; ANCA-COUCÉ, A. Experimental investigation on biomass shrinking and swelling behaviour: particles pyrolysis and wood logs combustion. *Biomass and Bioenergy*. 2019, vol. 123, pp. 1–13. issn 0961-9534. Available from doi: 10.1016/j.biombioe.2019.01.044.

- 
- [45] CHAUSSONNET, G.; BRAUN, S.; WIETH, L.; KOLB, T.; KOCH, R.; BAUER, H.-J.; SÄNGER, A.; JAKOBS, T.; DJORDJEVIC, N. SPH simulation of a twin-fluid atomizer operating with a high viscosity liquid. In: *Proceedings of the 13th Triennial International Conference on Liquid Atomization and Spray Systems (ICLASS 2015), 23-27 August 2015, Tainan, Taiwan*. Tainan, Taiwan: National Cheng Kung University, 2015. Available from doi: 10.13140/RG.2.1.4320.7128.
- [46] CHAUSSONNET, G.; KOCH, R.; BAUER, H.-J.; SÄNGER, A.; JAKOBS, T.; KOLB, T. SPH simulation of an air-assisted atomizer operating at high pressure: influence of non-Newtonian effects. In: *Proceedings of the ASME Turbo Expo 2017: Turbo-machinery Technical Conference and Exposition. Volume 3: Coal, Biomass and Alternative Fuels; Cycle Innovations; Electric Power; Industrial and Cogeneration Applications; Organic Rankine Cycle Power Systems, 26-30 June 2017, Charlotte, NC, USA*. Charlotte, NC, USA: American Society of Mechanical Engineers, 2017. No. GT2017-63033. Available from doi: 10.1115/gt2017-63033.
- [47] CHAUSSONNET, G.; KOCH, R.; BAUER, H.-J.; SÄNGER, A.; JAKOBS, T.; KOLB, T. Smoothed Particle Hydrodynamics simulation of an air-assisted atomizer operating at high pressure: influence of non-Newtonian effects. *Journal of Fluids Engineering*. 2018, vol. 140, no. 6. issn 0098-2202. Available from doi: 10.1115/1.4038753.
- [48] CHAUSSONNET, G.; BRAUN, S.; DAUCH, T.; KELLER, M.; SÄNGER, A.; JAKOBS, T.; KOCH, R.; KOLB, T.; BAUER, H.-J. Toward the development of a virtual spray test-rig using the smoothed particle hydrodynamics method. *Computers & Fluids*. 2019, vol. 180, pp. 68–81. issn 0045-7930. Available from doi: 10.1016/j.compfluid.2019.01.010.
- [49] CHEMVIRON CARBON. Bodenfelde, Germany, 2021. Available also from: <https://www.chemviron.eu>.
- [50] CHEN, J.-S.; GUNKEL, W. W. Modeling and simulation of co-current moving bed gasification reactors. Part I: a non-isothermal particle model. *Biomass*. 1987, vol. 14, no. 1, pp. 51–72. issn 0144-4565. Available from doi: 10.1016/0144-4565(87)90022-9.
- [51] CHEN, L.; DUPONT, C.; SALVADOR, S.; GRATEAU, M.; BOISSONNET, G.; SCHWEICH, D. Experimental study on fast pyrolysis of free-falling millimetric biomass particles between 800 °C and 1000 °C. *Fuel*. 2013, vol. 106, pp. 61–66. issn 0016-2361. Available from doi: 10.1016/j.fuel.2012.11.058.
- [52] CHEN, Y.; CHARPENAY, S.; JENSEN, A.; WÓJTOWICZ, M. A.; SERIO, M. A. Modeling of biomass pyrolysis kinetics. *Symposium (International) on Combustion*. 1998, vol. 27, no. 1, pp. 1327–1334. issn 0082-0784. Available from doi: 10.1016/s0082-0784(98)80537-7.
-

- 
- [53] CHIRONE, R.; MASSIMILLA, L. Primary fragmentation of a coal in fluidized bed combustion. *Symposium (International) on Combustion*. 1989, vol. 22, no. 1, pp. 267–277. issn 0082-0784. Available from doi: 10.1016/s0082-0784(89)80033-5.
- [54] CHUI, E. H.; RAITHBY, G. D. Computation of radiant heat transfer on a nonorthogonal mesh using the finite-volume method. *Numerical Heat Transfer, Part B: Fundamentals*. 1993, vol. 23, no. 3, pp. 269–288. issn 1040-7782. Available from doi: 10.1080/10407799308914901.
- [55] CLIFT, R.; GRACE, J. R.; WEBER, M. E. *Bubbles, drops, and particles*. New York, NY, USA: Academic Press, 1978. isbn 978-0121769505.
- [56] COIMBRA, C. F. M.; QUEIROZ, M. Evaluation of a dimensionless group number to determine second-Einstein temperatures in a heat capacity model for all coal ranks. *Combustion and Flame*. 1995, vol. 101, no. 3, pp. 209–220. issn 0010-2180. Available from doi: 10.1016/0010-2180(94)00208-a.
- [57] COSTA, F. F.; WANG, G.; COSTA, M. Combustion kinetics and particle fragmentation of raw and torrefied pine shells and olive stones in a drop tube furnace. *Proceedings of the Combustion Institute*. 2015, vol. 35, no. 3, pp. 3591–3599. issn 1540-7489. Available from doi: 10.1016/j.proci.2014.06.024.
- [58] COSTA, F. F.; COSTA, M. Particle fragmentation of raw and torrefied biomass during combustion in a drop tube furnace. *Fuel*. 2015, vol. 159, pp. 530–537. issn 0016-2361. Available from doi: 10.1016/j.fuel.2015.07.006.
- [59] CROWE, C. T. *Multiphase flow handbook*. Boca Raton, FL, USA: CRC Press, 2005. isbn 978-1-4200-4047-0. Available from doi: 10.1201/9781420040470.
- [60] DACOMBE, P.; POURKASHANIAN, M.; WILLIAMS, A.; YAP, L. Combustion-induced fragmentation behavior of isolated coal particles. *Fuel*. 1999, vol. 78, no. 15, pp. 1847–1857. issn 0016-2361. Available from doi: 10.1016/s0016-2361(99)00076-9.
- [61] DAHMEN, N.; ABELN, J.; EBERHARD, M.; KOLB, T.; LEIBOLD, H.; SAUER, J.; STAPF, D.; ZIMMERLIN, B. The bioliq process for producing synthetic transportation fuels. *WIREs Energy and Environment*. 2016, vol. 6, no. 3. issn 2041-840X. Available from doi: 10.1002/wene.236.
- [62] DAKIČ, D.; HONING, G. van der; VALK, M. Fragmentation and swelling of various coals during devolatilization in a fluidized bed. *Fuel*. 1989, vol. 68, no. 7, pp. 911–916. issn 0016-2361. Available from doi: 10.1016/0016-2361(89)90129-4.
- [63] DAMMANN, M.; MANCINI, M.; FLECK, S.; WEBER, R.; KOLB, T. Entrained flow gasification: experiments and mathematical modelling based on RANS. In: *Proceedings of the Joint Meeting of the German and Italian Sections of the Combustion Institute, 24-26 May 2018, Sorrento, Italy*. Sorrento, Italy: Italian Section of the Combustion Institute, 2018. Available from doi: 10.5445/IR/1000085909.

- 
- [64] DAMMANN, M.; MANCINI, M.; FLECK, S.; WEBER, R.; KOLB, T. Entrained flow gasification: experiments and mathematical modelling based on RANS. In: *Proceedings of the 29th Deutscher Flammentag: Verbrennung und Feuerung, 17-18 September 2019, Bochum, Germany*. Bochum, Germany, 2019. Available from doi: 10.5445/IR/1000131589.
- [65] DAMMANN, M.; MANCINI, M.; WEBER, R.; KOLB, T. Entrained flow gasification: mathematical modelling based on RANS for design and scale-up. In: *Proceedings of the 30th Deutscher Flammentag: für nachhaltige Verbrennung, 28-29 September 2021, Hannover-Garbsen, Germany*. Hannover-Garbsen, Germany, 2021. Available from doi: 10.5445/IR/1000140359.
- [66] DAMMANN, M.; MANCINI, M.; KOLB, T.; WEBER, R. Thermal radiation at high-temperature and high-pressure conditions: comparison of models for design and scale-up of entrained flow gasification processes. In: *Proceedings of the 13th European Conference on Industrial Furnaces and Boilers, 19-22 April 2022, Algarve, Portugal*. Algarve, Portugal, 2022. Available from doi: 10.5445/IR/1000145810.
- [67] DAMMANN, M.; MANCINI, M.; KOLB, T.; WEBER, R. Thermal radiation at high-temperature and high-pressure conditions: comparison of models for design and scale-up of entrained flow gasification processes. *Thermal Sciences and Engineering Progress*. 2023, vol. 40, p. 101772. issn 2451-9049. Available from doi: 10.1016/j.tsep.2023.101772.
- [68] DAMMANN, M.; WALKER, S. C.; MANCINI, M.; KOLB, T. Devolatilisation of beech wood char: kinetics from thermogravimetric and drop-tube reactor experiments. *Fuel*. 2024, vol. 375, p. 131967. issn 2451-9049. Available from doi: 10.1016/j.fuel.2024.131967.
- [69] DENG, J.; LI, Q.-W.; XIAO, Y.; SHU, C.-M.; ZHANG, Y.-N. Predictive models for thermal diffusivity and specific heat capacity of coals in Huainan mining area, China. *Thermochimica Acta*. 2017, vol. 656, pp. 101–111. issn 0040-6031. Available from doi: 10.1016/j.tca.2017.09.005.
- [70] DI BLASI, C. Heat, momentum and mass transport through a shrinking biomass particle exposed to thermal radiation. *Chemical Engineering Science*. 1996, vol. 51, no. 7, pp. 1121–1132. issn 0009-2509. Available from doi: 10.1016/s0009-2509(96)80011-x.
- [71] DI BLASI, C. Influences of physical properties on biomass devolatilization characteristics. *Fuel*. 1997, vol. 76, no. 10, pp. 957–964. issn 0016-2361. Available from doi: 10.1016/s0016-2361(97)00096-3.
- [72] DI BLASI, C. Combustion and gasification rates of lignocellulosic chars. *Progress in Energy and Combustion Science*. 2009, vol. 35, no. 2, pp. 121–140. issn 0360-1285. Available from doi: 10.1016/j.pecs.2008.08.001.
-

- 
- [73] DIN DEUTSCHES INSTITUT FÜR NORMUNG. *DIN 51046-1:1976-08. Prüfung keramischer Roh- und Werkstoffe. Bestimmung der Wärmeleitfähigkeit bei Temperaturen bis 1600 °C nach dem Heißdraht-Verfahren. Wärmeleitfähigkeit bis 2 W/(mK)*. 1976.
- [74] DIN DEUTSCHES INSTITUT FÜR NORMUNG. *DIN 66133:1993-06. Bestimmung der Porenvolumenverteilung und der spezifischen Oberfläche von Feststoffen durch Quecksilberintrusion*. 1993.
- [75] DIN DEUTSCHES INSTITUT FÜR NORMUNG. *DIN 51720:2001-03. Prüfung fester Brennstoffe. Bestimmung des Gehaltes an Flüchtigen Bestandteilen*. 2001.
- [76] DIN DEUTSCHES INSTITUT FÜR NORMUNG. *DIN 51734:2008-12. Prüfung fester Brennstoffe. Immediatanalyse und Berechnung des Fixen Kohlenstoffs*. 2008.
- [77] DIN DEUTSCHES INSTITUT FÜR NORMUNG. *DIN ISO 9277-1:2014-01. Bestimmung der spezifischen Oberfläche von Festkörpern mittels Gasadsorption: BET-Verfahren (ISO 9277:2010)*. 2014.
- [78] DOMBROVSKY, L.; SAZHIN, S. Absorption of thermal radiation in a semi-transparent spherical droplet: a simplified model. *International Journal of Heat and Fluid Flow*. 2003, vol. 24, no. 6, pp. 919–927. issn 0142-727X. Available from doi: 10.1016/s0142-727x(03)00084-5.
- [79] DOORMAAL, J. P. V.; RAITHEY, G. D. Enhancements of the simple method for predicting incompressible fluid flows. *Numerical Heat Transfer*. 1984, vol. 7, no. 2, pp. 147–163. issn 0149-5720. Available from doi: 10.1080/01495728408961817.
- [80] DUBIL, K. *Betrachtungen zum Partikelabbrand während der Vergasung unter Berücksichtigung der Entwicklung der Reaktivität*. Karlsruhe, Germany, 2017. Master's Thesis. Engler-Bunte-Institut, Brennstofftechnologie – Chemische Energieträger, Karlsruher Institut für Technologie.
- [81] DUBININ, M. M.; ZAVERINA, E. D.; RADUSHKEVICH, L. V. Sorption and structure of active carbons. I. Adsorption of organic vapors. *Zhurnal Fizicheskoi Khimii*. 1947, vol. 21, no. 3, pp. 151–162. issn 0044-4537.
- [82] DUNN-RANKIN, D.; KERSTEIN, A. R. Numerical simulation of particle size distribution evolution during pulverized coal combustion. *Combustion and Flame*. 1987, vol. 69, no. 2, pp. 193–209. issn 0010-2180. Available from doi: 10.1016/0010-2180(87)90031-9.
- [83] DUNN-RANKIN, D.; KERSTEIN, A. R. Influence of ash on particle size distribution evolution during coal combustion. *Combustion and Flame*. 1988, vol. 74, no. 2, pp. 207–218. issn 0010-2180. Available from doi: 10.1016/0010-2180(88)90018-1.

- 
- [84] DUPONT, C.; COMMANDRÉ, J.-M.; GAUTHIER, P.; BOISSONNET, G.; SALVADOR, S.; SCHWEICH, D. Biomass pyrolysis experiments in an analytical entrained flow reactor between 1073 K and 1273 K. *Fuel*. 2008, vol. 87, no. 7, pp. 1155–1164. issn 0016-2361. Available from doi: [10.1016/j.fuel.2007.06.028](https://doi.org/10.1016/j.fuel.2007.06.028).
- [85] DUPONT, C.; CHIRIAC, R.; GAUTHIER, G.; TOCHE, F. Heat capacity measurements of various biomass types and pyrolysis residues. *Fuel*. 2014, vol. 115, pp. 644–651. issn 0016-2361. Available from doi: [10.1016/j.fuel.2013.07.086](https://doi.org/10.1016/j.fuel.2013.07.086).
- [86] DURET, B.; REVEILLON, J.; MENARD, T.; DEMOULIN, F. X. Improving primary atomization modeling through DNS of two-phase flows. *International Journal of Multiphase Flow*. 2013, vol. 55, pp. 130–137. issn 0301-9322. Available from doi: [10.1016/j.ijmultiphaseflow.2013.05.004](https://doi.org/10.1016/j.ijmultiphaseflow.2013.05.004).
- [87] EBERHARD, M.; SANTO, U.; MICHELFELDER, B.; GÜNTHER, A.; WEIGAND, P.; MATTHES, J.; WAIBEL, P.; HAGENMEYER, V.; KOLB, T. The bioliq<sup>®</sup> Entrained Flow Gasifier: a model for the German Energiewende. *ChemBioEng Reviews*. 2020, vol. 7, no. 4, pp. 106–118. Available from doi: [10.1002/cben.202000006](https://doi.org/10.1002/cben.202000006).
- [88] ECKEL, G.; LE CLERCQ, P.; KATHROTIA, T.; SAENGER, A.; FLECK, S.; MANCINI, M.; KOLB, T.; AIGNER, M. Entrained flow gasification. Part 3: insight into the injector near-field by large eddy simulation with detailed chemistry. *Fuel*. 2018, vol. 223, pp. 164–178. issn 0016-2361. Available from doi: [10.1016/j.fuel.2018.02.176](https://doi.org/10.1016/j.fuel.2018.02.176).
- [89] ECKEL, G. *Large eddy simulation of turbulent reacting multi-phase flows*. Stuttgart, Germany: Universität Stuttgart, 2018. Available from doi: [10.18419/opus-9941](https://doi.org/10.18419/opus-9941). Ph.D. Thesis. Fakultät für Luft- und Raumfahrttechnik und Geodäsie, Universität Stuttgart.
- [90] ELLENDT, N.; LUMANGLAS, A. M.; MOQADAM, S. I.; MÄDLER, L. A model for the drag and heat transfer of spheres in the laminar regime at high temperature differences. *International Journal of Thermal Sciences*. 2018, vol. 133, pp. 98–105. issn 1290-0729. Available from doi: [10.1016/j.ijthermalsci.2018.07.009](https://doi.org/10.1016/j.ijthermalsci.2018.07.009).
- [91] ESPDEV. *csaps. Release 1.0.4* [<https://pypi.org/project/csaps/>]. 2021. Available also from: <https://pypi.org/project/csaps/>.
- [92] EUCKEN, A. Über die Temperaturabhängigkeit der Wärmeleitfähigkeit einiger Gase. *Physikalische Zeitschrift*. 1911, vol. 12, no. 17, pp. 1101–1107. issn 2366-9373.
- [93] EUCKEN, A. Über das Wärmeleitvermögen, die spezifische Wärme und die innere Reibung der Gase. *Physikalische Zeitschrift*. 1913, vol. 14, pp. 324–332.
- [94] EUROFINS UMWELT OST. Freiberg, Germany, 2021. Available also from: <https://www.eurofins.de/>.
-

- 
- [95] FARROW, T. S.; SUN, C.; SNAPE, C. E. Impact of CO<sub>2</sub> on biomass pyrolysis, nitrogen partitioning, and char combustion in a drop tube furnace. *Journal of Analytical and Applied Pyrolysis*. 2015, vol. 113, pp. 323–331. issn 0165-2370. Available from doi: 10.1016/j.jaap.2015.02.013.
- [96] FISCHER, S. Zur Messung hoher Temperaturen in strömenden Gasen mit Thermoelementen. *Die Technik*. 1968, vol. 23, no. 1, pp. 29–33. issn 0040-1099.
- [97] FLECK, S.; HOTZ, C.; STOESSER, P.; KOLB, T. Gasification of biomass-based suspension fuels in an atmospheric entrained flow gasifier. In: *Proceedings of the 27th Deutscher Flammentag: Verbrennung und Feuerung, 16-17 September 2015, Clausthal-Zellerfeld, Deutschland*. Düsseldorf, Germany: VDI-Verlag, 2015, vol. 2267, pp. 697–704. VDI-Berichte.
- [98] FLECK, S.; SANTO, U.; HOTZ, C.; JAKOBS, T.; ECKEL, G.; MANCINI, M.; WEBER, R.; KOLB, T. Entrained flow gasification. Part 1: gasification of glycol in an atmospheric-pressure experimental rig. *Fuel*. 2018, vol. 217, pp. 306–319. issn 0016-2361. Available from doi: 10.1016/j.fuel.2017.12.077.
- [99] FLECK, S.; KOLB, T. *Entrained flow gasification: data from gasification experiments with ethylene glycol and ethylene glycol-beech wood-char slurries (personal communication)*. 2022.
- [100] FLECK, S.; HAAS, M.; SANTO, U.; KOLB, T. Entrained flow gasification of glycol-beech wood-char slurry in an atmospheric-pressure experimental rig (in preparation). *Fuel*. 2025. issn 0016-2361.
- [101] FRADET, Q.; BRAUN-UNKHOFF, M.; RIEDEL, U. A sectional approach for the entrained-flow gasification of slurry fuels. *Energy & Fuels*. 2018, vol. 32, no. 12, pp. 12532–12544. issn 0887-0624. Available from doi: 10.1021/acs.energyfuels.8b02785.
- [102] FRADET, Q. *Novel modeling approaches for the entrained-flow gasification of bio-slurries*. Stuttgart, Germany, 2020. Available from doi: 10.18419/opus-10989. Ph.D. Thesis. Fakultät für Luft- und Raumfahrttechnik und Geodäsie, Universität Stuttgart.
- [103] FRITSCH. Idar-Oberstein, Germany, 2021. Available also from: <https://www.fritsch-international.com>.
- [104] GAO, X.; ZHANG, Y.; LI, B.; YU, X. Model development for biomass gasification in an entrained flow gasifier using intrinsic reaction rate submodel. *Energy Conversion and Management*. 2016, vol. 108, pp. 120–131. issn 0196-8904. Available from doi: 10.1016/j.enconman.2015.10.070.

- 
- [105] GILBERT, R. G.; LUTHER, K.; TROE, J. Theory of thermal unimolecular reactions in the fall-off range. II. Weak collision rate constants. *Berichte der Bunsengesellschaft für physikalische Chemie*. 1983, vol. 87, no. 2, pp. 169–177. issn 0005-9021. Available from doi: 10.1002/bbpc.19830870218.
- [106] GOODWIN, D. G.; SPETH, R. L.; MOFFAT, H. K.; WEBER, B. W. *Cantera: an object-oriented software toolkit for chemical kinetics, thermodynamics and transport processes* [<https://www.cantera.org>]. 2021. Available from doi: 10.5281/zenodo.4527812. Version 2.5.1.
- [107] GRANT, D. M.; PUGMIRE, R. J.; FLETCHER, T. H.; KERSTEIN, A. R. Chemical model of coal devolatilization using percolation lattice statistics. *Energy & Fuels*. 1989, vol. 3, no. 2, pp. 175–186. issn 0887-0624. Available from doi: 10.1021/ef00014a011.
- [108] GRØNLI, M. G.; MELAAEN, M. C. Mathematical model for wood pyrolysis: comparison of experimental measurements with model predictions. *Energy & Fuels*. 2000, vol. 14, no. 4, pp. 791–800. issn 0887-0624. Available from doi: 10.1021/ef990176q.
- [109] GRØNLI, M. G.; VÁRHEGYI, G.; BLASI, C. D. Thermogravimetric analysis and devolatilization kinetics of wood. *Industrial & Engineering Chemistry Research*. 2002, vol. 41, no. 17, pp. 4201–4208. issn 0888-5885. Available from doi: 10.1021/ie0201157.
- [110] GÜNTHER, R. *Verbrennung und Feuerungen*. Berlin, Germany [et al.]: Springer, 1984. isbn 978-3-540-13256-1.
- [111] GUO, J.; LUA, A. C. Kinetic study on pyrolytic process of oil-palm solid waste using two-step consecutive reaction model. *Biomass and Bioenergy*. 2001, vol. 20, no. 3, pp. 223–233. issn 0961-9534. Available from doi: 10.1016/s0961-9534(00)00080-5.
- [112] GUPTA, M.; YANG, J.; ROY, C. Specific heat and thermal conductivity of softwood bark and softwood char particles. *Fuel*. 2003, vol. 82, no. 8, pp. 919–927. issn 0016-2361. Available from doi: 10.1016/s0016-2361(02)00398-8.
- [113] HAAS, M.; FLECK, S.; KOLB, T. *Entrained flow gasification: data from atomisation and gasification experiments with ethylene glycol (personal communication)*. 2022.
- [114] HAAS, M.; DAMMANN, M.; FLECK, S.; KOLB, T. Entrained flow gasification: impact of fuel spray distribution on reaction zone structure. *Fuel*. 2023, vol. 334, p. 126572. issn 0016-2361. Available from doi: 10.1016/j.fuel.2022.126572.
- [115] HAFNER, S.; RASHIDI, A.; BALDEA, G.; RIEDEL, U. A detailed chemical kinetic model of high-temperature ethylene glycol gasification. *Combustion Theory and Modelling*. 2011, vol. 15, no. 4, pp. 517–535. issn 1364-7830. Available from doi: 10.1080/13647830.2010.547602.
-

- 
- [116] HAFNER, S. *Modellentwicklung zur numerischen Simulation eines Flugstromvergasers für Biomasse*. Heidelberg, Germany, 2010. Available from doi: 10.11588/heidok.00011309. Ph.D. Thesis. Naturwissenschaftlich-Mathematische Gesamtfakultät, Ruprechts-Karls-Universität Heidelberg.
- [117] HALAMA, S.; SPLIETHOFF, H. Numerical simulation of entrained flow gasification: reaction kinetics and char structure evolution. *Fuel Processing Technology*. 2015, vol. 138, pp. 314–324. issn 0378-3820. Available from doi: 10.1016/j.fuproc.2015.05.012.
- [118] HALAMA, S.; SPLIETHOFF, H. Reaction kinetics of pressurized entrained flow coal gasification: computational fluid dynamics simulation of a 5 MW Siemens test gasifier. *Journal of Energy Resources Technology*. 2016, vol. 138, no. 4. issn 0195-0738. Available from doi: 10.1115/1.4032620.
- [119] HANROT, F.; ABLITZER, D.; HOUZELOT, J. L.; DIRAND, M. Experimental measurement of the true specific heat capacity of coal and semicoke during carbonization. *Fuel*. 1994, vol. 73, no. 2, pp. 305–309. issn 0016-2361. Available from doi: 10.1016/0016-2361(94)90130-9.
- [120] HASHIMOTO, N.; SHIRAI, H. Numerical simulation of sub-bituminous coal and bituminous coal mixed combustion employing tabulated-devolatilization-process model. *Energy*. 2014, vol. 71, pp. 399–413. issn 0360-5442. Available from doi: 10.1016/j.energy.2014.04.091.
- [121] HASSE, C.; DEBIAGI, P.; WEN, X.; HILDEBRANDT, K.; VASCELLARI, M.; FARAVELLI, T. Advanced modeling approaches for CFD simulations of coal combustion and gasification. *Progress in Energy and Combustion Science*. 2021, vol. 86, p. 100938. issn 0360-1285. Available from doi: 10.1016/j.pecs.2021.100938.
- [122] HEGHEŞ, C. I. *C1-C4 hydrocarbon oxidation mechanism*. Heidelberg, Germany, 2006. Available from doi: 10.11588/heidok.00007379. Ph.D. Thesis. Naturwissenschaftlich-Mathematische Gesamtfakultät, Ruprechts-Karls-Universität Heidelberg.
- [123] HELBLE, J. J.; SAROFIM, A. F. Influence of char fragmentation on ash particle size distributions. *Combustion and Flame*. 1989, vol. 76, no. 2, pp. 183–196. issn 0010-2180. Available from doi: 10.1016/0010-2180(89)90066-7.
- [124] HELMHOLTZ VIRTUAL INSTITUTE FOR GASIFICATION TECHNOLOGY (HVIGAS-TECH). 2021. Available also from: <https://www.hvigastech.org/>.
- [125] HIGMAN, C.; BURGT, M. van der. *Gasification*. 2nd ed. Burlington, MA, USA: Gulf Professional Publishing, 2008. isbn 978-0-08-056090-8. Available from doi: 10.1016/b978-0-7506-8528-3.x0001-6.
- [126] HOLZKOHLEVERARBEITUNG SCHÜTTE. Schmallingenberg, Germany, 2021. Available also from: <http://www.holzkohleverarbeitung-schuette.de/>.
-

- 
- [127] HONG, J.; HECKER, W. C.; FLETCHER, T. H. Improving the accuracy of predicting effectiveness factors for  $n$ th order and Langmuir rate equations in spherical coordinates. *Energy & Fuels*. 2000, vol. 14, no. 3, pp. 663–670. issn 0887-0624. Available from doi: 10.1021/ef9902193.
- [128] HOTTEL, H. C.; SAROFIM, A. F. *Radiative transfer*. 1st ed. New York, NY, USA: McGraw-Hill, 1967. isbn 978-0070304505.
- [129] HOWELL, J. R.; MENGÜÇ, M. P.; DAUN, K.; SIEGEL, R. *Thermal radiation heat transfer*. 6th ed. Boca Raton, FL, USA: CRC Press, 2015. isbn 978-0-429-19059-9. Available from doi: 10.1201/b18835.
- [130] HÜTTINGER, K. J.; MERDES, W. F. The carbon-steam reaction at elevated pressure: formations of product gases and hydrogen inhibitions. *Carbon*. 1992, vol. 30, no. 6, pp. 883–894. issn 0008-6223. Available from doi: 10.1016/0008-6223(92)90011-k.
- [131] INSTITUTE OF GAS TECHNOLOGY. *Preparation of a coal conversion systems technical data book*. Chicago, IL, USA, 1977. Tech. rep., 8964-7. Department of Energy.
- [132] IRFAN, M. F.; USMAN, M. R.; KUSAKABE, K. Coal gasification in CO<sub>2</sub> atmosphere and its kinetics since 1948: a brief review. *Energy*. 2011, vol. 36, no. 1, pp. 12–40. issn 0360-5442. Available from doi: 10.1016/j.energy.2010.10.034.
- [133] ISO ORGANIZATION FOR STANDARDIZATION. *ISO 10780:1994-11. Stationary source emissions: measurement of velocity and volume flowrate of gas streams in ducts*. 1994.
- [134] J+G FEUERFESTBAU. *Data sheet for JUCAST FB 004 E. Dense refractory concrete*. 2003.
- [135] JAKOBS, T.; FLECK, S.; MANCINI, M.; WEBER, R.; KOLB, T. Gasification of high viscous slurry: R&D on atomization and numerical simulation. In: *Proceedings of the 36th International Technical Conference on Clean Coal and Fuel Systems 2010: The Clearwater Clean Coal Conference, 5-9 June 2011, Clearwater, FL, USA*. Clearwater, FL, USA: Coal Technologies Associates, 2011.
- [136] JAKOBS, T.; DJORDJEVIC, N.; FLECK, S.; MANCINI, M.; WEBER, R.; KOLB, T. Gasification of high viscous slurry. R&D on atomization and numerical simulation. *Applied Energy*. 2012, vol. 93, pp. 449–456. issn 0306-2619. Available from doi: 10.1016/j.apenergy.2011.12.026.
- [137] JAKOBS, T.; SÄNGER, A.; KOLB, T. *Atmospheric atomisation: data from atomisation experiments with ethylene glycol (personal communication)*. 2022.
-

- 
- [138] JAKOBS, T. *Einfluss des Reaktordrucks auf die Spraygüte außenmischender Zweistoffdüsen*. Karlsruhe, Germany, 2015. Available from doi: 10.5445/IR/1000048862. Ph.D. Thesis. Fakultät für Chemieingenieurwesen und Verfahrenstechnik, Karlsruher Institut für Technologie.
- [139] JAYAWICKRAMA, T. R.; HAUGEN, N. E. L.; BABLER, M. U.; CHISHTY, M. A.; UMEKI, K. The effect of Stefan flow on Nusselt number and drag coefficient of spherical particles in non-isothermal gas flow. *International Journal of Multiphase Flow*. 2021, vol. 140, p. 103650. issn 0301-9322. Available from doi: 10.1016/j.ijmultiphaseflow.2021.103650.
- [140] JOHANSEN, J. M.; GADSBØLL, R.; THOMSEN, J.; JENSEN, P. A.; GLARBORG, P.; EK, P.; MARTINI, N. D.; MANCINI, M.; WEBER, R.; MITCHELL, R. E. Devolatilization kinetics of woody biomass at short residence times and high heating rates and peak temperatures. *Applied Energy*. 2016, vol. 162, pp. 245–256. issn 0306-2619. Available from doi: 10.1016/j.apenergy.2015.09.091.
- [141] JOHANSEN, J. M.; JENSEN, P. A.; GLARBORG, P.; MANCINI, M.; WEBER, R.; MITCHELL, R. E. Extension of apparent devolatilization kinetics from thermally thin to thermally thick particles in zero dimensions for woody biomass. *Energy*. 2016, vol. 95, pp. 279–290. issn 0360-5442. Available from doi: 10.1016/j.energy.2015.11.025.
- [142] JOHANSEN, J. M.; JENSEN, P. A.; GLARBORG, P.; DE MARTINI, N.; EK, P.; MITCHELL, R. E. High heating rate devolatilization kinetics of pulverized biomass fuels. *Energy & Fuels*. 2018, vol. 32, no. 12, pp. 12955–12961. issn 0887-0624. Available from doi: 10.1021/acs.energyfuels.8b03100.
- [143] JOHNSTONE, H. F.; CHEN, C. Y.; SCOTT, D. S. Kinetics of the steam-carbon reaction in porous graphite tubes. *Industrial & Engineering Chemistry*. 1952, vol. 44, no. 7, pp. 1564–1569. issn 0019-7866. Available from doi: 10.1021/ie50511a026.
- [144] JONES, W. P.; LINDSTEDT, R. P. Global reaction schemes for hydrocarbon combustion. *Combustion and Flame*. 1988, vol. 73, no. 3, pp. 233–249. Available from doi: 10.1016/0010-2180(88)90021-1.
- [145] DE JONG, W.; DI NOLA, G.; VENNEKER, B. C. H.; SPLIETHOFF, H.; WÓJTOWICZ. TG-FTIR pyrolysis of coal and secondary biomass fuels: determination of pyrolysis kinetic parameters for main species and NO<sub>x</sub> precursors. *Fuel*. 2007, vol. 86, no. 15, pp. 2367–2376. issn 0016-2361. Available from doi: 10.1016/j.fuel.2007.01.032.
- [146] KAJITANI, S.; HARA, S.; MATSUDA, H. Gasification rate analysis of coal char with a pressurized drop tube furnace. *Fuel*. 2002, vol. 81, no. 5, pp. 539–546. issn 0016-2361. Available from doi: 10.1016/s0016-2361(01)00149-1.

- 
- [147] KANTOROVICH, I.; BAR-ZIV, E. Role of the pore structure in the fragmentation of highly porous char particles. *Combustion and Flame*. 1998, vol. 113, no. 4, pp. 532–541. issn 0010-2180. Available from doi: 10.1016/s0010-2180(97)00247-2.
- [148] KARLSRUHE INSTITUTE OF TECHNOLOGY. *bioliq*. Karlsruhe, Germany, 2021. Available also from: <https://www.bioliq.de>.
- [149] KATHROTIA, T.; NAUMANN, C.; OSSWALD, P.; KÖHLER, M.; RIEDEL, U. Kinetics of ethylene glycol: the first validated reaction scheme and first measurements of ignition delay times and speciation data. *Combustion and Flame*. 2017, vol. 179, pp. 172–184. issn 0010-2180. Available from doi: 10.1016/j.combustflame.2017.01.018.
- [150] KAZAKOV, A.; FRENKLACH, M. *Reduced reaction sets based on GRI-Mech 1.2*. 1994. Available also from: <http://combustion.berkeley.edu/drm/>.
- [151] KERSTEIN, A. R.; EDWARDS, B. F. Percolation model for simulation of char oxidation and fragmentation time-histories. *Chemical Engineering Science*. 1987, vol. 42, no. 7, pp. 1629–1634. issn 0009-2509. Available from doi: 10.1016/0009-2509(87)80167-7.
- [152] KIROV, N. Y. Specific heats and total heat contents of coals and related materials at elevated temperatures. *BCURA Monthly Bulletin*. 1965, vol. 29, no. 2, pp. 33–59. issn 0365-9461.
- [153] KOBAYASHI, H.; HOWARD, J. B.; SAROFIM, A. F. Coal devolatilization at high temperatures. *Symposium (International) on Combustion*. 1977, vol. 16, no. 1, pp. 411–425. issn 0082-0784. Available from doi: 10.1016/s0082-0784(77)80341-x.
- [154] KOLB, T.; AIGNER, M.; KNEER, R.; MÜLLER, M.; WEBER, R.; DJORDJEVIC, N. Tackling the challenges in modelling entrained-flow gasification of low-grade feedstock. *Journal of the Energy Institute*. 2016, vol. 89, no. 4, pp. 485–503. issn 1743-9671. Available from doi: 10.1016/j.joei.2015.07.007.
- [155] KREITZBERG, T.; HAUSTEIN, H. D.; GÖVERT, B.; KNEER, R. Investigation of gasification reaction of pulverized char under N<sub>2</sub>/CO<sub>2</sub> atmosphere in a small-scale fluidized bed reactor. *Journal of Energy Resources Technology*. 2016, vol. 138, no. 4, pp. 042207-1–042207-7. issn 0195-0738. Available from doi: 10.1115/1.4032791.
- [156] KREITZBERG, T.; KNEER, R. *Gasification kinetics of the wood chars HK02-500 and HK02-1600 (personal communication)*. 2018.
- [157] KREITZBERG, T.; PHOUNGLAMCHEIK, A.; HAUGEN, N. E. L.; KNEER, R.; UMEKI, K. A shortcut method to predict particle size changes during char combustion and gasification under regime II conditions. *Combustion Science and Technology*. 2022, no. 2, pp. 272–291. issn 0010-2202. Available from doi: 10.1080/00102202.2019.1678919.
-

- 
- [158] KREUTZKAM, B.; WIELAND, C.; SPLIETHOFF, H. Improved numerical prediction of ash formation and deposition using a novel developed char fragmentation model. *Fuel*. 2012, vol. 98, pp. 103–110. issn 0016-2361. Available from doi: 10.1016/j.fuel.2012.02.056.
- [159] KU, X.; LI, T.; LØVÅS, T. Eulerian-Lagrangian simulation of biomass gasification behavior in a high-temperature entrained-flow reactor. *Energy & Fuels*. 2014, vol. 28, no. 8, pp. 5184–5196. issn 0887-0624. Available from doi: 10.1021/ef5010557.
- [160] KUMAR, R.; KOLAR, A.; LECKNER, B. Shrinkage characteristics of Casuarina wood during devolatilization in a fluidized bed combustor. *Biomass and Bioenergy*. 2006, vol. 30, no. 2, pp. 153–165. issn 0961-9534. Available from doi: 10.1016/j.biombioe.2005.11.005.
- [161] KUMAR, M.; GHONIEM, A. F. Multiphysics simulations of entrained flow gasification. Part I: validating the nonreacting flow solver and the particle turbulent dispersion model. *Energy & Fuels*. 2011, vol. 26, no. 1, pp. 451–463. issn 0887-0624. Available from doi: 10.1021/ef200884j.
- [162] KUMAR, M.; GHONIEM, A. F. Multiphysics simulations of entrained flow gasification. Part II: constructing and validating the overall model. *Energy & Fuels*. 2012, vol. 26, no. 1, pp. 464–479. issn 0887-0624. Available from doi: 10.1021/ef2008858.
- [163] KUMAR, U.; SALEM, A. M.; PAUL, M. C. Investigating the thermochemical conversion of biomass in a downdraft gasifier with a volatile break-up approach. *Energy Procedia*. 2017, vol. 142, pp. 822–828. issn 1876-6102. Available from doi: 10.1016/j.egypro.2017.12.132.
- [164] KUMAR, U.; PAUL, M. C. CFD modelling of biomass gasification with a volatile break-up approach. *Chemical Engineering Science*. 2019, vol. 195, pp. 413–422. issn 0009-2509. Available from doi: 10.1016/j.ces.2018.09.038.
- [165] LALLEMANT, N.; SAYRE, A.; WEBER, R. Evaluation of emissivity correlations for H<sub>2</sub>O-CO<sub>2</sub>-N<sub>2</sub>/air mixtures and coupling with solution methods of the radiative transfer equation. *Progress in Energy and Combustion Science*. 1996, vol. 22, no. 6, pp. 543–574. issn 0360-1285. Available from doi: 10.1016/s0360-1285(96)00010-x.
- [166] LAUNDER, B. E.; SPALDING, D. B. *Lectures in mathematical models of turbulence*. London, UK [et al.]: Academic Press, 1972. isbn 0-12-438050-6.
- [167] LAUNDER, B. E.; SPALDING, D. B. The numerical computation of turbulent flows. *Computer Methods in Applied Mechanics and Engineering*. 1974, vol. 3, no. 2, pp. 269–289. issn 0045-7825. Available from doi: 10.1016/0045-7825(74)90029-2.

- 
- [168] LAURENDEAU, N. M. Heterogeneous kinetics of coal char gasification and combustion. *Progress in Energy and Combustion Science*. 1978, vol. 4, no. 4, pp. 221–270. issn 0360-1285. Available from doi: 10.1016/0360-1285(78)90008-4.
- [169] LEE, A. L. Heat capacity of coal. *ACS Division of Fuel Chemistry*. 1968, vol. 12, pp. 19–31. issn 0569-3772.
- [170] LEFEBVRE, A. H. *Atomization and sprays*. 1st ed. New York, NY, USA: Hemisphere Publishing, 1989. isbn 978-0891166030.
- [171] LEROUX, B.; DELABROY, O.; LACAS, F. Experimental study of coaxial atomizers scaling. Part II: diluted zone. *Atomization and Sprays*. 2007, vol. 17, no. 5, pp. 409–430. issn 1044-5110. Available from doi: 10.1615/atomizspr.v17.i5.20.
- [172] LESNIAK, B.; SŁUPIK, Ł.; JAKUBINA, G. The determination of the specific heat capacity of coal based on literature data. *CHEMIK*. 2013, vol. 67, no. 6, pp. 560–571. issn 0009-2886.
- [173] LI, T.; CHAUDHARI, K.; VANESSENDELFT, D.; TURTON, R.; NICOLETTI, P.; SHAHNAM, M.; GUENTHER, C. Computational fluid dynamic simulations of a pilot-scale transport coal gasifier: evaluation of reaction kinetics. *Energy & Fuels*. 2013, vol. 27, no. 12, pp. 7896–7904. issn 0887-0624. Available from doi: 10.1021/ef401887r.
- [174] LI, T.; KU, X.; LØVÅS, T. CFD simulation of devolatilization of biomass with shrinkage effect. *Energy Procedia*. 2017, vol. 105, pp. 505–510. issn 1876-6102. Available from doi: 10.1016/j.egypro.2017.03.348.
- [175] LI, T.; THUNMAN, H.; STRÖM, H. A fast-solving particle model for thermochemical conversion of biomass. *Combustion and Flame*. 2020, vol. 213, pp. 117–131. issn 0010-2180. Available from doi: 10.1016/j.combustflame.2019.11.018.
- [176] LIU, H.-F.; LI, W.-F.; GONG, X.; CAO, X.-K.; XU, J.-L.; CHEN, X.-L.; WANG, Y.-F.; YU, G.-S.; WANG, F.-C.; YU, Z.-H. Effect of liquid jet diameter on performance of coaxial two-fluid airblast atomizers. *Chemical Engineering and Processing: Process Intensification*. 2006, vol. 45, no. 4, pp. 240–245. issn 0255-2701. Available from doi: 10.1016/j.cep.2005.08.003.
- [177] LORENZETTO, G. E.; LEFEBVRE, A. H. Measurements of drop size on a plain-jet airblast atomizer. *AIAA Journal*. 1977, vol. 15, no. 7, pp. 1006–1010. issn 0001-1452. Available from doi: 10.2514/3.60742.
- [178] LU, T.; LAW, C. K. A criterion based on computational singular perturbation for the identification of quasi steady state species: a reduced mechanism for methane oxidation with NO chemistry. *Combustion and Flame*. 2008, vol. 154, no. 4, pp. 761–774. issn 0010-2180. Available from doi: 10.1016/j.combustflame.2008.04.025.
-

- 
- [179] LU, X.; WANG, T. Investigation of radiation models in entrained-flow coal gasification simulation. *International Journal of Heat and Mass Transfer*. 2013, vol. 67, pp. 377–392. issn 0017-9310. Available from doi: 10.1016/j.ijheatmasstransfer.2013.08.011.
- [180] LUU, T. D.; SHAMOONI, A.; STEIN, O. T.; KRONENBURG, A.; POPP, S.; NICOLAI, H.; SCHNEIDER, H.; WEN, X.; HASSE, C. Analysis of heat transfer effects in flamelet/progress variable LES of gas-assisted pulverised coal flames. In: *Proceedings of the 30th Deutscher Flammentag: für nachhaltige Verbrennung, 28-29 September 2021, Hannover-Garbsen, Germany*. Hannover-Garbsen, Germany, 2021.
- [181] MA, J.; ZITNEY, S. E. Computational fluid dynamic modeling of entrained-flow gasifiers with improved physical and chemical submodels. *Energy & Fuels*. 2012, vol. 26, no. 12, pp. 7195–7219. issn 0887-0624. Available from doi: 10.1021/ef301346z.
- [182] MACDONALD, R. A.; CALLANAN, J. E.; MCDERMOTT, K. M. Heat capacity of a medium-volatile bituminous premium coal from 300 to 520 K. Comparison with a high-volatile bituminous nonpremium coal. *Energy & Fuels*. 1987, vol. 1, no. 6, pp. 535–540. issn 0887-0624. Available from doi: 10.1021/ef00006a014.
- [183] MAGNUSSEN, B. F.; HJERTAGER, B. H. On mathematical modeling of turbulent combustion with special emphasis on soot formation and combustion. *Symposium (International) on Combustion*. 1977, vol. 16, no. 1, pp. 719–729. issn 0082-0784. Available from doi: 10.1016/s0082-0784(77)80366-4.
- [184] MAGNUSSEN, B. On the structure of turbulence and a generalized eddy dissipation concept for chemical reaction in turbulent flow. In: *Proceedings of the 19th Aerospace Sciences Meeting, 12-15 January 1981, St. Louis, MO, USA*. St. Louis, MO, USA: American Institute of Aeronautics and Astronautics, 1981. No. 81-31510. Available from doi: 10.2514/6.1981-42.
- [185] MANCINI, M.; BUCZYŃSKI, R.; WEBER, R.; FLECK, S.; STOESSER, P.; KOLB, T. Gasification of glycol: measurements and mathematical modelling. In: *Proceedings of the 25th Deutscher Flammentag: Verbrennung und Feuerung, 14-15 September 2011, Karlsruhe, Germany*. Düsseldorf, Germany: VDI-Verlag, 2011, vol. 2119, pp. 221–226. VDI-Berichte.
- [186] MANCINI, M.; WEBER, R.; WEIGAND, P.; LEUCKEL, W.; KOLB, T. Design of the entrained flow reactor for gasification of biomass based slurry. In: *Proceedings of the 26th Deutscher Flammentag: Verbrennung und Feuerung, 11-12 September 2013, Duisburg, Germany*. Düsseldorf, Germany: VDI-Verlag, 2013, vol. 2161, pp. 625–634. VDI-Berichte.

- 
- [187] MANCINI, M.; ALBERTI, M.; DAMMANN, M.; SANTO, U.; ECKEL, G.; KOLB, T.; WEBER, R. Entrained flow gasification. Part 2: mathematical modeling of the gasifier using RANS method. *Fuel*. 2018, vol. 225, pp. 596–611. issn 0016-2361. Available from doi: 10.1016/j.fuel.2018.03.100.
- [188] MANCINI, M. *Modeling of solid fuel conversion processes for CFD applications*. Clausthal-Zellerfeld, Germany: Papierflieger, 2019. isbn 978-3-86948-721-2. Available from doi: 10.21268/20200106-0. Habilitation thesis. Fakultät für Energie- und Wirtschaftswissenschaften, Technische Universität Clausthal.
- [189] MANSOUR, A.; CHIGIER, N. Air-blast atomization of non-Newtonian liquids. *Journal of Non-Newtonian Fluid Mechanics*. 1995, vol. 58, no. 2-3, pp. 161–194. issn 0377-0257. Available from doi: 10.1016/0377-0257(95)01356-z.
- [190] MARINOV, N. M. A detailed chemical kinetic model for high temperature ethanol oxidation. *International Journal of Chemical Kinetics*. 1999, vol. 31, no. 3, pp. 183–220. issn 0538-8066. Available from doi: 10.1002/(SICI)1097-4601(1999)31:3<183::AID-KIN3>3.0.CO;2-X.
- [191] MARKLUND, M.; TEGMAN, R.; GEBART, R. CFD modelling of black liquor gasification: identification of important model parameters. *Fuel*. 2007, vol. 86, no. 12-13, pp. 1918–1926. issn 0016-2361. Available from doi: 10.1016/j.fuel.2006.12.015.
- [192] MARKLUND, M.; TEGMAN, R.; GEBART, R. A self-consistent CFD-model for pressurised high temperature black liquor gasification. *IFRF Combustion Journal*. 2008, no. 200801. issn 1562-479X. Available also from: <https://ifrf.net/research/archive/a-self-consistent-cfd-model-for-pressurised-high-temperature-black-liquor-gasification/>.
- [193] MARKLUND, M. *Pressurized entrained-flow high temperature black liquor gasification: CFD based reactor scale-up method and spray burner characterization*. Luleå, Sweden, 2006. Available also from: <https://nbn-resolving.org/urn:nbn:se:ltu:diva-26275>. Ph.D. Thesis. Department of Engineering Sciences and Mathematics, Luleå University of Technology.
- [194] MATHWORKS. *MATLAB. Release 2019b*. 2019.
- [195] MÄTZLER, C. *Mie scattering with and without diffraction*. Bern, Switzerland, 2004. Tech. rep., 2004-02. Institute of Applied Physics, University of Bern.
- [196] MCBRIDE, B. J.; ZEHE, M. J.; GORDON, S. *NASA Glenn coefficients for calculating thermodynamic properties of individual species*. Cleveland, OH, USA, 2002. Tech. rep., NASA/TP-2002-211556. John H. Glenn Research Center at Lewis Field, National Aeronautics and Space Administration. Available also from: <https://ntrs.nasa.gov/citations/20020085330>.
-

- 
- [197] McDONALD, R. A. Heat content and heat capacity of an extruded graphite from 341 to 1723 K. *Journal of Chemical and Engineering Data*. 1965, vol. 10, no. 3, pp. 243–243. issn 0021-9568. Available from doi: 10.1021/jc60026a011.
- [198] McELIGOT, D. M.; SWANK, W. D.; COTTLE, D. L.; VALENTIN, F. I. *Thermal properties of G-348 graphite*. Idaho Falls, ID, USA: Office of Scientific and Technical Information (OSTI), 2016. Tech. rep., INL/EXT-16-38241. Idaho National Laboratory. Available from doi: 10.2172/1330693.
- [199] MENTER, F. R.; KUNTZ, M.; LANGTRY, R. Ten years of industrial experience with the SST turbulence model. *Turbulence, heat and mass transfer*. 2003, vol. 4, no. 1, pp. 625–632.
- [200] MENTER, F. R. Two-equation eddy-viscosity turbulence models for engineering applications. *AIAA Journal*. 1994, vol. 32, no. 8, pp. 1598–1605. issn 0001-1452. Available from doi: 10.2514/3.12149.
- [201] MENTSER, M.; ERGUN, S. *A study of the carbon dioxide-carbon reaction by oxygen exchange*. Washington D.C., USA: United States Government Printing Office, 1973. Tech. rep., 664. United States Bureau of Mines, United States Department of the Interior. Available also from: <https://digital.library.unt.edu/ark:/67531/metadc12808/>.
- [202] MERRICK, D. Mathematical models of the thermal decomposition of coal. 2. Specific heats and heats of reaction. *Fuel*. 1983, vol. 62, no. 5, pp. 540–546. issn 0016-2361. Available from doi: 10.1016/0016-2361(83)90223-5.
- [203] MERRICK, D. Mathematical models of the thermal decomposition of coal. 3. Density, porosity and contraction behaviour. *Fuel*. 1983, vol. 62, no. 5, pp. 547–552. issn 0016-2361. Available from doi: 10.1016/0016-2361(83)90224-7.
- [204] METHLING, T.; KATHROTIA, T.; RIEDEL, U. Rapid reduction of a chemical kinetic model for the combustion of the pyrolysis oil surrogate ethylene glycol. In: *Proceedings of the 16th International Conference on Numerical Combustion, 3-4 April 2017, Orlando, FL, USA*. Orlando, FL, USA, 2017.
- [205] METHLING, T. *Reduced reaction mechanism for the gasification of ethylene glycol (personal communication)*. 2019.
- [206] MEYER, B. XtL: development of synthesis fuels in Europe and South Africa. In: *Proceedings of the IEA-MOST Workshop: Advances in deployment of fossil fuel technologies, 24-25 June 2014, Beijing, China*. Beijing, China, 2014.
- [207] MITCHELL, R.; HURT, R.; BAXTER, L.; HARDESTY, D. *Compilation of Sandia coal char combustion data and kinetic analyses*. Albuquerque, NM, USA, 1992. Tech. rep. Available from doi: 10.2172/7045508.

- 
- [208] MITCHELL, R. E.; AKANETUK, A. E. J. The impact of fragmentation on char conversion during pulverized coal combustion. *Symposium (International) on Combustion*. 1996, vol. 26, no. 2, pp. 3137–3144. issn 0082-0784. Available from doi: 10.1016/s0082-0784(96)80158-5.
- [209] MODEST, M. F. *Radiative heat transfer*. 3rd ed. Academic Press, 2013. isbn 978-0-12-386944-9.
- [210] MOHAN, D.; PITTMAN, C. U.; STEELE, P. H. Pyrolysis of wood/biomass for bio-oil: a critical review. *Energy & Fuels*. 2006, vol. 20, no. 3, pp. 848–889. issn 0887-0624. Available from doi: 10.1021/ef0502397.
- [211] MORGANO, M. T.; LEIBOLD, H.; RICHTER, F.; SEIFERT, H. Screw pyrolysis with integrated sequential hot gas filtration. *Journal of Analytical and Applied Pyrolysis*. 2015, vol. 113, pp. 216–224. issn 0165-2370. Available from doi: 10.1016/j.jaap.2014.12.019.
- [212] MORSI, S. A.; ALEXANDER, A. J. An investigation of particle trajectories in two-phase flow systems. *Journal of Fluid Mechanics*. 1972, vol. 55, no. 2, pp. 193–208. issn 0022-1120. Available from doi: 10.1017/s0022112072001806.
- [213] MUELLER, A.; HAUSTEIN, H. D.; STOESSER, P.; KREITZBERG, T.; KNEER, R.; KOLB, T. Gasification kinetics of biomass- and fossil-based fuels: comparison study using fluidized bed and thermogravimetric analysis. *Energy & Fuels*. 2015, vol. 29, no. 10, pp. 6717–6723. issn 0887-0624. Available from doi: 10.1021/acs.energyfuels.5b01123.
- [214] MULARSKI, J.; PAWLAK-KRUCZEK, H.; MODLINSKI, N. A review of recent studies of the CFD modelling of coal gasification in entrained flow gasifiers, covering devolatilization, gas-phase reactions, surface reactions, models and kinetics. *Fuel*. 2020, vol. 271, p. 117620. issn 0016-2361. Available from doi: 10.1016/j.fuel.2020.117620.
- [215] MULHEM, B.; FRITSCHING, U.; SCHULTE, G.; BAUCKHAGE, K. Characterisation of twin-fluid atomization for suspensions. In: *Proceedings of the 9th International Conference on Liquid Atomization and Spray Systems, 13-17 July 2003, Sorrento, Italy*. Sorrento, Italy: ILASS, 2003.
- [216] MÜLLER, T.; HABISREUTHER, P.; ZARZALIS, N.; SÄNGER, A.; JAKOBS, T.; KOLB, T. Investigation on jet breakup of high-viscous fuels for entrained flow gasification. In: *Proceedings of the ASME Turbo Expo 2016: Turbomachinery Technical Conference and Exposition. Volume 3: Coal, Biomass and Alternative Fuels: Cycle Innovations: Electric Power; Industrial and Cogeneration; Organic Rankine Cycle Power Systems, 13-17 June 2016, Seoul, South Korea*. Seoul, South Korea: American Society of Mechanical Engineers, 2016. No. GT2016-56371. Available from doi: 10.1115/gt2016-56371.
-

- 
- [217] MÜLLER, T.; SÄNGER, A.; HABISREUTHER, P.; JAKOBS, T.; TRIMIS, D.; KOLB, T.; ZARZALIS, N. Simulation of the primary breakup of a high-viscosity liquid jet by a coaxial annular gas flow. *International Journal of Multiphase Flow*. 2016, vol. 87, pp. 212–228. issn 0301-9322. Available from doi: 10.1016/j.ijmultiphaseflow.2016.09.008.
- [218] MURTHY, J. Y.; MATHUR, S. R. Finite volume method for radiative heat transfer using unstructured meshes. *Journal of Thermophysics and Heat Transfer*. 1998, vol. 12, no. 3, pp. 313–321. issn 0887-8722. Available from doi: 10.2514/2.6363.
- [219] NAKOD, P. CFD modeling and validation of oxy-fired and air-fired entrained flow gasifiers. *International Journal of Chemical and Physical Sciences*. 2013, vol. 2, no. 6, pp. 28–40. issn 2319-6602. Available also from: <https://www.ijcps.org/0Site/issue8.html>.
- [220] NEWALKAR, G.; IISA, K.; D’AMICO, A. D.; SIEVERS, C.; AGRAWAL, P. Effect of temperature, pressure, and residence time on pyrolysis of pine in an entrained flow reactor. *Energy & Fuels*. 2014, vol. 28, no. 8, pp. 5144–5157. issn 0887-0624. Available from doi: 10.1021/ef5009715.
- [221] NIEMELÄ, N. P.; TOLVANEN, H.; SAARINEN, T.; LEPPÄNEN, A.; JORONEN, T. CFD based reactivity parameter determination for biomass particles of multiple size ranges in high heating rate devolatilization. *Energy*. 2017, vol. 128, pp. 676–687. issn 0360-5442. Available from doi: 10.1016/j.energy.2017.04.023.
- [222] NIEMELÄ, N. *Computational fluid dynamics modeling of pulverized biomass combustion using optimized reactivity parameters*. Tampere, Finland, 2016. Available also from: <http://urn.fi/URN:NBN:fi:ttty-201603223739>. Master’s Thesis. Faculty of Natural Sciences, Tampere University of Technology.
- [223] NIKRITYUK, P.; MEYER, B. (eds.). *Gasification processes: modeling and simulation*. Weinheim, Germany: Wiley-VCH, 2014. isbn 978-3-527-33550-3.
- [224] NIKSA, S.; LIU, G.-s.; HURT, R. H. Coal conversion submodels for design applications at elevated pressures. Part I: devolatilization and char oxidation. *Progress in Energy and Combustion Science*. 2003, vol. 29, no. 5, pp. 425–477. issn 0360-1285. Available from doi: 10.1016/s0360-1285(03)00033-9.
- [225] NIKSA, S. FLASHCHAIN theory for rapid coal devolatilization kinetics. 2. Impact of operating conditions. *Energy & Fuels*. 1991, vol. 5, no. 5, pp. 665–673. issn 0887-0624. Available from doi: 10.1021/ef00029a007.
- [226] NIKSA, S. FLASHCHAIN theory for rapid coal devolatilization kinetics. 3. Modeling the behavior of various coals. *Energy & Fuels*. 1991, vol. 5, no. 5, pp. 673–683. issn 0887-0624. Available from doi: 10.1021/ef00029a008.

- 
- [227] NIKSA, S. FLASHCHAIN theory for rapid coal devolatilization kinetics. 4. Predicting ultimate yields from ultimate analyses alone. *Energy & Fuels*. 1994, vol. 8, no. 3, pp. 659–670. issn 0887-0624. Available from doi: 10.1021/ef00045a022.
- [228] NIKSA, S. FLASHCHAIN theory for rapid coal devolatilization kinetics. 5. Interpreting rates of devolatilization for various coal types and operating conditions. *Energy & Fuels*. 1994, vol. 8, no. 3, pp. 671–679. issn 0887-0624. Available from doi: 10.1021/ef00045a023.
- [229] NIKSA, S. FLASHCHAIN theory for rapid coal devolatilization kinetics. 6. Predicting the evolution of fuel nitrogen from various coals. *Energy & Fuels*. 1995, vol. 9, no. 3, pp. 467–478. issn 0887-0624. Available from doi: 10.1021/ef00051a011.
- [230] NIKSA, S. FLASHCHAIN theory for rapid coal devolatilization kinetics. 7. Predicting the release of oxygen species from various coals. *Energy & Fuels*. 1996, vol. 10, no. 1, pp. 173–187. issn 0887-0624. Available from doi: 10.1021/ef9500671.
- [231] NIKSA, S. Predicting the rapid devolatilization of diverse forms of biomass with bio-flashchain. *Proceedings of the Combustion Institute*. 2000, vol. 28, no. 2, pp. 2727–2733. issn 1540-7489. Available from doi: 10.1016/s0082-0784(00)80693-1.
- [232] NIKSA, S. bio-FLASHCHAIN<sup>®</sup> theory for rapid devolatilization of biomass. 1. Lignin devolatilization. *Fuel*. 2020, vol. 263, p. 116649. issn 0016-2361. Available from doi: 10.1016/j.fuel.2019.116649.
- [233] NIKSA, S. bio-FLASHCHAIN<sup>®</sup> theory for rapid devolatilization of biomass. 2. Predicting total yields for torrefied woods. *Fuel*. 2020, vol. 263, p. 116645. issn 0016-2361. Available from doi: 10.1016/j.fuel.2019.116645.
- [234] NIKSA, S. bio-FLASHCHAIN<sup>®</sup> theory for rapid devolatilization of biomass. 3. Predicting total yields for torrefied grasses and agricultural residues. *Fuel*. 2020, vol. 263, p. 116646. issn 0016-2361. Available from doi: 10.1016/j.fuel.2019.116646.
- [235] NIKSA, S.; KERSTEIN, A. R. FLASHCHAIN theory for rapid coal devolatilization kinetics. 1. Formulation. *Energy & Fuels*. 1991, vol. 5, no. 5, pp. 647–665. issn 0887-0624. Available from doi: 10.1021/ef00029a006.
- [236] OLSSON, E.; KREISS, G. A conservative level set method for two phase flow. *Journal of Computational Physics*. 2005, vol. 210, no. 1, pp. 225–246. Available from doi: 10.1016/j.jcp.2005.04.007.
- [237] PAPADIKIS, K.; GU, S.; BRIDGWATER, A. V. CFD modelling of the fast pyrolysis of biomass in fluidised bed reactors: modelling the impact of biomass shrinkage. *Chemical Engineering Journal*. 2009, vol. 149, no. 1-3, pp. 417–427. issn 1385-8947. Available from doi: 10.1016/j.cej.2009.01.036.
-

- 
- [238] PARK, S.; JEONG, H.; HWANG, J. 3-D CFD modeling for parametric study in a 300-MW one-stage oxygen-blown entrained-bed coal gasifier. *Energies*. 2015, vol. 8, no. 5, pp. 4216–4236. issn 1996-1073. Available from doi: 10.3390/en8054216.
- [239] PHILIPP, E. Green synthetic fuels from CO<sub>2</sub> and biomass. In: *Proceedings of the 2021 Global Syngas Technologies Council Conference, 10-12 October 2021, San Antonio, TX, USA*. San Antonio, TX, USA, 2021.
- [240] PIELSTICKER, S.; GÖVERT, B.; KREITZBERG, T.; HABERMEHL, M.; HATZFELD, O.; KNEER, R. Simultaneous investigation into the yields of 22 pyrolysis gases from coal and biomass in a small-scale fluidized bed reactor. *Fuel*. 2017, vol. 190, pp. 420–434. issn 0016-2361. Available from doi: 10.1016/j.fuel.2016.10.085.
- [241] PIELSTICKER, S.; SCHLÖGEL, K.; KREITZBERG, T.; HATZFELD, O.; KNEER, R. Measurement of beech wood pyrolysis kinetics in a fluidized bed reactor. In: *Proceedings of the Joint Meeting of the German and Italian Sections of the Combustion Institute, 23-26 May 2018, Sorrento, Italy*. Sorrento, Italy, 2018.
- [242] PIELSTICKER, S.; KREITZBERG, T.; HATZFELD, O.; KNEER, R. Using the chemical percolation devolatilization model for analysis of pyrolysis kinetics in a fluidized bed reactor. In: *Proceedings of the 11th Mediterranean Combustion Symposium, 16-20 Juni 2019, Tenerife, Spain*. Tenerife, Spain, 2019.
- [243] POINSOT, T. *Theoretical and numerical combustion*. Toulouse, France [et al.], 2012. isbn 978-2-7466-3990-4.
- [244] POLING, B. E.; PRAUSNITZ, J. M.; O’CONNELL, J. P. *The properties of gases and liquids*. 5th ed. New York, NY, USA: McGraw-Hill, 2001. isbn 978-0-070-11682-5.
- [245] POPE, S. B. *Turbulent flows*. Cambridge University Press, 2000. isbn 978-0-521-59886-6.
- [246] RABAÇAL, M.; KOPS, R. B.; PEREIRA, F. M.; COSTA, M. Direct observations of single particle fragmentation in the early stages of combustion under dry and wet conventional and oxy-fuel conditions. *Proceedings of the Combustion Institute*. 2019, vol. 37, no. 3, pp. 3005–3012. issn 1540-7489. Available from doi: 10.1016/j.proci.2018.07.001.
- [247] RAGLAND, K. W.; AERTS, D. J.; BAKER, A. J. Properties of wood for combustion analysis. *Bioresource Technology*. 1991, vol. 37, no. 2, pp. 161–168. issn 0960-8524. Available from doi: 10.1016/0960-8524(91)90205-x.
- [248] RANZ, W. E.; MARSHALL, W. R. Evaporation from drops. Part I. *Chemical Engineering Progress*. 1952, vol. 48, no. 3, pp. 141–146. issn 0360-7275.
- [249] RANZ, W. E.; MARSHALL, W. R. Evaporation from drops. Part II. *Chemical Engineering Progress*. 1952, vol. 48, no. 3, pp. 173–180. issn 0360-7275.

- 
- [250] RASHIDI, A.; HAFNER, S.; RIEDEL, U. Gasification of ethylene glycol as model substance for biomass based pyrolysis oil: detailed reaction mechanism development and CFD simulation. In: *Proceedings of the 4th European Combustion Meeting, 14-17 April 2009, Vienna, Austria*. Vienna, Austria, 2009.
- [251] RASHIDI, A. *CFD simulation of biomass gasification using detailed chemistry*. Heidelberg, Germany: Ruprecht-Karls-Universität Heidelberg, 2011. Available from doi: 10.11588/heidok.00011654. Ph.D. Thesis. Naturwissenschaftlich-Mathematische Gesamtfakultät, Ruprecht-Karls-Universität Heidelberg.
- [252] RAUCH, R.; HRBEK, J.; HOFBAUER, H. Biomass gasification for synthesis gas production and applications of the syngas. *Wiley Interdisciplinary Reviews: Energy and Environment*. 2013, vol. 3, no. 4, pp. 343–362. issn 2041-8396. Available from doi: 10.1002/wene.97.
- [253] REACTION DESIGN. *CHEMKIN-PRO. Release 15112*. San Diego, CA, USA, 2011.
- [254] REACTION DESIGN. *CHEMKIN-PRO. Release 15113*. San Diego, CA, USA, 2012.
- [255] REHM, M.; SEIFERT, P.; MEYER, B. Theoretical and numerical investigation on the EDC-model for turbulence-chemistry interaction at gasification conditions. *Computers & Chemical Engineering*. 2009, vol. 33, no. 2, pp. 402–407. issn 0098-1354. Available from doi: 10.1016/j.compchemeng.2008.11.006.
- [256] REMACHA, M. P.; JIMÉNEZ, S.; BALLESTER, J. Devolatilization of millimeter-sized biomass particles at high temperatures and heating rates. Part 2: modeling and validation for thermally-thin and -thick regimes. *Fuel*. 2018, vol. 234, pp. 707–722. issn 0016-2361. Available from doi: 10.1016/j.fuel.2018.07.017.
- [257] RICHARDS, A. P.; FLETCHER, T. H. A comparison of simple global kinetic models for coal devolatilization with the CPD model. *Fuel*. 2016, vol. 185, pp. 171–180. issn 0016-2361. Available from doi: 10.1016/j.fuel.2016.07.095.
- [258] RICHTER, A.; NIKRITYUK, P. A. Drag forces and heat transfer coefficients for spherical, cuboidal and ellipsoidal particles in cross flow at sub-critical Reynolds numbers. *International Journal of Heat and Mass Transfer*. 2012, vol. 55, no. 4, pp. 1343–1354. issn 0017-9310. Available from doi: 10.1016/j.ijheatmasstransfer.2011.09.005.
- [259] RICHTER, A.; SEIFERT, P.; COMPART, F.; TISCHER, P.; MEYER, B. A large-scale benchmark for the CFD modeling of non-catalytic reforming of natural gas based on the Freiberg test plant HP POX. *Fuel*. 2015, vol. 152, pp. 110–121. issn 0016-2361. Available from doi: 10.1016/j.fuel.2014.12.004.

- 
- [260] RÖSSGER, P.; SEIDL, L. G.; COMPART, F.; HUSSLER, J.; GRÄBNER, M.; RICHTER, A. Integrating biomass and waste into high-pressure partial oxidation processes: Thermochemical and economic multi-objective optimization. *Journal of Cleaner Production*. 2022, vol. 358, p. 132053. issn 0959-6526. Available from doi: 10.1016/j.jclepro.2022.132053.
- [261] ROSSUM, G. van; DRAKE, F. L. *Python. Release 3.6* [<https://www.python.org>]. Ed. by PYTHON SOFTWARE FOUNDATION. 2021. Available also from: <https://www.python.org/>.
- [262] RYBDYLOVA, O.; AL QUBEISSI, M.; BRAUN, M.; CRUA, C.; MANIN, J.; PICKETT, L. M.; SERCEY, G. de; SAZHINA, E. M.; SAZHIN, S. S.; HEIKAL, M. A model for droplet heating and its implementation into ANSYS Fluent. *International Communications in Heat and Mass Transfer*. 2016, vol. 76, pp. 265–270. issn 0735-1933. Available from doi: 10.1016/j.icheatmasstransfer.2016.05.032.
- [263] SAFRONOV, D.; FÖRSTER, T.; SCHWITALLA, D.; NIKRITYUK, P.; GUHL, S.; RICHTER, A.; MEYER, B. Numerical study on entrained-flow gasification performance using combined slag model and experimental characterization of slag properties. *Fuel Processing Technology*. 2017, vol. 161, pp. 62–75. issn 0378-3820. Available from doi: 10.1016/j.fuproc.2017.03.007.
- [264] SAGAUT, P. *Large eddy simulation for incompressible flows: an introduction*. 3rd ed. Berlin, Germany [et al.]: Springer, 2006. isbn 978-3-540-26344-9.
- [265] SÄNGER, A. D. *Zerstäubung hochviskoser Fluide bei variierendem Systemdruck: Grundlagenforschung zur Hochdruck-Flugstromvergasung*. Karlsruhe, Germany, 2018. Available from doi: 10.5445/IR/1000087397. Ph.D. Thesis. Fakultät für Chemieingenieurwesen und Verfahrenstechnik, Karlsruher Institut für Technologie.
- [266] SANI, E.; DELL'ORO, A. Optical constants of ethylene glycol over an extremely wide spectral range. *Optical Materials*. 2014, vol. 37, pp. 36–41. issn 0925-3467. Available from doi: 10.1016/j.optmat.2014.04.035.
- [267] SAROFIM, A. F.; HOWARD, J. B.; PADIA, A. S. The physical transformation of the mineral matter in pulverized coal under simulated combustion conditions. *Combustion Science and Technology*. 1977, vol. 16, no. 3-6, pp. 187–204. issn 0010-2202. Available from doi: 10.1080/00102207708946804.
- [268] SAROFIM, A. F.; HELBLE, J. J. Mechanisms of ash and deposit formation. In: *Proceedings of the Engineering Foundation International Conference, Solihull, UK*. Solihull, UK, 1993. isbn 978-1560322931.
- [269] SASONGKO, D.; RASRENDRA, C. B.; INDARTO, A. Fragmentation model of coal devolatilisation in fluidised bed combustion. *International Journal of Ambient Energy*. 2017, vol. 39, no. 5, pp. 508–515. issn 0143-0750. Available from doi: 10.1080/01430750.2017.1318788.

- 
- [270] SAZHIN, S. S.; KRUTITSKII, P. A.; ABDELGHAFAR, W. A.; SAZHINA, E. M.; MIKHALOVSKY, S. V.; MEIKLE, S. T.; HEIKAL, M. R. Transient heating of diesel fuel droplets. *International Journal of Heat and Mass Transfer*. 2004, vol. 47, no. 14-16, pp. 3327–3340. issn 0017-9310. Available from doi: 10.1016/j.ijheatmasstransfer.2004.01.011.
- [271] SAZHIN, S. S.; AL QUBEISSI, M.; NASIRI, R.; GUN'KO, V. M.; ELWARDANY, A. E.; LEMOINE, F.; GRISCH, F.; HEIKAL, M. R. A multi-dimensional quasi-discrete model for the analysis of diesel fuel droplet heating and evaporation. *Fuel*. 2014, vol. 129, pp. 238–266. issn 0016-2361. Available from doi: 10.1016/j.fuel.2014.03.028.
- [272] SCALA, F.; CHIRONE, R.; SALATINO, P. Combustion and attrition of biomass chars in a fluidized bed. *Energy & Fuels*. 2006, vol. 20, no. 1, pp. 91–102. issn 0887-0624. Available from doi: 10.1021/ef050102g.
- [273] SCHIEMANN, M.; GRONARZ, T.; GRAESER, P.; GOREWODA, J.; KNEER, R.; SCHERER, V. A correlation between char emissivity and temperature. *Fuel*. 2019, vol. 256, p. 115889. issn 0016-2361. Available from doi: 10.1016/j.fuel.2019.115889.
- [274] SCHILLER, L.; NAUMANN, A. Z. Über die grundlegenden Berechnungen bei der Schwerkraftaufbereitung. *Zeitung des Vereins Deutscher Ingenieure*. 1933, vol. 77, pp. 318–320.
- [275] SCHNEIDER, C.; STOESSER, P.; RINCON, S.; KOLB, T. Determination of heterogeneous reaction kinetics of high-temperature biomass char. In: *Proceedings of the 28th Deutscher Flammentag: Verbrennung und Feuerung, 6-7 September 2017, Darmstadt, Germany*. Düsseldorf, Germany: VDI-Verlag, 2017, vol. 2161, pp. 331–343. VDI-Berichte.
- [276] SCHNEIDER, C.; WALKER, S.; PHOUNGLAMCHEIK, A.; UMEKI, K.; KOLB, T. Effect of calcium dispersion and graphitization during high-temperature pyrolysis of beech wood char on the gasification rate with CO<sub>2</sub>. *Fuel*. 2021, vol. 283, p. 118826. Available from doi: 10.1016/j.fuel.2020.118826.
- [277] SCHNEIDER, C.; ZELLER, M.; BÖHM, D.; KOLB, T. Influence of pressure on the gasification kinetics of two high-temperature beech wood chars with CO<sub>2</sub>, H<sub>2</sub>O and its mixture. *Fuel*. 2021, vol. 299, p. 120523. Available from doi: 10.1016/j.fuel.2021.120523.
- [278] SCHNEIDER, C. *Reaction kinetics of biogenic solid fuels under process conditions of technical entrained-flow gasifiers*. Karlsruhe, Germany, 2021. Available from doi: 10.5445/IR/1000139237. Ph.D. Thesis. Fakultät für Chemieingenieurwesen und Verfahrenstechnik, Karlsruher Institut für Technologie.
-

- 
- [279] SCHNEIDER, M. *Untersuchungen zur Pyrolysekinetik eines biogenen Festbrennstoffes im Fallrohrreaktor*. Karlsruhe, Germany, 2018. Master's Thesis. Engler-Bunte-Institut, Brennstofftechnologie – Chemische Energieträger, Karlsruher Institut für Technologie.
- [280] SCIPY DEVELOPERS. *SciPy. Release 1.5.1* [<https://pypi.org/project/scipy/>]. Ed. by PYTHON SOFTWARE FOUNDATION. 2021. Available also from: <https://pypi.org/project/scipy/>.
- [281] SENNECA, O.; RUSSO, S.; CHIRONE, R. Primary fragmentation of coal particles at high heating rate. *Chemical Engineering Transactions*. 2009, vol. 18, pp. 569–574. Available from doi: 10.3303/CET0918092.
- [282] SENNECA, O.; ALLOUIS, C.; CHIRONE, R.; RUSSO, S. Set up of an experimental apparatus for the study of fragmentation of solid fuels upon severe heating. *Experimental Thermal and Fluid Science*. 2010, vol. 34, no. 3, pp. 366–372. issn 0894-1777. Available from doi: 10.1016/j.expthermflusci.2009.10.015.
- [283] SENNECA, O.; URCIUOLO, M.; CHIRONE, R.; CUMBO, D. An experimental study of fragmentation of coals during fast pyrolysis at high temperature and pressure. *Fuel*. 2011, vol. 90, no. 9, pp. 2931–2938. issn 0016-2361. Available from doi: 10.1016/j.fuel.2011.04.012.
- [284] SENNECA, O.; URCIUOLO, M.; CHIRONE, R. A semidetailed model of primary fragmentation of coal. *Fuel*. 2013, vol. 104, pp. 253–261. issn 0016-2361. Available from doi: 10.1016/j.fuel.2012.09.026.
- [285] SENNECA, O.; URCIUOLO, M.; BARESCINO, P.; DIGLIO, G.; PEPE, F.; CHIRONE, R. Pyrolysis, combustion, and fragmentation model of coal particles: preliminary results. *Combustion Science and Technology*. 2016, vol. 188, no. 4-5, pp. 759–768. issn 0010-2202. Available from doi: 10.1080/00102202.2016.1138763.
- [286] SENNECA, O.; BARESCINO, P.; URCIUOLO, M.; CHIRONE, R. Prediction of structure evolution and fragmentation phenomena during combustion of coal: effects of heating rate. *Fuel Processing Technology*. 2017, vol. 166, pp. 228–236. issn 0378-3820. Available from doi: 10.1016/j.fuproc.2017.06.010.
- [287] SENNECA, O.; HEUER, S.; BARESCINO, P.; URCIUOLO, M.; PEPE, F.; SCHIEMANN, M.; CHIRONE, R.; SCHERER, V. Fragmentation of pulverized coal in a laminar drop tube reactor: experiments and model. *Proceedings of the Combustion Institute*. 2019, vol. 37, no. 3, pp. 2849–2855. issn 1540-7489. Available from doi: 10.1016/j.proci.2018.08.057.
- [288] SEPTIEN, S.; VALIN, S.; DUPONT, C.; PEYROT, M.; SALVADOR, S. Effect of particle size and temperature on woody biomass fast pyrolysis at high temperature (1000–1400 °C). *Fuel*. 2012, vol. 97, pp. 202–210. issn 0016-2361. Available from doi: 10.1016/j.fuel.2012.01.049.

- 
- [289] SHAH, K. V.; CIEPLIK, M. K.; BETRAND, C. I.; KAMP, W. L. van de; VUTHALURU, H. B. A kinetic-empirical model for particle size distribution evolution during pulverised fuel combustion. *Fuel*. 2010, vol. 89, no. 9, pp. 2438–2447. issn 0016-2361. Available from doi: 10.1016/j.fuel.2009.12.013.
- [290] SHINJO, J.; UMEMURA, A. Simulation of liquid jet primary breakup: dynamics of ligament and droplet formation. *International Journal of Multiphase Flow*. 2010, vol. 36, no. 7, pp. 513–532. issn 0301-9322. Available from doi: 10.1016/j.ijmultiphaseflow.2010.03.008.
- [291] SIMONE, M.; BIAGINI, E.; GALLETTI, C.; TOGNOTTI, L. Evaluation of global biomass devolatilization kinetics in a drop tube reactor with CFD aided experiments. *Fuel*. 2009, vol. 88, no. 10, pp. 1818–1827. issn 0016-2361. Available from doi: 10.1016/j.fuel.2009.04.032.
- [292] SIRIGNANO, W. A. *Fluid dynamics and transport of droplets and sprays*. 2nd ed. Cambridge, UK [et al.]: Cambridge University Press, 2010. isbn 978-0-521-88489-1.
- [293] SMITH, T. F.; SHEN, Z. F.; FRIEDMAN, J. N. Evaluation of coefficients for the weighted sum of gray gases model. *Journal of Heat Transfer*. 1982, vol. 104, no. 4, pp. 602–608. issn 0022-1481. Available from doi: 10.1115/1.3245174.
- [294] SMITH, G. P.; GOLDEN, D. M.; FRENKLACH, M.; MORIARTY, N. W.; EITENEER, B.; GOLDENBERG, M.; BOWMAN, C. T.; HANSON, R. K.; SONG, S.; GARDINER, W.; LISSIANSKI, V. V.; QIN, Z. *GRI-Mech 3.0*. 1999. Available also from: <http://combustion.berkeley.edu/gri-mech/>.
- [295] SOLOMON, P. R.; HAMBLIN, D. G.; CARANGELO, R. M.; SERIO, M. A.; DESHPANDE, G. V. General model of coal devolatilization. *Energy & Fuels*. 1988, vol. 2, no. 4, pp. 405–422. issn 0887-0624. Available from doi: 10.1021/ef00010a006.
- [296] SPALDING, D. B. Mixing and chemical reaction in steady confined turbulent flames. *Symposium (International) on Combustion*. 1971, vol. 13, no. 1, pp. 649–657. issn 0082-0784. Available from doi: 10.1016/s0082-0784(71)80067-x.
- [297] SREEKANTH, M.; PRASAD, B. V. S. S. S.; KOLAR, A. K.; THUNMAN, H.; LECKNER, B. Stresses in a cylindrical wood particle undergoing devolatilization in a hot bubbling fluidized bed. *Energy & Fuels*. 2008, vol. 22, no. 3, pp. 1549–1559. issn 0887-0624. Available from doi: 10.1021/ef700658k.
- [298] SRINIVASACHAR, S.; TOQAN, M. A.; BEÉR, J. M.; ETTOUNEY, H. M. Percolation model for coal char particle combustion and fragmentation. *Combustion Science and Technology*. 1988, vol. 57, no. 1-3, pp. 55–70. issn 0010-2202. Available from doi: 10.1080/00102208808923943.
-

- 
- [299] STEIBEL, M.; HALAMA, S.; GEISSLER, A.; SPLIETHOFF, H. Gasification kinetics of a bituminous coal at elevated pressures: entrained flow experiments and numerical simulations. *Fuel*. 2017, vol. 196, pp. 210–216. issn 0016-2361. Available from doi: 10.1016/j.fuel.2017.01.098.
- [300] STOESSER, P.; SCHNEIDER, C.; KREITZBERG, T.; KNEER, R.; KOLB, T. On the influence of different experimental systems on measured heterogeneous gasification kinetics. *Applied Energy*. 2018, vol. 211, pp. 582–589. issn 0306-2619. Available from doi: 10.1016/j.apenergy.2017.11.037.
- [301] STÖHR, M.; RUOFF, S.; RAUCH, B.; MEIER, W.; LE CLERCQ, P. Droplet vaporization for conventional and alternative jet fuels at realistic temperature conditions: Systematic measurements and numerical modeling. *Proceedings of the Combustion Institute*. 2021, vol. 38, no. 2, pp. 3269–3276. issn 1540-7489. Available from doi: 10.1016/j.proci.2020.05.015.
- [302] STOKES, G. G. On the effect of the internal friction of fluids on the motion of pendulums. *Transactions of the Cambridge Philosophical Society*. 1851, vol. 9, pp. 8–27.
- [303] STÖSSER, P. *Investigation of solid-phase processes during the conversion of biogenic slurry in entrained-flow gasifiers*. Karlsruhe, Germany: Dr. Hut, 2020. isbn 978-3-8439-4384-0. Ph.D. Thesis. Fakultät für Chemieingenieurwesen und Verfahrenstechnik, Karlsruher Institut für Technologie.
- [304] STUBINGTON, J. F.; LINJEWILE, T. M. The effects of fragmentation on devolatilization of large coal particles. *Fuel*. 1989, vol. 68, no. 2, pp. 155–160. issn 0016-2361. Available from doi: 10.1016/0016-2361(89)90316-5.
- [305] SUN, S.; TIAN, H.; ZHAO, Y.; SUN, R.; ZHOU, H. Experimental and numerical study of biomass flash pyrolysis in an entrained flow reactor. *Bioresource Technology*. 2010, vol. 101, no. 10, pp. 3678–3684. issn 0960-8524. Available from doi: 10.1016/j.biortech.2009.12.092.
- [306] SUTHERLAND, J. C. *Multicomponent mass transfer. Lecture notes*. 2013.
- [307] SYAMLAL, M.; BISSETT, L. A. *METC gasifier advanced simulation (MGAS) model*. Morgantown, WV, USA, 1992. Tech. rep. U.S. Department of Energy, Office of Fossil Energy. Available from doi: 10.2172/10127635.
- [308] SYRED, N.; KURNIAWAN, K.; GRIFFITHS, T.; GRALTON, T.; RAY, R. Development of fragmentation models for solid fuel combustion and gasification as subroutines for inclusion in CFD codes. *Fuel*. 2007, vol. 86, no. 14, pp. 2221–2231. issn 0016-2361. Available from doi: 10.1016/j.fuel.2007.05.060.

- 
- [309] TAYLOR, R.; KRISHNA, R. *Multicomponent mass transfer*. New York, NY, USA [et al.]: John Wiley & Sons, 1993. isbn 0-471-57417-1. Available also from: [https://www.ebook.de/de/product/7264215/taylor\\_krishna\\_multicomponent\\_mass\\_transfer.html](https://www.ebook.de/de/product/7264215/taylor_krishna_multicomponent_mass_transfer.html).
- [310] TCHAPDA, A. H.; PISUPATI, S. V. Characterization of an entrained flow reactor for pyrolysis of coal and biomass at higher temperatures. *Fuel*. 2015, vol. 156, pp. 254–266. issn 0016-2361. Available from doi: 10.1016/j.fuel.2015.04.015.
- [311] THIELE, E. W. Relation between catalytic activity and size of particle. *Industrial & Engineering Chemistry*. 1939, vol. 31, no. 7, pp. 916–920. issn 0888-5885. Available from doi: 10.1021/ie50355a027.
- [312] TOLVANEN, H.; KOKKO, L.; RAIKO, R. Fast pyrolysis of coal, peat, and torrefied wood: mass loss study with a drop-tube reactor, particle geometry analysis, and kinetics modeling. *Fuel*. 2013, vol. 111, pp. 148–156. issn 0016-2361. Available from doi: 10.1016/j.fuel.2013.04.030.
- [313] TOMECZEK, J.; PALUGNIOK, H. Specific heat capacity and enthalpy of coal pyrolysis at elevated temperatures. *Fuel*. 1996, vol. 75, no. 9, pp. 1089–1093. issn 0016-2361. Available from doi: 10.1016/0016-2361(96)00067-1.
- [314] TREMEL, A.; SPLIETHOFF, H. Gasification kinetics during entrained flow gasification. Part I: devolatilisation and char deactivation. *Fuel*. 2013, vol. 103, pp. 663–671. issn 0016-2361. Available from doi: 10.1016/j.fuel.2012.09.014.
- [315] TREMEL, A.; SPLIETHOFF, H. Gasification kinetics during entrained flow gasification. Part III: modelling and optimisation of entrained flow gasifiers. *Fuel*. 2013, vol. 107, pp. 170–182. issn 0016-2361. Available from doi: 10.1016/j.fuel.2013.01.062.
- [316] TREMEL, A. *Reaction kinetics of solid fuels during entrained flow gasification*. München, Germany, 2012. Available also from: <http://nbn-resolving.de/urn/resolver.pl?urn:nbn:de:bvb:91-diss-20121207-1092925-0-8>. Ph.D. Thesis. Fakultät für Maschinenwesen, Technische Universität München.
- [317] TRUBETSKAYA, A.; JENSEN, P. A.; JENSEN, A. D.; STEIBEL, M.; SPLIETHOFF, H.; GLARBORG, P. Influence of fast pyrolysis conditions on yield and structural transformation of biomass chars. *Fuel Processing Technology*. 2015, vol. 140, pp. 205–214. issn 0378-3820. Available from doi: 10.1016/j.fuproc.2015.08.034.
- [318] TRUBETSKAYA, A.; JENSEN, P. A.; JENSEN, A. D.; GARCIA LLAMAS, A. D.; UMEKI, K.; GLARBORG, P. Effect of fast pyrolysis conditions on biomass solid residues at high temperatures. *Fuel Processing Technology*. 2016, vol. 143, pp. 118–129. issn 0378-3820. Available from doi: 10.1016/j.fuproc.2015.11.002.

- 
- [319] TRYGGVASON, G.; BUNNER, B.; ESMAEELI, A.; JURIC, D.; AL-RAWAHI, N.; TAUBER, W.; HAN, J.; NAS, S.; JAN, Y.-J. A front-tracking method for the computations of multiphase flow. *Journal of Computational Physics*. 2001, vol. 169, no. 2, pp. 708–759. issn 0021-9991. Available from doi: 10.1006/jcph.2001.6726.
- [320] TURÁNYI, T.; TOMLIN, A. S. *Analysis of kinetic reaction mechanisms*. 1st ed. Berlin, Germany [et al.]: Springer, 2014. isbn 978-3-662-44561-7. Available from doi: 10.1007/978-3-662-44562-4.
- [321] VÁRHEGYI, G.; SZABÓ, P.; ANTAL, M. J. Kinetics of charcoal devolatilization. *Energy & Fuels*. 2002, vol. 16, no. 3, pp. 724–731. issn 0887-0624. Available from doi: 10.1021/ef010227v.
- [322] VASCELLARI, M.; ARORA, R.; POLLACK, M.; HASSE, C. Simulation of entrained flow gasification with advanced coal conversion submodels. Part 1: pyrolysis. *Fuel*. 2013, vol. 113, pp. 654–669. issn 0016-2361. Available from doi: 10.1016/j.fuel.2013.06.014.
- [323] VASCELLARI, M.; ARORA, R.; HASSE, C. Simulation of entrained flow gasification with advanced coal conversion submodels. Part 2: char conversion. *Fuel*. 2014, vol. 118, pp. 369–384. issn 0016-2361. Available from doi: 10.1016/j.fuel.2013.11.004.
- [324] VASCELLARI, M.; ROBERTS, D. G.; HLA, S. S.; HARRIS, D. J.; HASSE, C. From laboratory-scale experiments to industrial-scale CFD simulations of entrained flow coal gasification. *Fuel*. 2015, vol. 152, pp. 58–73. issn 0016-2361. Available from doi: 10.1016/j.fuel.2015.01.038.
- [325] VDI-GESELLSCHAFT VERFAHRENSTECHNIK UND CHEMIEINGENIEURWESEN (VDI-GVC). *VDI-Wärmeatlas*. 11th ed. Ed. by STEPHAN, P.; KABELAC, S.; KIND, M.; MARTIN, H.; MEWES, D.; SCHABER, K. Berlin, Germany [et al.]: Springer, 2013. isbn 978-3-642-19982-0. Available from doi: 10.1007/978-3-642-19981-3.
- [326] VICENTE, W.; OCHOA, S.; AGUILLÓN, J.; BARRIOS, E. An Eulerian model for the simulation of an entrained flow coal gasifier. *Applied Thermal Engineering*. 2003, vol. 23, no. 15, pp. 1993–2008. issn 1359-4311. Available from doi: 10.1016/s1359-4311(03)00149-2.
- [327] VIRTANEN, P.; GOMMERS, R.; OLIPHANT, T. E.; HABERLAND, M.; REDDY, T.; COURNAPEAU, D.; BUROVSKI, E.; PETERSON, P.; WECKESSER, W.; BRIGHT, J.; WALT, S. J. van der; BRETT, M.; WILSON, J.; MILLMAN, K. J.; MAYOROV, N.; NELSON, A. R. J.; JONES, E.; KERN, R.; LARSON, E.; CAREY, C. J.; POLAT, İ.; FENG, Y.; MOORE, E. W.; VANDERPLAS, J.; LAXALDE, D.; PERKTOLD, J.; CIMRMAN, R.; HENRIKSEN, I.; QUINTERO, E. A.; HARRIS, C. R.; ARCHIBALD, A. M.; RIBEIRO, A. H.; PEDREGOSA, F.; MULBREGT, P. van; SCIPY 1.0 CONTRIBUTORS. SciPy

- 
- 1.0: fundamental algorithms for scientific computing in Python. *Nature Methods*. 2020, vol. 17, pp. 261–272. Available from doi: 10.1038/s41592-019-0686-2.
- [328] WACHTER, S.; JAKOBS, T.; KOLB, T. Towards system pressure scaling of gas assisted coaxial burner nozzles – an empirical model. *Applications in Energy and Combustion Science*. 2021, vol. 5, p. 100019. issn 2666-352X. Available from doi: 10.1016/j.jaecs.2020.100019.
- [329] WACHTER, S.; JAKOBS, T.; KOLB, T. Mass flow scaling of gas-assisted coaxial atomizers. *Applied Sciences*. 2022, vol. 12, no. 4, p. 2123. issn 2076-3417. Available from doi: 10.3390/app12042123.
- [330] WARNCKE, K.; GEPPERTH, S.; SAUER, B.; SADIKI, A.; JANICKA, J.; KOCH, R.; BAUER, H.-J. Experimental and numerical investigation of the primary breakup of an airblasted liquid sheet. *International Journal of Multiphase Flow*. 2017, vol. 91, pp. 208–224. issn 0301-9322. Available from doi: 10.1016/j.ijmultiphaseflow.2016.12.010.
- [331] WATANABE, H.; OTAKA, M. Numerical simulation of coal gasification in entrained flow coal gasifier. *Fuel*. 2006, vol. 85, no. 12-13, pp. 1935–1943. issn 0016-2361. Available from doi: 10.1016/j.fuel.2006.02.002.
- [332] WEBER, R.; BOYSAN, F.; AYERS, W. H.; SWITENBANK, J. Simulation of dispersion of heavy particles in confined turbulent flows. *AIChE Journal*. 1984, vol. 30, no. 3, pp. 490–492. issn 1547-5905. Available from doi: 10.1002/aic.690300322.
- [333] WESTBROOK, C. K.; DRYER, F. L. Simplified reaction mechanisms for the oxidation of hydrocarbon fuels in flames. *Combustion Science and Technology*. 1981, vol. 27, no. 1-2, pp. 31–43. issn 0010-2202. Available from doi: 10.1080/00102208108946970.
- [334] WESTBROOK, C. K.; DRYER, F. L. Chemical kinetic modeling of hydrocarbon combustion. *Progress in Energy and Combustion Science*. 1984, vol. 10, no. 1, pp. 1–57. issn 0360-1285. Available from doi: 10.1016/0360-1285(84)90118-7.
- [335] WILCOX, D. *Turbulence modeling for CFD*. 3rd ed. La Cañada, CA, USA: DCW Industries, 1993. isbn 978-0-9636051-0-8.
- [336] WILCOX, D. C. Reassessment of the scale-determining equation for advanced turbulence models. *AIAA Journal*. 1988, vol. 26, no. 11, pp. 1299–1310. issn 0001-1452. Available from doi: 10.2514/3.10041.
- [337] WILEMSKI, G.; SRINIVASACHAR, S. Prediction of ash formation in pulverized coal combustion with mineral distribution and char fragmentation models. In: *Proceedings of the Engineering Foundation Conference, Solihull, UK*. Solihull, UK, 1993. isbn 978-1560322931.
-

- 
- [338] WILKE, C. R. A viscosity equation for gas mixtures. *The Journal of Chemical Physics*. 1950, vol. 18, no. 4, pp. 517–519. issn 0021-9606. Available from doi: 10.1063/1.1747673.
- [339] XIU, S.; LI, Z.; LI, B.; YI, W.; BAI, X. Devolatilization characteristics of biomass at flash heating rate. *Fuel*. 2006, vol. 85, no. 5-6, pp. 664–670. issn 0016-2361. Available from doi: 10.1016/j.fuel.2005.08.044.
- [340] YAGI, S.; KUNII, D. Studies on combustion of carbon particles in flames and fluidized beds. *Symposium (International) on Combustion*. 1955, vol. 5, no. 1, pp. 231–244. issn 0082-0784. Available from doi: 10.1016/s0082-0784(55)80033-1.
- [341] YAGI, S.; KUNII, D. Fluidized-solids reactors with continuous solids feed. I. Residence time of particles in fluidized beds. *Chemical Engineering Science*. 1961, vol. 16, no. 3-4, pp. 364–371. issn 0009-2509. Available from doi: 10.1016/0009-2509(61)80043-2.
- [342] YAMAMOTO, K.; MUROTA, T.; OKAZAKI, T.; TANIGUCHI, M. Large eddy simulation of a pulverized coal jet flame ignited by a preheated gas flow. *Proceedings of the Combustion Institute*. 2011, vol. 33, no. 2, pp. 1771–1778. issn 1540-7489. Available from doi: 10.1016/j.proci.2010.05.113.
- [343] YUEN, M. C.; CHEN, L. W. On drag of evaporating liquid droplets. *Combustion Science and Technology*. 1976, vol. 14, no. 4-6, pp. 147–154. issn 0010-2202. Available from doi: 10.1080/00102207608547524.
- [344] ZANZI, R.; SJÖSTRÖM, K.; BJÖRNBOM, E. Rapid pyrolysis of agricultural residues at high temperature. *Biomass and Bioenergy*. 2002, vol. 23, no. 5, pp. 357–366. issn 0961-9534. Available from doi: 10.1016/s0961-9534(02)00061-2.
- [345] ZEISSLER, R. *Modellierung der Gasphasenreaktion bei der autothermen katalytischen Erdgasspaltung unter hohen Drücken*. Freiberg, Germany: Medienzentrum der TU Bergakademie Freiberg, 2006. isbn 978-3-86012-296-9. Available also from: <https://d-nb.info/982186258>. Ph.D. Thesis. Fakultät für Maschinenbau. Verfahrens- und Energietechnik, Technische Universität Bergakademie Freiberg.
- [346] ZELLAGUI, S.; SCHÖNNENBECK, C.; ZOUAOU-MAHZOUL, N.; LEYSSENS, G.; AUTHIER, O.; THUNIN, E.; PORCHERON, L.; BRILHAC, J.-F. Pyrolysis of coal and woody biomass under N<sub>2</sub> and CO<sub>2</sub> atmospheres using a drop tube furnace: experimental study and kinetic modeling. *Fuel Processing Technology*. 2016, vol. 148, pp. 99–109. issn 0378-3820. Available from doi: 10.1016/j.fuproc.2016.02.007.
- [347] ZHANG, F.; ZIRWES, T.; MÜLLER, T.; WACHTER, S.; JAKOBS, T.; HABISREUTHER, P.; ZARZALIS, N.; TRIMIS, D.; KOLB, T. Effect of elevated pressure on air-assisted primary atomization of coaxial liquid jets: basic research for entrained flow gasification. *Renewable and Sustainable Energy Reviews*. 2020, vol. 134, p. 110411. issn 1364-0321. Available from doi: 10.1016/j.rser.2020.110411.

- 
- [348] ZHANG, R.; KU, X.; YANG, S.; WANG, J.; FAN, L. Modeling and simulation of the motion and gasification behaviors of superellipsoidal biomass particles in an entrained-flow reactor. *Energy & Fuels*. 2021, vol. 35, no. 2, pp. 1488–1502. issn 0887-0624. Available from doi: 10.1021/acs.energyfuels.0c03440.
- [349] ZHAO, Y.; SUN, S.; TIAN, H.; QIAN, J.; SU, F.; LING, F. Characteristics of rice husk gasification in an entrained flow reactor. *Bioresource Technology*. 2009, vol. 100, no. 23, pp. 6040–6044. issn 0960-8524. Available from doi: 10.1016/j.biortech.2009.06.030.
- [350] ZIMMERLIN, B.; EBERHARD, M.; FRIDBJARNARSON, G.; GALLA, U.; KOLB, T.; MAI, R.; MICHELFELDER, B.; NIEBEL, A.; WEIRICH, F.; WILLY, M. Status quo of the bioliq-process at KIT. In: *Proceedings of the 9th International Seminar on Gasification, 19-20 October 2016, Malmö, Sweden*. Malmö, Sweden, 2016.





